



DTIC FILE COPY

AD-A224 769

Proceedings of the Twenty-first Annual Precise Time and Time Interval (PTTI) Applications and Planning Meeting



A meeting held at the
Sheraton Hotel
Redondo Beach, California
November 28 - November 30, 1989

DISTRIBUTION STATEMENT A

**Approved for public release;
Distribution Unlimited**

DTIC:

Following are DESCRIPTOR terms suggested
by Dr. John Vig, Army Electronics Technology
and Devices Laboratory, LABCOM, of the Executive
Committee (who has sent the report, thru the
STINFO Office, Fort Monmouth):

clock
time
timekeeping
time interval
precise time
atomic clock
atomic frequency standard
rubidium standard
cesium standard
atomic resonator
radiation effects
vibration effects
temperature effects
resonator
oscillator
quartz oscillator
stability
aging
Allan variance
phase noise
frequency control
frequency standard

Proceedings of the Twenty-first Annual Precise Time and Time Interval (PTTI) Applications and Planning Meeting

**A meeting held at the
Sheraton Hotel
Redondo Beach, California
November 28 - November 30, 1989**

Sponsored by

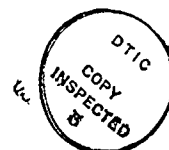
**U.S. Naval Observatory
NASA Goddard Space Flight Center
Space and Naval Warfare Systems Command
Naval Research Laboratory
National Institute of Standard and Technology
Army Electronics Technology and Devices Laboratory
Rome Air Development Center
USAF Space Command**

90 07 25 022

PRECISE TIME AND TIME INTERVAL (PTTI) APPLICATIONS AND PLANNING MEETING

ORDER FORM FOR PROCEEDINGS

	<u>Year</u>	<u>Cost</u>	<u>Available</u>	<u>Unavailable</u>
1	1969			X
2	1970	\$25.00	X	
3	1971	\$25.00	X	
4	1972	\$25.00	X	
5	1973	\$25.00	X	
6	1974	\$25.00	X	
7	1975	\$25.00	X	
8	1976			X
9	1977			X
10	1978	\$25.00	X	
11	1979	\$25.00	X	
12	1980	\$25.00	X	
13	1981	\$25.00	X	
14	1982	\$25.00	X	
15	1983	\$25.00	X	
16	1984	\$25.00	X	
17	1985	\$25.00	X	
18	1986	\$20.00	X	
19	1987	\$25.00	X	
20	1988	\$35.00	X	
21	1989	\$65.00	X	



\$ 65.00	
Distribution /	
Availability Codes	
Dist	Avail and/or Special
A-1	21

Please circle copy(ies) requested and make the check payable to "Treasurer, PTTI". Please do not add personal names or addresses to the pay line on the check. We cannot accept invoices. Please return the check and the Order Form to:

Mrs. Sheila Faulkner
Chairman, PTTI Executive Committee
U. S. Naval Observatory
Time Service Department
34th and Massachusetts Avenue, NW
Washington, DC 20392-5100

(202) 653-1460

It is with great regret that we must announce we can no longer absorb the cost of air mailing the "Proceedings" to international addresses; therefore, the "Proceedings" will be sent by Surface Mail. However, if you wish to pay the air mail postage, we will notify you of the cost before mailing. For example, Air Mail to Europe is currently estimated at \$26.00 for the first 4 pounds. Each additional half pound is \$3.00.

When you register for the PTTI Meeting or order the "Proceedings", your name is added to the Mailing list to automatically receive future meeting information and a copy of the Proceedings.

EXECUTIVE COMMITTEE

Sheila C. Faulkner, Chairman
U.S. Naval Observatory

David W. Allan
National Institute of Standards and Technology

James A. Buisson
U.S. Naval Research Laboratory

Jimmie B. Collie
Space and Naval Warfare Systems Command

Hugh S. Fosque
NASA Headquarters

Raymond Granata
NASA Goddard Space Flight Center

Dr. William J. Klepczynski
U.S. Naval Observatory

Dr. Arthur O. McCoubrey
National Institute of Standards and Technology

Dr. John R. Vig
Army Electronics Technology and Devices Laboratory

Dr. H. Beat Wackernagel
USAF Space Command

Dr. Joseph D. White
U.S. Naval Research Laboratory

Dr. Gernot M.R. Winkler
U.S. Naval Observatory

Dr. Nicholas F. Yannoni
Rome Air Development Center

OFFICERS

GENERAL CHAIRMAN

DR. HENRY FLIEGEL

The Aerospace Corporation

TECHNICAL PROGRAM COMMITTEE CHAIRMAN

PAUL F. KUHNLE

Jet Propulsion Laboratory
California Institute of Technology

ASSISTANT TECHNICAL PROGRAM COMMITTEE CHAIRMAN

S. CLARK WARDRIP

Bendix Field Engineering Corporation

EDITORIAL COMMITTEE CHAIRMAN

DR. RICHARD L. SYDNOR

Jet Propulsion Laboratory
California Institute of Technology

EDITORIAL COMMITTEE MEMBERS

T. Tucker

Jet Propulsion Laboratory
California Institute of Technology

M. Calhoun

Jet Propulsion Laboratory
California Institute of Technology

P. Clements

Jet Propulsion Laboratory
California Institute of Technology

G. J. Dick

Jet Propulsion Laboratory
California Institute of Technology

PUBLICITY COMMITTEE CHAIRMAN

JIMMIE B. COLLIE

Space and Naval Warfare Systems Command

TECHNICAL ASSISTANCE

PAUL KUSHMEIDER

Bendix Field Engineering Corporation

SESSION CHAIRMEN

SESSION I

Dr. John R. Vig

Army Electronics Technology and Devices Laboratory

SESSION II

Dr. William G. Melbourne

Jet Propulsion Laboratory

SESSION III

Paul F. Kuhnle

Jet Propulsion Laboratory

SESSION IV

Dr. Samuel R. Stein

Ball Aerospace

SESSION V

Dr. Victor R. Reinhardt

Hughes Aircraft Company

SESSION VI

Jack McNabb

TRAK Systems

ARRANGEMENTS

Sheila C. Faulkner

Paul J. Kushmeider

FINANCE COMMITTEE

Dr. William J. Klepczynski

Sheila C. Faulkner

RECEPTIONISTS

The names of the ladies who served as receptionists at the 21st Annual PTTI meeting are:

Linda Arquero (Hughes)

Sheila Faulkner (USNO)

Kathy Hibbard (Datum)

Nicolette Jardine (USNO)

Jennifer Stone (Brightline)

Betty Wardrip (Bendix)

PTTI ADVISORY BOARD COMMITTEES

1990

<u>OFFICE</u>	<u>NAME</u>	<u>ORGANIZATION</u>
Chairman	Mr. S. Clark Wardrip	BFEC
Vice Chairman	Mr. Martin B. Bloch	FEI
Finance Committee	Mr. Martin B. Bloch, Chairman Mr. S. Clark Wardrip Mr. James L. Wright Mr. Gary Smith	FEI BFEC CSC/RC KODE
Exhibits Committee	Dr. Martin W. Levine, Chairman Dr. James A. Barnes Mr. Roger J. Hesse Mr. Jack McNabb Mr. William J. Riley Mr. Don Mitchell Dr. Robert F. C. Vessot	Consultant Austron DATUM TRAK EG&G Austron/FTS SAO
Guest Speaker Committee	Mr. Robert H. Kern, Chairman Professor Carroll O. Alley Dr. Leonard S. Cutler Professor Bradford Parkinson Dr. Victor S. Reinhardt Dr. Samuel R. Stein Dr. Richard L. Sydnor	KERNCO University of MD HP Stanford University Hughes Ball/Efratom JPL
Reports Committee	Mr. Terry N. Osterdock, Chairman Mr. James M. Cloeren Mr. Paul F. Kuhnle Mr. Paul J. Kushmeider Professor Harry Robinson Mr. Philip E. Talley	SNI APL JPL BFEC Duke University Aerospace

NOTE: NON-GOVERNMENT OFFICERS OF THE PTTI ARE AUTOMATICALLY MEMBERS OF THE PTTI ADVISORY BOARD FOR THE YEAR(S) THAT THEY ARE IN OFFICE.

1990 ADVISORY BOARD MEMBERSHIP

Mr. S. Clark Wardrip, Chairman

Bendix Field Engineering Corporation

Professor Carroll O. Alley
University of Maryland
Department of Physics and Astronomy
College Park, Maryland 20742
(301) 454-3405

Dr. James A. Barnes
Austron, Inc.
3300 Mitchell Lane
Boulder, Colorado 80301
(303) 440-7282

Mr. Martin B. Bloch
Frequency Electronics, Inc.
55 Charles Lindbergh Boulevard
Uniondale, New York 11553
(516) 794-4500

Mr. James M. Cloeren
Johns Hopkins University
Applied Physics Laboratory
Johns Hopkins Road
Laurel, Maryland 20707
(301) 953-8821

Dr. Leonard S. Cutler
Hewlett-Packard Company
1651 Page Mill Road
Palo Alto, California 94304
(415) 857-5259

Dr. Henry F. Fliegel
The Aerospace Corporation
Building 120, M5/685
2350E El Segundo Boulevard
El Segundo, California 90245
(213) 336-1710

Mr. Roger J. Hesse
DATUM
1363 South State College Boulevard
Anaheim, California 92806
(714) 533-6333

Dr. Martin W. Levine
Consultant
P. O. Box 1513
Manchester, Massachusetts 01944
(508) 526-4218

Mr. Robert H. Kern
Kernco, Inc.
28 Harbor Street
Danvers, Massachusetts 01923-0678
(508) 777-1956

Mr. Paul F. Kuhnle
Jet Propulsion Laboratory
4800 Oak Grove Drive
M/S 298
Pasadena, California 90803
(818) 354-2715

Mr. Paul J. Kushmeider
Bendix Field Engineering Corporation
One Bendix Road
Columbia, Maryland 21045
(301) 964-7672

Mr. Jack McNabb
TRAK Microwave
4726 Eisenhower Boulevard
Tampa, Florida 33614-6391
(813) 884-1411

Mr. Donald Mitchell
Austron, Inc.
P. O. Box 14766
Austin, Texas 78761-4766
(512) 251-2313

Mr. Terry N. Osterdock
Stellar Navigation, Inc.
19075 Skyline Boulevard
Los Gatos, California 95030
(408) 354-0733

Professor Bradford W. Parkinson
Stanford University
Hansen Labs, Via Palou
Stanford, California 94305-4085
(408) 395-6521

Dr. Victor S. Reinhardt
Hughes Aircraft
Space and Communications
S12/W322, P. O. Box 92919
Los Angeles, California 90009
(213) 416-0160

Mr. William J. Riley
EG&G, Inc.
35 Congress Street
Salem, Massachusetts 01775
(508) 745-3200

Professor Harry Robinson
Duke University
Department of Physics
Durham, North Carolina 27706
(919) 684-8226

Mr. Gary Smith
KODE
1515 South Manchester Avenue
Anaheim, California 92802-2907
(714) 758-0400

Dr. Samuel R. Stein
Ball Efratom Division
P. O. Box 589
Broomfield, Colorado 80020
(303) 460-2017

Dr. Richard L. Sydnor
Jet Propulsion Laboratory
4800 Oak Grove Drive
M/S 298
Pasadena, California 91109
(818) 354-2763

Mr. Philip E. Talley
The Aerospace Corporation
550 Margo Avenue
Long Beach, California 90803
(213) 336-0484

Dr. Robert F. C. Vessot
Smithsonian Astrophysical Observatory
60 Garden Street
Cambridge, Massachusetts 01945
(617) 495-7272

Mr. S. Clark Wardrip
Bendix Field Engineering Corporation
P. O. Box 6147
Vandenberg Air Force Base,
California 93437
(805) 865-3214

Mr. James L. Wright
CSC and Raytheon Company
Eastern Test Range
Building 989, MU 840
Patrick Air Force Base, Florida 32925
(407) 494-2014

FOREWORD

These Proceedings contain the papers presented at the Twenty First Annual Precision Time and Time Interval Applications and Planning Meeting. The meeting was held at the Sheraton Hotel in Redondo Beach, California this year. A good attendance at the meetings and the banquet was an indication of the continuing interest in the field. We had a number of invited papers, some of which are included in this proceedings. Some papers are missing because they were not received in time for publication or were withdrawn from publication by sponsors. The question and answer periods following each talk are included, but they are marred this year by the lack of cooperation among the questioners in not speaking with the microphones. to p. XI/11

We had for the first time this year a Poster Session. Acceptance of this session was uniformly positive, both by attendees and by presenters. The advantage of this session is the one-on-one interaction between the presenter and the attendee.

There were 254 registered attendees (up from 205 last year).

The objective of these meetings is to provide an opportunity for program planners to meet those who are engaged in research and development and to keep abreast of the state-of-the-art and latest technological developments. At the same time, they provide an opportunity for engineers to meet program planners.

The success of these meetings depends on the efforts of the Program Chairman and the individual Session Chairmen and the organization of the entire meeting by the Chairman of the Executive Committee. Without their unstinting labor, such meetings could not be held.

CONTENTS

Keynote Address

Synchronization of Clocks	1
David Allan, National Institute of Standards and Technology	

SESSION I

Specification and Procurement of Frequency and Timing Equipment and Systems

Chairman: John R. Vig

Army Electronics Technology and Devices Laboratory

Invited Speaker, Timing in Swissnet, Specification, Development, Implementation and Operational Experience	19
P. Kartaschoff Swiss PTT Research and Development Laboratory, Switzerland	
Specification and Procurement of Frequency and Timing Equipment and Systems "Industry Opinion"	39
D. Mitchell, Austron, Inc. A Datum, Inc. Company	
Value Procurement	45
C. E. Youngberg Hewlett Packard Company	
Specification of Atomic Frequency Standards for Military and Space Applications	51
J. White, F. Danzy, E. Powers Naval Research Laboratory	

SESSION II

Time Synchronization, Methods, and Performance

Chairman: William G. Melbourne

Jet Propulsion Laboratory

Invited Speaker: Progress in Transferring Time Using GLONASS Satellites	59
P. Daly and I. D. Kitching University of Leeds, United Kingdom	
Results of A Block II GPS PTTI Users Survey	71
T. R. Bartholomew, TASC and S. M. Bloor, Department of Defense	
GPS—UTC Time Synchronization	77
C. H. McKenzie, W. A. Feess, A. L. Satin, R. H. Lucas and H. Holz The Aerospace Corporation	

Precise Ephemerides for GPS Time Transfer	95
W. Lewandowski, Bureau International des Poids et Mesures and M. A. Weiss, National Institute of Standards and Technology	
Accurate Delay Calibration for Two—Way Time Transfer Earth Stations	107
G. de Jong, Van Swinden Laboratory The Netherlands	
Satellite Two—Way Time Transfer: Fundamentals and Recent Progress	117
D. A. Howe, D. W. Hanson, J. L. Jespersen and M. A. Lombardi National Institute of Standards and Technology	
A New Two—Way Time Transfer Modem	131
G. P. Landis, J. D. White, A Gifford and R. L. Beard Naval Research Laboratory and J. A. Murray, Sachs Freeman Associates, Inc.	

SESSION III

Personal Interaction and Discussion Poster Session;

Chairman: Paul F. Kuhnle
Jet Propulsion Laboratory

Phase Distribution on Fiber Optic Cable	139
J. C. Webber and D. L. Thacker Interferometrics, Inc.	
GPS Synchronized Disciplined Rubidium Frequency Standard	145
D. E. Fossler TRAK Systems	
A GPS Disciplined Rubidium Clock	149
W. Dewey Kinematics/Truetime	
Steady State Oscillator Analysis in the Immittance Domain	161
B. Parzen, Consulting Engineer	
Final Results of a New Test of Relativity	171
T. P. Krisher, L. Maleki, L. E. Primas, G. F. Lutes, R. T. Logan and J. D. Anderson Jet Propulsion Laboratory C. M. Will, Washington University	
The NIST Digital Time Service	181
J. Levine, D. W. Allan and D. B. Sullivan National Institute of Standards and Technology	

A New Hydrogen—Maser Time and Frequency Standard at Sheshan VLBI Station of Shanghai Observatory	191
Z. C. Zhai, H. X. Huang, C. F. Lin, G. X. Jiang, W. H. Luo and J. F. Lu Shanghai Observatory, Peoples Republic of China	
Improvement of Time Comparison Results by Using GPS Dual Frequency Codeless Receivers Measuring Ionospheric Delay	199
M. Imae and C. Miki, Communications Research Laboratory, Japan and C. Thomas, Bureau International des Poids et Mesures, France	
Alternative Timing Networks with GPS	205
G. P. Landis, S. Stebbins, and R. L. Beard, U. S. Naval Research Laboratory A. F. Fliegel, The Aerospace Corporation	
A Comparison of Time Transfer Techniques	215
S. Stebbins, A. Gifford and R. L. Beard Naval Research Laboratory	
Atomic Velocity Distribution Out of Hydrogen Maser Dissociators	223
B. Jaduszliwer and Y. C. Chan The Aerospace Corporation	

SESSION IV

Fr. p. XIV → Analysis and Calibration, → p. XVI

Chairman: Samuel R. Stein
Ball Aerospace

Tropospheric Limitations to the Stability of Radio Metric Delay Measurements	233
R. N. Truehaft Jet Propulsion Laboratory	
On—Orbit Frequency Stability Analysis of GPS NAVSTAR Cesium and Rubidium Clocks	239
T. B. McCaskill and J. A. Buisson, Naval Research Laboratory and T. J. Hogan, SFA, Inc.	
Application of Hydrogen—Maser Technology to the Search for Gravitational Radiation	259
J. D. Anderson, E. L. Lau and J. W. Armstrong Jet Propulsion Laboratory	
Report on the Timescale Algorithm Test Bed at USNO	269
S. R. Stein, Ball Aerospace; A. Gifford, Naval Research Laboratory and L. A. Breakiron, U. S. Naval Observatory	
Observation Plan of High—Stable Pulsars in CRL	289
S. Hama, M. Imae, H. Kluchi, K. Takaba and P. Takahashi Communications Research Laboratory, Ministry of Posts and Telecommunications, Japan	

Accuracy Model for Phase Noise Measurements	295
F. L. Walls, C. M. Felton and A. J. D. Clements National Institute of Standards and Technology T. D. Martin, Gravity Research Institute	
New Hydrogen Masers at the National Research Council of Canada	313
D. Morris and J. Vanier National Research Council, Canada	
Status Report on a Synchronization Experiment Between European Time Scales Using ECS Geostationary Satellite	323
V. Pettiti, F. Cordara and P. G. Galliano Istituto Elettrotecnico Nazionale, Italy	
A New Time Scale Algorithm: AT1 Plus Frequency Covariance	343
M. Weiss and T. Weissert National Institute of Standards and Technology	

SESSION V

for p. xv ———> New Technology and Results, ———> to p. xviii/
Chairman: Victor S. Rheinhardt
Hughes Aircraft Company
xviii

The Cryogenic Hydrogen Maser: Projected Performance and Recent Progress Toward Spaceborne Applications	359
R. L. Walsworth and I. F. Silvera, Harvard University; R. F. C. Vessot and E. Mattison, Harvard-Smithsonian Center for Astrophysics and M. L. Dingus, Alabama Cryogenic Engineering	
Dielectric Resonator Oscillators Theory and State-of-the-Art	371
A. P. S. Khanna, Avantek, Inc.	
Determining Optimum C-Field Settings That Minimize Output Frequency Variations in Cesium Atomic Frequency Standards	385
S. K. Karuza, W. A. Johnson, J. P. Hurrell, F. J. Voit The Aerospace Corporation	
Modeling Fast Modulation Effects in Cesium Atomic Clocks	401
P. Hurrell, W. A. Johnson, S. K. Karuza and F. J. Voit The Aerospace Corporation	
Environmental Tests of Cesium Beam Frequency Standards at the Frequency Standards Laboratory of the Jet Propulsion Laboratory	409
R. L. Sydnor, T. K. Tucker, G. A. Greenhall, W. A. Diener and L. Maleki Jet Propulsion Laboratory	
Performance of Optical Fibers for Reference Frequency and IF Signal Transmissions in VLBI Observation	421
K. Sato and T. Hara, Division of Earth Rotation National Astronomical Observatory, Japan	

Reliability Studies of Lamp Cells for Use in Rubidium Vapor Frequency Standards	431
T. McClelland, Frequency Electronics, Inc.	
Analysis of Fundamental and Systematic Effects Limiting Hydrogen Maser Frequency Stability	433
E. M. Mattison and R. F. C. Vessot Smithsonian Astrophysical Observatory	
Microcomputer—Compensated Crystal Oscillator for Low—Power Clocks	445
S. S. Schodowski, R. L. Filler, J. A. Messina, V. J. Rosati and J. R. Vig U. S. Army Electronics Technology and Devices Laboratory	

fr. p. xvi

SESSION VI

Timing Systems and Equipment of Today and Tomorrow (SDW)

Chairman: Jack McNabb
TRAK Systems

PTTI Systems on the Eastern Test Range	467
C. S. Duffy and J. L. Wright Computer Sciences Raytheon	
NASA/JPL Deep Space Network Frequency and Timing	479
P. F. Kuhnle, Jet Propulsion Laboratory	
Synchronizing LORAN—C Master Stations to Coordinated Universal Time	491
G. R. Westling, M. D. Sakahara, and C. J. Justice United States Coast Guard	
Frequency and Timing System at the National Institute for Standards (NIS)	501
S. Samuel, National Institute for Standards, Egypt	
Ultrastable Quartz Oscillator for Spacecraft	509
J. R. Norton, Johns Hopkins University Applied Physics Laboratory	
An Unbiased Weighting Method for Data in GPS Common View	519
Zhuang Qixiang, Jian Shuguang and Fan Neng Shanghai Observatory, Chinese Academy of Sciences	
Simultaneous Transmission of a Frequency Reference and a Time Code Over a Single Opticle Fiber	527
G. Lutes and M. Calhoun Jet Propulsion Laboratory	
Common—View GPS Time Transfer Accuracy and Stability Results	537
J. R. Semler, Interstate Electronics Corporation	

KEYNOTE ADDRESS SYNCHRONIZATION OF CLOCKS

David W. Allan*
Time and Frequency Division
National Institute of Standards and Technology
Boulder, Colorado 80303

Abstract

Time metrology has moved from milliseconds to picoseconds in the last four decades, and frequency metrology from nine significant digits to sixteen. The ability to synchronize remote clocks has improved dramatically as well. With implementation of GPS (Global Positioning System,) the full long-term frequency stability as well as the frequency accuracy of the best atomic clocks can now be transferred to remote sites. GPS's selective availability, an intentional degradation of system performance, will adversely affect the accuracy and stability of GPS time and frequency for the average civilian user.

In this paper we define terms of reference, discuss various alternatives for clock synchronization and syntonization, and make some comparisons between various techniques used in synchronizing and syntonizing clocks. In the process we review the concepts of time stability and accuracy, frequency stability and accuracy.

INTRODUCTION

The synchronization of clocks is a subject which has been widely treated throughout the years. With the development of very accurate means for satellite time transfer, the subject has gained substantially in importance. This paper provides a discussion of the relevant issues surrounding clock comparisons and of the various means of comparing them when they are a significant distance apart.

Time transfer systems (or clock synchronization systems) are often characterized by a single number, designating a precision or an accuracy of some number of microseconds or nanoseconds. This is often ambiguous and it is the intent of this work to clarify the characterization of clock synchronization or comparison systems. We will apply these techniques to some current comparison systems for clocks located some distance apart, and project some of our future opportunities — given these techniques, constraints and guidelines.

BACKGROUND

We are not here generally concerned with measurement noise, that is divider or counter noise — though this can be problematic in some instances. As clocks continue to improve, more attention must be

*Contributions of the U.S. Government; not subject to copyright.

paid to the characterization of measurement systems, that is the systems which read the output of clocks. This is especially true if the clocks are remotely located from each other. Characterizing the measurement system is essential if a remote (slave) clock is intended to be optimally synchronized or syntonized to a master clock. In this latter situation, optimum design of the servo system, locking the slave to the master clock, requires a characterization of all of the contributing elements.

A free-running clock can almost always be characterized better than one whose output is servo controlled to another clock. Hence, a computed output or an external micro-phase stepper is useful in providing a synchronized or syntonized output which does not perturb the free-running clock^[1]. A local set of clocks can be better characterized if there are at least three of them of about the same quality^[2]. Once a set of clocks is available, then algorithms can be employed to intelligently combine their readings so that the algorithm-computed time and/or frequency can be more stable than that of the best clock in the set. In addition, algorithms can be designed to test for abnormal clock behavior and to desensitize the computed time to any abnormal behavior as well as to failures^[3].

If the clocks, as well as the comparison system, are well characterized, then an ensemble of clocks, can be constructed from a set of remotely located clocks. With full characterization of all components, the system of clocks and its associated comparison can be optimized for overall performance. As far as I know, while often applied to local ensembles, this concept has not yet been applied to clock ensembles whose member clocks are in different locations. There are some long-term plans to do this for GPS. We feel that there are potentially significant gains available in the proper application of this concept.

Figure 1 illustrates a straightforward comparison system which measures the time and frequency differences between Clock 1 and Clock 2. Our concern is the characterization of the full noise in the comparison including measurement noise, clock noise and noise introduced in the comparison path and system. In figure 2 we illustrate an additional concern which arises in designing a servo-loop to slave a remote clock to a master clock. The data from the comparison may not be available immediately; hence, in the feedback loop, the measurement noise, path deviations, the delay in acquiring the comparison data will effect the servo design very fundamentally. Practical delays in acquiring comparison data range from milliseconds to times longer than a month. For example, the delay time (data acquisition time) for servo controlling Coordinated Universal Time at NIST (UTC(NIST)) to the international UTC scale is more than a month. Though we will not go into the servo-design theory in this paper, we want to stress that the measurement noise and path noise characteristics and the delay in acquiring comparison data play very important roles in servo design.

Appendix A gives some relevant definitions of words (precision, accuracy, stability) that will be used in this paper. In characterizing systems for comparing clocks which are remotely located to each other, it is important to consider concepts such as: time accuracy, time stability, time prediction error, frequency accuracy, and frequency stability. Each of these has a unique interpretation.

Conceptually, time accuracy is the time difference between the readings of two clocks at some time in a given reference frame. We often define one of the clocks as perfect so that we are assessing the accuracy of a clock relative to some "ideal" clock. One can imagine the transport of a perfect portable clock to accomplish this time difference measurement. Time accuracy is often limited by systematic errors in the comparison system, such as uncertainties in cable delays, and propagation-path-length uncertainties, and is often very hard to measure or assess. In addition, systematic differences between the clocks will contribute to the time inaccuracy. The time accuracy can never be better than time stability and is often much worse.

One of the best ways to observe the time stability is to plot the time residuals, often denoted $x(t)$,

between two clocks after the systematics have been subtracted. Time stability is, often affected by environmental variations (which affect clock and comparison system performance), in addition to the usual kinds of random variations. People commonly measure time stability as the rms deviation of the time residuals from a linear regression to the time deviations. This practice, which can be very misleading, will be discussed in some detail in the body of the paper. If there are periodic terms affecting a time comparison system, then measuring the spectral density of the time or the phase fluctuations may be a very good measure. One may also measure the effect of these periodic terms using $\sigma_y(\tau)$ (see ref. 2). We will show that for time stability there is often a τ (averaging-time) dependence. This is an important consideration which will be discussed later. We also show that $\tau * \text{mod}\sigma_y(\tau)$ is a useful measure of the time stability of a comparison system.

The quantity $K\tau\sigma_y(\tau)$ is a useful measure for estimating the time prediction error in a comparison. We often have a particular power-law spectral density process which is the dominate model for the signal variations from the clocks and/or the comparison system. The value of K is $1/\sqrt{3}$ for white-noise PM, 1 for white-noise FM and for random-walk FM, and 1.2 for flicker-noise FM under the assumption of optimum prediction. Sometimes white noise phase modulation is the predominant noise model, in which case the quantity $\tau * \text{mod}\sigma_y(\tau)/\sqrt{3}$ is the optimum rms time prediction error for an average over τ of $x(t)$ measurements.

Frequency accuracy for a given primary standard is not a function of integration time and is properly stated as a single number. But the ability of a comparison system, to determine absolute frequency difference between two standards is often a function of the sampling or integration time, τ . We will show that the frequency accuracy of a comparison system is also a function of the data processing method. This leads to the idea that there is an optimum method for estimating the absolute frequency difference between two remote clocks or for controlling the frequency of a remote clock.

Frequency stability, similar to time stability, is observed by looking at a plot of the fractional frequency offset, $y(t)$, where $y(t) = \nu(t) - \nu_0/\nu_0$ with $\nu(t)$ being the time varying frequency output of a clock and ν_0 is the clock's nominal frequency. In practice, measured values of $y(t)$ are observed over some averaging time, τ . It is often very useful to observe a $y(t)$ plot at different averaging times. The frequency stability of a comparison system can be quantified in the same way clocks are characterized, using a $\sigma_y(\tau)$ or $\text{mod}\sigma_y(\tau)$ plot. It is sometimes useful to measure the spectral density of the frequency fluctuations to supplement the above time-domain methods, in order to ascertain the presence of different kinds of noise. The kind of noise observed in comparisons between two clocks, and that which may be added by the comparison system, will determine how to optimize estimates of characterization parameters (both systematic and noise) for the clocks and the comparison system. One important example of a characterization parameter is the frequency drift between two clocks.

There are of course important relationships among time accuracy, time stability, time prediction error, frequency accuracy, and frequency stability. These will be discussed later.

CHARACTERIZATION OF COMPARISONS SYSTEMS

Figure 3 shows the improvement in the U.S. primary frequency standard since the advent of cesium beam technology. The trend line shows an improvement of about a factor of 10 every seven years. We expect to see further improvement, but extrapolations from data such as this are dangerous. There are now good indications that standards based on trapped and cooled ions will yield dramatic improvements. The ultimate potential for these devices is an accuracy of about one part in 10^{18} , but

practical considerations will make this limit difficult to achieve.

In the past, the accuracy of operational comparisons between primary standards fell behind the accuracy of the standards. Further improvements in primary standard accuracy were thus of limited use. However, during the last decade the development and application of two-way satellite and GPS time transfer dramatically changed the picture. With the excellent comparison accuracy available with GPS common-view technique, comparison accuracy is now ahead of clock accuracy. This was a major breakthrough for international time and frequency comparisons, and the GPS technique become the de-facto international standard for comparisons^[5]. A decision by GPS system operators to intentionally degrade performance as observed by civilian users, the so-called process of selective availability, raises questions which are important in time transfer applications. These will be discussed shortly.

Time transfer using the two-way satellite technique now looks to be a very attractive alternate available to primary timing centers. More information is needed on the accuracy and long-term time stability of this comparison technique as early work has not focussed on these^{[6],[7]}. Most of the published results are on short-term time stability.

Important factors for all of these comparison systems include cost and simplicity of use and means for accurately assessing comparison accuracy. The ideal comparison system is one which provides the time difference, the frequency difference, and the relative time and frequency stability of the clocks along with the uncertainties associated with the comparison system. If the comparison system is to be widely used, the cost should be low. Of course, there is no single system which now meets this ideal. Figure 4 shows a plot of some of the more common comparison techniques now being used. We have used both $\sigma_y(\tau)$ and $\text{mod}\sigma_y(\tau)$ to characterize the frequency stability of these comparison systems, because, in some cases, white-noise phase modulation (PM) is the limiting random process and $\sigma_y(\tau)$ characterization is ambiguous for that process.

When white-noise phase modulation is the predominant noise in a comparison system, some important equations for optimal estimation of time and frequency between the clocks are:

$$\hat{x}(i) = a_0 + a_1 \cdot i \quad \text{and} \quad (1)$$

$$s_x = \sqrt{\frac{1}{N-2} \sum_{i=1}^N (x(i) - \hat{x}(i))^2} \quad (2)$$

Here the $\hat{x}(i)$ is the optimal estimate of the time difference between the clocks at the measurement point i . The " a_0 " and the " a_1 " coefficients are determined by minimizing the variance around the linear regression line, so the meaning of optimum is for a minimum variance. The $x(i)$'s are the measured time difference over the N measurements. The confidence on the estimate of the intercept " a_0 " is s_0 :

$$s_0 = 2s_x/\sqrt{N} \quad (3)$$

and the confidence of the estimate of the mean value $\left(\bar{x} = \frac{1}{N} \sum_{i=1}^N x(i)\right)$ is s_{mean} :

$$s_{mean} = s_x/\sqrt{N}. \quad (4)$$

The confidence of the estimate of the slope, (" a_1 " the frequency difference) is s_1 :

$$s_1 = \frac{\sqrt{12}s_x}{\tau_0 N^{3/2}} = 2\text{mod}\sigma_y(\tau) \quad (5)$$

Equation 1 is the classical equation for a linear regression, which is often computed as a fit to the time residuals. The application of this equation is optimal only for white noise processes. We assume there are N values each τ_0 apart. In this case, the standard deviation (given by Equation 2) is a measure of the time stability at the data sampling rate — sometimes called the time of the time difference measurements. The $N - 2$ expression in the denominator shows that two degrees of freedom have been removed with the estimation of the a_0, a_1 terms of Equation 1. The mean value confidence interval in Equation 4 is half that of the intercept, and is the optimum estimate of the time difference between the clocks at the mid-point time. The solution to equation 1 at the midpoint is equal to the mean value. Equation 5 shows the value of using $\text{mod}\sigma_y(\tau)$ to determine the confidence of the estimate of the frequency difference, a_1 . If the residuals are not white, then the τ dependence will not be $\tau^{-3/2}$, and the linear regression will not give the optimum estimate of the time and frequency difference of the clocks. If the residuals are white, the value of $\text{mod}\sigma_y(\tau)$ gives the proper value of the confidence for any averaging time, τ . The rapid improvement ($\tau^{-3/2}$) gained in estimating the absolute frequency difference by increasing the averaging time is clearly illustrated by the use of $\text{mod}\sigma_y(\tau)$.

Linear regression analysis is often used to model processes which do not have a white spectrum for the residuals. In this case, the linear regression coefficients and their confidences can often be very misleading. A $\text{mod}\sigma_y(\tau)$ diagram will indicate if one is or is not legitimate in using linear regression analysis, and if not then it gives a measure of the effects of the degradation caused by the actual random processes on the estimate of the frequency difference between the two remote clocks.

Figure 5 is a plot of the rms time prediction error seen in currently available clocks and oscillators. The data has been used in an optimum fashion to predict into the future over an interval, τ_p . The rms time deviation can be defined in many ways. This is one useful approach. The next four Figures, 6, 7, 8, and 9, are plotted with exactly the same ordinate and abscissa as Figure 5. They can then be overlaid to see the effects of various systematic effects, either in the clocks or in the comparison system. Figure 6 has the ordinate labeled with both the white PM level (usually arising from the comparison system) and the time accuracy. The time accuracy number provides a hard limit in comparing the time difference between two clocks. In contrast, the white PM level is a function of integration time, and if other processes are not limiting, knowledge of the time difference improves as the square root of the number of measurements averaged — consistent with equation 4. If the residuals are white PM, one may also write from the concept of time averaging of measurements the following equation:

$$s_{rms}(\tau_0) = \frac{\tau^{3/2}}{\sqrt{3\tau_0}} \text{mod}\sigma_y(\tau), \quad (6)$$

where “ s ” denotes the classical standard deviation of the $x(i)$ taken τ_0 apart ($\tau = n\tau_0$) as in Equation (2). Since the numerator in Equation 6 is constant for white PM, the improvement in $s_{rms}(\tau_0)$ is proportional to $\tau_0^{-1/2}$. This is not surprising since τ_0 is the window over which the phase (or the time) has been averaged. If τ_0 becomes the full data length, then, as expected, Equation 6 is the standard deviation of the mean. Here again, a $\text{mod}\sigma_y(\tau)$ diagram provides a good visualization of the estimate of the time difference estimate uncertainty and of the time stability (as limited by the clocks and/or the comparison system).

Figure 7, 8 and 9 are included for the readers convenience. Figure 7 shows the accumulated time

difference as a function of time for two clocks whose frequencies differ by various fixed amounts. In this case the abscissa could also be the prediction interval. Figure 8 shows the rms time deviation as a function of the prediction interval as caused by flicker noise frequency modulation (FM) (a common noise in clocks). Notice that the slope is the same as for frequency offset. The factor 1.2 is the K factor for flicker noise where optimum prediction has been assumed. Figure 9 shows the large time deviation error that results from frequency drift. The labels for the different lines are fractional frequency drift per day expressed as powers of 10. The quadratic nature of the time deviation resulting from frequency drift often causes this kind of error to be the predominate long-term systematic error.

Figure 10 is a plot of $\tau \text{mod} \sigma_y(\tau)$ as a function of τ . With $\tau = n\tau_0$, this shows whether or not one benefits from averaging n values of the $x(i)$ time-difference measurements. One of the advantages of this new approach is that it illustrates the benefit of averaging the time difference measurements, whether or not the instabilities are in the comparison system or in the clocks. If the measurement noise residuals are a white PM process, then the time stability will improve as the square root of τ . If it is a flicker PM process there will be no improvement with averaging. If the plot degrades with increasing τ (slope greater than 0), then there are probably non-stationary processes perturbing the comparison system. In the case of Loran-C, we see a double hump at one-half day and at one-half year caused by diurnal variations and annual variations. We have longer-term common-view data using GPS than are plotted, and know that the time stability does not continue to improve as square root of τ . In this case, the nonstationary processes are probably related to ionospheric modeling errors and errors in the Kalman estimates of the satellites' ephemerides. Multipath distortion effects at the antenna can sometimes cause several nanoseconds of bias in the time inaccuracy, but do not change the slope in this type of plot, if the bias is constant.

For two-way-satellite time transfer, the noise limit does not continue decreasing as indicated by the short-term results in Figure 10. Daily deviations of the order of a few nanoseconds have been observed, but these will likely be reduced as the systems are improved and better characterized. This characterization of the two-way satellite time transfer technique will be very important for the future — especially for averaging of one day and longer. A determination of the time accuracy of this technique will be very important as well. Theoretically, both the time stability and the time accuracy of two-way time transfer should provide an excellent means for comparing widely separated clocks. The primary drawback to this technique is the need for broadcasting from each station, a requirement which adds cost and involves licensing with government agencies.

THE FUTURE OF COMPARISON SYSTEMS

It is clear that the best means for comparing widely separated clocks involves satellite techniques. For clocks in close proximity (that is, within a modest number of kilometers) perhaps optical fibers will provide the best comparisons^[9]. As we develop higher accuracy and more stable clocks, we will need to use higher frequencies to achieve better phase resolution for the comparisons.

It appears that the GPS system could be pushed to a time accuracy approaching a few nanoseconds. For short-baseline comparisons, studies suggest that one might achieve accuracies as low as 0.1 ns^[9]. Time stabilities for GPS common-view comparisons yield $\tau \text{mod} \sigma_y(\tau)$ of about 1 nanosecond times $\tau^{-1/2}$, where τ is in days. At $\tau = 1$ day, this product actually ranges from 0.8 to 8 ns for the many international time stability measurements which use the GPS common view method. With ionospheric calibrators and more-exact, a post-ephemeris data for the satellites, the GPS common-view technique could yield a comparison limit for frequency accuracy approaching 10^{-17} . This would require about

three months of integration under the assumption of ideal white-noise phase modulation. Codeless ionospheric calibrators, which measure the real ionospheric delay, are now becoming available for GPS. There is also the promise that precise post-measurement ephemerides will be made available to the civilian sector (the non-PPS user). With these advances the GPS common-view method for time and frequency transfer could be even better than it has been, but the price for this would be additional processing along with a significant delay in access to data needed to calculate all errors. The following table summarizes the anticipated compensation for using GPS in the common-view mode.

TABLE				
GPS COMMON-VIEW TIME-TRANSFER ERROR SOURCES				
(WITH SELECTIVE AVAILABILITY ON)				
SOURCE	COMMENTS	RMS TIME ACCURACY (ns)		
CLOCK DITHER	CANCELS IN C-V MODE	--		
EPSILON	DEPENDS ON THE BASE-LINE	30	to	50
IONOSPHERE (BDCST)	DEPENDS ON TOD AND COORD.	5	to	40
TROPOSPHERE	DEPENDS ON ELEV. AND WEATHER	2	to	5
MULTIPATH	DEPENDS ON GROUND PLANE AND REFLECTION	4	to	8
RECEIVER	DEPENDS ON THE MAKE AND MODEL	1	to	100
C-V TIME TRANSFER ERRORS (NO COMPENSATION)		31	to	120
(WITH SELECTIVE AVAILABILITY ON AND WITH COMPENSATION)				
SOURCE	COMMENTS	RMS TIME ACCURACY (ns)		
CLOCK DITHER	CANCELS IN C-V MODE	--		
EPSILON	COMPUTED EPHEMERIS (Some Days After)	3	to	5
IONOSPHERE	WITH IONOSPHERIC CALIBRATOR	2	to	3
TROPOSPHERE	DEPENDS ON ELEV. AND WEATHER	2	to	5
MULTIPATH	WITH CHOKE-RING ANTENNA GND. PLANE	2	to	4
RECEIVER	DEPENDS ON MAKE AND MODEL	1	to	100
C-V TIME TRANSFER ERRORS (WITH COMPENSATION)		5	to	100

The right column lists rms estimates for each of the time accuracy error elements with the sum at the end of each column being the square root of the sum of the squares. EPSILON is the intentional insertion of errors in the broadcast ephemeris. The meanings of other terms in the table are:

C-V	-	GPS common-view mode	Elev.	-	Elevation
TOD	-	Time of Day	Refl.	-	Reflections
GND	-	Ground	BDCST	-	As Broadcast

How well the systematics of the two way satellite timing technique can be understood is yet to be determined. From a theoretical point of view this technique should be better, in both time stability

and time accuracy, than the GPS common-view technique. The method could provide about an order of magnitude of improvement.

An often overlooked experiment which could lead to time transfer improvement is the Scout Rocket Experiment which involved flight of a hydrogen maser^{[10],[11]}. This experiment used a microwave Doppler cancellation method and an ionospheric calibration system. From the published data it is estimated that time stability, $\tau_{\text{mod}\sigma_y}(\tau)$ over several hours was about ten picoseconds. With this level of stability available from a satellite-born hydrogen maser, cycle ambiguity of the clocks microwave signal could be resolved from pass to pass or from day to day. This could yield frequency comparisons over 24 hours of 10^{-16} . If the residuals for the comparison process were white PM from day to day, it would take only a few weeks to measure frequency difference at the 10^{-18} level. At this level, relativity considerations become very important, and they will be very difficult to calculate. But, with bigger and better computers coming in the future, perhaps the relativity issues would be solvable.

CONCLUSION

In order to synchronize (or syntonize) a system of clocks in an optimum way, it is necessary to know both the stability characteristics of the clocks as well as those of the comparison system. The characterization the random variations in clocks is pretty well understood, but that of comparison systems is not. It is often the case that the standard deviation of the time residuals is non-convergent for both clocks and comparison systems, in which case it is not a useful measure. In this paper we have presented some reasonable ways to describe and to characterize comparison systems. These allow us to better specify time and frequency comparisons. This issue is becoming more important as system synchronization and syntonization requirements become more stringent.

We have explained how time accuracy, time stability, time predictability, frequency accuracy and frequency stability are separate and distinct concepts. Important relationships between these concepts were presented. These have implications for accurate time comparisons. For example, knowing the kinds of random instabilities in the clocks and in the comparison system allows one to optimally estimate the absolute time and frequency differences between widely separated clocks. As we anticipate more accurate frequency standards, very careful design as well as characterization of comparison systems will be required to take advantage of the improved standards. Even at current time comparison levels, there is a need for better specification of the performance of comparison systems. We have presented one reasonable approach with the hope that this will stimulate discussion and even adoption of a standard method for characterizing the accuracy and stability of the comparison process.

ACKNOWLEDGEMENTS

The author is indebted to Dr. Wilfred K. Klemperer and Ms. Trudi K. Peppler, Dr. Donald B. Sullivan and Dr. Matthew Young for contributions and suggestions. Dr. Marc A. Weiss and Mr. Dick D. Davis helped with the data acquisition and analysis for which I am grateful. Mr. Thomas Weissert was extremely helpful with the figures.

APPENDIX

DEFINITIONS

- **ACCURACY**

The degree of conformity of a measured or calculated value to its definition (see Uncertainty).

- **PRECISION**

The degree of mutual agreement among a series of individual measurements; often, but not necessarily, expressed by the standard deviation.

- **UNCERTAINTY**

The limits of the confidence interval of a measured or calculated quantity.

- **FREQUENCY INSTABILITY**

The spontaneous and/or environmentally caused frequency change within a given time interval.

- **REPRODUCIBILITY**

A) With respect to a set of independent devices of the same design, the ability of these devices to produce the same value.

B) With respect to a single device, put into operation repeatedly without adjustments, the ability to produce the same value.

- **ERROR**

The difference of a value from its assumed correct value.

- **DRIFT**

The systematic change in frequency of an oscillator with time.

- **AGING**

The systematic change in frequency with time caused by internal changes in the oscillator.

REFERENCES

- [1] D.W. Allan, M.A. Weiss, and T.K. Peppler, "In Search of the Best Clock," IEEE Transactions on Instrumentation and Measurement, IM-38, 624-630 (1989).
- [2] D.W. Allan, "Time and Frequency (Time-Domain) Characterization, Estimation, and Prediction, of Precision Clocks and Oscillators", IEEE Transactions on Ultrasonics, Ferroelectrics, and Frequency Control, UFFC-34, 647-654 (1987).
- [3] M.A. Weiss and T. Weissert, "A New Time Scale; AT1 Plus Covariance," submitted to Proc. of 20th Annual Precise Time and Time Interval Planning Meeting (PTTI), Redondo Beach, CA, Nov. 30 - Dec. 1, 1989.
- [4] D.J. Wineland, J. Bergquist, J. Bollinger, W. M. Itano, D. Heinzen, S. Gilbert, C. Manney, and C. Weimer, "Progress at NIST Toward Absolute Frequency Standards Using Stored Ions," Proc. of 43rd Annual Symposium on Frequency Control, Denver, CO, May 31 - June 2, 1989, pp. 143-150.
- [5] D. W. Allan, et. al., "Accuracy of International Time and Frequency Comparisons via Global Positioning System Satellites in Common-View," IEEE Transactions on Instrumentation and Measurement, IM-34, 118-125 (1985).

- [6] D. Hanson, "Fundamentals of Two-Way Time Transfers by Satellite," Proc. of 43rd Annual Symposium on Frequency Control, Denver, CO, May 31 - June 2, 1989, pp. 174-178; D.A. Howe, et. al., "NIST-USNO Time Comparisons Using Two-Way Satellite Time Transfers," 43rd Annual Symposium on Frequency Control, Denver, CO, May 31 - June 2, 1989, pp. 193-198.
- [7] M. Imae, H. Okazawa, T. Sato, M. Urazuka, K. Yoshimura, and Y. Yasuda, "Time Comparison Experiments with Small K-Band Antennas and SSRA Equipments via a Domestic Geostationary Satellite," IEEE Transactions on Instrumentation and Measurement, IM-32, 199-203 (1983).
- [8] G. Lutes and M. Calhoun, "Simultaneous Transmission of a Frequency Reference and a Time Code Over a Single Optical Fiber", submitted to Proc. of 20th Annual Precise Time and Time Interval Planning Meeting (PTTI), Redondo Beach, CA, Nov. 30 - Dec. 1, 1989.
- [9] P.F. MacDoran, D.J. Spitzmesser, L.A. Buennagel, "SERIES: Satellite Emission Range Inferred Earth Surveying," Proc. of the Third International Geodetic Symposium on Satellite Positioning, Las Cruces, N. Mexico, February 1982.
- [10] R.F.C. Vessot and M.W. Levine, Gen. Relativ. Gravit. 10 (1979) 181; R.F.C. Vessot et. al., Phys. Rev. Lett. 45 (1980) 2081.
- [11] D.W. Allan, C.O. Alley, N. Ashby, R. Decher, R.F.C. Vessot and G.M.R. Winkler, Ultra-Accurate International Time and Frequency Comparison Via an Orbiting Hydrogen-Maser Clock, Journal De Physique, Colloque C8, 395-413, 1981.

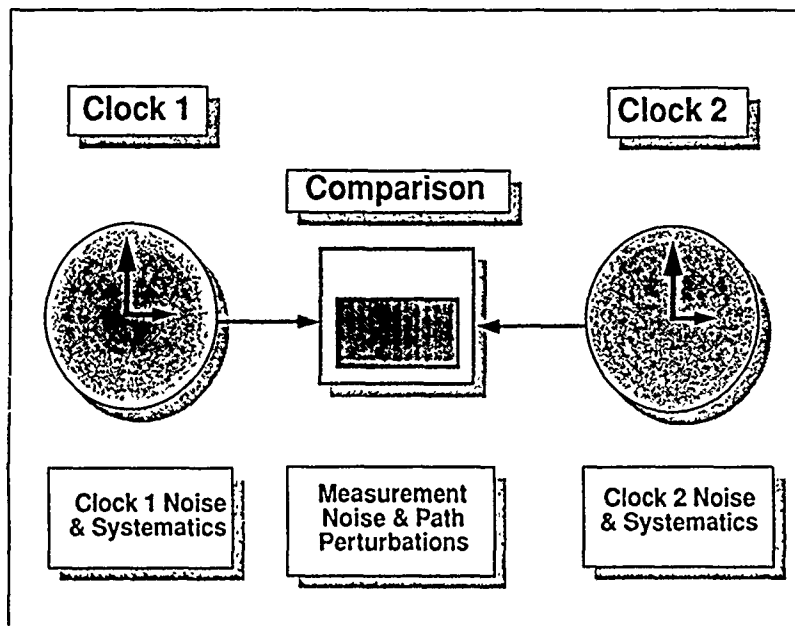


Figure 1. This figure shows two clocks, some arbitrary distance apart, being compared by some generic comparison system. In principle, the comparison system can be co-located with either or both of the clocks or with neither of the clocks. In general, the measured values coming from the comparison system will have variability due to the clocks noise, delay variations in the connecting links, and variations in the comparison system itself. Characterizing the performance of the links and the comparison system is important. Otherwise, understanding what variations come from the clocks and what comes from the comparison system and the links would be impossible.

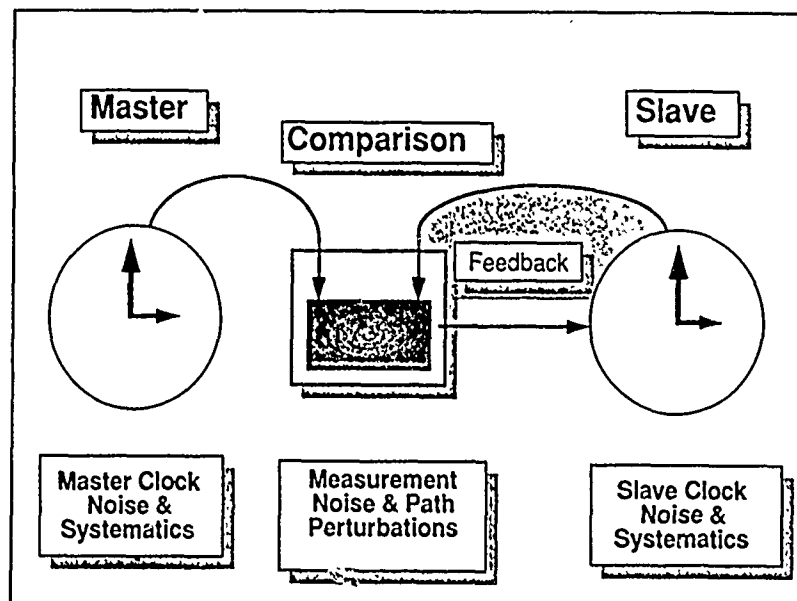


Figure 2. This figure is similar to Figure 1. Again, we are measuring the time and frequency difference between two clocks located some distance apart. In this case we wish to servo control the time and/or frequency of the slave to the master. A proper characterization of the links between the clocks in combination with the comparison system is essential for the proper design of a feedback system to control the slave clock. Another important parameter for the feedback design is the delay associated with the comparison system.

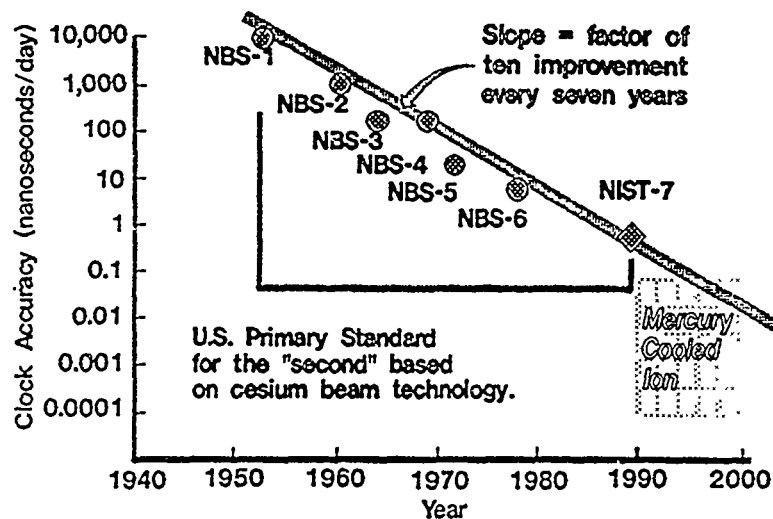


Figure 3. Depicted here is the continual improvement in atomic frequency standards of the U.S. The overall trend is a factor of 10 improvement every seven years. If this trend line continues, and there is good indication that it may, then more careful attention is needed both on the design as well as on the proper characterization of comparison systems for these standards. Note. one nanosecond per day corresponds to a fractional frequency of about a part in 10^{14} .

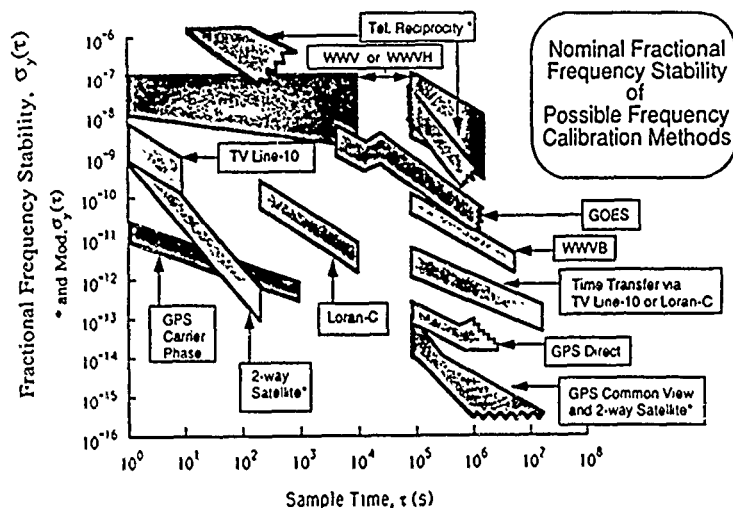


Figure 4 This plot gives nominal frequency stability of several important comparison systems. The stabilities are characterized using $\sigma_y(\tau)$ except where indicated by an "**". $\text{Mod}\sigma_y(\tau)$ was used in those cases where white noise PM was predominant for some range of sample times τ , and an asterisk "*" denotes those. The "Tel. Reciprocity" data were analyzed under the assumption of reciprocity of the path (measure the round trip time and divide by two to calibrate the path delay). The short-term data were measured locally and the long-term data were measured between Colorado and Hawaii via communication satellite. We often found that telephone modems contributed more noise than the path. What is plotted is the composite. The WWV and WWVH time-and-frequency transmissions at 2.5, 5, 10 and 15 MHz (WWV also broadcasts at 20 MHz) are limited in their stabilities by sky-wave-path variations. GOES East and GOES West are NOAA weather satellites broadcasting UTC(NIST) on two slightly different frequencies near 468 MHz. Here, the stability is limited by the knowledge of the satellites' ephemerides. WWVB is NIST's 60 kHz time-and-frequency broadcast service; in this case the propagation path stability is limited by the fluctuations in the earth-ionosphere waveguide. The TV Line-10 method involves line of sight transmissions in the TV band. It can operate with an atomic clock at the transmitter or with two clock sites receiving the TV Line-10 arrival times concurrently and subtracting one set of numbers from the other. Stability limitations here are often caused by the receiving equipment. Loran-C is a ground-wave navigation signal (at 100 kHz) operated by the U.S. Coast Guard. The time is monitored and controlled with respect to UTC(USNO). The stability is limited by propagation path variations. Two-way satellite time transfer uses spread-spectrum modems operating with different up-link and down-link carrier frequencies in one of several different bands (C, Ku, and K). The short-term stability for two-way satellite time transfer is basically limited by signal to noise and bandwidth considerations. Currently, the long-term performance seems to be limited by equipment instabilities. One can only extract frequency information from the "GPS Carrier Phase" measurements, and the stability seems to be limited by the GPS on board clocks. Time and frequency stability of directly received GPS signals is limited mainly by variations in the GPS Kalman state estimates for the system. If one is using an L1 GPS timing receiver only, then the ionospheric modeling errors can contribute additional instabilities. In some cases, signal multipath errors and/or receiver instabilities can also contribute significant instabilities. Using GPS in the common-view mode cancels out the clock instabilities of the GPS satellites and cancels some of the broadcast satellite-ephemeris instabilities. The stability limits for the common-view mode arise from the same mechanisms as for GPS direct measurements except that some of the mechanisms are reduced by common-mode cancellation.

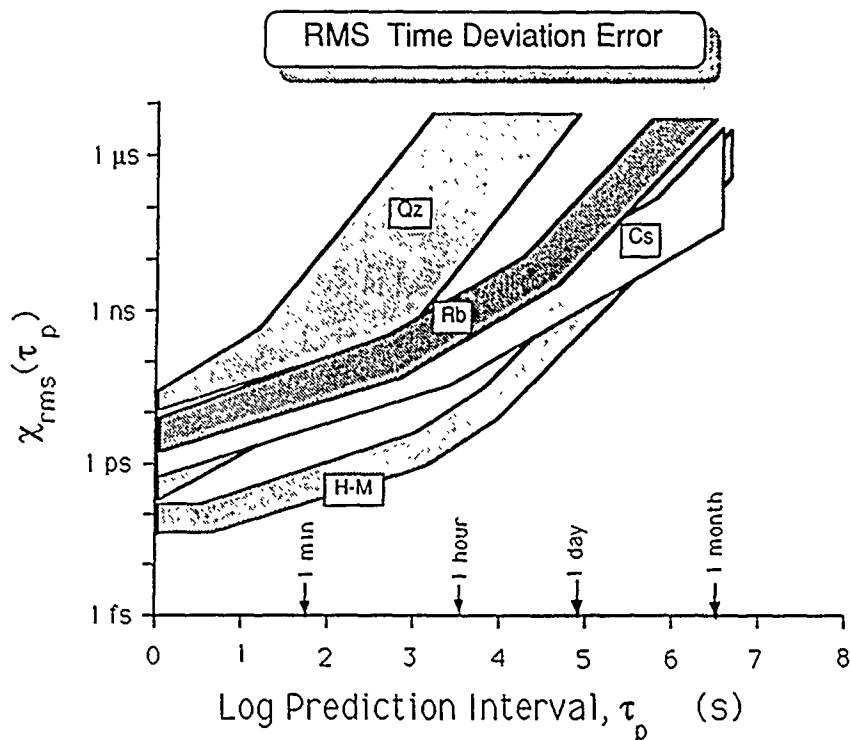


Figure 5 This is a plot of the time prediction error, $\chi_{rms}(\tau_p)$, as a function of the prediction interval for commercially available precision clocks. Qz denotes quartz-crystal oscillator clock, Rb denotes rubidium gas-cell frequency-standard clock, Cs denotes cesium-beam frequency-standard clock, and H-M denotes active hydrogen maser clock. This prediction error is calculated from $K\tau\sigma_y(\tau)$ with K being chosen for an optimum prediction estimate. The value of K depends on the type of noise.

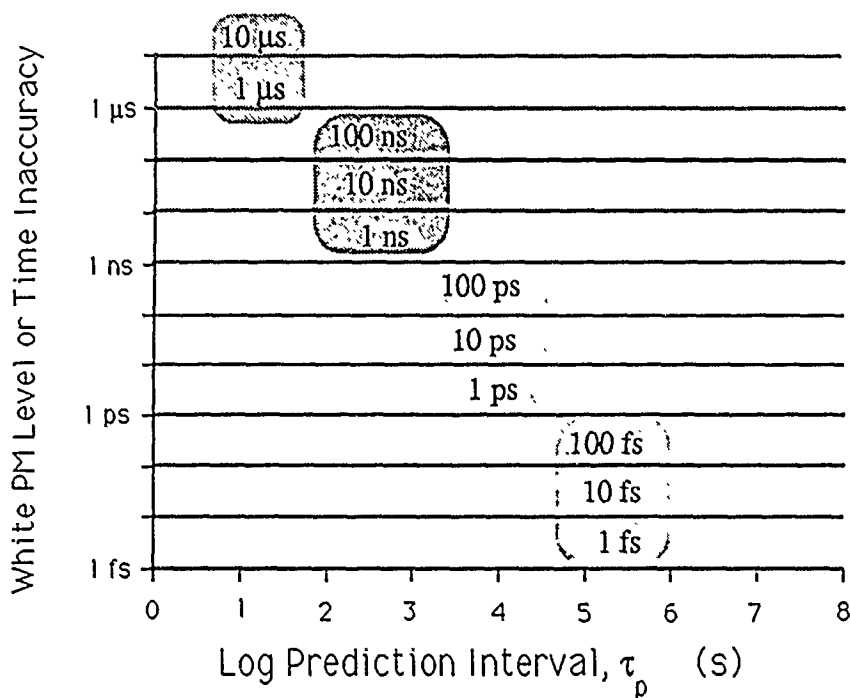


Figure 6

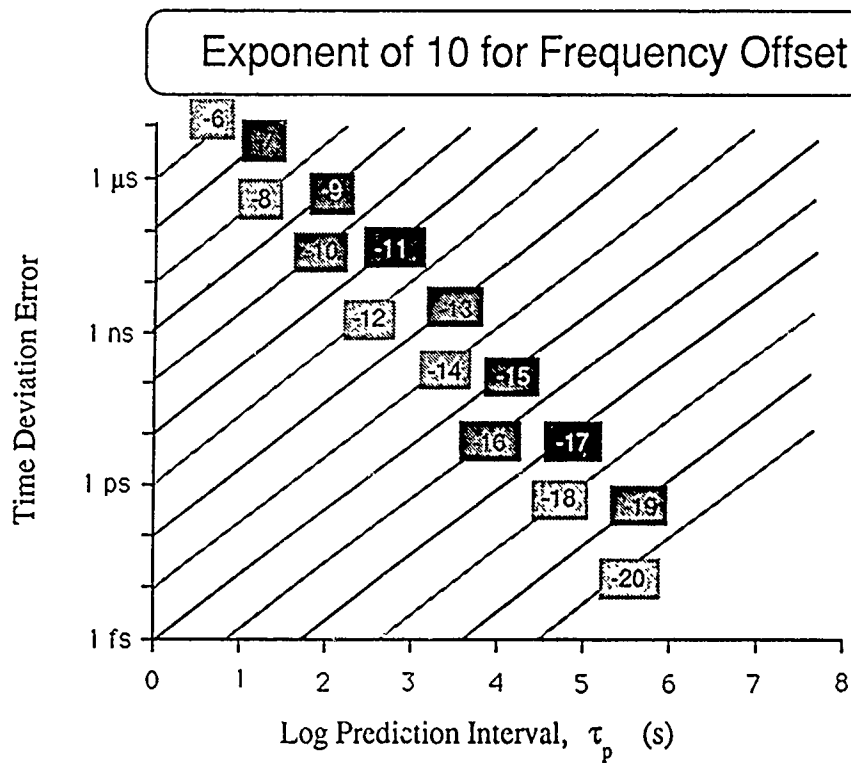


Figure 7

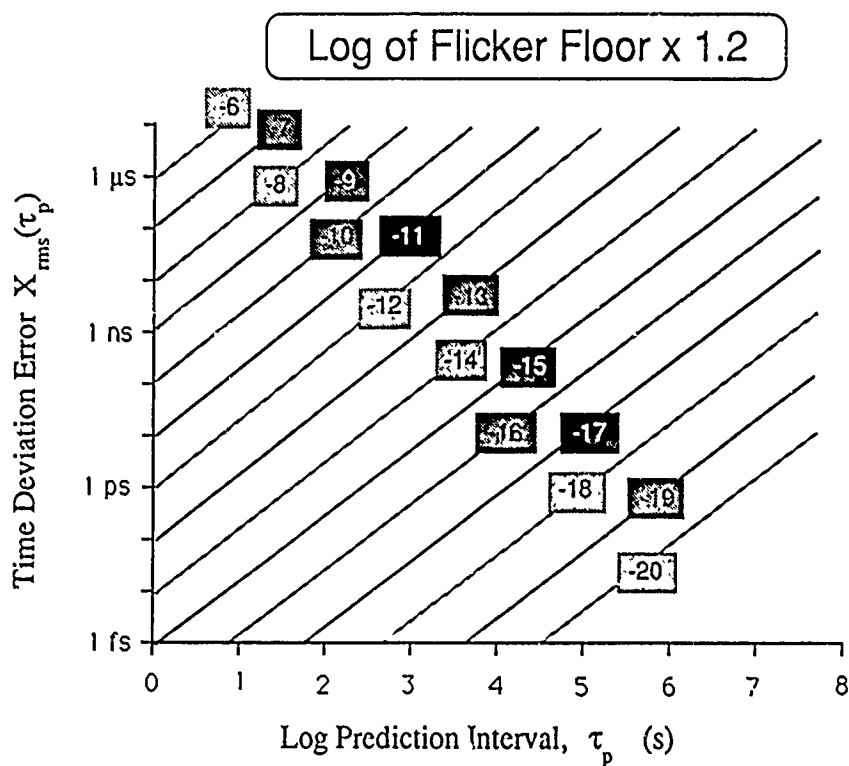


Figure 8

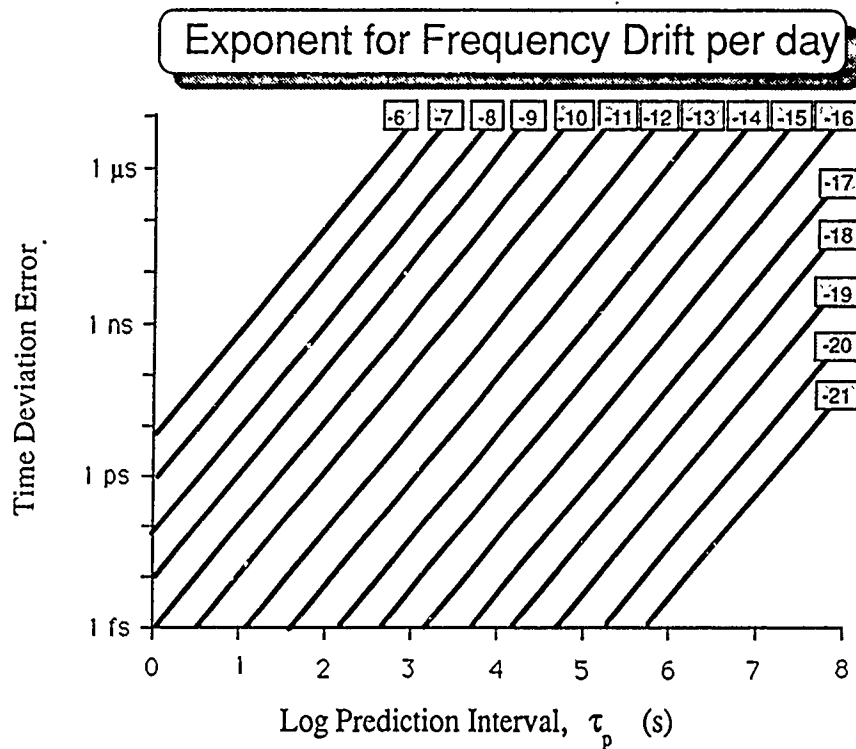


Figure 9

Figures 6, 7, 8 and 9 The ordinates and abscissas of these four plots are the same as those for Figure 5. Figure 6 can represent either the time accuracy or the white noise PM level. The time accuracy is often limited by systematic effects and averaging values does not improve it. The white noise PM is well represented by the standard deviation of the measurements, and, if this noise is the limiting noise, then averaging values will improve the knowledge of the time as the square root of the number of values averaged. Figure 7 is the time accumulation over some interval, τ_p , due to a systematic frequency difference (or offset) between the two clocks being compared. Figure 8 is the rms time deviation resulting from a random flicker FM process — often observed in long-term clock comparisons. The $1.2 (1/\sqrt{\ln 2})$ factor is the K factor for flicker noise FM. "Flicker Floor" means the value of $\sigma_y(\tau)$ where there is a τ^0 dependence, that is, where there is no further improvement in stability with increasing τ . The curves in Figures 7 and 8 have the same slope (+1) even though they arise from different mechanisms. Figure 9 demonstrates the long-term significance of time deviation errors resulting from a linear frequency drift in a clock. The plus-two (+2) slope corresponds to the quadratic departure of the time of the drifting clock. If frequency drift exists in a clock, this error along with environmental perturbations is often the main cause of long-term time deviations.

RMS Time Estimate due to Random Noise

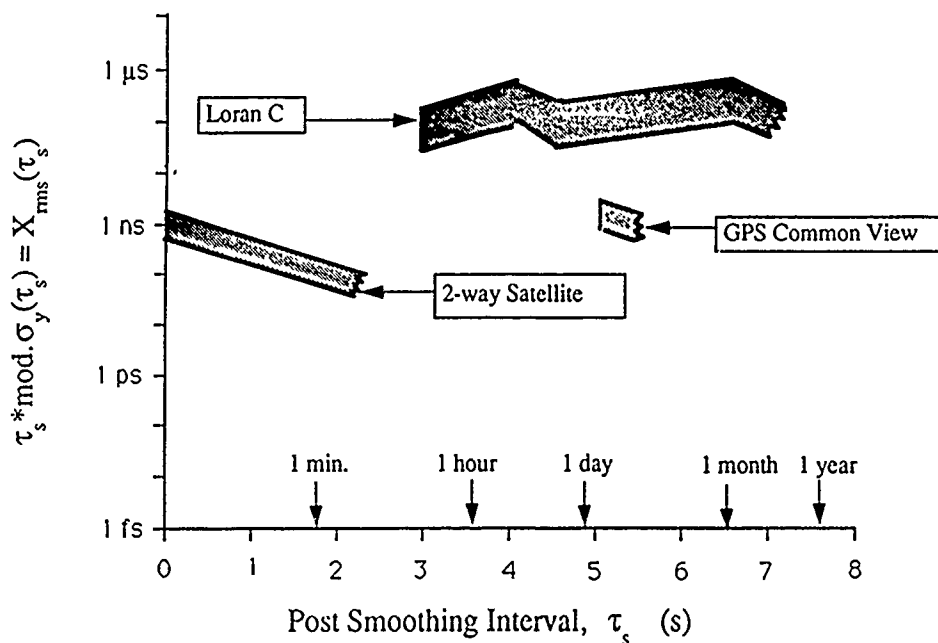


Figure 10. This type of plot can be used to determine whether or not smoothing or averaging the data is beneficial. We have here defined the time stability as the product $\tau \text{mod} \sigma_y(\tau)$. For flicker noise PM, white noise FM, flicker noise FM and random-walk noise FM the standard deviation of the time residuals grow without bound as the data length increases. Hence, it is not a good measure. The above product is a good measure, is convergent and is data-length independent. This measure can also show the effects of systematic effects, of environmental perturbations as well as the different kinds of noise processes that may be driving the instabilities in the comparison system and/or in the clocks. The different comparison methods plotted are explained in Figure 4.

QUESTIONS AND ANSWERS

GERNOT WINKLER, USNO: I have two comments. First; the telephone capability was not invented here, unfortunately. The Japanese reported in 1984, tests made over a 400 kilometer range between Mitsusaba and Tokyo. They reported noise of approximately 100 microseconds over that range. The second thing is maybe more important; that is we expound the virtues of efficient statistical measures, with the average over sufficient points, in the case of phase noise. This is, of course, precisely accurate, but what is good and necessary for laboratory conditions is not the best for actual field operations. If we have a system where you must make robust measurements of clock differences, the robustness is what has to be observed. You have to remember that efficiency and robustness are opposite extremes. For that reason, it is much easier to recognize outliers if you make direct fits, even though it is a far less efficient measure of the offset.

MR. ALLAN: In response to that I guess that I would say two things. First, I agree that one has to take the robust statistical approach, there is a lot of power in that. The only slight exception that I would make is that if one does optimum estimation, then you are more efficiently able to see outliers. There are different ways to use robust statistics, I believe. I do fully agree with the concern in these issues, because in field operation you have to deal with abnormal behavior.

TIMING IN SWISSNET
SPECIFICATION, DEVELOPMENT, IMPLEMENTATION
AND OPERATIONAL EXPERIENCE

Peter Kartaschoff
Swiss PTT
Research and Development Laboratory
CH-3000 Bern 29, Switzerland

A b s t r a c t

This is a report on a team effort started in 1974. During the past 15 years two generations of frequency control and timing equipment have been developed. The installation of the second generation equipment started in 1985. The principles of the clock hierarchy is recalled and compared to more recent proposals. The Swiss Integrated Services Digital Network (SWISSNET) derives its timing from its own three geographically separated primary reference clocks. It is designed to comply with the relevant CCITT Recommendations at the second highest level of hierarchy, consisting of about sixty timing nodes. These in turn control the clock units of all digital switches. The switching equipment is supplied by three different vendors which all have been able to satisfy the specifications imposed on their timing equipment. Some examples of problems and how they were solved will be reported and offered for discussion.

1. Introduction

SWISSNET is the name of the evolving Integrated Services Digital Network (ISDN) in Switzerland. The country has a surface of 40'000 square kilometers, 6.3 million inhabitants and 3.6 million telephone subscribers. The telecommunications network is operated by the Swiss Post and Telecom Enterprise (PTT), owned by the Swiss Federal Government. PTT has a staff of 60'000, 40'000 in the Postal Department and 20'000 in the Telecom Department. The ratio of staff to customers served has been kept stable at about 5 per 1'000 during the last years through continuous high effort in management, planning and organization. The first ISDN version, SWISSNET 1, has started operating on a trial basis with a group of selected business customers in Summer 1988 and became a commercial service in Summer 1989 [1]. Further steps are following rapidly. Moreover, broadband switched services are being introduced at a rapid pace. On the international level, major efforts in standardization of new concepts are underway in the CCITT, this work being based on proposals from regional bodies such as the ANSI T1 committee in the U.S., the European Telecommunications Standards Institute (ETSI), created early in 1988 and from national telecom operators.

The history and current state of digital network timing developments are well documented in the April 1989 issue of the IEEE Communications magazine [2, 3] which contains five interesting review papers on network performance aspects. A few remarks on terminology are necessary at this point with the hope to reduce confusion among the many authors (and readers) in this field.

The term digital Network timing is used here in a general sense comprising other more restricted terms such as clock signal distribution, synchronization, frequency control etc. On the other hand, the current timing systems do not distribute time in the meaning of date on a time scale. They only perform frequency control on all clocks in the network in order to keep the clock rates within the limits required for acceptable performance of the transmission, storage and switching operations in the network.

2. Specification and development

2.1 General

There is a voluminous and evolving set of rules in the Swiss PTT for specification, development and procurement of hardware and software. Since we cover a period of over 15 years, space does not allow to discuss all aspects of this process. We limit the discussion to some key elements which illustrate the way of operation, some changes and possible future trends.

Being a public service/network operator the Swiss PTT does not manufacture any equipment. Compared to the larger European PTT's it is a small organization. The R + D laboratory with a staff of about 300 is in charge of much non - R + D work such specification, testing and consulting work. Therefore only about 60 of our Engineers are actively engaged in R + D work. The team working on the subject described here never exceeded 6 PTT engineers and was smaller during most of the time, some changes occurred due to promotion or shift to other activities.

We however had the advantage of being flexible, in close contact and not impeded by administrative barriers. Last but not least we started early and had the time required to get into the subject.

The classical cycle:

- setting specifications
- call for proposal
- development contract
- testing of prototype

- review and correction
- retesting
- quotation for procurement
- prototype approval testing
- production order
- delivery and installation
- acceptance test
- correction of faults if any

was followed, not only once but several times in an iterative manner. We did not have any legal problems concerning calls for proposals and contract awards. In each case, the amounts involved were far below the limit requiring a public "call for tender".

Whatever the type of contract, i.e. single source or competitive bidding, the prospective supplier must quote in detail. All offers are scrutinized by a special office in the material procurement division.

The invoices are checked again and all accounting operations are audited by an office called "Financial Inspectorate" (FISP) which is independent of PTT management but reports directly to the Government and can even be called to hearings before parliamentary committees. FISP can become very active in cases of real trouble with a project. Normally it also constitutes a safeguard and often helps the management in the choice of correct procedures. During the developments described in the following sections no problem ever occurred concerning these controlling offices.

2.2 First generation

The first informal talks concerning new developments of frequency generating equipment started early in 1973 between Engineers of the PTT Research Laboratory in Bern and the Oscilloquartz Company (OSA) in Neuchâtel. This company founded in 1949 as a small affiliate to a major watch manufacturer had supplied carrier frequency generating equipment for the PTT telephone transmission network since 1952. 20 years experience and an excellent record of performance and reliability had then already put it ahead of possible competitors. It was therefore logical that the PTT continued working with OSA.

The key technical persons participating in the initial contacts were Walter Neu, Hans Karl Pfyffer, Christian Stäger and the author all from the PTT R&D division and Erhard Graf and Bernard Walther from OSA.

Two problem areas were identified at that time. One concerned data transmissions using modems and analog Frequency Division Multiplex transmission systems. The existing carrier frequency generating equipment installed between 1962 and 1966 was designed for voice transmission (carrier telephony) with maximum carrier frequencies of 12 MHz, using master crystal oscillators on 124 kHz. Very reliable and aging less than 1 part in 10^{10} per day, these sources had too high phase noise for the operation of planned transmission systems with a bandwidth extended to 60 MHz.

The other, more long term problem was how to deal with the future switched digital networks. Here the situation as known from the then published literature and from contributions to the CCITT Special Study Group D (now known as CCITT SG XVIII) was confusing at best.

The time available to agree on specifications and develop prototype equipment was limited. Two major network capacity extension projects had already started:

- 60 MHz main coaxial cable trunk network
- PCM trunk Zurich-Berne-Geneva for leased data lines, gross bit rate 140 Mbit/s.

Early tests for these systems were then planned to start late in 1975. However, these large projects slipped towards 1977, so that the frequency generating equipment was ready in time.

The first rough specifications were drafted in 1974. The principal objectives were:

Frequency offset:	less than 1 part in 10^{-9} /6 months
Spectral purity:	$S_0(f)$ less than -105 dB for $50 \text{ Hz} \leq f \leq 4 \text{ kHz}$
MTBF:	minimum 30 years for the master oscillator unit.

All other specifications, electrical, mechanical and environmental were to be conformal to all the other transmission line equipment, based on internal standards established in 1972.

Figure 1 shows a block diagram of a frequency generator unit proposed [4] in February 1974 to the internal expert team. Two Rubidium and one crystal oscillator generate each a 10 MHz signal. The oscillator frequencies are controlled in order to keep the three signals in phase. These signals can thus be combined on a common bus. The control unit contains phase comparators, amplitude monitors, D/A converters for step frequency control of the oscillators and an external reference frequency input. This proposal was thoroughly discussed in the team and then abandoned. The decision to pro-

ceed with another design [5], shown in Fig. 2, was unanimous and based on a cautious assessment of the risks in its development. We would not have been able to meet the deadline. Keeping the pace of the evolution in the CCITT Recommendations would have been very difficult.

The Frequency generator rack developed during 1975/77 comprised two crystal oscillator units (OSA B5400) locked to each other and feeding two decoupled 5 MHz reference bus lines. These in turn feed up to 2x9 PLL synthesizer units generating the required output signals at 4, 12, 124, 2108, 2200 kHz for FDM analog systems and 2048, 4096 kHz for PCM systems.

The outputs are 75 ohm coaxial with a sinusoidal signal level of 0 dBm. Each equipment rack can have up to 440 output connectors; installed in the upper part of the rack. Each reference frequency signal is supplied twice over two independent outputs to the multiplexer racks. Switchover in case of failure is done on the receiving end.

The technical basis of the requirements of the specifications and the main features of the equipment have been presented in June 1977 at the 31st Annual Frequency Control Symposium [6, 7]. Compared to the 1974 specifications mentioned above two major enhancements were introduced:

Frequency uncertainty	: less than $\pm 1 \cdot 10^{-11}$
Spectral purity for the FDM outputs	: $S_g(f)$ less than -117dB/Hz for 50 Hz $\leq f \leq$ 4 kHz

The increased accuracy to be referred to the UTC timescale was a result obtained in the CCITT, contained in the then new Recommendation G.811. This feature was required only in the nodes along the PCM data line which at that time constituted only a few nodes of a total of about 60.

All other nodes having FDM systems only were installed with only the two crystal oscillators and without the cesium unit.

The increased spectral purity requirement was based on studies made by H.K. Pfyffer and reported in [6]. We were able to test this performance in the field with phase noise measuring equipment developed by Kurt Hilty [8].

During the two years design phase, the main effort was concentrated on reliability rather than highest technical performance. Therefore, a large part of the engineering man-hours spent at PTT and at OSA were devoted to subjects such as redundant power supplies, monitoring and alarm circuits, signal cut-off circuitry in out-of-lock states of the PLL's, minimizing the number of common elements (only passive elements allowed).

The contributions to this work by Max Suremann who edited and revised the specifications and by René Payern who brought in the experience from network operations are to be acknowledged.

2.3 Second generation

The first generation equipment installed and operating from 1977 onwards was satisfactory with respect to time of delivery and reliability. The short time available did however not allow to solve many problems recognized during this first phase. The team members which all had many other often more urgent tasks to do, felt that additional help was required. W. Neu, one of the initiators had moved to ISDN research. H.K. Pfyffer was even more drawn into Digital Network planning and standardisation activities which culminated in his election as Chairman of CCITT SG XVIII in 1983 and promotion to Deputy Director of Research at PTT in 1985. C. Stäger had returned to his microwave research already in 1974. On the OSA side, B. Walther left the company for a teaching position in an engineering college. Those who stayed on received help. On the research side, Pierre André Probst and Paul Vörös joined the team.

From the engineering division came Hans Ulrich Stettler and Hans Friederich.

The problem in 1977 was that, although we had clock units and all the associated equipment of superb quality and good reliability, we had no good network timing control concept. Academic research as known from the published literature was, in quantity and scientific quality biased towards sophisticated system theory using mutual synchronization. On the other hand all colleagues we knew that were already building networks used master-slave synchronization. As we had to build a network and be sure it works we followed this way.

One important concern was to introduce new concepts in an organic and evolutive process, well coordinated with the much larger effort devoted to the transition from the conventional telephone network to the future digital network.

One possibility for reference clock distribution was created in the period 1975-78 when an old standard frequency distribution system dating back to the fifties was replaced by new equipment. An accurate pilot signal at 4300 MHz is distributed over the coaxial cable trunk network to all nodes. Various standard frequency signals, including 5 MHz are derived at each node and used e.g. for periodic manual readjustment of the FDM carrier generators within the margin of ± 1 part in 10^8 . This could have offered a temporary relief in case of urgency but would have left the new digital network dependent on a obsolescent infrastructure.

The solution to be developed was to use the 30 channel PCM multiplex with a bit rate of 2048 kbit/s from which a 2048 KHz reference frequency could be derived at any place in the network.

The main effort in the studies leading to the hierarchy depicted in Fig. 3 was carried by P.A. Probst and P. Vörös, with assistance from the other team members.

Results of these investigations were published in 1982 [9]. In the meantime revised specifications were introduced and discussed with OSA. The main problem was the definition of optimum filter characteristics of the slave oscillator control system in order to reduce the effects of jitter present at the receiving end of the transmission system [10]. The PLL circuits of the first generation master oscillators had not been designed for this purpose and could not absorb the level of jitter encountered in practice. Another major difficulty was the impossibility of dealing with some states of oscillator failure locally when you have only two oscillators. If an abnormal phase excursion is detected, there is no arbiter to unambiguously and quickly decide which unit is in trouble. Finally, after lengthy deliberations and sometimes protracted discussions we came to the conclusion that there was only one safe way out, at the additional cost of a third unit. We thus introduced the triad principle with majority decision in the first and second order centers.

Figure 4 shows the first order center arrangement. A careful observer will notice that if all three cesium units, located in different places, simultaneously fail, the first level falls back into a mutual mode. Based on current experience and supposing proper maintenance, such an event may occur once in a thousand years.

The second order centers of which now 66 units are operating have three identical master oscillator units, as shown in Fig 5. The network concept and the design features of the second generation clock signal generator units have been described and presented at the 17th PTTI meeting in 1985 [11, 12].

The revised specifications for the development of the second generation concerned the following main items:

- Timing extractor. Input: PCM 2048 kbit/s, HDB3 Code, as in CCITT Rec G703, option 75 ohm, level attenuated to range 226...946 mVpp.
Output: 2048 kHz sinusoidal, level to be fixed by the manufacturer of the system.

Alarms: Signal below minimum and detection of AIS (Alarm Indicator Signal sent on the PCM line).

- Jitter Transfer Function (see Ref [12]).
- Holdover: Frequency offset less than 5 parts in 10^{-10} during 18 hours.
- Out of lock: VCX0 control voltage below 10 % or above 90 % of control range.
- Frequency Offset Detection: The unit which drifts away more than 4 parts in 10^{11} from either of the two others is disconnected from the bus and a non urgent alarm is generated.

As shown in the figures 4 and 5 the first and second order equipment racks are identical except that in Fig 4 the PLL B is replaced by a cesium standard and the reference signals for PLL A and C are derived from other first order clock generators.

3. Implementation

The first and second order clock signal generating equipment has been designed as a part of the digital trunk transmission network. All switching equipment is in the third order level of hierarchy. In this and the lower levels of hierarchy the PTT is dealing with several vendors and a large variety of customers. Until 1983 there was a project to develop a Swiss digital switch family. In June 1983 this project was abandoned. Specifications based on the then existing CCITT and CEPT recommendations were published and three vendors were selected:

<u>Company</u>	<u>Type</u>	<u>Swiss representative</u>
- Siemens	EWSD	Siemens-Albis
- Ericsson	AXE	Ascom
- Alcatel (ex-ITT)	S12	Standard Telephone and Radio

as suppliers for public digital switches.

For the third order clock units the minimum configuration principle is shown in Figure 6. The specifications are a very small part of the books containing the general switch specifications [13]. They are limited to standard (CCITT and CEPT) input and output signal levels, impedance and matching, jitter transfer function (CCITT Rec. G742, Chapter 6.1), Holdover (CCITT G.811, Table 2, Red Book 1984) specifications. One transit and one local switch of each Type were tested during 1988. These clock units

contain oven controlled crystal oscillators with memory for holdover. The problems encountered during these tests were mostly non-technical. The people on site were not competent in our special field and usually had strict instruction not to touch these precious devices. Our engineers always succeeded finally to get hold of the right persons through the headquarters of the companies by using many telephone calls to find the way through the maze of organizational layers and divisional frontiers. Once a unit refused to lock. It was delivered with a gross misadjustment and our engineer's screwdriver solved the problem.

One important detail on which we had to fight a little bit with one supplier was the absence of a test point for getting at the VCXO output signal. The requirement was in the specifications but had been ignored.

Since we were not sure how the switch clocks would be made and behave, the hierarchy of Figure 3 was strictly adhered to. All reference links between the three first order centers and the second order centers do not pass through the switches but are sections of the fixed network constituted of PCM lines leased to large customers. The ensemble of the first and second order centers thus form a permanently connected network covering the whole country and bringing the high performance timing reference signal relatively close to the customer.

Slow path delay variations on the reference links have been investigated by means of a measurement system developed by K. Hilty and J.P. Mellana and described at the 19th PTTI Meeting in 1987 [14].

The first second order equipment rack of the second generation was installed at an Intelsat Business Service Satellite Earth Station in Vernier near Geneva in June 1986. It was locked to a PCM Signal from the Transmission Center of Rue du Mt. Blanc in Geneva, a few kilometers away, where a cesium controlled first generation rack was installed several years before.

The three new second generation first order reference sources were delivered in December 1986 and provisionally installed in Berne for a burn-in and acceptance test period of ten months. The three units were dispatched to their final locations and became operational in December 1987.

In October 1989, 60 second order centers have become operational. Due to restructuring and extension of the digital trunk network the number of second order centers will be increased to 70 during the coming two years.

The maximum length of a time reference link is currently about 100 km, the average being about 50 km. The excellent stability of the links on those

sections and nodes where there is no construction work in course, has allowed the network management to introduce some crossover links, i.e. these three reference lines entering each 2nd order unit do not all come from the same primary center. On the lower (3rd and 4th) levels, the network is still in an early state of implementation but has reached its maximum annual growth in order to reach total ISDN coverage in a few years. Many subscribers already receive their timing reference via 2048 kbit/s PCM lines or 64 kbit/s through synchronous demultiplexers.

4. Operational experience

During the first phase, from 1977 to beyond 1986, since first generation equipment is still operating now and during the coming years, the experience regarding reliability and performance, has been very satisfactory.

Especially the cesium units have shown better reliability than predicted from a worldwide survey made by the CCIR on commercial units [15]. Based on about 200 unit years of operation, the mean time before failure is about 6 years. Most of the first generation cesium tubes go down after 8 years, the cesium oven being exhausted. The repair records show that the most sensitive parts concerning outages are the monitoring and alarm circuits rather than the oscillators and amplifiers.

During this first phase, no remote controlled oscillators were used in the data network. The nodes were fed by free running cesium units. At the maximum we had 14 such sources in operation. One of the most important effects, not technical but psychological, was the demystification of the cesium unit. The term "atomic clock" was deliberately not used. The personnel now has gained good confidence in the equipment.

The second generation equipment still has a relatively short record of life but looks very good. The ten month burn-in and testing period of the three primary units has allowed to correct some bugs remaining in the hard- and software.

In the 150 PLL-Units during about 2 years we had 4 failures. Thus a first estimate of the MTBF is 75 years for one unit, however, the narrow statistical base indicates that the real meaning of such an estimate is doubtful.

On the other hand, we have lived two examples of the effect of failures.

Once a 5 MHz/2048 kHz synthesiser module went out of lock without signaling the alarm on the central panel. This module fed a multiplexer in the data lines in a local district near Lausanne. The usual second redun-

dant line was not operative since the signal with a few ppm offset frequency was still on. The data traffic of a few banks, insurance and some other companies broke down until the culprit was found and removed from the rack.

The other case occurred a few months after the IBS satellite earth station mentioned above went into service. Some important businessmen had been invited to one of the first videoconferences between Geneva and the U.S. It was a flop because one intermediate network operating company apparently ignored the synchronization requirement. The next time, a few weeks later it worked since everybody involved had learnt the lesson.

The three 1st order master centers have currently been adjusted to within a few parts in 10^{13} by the operators. Otherwise they are free running.

Currently, the standard frequency distribution network mentioned before is being used for occasional checks. Its reference is derived from one of the cesium standards in our Research Laboratory, where the connection to UTC is provided.

We use TV time comparisons to the Swiss Federal Office of Metrology which also has a GPS-receiver, and directly to the LPTF in Paris via the French TV-Network. Finally, we still use LORAN-C and monitor two LF transmitters, HBG and DCF 77.

For special cases we still use portable units, one cesium and two rubidium devices. The latter are very convenient for short time operations and appear to be less sensitive to magnetic fields than some of the portable cesium units.

5. Conclusions and Outlook

When the concept was presented four years ago [11] the prototype development of the second generation timing reference generation and distribution equipment was just finished. Now it is operating very well. Even with only a part of the digital network already built, the investment in this equipment is a minute fraction of the many billions of dollars already invested in the optical fiber and radio relay network, the multiplexers and switches.

The backbone, i.e. the upper part of Figure 3, is characterized by a feature which I would like to call the Triad Principle, i.e. use three units not just for signal availability but for rapid failure detection. As far as we know at this time, no other network operator has yet followed this

concept. It had its price but we feel very comfortable with it, now and for the foreseeable future.

The introduction of the new Synchronous Digital Hierarchy (SDH) by the CCITT, based on the SONET concept proposed by the U.S., will require only the development of synthesizer modules to generate the new frequencies. Starting with 5 MHz with the highest spectral purity now available, multiplication into the GHz range is feasible.

The work reported in this paper was not always easy but we had a few advantages. We are in a relatively small organization, are only a few individuals but with the background required: Digital transmission, frequency standards, reliability statistics, network planning and practical experience in transmission systems management. Finally we had the advantage of starting early, working out a preliminary solution under healthy pressure and improving it in the second phase.

6. Acknowledgments

The names of all the participants to this work have already been mentioned with their contributions, most of it published. However a special thanks is due to Hans Friederich from Network Operations, whose workload did not allow him to write papers. The author thanks all his colleagues and the past and present higher level managers who always supported our work.

References

- [1] K.E. Wuhrmann, Swissnet und Breitbandnetze, Bull. Tech. PTT, Vol. 66, 12-1988, pp. 478-489 (December 1988).
- [2] Masami Kihara, "Performance Aspects of Reference Clock Distribution for Evolving Digital Networks", IEEE Communications Magazine, Vol. 27, No. 4, pp. 24-34, (April 1989).
- [3] John E. Abate et al., "AT&T's New Approach to the Synchronization of Telecommunications Networks.", IEEE Communications Magazine, Vol. 27, No. 4, pp. 35-45, (April 1989).
- [4] K. Hilty and P. Kartaschoff, PTT Report VD 22.001 A, 18. February 1974 (unpublished).
- [5] PTT 839.10, 1. February 1975 (unpublished).
- [6] P. Kartaschoff, "Frequency Control and Timing Requirements for Communications Systems", Proc. 31st Ann. Freq. Contr. Symp. USA ECOM, Ft Monmouth, NJ (1977) pp. 478-483.
- [7] E.P. Graf and B. Walther, "Generation of Base-Band Frequencies for FDM and TDM Telecommunications, Proc. 31st Ann. Freq. Contr. Symp. USA ECOM, Ft. Monmouth, NJ (1977), pp. 484-488.
- [8] K. Hilty, "Messtechnik zur Bestimmung des Phasenrauschspektrums", Bull. Tech. PTT, Vol. 58, No. 1 (January 1980).
- [9] P.A. Probst & P. Vörös, "Synchronisierung digitaler Netze - Synchronisation des réseaux numériques",
Part 1: "Plesiochroner Betrieb - Exploitation plésiochrone", TM PTT Vol. 60, Nr. 2, pp. 93-101 (February 1982)
Part 2: "Synchroner Betrieb - Fonctionnement synchrone", TM PTT Vol. 60, Nr. 3, pp. 125-138 (March 1982).
- [10] P. Kartaschoff, "Reference Clock Parameters for Digital Communications Systems Applications, Proc. 12th Annual PTTI Meeting, NASA Conference Publication 1275, pp. 515-549 (1980).
- [11] P. Kartaschoff, P.A. Probst and P. Vörös, "A Network Timing Concept for Switzerland"
Proc. 17th PTTI, pp. 287-300, Washington D.C. 1985.

- [12] E. Graf, P. Girardet and P. Rochat
"Network Timing Equipment for Synchronous Digital Communications"
Proc. 17th PTTI, pp. 303-316, Washington D.C. 1985.
- [13] PTT 838.00, Pflichtenheft IFS (First Edition 1985).
- [14] K. Hilty and J.P. Mellana, "Measurement of Delay Variation in Digital
Communications Networks"
Proc. 19th PTTI, pp. 96-105, Redondo Beach CA 1987.
- [15] CCIR Report 898, ITU Geneva 1988, Vol. 7

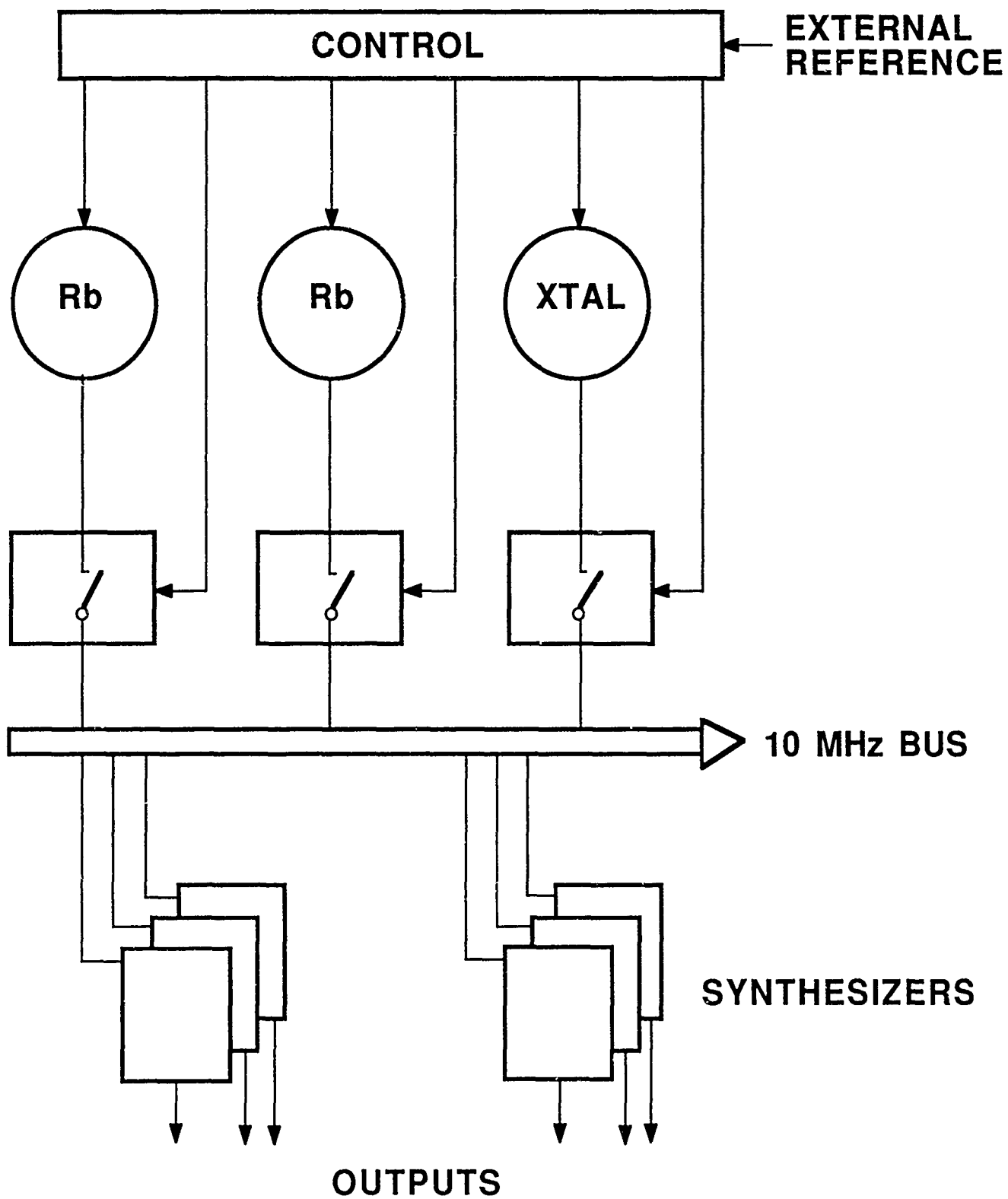


Fig. i Master Clock Unit, proposal February 1974

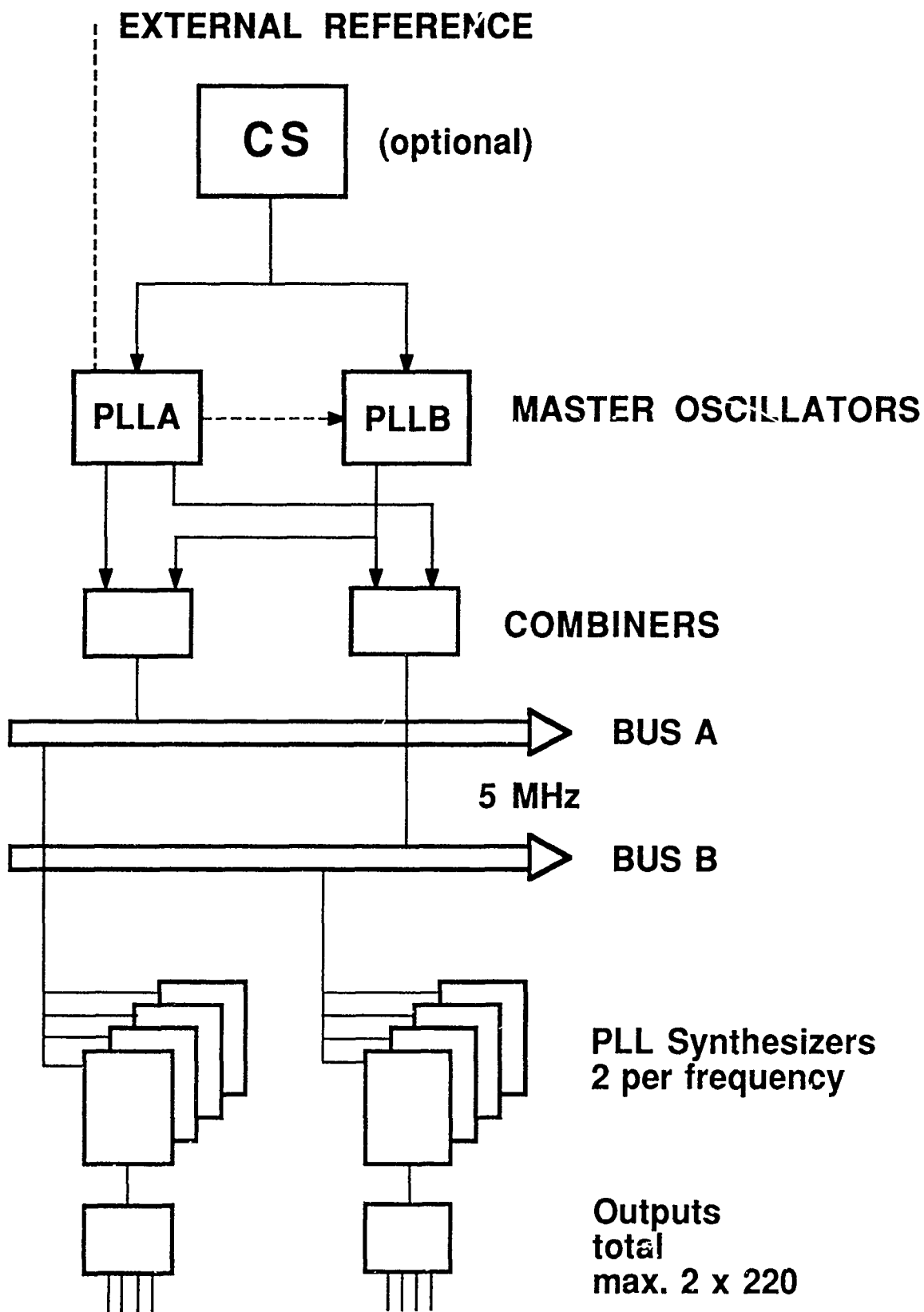


Fig. 2 First Generation Master Clock Unit with optional Cesium reference

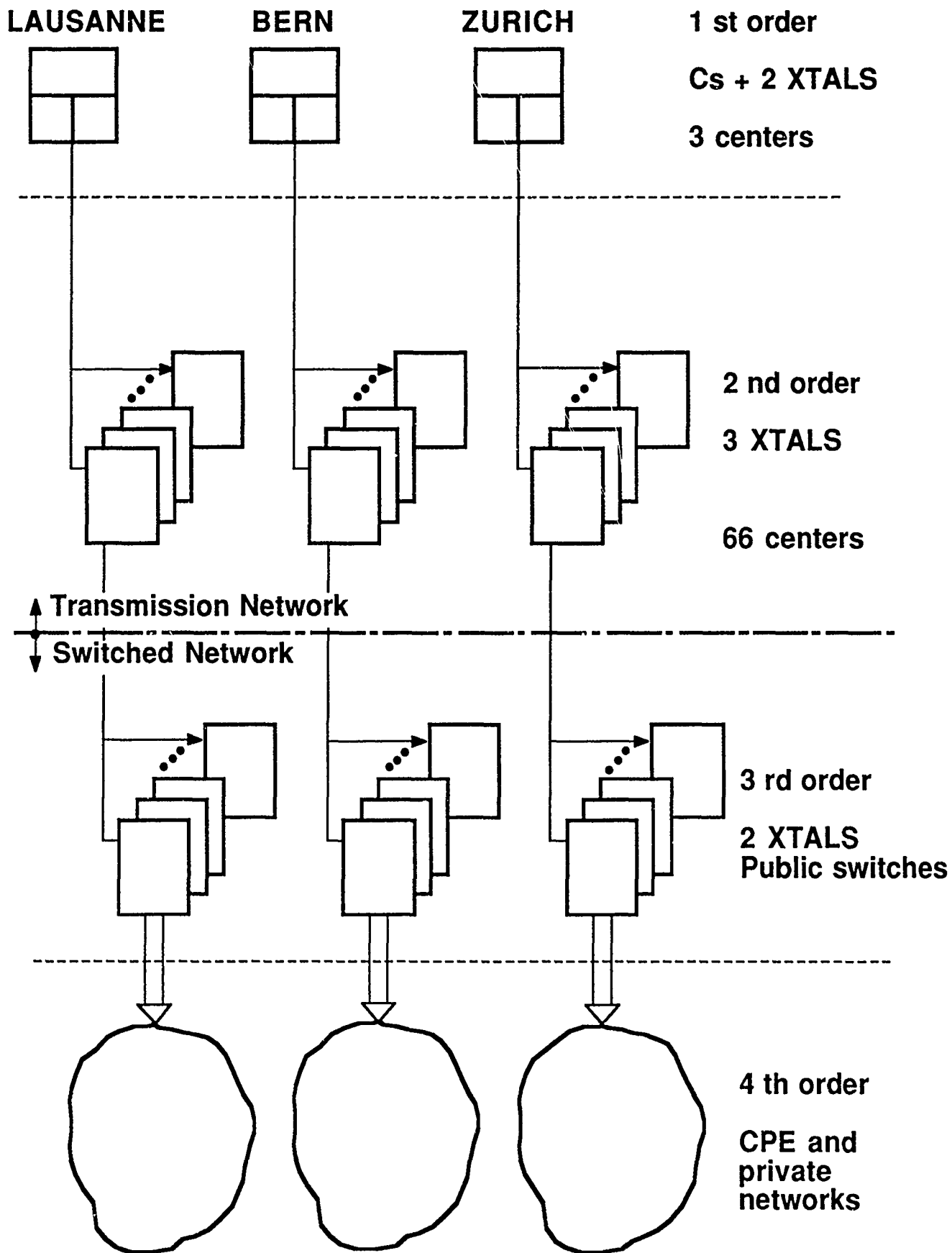


Fig. 3 Network Hierarchy for Clock Signal Distribution

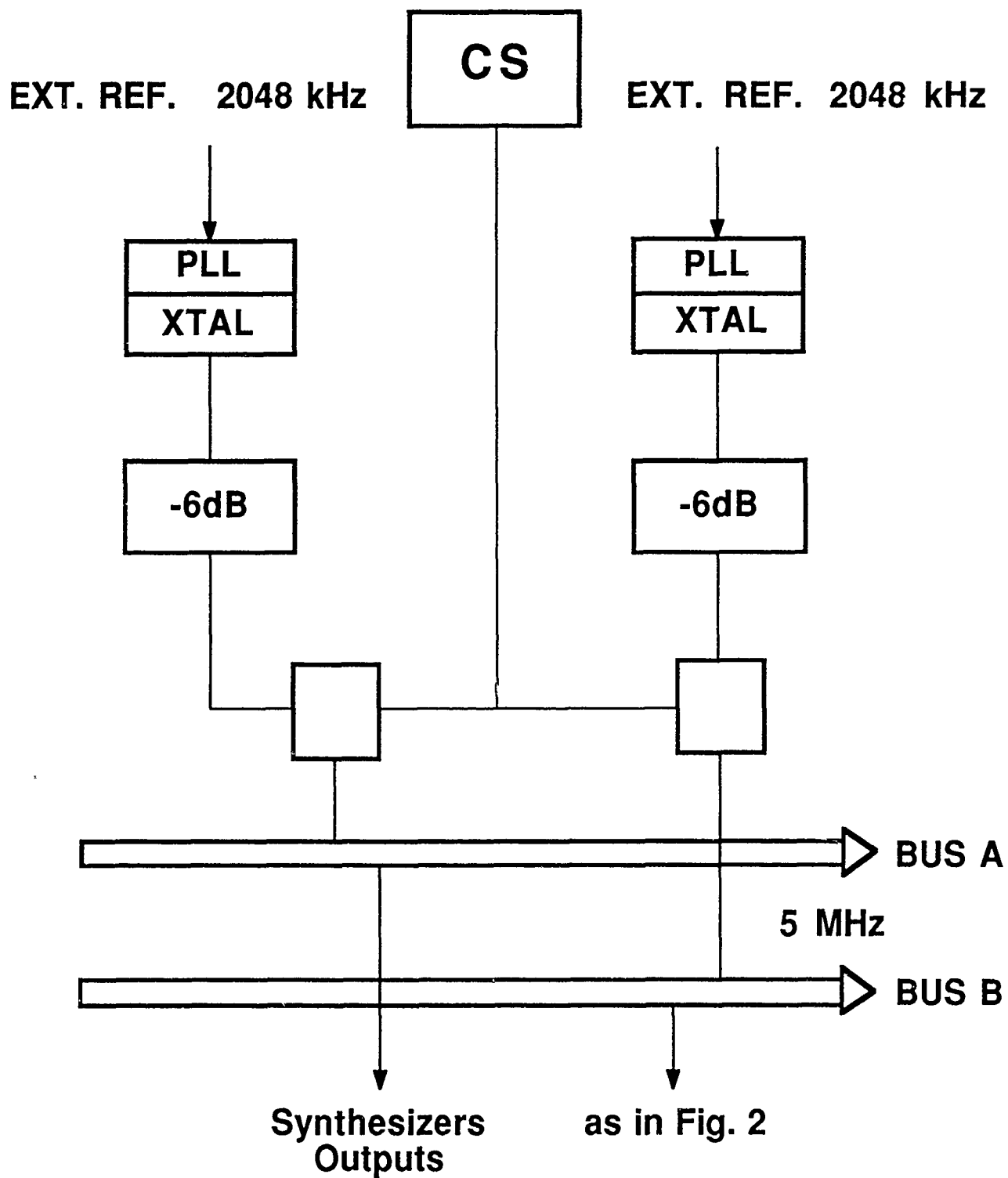


Fig. 4 First order clocks

3 INDEPENDENT REFERENCES 2048 kHz

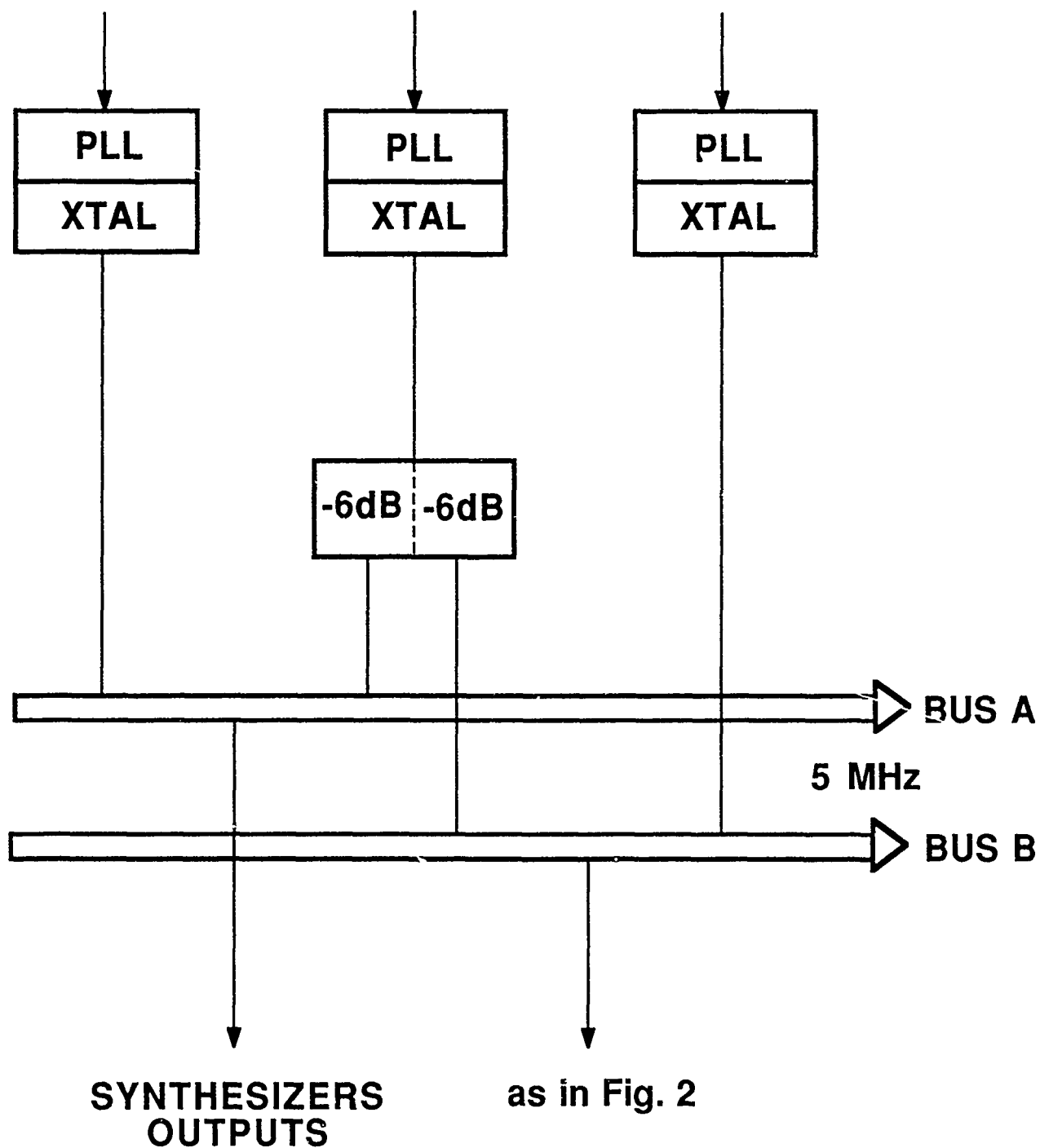


Fig. 5 Second order clocks

2 EXTERNAL REFERENCES 2048 kHz

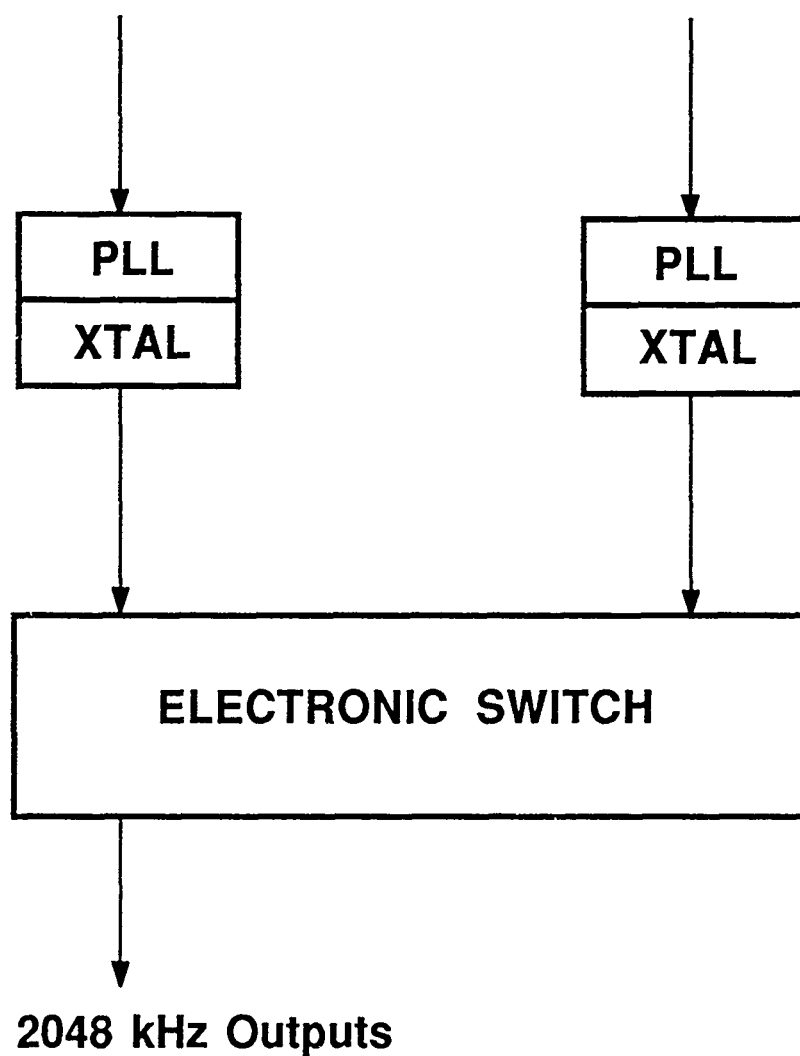


Fig. 6 Third order clocks

SPECIFICATIONS AND PROCUREMENT OF FREQUENCY AND TIMING EQUIPMENT AND SYSTEMS "INDUSTRY OPINION"

Don Mitchell
Austron, Inc.
P. O. Box 14766
Austin, Texas 78761

Abstract

This paper presents the results of a survey of some time and frequency manufacturers on "industry opinion" as to what can be done to improve the specifications and procurement of time and frequency instrumentation and systems.

Of prime importance in this discussion is the Statement of Work (SOW) and the item specifications which are the heart of any request for proposal and resulting contract. The SOW and specification must adequately spell out exactly what needs to be done, how, when and where. The SOW and specifications should be written simply, thoroughly, logically, accurately, concisely and precisely, all of which makes it a real challenge to write. The writer should have a basic understanding of the legal implications of contract language as it relates to the SOW and specifications of a request for proposal which will result in a binding contract.

INTRODUCTION

When requested to present this paper I saw it as a means of providing positive feedback to the equipment end user in his efforts to specify and ultimately procure hardware or services to satisfy his requirement.

Since I was tasked to present this as an "industry opinion", I formulated a letter soliciting comments and sent it to 37 selected individuals associated with the time and frequency industry. Selections were made from the PTTI and Frequency Control Symposium mailing lists. Written responses were not received but we did receive several informative telephone calls. Generally, comments were similar in that all agreed that there was need for improvement, but no one volunteered a specific example since their customers might think they were being singled out. Therefore, the comments for this paper were sourced from a wide range and were not limited to the time and frequency community. I do believe that most are germane to this community although they apply to other areas as well.

Since 1982 Congress has enacted eight major reforms of the defense procurement system, generating a multitude of new rules and regulations that business concerns of all sizes are required to comply with. These reforms were written to protect the government from "wrongdoers", but instead have created

a complexity of rules and regulations that make it possible to find a regulation that states one thing, and another that, in fact, contradicts the first. This scenario has not helped to eliminate contract abuses as intended, but in many cases has added cost to doing business with the government and in some cases allowed unscrupulous suppliers to propose and deliver substandard equipment with virtual immunity to government review or rejection.

Daily we hear of alleged abuses such as high cost hammers, toilet seats, coffee pots and defective components in our missile systems. I am sure that at least some of you in attendance have at some time experienced an anomaly that your procurement system did not allow you to remedy. To prevent such occurrences, it is of utmost importance that each of you become personally involved in your procurements to the extent that you write complete specifications and statements of work.

The following are major areas of the procurement process that you, the end user, should be familiar with. Also note that if you will be writing specifications on a continuing basis, a dialog should be maintained with your procurement group.

Source Selection:

You should understand what your procurement sections policies are on source selection, their organization and processes. Understand your role or what it can be in source selection. Become familiar with the Federal Acquisition Regulations (FAR) on source selection.

Type of Procurement:

You should understand types of procurements and which type will most likely result from your submitted requisition. These are likely to be: Request for Quotation (RFQ); Request for Proposal (RFP); or Invitation for Bid (IFB). Determine if you have any input in selecting the type of procurement.

Discussions and Negotiations:

You should understand the difference between discussions and negotiations. Who will be involved in discussions and what are the limitations on discussions. Should discussions be limited to technical or management or both? Changes as a result of discussion should be fully documented.

Award Decision:

How will the decision be made? Who will make the award decision? What are the important trade-offs.

- Technical
- Management
- Probable Cost

- Best and Final Price
- Past Performance
- Experience
- Delivery
- Service
- Life Cycle

Below I have listed some of the problems we in industry see that seem to occur repeatedly in government procurements. Some of those listed, you the end user writing the specification and statement of work (SOW) have some direct control over. Understandably you the end user will not have control over some of the items listed, but you can exert pressure on your procurement section to rectify these problems as they will affect the ultimate procurement.

Problem

RFPs and IFBs are issued for commercial "off-the-shelf" or modified commercial "off-the-shelf" equipment with numerous listings of MIL-type requirements imposed as a requirement of the specification and/or SOW. We in industry are unable to determine if you really desire commercial "off-the-shelf" equipment that meets all of these MIL requirements and are in fact exposing ourselves to a charge of non-compliance when bidding standard commercial equipment in response to the RFP or IFB.

Possible Solution

Fully understand your requirement. Will commercial "off-the-shelf" equipment satisfy your requirement? Is commercial "off-the-shelf" or modified commercial "off-the-shelf" equipment available to satisfy your requirement? Do a market survey or issue a draft RFP. Ninety percent of your requirements can probably be fulfilled with commercial equipment. Write your specification and SOW to clearly reflect commercial specifications unless, of course, you need MIL-spec.

Problem

RFPs and IFBs are issued with TBDs and TBRs listed throughout the specification and SOW. These create problems not only for the vendor bidding this requirement, but also for you the end user evaluating the responses you may get to those TBDs or TBRs or, worse yet, not getting responses and a contract being issued with several TBDs and TBRs remaining unresolved.

Possible Solution

If possible determine what your exact requirement is and eliminate TBDs or TBRs from your specification or SOW. If you the end user are unclear in your requirements, how can the bidder be responsive. Bidding to a government requirement should not be a guessing game, clearly state the requirement. This protects you, the government.

Problem

RFPs and IFBs are issued with Section B Supplies or Services description for a brand name/model number or equal, but with Section C Description/Specification/Work Statement equipment salient characteristics which do not fully describe the brand name/model number. The brand name/model number that you require will most likely not be what you will get on this procurement. The brand name manufacturer will most likely bid to model number or face the possibility of an irate requisitioner. The other name bidders can bid only per the salient characteristics even if they know that they will not meet your requirements. Another example of what can occur is the procurement becomes a small business set-a-side and the brand name manufacturer is large business making it impossible for the brand name manufacturer to even offer a bid.

Possible Solution

Don't requisition by brand name or equal model number. If, for whatever reason you need a brand name/model number equipment, then you should write a sole source justification. Nine times out of ten you will not get the brand name unit.

If you do not have adequate salient characteristics specified, you will probably not receive the brand name unit and you will most likely be totally surprised when the unit is delivered. The delivered unit will probably not even accomplish the desired result. Write a specification to submit with your requisition, it will save you time and ensure that what you procure does your job.

Problem

Negotiated RFPs have been handled as two-step procurements without the protection provided under FAR regulations for a real two-step procurement.

Possible Solution

Procurement should follow the Federal Acquisition Regulation procedures.

Problem

All of us at one time or another have been witness to an instrument or equipment being delivered only to find it does not comply with the specification, is of substandard quality and in some cases non-functioning. When we try to reject the unit we find the DD250 has been signed and often the payment issued. Often after days or months of effort to rectify the problem we realize we are spinning our wheels and are forced to try to use the unit or discard it and go out on a new procurement.

Possible Solution

Ask for Certificates of Performance or Factory Acceptance Testing. Don't hesitate on rejecting non-functioning units or units that don't meet the specification. Make sure all procurements have quality assurance provisions included. Most manufacturers will work with you to rectify any problems that may exist even if they are not at fault.

There are many other problems you encounter in procuring equipment and/or services and in order to minimize these you must at least maintain a familiarity of the acquisition process. I realize this will be difficult, but feel it will help in the long run if you understand the process.

Part of the problems may be self-created as evidenced by the following story.

The procurement section receives a requisition for a very sophisticated item of instrumentation. Attached is a one-page specification describing the requirement and listing the salient characteristics of the instrument.

That same procurement section receives a requisition for the procurement of chocolate chip cookies with a seventeen page specification describing the requirements and listing the salient characteristics of the chocolate chip cookie to include the circumference, the thickness, the minimum and maximum number of chocolate chips and the shade of brownness when done.

Which procurement stands the best chance of being what the end user really wants?

We do not have to be like the chocolate chip cookie end user to get what we need, but I feel that most of us are lax in writing specifications for the item we need to accomplish our job.

QUESTIONS AND ANSWERS

HELMUT HELWIG, NIST: I wanted to make a comment. You touched on a very complex issue, just the surface of it. There are peripheral issues that are very important relating to quality, quality audit, cost accounting, cost audit, and so on which are very complex and confusing. I just want to comment that that is well recognized in the government, particularly in the Department of Defense. It is not only a Department of Defense issue when you talk about regulations and rules of the game, it is also the legislation which is confusing. New legislation is passed, sometimes in an uncoordinated way, and that creates an increasingly complex issue. I also wanted to mention that the document which describes the issues in general, especially in Defense procurements, was issued by the last Undersecretary for (not clear on the tape). It is a beautifully bound form called "Fostering U.S. Industrial Defense Readiness", or something like that. If anyone wants copies of that, I think that I could make some available.

UNIDENTIFIABLE QUESTIONER, ROCKWELL: I can really sympathize with you, Don. We had to write specs for the Block Two and the Block One satellites. As a little history, the rubidiums were started early and we are on the twelfth iteration of that spec. On the cesiums we are only at the second or third. Another thing that you have to worry about is the applicable documents. The customer will say that 'we are going to use 1540', when 1540 doesn't have anything to do with the environment that the clock is going to see, or even how you are going to test it and that drives up the cost unrealistically. You have to worry about the applicable documents.

MR. MITCHELL: My paper is longer than what I presented and I did include in the paper some of the very important problem areas and the suggested solutions. If you do require a Mil-spec component, for goodness sakes specify that, but if you can use an off the shelf component, don't have us, the manufacturer, go through reams of documentation and taking exception to it. Write what you want. If you want commercial off the shelf, then state that. Don't require us to do a lot of un-needed documentation because, in the long run, it costs more to you, the customer.

VALUE PROCUREMENT

C. Eric Youngberg
Hewlett Packard Company
5301 Stevens Creek Boulevard
Santa Clara, California 95052

Abstract

Like their commercial counterparts, military users expect the best value for their purchase dollar. This value includes meeting specifications and price requirements, as well as less quantified needs in product support and cost-of-ownership.

Reputable commercial suppliers are conscious of these needs with respect to their markets. These needs must be fulfilled on a daily basis in order to survive. The procurement process, which actually starts before any product is delivered, is tailored in the commercial world to effectively match the requirements of suppliers and users.

This paper will discuss methods in which the procurement process which matches the needs of commercial suppliers and military users may also be tailored to the increased satisfaction of both groups.

INTRODUCTION

Planning and writing specifications is part of what Hewlett Packard considers to be the establishment of mutual performance expectations and measures between supplier and buyer. This is the essence of a "working" vs. "adversarial" relationship, and what we consider to be critical to procuring value from our vendors.

We believe that any further clarification with regard to writing specifications which support procurement of our products by our customers should be preceded by first establishing this same type of procurement process; one which allows a buyer to truly purchase lasting value through the establishment of mutually beneficial, long-term relationships with its vendors. This paper addresses, in outline fashion, how HP is solving the problem of procuring value from its vendors, in the hope that the concepts presented may assist our customers in doing the same.

TQRDC&F

Results HP seeks from its suppliers do not occur from random sourcing or selection of suppliers based solely on specifications and competitive bid prices. They result from making the correct selection of suppliers and then working closely with them to improve quality and productivity. Thus, the strategy of establishing "working relationships" with suppliers involves the following general strategy:

1. establish mutual performance expectations and measures (of which specifications are a part),
2. feed back results,
3. initiate corrective actions to ensure continuous performance improvements, and

4. continue to reward the best performers with more business.

By setting supplier expectations, we:

- * maximize customer satisfaction,
- * maximize profitability for all contributors in the system,
- * maximize responsiveness to change,
- * provide a framework for effective communications.

To accomplish these objectives, we set out to do the following with each vendor interested doing business with us:

- * establish and maintain long-term commitments,
- * promote effective communications,
- * obtain mutual agreement on expectations and goals,
- * treat their processes as extensions of our own,
- * utilize a team approach to achieve performance improvements in a proactive/cooperative manner.

The success of this program is rightfully shared with our suppliers who specifically contribute to our commitment to excellence. Successful supplier performance is measured in the areas of technology, quality/ reliability, responsiveness, delivery, cost of ownership, and financial stability, or **TQRDC&F** as we call it, and will always have rewards of repeat business, increased sales, and profitable growth.

An effective procurement process, constructed using the strategy outlined above, enables the customer to obtain far greater value from products than that obtained by purely meeting the "letter of the law" specifications.

COMMON PROCUREMENT OBJECTIVE

"Maintain a competitive advantage by providing materials of the highest quality and lowest cost, with the best delivery, responsiveness and technology available, by selecting fewer but better suppliers."

TQRDC&F MEASURES

TECHNOLOGY

Hewlett Packard competes on the basis of its strength in design and manufacturing technology. Likewise, HP expects its suppliers to be technological leaders in their respective fields of design and manufacturing. Suppliers are expected to participate in mutual engineering throughout HP's products' life cycle to enable timely introductions and continuous quality and cost improvements. Suppliers are graded on three key areas:

- New Technology - suppliers must be prepared to:
 - * provide leading edge technology,
 - * introduce new products in a timely fashion.

- **Mutual Engineering** — participate with HP in continually redesigning for reduced cost, as well as providing design and application assistance on existing and new products.
- **Commitment to R&D** — strength of management commitment to R&D funding is a prime indicator of present technical innovation and capability to respond to change.

QUALITY/RELIABILITY

HP expects zero defective products for electrical, mechanical, cosmetic and administrative reasons. Quality and Reliability are expected to be achieved through superior design, process control and continuous process improvements. Suppliers are graded according to:

- **Process Control** — using HP-qualified processes and SQC (Statistical Quality Control) methods to control/improve them, vendors will hold to the basic tenet in HP that quality is a result of the suppliers internal process, not external quality control. Specifically, suppliers must continually demonstrate:
 - * * that they can meet or exceed HP specification requirements,
 - * * Q/R improvements through application of SQC and TQC methods,
 - * * that outgoing quality verification is high enough make incoming inspection unnecessary.
- **Demonstrated Product Reliability by Test** — provide reliability data to HP when requested.
- **Documentation** — accurate manufacturing documentation, including tooling information, is willingly supplied by vendors to HP, along with a commitment to give:
 - * * advance notice of major process & product changes
 - * * **Responsive To Alerts And Corrective Action Requests** — suppliers work quickly and effectively with HP to resolve reported Q/R problems.

RESPONSIVENESS

Suppliers are expected to be responsive to swings in demand with short cycle time, appropriate inventory management, while maintaining flexible capacity capabilities to successfully resolve and improve worldwide service. Suppliers are graded in four areas:

High Level Management Commitment to HP — the suppliers management should understand HP's expectations, develop strategic/tactical plans to address them, strive to resolve problems quickly, and provide effective two-way communication of these needs in the organization. Important parameters:

- * * responsive to changing needs
- * * initiate communication on potential problems
- * * timely response and resolution to inquires
- * * support of sole sourced parts

Effective Worldwide Factory and Field Support for All HP Entities — our suppliers must understand the requirements of doing international business and HP's expectations for equity, consistency and support.

Long Term Product Support — committed to supplying parts through the discontinuance phase of HP product sales and support life.

Flexibility to Changes — HP views suppliers manufacturing process as an extension of its own, and commits to minimizing operational problems by sharing forecasts of needs.

DELIVERY

HP expects deliveries to be 100% on time all the time with a window of -3/+0 days. To achieve this expectation, there must be continuous improvement in overall delivery performance and our suppliers must be prepared to meet commitments worldwide. Lead times must be short by industry standards, reliable and decreasing over time.

On-Time Delivery — 100% on time delivery is expected. HP will assist with forecasts and freight clusters where appropriate.

Lead Time — HP expects high performance with respect to lead times as well as continued improvement, and provides forecast information to support this performance. Important parameters:

- * * stable lead times, decreasing over time
- * * progressively shorter manufacturing cycle times
- * * progressively shorter order processing times
- * * assurance of material in market upturns

Packaging — must be done to HP expectations.

Backup Shipment Strategy — must have a mutually agreed upon plan.

COST OF OWNERSHIP

HP must have low-cost, high quality products on a worldwide basis. Supplier performance is measured by how well cost reduction techniques and improvements are being put in place.

Cost Reduction — suppliers enter into cost analysis discussions with HP on specific parts, with the purpose of establishing mutually beneficial prices. Programs to reduce cost must also be implemented. Important parameters:

- * * continuous price reductions through process improvements
- * * two-way feedback on opportunities for improvement
- * * leadership toward standard parts and processes

FINANCIAL STABILITY

Part of establishing long-term business relationships with suppliers is the verification of financial stability, to ensure ability to grow financially as well as technically. Measures include:

- * * D&B credit ratings
- * * financial questionnaires
- * * output from financial stability models

SUMMARY

Planning and writing specifications is an important part of setting supplier/buyer expectations. However, it is only a small part of the relationship which is formed in the procurement process. Much more central to the issue is the establishment of a win-win working relationship through a whole set of mutual performance expectations and measures, including specifications. The extent to which this is done and results are fed back, and corrective actions are initiated, will ensure that continuous performance improvements will occur and provide for the procurement of real value.

CREDIT

HEWLETT-PACKARD SUPPLIER PERFORMANCE EXPECTATIONS, June 1989
ELECTRONIC BUSINESS, October 16, 1989

QUESTIONS AND ANSWERS

JOHN VIG, AETDL: How do you control improvements? I know that some people are very afraid of having things change because that some innocent change that is supposedly an improvement can result in nasty problems later on. How do you control these?

MR. YOUNGBERG: That does happen from time to time and what we will do is to go back to the vendor, after we have made tests, and work with them on a solution to that particular problem. I am thinking of one that we had recently, a connector, where we went back, since we have a long term relationship, and try to help them understand their process and how they can change it and make it work for us.

SPECIFICATION OF ATOMIC FREQUENCY STANDARDS FOR MILITARY AND SPACE APPLICATIONS

J. White, F. Danzy, E. Powers
U.S. Naval Research Laboratory (NRL)
4555 Overlook Avenue, S.W.
Washington, D.C. 20375-5000

Abstract

This paper provides a detailed review of a typical specification for a cesium clock to be used in an orbiting satellite. Area of the specifications to be discussed include the use of military standards and other government documents as references, performance criteria, electrical and mechanical interface details, parts selection, quality assurance standards, and reliability requirements. The relationship between the specifications, the statement of work, and test procedures will also be discussed.

I INTRODUCTION

Specifying an atomic clock for use in a space environment requires an understanding of the requirements and environment not just in the sense of timekeeping or frequency stability, but also of the highly specialized conditions required to be met for flight. In space applications, the ability of the clock to survive and keep stable time over a number of environments at a very high reliability is usually at least as important as exactly how stable it is. For example, since it is not generally practical to recover a failed clock to repair it, satellite systems may carry several clocks just to assure that there will be an operating clock available throughout the expected mission. Similarly, the vibration levels encountered during a rocket launch are much more severe than a laboratory clock would ever see. The transition from an existing laboratory or commercial device requires a broad understanding of what is to be expected from the clock and under what conditions it must provide that performance.

The approach to be presented in this paper defines the steps that are necessary to specify a space clock. Not all performance parameters will be covered, but attention will be given to those that are unique to high precision clocks and also to items that have been found to be especially troublesome. In addition, there are a number of applicable documents and standards available which can be cited in clock specifications. Reliability is another key area where experience has shown difficulties due to the low volume production of space clocks and the uniqueness of atomic resonator packages. Finally, there is the question of what parameters need to be tested and to what extent it is practical to test them to verify that the delivered item really has the desired characteristics. Our experience has been that performance, reliability and acceptance criteria are the principal areas which must be given consideration when developing clock specifications. Figure 1 depicts the relationship of the areas we feel had the greatest influence in the development of the specifications. Table I provides a listing

of the military handbooks and specifications we found to be particularly helpful when developing specifications for atomic clocks intended for space applications. We recommend that one become at least familiar with these documents when developing specifications for a militarized clock system. It should be pointed out that table I is not intended to be all inclusive, other applicable documents may be required including program specific reliability/quality documentation which could have been added to this list.

II PERFORMANCE

Frequency standards performance specifications must be realistic and based on an appreciation of the operating environment. For a given technology one can not expect to achieve the level of performance with space hardware as one can get with a laboratory instrument of the same technology. Normally sacrifices in performance must be made in order to reduce the clock's sensitivities to the operational profile of the space mission. The base line performance requirements are generally a derivative of a laboratory instruments capability tailored to conform with the host system's operational and environmental requirements. Typically a performance hierarchy is established with adjustments being made as the clock design become better defined. The following is a listing which illustrates the starting order we used in establishing performance requirements.

Baseline Performance

- Long and Short Term Stability
- Accuracy
- Settability
- Phase Noise
- Spectral Purity

Environment

- Thermal
- Radiation
- Magnetic

Interface

- Output Signal Characteristics
- Diagnostic Monitors
- Electromagnetic Interference and Compatibility
- Telemetry Commands
- Power (turn-on and nominal)
- Warm-up time

It should be emphasized that a lower-order performance requirement can influence a higher-order requirement. That is one might have to sacrifice on the settability requirements because of the spacecraft telemetry capability. Stability or accuracy requirements may have to be reduced due to the thermal or magnetic environment of the spacecraft. Our experience has been the higher the order the more likely requirements sacrifices will be made. If the effort is structured to include a full development program,

prototype, engineering and pre-production models, fewer performance sacrifices will be experienced in the end product. It can not be stressed too strongly that the more effort devoted to the engineering and pre-production stages the more likely one is to achieve the desired higher order performance goals. The clocks developed by NRL with the more comprehensive efforts in the engineering development stages have resulted in better demonstrated performance.

III RELIABILITY

Reliability requirements are generally based on the level of risk acceptable to meet mission requirements. If it is an economically re-flyable mission, reliability requirements can be somewhat relaxed. But if it is a high priority, minimum risk mission reliability requirements can be quite stringent. The effort to develop clocks for the GPS program would be a good example of a program with a minimum risk mission requirement. If the mission requires a highly reliable clock and the manufacturer doesn't have extensive experience in building space qualified clocks for efforts which requiring high reliability you can expect to experience considerable difficulty. Unfortunately our experience has shown there is a flip side to this coin. Sometimes a manufacturer with space hardware experience has established in-house production procedures based on what was considered acceptable for other programs. When this is the case, one might experience difficulty in introducing program specific reliability and quality program requirements. Specifications should include requirements for the manufacturer to provide a detailed reliability/quality program plan, even for an engineering development effort. We feel that at a minimum the program plans should include the items listed below in order their of priority:

- Parts, Materials and Processing program
- Vendor Performance Requirements
- Workmanship Standards
- Configuration Management
- Documentation Control
- Test Procedures
- Test system configurations

The hierarchy of this list should be modified as the program progresses. Test plans/procedures and documentation control will eventually become the more critical. Reliability requirements must be address at the very beginning of the effort. Attempts to introduce reliability practices after the baseline design has been established is one mistake one does not want to make. If the host system has stringent piece part quality requirements, specifications should clearly reflect these requirements in any effort above the level of prototype. If reliability predictions are to be required, the ground rules for performing the predictions should be clearly stated in the specifications. Mechanical reliability is an area often taken for granted in the early design stages. An attitude frequently encountered was "I can always make it strong enough to survive the launch environment". Our experience has been obtaining the mechanical reliability which meets the launch, shock and vibration environment, was one of the hardest to achieve and generally this requirement has zero room for sacrifice. As an aside one can expect to become familiar with DOD-STD-480 (waivers and deviations) the degree will depend on (a) experience of the manufacturer, (b) specification clarity/detail, and (c) adequacy of development effort.

IV ACCEPTANCE CRITERIA

Qualification requirements are generally used as the base line for the acceptance criteria. The qualifications requirements are generated from the host system operating environment and system specified performance and survivability requirements. Requirements imposed by military standards influence the acceptance criteria, but one must recognize that atomic clock technology is somewhat unique to space applications and tailoring of some of the requirements imposed by military standards is necessary. Verification that a given design will meet or exceed the minimum acceptance criteria can only be accomplished from the results obtained through the qualification and acceptance testing programs. Design analysis and predictions will only give a reasonable estimate of product performance. The decision to fly a candidate unit will be based solely on the test results. It is therefore very important that the qualification and acceptance test plans be carefully thought out to insure the data you get from testing will provide the information you really need to know. To insure that the data packages contained the right information the qualification and acceptance test plans are made part of our specifications. The test plans include the basic format for data presentation, but variations to accommodate a manufacturer's data collection schemes may be acceptable. The following is a list of some of the areas we consider to require special attention in the specifications:

- (1) Ambient or Thermal Vacuum Environment
- (2) Magnetic field
- (3) EMI/EMC
- (4) Cyclic or Incremental Profiles
- (5) Testing Sequence

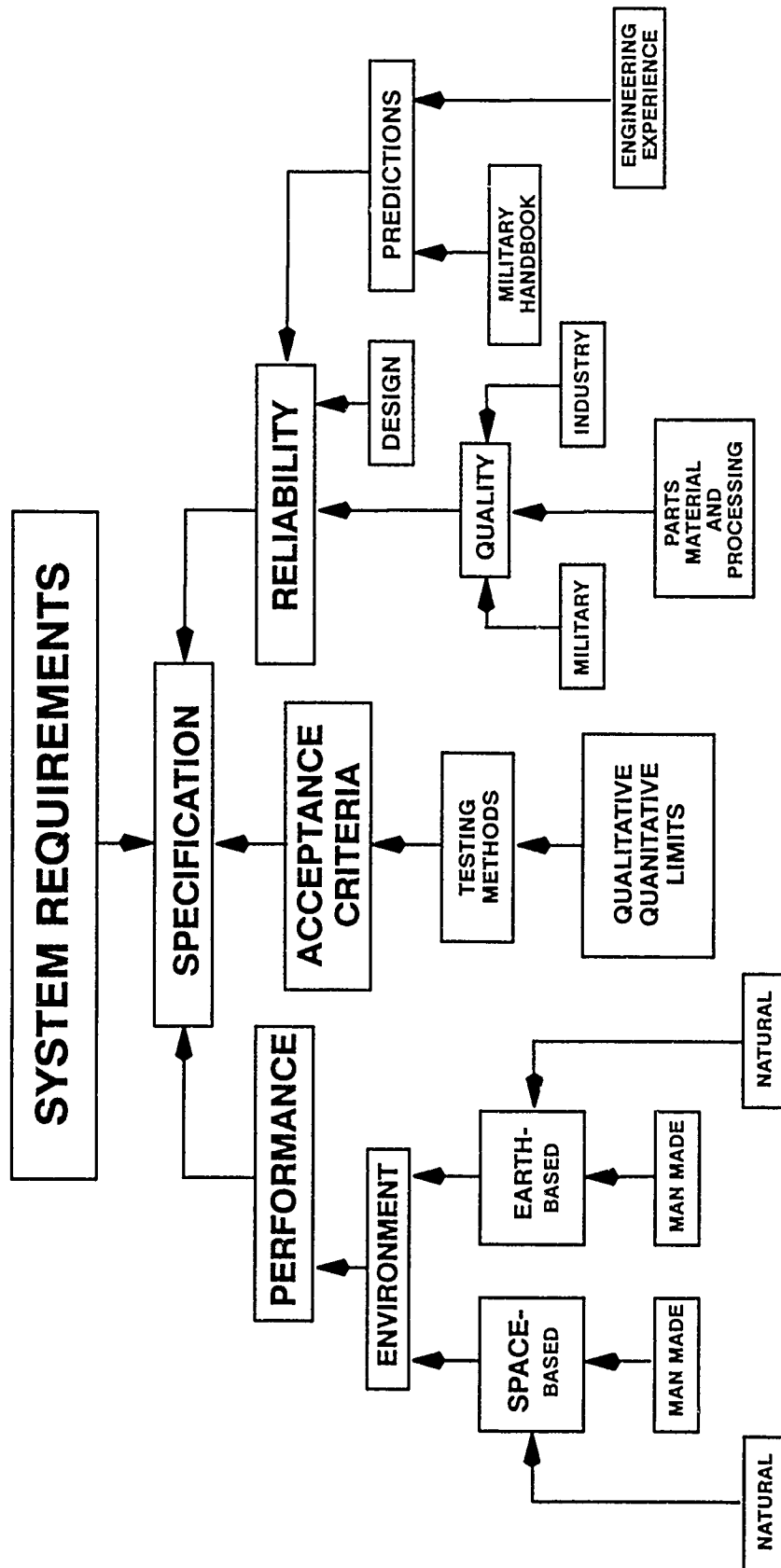
Figure 2 is an example of what can result when test plans are not spelled out in detail. The manufacturer's initial estimate of the unit's temperature coefficient was based on figure 2a. To verify the unit's temperature coefficient the test was repeated at NRL with smaller temperature steps, the results are shown in figure 2b. Operationally the unit's nominal base plate temperature would be in the range from 20 to 35 degrees celsius. In this range the unit exhibited a temperature coefficient of approximately $+1.55 \times 10^{-13}$ per degrees celsius, significantly greater than the manufacturer's initial estimate of 4.0×10^{-15} per degree celsius. The task of developing the test procedures was left to the manufacturer, but approval was required prior to their being instituted. The test procedures submitted by the manufacturer for approval should include schematics of test system configurations. Additionally pictorial drawings illustrating test article position and orientation should be included. The test data required by the specifications does not have to be limited to the qualification or acceptance test results obtained from the clock system. Specifications might include data requirements for subassemblies, especially parametric measurements made on the physic package. This information can be used to measure product variability.

The recommendations for specifications preparations for space qualified atomic frequency standards are based on our experience while developing cesium clock for GPS applications. Areas given special emphasis were done so because of the major difficulties we encountered in achieving these requirements.

TABLE I
Typical Reference Documents Encountered

(1)	DOD-HDBK-248	Guide for Application and Tailoring of Requirements for Defense Material Acquisitions
(2)	DOD-HDBK-343	Design, Construction, and Testing Requirements for One of a Kind Space Equipment
(3)	DOD-HDBK-344	Environmental Stress Screening(ESS) of Electronic Equipment
(4)	MIL-STD-461	Electromagnetic Emission and Susceptibility Requirements for the Control of Electromagnetic Interference
(5)	DOD-STD-480	Configuration Control-Engineering Changes, Deviations and Wavers
(6)	MIL-STD-490	Specification Practices
(7)	MIL-STD-781	Reliability Design Qualification and Production Acceptance Test: Exponential Distribution
(8)	MIL-STD-785	Reliability Program for System and Equipment Development and Production
(9)	MIL-STD-1540	Test Requirements for Space Vehicle
(10)	MIL-STD-1541	Electromagnetic Compatibility Requirements for Space System
(11)	MIL-STD-1543	Reliability Program Requirements for Space and Missile System
(12)	MIL-STD-1546	Part, Materials, and Processes Standardization, Control and Management Program for Spacecraft and Launch vehicles
(13)	MIL-STD-1546	Part, Materials, and Processes for Space and Launch Vehicles, Technical Requirements for
(14)	DOD-E-8983C	Electronic Equipment, Aerospace, Extended Space Environment
(15)	MIL-Q-9858	Quality Program Requirements
(16)	MIL-F-28811a(EC)	Frequency Standard, Cesium Beam Tube
(17)	FED-STD-209	Clean Room and Work Station Requirements, Controlled Environment

FIGURE 1



Frequency Offset x 1E12 Temperature Coefficient Two Point Method

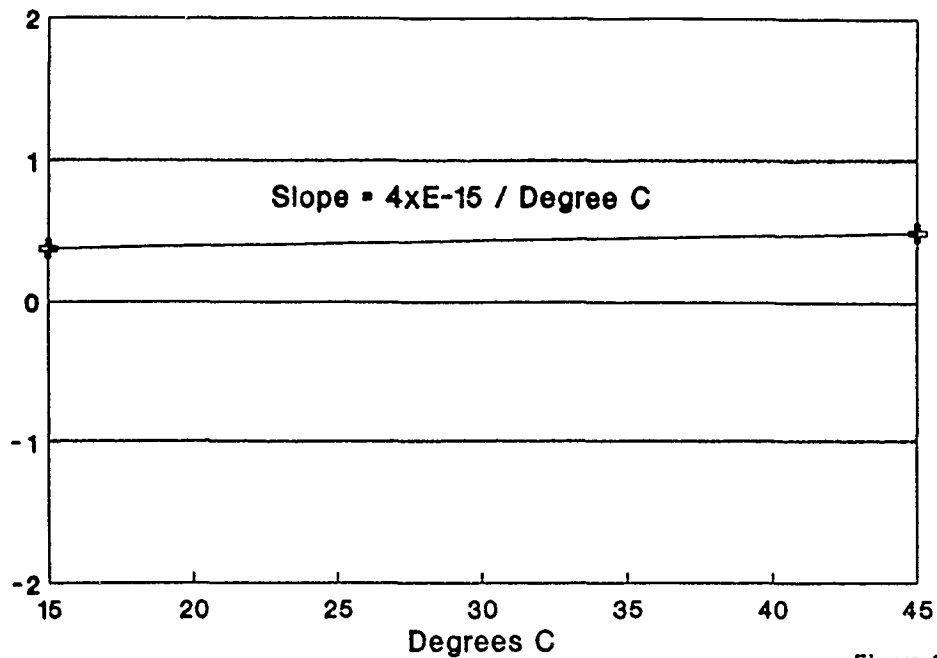


Figure 2A

Frequency Offset x 1E12 Temperature Coefficient Other Possibilities

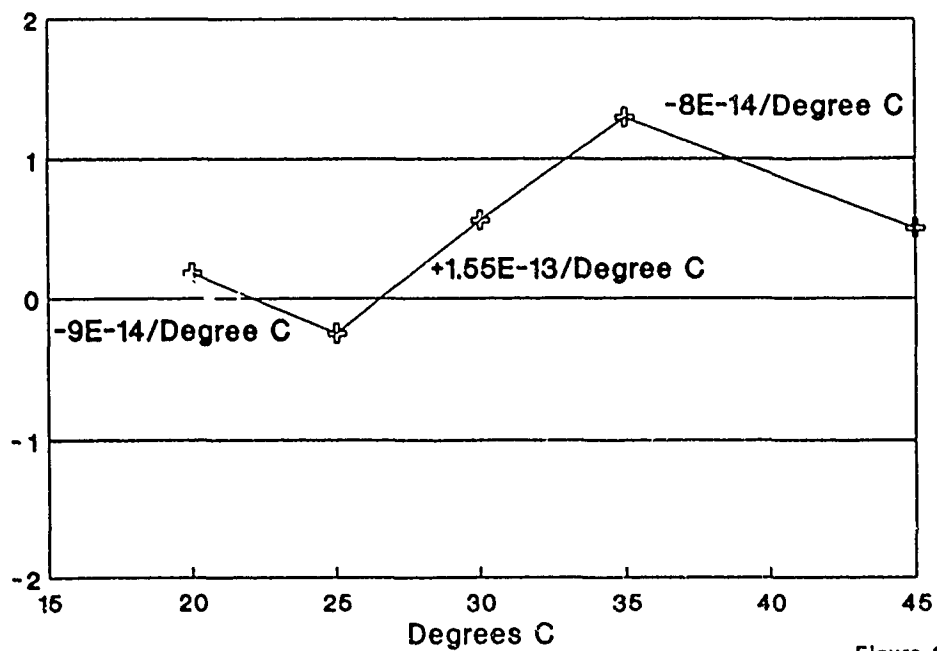


Figure 2B

Progress in transferring time using GLONASS satellites

P Daly & I D Kitching

Department of Electrical and Electronic Engineering
University of Leeds, Leeds LS2 9JT, United Kingdom

ABSTRACT

The Soviet Union's global navigation satellite system, GLONASS, currently has nine pre-operational satellites with the full complement of twenty-four satellites available possibly in two years at the present launch rate. Since only a single satellite is required for time transfer to a known location, the potential of Glonass as a disseminator of time and frequency can be evaluated in this pre-operational phase.

This paper discusses the timing references available from Glonass and how they are employed in a satellite-to-user time transfer link. Using the Glonass low precision codes, and without making dual frequency corrections, time transfer with Glonass is obtainable to precisions of the order of 100 nanoseconds or better. Data is presented showing the relationship between Glonass system time and UTC(USNO) over an extended period of time. Finally the linking of Glonass system time to UTC(SU) is shown to have been established since late 1988.

INTRODUCTION

Glonass provides worldwide time dissemination and time transfer services in the same manner as the NAVSTAR GPS and exhibits the same advantages as Navstar does over other existing timing services [1]. Time transfer is both efficient and economic in the sense that direct clock comparisons can be achieved via Glonass between widely separated sites without the use of portable clocks. Event time tagging can be achieved with the minimum of effort and users can reacquire Glonass time at any instant due to the continuous nature of time aboard the satellites.

The first release from the Soviet Union of detailed Glonass information occurred at the International Civil Aviation Organisation (ICAO) special committee meeting on Future Air Navigation Systems (FANS) in Montreal in May 1988 [2]. The report contained nominal orbital information as well as detailed descriptions of the Glonass C/A code structure and transmitted data message. Most of this information had already been made available via other publications [3], [4], [5]. The reader's attention is directed to the references at the end of this paper for more general Glonass information. Currently nine Glonass satellites are in full operation giving single satellite coverage at most locations almost 24 hours a day. These satellites are listed in Table 1 (Glonass 38 is included in the Table although its health gives cause for concern).

SAT ID	COSMOS	GLONASS	CHN	L1/MHz
1988-43A	1946	34	12	1608.7500
1988-43B	1947	35	23	1614.9375
1988-43C	1948	36	24	1615.5000
1988-85A	1970	37	18	1612.1250
1988-85B	1971	38	7*	1605.9375
1988-85C	1972	39	10	1607.6250
1989- 1A	1987	40	9	1607.0625
1989- 1B	1988	41	6	1605.3750
1989-39A	2022	42	16	1607.0625
1989-39B	2023	43	17	1605.3750

* health marginal
Current Active Glonass Satellites 1-11-89.
Table 1

TIME FROM GLONASS

Time transfer from Glonass is achieved in a straightforward manner, Figure 1. Each satellite transmits signals referenced to its own on board clock. The Control Segment monitors the satellite clocks and determines their offsets from the common Glonass system time. The clock offsets are then up loaded to the satellites as part of the transmit data message. A user at a known location receives signals from the satellite and by decoding the data stream modulated on to the transmission is able to obtain the position of the satellite, as well as the satellite's clock offset from the common system time, as a function of time. Hence the signal propagation time can be calculated at any instant. The time at which the signals are transmitted is also contained in the data message; by combining this with the propagation time and correcting for the satellite clock offset, the user can effect transfer to Glonass system time. Any other user who has a satellite visible is also able to transfer to the same time scale.

Though this simplistic approach will provide time transfer to the Glonass system time additional errors occur which must be corrected for or an allowance made for them in the error budget.

- 1) Position errors. Both the transmitted satellite ephemeris and the user's known location can contain errors which appear as biases in the measurements. This is particularly relevant in the case of Glonass as the co-ordinate system reference frame which is used is at present unknown and thus it would prove more profitable to solve for user position as well as time offset to remove position uncertainties.
- 2) Atmospheric delays. The transit time of the signals are affected by delays in the troposphere and ionosphere. Tropospheric delay can be minimised by selecting satellites at high elevation angles and can also be accurately modelled. The ionospheric delay is usually the largest error in time transfer. Models also exist for this, such as that used by the Navstar GPS, but are generally less accurate. The Navstar model results in a rms reduction in range error of 60 percent [6]. Ionospheric effects can be removed most effectively by making dual frequency measurements.

- 3) Errors may result in the calculation of signal propagation time if proper account is not taken of delays due to the rotation of the earth during the signal propagation time. This is a function of satellite position and user latitude. For the worst case of a user at the equator and a satellite due east or west on the horizon this effect can result in an error of

approximately 128 nanoseconds in the case of Glonass. The earth rotation error can be easily calculated and removed.

- 4) Receiver noise and biases. Receiver noise with zero mean can be removed by simple averaging, which can be readily applied for a stationary user. Biases such as receiver delay can also be subtracted from the measurements.
- 5) Other errors exist such as imprecision in satellite clock correction parameters and affects such as multipath.

SIGNAL TIMING REFERENCES

Timing references are contained in both the satellite code and transmitted data. The Glonass C/A code is a 511 bit maximal length sequence transmitted at a rate of 511 Kbits/s giving a code epoch every millisecond. The Glonass data message is represented as 50 baud data modulated on to the satellite code. The data transitions are co-incident with code epochs. The data is transmitted as 2.5 minute superframes; each superframe is divided into 5 half-minute frames and each frame consists of 15 two-second lines of data. Each frame contains the current time, satellite ephemeris, clock correction parameters and almanacs for five other satellites. Hence five frames are required to obtain all the almanacs. The 1 second epochs occur in the data at the beginning (even second) and middle (odd second) of each line. Figure 2 shows the content of one data frame.

GLONASS DATA MESSAGE

SATELLITE EPHEMERIS

Glonass ephemerides are represented by satellite ECEF position and velocity vectors as well as acceleration correction components. In general the ephemerides are updated half hourly giving a maximum ephemeris extrapolation period of 15 minutes. To calculate the satellite position the equations of motion of the satellite can be numerically integrated over the prediction period.

$$\ddot{\underline{r}} = -\frac{\mu}{r^3}\underline{r} + \nabla \left[\frac{3}{2} J_2 \frac{R_{\oplus}^2}{r^3} \left(\frac{1}{3} - \frac{z^2}{r^2} \right) \right] \quad (1)$$

Equation (1) gives the equation of motion of the satellite with a correction for the second zonal harmonic (J_2) of the earth's oblateness which is by far the largest perturbation on the Glonass satellites over the ephemeris validity period. Translation of position and velocity from the ECEF frame to the inertial frame is necessary before integration. The equation of motion can be expressed [7] in constituent components by equations (2) to (4).

$$\ddot{x} = -\frac{\mu}{r^3}x - \frac{3J_2\mu R_\oplus^2}{2r^5}\left(1 - \frac{5z^2}{r^2}\right) \quad (2)$$

$$\ddot{y} = -\frac{\mu}{r^3}y - \frac{3J_2\mu R_\oplus^2}{2r^5}\left(1 - \frac{5z^2}{r^2}\right) \quad (3)$$

$$\ddot{z} = -\frac{\mu}{r^3}z - \frac{3J_2\mu R_\oplus^2}{2r^5}\left(3 - \frac{5z^2}{r^2}\right) \quad (4)$$

These equations can be integrated by any suitable technique (Runge-Kutta 4th order for example) and with a suitable step size the satellite's position can be easily calculated to within 3 metres over half an hour. The acceleration terms in the data message correct for additional perturbations to the satellite's motion which are predominantly luni-solar in origin.

SATELLITE CLOCK OFFSETS

The satellite clock offset from the common Glonass system time is represented by two parameters [2].

- 1) γ_n - the relative frequency offset between the nth. satellite navigation signal frequency, f_n , and the nominal value, f_{hn} , of the nth. satellite frequency.

$$\gamma_n = \frac{f_n - f_{hn}}{f_{hn}} \quad (5)$$

- 2) τ_n - the nth. satellite time scale shift relative to the Glonass time scale.

The Glonass system time, t_{sys} , is related to the satellite time, t_{sv} , by,

$$t_{sys} = t_{sv} + \tau_n - \gamma_n(t - t_o) \quad (6)$$

$$\dot{\tau}_n = -\gamma_n \quad (7)$$

where t_o is the time of validity of τ_n and γ_n . In addition a third parameter τ_c representing the difference between Glonass system time and Moscow Time is transmitted.

Table 2 shows the range and resolution of the Glonass clock correction parameters.

Glonass	Bits*	Scale	Range	Resolution	Units
τ_n	22	2^{-30}	$\pm 2 \times 10^{-3}$	9×10^{-10}	s
γ_n	11	2^{-40}	$\pm 9 \times 10^{-10}$	9×10^{-13}	s/s
τ_c	28	2^{-27}	± 1	7×10^{-9}	s

* MSB = sign bit.

Glonass clock correction parameters.

Table 2

GLONASS TIME TRANSFER MEASUREMENTS

A series of measurements have been conducted of the difference between UTC(USNO) and Glonass system time. The arrangement of equipment to carry out these measurements is shown in Figure 3. A prototype single channel Glonass/Navstar GPS receiver has been constructed [8] which allows time comparisons between Glonass or Navstar system time and a 1 pps reference synchronised to UTC(USNO) available from a commercial Navstar receiver specified to be within 100 nsec of UTC(USNO) but in practice significantly better than this figure. The Navstar

system time / UTC(USNO) comparison is used as a calibration and confidence measurement since the offset between GPS time and UTC(USNO) is known and transmitted as part of the GPS data message. The measurements are conducted as follows.

A time interval counter measures the interval between the UTC(USNO) 1 pps and millisecond epochs decoded from the code generator of the test receiver. Whilst tracking a satellite time interval measurements are thus made of UTC(USNO) against the clock of the satellite currently being tracked but also including the signal propagation time. This measurement is then related to UTC(USNO) against system time by the following equations.

$$\rho = \text{UTC(USNO)} - t_{sv} + t_p \quad (8)$$

where, ρ = counter reading.

t_{sv} = satellite time.

t_p = signal propagation time (modulus 1 ms)

$$t_{sv} = t_{sys} - \delta t \quad (9)$$

where, t_{sys} = system time.

δt = difference in system time and satellite time.

$$\rho = \text{UTC(USNO)} - t_{\text{sys}} + \delta t + t_p \quad (10)$$

$$\text{UTC(USNO)} - t_{\text{sys}} = \rho - t_p - \delta t \quad (11)$$

The resolution on each measurement is 2 ns and the UTC(USNO) 1 pps is certainly accurate to within 100 ns. Measurements are made once per second, averaged over 3 minutes; the data is then stored for off-line processing.

DATE	SATELLITE	READINGS (1/SEC)	AVERAGE OFFSET/ns	STANDARD DEVIATION/ns
12/3/89	NAVSTAR 3	4320	-336	22
12/3/89	NAVSTAR 6	2520	-325	18
12/3/89	NAVSTAR 9	2340	-327	23
12/3/89	NAVSTAR 11	5580	-336	19
12/3/89	NAVSTAR 12	3420	-330	14
12/3/89	NAVSTAR 13	4990	-352	16
12/3/89	GLONASS 34	3960	29696	24
12/3/89	GLONASS 35	4860	29700	24
12/3/89	GLONASS 36	4320	29699	26
12/3/89	GLONASS 38	4320	29705	35
12/3/89	GLONASS 39	3780	29703	35
12/3/89	GLONASS 40	4140	29740	24
12/3/89	GLONASS 41	4680	29713	19

Navstar and Glonass system time offset from UTC(USNO).

Table 3.

Table 3 shows a set of measurements over a typical 24 hour period. The data has been corrected for tropospheric, relativistic and earth rotation effects but not for ionospheric effects. Since the measurements are taken over one day then the data is obtained from two passes of each satellite. An elevation mask of 10 degrees is used. The offset of UTC(USNO) from Navstar system time over this period as transmitted by the Navstar data message is about -344 ns demonstrating the effectiveness of the cross-calibration and lending confidence to the measurements of Glonass system time. The results relating Glonass system time to UTC(USNO) are very encouraging from the point of view of both consistency from one Glonass satellite to another (maximum difference in offset of the order of 50 nsecs) and of precision of the measurement (typically 20-30 nsecs). Since the largest unaccounted error (ionospheric propagation) is also of the order of 30 nsecs), the measurement limits have been reached.

GLONASS TIME SCALES & UTC(SU)

Figure 2 shows a plot of UTC(USNO) against Glonass system time over a period of about 12 months using an ensemble of available satellites. The plot shows clearly two phases of operation, the change-over occurring in March 1989. The first phase is characterised by a frequency offset of 0.18 ps/s and the second by an offset of 0.64 ps/s clearly indicating a frequency adjustment of the Glonass system time clock at the change-over point.

An additional clock correction parameter is included in the Glonass data message which relates the Glonass system time scale to the time scale at which ephemeris and satellite clock offsets are calculated. We will call this time scale Glonass ephemeris time; the offset between Glonass ephemeris time and Glonass system time is denoted in the transmitted data message by the parameter τ_c . Observations of τ_c over a period in excess of two years shows the offset between the time scales τ_c always maintained within approximately $\pm 30\mu\text{s}$ of each other. Under normal circumstances application of this parameter in the calculation of satellite location and clock offset is unnecessary since a nominal satellite velocity of 4 km/s and clock frequency offset of the order of 10 ps/s will provide insignificant corrections when changing from Glonass system time to ephemeris time. Figure 3 shows a plot of τ_c over the same time period as Figure 2. It can be seen that τ_c provides a somewhat less continuous time scale than Glonass system time. There is clear evidence of frequency changes in the plot and in addition a phase shift of about $3\mu\text{s}$ early in December 1988. The major significance of this phase change is seen in Figure 4 which portrays how the various Glonass time scales are linked. There are three separate traces on the plot which are as follows:-

- 1) Measurements at the University of Leeds of UTC(USNO) against Glonass system time as in Figure 2 but to a new time scale.
- 2) The same results as in 1) referred to Glonass ephemeris time by subtracting the transmitted parameter τ_c .
- 3) BIPM data giving UTC(USNO) - UTC(SU) as referred to the international reference centre in Paris for coordination of universal time (UTC).

Before early December 1988 Glonass ephemeris time was not identical with UTC(SU) but the phase reset at that time referred to earlier clearly initiated the synchronism of the two scales. This move was probably planned to take place by the start of 1989; during the whole of 1989 Glonass ephemeris time has been identical to UTC(SU). Reference of UTC(SU) to the BIPM by conventional means has been sporadic since July 1988. Clearly the time has arrived when international time coordination will be carried out primarily by means of navigation satellites, either those of the United States (Navstar GPS) or the

Soviet Union (Glonass). The implications for high-quality international time transfer as well as accurate and precise position-fixing on a continuous, global basis are

CONCLUSIONS

It has been demonstrated that time transfer with Glonass to a static user can be achieved to accuracies of the order of 100 ns or better while using the Glonass low precision C/A code phase and without dual frequency measurements. Results are repeatable cross-calibration with Navstar GPS provides a high confidence level. Glonass system time provides a time scale which has reliability and performance comparable to that of other international time scales and can be used as an intermediate time scale for clock comparisons between widely separated sites.

A direct linking has now been confirmed between Glonass system time and UTC(SU) as of late 1988. Previously Glonass system time had been referred to Moscow Time which was clearly not the same as UTC(SU). Now that both Navstar GPS and Glonass are both referred to their respective national time standards, UTC(USNO) and UTC(SU) respectively, the prospects for international time transfer by satellite are very encouraging.

Allan variance stability profiles of satellite system time as measured against UTC(USNO) have been produced extending from 1 to 64 days indicating the use of high-quality atomic oscillators, either Cesium or more likely Hydrogen Maser clocks, as the fundamental reference for Glonass system time.

Clearly the time has arrived when international time coordination will be carried out primarily by means of navigation satellites, either those of the United States (Navstar GPS) or the Soviet Union (Glonass). The implications for high-quality international time transfer as well as accurate and precise position-fixing on a continuous, global basis are extremely important.

REFERENCES

- [1] A J Van Dierendonck and W C Melton :
"Applications of Time Transfer Using Navstar GPS", The Institute of Navigation, Washington D.C., U.S., Special Issue on GPS, Volume 2, pp 133-146.
- [2] T G Anodina :
Working Paper -
"Global Positioning System GLONASS", Special Committee on Future Air Navigation Systems (FANS/4), International Civil Aviation Organisation (ICAO), Montreal, 2-20 May, 1988.
- [3] S A Dale and P Daly :
"Recent observations on the Soviet Union's Glonass Navigation Satellites", IEEE PLANS' 86 (Position Location & Navigation Symposium), Las Vegas, 4-8 November, 1986, pp 20-25.
- [4] S A Dale and P Daly :
"Developments in Interpretation of the Glonass Navigation Satellite Data Structure", IEEE NAECON'88 (National Aerospace & Electronics Conference), Dayton, Ohio, 23-27 May, 1988, pp 292-297.
- [5] S A Dale, P Daly and I D Kitching:
"Understanding Signals from Glonass Navigation Satellites", International Journal of Satellite Communications (John Wiley), Vol. 7, 1989, pp 11-22.

- [6] W A Fees and S G Stephens:
"Evaluation of GPS Ionospheric Time Delay Algorithm for Single-Frequency Users", IEEE PLANS' 86 (Position Location & Navigation Symposium), Las Vegas, 4-8 November, 1986, pp 206-213.
- [7] F T Geyling and H R Westerman:
"Introduction to Orbital Mechanics", Bell Telephone Laboratories, Addison-Wesley Publishing Company, 1971.
- [8] S A Dale, I D Kitching and P Daly :
"Position-Fixing using the USSR's Glonass C/A Code", IEEE PLANS' 88 (Position Location & Navigation Symposium), Orlando, 29 November - 2 December, 1988, pp 13-20.

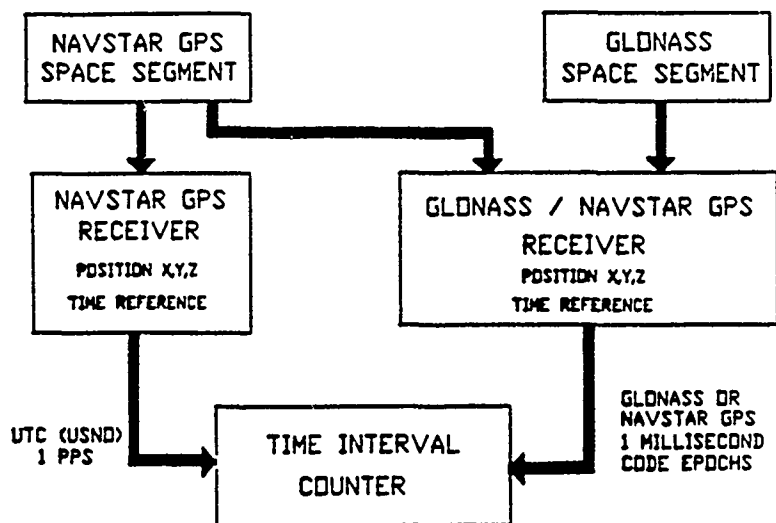


FIGURE 1.

TIME TRANSFER EQUIPMENT ARRANGEMENT

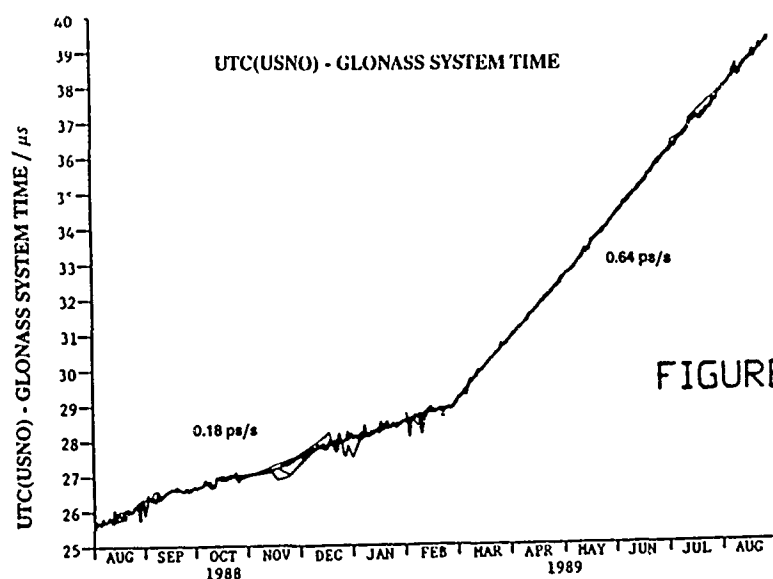


FIGURE 2.

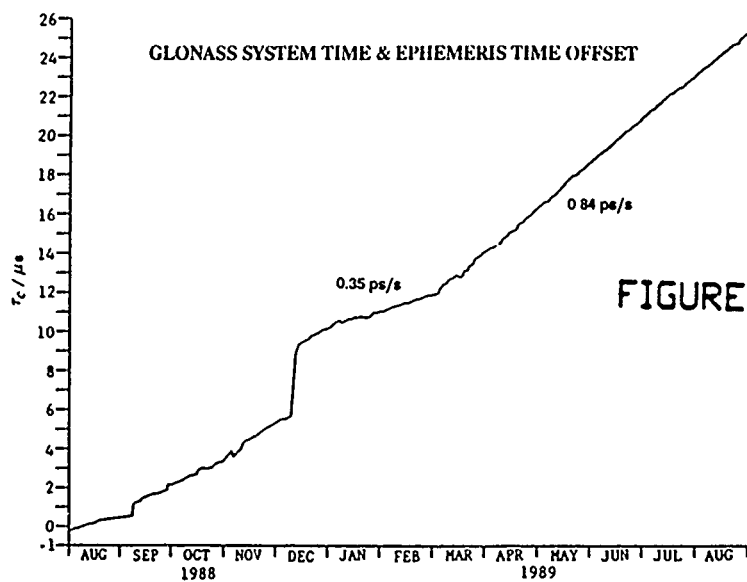


FIGURE 3.

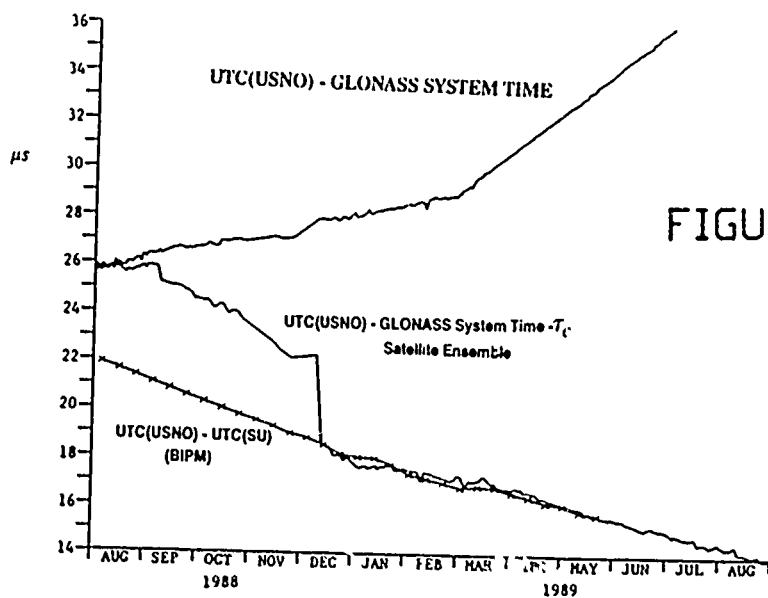


FIGURE 4.

QUESTIONS AND ANSWERS

ROBERT VESSOT, SAO: Can you tell me, in your opinion, what is the species of clock that they are most likely to have in orbit? I have heard reports of vastly improved rubidiums and ghastly cesiums, etc. What is your professional opinion?

MR. DALEY: Somebody put you up to that, right? I really don't want to say a lot about it, except that our evidence is that they are carrying atomic clocks. We have seen increasing performance of the on-board clocks. Evidence is that the present clocks are probably every bit as good as the NAVSTAR clocks. I say probably, because we have not finished our analyses yet. The early clocks were, as you say, representative of poor or mediocre rubidiums. Those steps in performance have been made over the last three years and I have no doubt that they will go on.

CARROLL ALLEY, U OF MARYLAND: Is there any evidence that the Soviet system itself is degraded, or is it working at its maximum performance?

MR. DALEY: We have no evidence of any degradation in performance, deliberate or otherwise. That doesn't say that it is not happening or couldn't happen. We look at the (edges ?) from GLONASS everyday, probably several hours a day, and we have never seen any evidence of SA or any other form of degradation. I believe that the Russians have announced that they can't do it even if they want to. Whether that is true or not, I don't know.

MR. VESSOT, SAO: Have you seen any evidence of cross-linking, satellite-to-satellite, in order not to wait for an orbit to send commands?

MR. DALEY: That one is easy—no, I don't know.

ROBERT VESSOT, SAO: What about corner reflectors? Do they have them? Professor Alley has, for at least a decade, been pleading with our people to put a corner reflector on one of these to resolve the clock vs. propagation and ephemeris issue. Do they have these?

MR. DALEY: My understanding is that some if not all of the GLONASS's do have corner reflectors on them.

MR. VESSOT: Can we track them then? We should be able to.

MR. DALEY: There are people in the audience who can answer that question much better than I can.

PROFESSOR ALLEY: Let me respond to that. Bob, there is an (name not clear) satellite which is totally covered with corner reflectors in the GLONASS orbits. It would be nice if there were corner reflectors on the GLONASS satellites themselves.

MR. DALEY: It is only hearsay, I have been told that they do.

PROFESSOR ALLEY: The half hour changes in the ephemeris message, is that transmitted from the ground to the satellites, or is it just a programmed change?

MR. DALEY: It is a programmed change.

PROFESSOR ALLEY: Do you have any idea how often they update the ephemeris?

MR. ALLEY: Almost certainly once a day.

RESULTS OF A BLOCK II GPS USERS SURVEY

Thomas R. Bartholomew
The Analytic Sciences Corporation (TASC)
1190 Winterson Road
Linthicum, MD 21090
and
Stephen M. Bloor
Department of Defense
Ft. Meade, MD

Abstract

As part of a system development the authors were required to select appropriate standards and cost-effective techniques for time recovery and frequency control. It quickly became apparent that GPS offered a good across-the-board solution to the system requirements for:

- time recovery
- synchrony
- frequency control
- syntony
- precise positioning.

It was also apparent, with the advent of Block II, selective availability (SA) and anti-spoofing (AS), that the performance of presently available time recovery receivers would potentially be inadequate to meet our system requirements. It was further evident that readily available, cost-effective receivers were not in the near-term plans of any of the contacted manufacturers. We therefore undertook to encourage the development and competitive availability of "authorized user" receivers capable of achieving the full time and frequency performance capabilities of GPS within the Block II environment. As part of that effort we reviewed our requirements with a representative set of receiver manufacturers. In addition, we distributed a questionnaire to over 1300 projected "authorized users". This was an attempt to determine:

1. the range of user requirements;
2. the size of the potential market; and
3. the degree of user interest in establishing an "authorized user" users group (AUUG).

This paper presents the results of the survey, reports on our progress in organizing the user/working group and briefly describes some of the concepts proposed to provide cost-effective solutions to the problem.

APPROACH

The initiative for the questionnaire was a direct result of an action item proposed at the May 11, 1989 USNO GPS Workshop.

The mailing list for the questionnaire was derived from the registration lists for the 1988 and 1989 Annual PTTI meetings, and the "Publication Series 4" mailing list provided by the USNO. The final list of 1100 names was assembled and culled to remove duplicates, foreign addresses and blunders.

The questionnaire was designed to be as simple as possible and was provided with a cover letter which contained essentially the same material as the above abstract. The seven questions posed in the questionnaire asked the user to:

1. Compare the users requirements to the attainable accuracy estimates of Table I. Table I was obtained from the USNO and is their estimate of the one sigma time recovery accuracy obtainable with SA and AS in Block II;
2. Provide estimates of required time and frequency accuracies if "authorized user" performance levels are required;
3. Estimate the number of "authorized user" GPS receivers required immediately and over the next 5 years;
4. Express interest in a "survey" option (probably a software option or addition) which would allow the timing receiver to be used as the reference end of a relative positioning system;
5. Provide any comments regarding SA and AS;
6. Express interest in an "authorized user" users group; and
7. State any restrictions on use of the responses.

The questionnaire, which is presented in its entirety in the following section, suffered from at least two major deficiencies. The three words "SPS (Standard Positioning Service) 'unauthorized user' " were omitted from the first question in the first mailing. This caused some "authorized users" to ignore the second question on specific requirements. Respondents in this category will be contacted by telephone as time and resources permit. The second difficulty occurred in questions 2) and 3) in that the time, frequency, and quantity categories were broken down into rather broad and unequal ranges. This caused some difficulty in our analysis in assigning specific values to the responses.

RESULTS

At this writing (November 22, 1989) responses are still coming in. We have received a total of about 175 replies with several classified as "non-responsive". Non-responsive was defined as follows.

1. not in time/frequency business at all;
2. total lack of understanding - "what is GPS?"; and
3. not now using and/or no future plans to use GPS.

There seemed to be a significant secondary distribution in that we received more than 20 responses from individuals in organizations who were not on our original mailing list. We had restricted our distribution to the USA and some of these came from other countries.

The data was entered into a simple data base and analyzed for "frequency of occurrence" in each of the question areas. There was no attempt to project the results of the survey to the total user population.

The following section presents the questions exactly as stated and shows the actual number of responses to each along with computed percentages from the 124 "responsive" questionnaires analyzed to date.

Q1. Will your (or your customers') time and frequency requirements be met by the projected Block II GPS SPS "unauthorized user" performance levels as estimated in Table I?

Yes 34 27% No 90 73%

[All of the 90 negative responses were found to be at least potentially eligible for AU status.]

Q2. If the answer to Q1. above is No, please indicate the required performance level:

Time		Frequency		Number
< 100 ns	19	1×10^{-10}		3
< 50 ns	5	1×10^{-11}		4
< 25 ns	15	1×10^{-12}		25
Other (1 ns to 15 ns)	16	Other (1×10^{-13} to 1×10^{-14})		10
Total		Total		42

[Of the 56 AU time requirement responses 31 (55%) need time recovery to 25 Ns or better. Of the 42 frequency requirement responses 35 (83%) need frequency to a part in 1×10^{-12} or better. Note that not all of the 90 potential "authorized users" responded to one or both elements of the requirements question.]

Q3. Please estimate the number of "authorized user" Block II GPS receivers equipped with security modules (PPS-SM's) which would be necessary to satisfy your (or your customers) requirements.

Immediate Total over 5 years

> 100	5	>100	14
50-99	3	50-99	1
20-49	4	20-49	12
10-19	6	10-19	9
01-09	59	01-09	59

[For the 90 AU responses only:

1. Estimated immediate requirement = 800-1000 receivers; and

2. Estimated total requirement over 5 years = 1600-2000 receivers.]

Q4. Would you (or your customers) be interested in a "survey" option which would allow centimeter level relative positioning?

Yes 63 [51% of all responses] No 49 [40% of all]

[Totals less than 100% because not all respondents replied to this question]

Q5. Please provide any other comments which you may have regarding SA-AS as it impacts your time, frequency, and positioning requirements.

[58% of all respondents provided comments. Several of these fell into 4 general areas as follows:

1. Hostility towards SA;
2. Questions and misconceptions regarding SA;
3. Questions and statements regarding alternative time recovery/time transfer methods including LORAN-C, two way communications via commercial COMSAT using spread spectrum modems, and similar schemes; and
4. Questions on the requirements for becoming an authorized user and participation in the planned users group.

Q6. If you are an "authorized user" would you be interested in participating in an "authorized user" users group (AUUG)?

Yes 66 *[79% of the AU responses]* No 24

Q7. Please detail any security, proprietary, or attribution restrictions you wish us to observe regarding your responses.

[Less than 2% had any sort of restrictions.]

PLANS

Where do we go from here? The time and frequency standards and requirements mentioned in Section I. have been determined and specified. The improvement of current systems and the development of future systems will require a series of steps with the following specific activities underway:

1. Propose the implementation/development of time recovery/frequency control receivers equipped with the necessary hardware (PPS-SM's and AOC's) to provide full access to GPS Block II performance capabilities for AU. It will be suggested that the initial acquisition be conducted such that 2 receivers are procured from each of 2 different manufacturers. The contracts could be written such that procurement options for 20 - 50 more receivers can be exercised.
2. Authorized User Users Group. This activity has been somewhat overtaken by events in that there is now an organized DoD PTTI AU Planning Group. They are in the first steps of planning, requirements definition and generating a receiver specification. This group is established under the auspices of the Superintendent of the USNO. The NRL will act as the technical coordinator.
3. Future activities with respect to this survey. We plan to analyze the remaining 40-50 responses received after our cutoff date. We will then total the results and provide a summary to all the respondents. We will further provide the survey in its entirety to the DoD PTTI AU Planning Group.

TABLE I
ESTIMATED ONE SIGMA TIME RECOVERY INCLUDING
THE EFFECTS OF S/A AND A/S

WITH A/S		UNAUTHORIZED USER NO KEYS	AUTHORIZED USER KEYS
NO S/A	SPA	40 ns.	40 ns.
	PPS	?	15 ns.
S/A	SPS	300 ns.	40 ns.
	PPS	?	15 ns.

QUESTIONS AND ANSWERS

UNIDENTIFIED QUESTIONER: Did the questionnaire go to people who had geodetic requirements, or were they excluded in principle?

MR. BLOOR: No, they weren't excluded at all. The questionnaires went to people who had always been on the PTTI mailing list or the PUB-4 mailing list. If there are geodetic users that were not surveyed, we are certainly interested in their responses.

SAME PERSON: I think that there are people that are not currently using GPS for geodetic purposes but who might benefit from it. I think that you have missed a significant number of folks. I am not not an authorized user, in your sense of the word, but I think that you have missed a large number of people that have a much stiffer requirement than you talked about.

MR. BLOOR: Stiffer time transfer requirements?

SAME PERSON: No, geodetic requirement.

MR. BLOOR: Yes, our geodetic requirements were very minor. I am mainly interested in time and frequency control.

UNIDENTIFIED QUESTIONER AND INDECIPHERABLE QUESTION:

MR. BLOOR: No, I am not the right person to state DoD policy. The term 'authorized user' has not been defined. Certainly, any military user could be an authorized user, however, that does not preclude others from being authorized users. Even, under certain interpretations of the draft policy, members of the civilian community. The keys are designed such that some keys are good for days and some are good for years. There has been discussion that certain civilian users might be authorized access via short term keys. I am not in the authorized user policy business.

GPS-UTC TIME SYNCHRONIZATION

C. H. MCKENZIE
W. A. FEES
R. H. LUCAS
H. HOLTZ
A. L. SATIN

The Aerospace Corporation
El Segundo, California

Abstract

Two automatic algorithms for synchronizing the GPS time standard to the UTC time standard are evaluated. Both algorithms control GPS-UTC offsets to within 10 nanoseconds, reduce operator workloads, and are simple to implement and maintain.

INTRODUCTION

The Global Positioning System (GPS) is required to synchronize its broadcast time standard to within one microsecond of the time standard maintained by the US Naval Observatory (USNO), Coordinated Universal Time (UTC) (Figure 1). (GPS will also broadcast the measured difference between GPS and UTC standards with an error no larger than 10% of the maximum allowed offset, allowing GPS users to synchronize to UTC time within 100 nanoseconds.)

Currently, GPS-UTC offsets measured at USNO are relayed to the GPS master control station at Falcon Air Force Base where master clock

corrections are manually computed to "steer" the GPS time to UTC time (Figure 2).

New ground software, developed by IBM Federal Systems Division, to be implemented in early 1990 will automatically steer GPS clock states under supervision by an operator. A modified bang-bang control law will be used to compute steering commands. We analyzed this law and a proportional phase-plus-frequency law to assess performance.

An automatic master-clock steering algorithm will improve synchronization and reduce operator workloads. The steering law must not exceed a GPS frequency-drift command limit of 1.5 nsec/day^2 , imposed to maintain user accuracy. The steering law must also be robust (insensitive to bad or missing data, human error, degraded clock performance, etc.) and simple to implement and maintain.

SYSTEM MODELS

Figure 3 shows a highly-aggregated block diagram of the GPS clock-steering process. The frequency-drift command is integrated twice (GPS-steering block) to obtain a GPS-time correction. We ignore satellite updating lags because the update process is fast compared to the clock-steering response. Feedback drives compensated GPS time (GPS physical clock output plus steering time correction) to UTC time. GPS-UTC phase-offset measurements drive the steering law.

GPS clock phase is modeled as a two-stage integration process with random walk phase and frequency components (Figure 4). Two types of clocks are considered, a single Cesium clock and an ensemble of hydrogen-maser (H-Maser) clocks.

GPS-UTC phase-offset measurements to different GPS satellites are obtained at about 15-minute intervals. Our model assumes 20 nsec (1σ)

white measurement noise, reflecting primarily satellite-clock and ephemeris errors and assuming independence between satellites. USNO phase-offset measurements are directly transmitted to Falcon and processed by a two-state Kalman filter. (Currently, phase and frequency offsets derived from least-squares-processing of measurements are transmitted from USNO to Falcon.) The filter is supplied with the steering-command time history and measurements are edited to remove outliers.

STEERING CONTROL LAWS

Two automatic steering control laws have been proposed, one by the GPS ground-system contractor (IBM) and the other by The Aerospace Corporation.

IBM's modified bang-bang control law (Reference 1) attempts to null phase and frequency offsets in minimum time subject to a frequency-drift command limit of 1.5 nsec/day^2 (Figure 5). The algorithm computes a discriminant, D , every ΔT seconds which is used to determine the frequency-drift command for that interval. Aerospace's proportional phase-plus-frequency law (Figure 6) is a standard position-plus-rate feedback law modified by the addition of a limiter on the frequency-drift command.

LINEAR ANALYSIS OF AEROSPACE LAW

A covariance analysis of the proportional Aerospace law is possible (see Appendix). (The nonlinear IBM law can only be evaluated by simulation.) Figures 7-10 summarize predicted performance and parameter sensitivities of the Aerospace law. The control gains can be selected to minimize the phase-error covariance while keeping the maximum RMS frequency-drift command less than 1.5 nsec/day^2 . The covariance analysis predicts a steering error of about 7 nsec for the cesium clock

(Figure 7) and 1.5 nsec for the H-Maser ensemble (Figure 8). Control gains can be varied significantly about their optimal values without significantly degrading steering performance, which allows the same gains to be used for either cesium and H-Maser clock systems. The cesium clock system is more sensitive than the H-Maser clock ensemble to clock noise variations, however.

SIMULATION OF IBM AND AEROSPACE CONTROL LAWS

Typical time response of the two control laws is illustrated in Figure 11. The IBM bang-bang law nulls the initial rate offset slightly faster than the Aerospace proportional law. Averaged steady-state errors are summarized for simulated cesium clock (Table 1) and H-Maser ensemble (Table 2) systems. The performance of the Aerospace law agrees with covariance analysis predictions. The performance of the IBM law is comparable to the Aerospace law for 15-minute updates, but worse with daily updates because its bang-bang action generates maximum RMS frequency-drift commands.

CONCLUSION

Both the IBM and Aerospace laws control GPS-UTC offsets to within 10 nsec, significantly better than the one microsecond requirement and the 100 nsec required broadcast accuracy. In fact, the residual steering error will likely be dominated by unmodelled factors such as data transmission errors between USNO and Falcon. The Aerospace law is smoother; the bang-bang IBM law reduces large initial offsets more quickly. Either law is straightforward to implement and maintain.

APPENDIX
COVARIANCE ANALYSIS OF AEROSPACE STEERING LAW

The Aerospace clock-steering model in Figure 6 (neglecting the limiter on the steering command) is described by:

$$x(k+1) = Ax(k) + Bw(k) \qquad \text{cov}[w] = Q \qquad (A1)$$

$$A = \begin{bmatrix} 1 & T & 0 & 0 \\ 0 & 1 & -K_1 T & -K_2 T \\ G_1 & G_1 T & 1-G_1 & T(1-G_1) \\ G_2 & G_2 T & -G_2-K_1 T & 1-T(G_2+K_2) \end{bmatrix}$$

$$B = \begin{bmatrix} T & 0 & 0 \\ 0 & T & 0 \\ G_1 T & 0 & G_1 \\ G_2 T & 0 & G_2 \end{bmatrix}$$

$$x(k) = \begin{bmatrix} \theta(k) \\ \omega(k) \\ \hat{\theta}(k) \\ \hat{\omega}(k) \end{bmatrix} \qquad w(k) = \begin{bmatrix} w_1(k) \\ w_2(k) \\ v(k) \end{bmatrix}$$

where

$\theta(k)$ = clock-phase offset

$\omega(k)$ = clock-frequency offset

$\hat{\theta}(k)$ = estimated clock-phase offset

$\hat{\omega}(k)$ = estimated clock-frequency offset

K_1 = phase-control gain

K_2 = frequency-control gain

T = time step

G_1 = phase Kalman gain

G_2 = frequency Kalman gain

$w_1(k)$ = phase clock noise

$w_2(k)$ = frequency clock noise

$v(k)$ = measurement noise

The covariance of $x(k)$ is given by

$$P(k+1) = AP(k)A' + BQB' \quad (A2)$$

The steady-state covariance was determined by the methods in References 2 and 3. The covariance of the frequency-drift command is given by

$$\text{cov}[\theta_c] = K_1^2 \text{cov}[\theta] + 2 K_1 K_2 \text{cov}[\theta, \omega] + K_2^2 \text{cov}[\omega] \quad (A3)$$

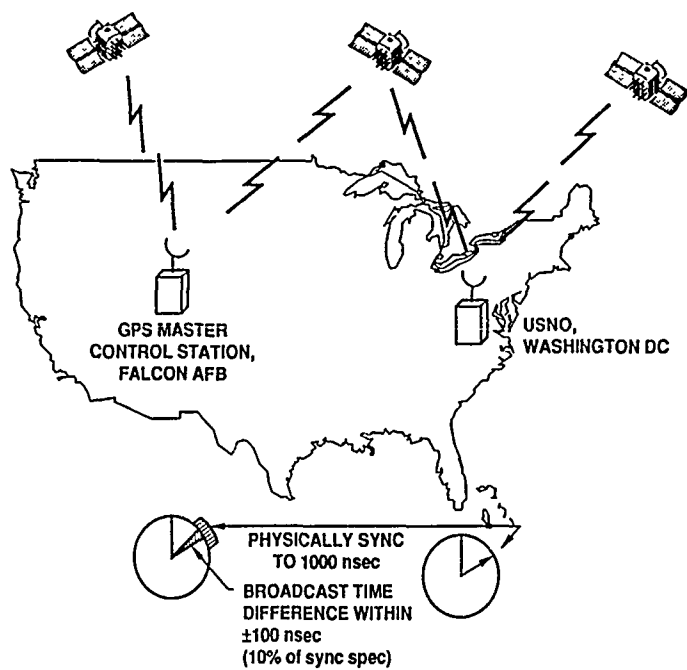


FIGURE 1. GPS-UTC SYNCHRONIZATION REQUIREMENTS

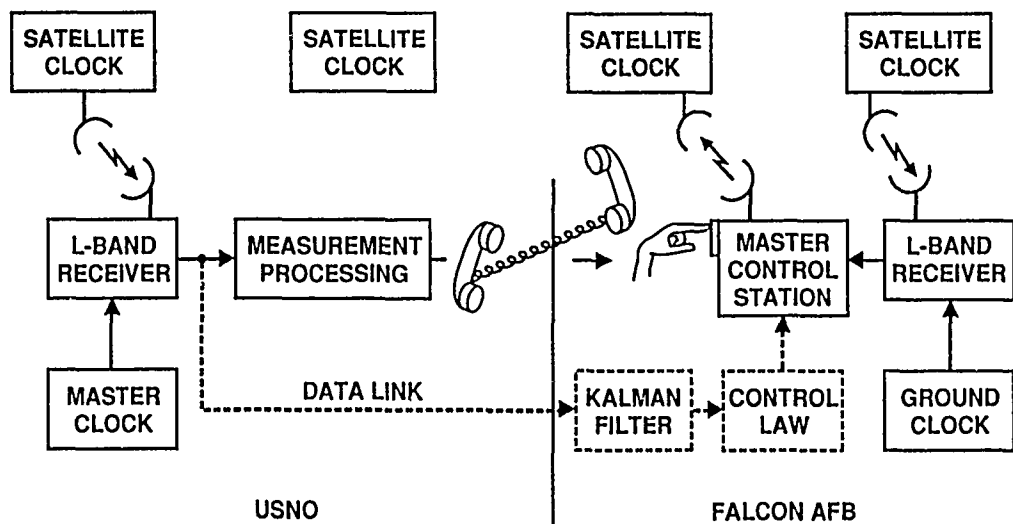


FIGURE 2. GPS-UTC SYNCHRONIZATION

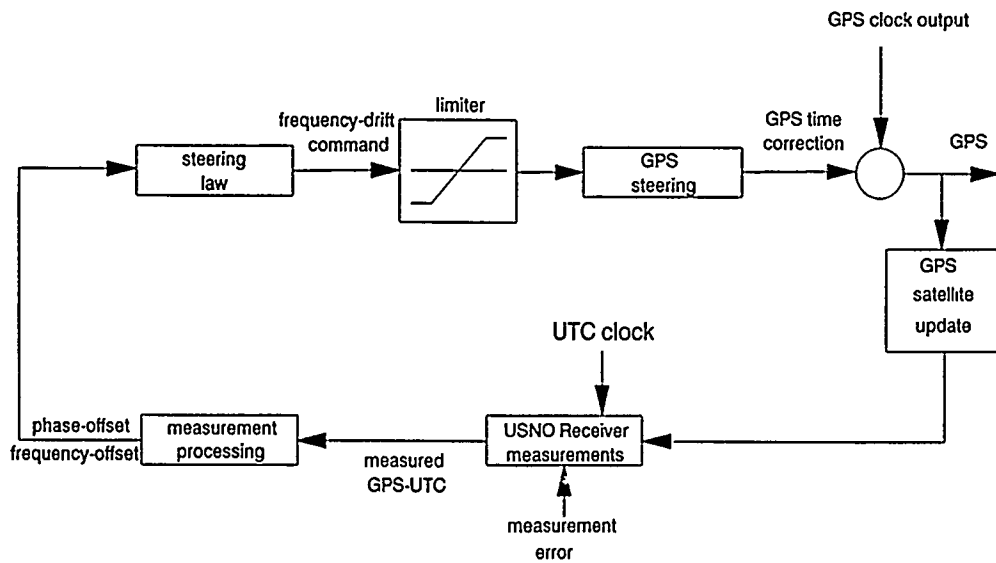


FIGURE 3. GPS CLOCK STEERING MODEL

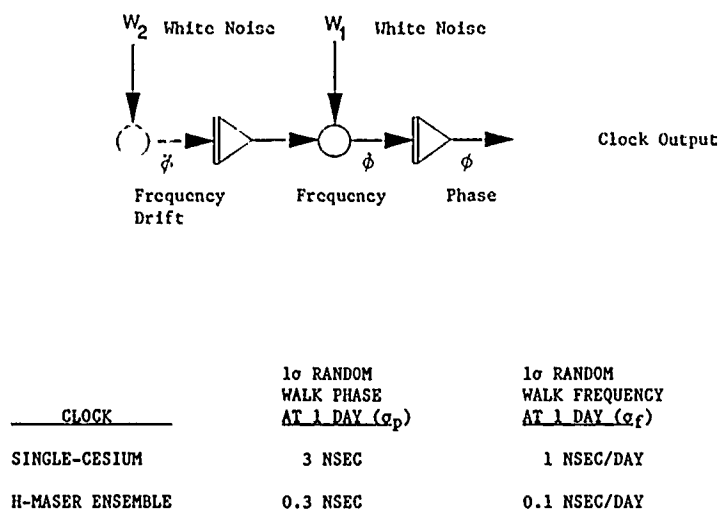


FIGURE 4. GPS CLOCK MODELS

DEFINE DISCRIMINANT = D

$$D(b, f) = b + \frac{f|f|}{2U}$$

b = CURRENT GPS-UTC PHASE OFFSET (SEC)

f = CURRENT GPS-UTC FREQUENCY OFFSET (SEC/SEC)

COMPUTE FREQUENCY-DRIFT STEERING COMMAND = \dot{f}

IF $|D(b, f)| < \text{TOL}$ THEN $\dot{f} = -\text{SGN}(f) \cdot \text{MIN}(U, |f|/\Delta T)$

IF $|D(b, f)| \geq \text{TOL}$

IF $|f| < f_{\text{max}}$ or $f \cdot D(b, f) > 0$

$$\dot{f} = -U \cdot \text{SGN}(D(b, f))$$

OTHERWISE

$$\dot{f} = 0$$

PARAMETERS: $U = 2 \times 10^{-19}$ SEC/SEC² (MAXIMUM FREQUENCY DRIFT)

$f_{\text{max}} = 5 \times 10^{-14}$ SEC/SEC (MAXIMUM FREQUENCY)

TOL = 10^{-9} SEC (BIAS ERROR TOLERANCE)

ΔT = STEERING-LOOP UPDATE PERIOD (NOMINALLY 900 SECONDS)

FIGURE 5. IBM STEERING LAW

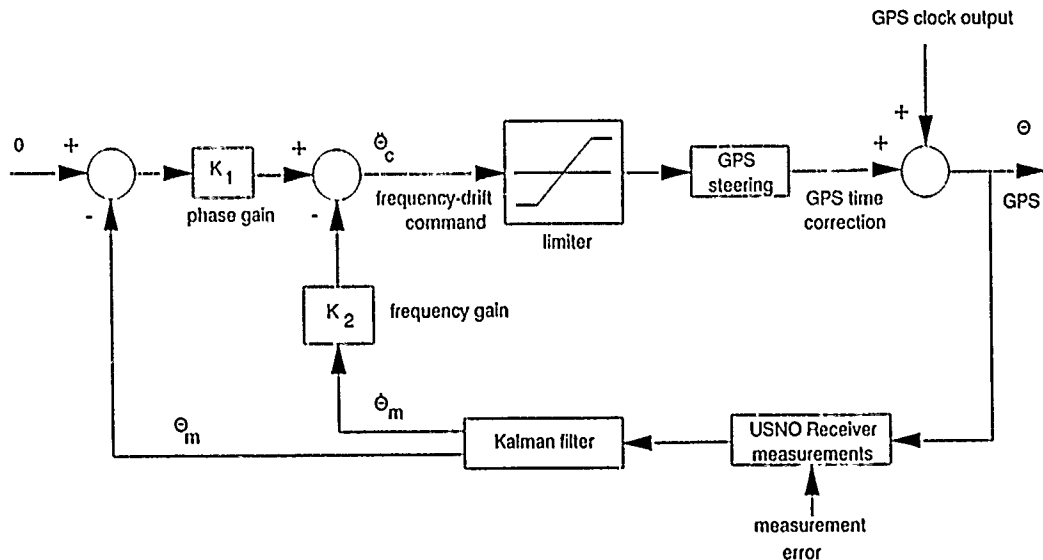


FIGURE 6. AEROSPACE STEERING SYSTEM

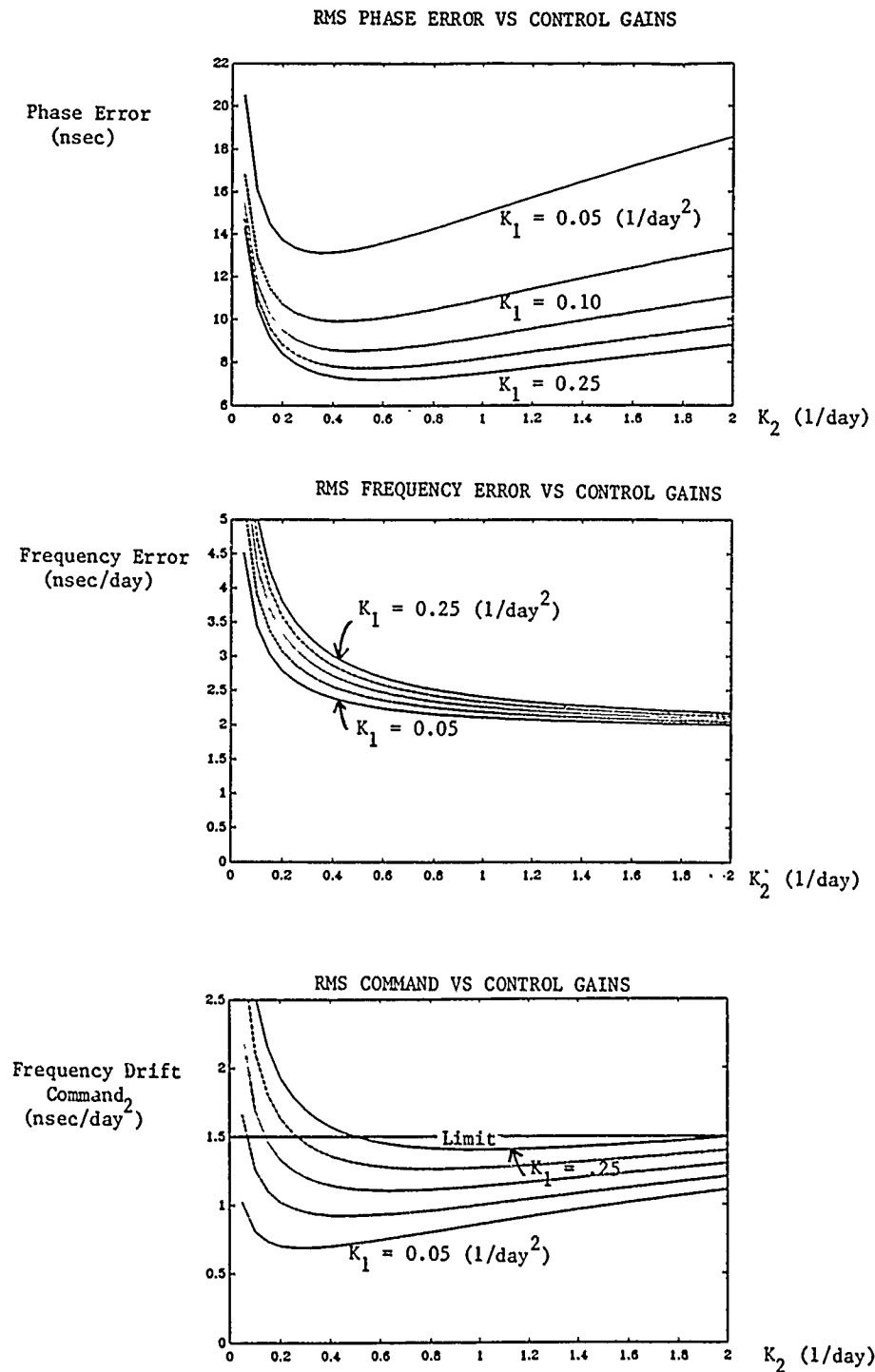


FIGURE 7. STEERING PERFORMANCE VS. CONTROL GAINS FOR CESIUM CLOCK

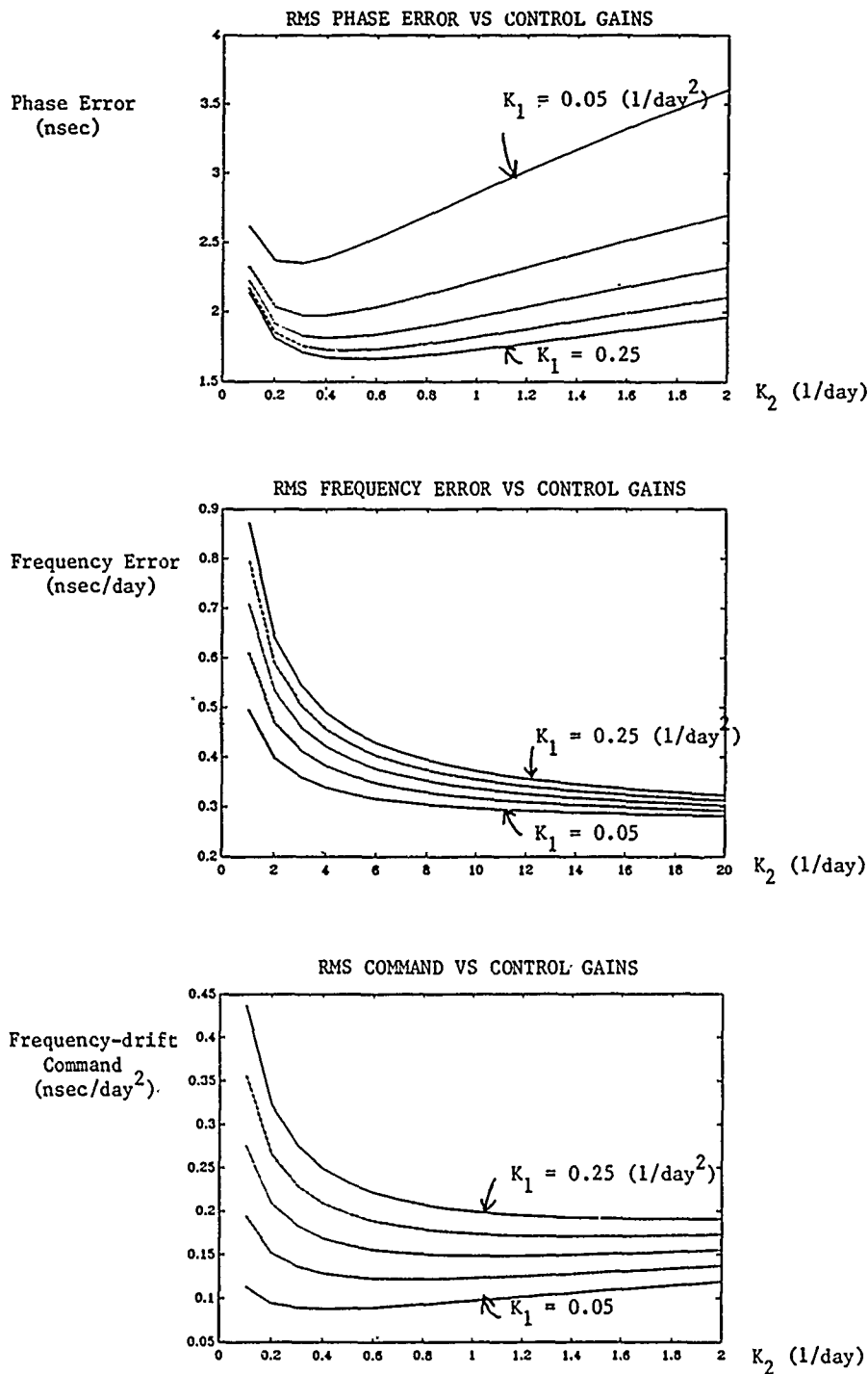


FIGURE 8. STEERING PERFORMANCE VS. CONTROL GAINS FOR H-MASER CLOCK ENSEMBLE

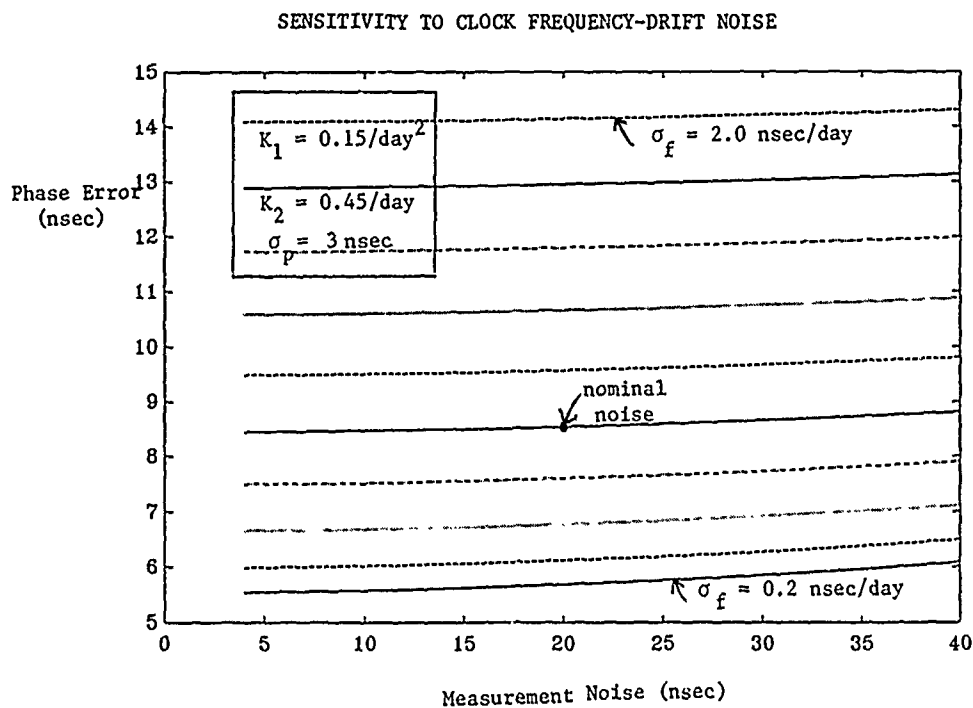
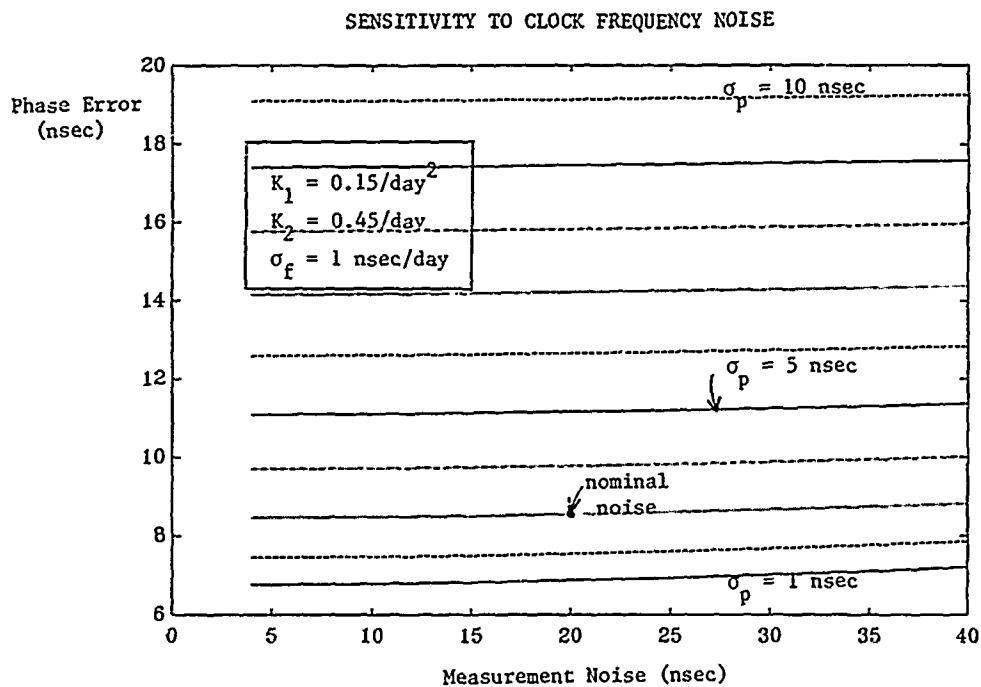


FIGURE 9. STEERING PERFORMANCE SENSITIVITY TO CLOCK AND MEASUREMENT NOISE FOR CESIUM CLOCK

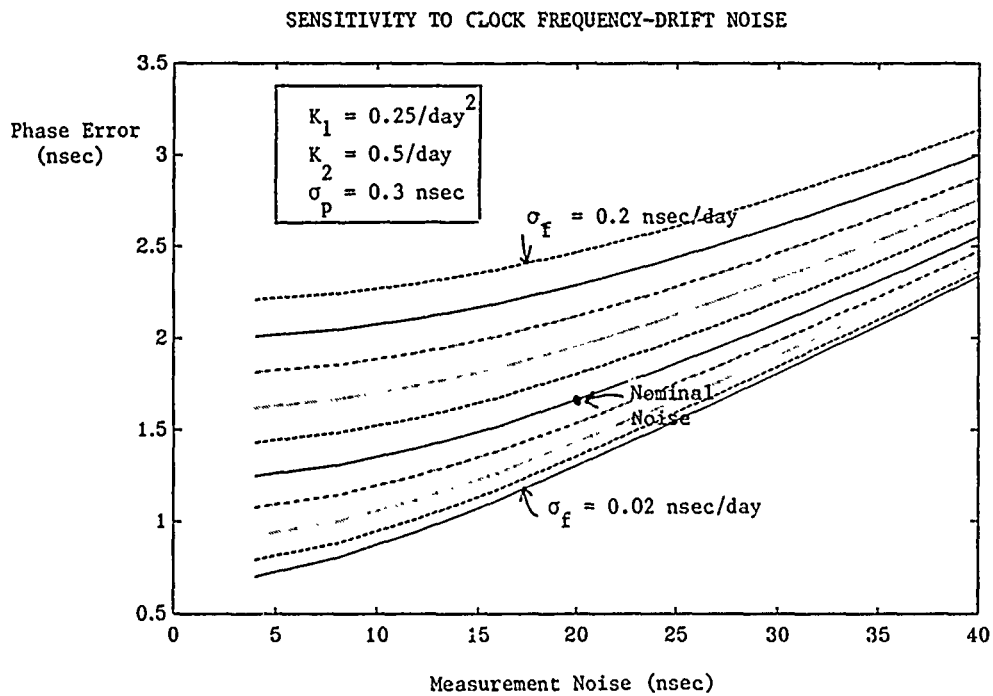
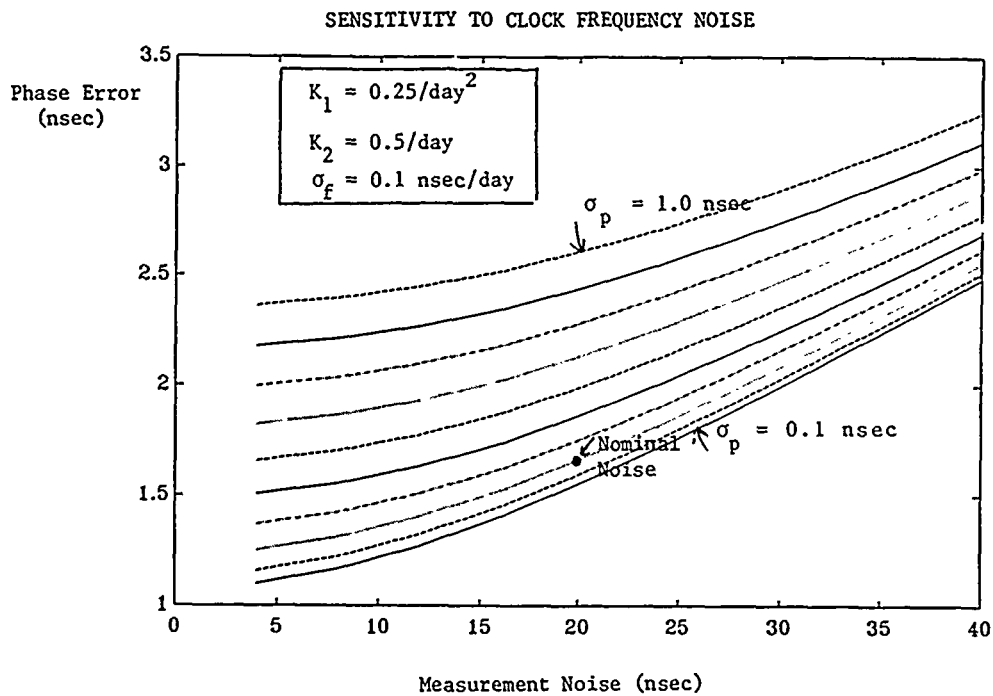


FIGURE 10. STEERING PERFORMANCE SENSITIVITY TO CLOCK AND MEASUREMENT NOISE FOR H-MASER CLOCK ENSEMBLE

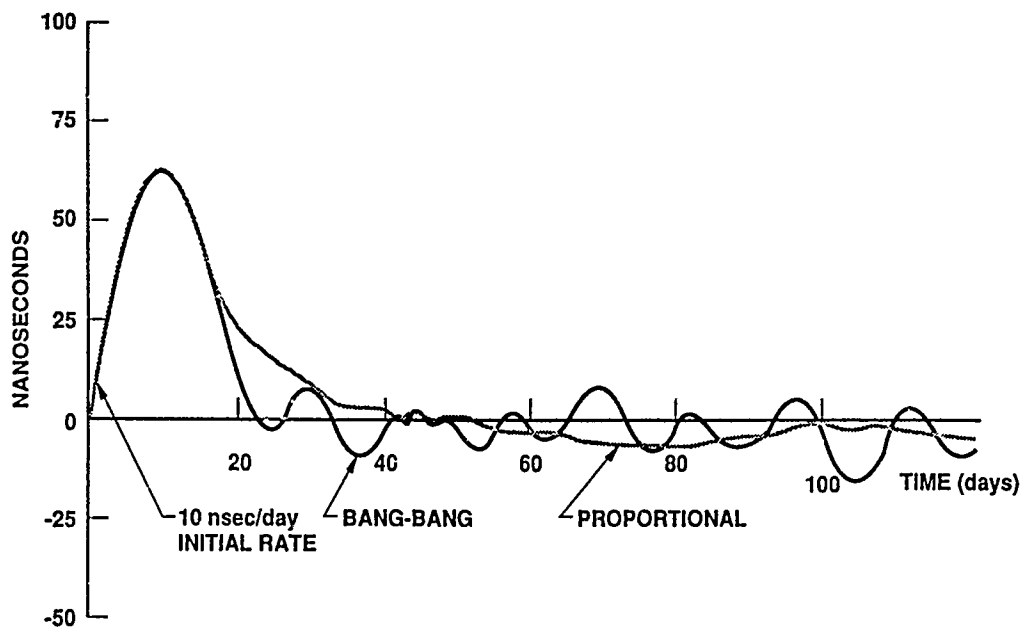


FIGURE 11, TRANSIENT RESPONSES

References

- (1) Brown, K., "Optimal Ensembling for GPS and Other Systems of Clocks", IBM Federal Systems Division Draft, 14 July 1987.
- (2) Lewis, Frank L., "Optimal Estimation", 1986.
- (3) Brewer, John W., "Kronecker Products and Matrix Calculus in Systems Theory", IEEE Transactions on Circuits and Systems, September 1978.

QUESTIONS AND ANSWERS

AL KIRK, JPL: Are you trying to steer all the clocks on the satellites, or only the master clock at Falcon?

MS MCKENZIE: Currently, only the master clock is steered.

MR. KIRK: But you do plan to steer all the clocks eventually?

ANSWER FROM THE AUDIENCE, NOT INTO THE MICROPHONE, INDECIPHERABLE

UNIDENTIFIED QUESTIONER: Since this is one of my favorite subjects at (unclear on the tape), I couldn't resist making some comments here. One is that the current implementation, I believe there is a requirement that there be a man in the loop to steer them rather than using an automatic control. We have had a great deal of discussion with them on the installation of timing systems out there and they insist on that. An automatic control would not be implemented in that case.

MS MCKENZIE: My understanding is there is automatic control under the supervision of an operator.

SAME PERSON: He would control it, input it or simply watch its operation? I am not sure about that. Automatic control is what bothers me about that. The other comment is about orbital errors being significantly less than clock errors. I would have to disagree about that. I think that the basic error of the system shows the clock and orbital errors being about the same magnitude. It is not clear that they have been separated out in the system so you can discount them in a steering mode like this.

ANSWER FROM THE AUDIENCE: The clocks that are in the current GPS are performing, most of them at least, much better than specifications. The comments are related mostly to the specifications than to actual achieved performance at this point in time. The original Block One clocks were specified at 2×10^{13} . We are achieving much better than that, and therefore the clock performance is good. What we are talking about in terms of clock performance is the ability to predict the clock, and the ability to predict the ephemeris. Ephemeris predictions are pretty stable. They are more bounded, but pretty stable in the prediction time, whereas the clocks randomly deviate from their upload values. For that reason we are saying that the clocks themselves, in prediction, are worse than the ephemeris in prediction. In the analysis the clock and ephemeris are part of the noise as received by USNO. In other words, when they receive time, it is a summation of the two. That was modeled as noise in the simulation. As to the question of manual vs. automatic: daily reports are received from USNO and are used for steering currently. It's a manual process and maybe the steering commands are set up once a month, or something like that, because of stability of the system and the requirements of the system don't dictate more frequent steering. This concept, and what is going to be implemented shortly, is that daily things are received and are input manually, not automatically, but still daily. The analysis included the time delay of one day in the steering.

UNIDENTIFIED QUESTIONER: You seemed to indicate that the proportional steering law resulted in a smaller rms than the bang-bang steering law. Why are you implementing the bang-bang steering law?

MS MCKENZIE: The bang-bang law does have a couple of advantages, one is that it is not necessary to select control gains, it also has a slightly faster response to transients. On the other hand, the proportional law gives a slightly better steady state result. There is not enough evidence to push for the implementation of the proportional law. IBM, the contractor, had experience with the bang-bang law and decided to implement that one. The steady state error for both laws is much better than the requirements.

AL GUEVARA, MCS: I am one of the individuals involved in determining the steering for GPS. One of my concerns with the bang-bang law—how often are you assuming the frequency and phase offsets are being updated in the MCS?

MS MCKENZIE: Measurements are processed daily, but there is a fifteen minute interpolation loop,

so the commands can change every fifteen minutes.

MR. GUEVARA: So every fifteen minutes they are supposedly going to be looking at the data base inputs as the steering is implemented. Is that a correct assumption?

ANSWER FROM THE AUDIENCE, INDECIPHERABLE

GERNOT WINKLER, USNO: There is another point. That is the reliability and robustness of operation. It is a weakness of the bang-bang method that, in the absence of steering information or severance of the control loop, you are going to go off at maximum rate. I think that that is a mistake.

MS MCKENZIE: That is a good point.

PRECISE EPHEMERIDES FOR GPS TIME TRANSFER

W. Lewandowski
Bureau International des Poids et Mesures
Pavillon de Breteuil
92312 Sevres Cedex, France
and
M. A. Weiss
United States Department of Commerce
National Institute of Standards and Technology
325 Broadway, 576
Boulder, Colorado 80303-3328

Abstract

The present technology of atomic clocks motivates time transfer techniques with nanosecond accuracy. Global Positioning System (GPS), the most common means for international time comparisons could achieve such accuracy over short distances (up to 1000 km). Over intercontinental distances the accuracy of the GPS time transfer ranges between 20 and 30 ns. Some of the principal error sources are the broadcast ephemerides, the broadcast ionospheric model, and the local antenna coordinates. This study investigates the quality of broadcast ephemerides by comparing them with precise ephemerides and by using precise ephemerides for time transfer. Another aspect of this work is to suggest a strategy to overcome the planned degradation of GPS satellite messages via Selective Availability (SA).

INTRODUCTION

The use of the Global Positioning System (GPS) for international time comparisons is continuously improved by adoption of more accurate antenna coordinates, introduction of double frequency ionospheric calibrators, organization of differential calibrations of receivers and refinement of data processing. This study examines the impact of the error in satellite position from the use of broadcast ephemerides on common-view time transfer^[1].

Table 1 demonstrates the impact for the most unfavorable case, when a bias in satellite position is parallel to the baseline between two timing centers. For a baseline of 9000 km (Europe-Japan) a bias of 15 m will introduce an error of 43 ns in time transfer using a single common-view measurement. Of course in practice a time comparison between two laboratories is realized by an averaging of a number of common-view measurements and so this error is reduced.

The quality of broadcast ephemerides over a two month period was studied in two ways: a direct comparative study of broadcast versus precise ephemerides, and a comparison of common view transfer using broadcast versus precise ephemerides.

The precise ephemerides used in this work were produced by the Naval Surface Warfare Center (NSWC); the broadcast ephemerides were recorded in Wettzel (Federal Republic of Germany).

Error in satellite position can be a major problem during the future implementation of Selective Availability (SA); the use of precise ephemerides and other possible ways of facing this challenge are discussed.

BROADCAST EPHEMERIDES

The GPS broadcast ephemerides are computed by the Air Force Operational Control Segment (OCS). The OCS has global tracking and monitor stations located at:

- -Falcon (U.S.A., Colorado Springs, Long.= 255.5 deg. E, Lat.= 38.5 deg. N),
- -Kwajalein Island (U.S.A., Pacific Ocean, Long.= 167.3 deg. E, Lat.= 9.1 deg. N),
- -Ascension Island (Great Britain, Atlantic Ocean, Long.= 345.8 deg. E, Lat.= 7.6 deg. S),
- -Diego Garcia Island (Great Britain, Indian Ocean, Long.= 72.2 deg. E, Lat.= 6.3 deg. S),
- -Hawaii (U.S.A., Pacific Ocean, Long.= 202.5 deg. E, Lat.= 20.5 deg. N).

Multichannel double frequency receivers are deployed at each of these sites to allow all satellites in view to be tracked simultaneously. Performed measurements are pseudo-range, Doppler, and ionospheric delay.

Data are sent in real time to the master control station for use in the Kalman filter which estimates the clock and orbit states for each satellite. These states are used to upload information to the satellites, which they in turn transmit to users. The ephemerides are among these broadcast data.

The orbit states in the Kalman filter for a given satellite are estimated as corrections to a reference orbit. The reference orbit is based on previous data and predicted once per week for the next week. With a reference orbit thus established, the tracking data are used to improve the orbit, and compute corrections to the reference orbit once every 15 min.

When an upload is required, the most recent corrections to the reference orbit are applied linearly to predict the next two weeks of ephemerides. The information in the upload consists of fourteen days of one-pages, though normally a new upload is done at least once a day. A satellite transmits a new page of parameters during each hour. Each one-hour page is the first hour of a fit optimizing parameters to four hours of estimates of the satellite orbit from the Kalman filter. The reference time for this fit is in the center of the four hours. Thus, a satellite transmits the same parameters for an hour, and these parameters are actually good for four hours.

The frequency of uploads is driven by a 6 meter User Range Error (URE). The actual time of an upload is decided by a number of considerations such as URE, location of satellite, and availability of the uplink. Currently the OCS is uploading the GPS satellites 1 to 3 times per day. It can happen that an upload does not improve the URE, in which case it can be immediately followed by another.

PRECISE EPHEMERIDES

The GPS precise ephemerides and clocks were computed at the Naval Surface Warfare Center (NSWC) from the beginning of 1986 until the GPS week 498 ending July 29, 1989. Since GPS week 499, July 30, 1989, they have been computed at the Defense Mapping Agency (DMA). The block II satellites are not yet included in the precise ephemerides computations.

The pseudo-range measurements used for the computations of precise ephemerides are performed at ten tracking stations^[8]. Five of the stations are the Air Force's OCS monitoring stations mentioned in the previous paragraph. The other five stations are operated by DMA and are located in:

- - Australia (Long.= 138.7 deg. E, Lat.= 34.7 deg. S),
- - Argentina (Long.= 301.5 deg. E, Lat.= 34.6 deg. S),
- - England (Long.= 358.7 deg. E, Lat.= 51.5 deg. N),
- - Bahrain (Long.= 50.6 deg. E, Lat.= 26.2 deg. N),
- - Ecuador (Long.= 281.5 deg. E, Lat.= 0.2 deg. S).

A 4-channel double-frequency receiver is deployed at each of these stations. The receivers are driven by high performance cesium frequency standards. The minimum observation angle for observation is 10 degrees. Temperature, pressure, and humidity are recorded at each site. The range measurements are corrected for ionospheric delay (two-frequency first order correction), tropospheric refraction (Hopfield model), periodic relativistic effects, offset between center of phase of antenna and center of mass of satellite (about 1 meter), and station displacements due to earth tides. The range observations collected at a 1.5 s rate are smoothed using carrier phase, in order to give 15 min of smoothed range observations. An observation standard deviation of 75 cm is assigned to each smoothed pseudo-range.

The DMA and the OCS monitor stations use essentially identical procedures for data collection and smoothing. These smoothed pseudo-range data are used as an input to the OMNIS Multisatellite Filter/Smoothing software using the Kalman filter^[9,10]. The computations are done in one hour batches processing simultaneously eight days of data of all stations and all satellites. The eight days allow one-half day overlaps with consecutive weeks.

Reference trajectories for all satellites are integrated using a truncated WGS 84 Earth Gravity Model (degree 8, order 8), mass gravity fields for the Sun and Moon, solid Earth tides, the Rockwell Rock4 model of radiation pressure including acceleration perpendicular to the direction of the sun, nutation, Earth rotation, UT1-UTC (using DMA initial values generated the week before the orbit fit), and a 5 min integration step.

Each weekly fit estimates:

- -for each satellite. orbital elements, radiation pressure modelled stochastically including acceleration perpendicular to the sun, and clock parameters,
- -for each monitor station, station clock parameters,
- -polar motion and UT1-UTC modelled as random constants.

The above described procedure generates fitted trajectory and clock files containing:

- -for every 15 min the position of the center of mass of each satellite expressed in WGS 84 coordinate system (X, Y, Z in km, DX/DT, DY/DT, DZ/DT in km/s, GPS time in year, month, day, hour, minute),
- -at one-hour intervals the time and frequency offsets between each satellite's clock and GPS time and frequency.

The uncertainty of precise ephemerides ranges from 1 m to 5 m.

COMPARISON BETWEEN BROADCAST AND PRECISE EPHEMERIDES

Although it is not the main purpose of this paper to examine differences between broadcast and precise ephemerides, we present the results of a comparison study which are necessary for further analysis. The sample of data we examine starts February 29, 1988 and ends April 23, 1989. The broadcast ephemerides were provided by the National Geodetic Survey (NGS). They were recorded in Wettzell (West Germany) as Keplerian parameters for each satellite for every hour of satellite visibility. The precise ephemerides come from NSWG and are presented as described at the end of the previous paragraph.

The satellite positions expressed in precise and broadcast ephemerides are compared in radial, on-track, and cross-track components at the time of the recording of the broadcast ephemerides. We have about seven comparisons per day for each satellite. Comparisons are made for all 53 days of the examined period in two intervals: Feb. 29 to March 31, 1988 and April 1-23, 1988. This has been done to separate the eclipse seasons.

During each year there are two periods when a given GPS satellite enters the Earth's shadow on every revolution. During these eclipse seasons larger thermal variations occur within the spacecraft than the rest of the year and accordingly may cause larger clock frequency variations. These variations are removed during the production of precise ephemerides, but they are not removed during the generation of broadcast ephemerides and may have a direct impact on their quality. In 1988 the eclipse seasons were the following: February 18-March 31, August 14-September 25, for PRN6/NAV3, PRN9/NAV6 and PRN12/NAV10; January 10-February 6, July 5-August 6, for PRN3/NAV11, PRN8/NAV4, PRN11/NAV8 and PRN13/NAV9. Thus for the period we are studying three satellites were in eclipse from Feb. 29 to March 31, 1988.

The results of this comparison are given in Table 2, in the form of quadratic means for radial, on-track, and cross-track components. We can observe first that satellites equipped with cesium clocks had broadcast ephemerides differing from precise by only a few meters, even for the eclipse period of PRN12/NAV10. Second, satellites using rubidium clocks had much larger differences, mainly during the eclipse periods. PRN6/NAV3 particularly, had very poor broadcast ephemerides during the eclipse period. PRN9/NAV6 did not exhibit the same degradation of broadcast ephemerides during its eclipse. PRN9/NAV6 had a cesium clock on board whereas PRN6/NAV3 did not. This cesium clock, though not in use, may have provided thermal mass, thus decreasing daily thermal variations. The two satellites were operating the same kind of rubidium clock. PRN8/NAV4 using a quartz oscillator has ephemerides comparable to spacecrafts using rubidium clocks.

Another study of the comparison of broadcast and precise ephemerides with an emphasis of geodetic differential positioning can be found in^[6].

BROADCAST EPHEMERIDES AS USED BY A TYPICAL GPS TIME RECEIVER

There is an internationally agreed-upon format for the collection and transmission of GPS time data, as used by the BIPM. A GPS time receiver collects data during its 13 min period. The received broadcast message contains, among other information, Keplerian orbital parameters and their perturbations. The 13 min tracks are determined by a tracking schedule issued by the BIPM.

First the receiver processes short term raw pseudo-range measurements, smoothing them over a period of seconds (typically 6 or 15) points through use of a second degree fit or phase accumulation (depending of the manufacturer). These short-term smoothed pseudo-ranges are corrected by the geometrical delay, the ionospheric delay, and various other parameters. The geometrical delay is computed from the positions of the satellite and user's antenna, both expressed in WGS 84 X,Y,Z coordinates, after the necessary transformations are performed by the receiver software.

A linear fit of the short-term data is used to reduce the comparison of satellite clock versus laboratory clock over the 13 min track to a slope, an intercept and a standard deviation. These data are reported in the BIPM format. If an upload of new ephemerides occurs during the 13 min track, two different broadcast ephemerides can be used during a single 13 min track.

APPLICATION OF PRECISE EPHEMERIDES TO TIME TRANSFER

To examine the impact of precise ephemerides on time comparisons we have chosen a pair of laboratories separated by a 6000 km baseline, Paris Observatory (OP) and U.S. Naval Observatory (USNO). The criterion chosen for this study is the dispersion of residuals of UTC(OP)-UTC(USNO) obtained from individual common view tracks with respect to the mean over all tracks, after correction for the rates of master clocks. The differences between precise and broadcast ephemerides computed in X, Y, Z coordinates (as defined in WGS 84) are interpolated to the middle of considered tracks, then projected on the direction vectors from laboratories to the spacecraft in order to correct time transfer. If there is an abrupt change of these differences (likely due to an upload of broadcast ephemerides) during interpolation period, the track is not corrected but rather is abandoned.

In the first approach we use observations of all available satellites (except PRN8/NAV4). The results are given by Figure 1. The use of precise ephemerides greatly diminishes the dispersion of residuals during the eclipse period for PRN6/NAV3, PRN9/NAV6, and PRN12/NAV10, but during the period following eclipse the amelioration is only slight.

In the second approach, we use only the observations of the satellites equipped with cesium clocks (Figure 2). In this case there is not observable improvement of time transfer using precise ephemerides. Sometimes the standard deviations of the residuals of the time comparison with precise ephemerides are better than those with broadcast ephemerides, sometimes worse (Fig. 2.c). The PRN12/NAV10 does not seem to be affected by its eclipse period. This experiment confirms the results of our comparative

study presented in table 2: broadcast ephemerides of satellites with cesium clocks are very close to the precise ephemerides.

EPHEMERIDES DURING SELECTIVE AVAILABILITY

The international community of time metrology is facing a major challenge with the SA degradation of GPS satellites. A recent experiment of the degradation of messages of Block I satellites (Sept. 29 – Oct. 2, 1989), which might be a test of SA, showed:

1. a phase jitter of the satellite clocks, the effect of which will be removed by a strict common view, and
2. a frequently changeable bias in the ephemerides of about 100 meters, the effect of which in common view is roughly proportional to the distance.

To overcome the problem of degraded ephemerides various approaches are being considered. These include the use of precise ephemerides, the use of the differences between broadcast undegraded and broadcast-degraded ephemerides provided by OCS^[1], the dynamical or geometrical^[2] determination of orbits by the timing community itself.

If either the timing community could have regular access to precise ephemerides or the community computed its own ephemerides, the following arrangements would be useful:

- -the records of broadcast ephemerides should be organized in a few principal laboratories around the world (one per area),
- -in a computation center the differences between broadcast and precise would be applied to time comparisons (as have been done during this study),
- -to avoid the problem of frequently changeable bias in the degraded ephemerides the software of time receivers should be modified so that during one track only one set of Keplerian parameters would be used, even if a new upload of broadcast ephemerides occurs during this track (section 5).

In the case of orbit determination by the timing community itself, the precise coordinates of GPS antennas are essential. Good differential coordinates for short baselines can be derived from time comparisons themselves^[3]. The links with the global terrestrial frame ITRF^[6], with few exceptions, are not yet satisfactorily realized.

There is another theoretical possibility^[5]. A center computing time comparisons instead of receiving 13 minute tracks from the time laboratories could receive 6 or 15 second smoothed pseudo-ranges as described in section 5. Then, using consistent software, all corrections including that of geometrical delay could be computed using precise ephemerides. The advantage of this approach is the uniqueness of the software, the disadvantage is the difficulty of the procedure.

CONCLUSIONS

Concerning the ephemerides of Block I satellites:

1. Broadcast ephemerides of satellites using cesium clocks differ from precise ephemerides by no more than a few meters.
2. Precise ephemerides do not improve the transfer of time if satellites are equipped with cesium clocks.
3. Broadcast ephemerides of rubidium-equipped satellites differ from precise by less than 15 m outside eclipse seasons, and up to 30 m in the case of PRN6/NAV3, during eclipse seasons.
4. When performing intercontinental GPS time transfer, broadcast ephemerides are sufficient when using cesium-equipped satellites, though the use of precise ephemerides with rubidium equipped satellites is recommended.

Concerning ephemerides during the implementation of SA:

1. Precise ephemerides can resolve the problem of SA orbit degradation, provided that the timing community has regular access to these ephemerides with a delay not exceeding 2 weeks.
2. Differences between broadcast undegraded and broadcast-degraded ephemerides, if released with a delay not exceeding 2 weeks, could be another satisfactory solution for SA orbit degradation.
3. For autonomy the timing community should actively investigate methods of independent orbit determination.

ACKNOWLEDGMENTS

The authors gratefully thank Dr W. Strange of NGS for providing the data used in this study, Prof. B. Guinot of BIPM, Dr. E.R. Swift of NSWC, Dr D.W. Allan of NIST and Dr P. Clements of JPL for most helpful discussions during the writing of this paper.

REFERENCES

1. Allan, D.W., Weiss, M.A., 1980, "Accurate time and frequency transfer during common view of a GPS satellite", Proc. 34th Ann. Freq. Control Symp., Ft Monmouth, pp 334-346.
2. Fliegel, H.F., Beard, R.L., Landis, G.P., Stebbins, S.B., Sept.1989, "An Alternative Common View Method for Time Transfer with GPS", Proc. of the 2nd International Meeting of the Institute of Navigation, Colorado Springs (in press).
3. Guinot, B., Lewandowski, W., 1989, "Improvement of the GPS time comparisons by simultaneous relative positioning of the receiver antennas," Bull. Geodesique (in press).

4. Guinot, B., BIPM, Pavillon de Breteuil, F-92312 Sevres, France. 1989 (private communication).
5. Kirchner, D., Ressler, H., Fassl, S., March 1989, "Experience with two collocated C/A-code GPS receivers of different types," Proc. 3rd European Frequency and Time Forum (in press).
6. Lewandowski, W., Douglas, R.J., Klepczynski, W.J., Strange, W., Suter, J., Weiss, M.A., June 1989, "Positioning of GPS Antennas in Time-Keeping Laboratories of North America," Proc. of the 43rd Annual Symposium on Frequency Control, Denver, Colorado, pp. 218-224.
7. Remondi, B.W., Hofmann-Wellenhof, B., August 1989, "GPS Broadcast Orbits Versus Precise Orbits: A Comparison Study," Proc. of the Meeting of Int. Ass. of Geodesy, Edinbourg (in press).
8. Swift, E.R., "NSWC's GPS Orbit/Clock Determination System," Proc. of the First Symposium on Precise Positioning with the Global Positioning System, Rockville, Maryland, April 15-19, 1985.
9. Swift, E.R., "Mathematical Description of the GPS Multisatellite Filter/Smoother," NSWC TR 87-187, Naval Warfare Center, Virginia, October, 1987.
10. Swift, E.R., "Orbit Period Frequency Variations in the GPS Satellite Clocks," Proc. 20th Annual PTTI Meeting, p. 87-100, Tysons Corner/Vienna, Virginia, Nov. 29 - Dec. 1, 1988.

ACRONYMS USED IN THE TEXT

BIPM	Bureau International des Poids et Mesures (International Bureau of Weights and Measures)
DMA	Defense Mapping Agency.
GPS	Global Positioning System.
IERS	International Earth Rotation Service, Central Bureau, Paris, France.
ITRF	IERS Terrestrial Reference Frame.
NGS	National Geodetic Survey, Rockville, Maryland, USA.
NSWC	Naval Surface Warfare Center.
OCS	Operational Control Segment.
OP	Observatoire de Paris, Paris, France
SA	Selective Availability.
USNO	U.S. Naval Observatory, Washington D.C., USA.
WGS	World Geodetic System.

OP-USNO by PRN 3,6,9,11,12,13

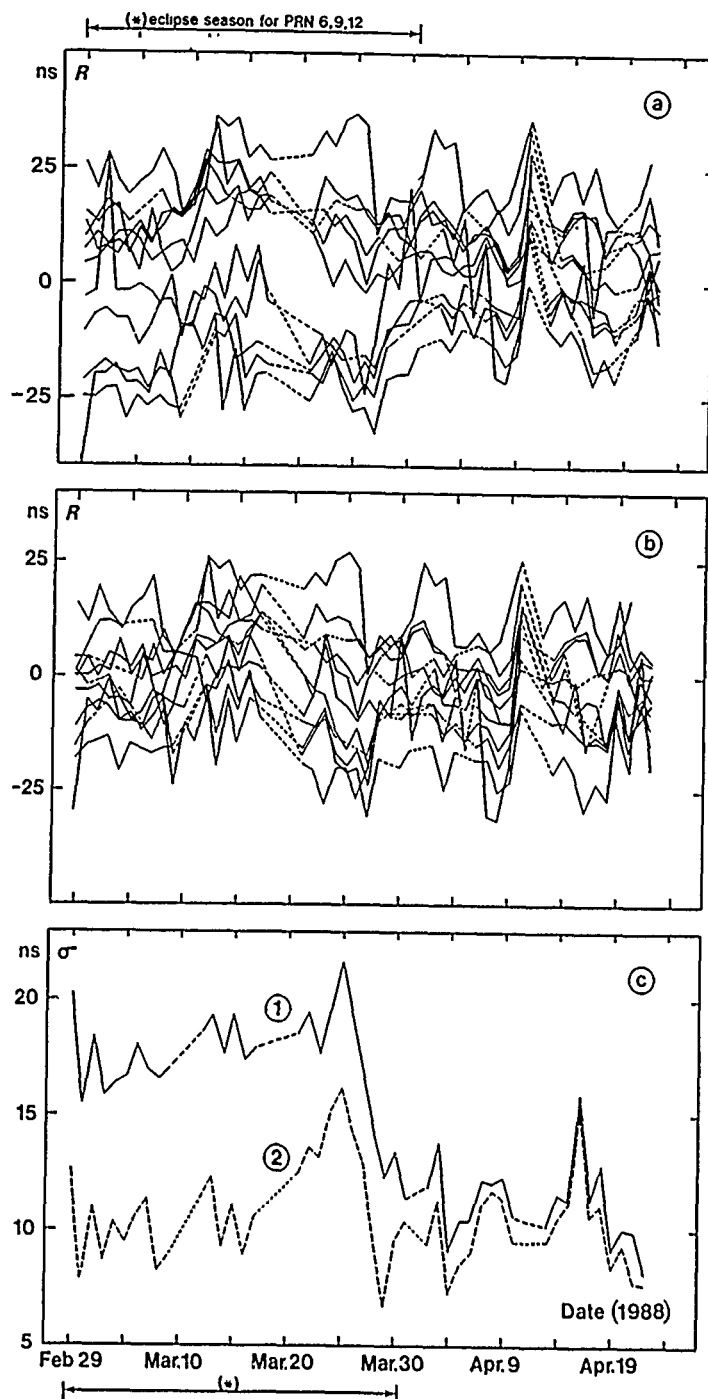


Fig. 1. Residuals (R) of UTC(OP)-UTC(USNO) as given by individual tracks, with respect to the mean (after correction for the rates of master clocks).

(a) - with broadcast ephemerides

(b) - with precise ephemerides

(c) 1 - standard deviations of residuals of (a)

2 - standard deviations of residuals of (b).

OP-USNO by PRN 3,11,12,13

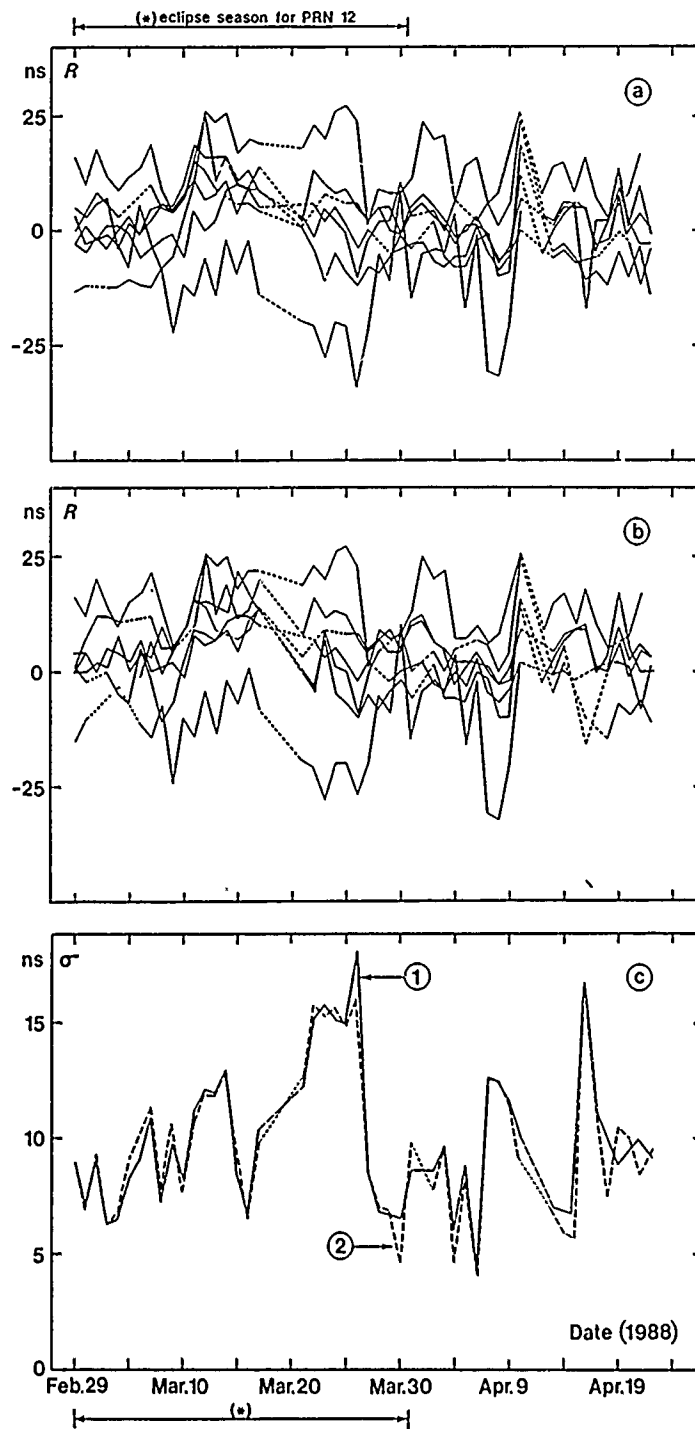


Fig. 2. Same as fig.1 but using only satellites with caesium clocks.

QUESTIONS AND ANSWERS

CARROLL ALLEY, U OF MARYLAND: Could you show again one of your slides showing the fits. There seems to be a periodicity there.

MR. LEWANDOWSKI: I didn't have time to explain what we saw above the noise. I don't know what periodicity you are talking about.

PROFESSOR ALLEY: Have you done a spectral analysis to determine what periodicities are there?

MR. LEWANDOWSKI: We only finished the report last week and haven't had time to do any more analysis. What I can say about this noise is that it is probably coming from ionospheric delay.

HENRY FLIEGEL, AEROSPACE: I wanted to underline something that you just said. I really don't think that you are seeing a good comparison of precise ephemerides *vs.* broadcast at all because I think that all of your error sources are dominated by the error sources that you just mentioned, ionosphere and especially station location. I think that the only conclusion that you can make is that you can't use precise ephemerides yet, until you get rid of those other sources of error. Then I imagine that you will see a substantial difference.

MR. LEWANDOWSKI: What I wanted to show was an improvement. Of course there are other noises. I see an improvement and ask 'why not use the precise ephemerides to get this improvement?' before we solve all the other problems.

ACCURATE DELAY CALIBRATION FOR TWO-WAY TIME TRANSFER EARTH STATIONS

Gerrit de Jong
Van Swinden Laboratory
P.O.Box 654, 2600 AR Delft
The Netherlands

INTRODUCTION

The most accurate clocks are using cesium beam frequency standards as their source of accuracy. The atomic time scale TAI is built from the SI seconds after adopting the definition of its origin. As a practical time scale close to the astronomic time, UTC has been introduced, which is equal to TAI, but kept in close agreement with universal time by addition or subtraction of leap seconds. UTC and TAI are computed by the BIPM from the time comparison data of laboratory and commercial cesium clocks. The accuracy of comparing clocks all over the world has been improved significantly by the use of the GPS common view method. This one way method is capable of precision around 8 ns and accuracies of about 30 ns if not deteriorated by Selective Availability measures.

A further improvement can be realized by using two-way methods, as demonstrated in several experiments using groundstations at each clock site capable of reception and transmission. This paper addresses the calibration of the groundstations to achieve high accuracy in such two way time comparisons.

GENERAL PRINCIPLES OF TIME COMPARISON

To measure the difference of the time scales of two clocks a time interval counter is used. One clock output is connected to the start of the counter, and the other clock output (1 pps) to the stop input. State of the art counters measure the difference with a resolution of 20 ps, and an accuracy of 100 ps or 0.1 ns.

If the clocks are not adjacent to each other, a cable can be used to transport the output signal of the second clock to the stop input of the time interval counter. However, the time interval reading is not correct because of the propagation delay of the 1 pps signal in the cable. This delay is to be measured and corrected for. A 50 Ω coaxial cable has typically a delay of about 5 ns/m.

If the cable is relative long then distortion of the pulse occurs which gives an extra delay. In a cable the higher frequency components are attenuated more than the lower frequency components, and the cable acts as a low pass filter. To avoid such a group velocity distortion, modulation of the 1 pps signal on a carrier frequency can be done. In this manner the additional delay from distortion can be minimized.

Instead of using a cable for transportation of such a modulated carrier the space can be used by means of transmitters and receivers with the appropriate antennas. This is done with low frequency

transmitters for time signals such as WWVB at 60 kHz in the U.S. and in Europe: DCF77 at 77.5 kHz, MSF60 at 60 kHz, HBG at 75 kHz; also in Loran-C and HF standard frequency and time transmitters. The maximum reception distance is several thousands of kilometers.

A problem for accuracy is the determination of the distance from transmitter to receiver and to correct for propagation properties of the medium: troposphere, ionosphere, (barometric pressure, humidity, degree of ionization).

Recently satellites are being used. One problem here is the very long distance and the accuracy of the determination of this distance. Another problem is the ionospheric delay; the latter however is inversely dependent by the square of carrier frequency and amounts less than 1 ns at 12 GHz.

The two-way method using satellites eliminates the need to determine separately the exact distance from each station to the satellite, as is shown in the next section.

TWO-WAY TIME COMPARISON

From Figure 1 we can see that the difference of the clocks at station 1 and 2 can be determined. In this figure:

TA(k) is the time scale at station k;
 TI(k) is the time interval reading;
 TT(k) is the transmitter delay;
 TR(k) is the receiver delay;
 TU(k) is the uplink delay;
 TD(k) is the downlink delay;
 TS(k) is the satellite delay;
 TC(k) is the correction for relativistic effects.

The difference $TA(1) - TA(2)$ is to be determined. The reading at station 1 is:

$$TI(1) = TA(1) - TA(2) + TT(2) + TU(2) + TS(2) + TD(1) + TR(1) + TC(1)$$

The reading at station 2 is:

$$TI(2) = TA(2) - TA(1) + TT(1) + TU(1) + TS(1) + TD(2) + TR(2) + TC(2)$$

The difference gives:

$$\begin{aligned} TI(1) - TI(2) = & 2\{TA(1) - TA(2)\} + TT(2) - TT(1) + TU(2) \\ & - TU(1) + TS(2) - TS(1) + TD(1) \\ & - TD(2) + TR(1) - TR(2) + TC(1) - TC(2)\} \end{aligned}$$

or:

$$\begin{aligned} TA(1) - TA(2) = & \frac{1}{2}\{TI(1) - TI(2) + TT(1) - TT(2) + TU(1) \\ & - TU(2) + TS(1) - TS(2) + TD(2) \\ & - TD(1) + TR(2) - TR(1) + TC(2) - TC(1)\} \end{aligned}$$

If the same transponder in the satellite is used, then:

$$TS(1) = TS(2)$$

If the satellite is not moving too fast then:

$$TU(1) = TD(1) \text{ and } TU(2) = TD(2),$$

and their delays cancel.

The TC(1) and TC(2) can be calculated accurately enough.

The remaining terms are now:

$$TA(1) - TA(2) = \frac{1}{2} \{ (TI(1) - TI(2) + TT(1) - TT(2) + TR(2) - TR(1) + C) \}$$

If the transmit delays TT and the receive delays TR at both stations were equal then they would cancel. But that can only be proved by measuring the difference by locating two groundstations close enough together, which is not a simple action. Even then the sum of the transmit difference and the receive difference is determined, not their values separately.

Therefore here a method to determine the absolute value of the transmit- and receive-delays separately is described.

THE TIME TRANSFER MODEM

The MITREX modem (Figure 2) has a modulator section in which the 1 pps signal is impressed on a bi-phase modulated carrier. The PRN generator is clocked at a 2.5 MHz rate and every 4 ms a bit sequence is generated. As soon as the 1 pps signal appears, then one sequence of 4 ms is inverted. The sequence is reclocked simultaneously with the 1 pps transmit output pulse and it then modulates the phase of a 70 MHz carrier frequency. The signal is band pass filtered and is fed as the IF signal to the upconverter and transmitted.

The demodulator section receives the 70 MHz downconverted signal and provides a 1 pps received pulse as soon as it detects the 4 ms inverted PRN sequence.

The sum of the internal delays in the modem can be measured by connecting the 70 MHz output with the 70 MHz input and connecting the 1 pps transmitted output to the start input of a time interval counter and the 1 pps received output to the stop input. The delay of any external cable can be measured by connecting the cable also between modem output and input. The cable delay is found by subtracting the internal modem delay.

THE CALIBRATION OF THE GROUND STATION DELAYS

A typical earth station is shown in Figure 3. The delay between the reference plane at the time interval counter and the plane at the antenna is to be determined. First the delay between the antenna and the modem reference plane will be measured. For this purpose a passive satellite transponder simulator is constructed. It is consisting of two double balanced mixers connected in series between two SMA to wave guide transitions acting as antennas. The mixers convert the transmit frequency (14 GHz) to the receive frequency (11 GHz). So one local oscillator is tuned to 2.93 GHz and the other is at 70 MHz.

The modem is used to measure the sum (TT + TR) of the transmit delay TT and the receive delay TR through the satellite simulator at the modem reference plane.

This is similar to the test loop translator which in some groundstations is installed between the output of the upconverter and the downconverter input, but now the delay in the antenna feeds is also included.

In order to determine the values of the transmit and receive delay separately, the 70 MHz cable to the satellite simulator is used. The delay of this cable CS is measured first. Therefore it is disconnected from the simulator and so are the 70 MHz cables CT and CD to the up- and the downconverter respectively.

First cable CT is interconnected to cable CD at the far end and the sum delay (CT + CD) is measured.

Then cable CS is substituted for CT and the sum delay (CS + CD) is measured.

Finally (CS + CT) is measured. From the obtained 3 measurements the delay of cable CS is calculated:

$$CS = \frac{1}{2}\{(CS + CD) + (CS + CT) - (CT + CD)\}.$$

Also the other cable delays are calculated in this way.

The calibrated cable CS is reconnected to the satellite simulator and the other cables are also reconnected. The next step is to connect cable CT to the 70 MHz continuous carrier and cable CS to the modulated 70 MHz modem output. Now the CW carrier of 14 GHz is PRN modulated in the satellite simulator. The sum of CS and the receive delay TR from simulator to modem input is measured: (CS + TR).

The delay CS is known, so TR can be calculated. The sum (TT + TR) of transmit delay TT and TR was already measured, so TT can also be calculated.

DETERMINATION OF THE INTERNAL DELAYS IN THE MITREX MODEM

It should be emphasized that in the preceding paragraph TT and TR are measured to the reference plane at the modem 70 MHz in- and output. Still undetermined is the internal transmit delay Tt with respect to the 1 pps received output.

Let us look again at the modem in Figure 2. The transmit part is the simpler, after the reclocking a wide-band mixer is used (delay estimated <2 ns) followed by a band-pass filter. Filters exhibit always delays, inversely proportional to their bandwidth. Also the receiver has a band-pass filter at its input. So the transmit filter was taken out of the circuit and then the total internal delay was measured again. The difference in delay between filter in and out the circuit gives the delay of the filter.

The other internal transmit delays are calculated from the measured internal cable lengths from the wideband mixer to the 70 MHz output connector of the modem. Once the total internal transmit delay Tt being determined, the internal receive delay Tr is calculated by subtracting the transmit delay Tt from the total internal delay.

FINAL CALIBRATIONS

Now the internal delays Tt and Tr can be added to the external groundstation delays to find the total receive delay as well as the total transmit delay from the antenna reference plane to the time interval

counter reference plane.

The systematic uncertainty, appearing from estimation of the internal delays of the mixer in the modulator and in the satellite simulator, is estimated to be less than 2 ns. The statistical uncertainty, or precision, is of the order of 1 ns but is depending upon the averaging time.

At VSL, the antenna is connected to the modem with IF coaxial cables of about 120 m. The values found were: $TT = 669.2$ ns, $TR = 648.6$ ns, $CS = 628.7$ ns, $Tt = 319.3$ ns and $Tr = 845.3$ ns. So an asymmetry of 505.4 ns exists.

CONCLUSION

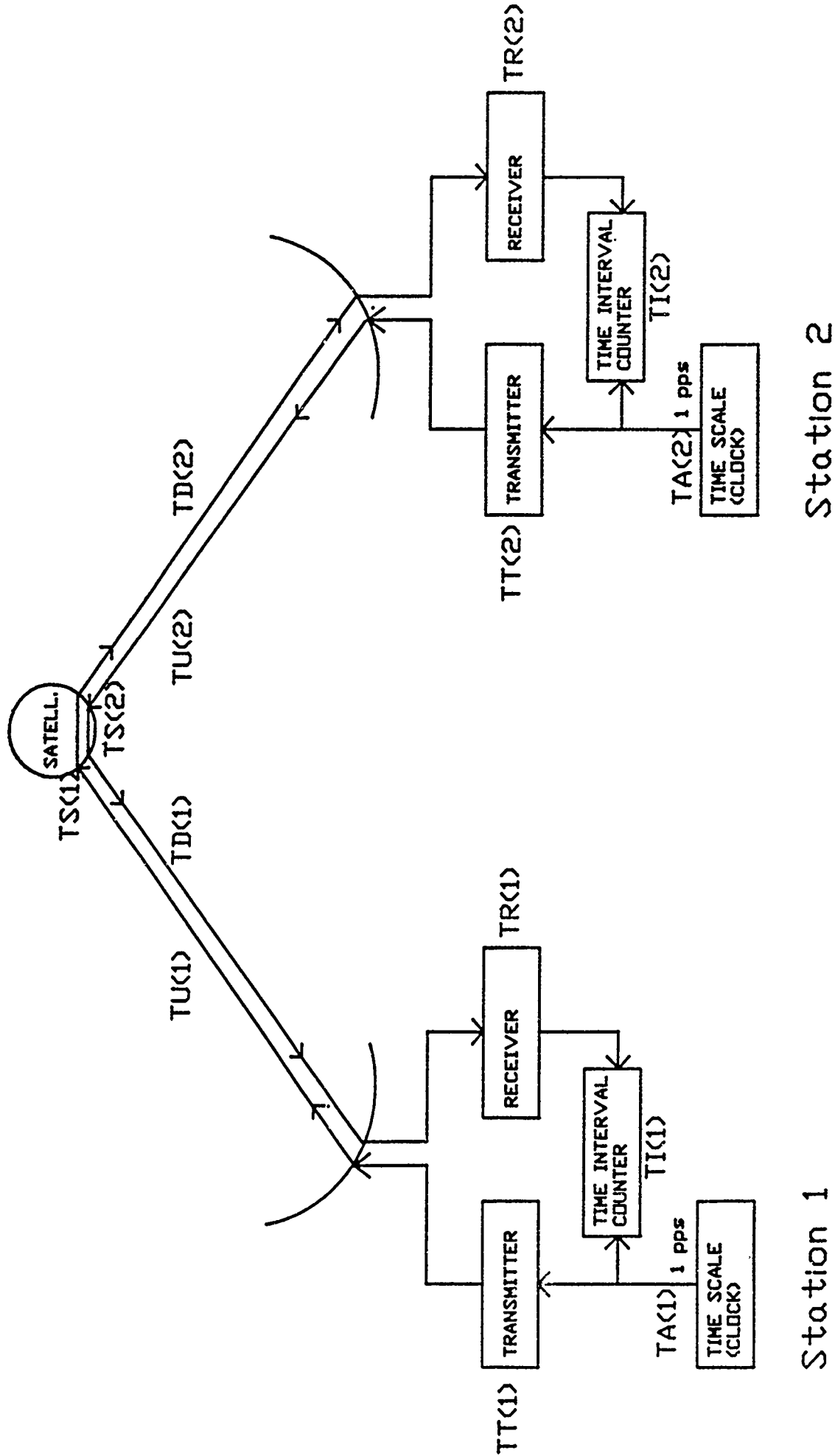
In this paper it has been shown that with the described calibration method using a satellite simulator all transmit and receive delays can be determined to the nanosecond level accuracy. It is important to measure accurately the transmit and receive delays at each two-way earth station; symmetry should not be assumed at the nanosecond accuracy level.

The internal delays between input and output antennas of the satellite and the difference in position of the satellite antennas relative to each earth stations should be treated similarly.

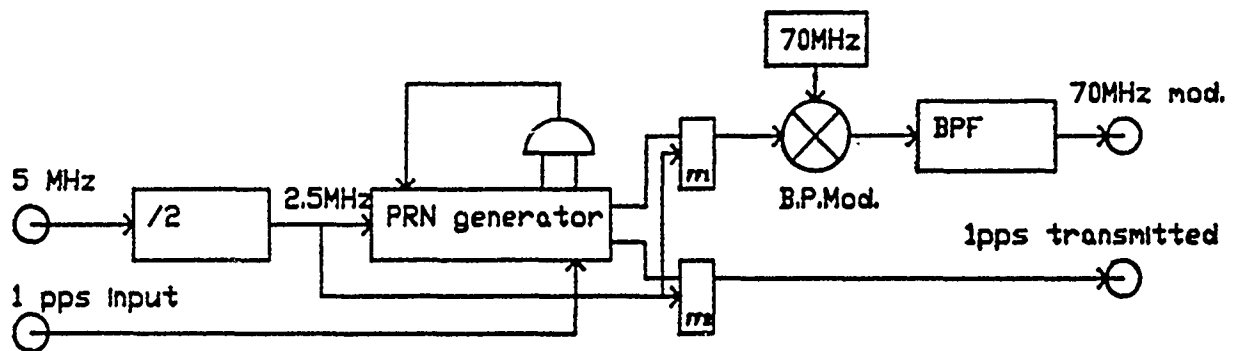
REFERENCES

1. Ph. Hartl et al., "High accuracy global time transfer via geosynchronous telecommunication satellites with Mitrex", *Journal Flight Science & Space Research*, vol. 7, no. 5, pp. 335 - 342, 1983.
2. D. Kirchner et al., "A two-way time transfer experiment via ECS-1 using the MITREX modem", *IEEE Trans. on Instr. and Meas.*, vol. 37, no. 3, Sept. 1988.
3. G. de Jong, "Measuring the propagation time of coaxial cables used with GPS receivers", *Proceedings 17th Annual PTTI Applications and Planning Meeting*, Dec. 3-5, 1986, Washington DC, USA.
4. G. de Jong, "Results of several years of comparison of European Time scales by means of a receive only satellite method", *Conference on Precision Electromagnetic Measurements*, June 1984, Delft, the Netherlands.
5. W. Klepczynski et al., "Preliminary comparison between GPS & two-way satellite time transfer", *Proceedings 42nd Annual Symposium on Frequency Control*, 1-3 June 1988, Baltimore, USA, *IEEE Cat. no. 88CH2588-2*, pp. 472-477.

Fig. 1 Two-way Time Comparison Principle



Mitrex Modulator section



Mitrex Demodulator section (receiver)

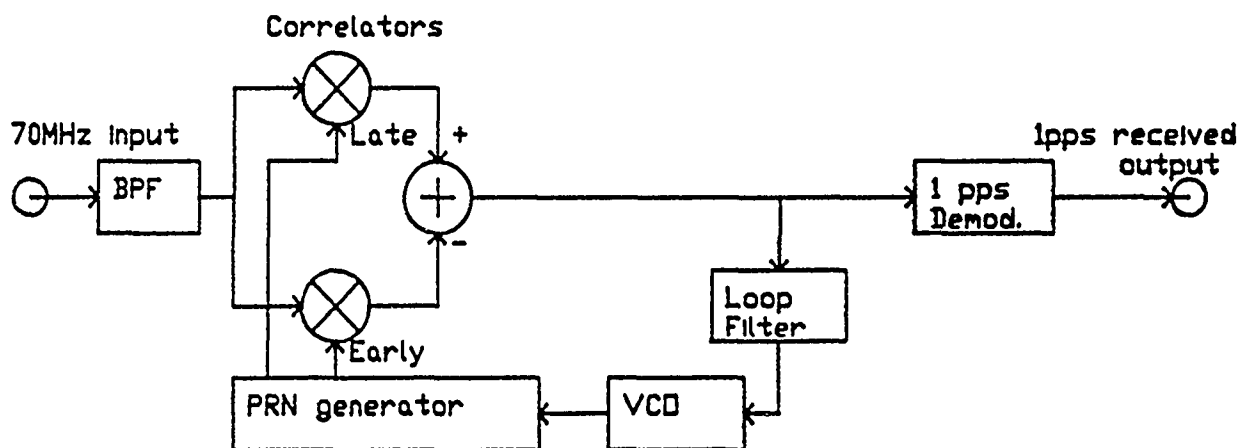


Fig. 2 Mitrex Modem

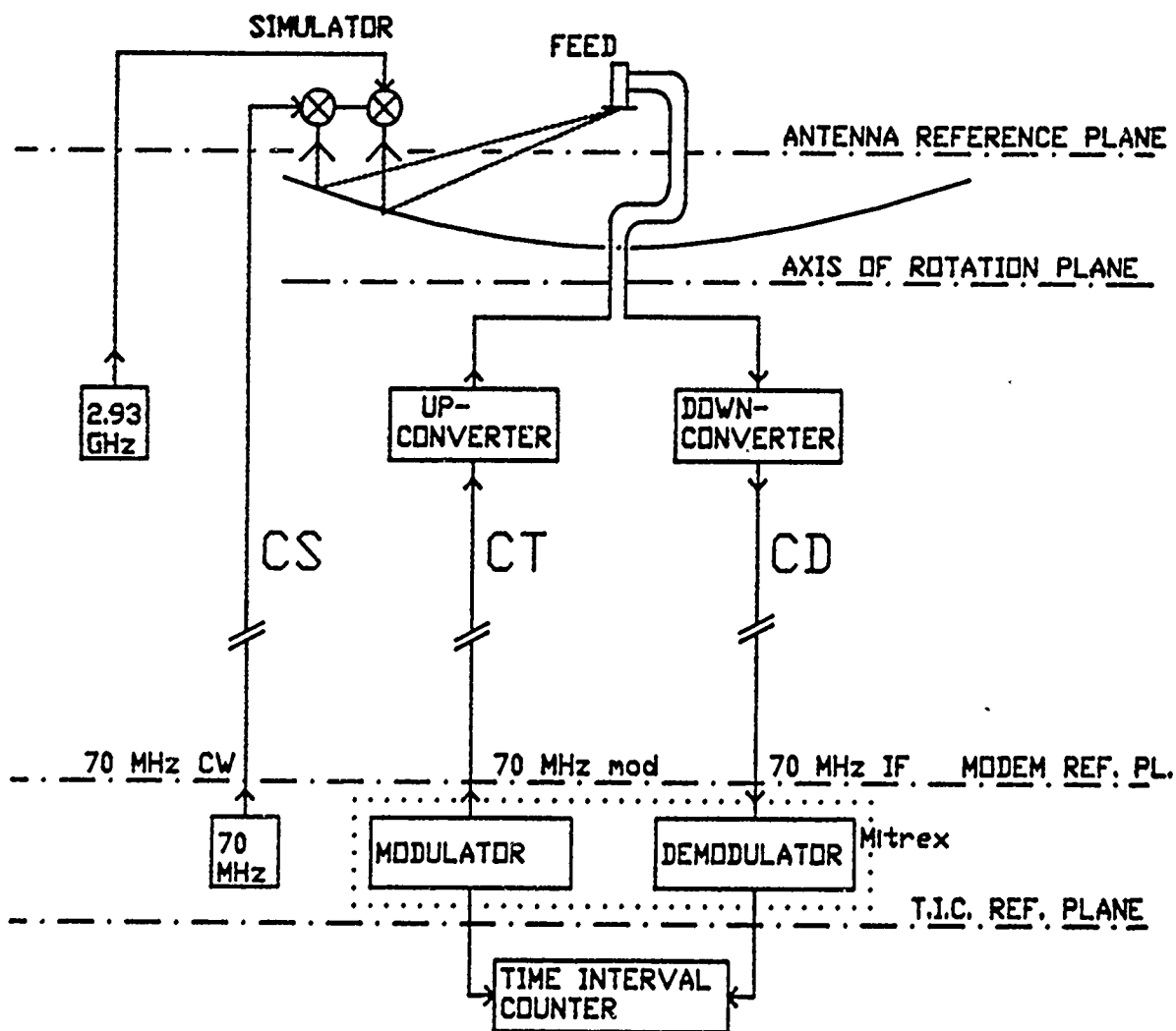


Fig. 3 Earth Station Calibration

QUESTIONS AND ANSWERS

DAVID ALLAN, NIST: Do you have a way of checking the one nanosecond accuracy number, or is that an internal calculation?

MR. DE JONG: It is the sum of the uncertainties of the readings of the time interval counter and the uncertainty in the measurement of the lengths of the coaxial cables and of the two mixers of the simulator. The mixers have not been measured, but we could take out, for example, the 70 MHz mixer and see what the difference would be in the total delay. It would be a lot of work and it is of the right order of magnitude for the total uncertainty.

SATELLITE TWO-WAY TIME TRANSFER: FUNDAMENTALS AND RECENT PROGRESS

D.A. Howe, D.W. Hanson, J.L. Jespersen, and M.A. Lombardi *
Time and Frequency Division
National Institute of Standards and Technology
325 Broadway
Boulder, Colorado 80303

Abstract

Experiments in precise clock comparisons using the two-way time transfer technique via satellite began in 1962. Experience gained from a variety of experiments since that time steadily improved the precision and accuracy of such comparisons. Recent growth in the fixed satellite service, or FSS, has created new opportunities at moderate costs for high-accuracy time transfers using geostationary satellites. We discuss fundamental aspects of two-way timing and show an implementation of a satellite two-way time transfer system which has been used for two-years between USNO, Washington, D.C. and NIST, Boulder, CO. The raw data collection procedure will be discussed. We also outline the rationale for the choice of satellite uplink/downlink frequencies, signal structure, and reduction of data.

Short-term noise in the time transfer limits the precision to about 300 ps in a 300 s average. Uncertainty in accuracy is due to uncertainty in the non-reciprocity of the two-way signal path. Accuracy limits due to the atmosphere, earth-satellite rotating system (Sagnac effect), and the equipment are discussed. The goal is to achieve an accuracy level of 1 ns after a suitable calibration of earth-station (differential) equipment delays.

Satellite Two-way Time Transfer

We discuss fundamental aspects of two-way time transfers first. Synchronization of clocks between two locations A and B in the two-way mode involves three elements. These are: the clocks which generate a signal, usually a pulse once per second, some method to transmit the pulses between locations A and B , and a time-difference measuring instrument, or time-interval counter (TIC), at each location. Figure 1 illustrates the principle of the two-way technique using two cables as the interconnecting medium. The difference of the clocks is given by

$$A - B = 1/2[R(A) - R(B)] + 1/2[d_{AB} - d_{BA}] \quad (1)$$

where $R(A)$ and $R(B)$ are the counter readings at A and B respectively and d_{AB} and d_{BA} are the cable signal delays from locations A to B and B to A respectively. If the electrical length of each

*Contribution of the U. S. Government; not subject to copyright.

cable is the same, i.e., $d_{AB} = d_{BA}$, then the clock difference is simply one-half of the difference of the time-interval counter readings.

Figure 2 shows the two-way time transfer method through a satellite. The scheme is basically the same as in Fig. 1 except both signals are transmitted through a satellite rather than through cables. Note that additional delay terms indicated represent the earth station transmitters (d_{TA} and d_{TB}) and receivers (d_{RA} and d_{RB}), the propagation delay to and from the satellite at A and B (d_{AS} , d_{SA} , d_{BS} , d_{SB}) and the delay through the satellite itself (d_{SAB} and d_{SBA}). Taking into account the various delays and using the formalism of Eq. 1, we have

$$A - B = 1/2[R(A) - R(B)] + 1/2[(d_{TA} - d_{RA}) - (d_{TB} - d_{RB})] \\ + 1/2[(d_{AS} - d_{SA}) - (d_{BS} - d_{SB})] + 1/2[d_{SAB} - d_{SBA}] - 2\omega A/c^2 \quad (2)$$

where the last term ($2\omega A/c^2$) is due to the Sagnac effect which will be discussed later. Figure 2 does not explicitly indicate the subtraction (the difference) of the TIC readings as in Fig. 1. The TIC readings can be exchanged by any means such as via telephone modem or through the satellite itself using its own communications capability. Cables of equal electrical length in Fig. 1 are analogous to equal, free-space path lengths to and from each earth station through the satellite in Fig. 2^[1].

Factors Affecting Signal Reciprocity

A fundamental issue of high accuracy synchronization in the satellite two-way technique is the determination of the value and uncertainty of path nonreciprocity. A direct-sequence, spread-spectrum (DSSS) signal structure has benefits for satellite two-way time transfer. This type of signal has good time transfer resolution at low power density^[2]. Using DSSS, each data bit is represented by a pseudo-random noise (or PN) sequence. Different PN sequences having low cross-correlation allow two DSSS signals to pass through a satellite transponder simultaneously with minimal interference. This so-called code division multiple access (CDMA) allows signal path reciprocity through the satellite transponder, i.e., $d_{SAB} = d_{SBA}$ in Eq. 2 (hence the term is zero).

The transmission and reception of a timing signal through a satellite involves waveguides, cables, amplifiers, converters, and filters, as well as the spread-spectrum, modulator-demodulator (modem). The non-reciprocal time delay through the earth station equipment is the difference between the equipment-related, receive-signal delay and transmit-signal delay, or the "differential" delay. Referring to Fig. 2 and Eq. 2, the equipment-related nonreciprocity involving two stations, A and B , is given by

$$\Delta E_{qA,B} = 1/2[(d_{TA} - d_{RA}) - (d_{TB} - d_{RB})] \quad (3)$$

in the case of a measurement of $A - B$.

One can measure equipment-related nonreciprocity by using a transportable earth station which can perform a two-way time transfer at each of two main earth station locations, A and B . The procedure is as follows. A common clock is used for both the main and transportable earth stations as shown in Fig. 3. The transportable station is located in close proximity to the main station in order to

minimize propagation and Sagnac nonreciprocity which is discussed next. If we call the transportable earth station "C", then the differential equipment delay between A and C would be given by

$$\Delta E_{qA,C} = 1/2[(d_{TA} - d_{RA}) - (d_{TC} - d_{RC})] \quad (4)$$

where d_{TC} and d_{RC} are the delays through the transmitter and receiver respectively at C. A - C between the stations is known since a common clock is used; therefore Eq. 2 makes the differential equipment delay between A and C determinable. (Other factors are assumed to be zero or, in the case of the Sagnac effect, determinable as will be discussed next.) The transportable earth station is then moved to location B where the same setup is again used to measure a differential equipment delay between B and C. The difference of the values obtained at A and B is thus the difference of their differential delays which is the equipment related nonreciprocity between locations A and B. The differential-equipment delay for A - B is thus given by

$$\Delta E_{qA,B} = \Delta E_{qA,C} - \Delta E_{qB,C} \quad (5)$$

or

$$1/2[(d_{TA} - d_{RA}) - (d_{TB} - d_{RB})] = 1/2[(d_{TA} - d_{RA}) - (d_{TC} - d_{RC})] - 1/2[(d_{TB} - d_{RB}) - (d_{TC} - d_{RC})] \quad (6)$$

and the expression on the right in Eq.6 is determinable. Day-to-day measurements of differential-equipment delay variations between earth stations typically do not exceed 1 ns with the present NIST hardware^[3].

The Fixed Satellite Service (or FSS) in the U.S. has frequency allocations in the Ku-band. The uplink and downlink frequencies are approximately 14 GHz and 12 GHz respectively. A frequency-dependent delay through the ionosphere causes the transmit and receive path delays to be different. For a given operating frequency f , the time delay varies as $1/f^2$. The use of Ku-band is favorable for satellite two-way time transfers because of the high signal reciprocity. Ionospheric signal dispersion at C-band (6/4 GHz) is substantially greater. Figure 4 shows nonreciprocal time difference for uplink and downlink frequencies of 14.307 and 12.007 GHz respectively as a function of elevation angle. The calculation assumes a total electron content in a vertical column of 1×10^{18} electrons per meter squared, considered a worst-case condition. Typical propagation (ionospheric) nonreciprocity, given as $1/2[(d_{AS} - d_{SA}) - (d_{BS} - d_{SB})]$ in Eq. 2, is expected to be of the order of 100 ps^[4].

The level of nonreciprocity due to the troposphere is regarded as insignificant at the frequencies used in these experiments. Tropospheric delay is dependent predominantly on water vapor, elevation angle, user altitude, temperature, and pressure. At our frequencies the error due to tropospheric delay is well below 100 ps.

The last noteworthy, nonreciprocal term is caused by the Sagnac effect. This effect is due to the rotation of the earth relative to universal coordinates. Clocks on the surface of the earth are not in a fixed inertial frame due to earth rotation. The exchange of timing information is subject to a relativistic correction, but the effect can be described if one simply considers that the relative locations of two points (A and B) have moved after information is received at A, for example, from B. This is shown pictorially in Fig. 5 where the view is from above the North Pole. At transmission of a timing pulse from earth station B, the location of station A, station B, and the satellite are shown as "1"

The satellite has moved to "2" by the time it receives and retransmits the pulse. Station A has moved to location "3" by the time the signal arrives at A. The signal path has been effectively lengthened in the case of a pulse communicated from west to east. Conversely, the path is shortened for a signal going from east to west. These changes in path length are equal to $2\omega A/c^2$ where c is the speed of light, ω is the earth's rotation rate, and A is the area defined by the projections onto the equatorial plane by the line segments connecting the satellite and the earth's center to the earth stations. This nonreciprocity is easily calculatable without high accuracy knowledge of satellite and earth station positions. For example, a time transfer between NIST (Boulder, CO) and USNO (Washington, D. C.) through SBS-3 at $95^\circ W$ involves only a 100 ps error for a 1° error in satellite longitude. A position error of 300 m in any direction at NIST's station produces an error of no more than 100 ps. In addition, if a perfectly circular geostationary orbit is assumed for the satellite, the slight eccentricity actually encountered produces less than 50 ps error^[1].

NIST-USNO Time Transfers

NIST and USNO have been making routine two-way satellite time transfers in the Ku-band since August 1987. The configuration at each location is the same except that NIST has a steerable 6.1 m dish and USNO has a 4.5 m dish with a fixed mount. Figure 6 shows a diagram of the principal earth station components. Reference [3] contains a description of the earth station equipment at NIST. The 1 pps signal is transmitted from each earth station and received by the other earth station by means of a spread-spectrum modem that operates with an intermediate frequency of 70 MHz^[5].

During two-way time transfer, NIST and USNO simultaneously transmit and receive two spread-spectrum signals. Each signal is initiated by a 1 pps clock signal that represents UTC(NIST) and UTC(USNO), respectively. The time difference between the locally transmitted 1 pps signal and the received 1 pps signal from the other station is measured and recorded at each site for a 300 s interval. The time differences are recorded at both sites and stored on a central computer at USNO. These data are then aligned for matching one second times, and one-half the difference of the two values is obtained. The resulting data show a second-by-second time difference between the clocks at NIST and USNO. At this point the data are not yet compensated for earth station equipment differential delay, Sagnac effect, and cable or other equipment delays. This is referred to as the raw, uncalibrated, two-way time comparison.

The mean and standard deviation are computed for each 300 s measurement session to obtain a single estimate and measurement precision for the time scale difference. Regression analysis shows no discernible slope above the residual white noise, and tests of the residuals show that they follow white noise behavior. Thus, the simple mean is the best estimate of the time comparison midway (at 150 s) through the measurement. Values of precision (standard deviation) are typically about 300 ps^[6].

The internal signal delay in each spread-spectrum modem (one at NIST and one at USNO) is measured and recorded before starting each measurement run. These delays are subtracted from the average, raw, time comparison to obtain an (uncalibrated) final comparison. Figure 7 is a plot of time comparison results for almost two years of scheduled two-way sessions. Each point represents a 300 s average.

Future International Comparisons

Intelsat, the International Telecommunications Satellite Organization, provides a satellite service which can accommodate two-way time transfers of the type described here. This is a specialized Ku-band service which is intended for digital links to small earth stations. An Intelsat satellite located at $307^{\circ}E$. longitude ($53^{\circ}W$) can support two-way time transfers between Europe and North America using antennas as small as 1.8 m. A transmitter power of 1W is sufficient to yield a carrier-to-noise-density ratio (C/N_0) of at least 54 dB-Hz, a minimum level for the modem involved here. Figure 8 shows the West and East Ku-band spot-beam coverages. A thorough explanation of the Intelsat service including implementation requirements, link calculations, and agencies to contact is included in reference [7].

NIST-USNO Facilities

NIST, in cooperation with USNO, has expanded its facilities to include the mobile earth terminal shown in Fig. 9. This is a self-contained earth station with a 1.8 m-offset, Gregorian-feed, steerable dish. The mobile system will be used to provide a "calibration" between two-way, satellite time-transfer earth stations. Its principal function is to determine equipment-related nonreciprocity as described earlier in this paper.

NIST Facilities

Figures 10 and 11 show NIST's 6.1 m, motor-steerable, dish antenna and earth-station laboratory, respectively. The dish is permanently located on the roof of a wing of a NIST building and the associated earth station equipment is in a room about 30 m away. Data reduction and equipment control are partially handled using a PC-type computer. The computer has enough control that a two-way time transfer can be scheduled to run automatically without an operator. As the number of participants in two-way time transfer increases, computer support of operations will be needed to minimize operational costs.

Conclusion

Starting with fundamental principles, we examined the application of two way time transfer using present-day commercial satellite resources. The four notable sources of signal nonreciprocity (directly affecting accuracy estimates) which were described are:

1. Satellite transponder effects
2. Earth-station equipment-related effects
3. Atmospheric (tropospheric and ionospheric) effects
4. Relativistic (Sagnac) effect

. . .

Using Ku-band (14/12 GHz) equipment, combined uncertainties yield a projected accuracy in the neighborhood of 1 ns.

Results of NIST-USNO, two-way, satellite time transfers taken for two years were presented. Time transfers were done three times per week through SBS-3 at 95°W longitude. Second-by-second time differences were measured for 300 s (5 min); the simple mean and standard deviation were computed for the value and precision of the time comparison, respectively. Typical precision was approximately 300 ps.

The Intelsat satellites offer an opportunity for two-way satellite experiments between Europe and North America using small dish antennas. These experiments are in the planning stages. NIST facilities have been expanded to support these and other satellite experiments.

References

1. Hanson, D. W., "Fundamentals of two-way time transfers by satellite," Proc. of 43rd Annual Symposium on Frequency Control, Denver, CO, June, 1989, pp. 174-178.
2. R. C. Dixon, Spread Spectrum Systems, 2nd Edition, John Wiley and Sons, New York, NY, 1984, pp. 291-295.
3. Howe, D. A., "Progress toward one-nanosecond two-way time transfer accuracy using Ku-band geostationary satellites," IEEE Trans. on Ultrasonics, Ferroelectrics, and Frequency Control, UFFC-34, No. 6, Nov., 1987.
4. Jespersen, J., "Impact of atmospheric non-reciprocity on satellite two way time transfers," Proc. of 43rd Annual Symposium on Freq. Control, Denver, CO, June, 1989, pp. 186-192.
5. Mitrex 25000 documentation, P. Hartl et. al., Institute for Navigation, Univ. Stuttgart, Germany, Jan., 1985.
6. Howe, D. A. et. al, "NIST-USNO time comparisons using two-way satellite time transfers," Proc. of 43rd Annual Symposium on Freq. Control, Denver, CO, June, 1989, pp. 193-198.
7. Veenstra, L. B. and Hanson, D. W., "Two-way satellite time transfers between and within North America and Europe," Proc. of 43rd Annual Symposium on Freq. Control, Denver, CO, June, 1989, pp. 179-185.

Two-Way Technique

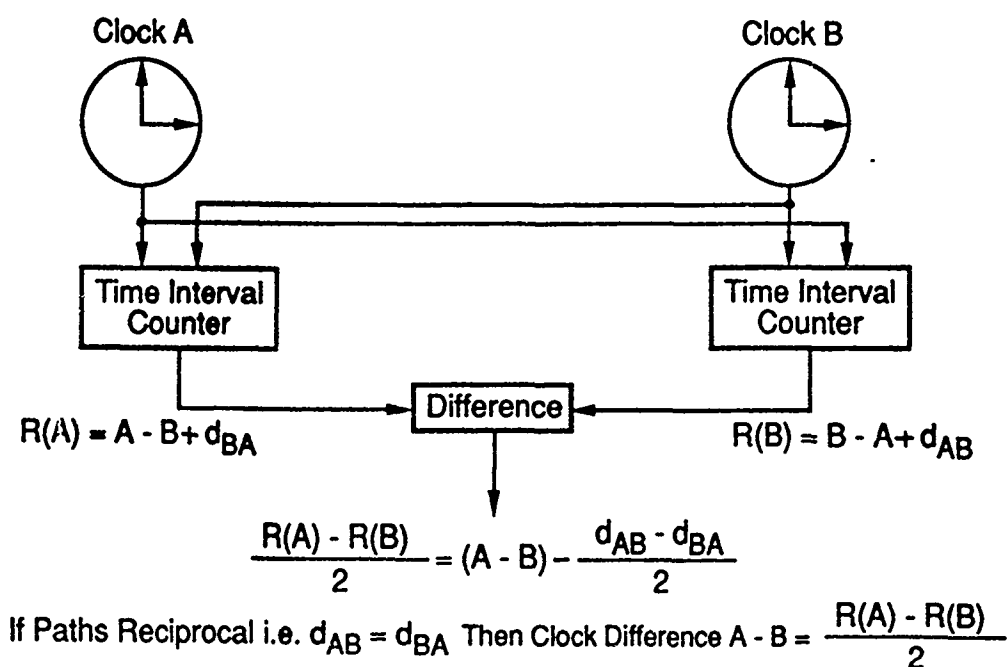


Fig. 1. Two-way technique using cables.

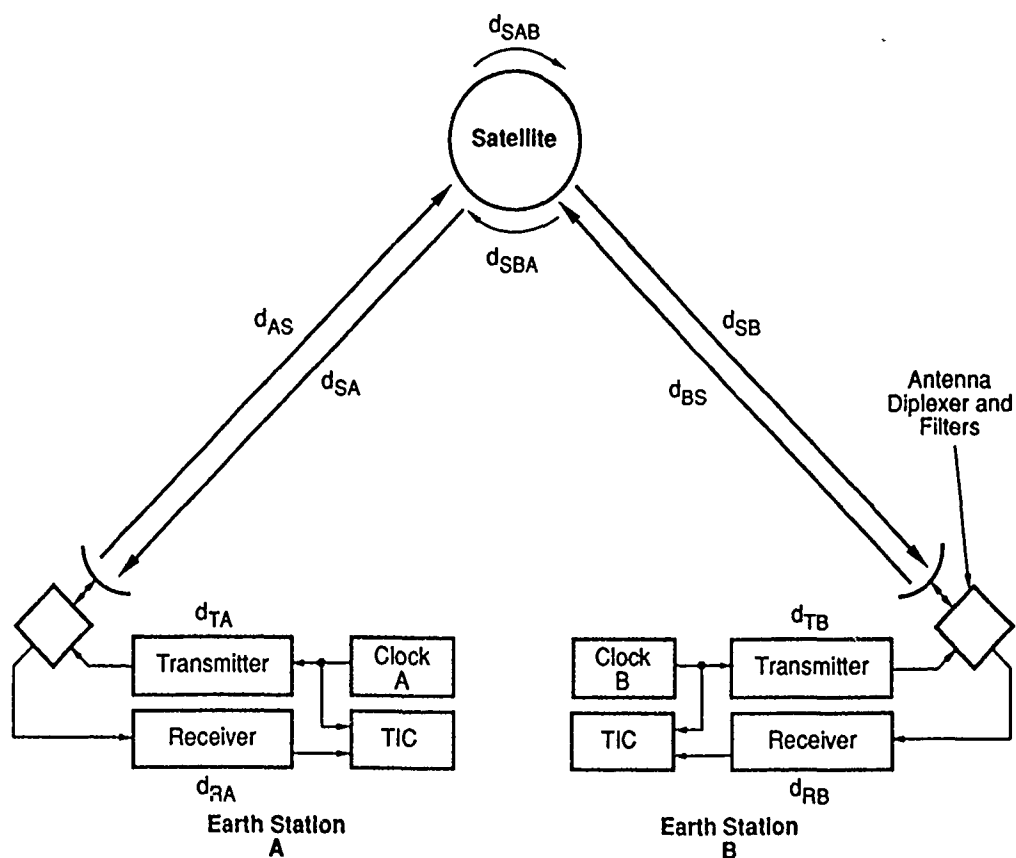


Fig. 2. Two-way time transfer using a satellite.

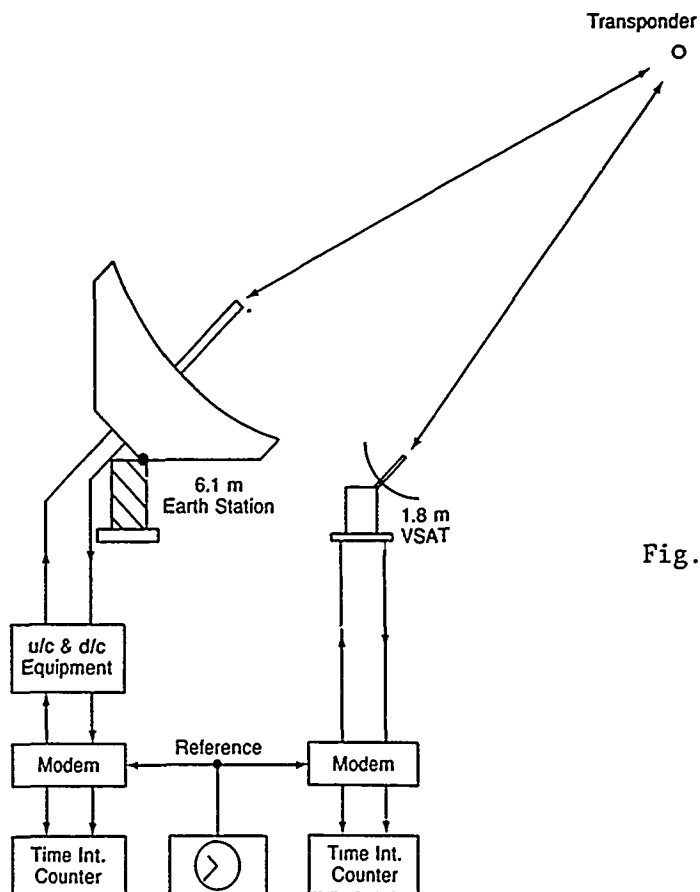


Fig. 3. Measurement procedure for differential delay between a fixed earth station and a transportable earth station, both collocated with a common reference clock.

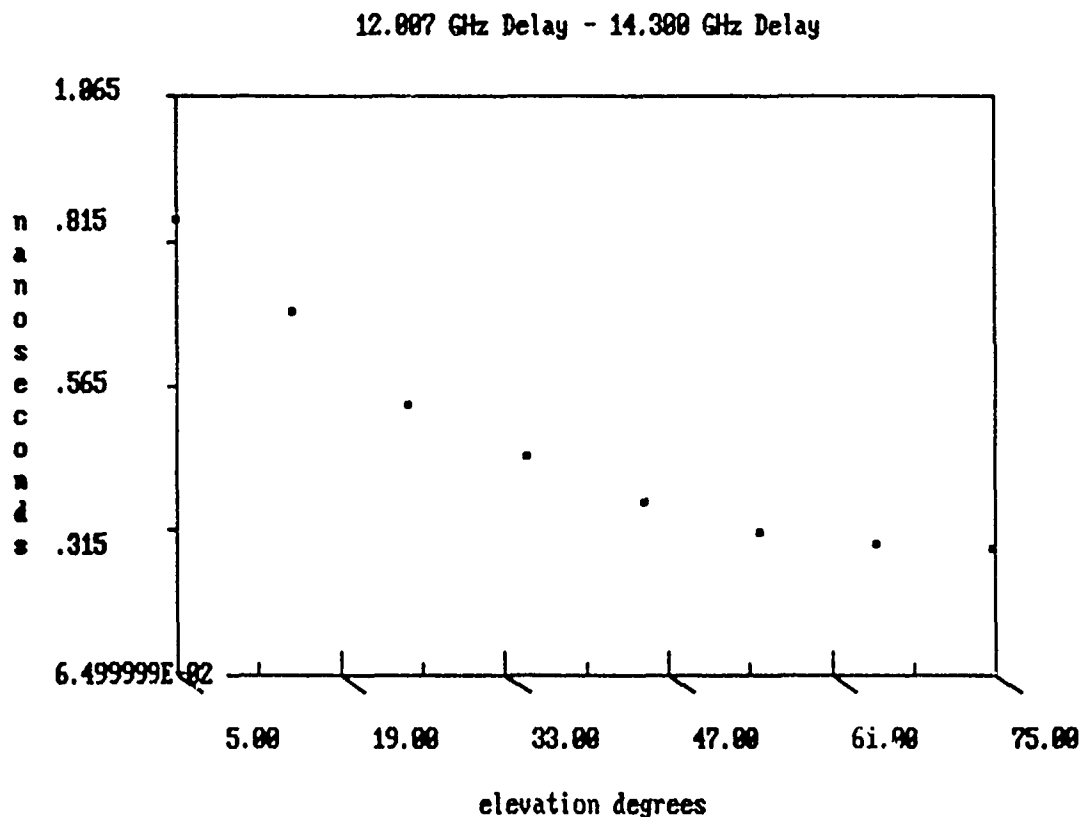


Fig. 4. Ionospheric nonreciprocity at Ku-band for various elevation angles.

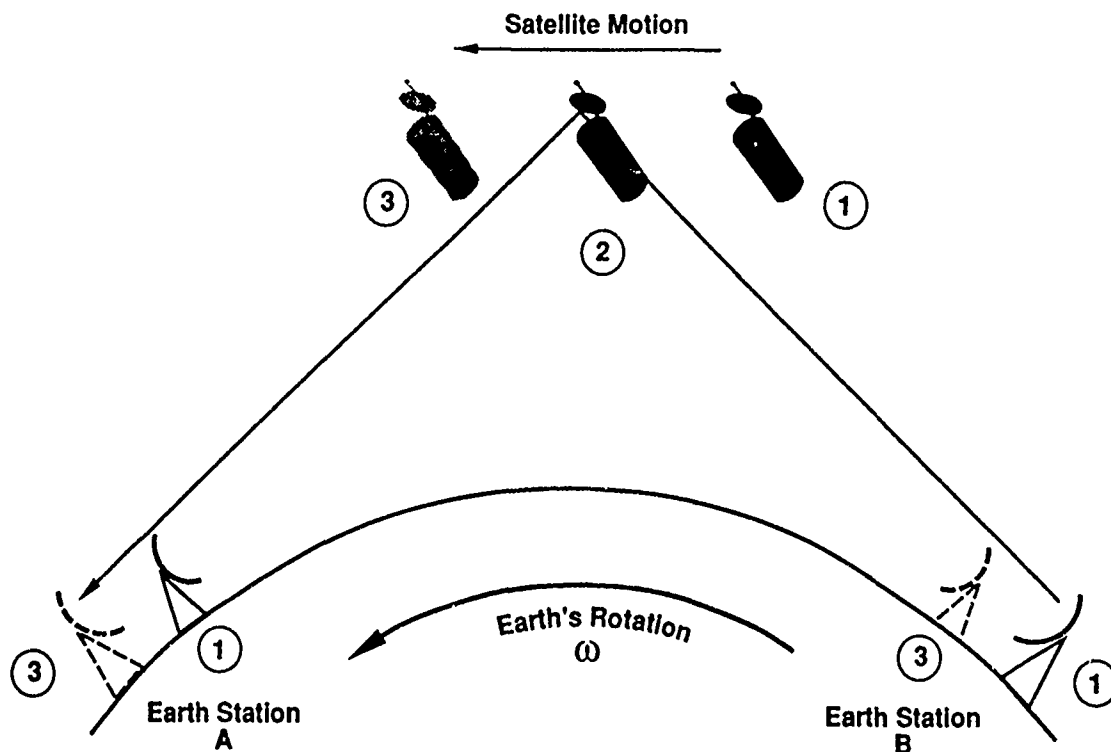


Fig. 5. Sagnac effect. View is from above the north pole.

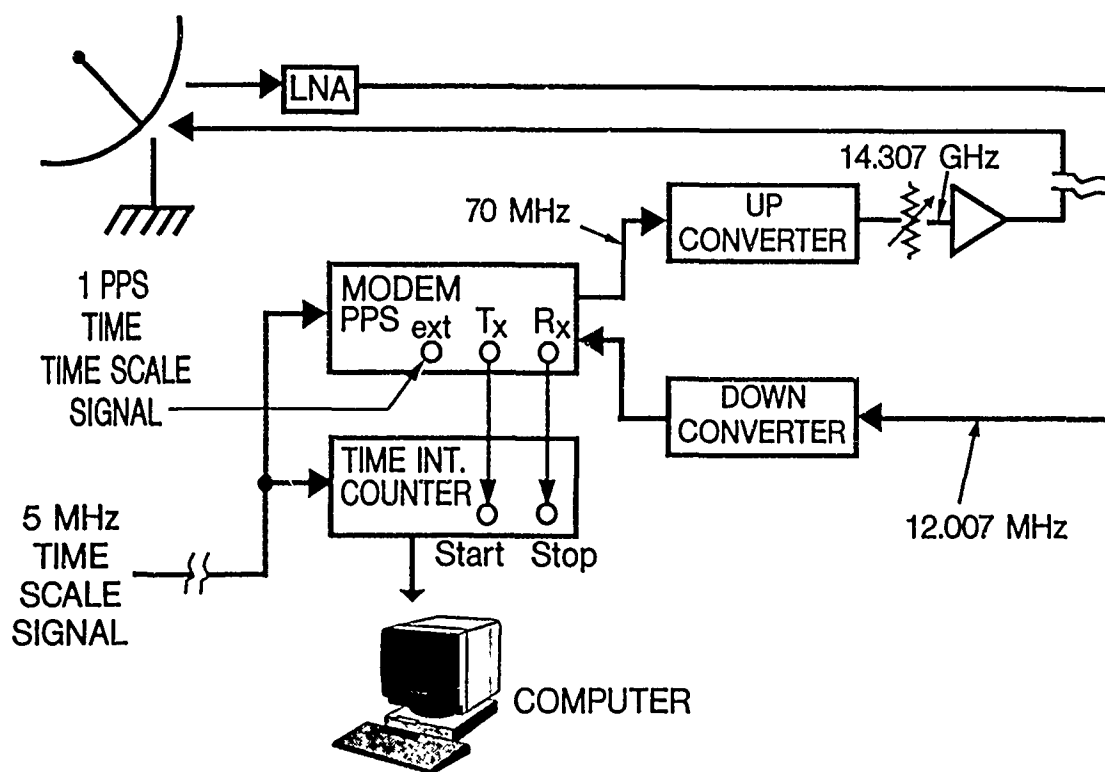


Fig. 6. Earth station equipment.

UTC(USNO) - UTC(NIST) TWO-WAY TIME TRANSFER DATA

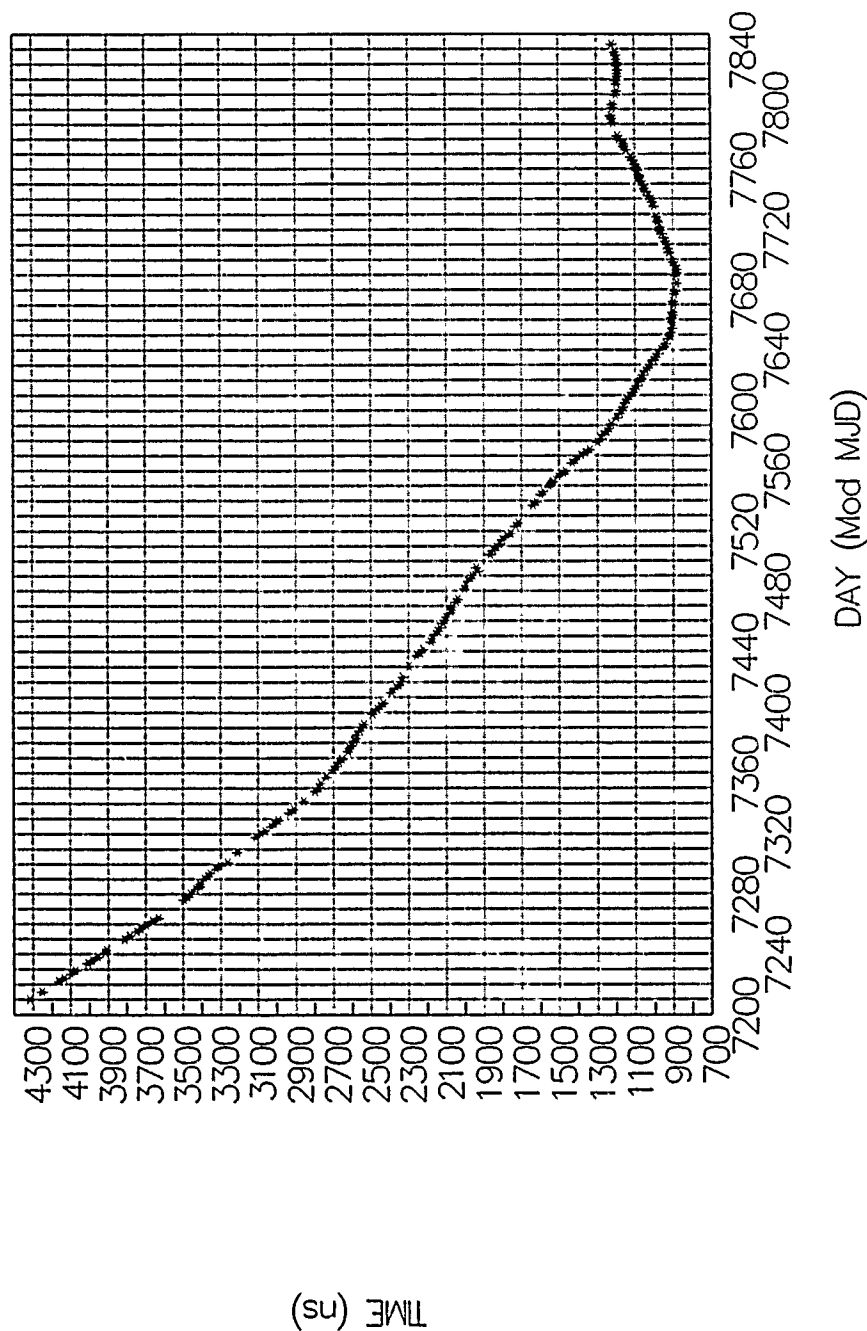
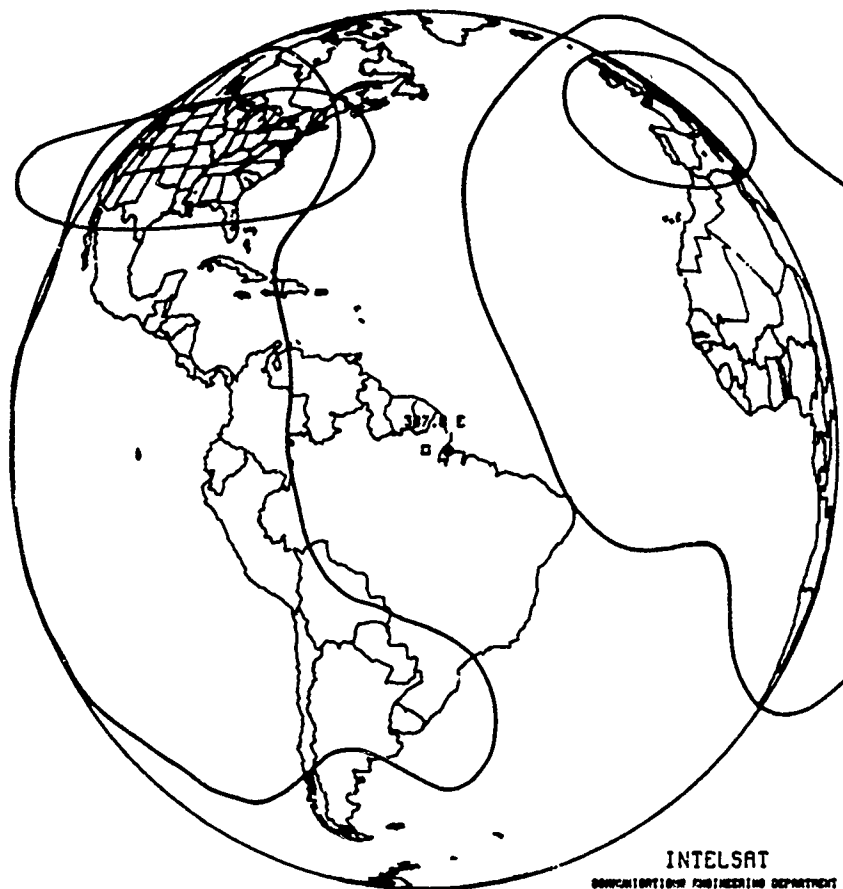


Fig. 7. Mean values of 5-minute two-way satellite sessions between NIST and USNO.

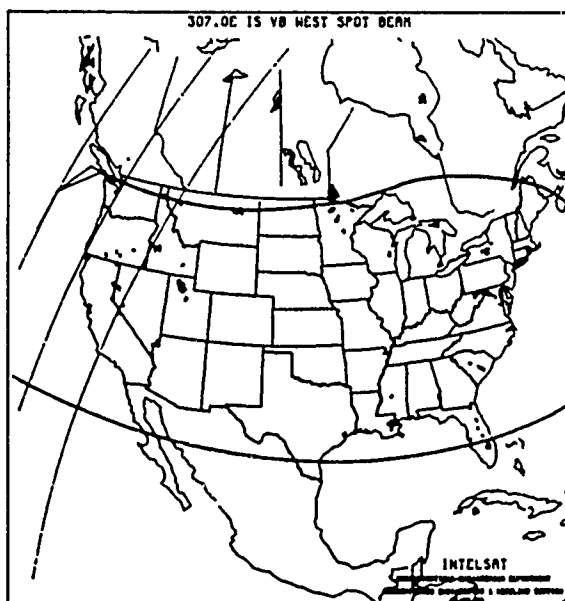
307.0E IS VB (F-13) (INCLINATION 0.0 BIAS .5E)



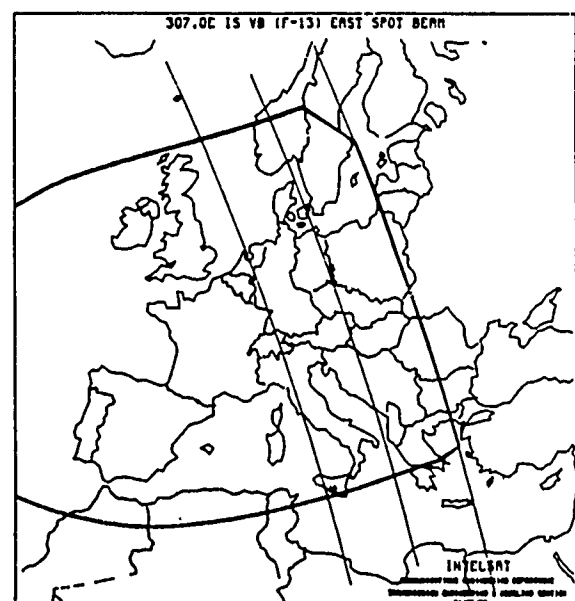
INTELSAT

COMMUNICATIONS ENGINEERING DEPARTMENT
TRANSMISSION ENGINEERING & MODELING SECTION
06/05/80

INTELSAT VA(1B) Interconnections from 307° East



INTELSAT VA(1B) West Spot Coverage
from 307° East



INTELSAT VA(1B) East Spot Coverage
from 307° East

Fig. 8. Coverage in North America and Europe by Intesat VA.



Fig. 9. Ku-band mobile earth station with 1.8 m dish.

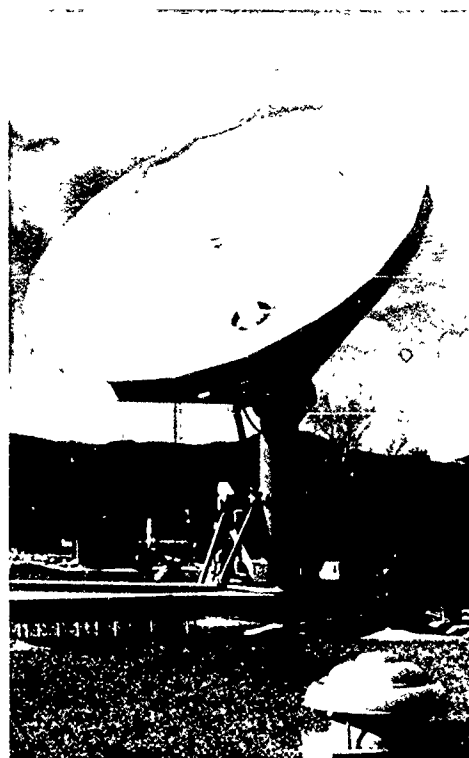


Fig. 10. Steerable 6.1 m dish at NIST.



Fig. 11. NIST earth-station laboratory.

QUESTIONS AND ANSWERS

CARROLL ALLEY, U OF MARYLAND: Would you say a few words explicitly about how you correct for the Sagnac effect?

MR. HOWE: I don't remember the number, but we calculate it and correct the data.

DAVID ALLAN, NIST: The size of the effect is 1.6 nanoseconds per square megameter of the path as projected on the equatorial plane. You don't need to know the area projected to much better than a square megameter to get one nanosecond accuracy.

MR. HOWE: The question was not so much what the value was, but the differences that we would encounter with some variables which we can't control.

A NEW TWO-WAY TIME TRANSFER MODEM

G. P. Landis, J. D. White, A. Gifford, and R. L. Beard

Naval Research Laboratory

Washington, DC

and

J. A. Murray

Sachs Freeman Associates, Inc.

Landover, Maryland

Abstract

The use of commercial communications satellites for precise time transfer has been performed with a variety of techniques for a number of years. Military communications systems can also provide this function in a few deployed systems. This paper will describe a new design of a time transfer modem that can be produced at a reasonable cost and enable users to make direct comparisons with the Naval Observatory with nanosecond precision. A flexible, all-digital design is being implemented that will enable a variety of different codes to be employed. Compatibility with existing equipment, such as the HARTL Modem, is a goal of this development. The design and operating modes of this equipment will be described.

INTRODUCTION

The United States Naval Observatory (USNO) routinely makes two-way time transfers through the Defense Satellite Communications System (DSCS). An interface with the system's spread-spectrum communications modems is used to provide a precise-time trunk line for interests located near the DSCS terminals. For a link with no communications modem, spread-spectrum time-transfer modems designed by the Naval Research Laboratory (NRL) were used. NRL is developing a modem that will work with very small aperture terminals and commercial satellites to serve other users requiring greater accuracy.

DESIGN APPROACH

A two-way spread-spectrum method (Figure 1) will be used because of its performance and its insensitivity to positions of receivers and satellites. Digital hardware is used in the modem design as much as possible to meet requirements for accuracy, long-term stability and versatility. The digital techniques also meet requirements for reliability and cost. The modem is being designed for maximum compatibility with other time transfer systems. Off-the-shelf equipment will be combined with some special purpose hardware. The off-the-shelf parts will include the satellite terminal (VSAT), the Personal Computer (PC) and the Digital Signal Processor (DSP) card. Items of special equipment will be an analog box and a digital board (Figure 2).

To avoid drift of analog circuits, the received signal will be digitized at as high a frequency as possible, 25 million samples per second (Figure 3). All processing after this point will use digital signal processing methods. The faster functions will be done with the dedicated special digital board hardware (Figure 4), and the slower phases with the programmable DSP card.

For versatility, a numerically controlled oscillator (NCO) will be used to generate a programmable code rate. For code selection a code generator chip with programmable taps will be used. The combination of an NCO and a programmable code generator give almost unlimited possibilities in code generation. It will be easy to generate a code compatible with the Hartl Mitrex modem or the Global Positioning System (GPS) clear/acquisition (C/A) code.

Under some conditions, problems arise in using digital method due to time quantization in the sampling of the data. It is possible by adding random noise at appropriate places in the processing to improve the time resolution of the measurements beyond a small fraction of the sampling period.

A 32-bit floating-point DSP will be used as the microprocessor. This DSP will be a commercial card that will plug into the PC backplane. The DSP systems are very fast, over 10 Million Floating Point Operations per Second (MFLOPS), and have C compilers. This will give expansion capabilities and make software development easier. The DSP system will configure the system hardware, control acquisition and tracking of the signals, demodulate and format the data on the received signal, make the range measurements, process the range measurements into time transfer information and control all communications functions with the PC.

All operator controls other than VSAT controls, power levels, frequency selection and antenna pointing, will be handled by the PC. In the communication mode, files will be transferred between the PCs of the participating stations.

SIGNAL STRUCTURE

The modem, which is under software control, can accommodate a wide variety of signal structures. For the planned bandwidth of about 3 MHz, binary phase shift keying (BPSK) will be used with a chipping rate in the order of 2 Mb/s. (It can easily be changed for compatibility with other systems). A 4095-bit maximal-length sequence is currently planned. To produce a code length of 1/600 second, a chipping rate of approximately 2.457 Mb/s will be used. The code length is chosen for quick synchronization, while still maintaining a robust capability to recover BPSK data sent at one bit per code cycle. A data rate equal to or at a submultiple of the code cycle rate makes for easier handling, since a part of the computation involves determining after the fact the state (1 or 0) of the previous data bit. (To resolve the PRN code's (1.66... ms) ambiguity, the receiver must recover a time tag having resolution to within a code cycle). From a signal-to-noise standpoint, the channel would support a considerably shorter code and higher data rate, and they might be used eventually, but a shorter code, when not modulated with data, would contain brighter spectral lines spaced farther apart and is currently being avoided.

DATA EXCHANGE FORMAT

No specific data exchange format has yet been adopted. Besides the time tag, which must be transmitted both ways, measurement data must be transmitted at least one way. Other coordination and

identification data are also needed. (Note that all but an unambiguous time tag can be sent via another channel or a different medium). A time tag need be sent only once during a continuous session, but the measurement data are probably best exchanged about once per second. Since one pulse per second is a common output signal for clocks, and measurements will be made by most users with reference to that timing signal, a one-second measurement cycle and time tag seems apt. (Measurements in the NRL receiver will be made over shorter intervals and averaged for the one-second reading). To resolve the ambiguity of the once-per-second time tag, a time-of-day (TOD) message giving hours, minutes and seconds of the day and a day-of-year (DOY) word may be needed by some users. Also of interest to some timekeepers is the date and sign of the next leap second.

The message format could and may be left completely open (except for the time tag). However, the most generally useful information for a timekeeper might be included in a fixed-format segment for efficient transmission without framing delimiters. Optional data may be transmitted during the rest of the second. One possibility for character representation would be 7-bit ASCII plus start and stop bits (a 9-bit asynchronous version) to maintain time-tag integrity. Tables 1a and 1b show a possibility for message formats. (A BCD version which would preserve the integrity of the time tag is also being considered; it is much more efficient in transmitting the numbers in the fixed field and, at 8 bits per character (2 decimal digits), would support all the ASCII characters needed to send numbers, the capital alphabet and all required punctuation).

TABLE 1a. Data Possibilities
600 bit/sec Asynchronous, 9 bits/character, 7-bit ASCII
Data Sent by USNO

Data	Characters	No-Data Characters	Bits	Cum. Bits
TOD	6	ASCII NUL	54	54
Current DOY	3	ASCII NUL	27	81
Leap-Second (DOY+Sign)	4*	ASCII NUL	36	117
Sta. ID + Reply Code #	4	ASCII NUL	36	153
Optional Data	48	ASCII NUL	432	585
Remainder of Second**	Marking	All mark bits	15	600

The structure shown in Table 1 could designate 36 different pseudo-random noise (PRN) reply codes and 1296 different stations using alphanumeric characters. Station 00 might call for no one, while station ZZ might designate a USNO broadcast of general information. A broadcast mode, either for modest-accuracy users or for more detailed information, is easily accommodated.

GENERAL DESCRIPTION OF OPERATIONS

It is expected that USNO would ordinarily operate with one station at a time, but could operate with multiple stations using code-division multiplexing. (Note that USNO need transmit only one PRN code but would receive different codes from the other stations). The identification code of a single user would be sent each second by USNO in the proper slot. However, more stations can be

TABLE 1b
Data Possibilities
600 bit/sec Asynchronous, 9 bits/character, 7-bit ASCII
Data Sent by Remote Stations

Data	Characters	No-Data Characters	Bits 7	Cum. Bits
TOD (hh:mm:ss)	6	ASCII NUL	54	54
Current DOY	3	ASCII NUL	27	81
Leap-Second (DOY+Sign)	4*	ASCII NUL	36	117
Sta. ID	2	ASCII NUL	18	135
Measurement Data	11	ASCII NUL	99	234
Optional Data	39	ASCII NUL	351	585
Remainder of Second**	Marking	All mark bits	15	600

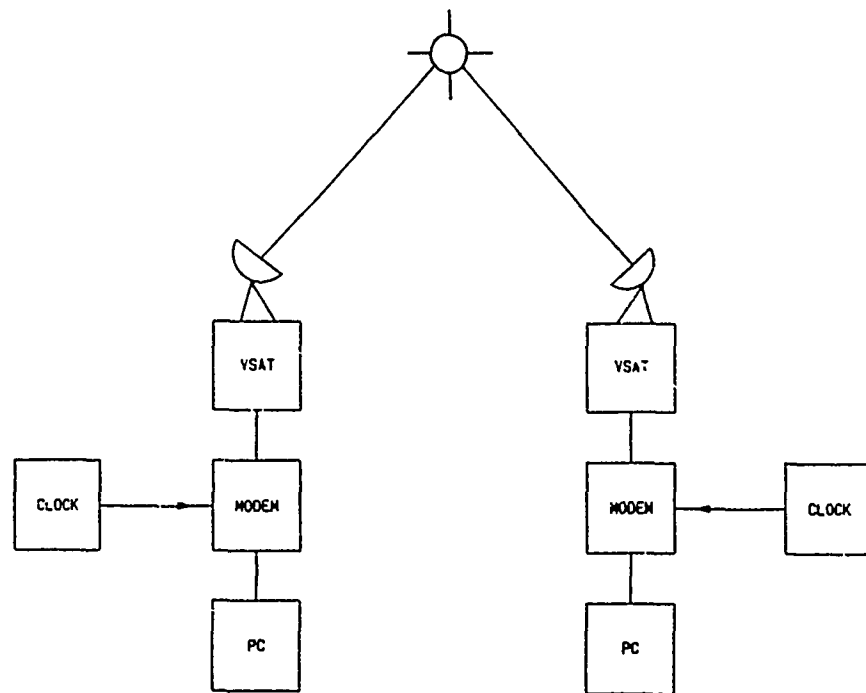
* The entire leap-second information could be represented more compactly by three decimal characters or by 2 alphanumeric characters.

** The first start (space) bit in the TOD message denotes the beginning of the second.

worked by sending their IDs less frequently. To give USNO the required single point of control over the network, a user station would monitor the USNO primary code (continuously or on schedule) and would transmit only while being polled by USNO. If one fails to receive its ID over a pre-established number of seconds, it would stop transmitting and would not come on again until its ID is received at least several times.

a specially designated PRN code might be reserved for user requests for service from USNO, who could then poll the station on the primary USNO transmitting code and specify a reply code. To preserve single-point control, the user must receive USNO on the primary code before initiating a request.

A large increase the communications capability could be had by using additional PRN sequences. With both carrier and code synchronization already established on the primary code, a second code could be received with very little additional complication. The data rate used with the second code need not be related to the code cycle length and might be considerably higher than that of the primary code. There are no current plans to implement this mode in the first model of the modem.



TIME TRANSFER SYSTEM

FIGURE # 1

FIGURE # 2

TIME TRANSFER SYSTEM

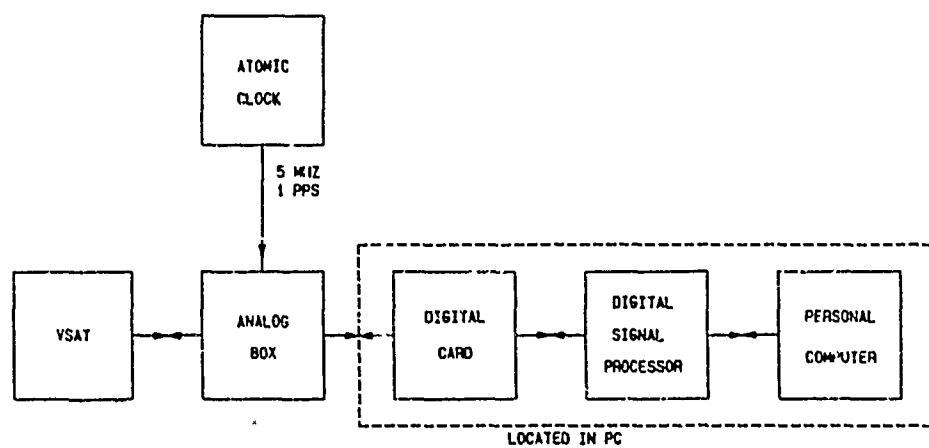


FIGURE # 3

ANALOG BOX

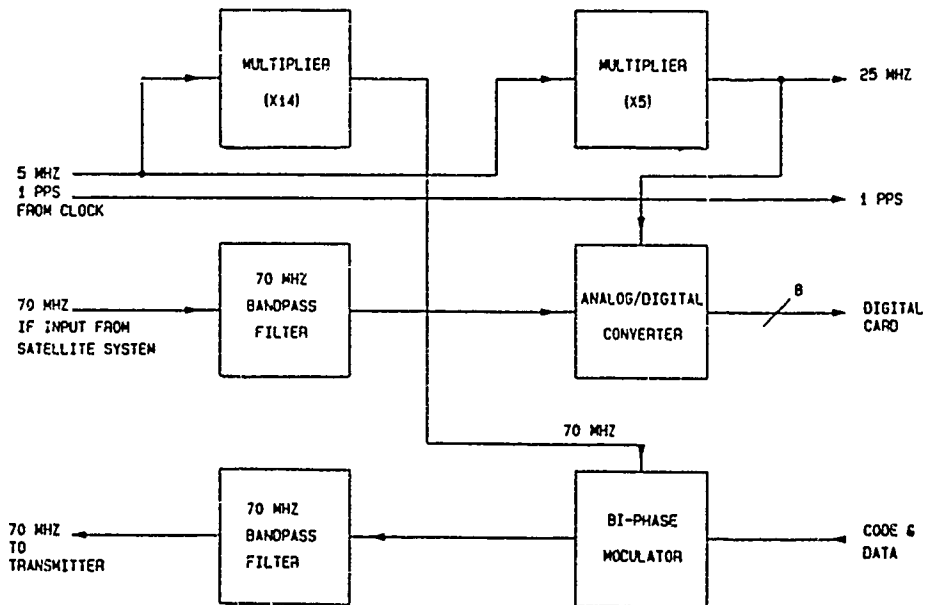
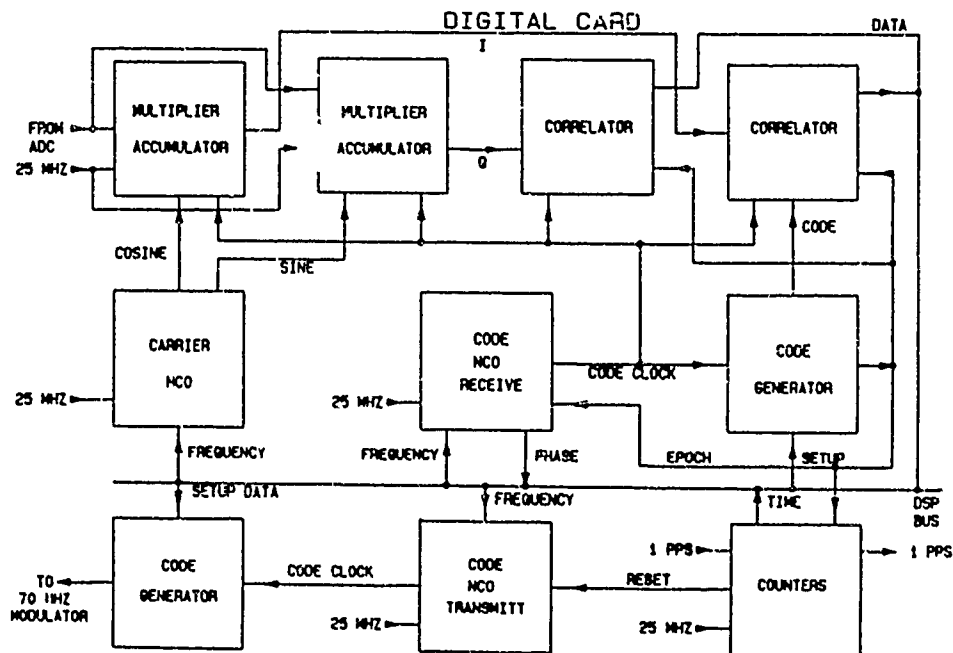


FIGURE # 4



QUESTIONS AND ANSWERS

DAVID ALLAN, NIST: what is your time table for this project?

MR. LANDIS: We would like to have it finished within a year. That is the modem part, not the GPS part.

PHASE DISTRIBUTION ON FIBER OPTIC CABLE

John C. Webber and Dorsey L. Thacker
Interferometrics Inc.
8150 Leesburg Pike, Vienna, VA 22182

Abstract

A fiber optics link has been tested for distributing stable phase information at a frequency of 216.98 MHz for the Kickapoo transmitter of the Naval Space Surveillance radar. Laboratory experiments have been carried out with a specially modified laser and no special precautions were taken to minimize reflections. The relative stability of different fibers in the same cable was tested with repeated cycling of the cable temperature. The relative stability of two fibers each 1 km in length over hundreds of hours including temperature changes of 25 kelvins was better than 25 psec peak-to-peak, or about 1 part in 200,000.

INTRODUCTION

The Naval Space Surveillance Kickapoo transmitter near Wichita Falls, Texas is a 10,500-foot long north-south linear array of 2556 dipole radiators which produce a fan-shaped beam at a frequency of 216.98 MHz. This beam covers essentially the entire continental U.S. so that any satellite which penetrates it produces reflections. These are received at multiple sites and the positions and orbits of the satellites deduced. Since its construction 25 years ago, the performance of the array has degraded due to difficulties in maintaining precise phasing of the array. The array is presently phased by returning reference signals through buried coaxial cables which have experienced physical deterioration. The objective of this project was to investigate the feasibility of replacing the phase reference cables with their fiber optic analog.

In order to determine the expected performance of such a system, laboratory experiments were conceived and executed to measure the characteristics of a fiber optic link operating at the transmitter frequency. After extensive consultation with pioneers in this field, a set of components was identified which appeared likely to have the desired stability and ease of handling in both laboratory and field environments. Critical to this study were commercial availability, reliability, and ease of installation and repair by field personnel.

EXPERIMENTAL SETUP

The components chosen included a 1300 nm laser and two receivers, both manufactured by Ortel Corporation. The laser was specially modified to reduce the effect of cable reflections on the output signal. Such reflections have long been observed to have deleterious effects on the phase of the laser output in such systems^[1-3]. No additional isolation between the laser and the remainder of the optical

system was used. For ease of configuration of the experimental apparatus for making several different measurements, it was decided to connect all optical elements by means of the field-installable AT&T ST connectors. These connectors have moderate return loss (about 30 dB), which is undesirable, but they are easy to install and replace if necessary. Reflections in a field installation could be reduced by fusion splicing if necessary.

The fiber optic cable chosen was of loose-tube construction, built by Siecor Corporation. The advantage of this cable over tight-buffered cable for this application is that the fibers within their large-diameter tubes are not tightly constrained. Thus, when mechanical stresses are imposed by temperature changes, the fiber is free to adjust itself and minimize the stress. This in turn results in smaller changes of the reflection properties than with other constructions. The cable was kept tightly wound on its original drum and placed in an insulated chamber whose temperature could be elevated above ambient by 25 kelvins, an amount sufficient to cause easily measurable changes in the total delay.

The experimental setup for the measurements described here is shown in Figure 1. A 5 MHz signal derived from a hydrogen maser frequency standard was split and sent to two high-stability frequency synthesizers. In the upper path, a generated signal at 216.98 MHz was applied to the modulation input of the fiber optic transmitter. This transmitter is equipped with an internal oven but none of the remainder of the apparatus was temperature-controlled. The optical signal was split in a Gould coupler and sent to two separate fibers in the cable. After the trip through the 1-km cable, the two optical signals were separately detected by identical receivers. The resulting electrical signals were filtered and amplified. Both passive bandpass filters and active crystal-controlled phase-lock loops were used and in the long-term measurements described here there was no measurable difference in the results using different types of filters.

Each 216.98 MHz signal from the fiber optic system was then mixed with a signal at 211.98 MHz derived from a second identical frequency synthesizer. The resulting 5 MHz signals were filtered and amplified, then sent to the NRL frequency standard measurement system. They were compared to the 5 MHz signal derived directly from the maser; it was thus possible to measure the relative phases of the 216.98 MHz signals propagated through separate fibers. The frequency standard measurement system is regularly used for evaluating the performance of high-stability oscillators and has a resolution of 20 psec at a frequency of 5 MHz. The equivalent noise at our frequency is reduced by a factor of $216.98/5$, and is thus expected to contribute only 0.5 psec of noise. The system measures a point once per hour.

RESULTS

Many different tests were performed to evaluate separately the stability and noise contributions of the electronics, the fiber optic transmitter/receiver pairs, and the fibers themselves. The noise level of the relative phase measurements using the entire system without including the 1 km cable was about 20 psec peak-to-peak, measured at 216.98 MHz. This noise comes from several sources, including the relative stability of the two frequency synthesizers, temperature variations of the other electronic components, and the 250-foot coaxial cables used to carry the 5 MHz signals from the maser to the experiment room and back to the measurement system.

One measurement sequence covering 48 days of continuous data is shown in Figure 2. The delay measurements of the two separate fiber and receiver channels are superimposed and lie on top of each

other; the difference is plotted in the center. The differential delay for the same period is plotted (using 11-point boxcar averaging) on an expanded vertical scale in Figure 3. At about 1130 hours, the heater was turned on and the temperature increased by 25 kelvins; the fiber responded with a time constant of about a day due to being wrapped tightly on its shipping drum. At 1400 hours, the temperature was allowed to drop back to ambient. At about 1250 hours, the building ventilation equipment began to malfunction, with excursions of a few kelvins evident from then until the end of the measurement period.

The total delay through each fiber was about 4.89 microseconds. The change in delay with the controlled temperature change was 1.6 nsec, corresponding to a temperature coefficient of delay of 1.3×10^{-5} /kelvin. The differential delay between the two fibers experienced a maximum excursion of 20 psec peak-to-peak and the effect of the controlled temperature change of the fibers alone is not seen in the differential data. Note, however, that the scatter of the points from the mean is somewhat worse during the period in which the building ventilation was malfunctioning. We conclude that most of the differential delay excursion is caused by changes in the electronics and not by differences in the fibers themselves. If we restrict our attention to the data taken before the building ventilation malfunctioned, and correct for the difference of a factor of 1.0021 in the electrical length of the two fibers, we obtain a differential temperature coefficient of 22 femtosec/kelvin for a combination of the fibers and electronics.

Since the phase stability requirement target for the Kickapoo transmitter is 51 psec, or ± 2 degrees of phase at 216.98 MHz, we also conclude that a fiber optic system using the components chosen for this experiment will easily satisfy the requirement. In early 1990, the first cable will be laid at the site for extended testing in the field, which should ultimately lead to a complete system for controlling the transmitter phases.

ACKNOWLEDGEMENTS

We thank G. F. Lutes for helpful conversations during the design phase of this project. We also thank J. D. White and E. Powers of the Naval Research Laboratory for their assistance in installing our equipment and instruction in the use of the frequency standard measurement system. We thank E. J. Wadiak of Interferometrics for his frequent assistance in monitoring the operation of the system. This work was sponsored by Naval Research Laboratory contract number N00014-87-C-2547.

BIBLIOGRAPHY

1. Reference Frequency Transmission over Optical Fiber (1986), G. F. Lutes and A. Kirk, Proceedings of the 18th Annual PTTI Meeting
2. Optical Fibre Link for Reference Frequency Distribution (1988), N. V. G. Sarma, Australia Telescope Memorandum
3. Interferometer Analog Optical Link Lines (1989), James R. Coe, NRAO Electronics Division Technical Note No. 149
4. Theoretical Radiation Patterns of NAVSPASUR Transmitting Antennas (1988), Steven L. Berg (Interferometrics Inc.)

5. Fiber Optic Frequency Transfer Link (1988), G. F. Lutes et al., Proceedings of the 42nd Annual Frequency Symposium
6. The NRAO 85-3 Fiber Optic Receiver Link, John C. Webber and D. L. Thacker, Interferometrics Laboratories Technical Report

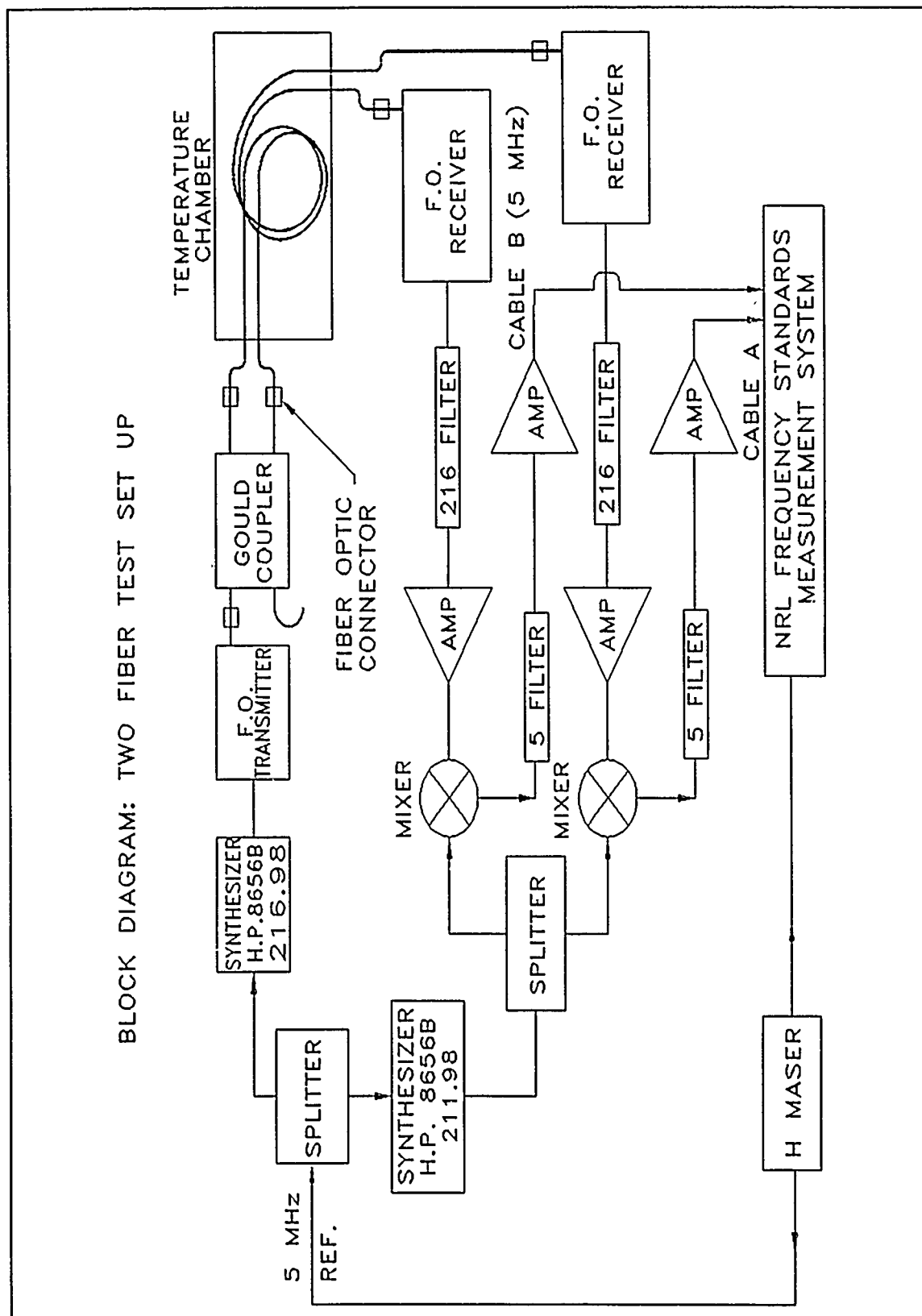


Figure 1 Experimental setup for the measurements.

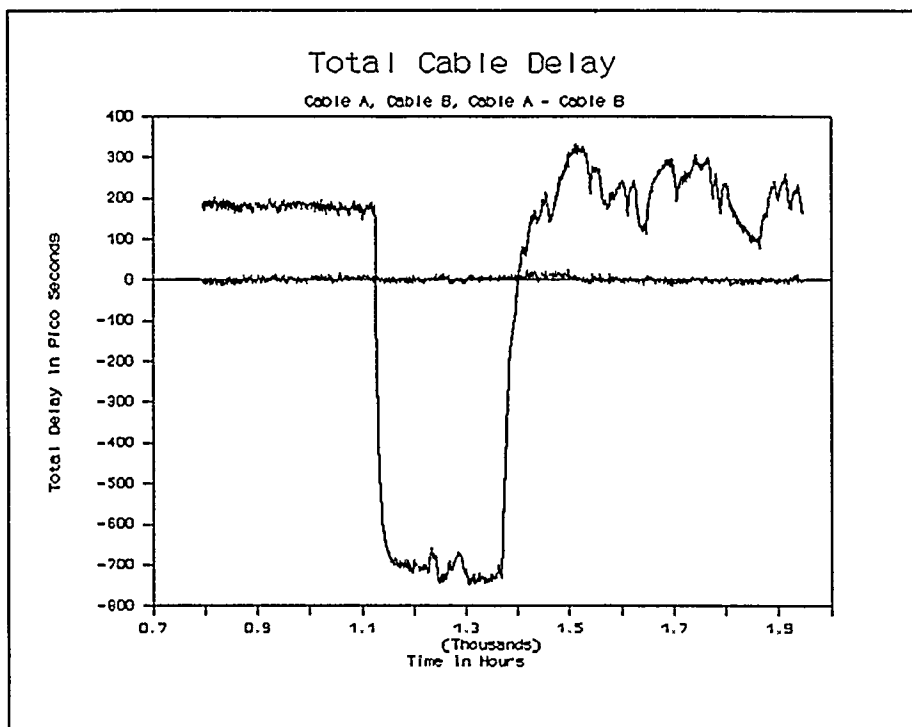


Figure 2 The total delay for two fibers is plotted and almost overlap each other exactly. The difference between the two fibers is also shown.

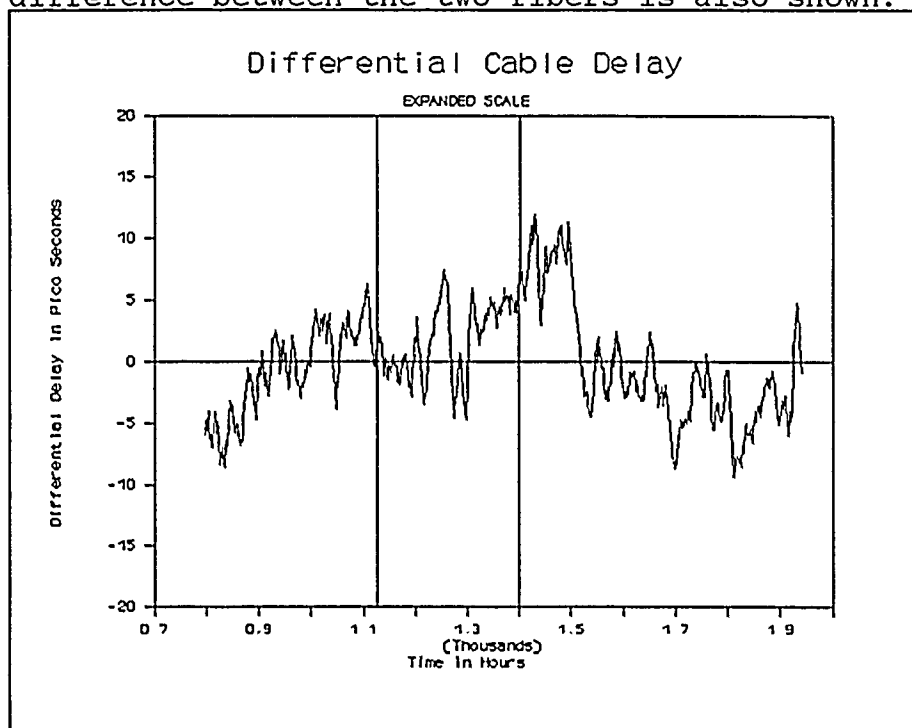


Figure 3 Differential Delay between two fibers with an expanded scale. The two vertical bars are at the times of the temperature change.

GPS SYNCHRONIZED DISCIPLINED RUBIDIUM FREQUENCY STANDARD

D. Earl Fossler
TRAK Systems
Div. of TRAK Microwave
Tampa, Florida

Abstract

A disciplined rubidium frequency standard steered by the corrected 1 PPS output from a GPS timing receiver or other stable 1 PPS source can provide a low phase noise, modest cost, frequency standard with long term frequency stability of a cesium standard and short term stability of better than 1×10^{-11} . Phase correlation to the 1 PPS input is maintained to within 50 nanoseconds during disciplining and within 100 nanoseconds during a five hour coasting period with no disciplining input.

INTRODUCTION

Disciplined crystal frequency oscillators have been around for many years. They are used mostly as "cleanup" oscillators following noisy frequency sources and as failsafe outputs driven by atomic frequency standards. Cesium and rubidium frequency standards incorporate disciplined crystal oscillators as part of their control loop. Even though rubidium frequency standards are used for many timing applications, disciplined rubidium frequency standards are not in wide use.

GPS timing receivers have been used for several years as a time correlation measuring instrument or time transfer instrument. One version of these receivers generates 1 PPS corrected to the GPS satellite epoch. There has been a lot of interest in using an output from this type of receiver as a disciplining source for 5 or 10 Mhz oscillators. The 1 PPS output from most of these receivers exhibits a very accurate long term stability, but, until we have full GPS satellite coverage, this output is present for only a portion of the day. Several timing instruments on the market provide a frequency output synchronized to GPS, but most of these units do not have the necessary long term frequency and temperature stability required for accurate time generation.

Over the past several years, TRAK Systems has gained considerable knowledge in using 1 PPS reference signals such as range time codes to discipline precision crystal oscillators used in synchronized time code generators. All of these oscillators have used CPU control and nonvolatile digital memory, and all of the units maintained both a frequency lock and precise phase lock to the disciplining 1 PPS. During our studies, we also investigated the various types of control loop approaches that provide satisfactory disciplining under a variety of laboratory and field conditions. Some algorithms provided fast attack for initialization, while others provided good long term smoothing through various noise conditions. All of these experiments were conducted with ovencontrolled oscillators, and over 200 units were successfully deployed worldwide.

In 1987, we were faced with a requirement to maintain precise time and frequency using a GPS receiver and a rubidium frequency standard. The required accuracy relative to GPS or UTC was on the order of 100 nanoseconds, with a required phase resolution of approximately 20 nanoseconds. Knowing that the GPS satellite coverage had gaps of up to six hours, we knew that, for several years at least, the design would have to provide for very low drift during coasting periods when there is no disciplining signal available. A market survey revealed that, although there were several good rubidium oscillators on the market, there were no suitable disciplined oscillators or oscillator disciplining modules available. It was decided that we would draw upon the knowledge gained from disciplining crystal oscillators and develop a rubidium standard operating at a constant temperature and using "C-field" voltage control. Of course, existing control algorithm would have to be translated three orders of magnitude from 1×10^{-9} to 1×10^{-11} . It was obvious from the beginning that three primary conditions had to be met:

1. A means had to be devised to overcome the rather large temperature drift problem that exists in commercially available rubidium modules, even over a limited temperature range.
2. Average frequency would have to be calculated with high precision, on a continuing basis, with the control voltage digitally stored. This would provide for minimum drift during coasting periods.
3. Vernier phase corrections, which were to be made by momentarily adjusting the frequency up or down, would have to be made almost continuously while tracking, but each increment would have to be small enough to preclude introducing measurable phase noise.

The task was undertaken, and we have designed a disciplined rubidium frequency standard that exhibits some very desirable characteristics previously not available on the market. This unit was designed especially to generate 10 Mhz, 5 Mhz, and 1 PPS outputs phase coherent to the long term average of a 1 PPS input. The 1 PPS input does not need to be continuous and may have jitter. This is important because the 1 PPS output from most GPS timing receivers exhibit these undesirable characteristics. The long term stability of the disciplined rubidium frequency standard takes on the long term stability of the 1 PPS input and keeps the short term stability of its rubidium oscillator.

THE DESIGN

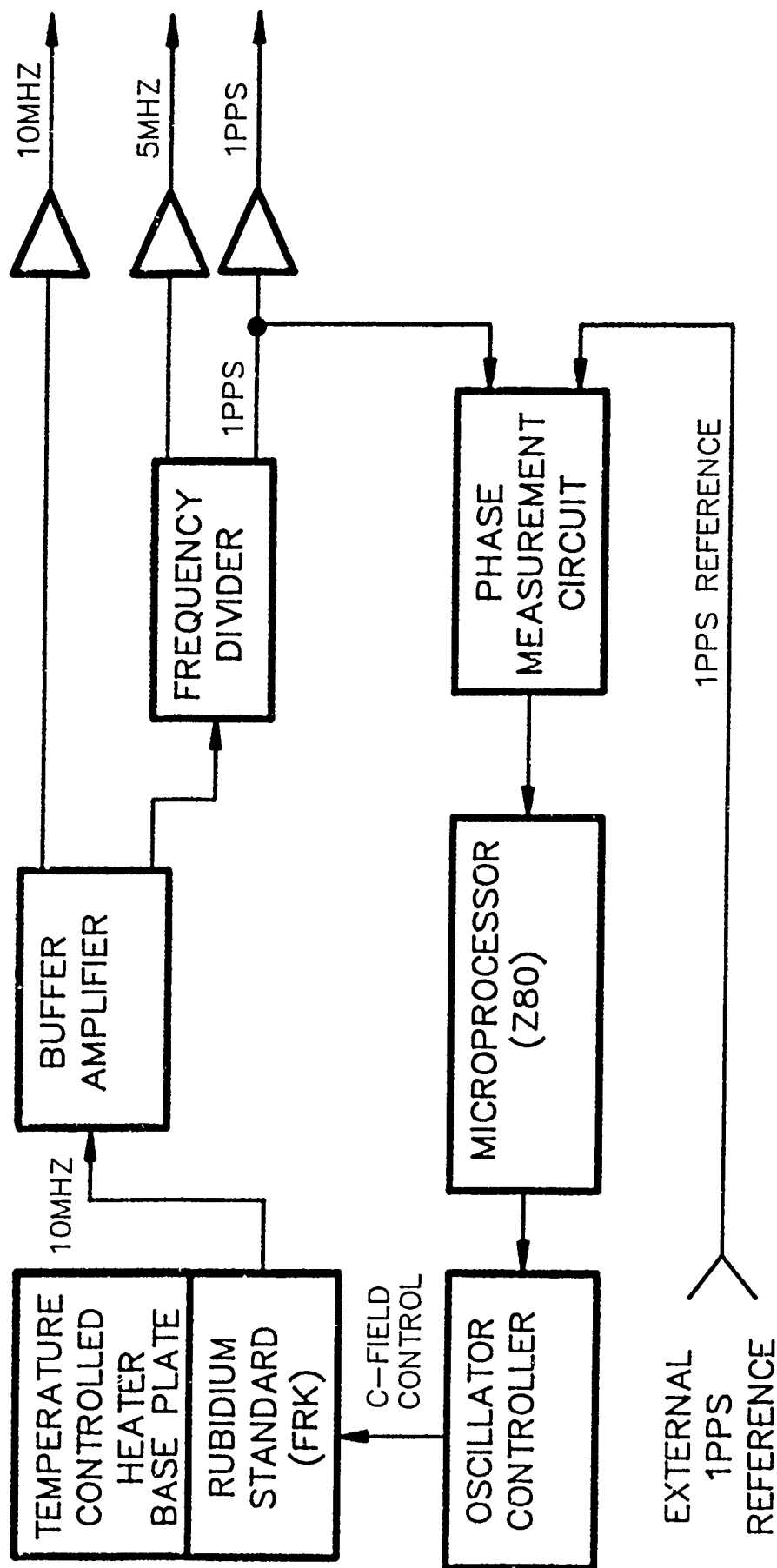
Precise frequency compensation for environmental temperature changes for rubidium oscillators is difficult to accomplish. The algorithm for temperature compensation is not the same for each unit; therefore, each unit must be characterized in order to assure accuracy over a wide temperature range. Furthermore, periodic recalibration is required to maintain this accuracy. We therefore chose to use a heated baseplate with dual proportional controlled heaters to maintain a constant rubidium module temperature. To further assure temperature stability, we purchased rubidium modules with internal compensation characteristic that is flat in the range close to the baseplate set point. Base plate temperature is held to within a plus or minus one degree Celsius. This design provides for the most stable frequency output over a normal temperature range.

The block diagram for the disciplined frequency standard shows the active elements used in our design. There are six major elements in this unit: the rubidium standard, an isolation amplifier, frequency dividers to provide the 5 Mhz and 1 PPS signals, a phase measurement circuit, the microprocessor,

and the oscillator frequency control circuit. The rubidium standard produces a 10 Mhz output, which is buffered to supply the 10 Mhz sinewave output from the unit and is also used to supply the input to the frequency dividers. The frequency dividers generate the 5 Mhz and 1 PPS outputs from the unit and one of the 1 PPS inputs to the phase measurement circuit. The second input to the phase measurement circuit is the external reference 1 PPS. Since maintaining phase coherence of the output 1 PPS to the input 1 PPS reference is just as important as maintaining precise frequency from the 10 Mhz output, the phase measurement is done at 1 PPS. This phase detector measures the difference as a signed number between zero and one-half second with 20 nanosecond resolution.

The output of the phase measuring circuit is processed by the microprocessor and stored. Next, the stored digital number is converted to an analog output from the oscillator control circuit that directly controls the C-field input of the rubidium frequency standard. This closes the loop.

The characteristics of the control loop are provided by the microprocessor program. In order to assure the required disciplining characteristics, several modes of operation are used, with a different algorithm being employed for each mode. The first mode is entered upon power turn-on. After the 1 PPS reference signal is present and the rubidium module has obtained frequency lock, the microprocessor generates a jam-sync to synchronize the two 1 PPS signals to within 200 nanoseconds. During the first hour, a fast algorithm disciplines the rubidium to produce a 1 PPS phase coherence of better than 100 nanoseconds and a drift rate of less than 20 nanoseconds per hour. After two hours, the phase coherence is reduced to less than 50 nanoseconds, and After a day of disciplining, the unit can coast without a reference input with its 1 PPS output drifting less than eight nanoseconds per hour including the combined effects of frequency offset, aging, and temperature changes between $+5^{\circ}\text{C}$ to $+40^{\circ}\text{C}$. When the disciplined standard is driven by the 1 PPS output from our Model 8800 GPS Station Clock, the 1 PPS output of the disciplined frequency standard is maintained within 100 nanoseconds of UTC time using Block I satellites.



BLOCK DIAGRAM
DISCIPLINED RUBIDIUM
FREQUENCY STANDARD

SK0306

A GPS DISCIPLINED RUBIDIUM CLOCK

Wayne Dewey
Kinematics/TrueTime
3243 Santa Rosa Ave.
Santa Rosa, CA 95407

Abstract

Sub-microsecond timing accuracy for event tagging and multi-site synchronization is possible using the Global Positioning System. In order to maintain a high degree of accuracy during periods when no satellites are visible, a highly stable local time base is required. For those cases which require Cesium oscillator stability, initial cost and continuing maintenance of the Cesium oscillator must be considered. A viable alternative is to use the Global Positioning System and an oscillator disciplining process. With this system, near Cesium performance can be achieved using a more rugged lower cost Rubidium oscillator. Additionally, when 24 hour satellite coverage becomes available, system performance may surpass that of a Cesium in long term stability.

INTRODUCTION

In recent years, time synchronization requirements between remote sites has become more demanding in terms of accuracy and stability. Power utilities are now looking to synchronize sites to under one microsecond to allow a means of maintaining grid stability while increasing power flow, and to time-tag power disturbances for location and analysis. Increasing demands for synchronous telecommunications requires both precise time and a stable frequency source at all sites.

The Global Positioning System (GPS) presently offers the means to satisfy sub-microsecond timing requirements worldwide on a daily basis. Additionally, while the short term stability of the GPS is fair, the long term stability of the GPS is excellent and approaches the stability of the UTC time source for GPS.

Is it possible to instill the long term stability characteristics of GPS into a low cost local oscillator which has good short term stability, thus satisfying both inter-site timing and local stability requirements with one system? In order to do so, all long term drift and aging characteristics of the Rubidium must be removed without disturbing the short and medium term stability of the oscillator. Additionally, long term frequency accuracy must be improved while maintaining accurate time.

This paper presents the results achieved when a local Rubidium oscillator is disciplined to GPS. Two control algorithms were tested, one controlling for zero frequency error and one for zero time error. The results of each are presented.

THE COMPONENTS

Both of the algorithms tested are designed to remove aging and long term drift components of the Rubidium oscillator while maintaining an accurate frequency. The first algorithm, Time and Rate

control, is an order 2, type 2 Phase Locked Loop which controls the Rubidium for zero time (or phase) error. This loop is designed to minimize the integral of frequency error over long term. The second algorithm, Rate control, is a Frequency Locked Loop which controls for zero frequency error. Both algorithms remove accumulated 1 Hz time error once per day.

THE UNIT UNDER TEST is a GPS-based Digital Clock (GPS-DC) with integral GPS time receiver and miniature Disciplined Rubidium oscillator. The Rubidium oscillator serves as the local time base for both the GPS-DC clock electronics and the GPS receiver. The GPS-DC has a specified accuracy of 100 ns to GPS and 250 ns to UTC(USNO) when tracking satellites.

THE GLOBAL POSITIONING SYSTEM is the standard upon which the disciplining process is based, and as such must be accurate and stable. Timing accuracy of GPS to UTC(USNO) is specified at 150 ns but has been reported to be as low as 35 ns^[5,9]. The long term stability of GPS is shown in Figure 1, which is the Allan Variance of GPS time transfer stability. Note with a 16 day τ or sample period, the frequency stability $\sigma_y(\tau)$ is 1.9×10^{-14} ^[1].

THE GPS RECEIVER is a Rockwell Collins Navcore I receiver. The receiver has a basic timing accuracy of 100 ns to GPS time and 250 us to UTC(USNO) time when the receiver's antenna position is known within 25 meters^[4,5]. The GPS receiver outputs information in the forms of a 1 Hz on-time pulse and various serial data. Among the serial information outputted is the variable Range Bias, used in the disciplining process. With the GPS receiver placed in position hold mode, Range Bias effectively represents the difference between the GPS receiver's local internal time and GPS time in units of meters, directly translatable into seconds of error. Because the GPS receiver's local time base is the Rubidium oscillator, any medium to long term changes in Range Bias are directly attributable to changes in the Rubidium oscillator. Range Bias has a usable resolution of a few nanoseconds.

THE DISCIPLINED RUBIDIUM OSCILLATOR is an FRS-C Miniature Rubidium Oscillator manufactured by Ball-Efratom. The oscillator has a C-field electrical tuning input which allows an adjustment range of 7.5×10^{-10} over 5 volts. The present FRS-C specifications (which will be improved) include a frequency stability of 5.0×10^{-11} per month and 2.0×10^{-10} per year. The frequency accuracy specification is 1.0×10^{-9} per year. The temperature specification for this oscillator is 3.0×10^{-10} from -5 to +55 degrees C. and is not linear over the range. By limiting changes in ambient temperature to ± 3 degrees and applying temperature compensation directly to the Rubidium oscillator, the effects of ambient temperature fluctuations are minimized.

A block diagram of the disciplining process is shown in Figure 2. The Rubidium oscillator is used as the primary local time base for both the clock and the GPS receiver. The GPS-DC averages 2,048 seconds of Range Bias values into a single datum once per day. In conjunction with the previous day's datum, the oscillator's average frequency error for the previous 24 hour period is calculated. The clock then calculates the required disciplining voltage correction, sums the result with the temperature compensating voltage for the oscillator, and applies the resulting disciplining voltage to the Rubidium oscillator.

THE TEST CONFIGURATION, shown in Figure 3, was designed to allow cross-checking of acquired data, assuring unambiguous identification of error sources. All critical parameters were acquired using the data acquisition system. This system consists of a 16 channel 12 bit Analog to Digital subsystem and an RS-232C data acquisition program running concurrently within a PC-AT clone. Approximately 1.2 Mbytes of data was accumulated per week using this system.

Cesium to Rubidium timing performance was monitored using the clock's Time Interval input with 100 ns resolution. Performance was also monitored using an analog phase comparison of Cesium 5 Mhz

and Rubidium 10 Mhz (both divided to 1 Mhz) with an effective resolution of 2 ns. This information was used to compare time and frequency stability over a range of 100 seconds to 40,000 seconds.

The Loran-C 1 Hz and GPS receiver 1 Hz comparison was used as an aid in initial system setup and to monitor GPS and receiver time error events during the test.

Rubidium disciplining voltage and baseplate temperature were acquired via analog channels for monitoring purposes.

TEST RESULTS

First to be examined is the Rubidium medium term stability (under one day) characteristic which is measured using the Cesium oscillator. Figure 4 shows the Allan Variance between the Rubidium and the Cesium oscillators. As can be seen by the plot, the oscillators are well behaved, reaching a low of 2.5×10^{-13} at a τ of 20,000 seconds. Both control algorithms exhibit the same performance for sample periods of less than one day.

Figure 5 is the same Allan Variance plot now extended out to 5 days with GPS data obtained using the Time and Rate control algorithm. A peak of 1.2×10^{-12} is seen at a τ of 2 days, caused by the disciplining process. The upper (+) plot represents the undisciplined Allan Variance plot of an FRS-C Rubidium oscillator. The upward trend representing long term drift and aging of the oscillator is not present in the disciplined oscillator Allan Variance plot.

Figure 6 is an Allan Variance plot of the Rate control algorithm. Note the consistent trend downwards until again the disciplining process brings the stability up to a 1.2×10^{-12} peak, this time at a τ or sample average of 1 day. Afterwards the graph peaks again at 3 days at 7.0×10^{-13} due to the cyclic effects of the disciplining process. Again note the elimination of long term drift and aging of the oscillator.

The daily frequency error for the Disciplined Rubidium using Rate control can be seen in Figure 7. A weekly cyclical frequency error between GPS and the Rubidium can be seen in this plot. It is unclear as to why this cyclical error exists, but it is evidently in the Rubidium oscillator and disciplining process as Figure 8 shows the same cyclic error when the Rubidium is compared to the Cesium. A possible reason could be the response characteristic of the Rubidium to small control voltage changes. The average frequency error offset of this algorithm is 1.2×10^{-12} and the peak error is 2.2×10^{-12} .

With the frequency offset and stability performance above, Figure 9 shows the peak daily time error of the Rubidium when time error is removed once per day. The maximum daily peak error measured was 180 ns to the GPS receiver. For smaller time errors, the error removal process could be performed more frequently.

Figure 10 is a graph of daily frequency accuracy of the Time and Rate control algorithm with respect to GPS. The maximum daily averaged frequency error seen is 3.0×10^{-12} , and, because of the Time control component of the algorithm, the frequency error is centered about zero. The large full cycle transient seen beginning at MJD 47,771 was initiated by a random walk frequency modulation process. The control algorithm required 2 days to remove the step, then proceeded to reverse the effects of the step on time accumulation with an equal transient in the positive direction. This algorithm was initially designed for applications prohibiting the use of microstepping in the 1 Hz output.

Timing accuracy of the Time and Rate control algorithm can be seen in Figure 11. Again, time error is allowed to accumulate for a 24 hour period before removal. The time error peaks are shown in this

plot and do not exceed 250 ns with respect to the GPS receiver.

CONCLUSIONS

Timing Accuracy

Timing accuracy of the GPS-DC clock when corrected daily was 250 ns to the GPS receiver and 500 ns to UTC(USNO). By removing time error more frequently than the once per day period used for these tests, error to UTC(USNO) would be reduced to 250 ns plus the error of the time error removal scheme.

Frequency Accuracy

Frequency accuracy for the Disciplined Rubidium oscillator was improved from 1.0×10^{-9} per year to 3.0×10^{-12} for Time and Rate control and 2.2×10^{-12} for Rate control. As all effects of aging and long term drift have been removed, these values are now constant.

Frequency Stability

Long term frequency stability achieved with this oscillator was 1.0×10^{-12} with Rate control and 3.0×10^{-12} with Time and Rate control. The Rate control algorithm also shows a trend towards better long term stability, achieving 3.0×10^{-13} at 5 days (Figure 9). Aging and long term drift effects have been removed through the disciplining process. Short term frequency stability was not affected.

TABLE I		
	Frequency Accuracy	Frequency Stability
CESIUM ^[2,7] (typical performance)	3.0×10^{-12} 3.0×10^{-13}	2.0×10^{-12} (over Cs tube life) 2.0×10^{-13} @ 1 day) 7.0×10^{-14} @ 10 days)
RUBIDIUM DISCIPLINED WITH TIME AND RATE CONTROL	3.0×10^{-12}	2.5×10^{-12} (@ 1 day) 1.0×10^{-12} (@ 5 days)
RUBIDIUM DISCIPLINED WITH RATE CONTROL	2.2×10^{-12}	1.0×10^{-12} (@ 1 day) 3.0×10^{-13} (@ 5 days)

The Rubidium oscillator's long term drift specifications of 5.0×10^{-11} per month and 5.0×10^{-10} per year have effectively been reduced to the long term drift of UTC(USNO), the time source for the GPS system.

A direct comparison of Cesium oscillator frequency accuracy and stability specifications to results obtained with the Rubidium Disciplining process is summarized in Table 1.

This test has shown that a local Rubidium oscillator disciplined to GPS can approach the long term stability and frequency accuracy of a Cesium oscillator, with the added advantage of offering time traceable to UTC(USNO). Performance may be improved by disciplining an oscillator with better stability specifications, and by reducing the control sample period.

APPENDIX

A word on algorithm development:

The Time and Rate control algorithm was designed to address the following basic clock mathematical model:

$$x(t) = x_0 + y_0 t + \frac{1}{2} D t^2 + e(t) \quad [6] \quad (1)$$

Where $x(t)$ is the time error of the clock at time t , x_0 is the initial synchronization error at $t = 0$, y_0 is the initial frequency offset at $t = 0$ (syntonization error), D is the frequency drift term and $e(t)$ represents all random fluctuations of the clock.

The Time and Rate control algorithm responds to the first 2 terms of the equation with zero error and can effectively remove them. The algorithm responds to the third term, Dt^2 with a constant time error, the magnitude proportional to D , the 2nd derivative of this third term. For the fourth and last term, $e(t)$, the algorithm will minimize the effects of Random Walk of Frequency on time error over the long term by forcing an artificial and opposite Random Walk event. Frequency stability in the range of 1 to 3 days is degraded using this method. In summing up the response to Equation 1, the Time and Rate control algorithm will exhibit zero frequency error and a small, constant timing error.

The Rate control algorithm is a frequency locked loop and is designed according to Equation 2:

$$y(t) = y_0 + Dt + e(t) \quad (2)$$

Where $y(t)$ is the frequency error of the clock source at time t , y_0 is the initial frequency error at $t = 0$, D is again the long term drift of the clock source, and $e(t)$ represents the random fluctuations of the clock. The algorithm will respond to Equation 2 with a small frequency error proportional to the derivative of the second term, D , and will minimize Random Walk FM contained within $e(t)$. In summing up the response to Equation 2, the Rate control algorithm will minimize frequency instability and will exhibit a small constant frequency offset.

REFERENCES

1. Weiss, Mark A. and Allan, David W. "The NBS Calibration Procedure for Providing Time and Frequency at a Remote Site by Weighting and Smoothing of GPS Common View Data", National Institute of Standards and Technology, Time and Frequency Division.
2. Hellwig, H. "Frequency Standards and Clocks: A Tutorial Introduction", U.S. Department of Commerce / National Institute of Standards and Technology Technical Note # 616, 2nd Revision.

3. Allan, David W. "Time and Frequency (Time-Domain) Characterization, Estimation, and Prediction of Precision Clocks and Oscillators" IEEE Transactions on Ultrasonics, Ferroelectrics, and Frequency Control Volume UFFC-34, No. 6, November 1987.
4. Knoernschild, G.F. "Global Positioning System for Time and Frequency Measurements" Proceedings of the Nineteenth Annual Precise Time and Time Interval (PTTI) Applications and Planning Meeting, December 1-3, 1987.
5. Global Positioning System Joint Program Office, ICD-GPS-200 Navstar GPS Space Segment, Navigation User Interfaces.
6. Allan, David W. Clock Characterization Tutorial, NIST Time and Frequency Seminar, June 5, 6, 7 1989.
7. Precision Time and Frequency Handbook, Ball Corporation, Efratom Division, Sixth Edition, 1987.
8. Weiss, Mark "Design of Kalman Smoothers in GPS Data", IEEE Instrumentation and Measurement Society, April 1989 Vol. 38 #2 p 652.
9. USNO Automatic Data System, GPS Time Transfer Information, @GPSAC.

GPS TIME TRANSFER

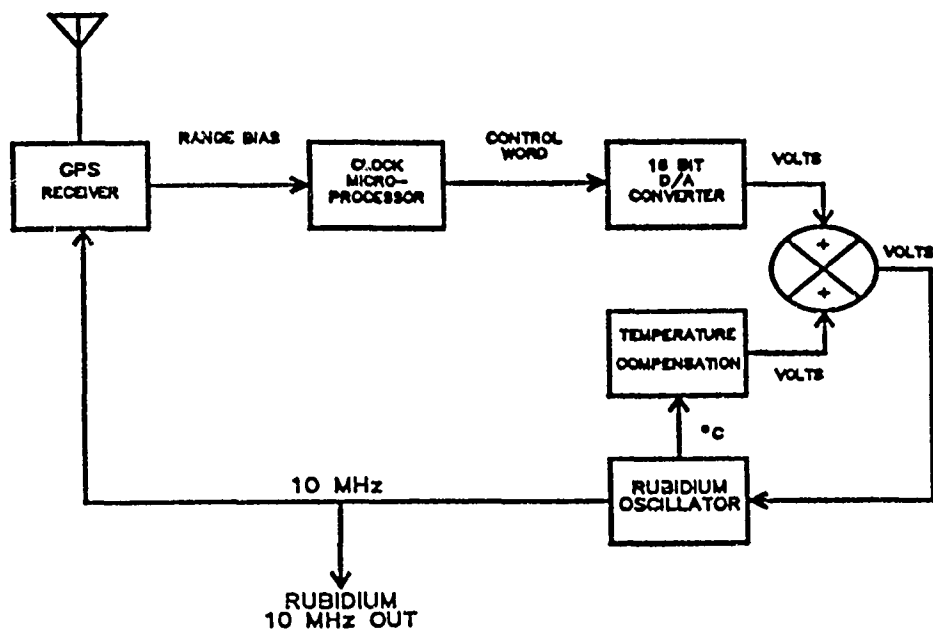
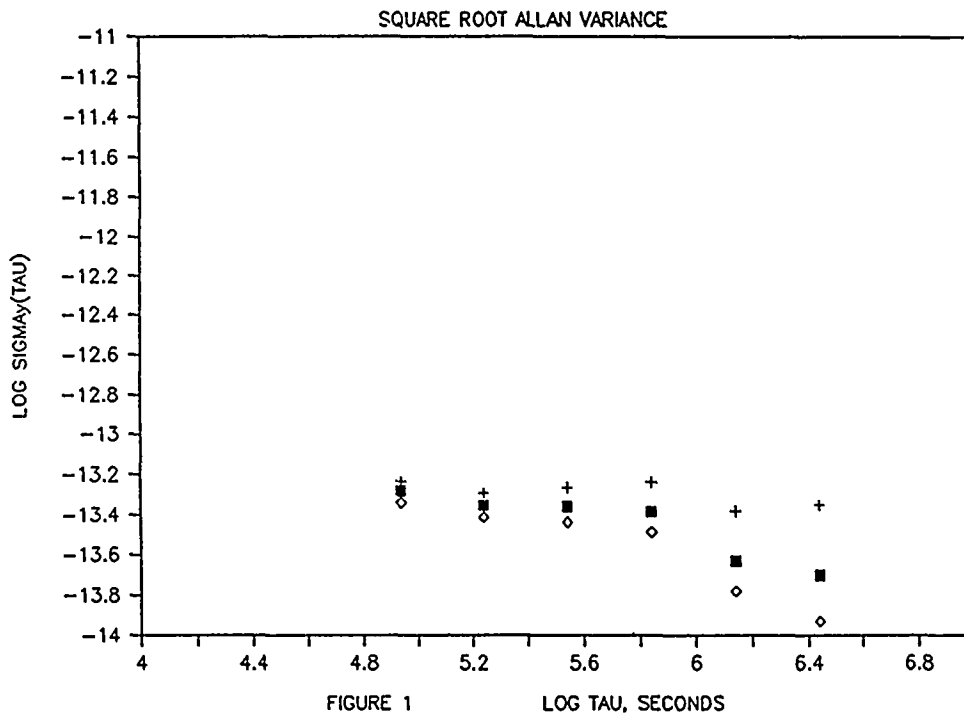


FIGURE 2 DISCIPLINED RUBIDIUM CONTROL LOOP

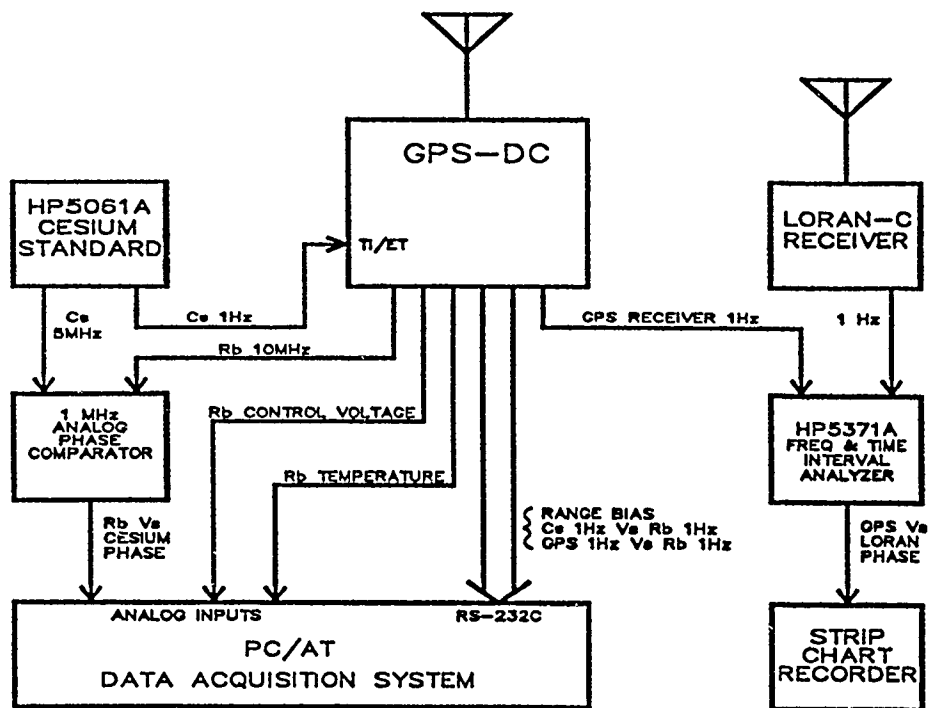


FIGURE 3 DISCIPLINED RUBIDIUM TEST CONFIGURATION

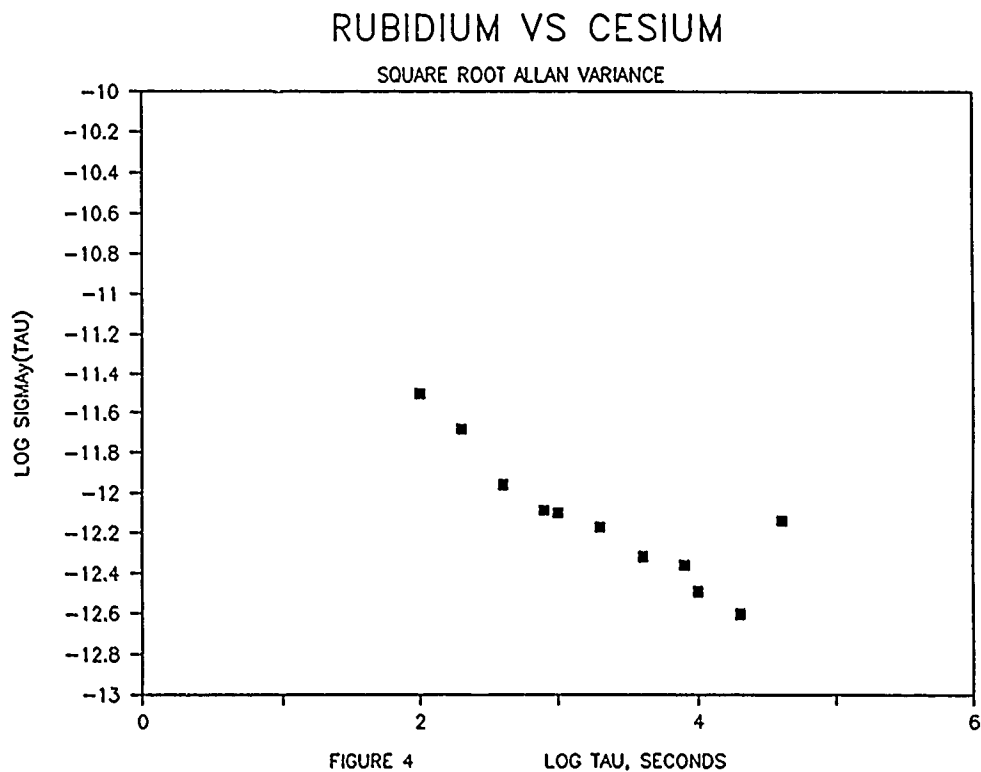
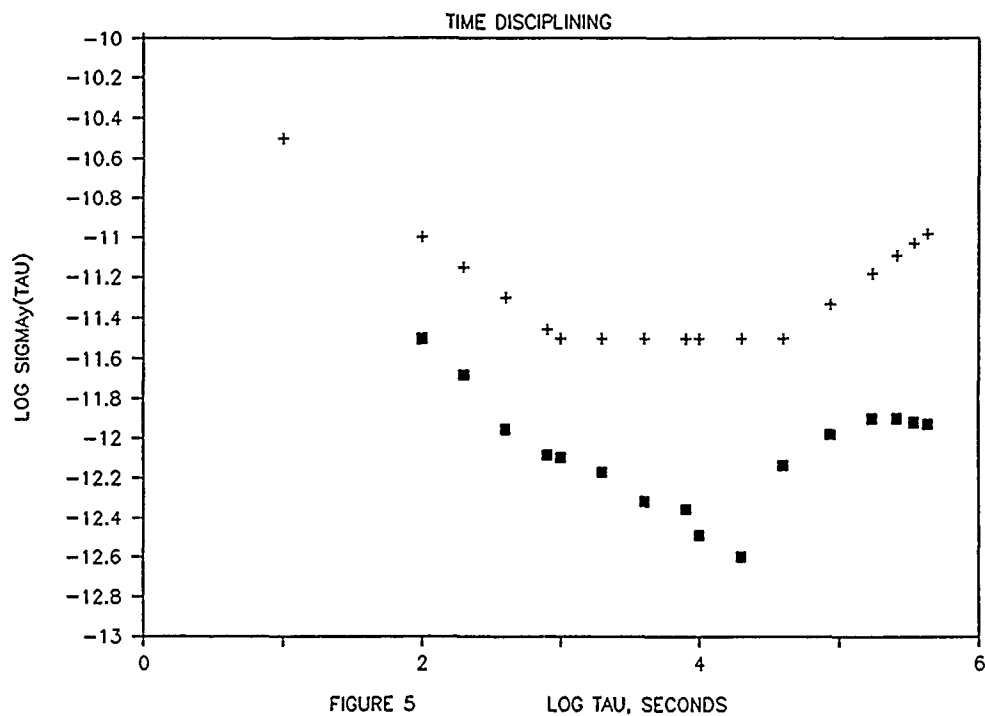
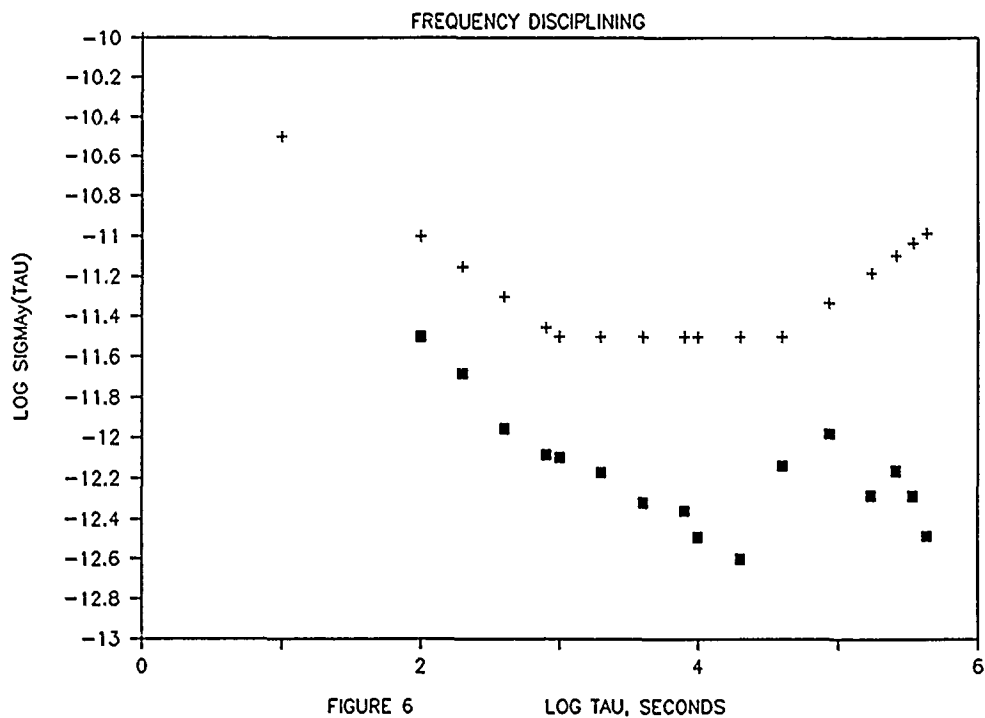


FIGURE 4 LOG TAU, SECONDS

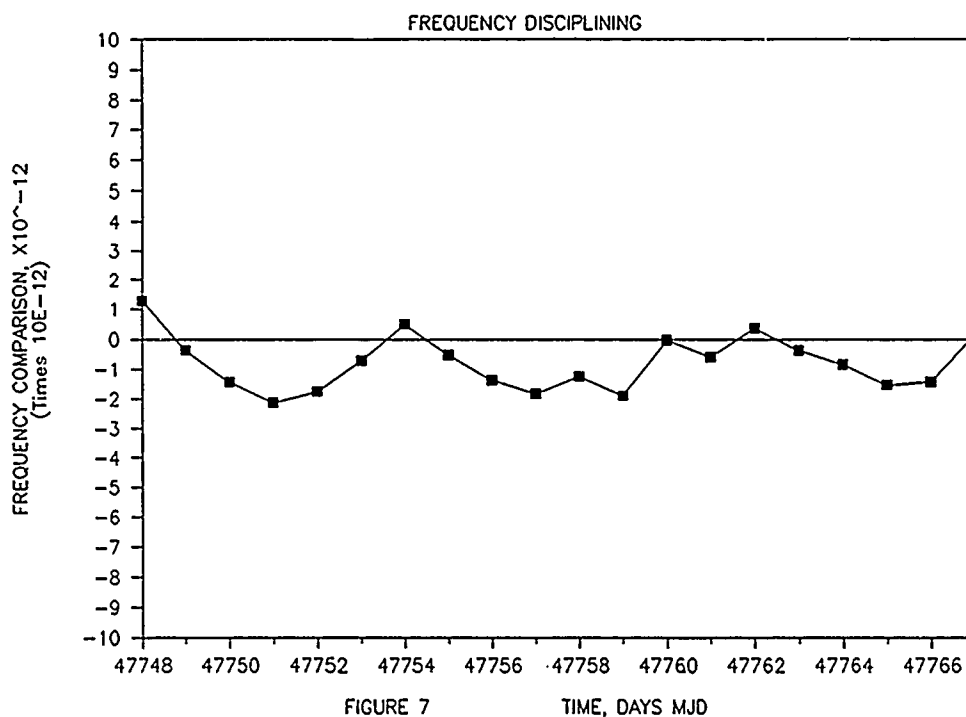
DISCIPLINED RUBIDIUM VS Cs AND GPS



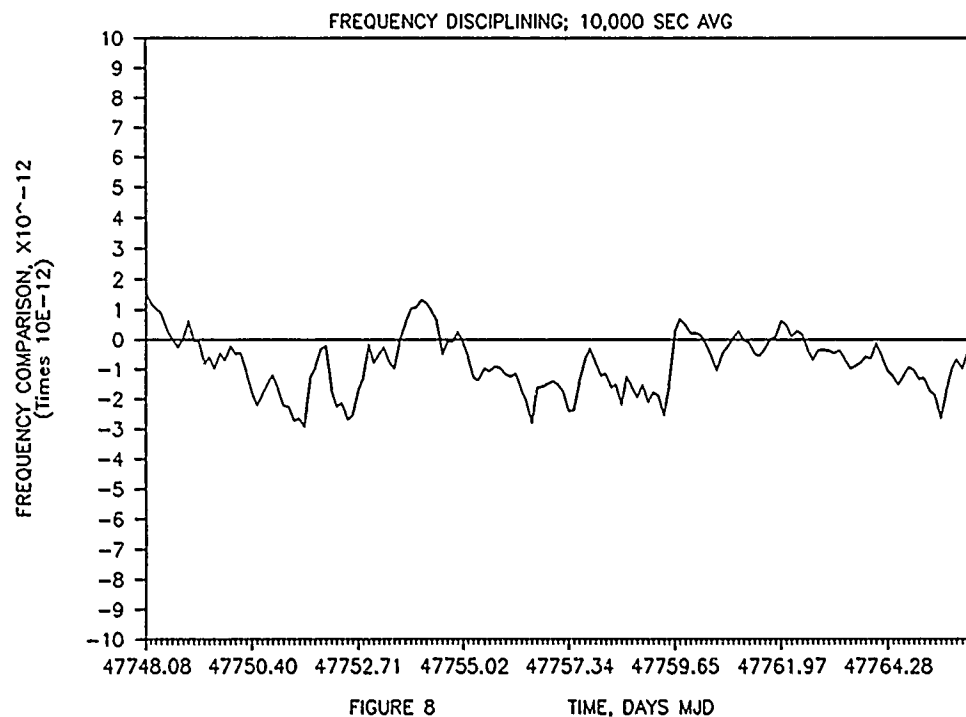
DISCIPLINED RUBIDIUM VS Cs AND GPS



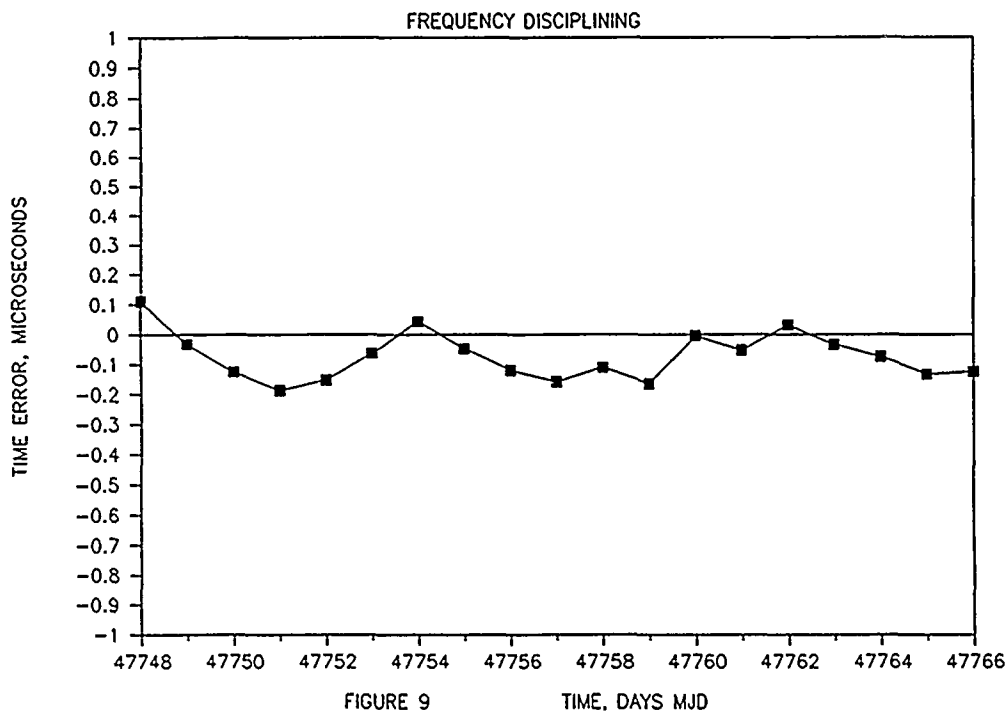
FREQUENCY COMPARISON, Rb VS GPS



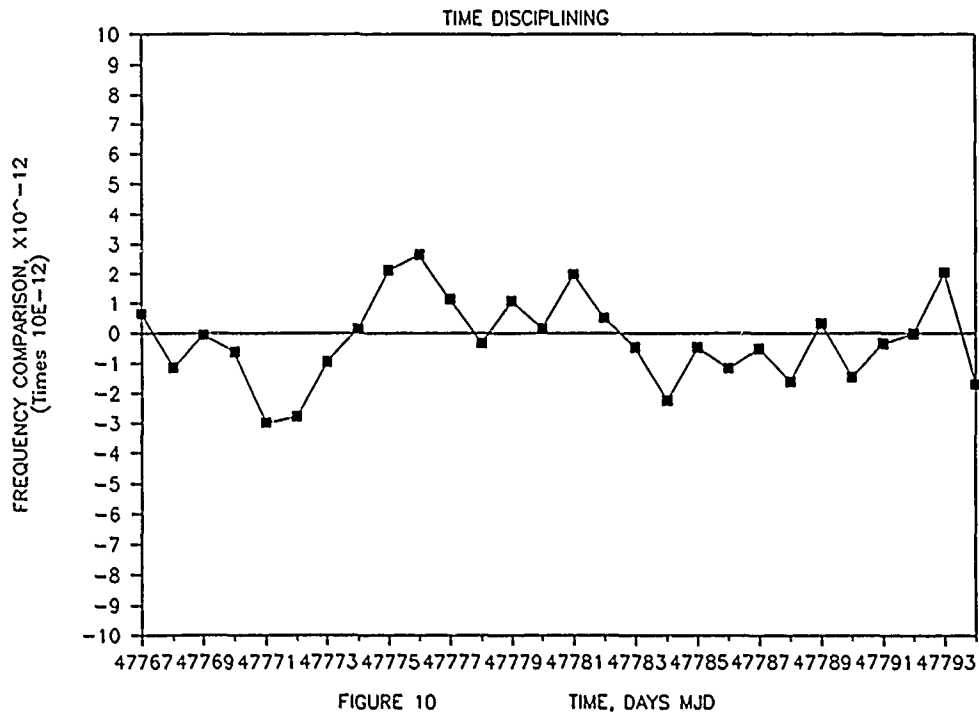
FREQUENCY COMPARISON, Rb VS Cs



DAILY PEAK TIME ERROR TO GPS RECEIVER



FREQUENCY COMPARISON, Rb VS GPS



RUBIDIUM DAILY PEAK TIME ERROR TO GPS

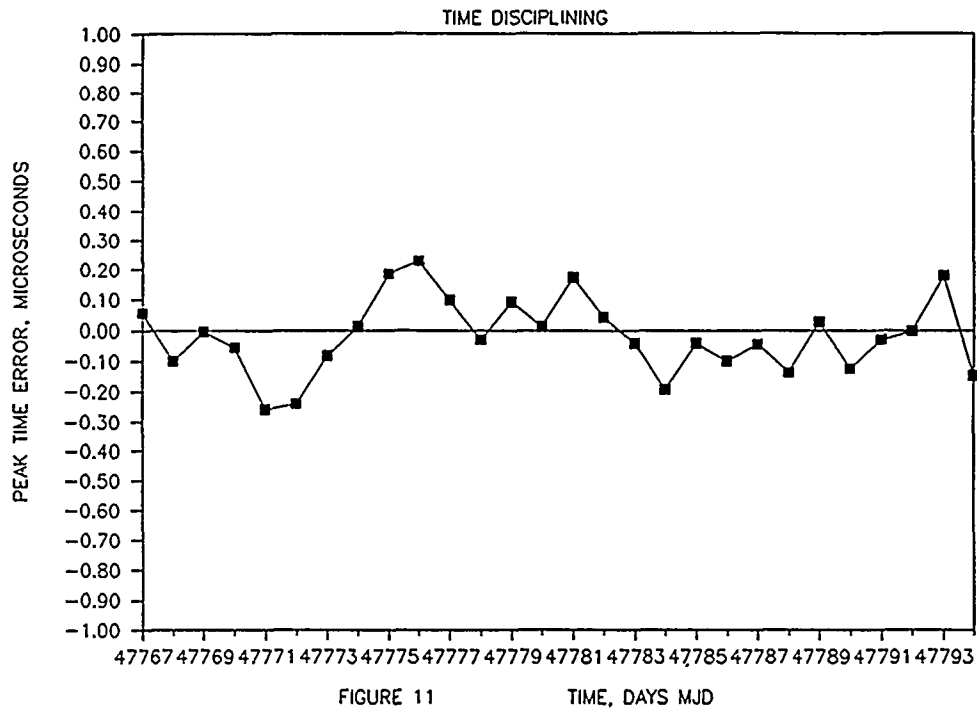


FIGURE 11

TIME, DAYS MJD

STEADY STATE OSCILLATOR ANALYSIS IN THE IMMITTANCE DOMAIN

Benjamin Parzen
Consulting Engineer
San Diego, CA 92103

Abstract

The theory of oscillator analysis in the immittance domain is presented. This theory enables the computer simulation of the steady state oscillator. The simulation makes practical the calculation of the oscillator total steady state performance, including noise. Some oscillator applications of the PC program, BPT, created for the simulation, are listed.

1 INTRODUCTION

During the past 11 years, the writer has been developing theory for oscillator analysis in the immittance domain. "IMMITTANCE DOMAIN" means that the basic relationships are expressed in terms of immittance, $Z = R + jX$ or $Y = G + jB$.

Effective and facile application of the theory to real problems also necessitated the creation of a PC computer circuit analysis program. The results of this effort are:

- A remarkably simple oscillator theory which fully describes the oscillator operation and which is readily translatable into the real world.
- A very user friendly multipurpose circuit analysis program, BPT.

The theory and program are universal in that they apply to all oscillators, past, present, and future. The theory and program are symbiotic, in that:

- To apply the program to oscillators, the theory must be used.
- The program is very helpful and almost indispensable in applying the theory to real oscillator problems including that of improving the theory.

It should be noted that, as BPT does not incorporate any basic information peculiar to oscillators, it follows that the theory may be used, in conjunction with other circuit analysis programs, to analyze oscillators but with much greater, and perhaps prohibitive, difficulty.

The theory is based upon the combination of 2 compatible oscillator models:

- The negative resistance model (2) as the primary model.
- The noise source, amplifier, and filter, model (3) in which positive feedback produces the necessary extremely high effective amplifier gain, as the secondary model.

2 THE NOISELESS OSCILLATOR [2]

2.1 Fundamental relationships

At steady state, in any mesh, of a hypothetically noiseless oscillator,

$$Z_t = \sum Z = 0 \quad (1)$$

From which,

$$\sum R = 0 \quad (2a)$$

$$\sum X = 0 \quad (2b)$$

Defining,

$$RN = \sum R_{negative} \quad RT = \sum R_{positive}. \quad (3)$$

Then,

$$RT = -RN. \quad (4)$$

2.2 Non-linearity considerations

If the linear and non-linear elements are grouped together, then, from Eqs 2:

$$\sum Z_{lin} + Z_{nlin} = 0 \quad (5)$$

From which,

$$\sum R_{nlin} = -\sum R_{lin} \quad (5a)$$

Similarly,

$$\sum X_{nlin} = -\sum X_{lin} \quad (5b)$$

where the non-linear values are the effective values.

Eqs 5 are very important since they state that it is only necessary to study the linear R and X elements to compute the totals of the non-linear R and X elements. This fact drastically reduces the labor involved in the analysis and, very often, it eliminates the need for considering the detailed behavior of non-linear elements.

2.3 Noiseless oscillator model

Fig 1 is the simplified diagram of the oscillator resonator mesh. (The mesh containing the resonator is usually chosen for analysis as it has the most information.)

As shown in Fig. 1, that part of the oscillator containing the resonator circuitry is called the osci, symbol os. The remainder is called the llator, symbol LL.

From Eq 1,

$$Z_{os} = -Z_{LL}. \quad (6)$$

Also,

$$\Delta f = -\Delta X_{LL}/(\delta X_{os}/\delta f). \quad (7)$$

Eq 7 enables the easy determination of oscillator frequency shifts caused by llator changes.

3 THE REAL OSCILLATOR

3.1 Introduction

The real oscillator always includes one or more llator noise sources in addition to the resonator frequency noise. The calculation of the contribution of the resonator noise to the oscillator noise is very simple (See Section 3.3) However, the calculation of the contributions of the llator noises is extremely difficult and constitutes a major topic of this paper.

3.2 Frequency relationships

The total frequency, F is described by,

$$F = f_0 + f \quad (8)$$

where f_0 is the carrier frequency and f is the offset or Fourier frequency.

3.3 Contribution of the resonator frequency noise to the oscillator noise.

Let the resonator frequency noise be described as:

$$[S_f(f)]_{os}. \quad (9)$$

Then the resonator frequency noise contribution to the oscillator frequency noise at all oscillator locations is identical to that in Eq 9.

The resonator frequency noise contribution to the oscillator phase noise at all oscillator locations is:

$$[S_f(f)]_{os}/f^2. \quad (10)$$

The total phase noise at any oscillator location is given by the sum of that of Eq 10 and the sum of the contributions of the llator noise sources to the phase noise at that location.

3.4 Contributions of the llator noise sources to the oscillator noise at location m.

Let the noise of noise source n be given by power spectrum,

$$PS_n(f). \quad (11)$$

Then the contribution of this source to the oscillator noise power spectrum at location m is:

$$PS_{mn}(f) \quad (12)$$

and

$$PS_{mn}(f) = PS_n(f) * TF_{mn}(f) \quad (12a)$$

where $TF_{mn}(f)$ is defined as the transfer function of noise source n to the oscillator noise at location m.

The total oscillator noise, PS_t at location m, obviously is

$$PS_t(f) = \sum_1^n PS_{mn}(f). \quad (13)$$

3.5 Real oscillator, special case, N configuration.

Fig 2 is the complete diagram for the N configuration (N meaning noise) of a special case real oscillator. The fact that makes this oscillator a special case is that the noise source, V_n , represents the total equivalent noise contributions of all the noise sources in the llator.

All real oscillators always contain a non-physical resistance, dR . The value of dR is determined by the oscillator limiting, or ALC, system which sets the level of the oscillator output.

Fig 2 includes the input, output, and common networks and the multiple potential output points, available in every real oscillator. The noise in the output depends upon the output point location.

Fig 2 also shows RV and XV which do not exist in the real oscillator. Their function is described in Sect 3.7.

The oscillator, at steady state, at $f = 0$, (the carrier frequency) satisfies Eqs 14 to 16, similar to, and derived from, Eqs 1 to 4.

$$Z_t = \sum Z = dR. \quad (14)$$

From which,

$$\sum X = 0, \quad \sum R = dR \quad (15)$$

and

$$RT = -RN + dR. \quad (16)$$

Also, it has been proven (5) that

$$\left| \frac{RN}{dR} \right|^2 = \left| \frac{V_s(0)}{V_n(0)} \right|^2. \quad (17)$$

This equation is used in calculating the oscillator operating Q.

Let

$$|RN/dR|^2 = (A_r)^2. \quad (18)$$

3.6 Real Oscillator Operation

- The oscillator is constructed and power is applied.
- The operator sets the output level by adjusting the limiting circuitry and thus setting dR .
- The oscillator determines f_0 , V_n , RT , dR and all other operating conditions.
- The oscillator determines the phase noise as a function of f .

3.7 The real oscillator, special case, Z configuration

Fig 3 is the complete diagram for the Z configuration (Z meaning impedance) of the special case real oscillator.

The purpose of this configuration is to enable the precise setup of the necessary and sufficient oscillatory condition of Eq 14. Once this is done, we are certain that this configuration when converted to the N configuration represents a true oscillator at the desired frequency.

As will be noted, the Z configuration differs from the N configuration in the following:

- The value, V_n , of the noise is 0.

- b. The circuit has been broken and a 1 A current source inserted. The value of the voltage, V_z , across this source is the value of the impedance Z_t of Eq 14. When Z_t has been precisely adjusted to dR at the desired frequency, f_0 , then this Z configuration is ready for conversion to a N configuration. The adjustment procedure is called "zeroing".

RV and XV are very small value trimmable resistor and reactor, respectively, provided to facilitate zeroing. Their values are identical in the Z and N configurations.

The zeroing procedure has been automatized in the computer simulated laboratory and thus makes practical the computer oscillator simulation.

3.8 Computer simulated oscillator operation

In the program oscillator, Z config. (See Fig 3)

- a. The oscillator is constructed by entering the circuit into the computer.
- b. The operator sets f_0 , $dR = 0$, and $V_n = 0$.
- c. The program sets the effective gain of the active circuitry, so that Eq 14 is almost satisfied.
- d. The program adjusts RV and XV so that the mesh impedance, $Z_t = V_z$ in Fig. 3, satisfies Eq 14 to a very high degree of precision. The Z configuration is then converted into the N configuration.

In the program oscillator, N config. (see Fig 2)

- e. The operator sets V_n to V_n real.
- f. The operator sets dR to the value where the desired oscillator output is obtained as measured by the AC current at any 1 point or ac voltage between any 2 points.
- g. The program determines the voltages and currents at all other points.
- h. The program determines the phase noise at and between all points.
- i. The program determines $Z_t(f)$, (see Fig 3) when dR is at the value of Step f, and V_n is set to 0.

3.9 Computation of the transfer functions, $TF_{mn}(f)$ in the real oscillator

This is best done by using the program. The procedure is the following

- a. Start with the oscillator configured as in Sect 3.8, Step d. Include all the noise sources, which are assumed to be uncorrelated.
- b. Create the equivalent N configuration, with the correct value of dR .
- c. To compute $TF_{mn}(f)$, set the magnitudes of all noise sources to 0, excepting the source at location n.
- d. Make the source, n, a unit white noise source.
- e. Determine the noise response at location m, $PS_{mn}(f)$.
- f. Then from Eq 12,

$$TF_{mn}(f) = PS_{mn}(f). \quad (19)$$

- g. Repeat steps c to f for all noise sources.

3.10 Oscillator noise, in all real oscillators, due to V_n (See Fig 2)

3.10.1

The resonator current, I_x , phase noise, due to V_n , is given by:

$$\mathcal{L}_{I_x}(f) = \mathcal{L}_{V_n}(f) * \left| \frac{RT}{Z_t(f)} \right|^2. \quad (20)$$

$Z_t(f)$ is obtained with the Z configuration and

$$\mathcal{L}_{V_n}(f) = PS_{V_n}(f)/(V_s)^2. \quad (21)$$

3.10.2 Noise at other locations

The phase noise in V_s is almost the same as that in I_x , except at the higher values of f .

Now that the phase noise in I_x is known, the determination of the phase noise, at all other locations, is straightforward but, depending upon the circuit complexity, can be very difficult and tedious and is best done with the program.

However, those desiring to perform the calculations should keep in mind the following rules when combining noises at any location:

- a. Noise voltages and currents, due to the same noise source, should be combined as phasors.
- b. Noise powers, due to different uncorrelated noise sources, should be combined as scalars.

3.11

The general relationship between $PS(f)$ and the phase noise, $\mathcal{L}(f)$ at the same location, is

$$\mathcal{L}(f) = PS(f)/\text{CarrierPower} \quad (22)$$

$$= PS(f)/PS(0) \quad (23)$$

for all values of f , when $PS(0)$ does not approach infinity.

Eq 22 is also useful for the case where $V_n(f)$ has a flicker or other noise component which theoretically approaches infinity as f approaches 0 and thus theoretically also makes $PS(f)$ approach infinity as f approaches 0. In this case, the oscillator noise power spectrum, at f when $|X_t(f)| \gg dR$, is independent of dR which is set by the oscillator limiting system at the desired carrier. Therefore, at these values of f ,

$$\mathcal{L}(f) = PS(f)/PC \quad (24)$$

where PC is the arbitrary desired carrier reference power.

4 PROGRAM APPLICATIONS IN OSCILLATORS

The following applications to oscillators are cited to demonstrate the utility and power of program BPT when used in conjunction with the theory.

- #### 4.1 Automatic zeroing of the Z oscillator configuration (coarse, active device gain setting and fine, impedance trimming) for the derivation of the $Z_t(f)$ relationship.

- 4.2 Automatic calculation of the oscillator operating frequency. Both 4.1 and 4.2 functions are high speed and high resolution executions of their respective functions.
- 4.3 Calculation of the DC operating point of oscillators.
- 4.4 Includes a procedure for determining the AC operating point of a self-limiting oscillator.
- 4.5 Includes a procedure for setting the AC and DC operating points in ALC type oscillators.
- 4.6 The program is a linear one but is designed to be capable of being interfaced with non linear operating conditions. Items 4.3 to 4.5 are examples.
- 4.7 Investigation of the $Z_t(f)$ or $Z_t(?)$ function of an oscillator or circuit such as a llator.

The following 5 examples illustrate the very useful information obtained from llator studies.

- 4.7.1 The effect of component changes upon frequency.
- 4.7.2 Overtone and mode selector gain margins and the effect of the resonator overtone and mode selector circuitry upon the oscillator stability.
- 4.7.3 Starting gain margin (loop gain, ALo)
- 4.7.4 Effect of power dissipating components upon the loop gain and the operating Q.
- 4.7.5 Effect of component tolerance and environment upon the above 4 items.
- 4.8 Determination of bypass and coupling capacitor adequacy.
- 4.9 The performance of subcircuits such as tuning networks.
- 4.10 The determination of circuit isolation properties.
- 4.11 Calculation of operating Q, from Eq 17.
- 4.12 Studies of impedance properties of resonators and other devices requiring high resolution.
- 4.13 Investigation of the effect of component and subcircuit noise upon oscillator noise.
- 4.14 Determination of the circuit configuration for optimum noise performance.
- 4.15 Calculating and plotting oscillator phase noise. It is not necessary to assume symmetrical noise sidebands.
- 4.16 Calculating and plotting the resonator current phase noise for a llator white noise source from the $Z_t(f)$ relationship.
- 4.17 In setting up an oscillator, the oscillator Z configuration is first created and then zeroed. (See Item 4.1). A facility is provided to automatically convert the zeroed Z configuration into an N configuration and vice versa.

5 THE PROGRAM AS A RESEARCH TOOL

The following suggested applications illustrate the power and usefulness of the program in research activities:

- 5.1 The formulation, checking, and confirmation of new theory. and new oscillator designs.

- 5.2 Determination of component aging from experimentally derived llator aging.
- 5.3 Determination of component temperature characteristics from experimentally derived llator temperature performance.
- 5.4 Determination of llator noise by experimentally deriving the oscillator phase noise and then program calculating the $V_n(f)$ function required to produce that oscillator noise.

6 CONCLUSIONS

Extremely simple and powerful oscillator theory has been presented. This theory has been used in the creation of a computer program for the universal analysis of oscillator steady state performance.

The importance of $Z_t(f)$, RT , and dR and the tremendous power of analysis in the immittance domain complemented by computer aided analysis have been demonstrated. An important additional advantage is that this analysis method provides considerably greater understanding of the operation of the real oscillator.

7 REFERENCES

1. Leeson, D. B., "A Simple Model of Feedback Oscillator Noise Spectrum.", Proc. I.E.E.E. 54, 329-330 (Feb. 1966)
2. Parzen, B. "Design of Crystal and Other Harmonic Oscillators", Wiley, New York, 1983
3. Robins, W.P. "Phase Noise in Signal Sources", Peter Peregrinus Ltd., London, 1982
4. Parzen, B. "Clarification and a Generalized Restatement of Leeson's Oscillator Noise Model", Proc. 42nd Annual Frequency Control Symposium, pp.348-351, June 1988
5. Parzen, B. "Oscillator and Stability Analysis in the Immittance Domain", in preparation.

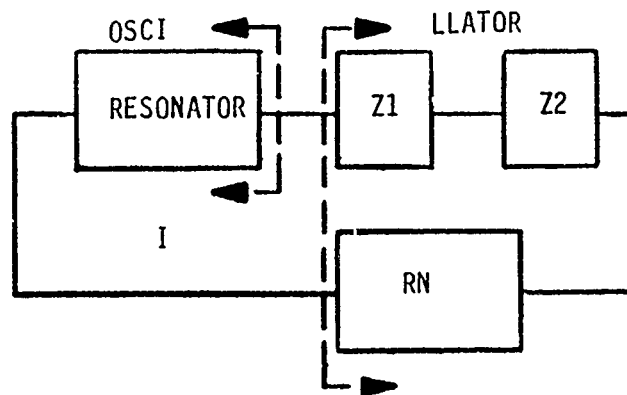


Figure 1: Noiseless Oscillator Model

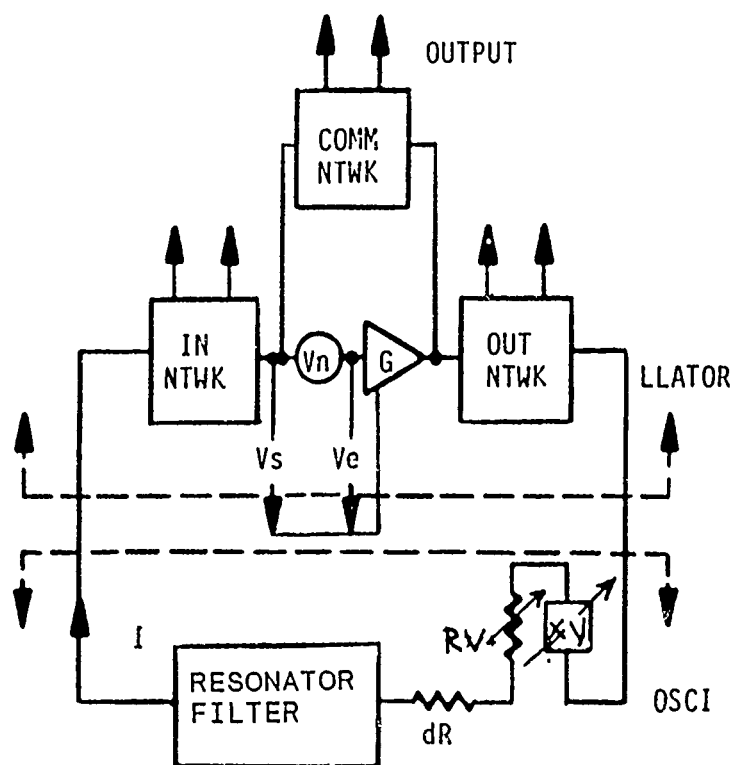


Figure 2: Real Oscillator, Special Case, N Configuration

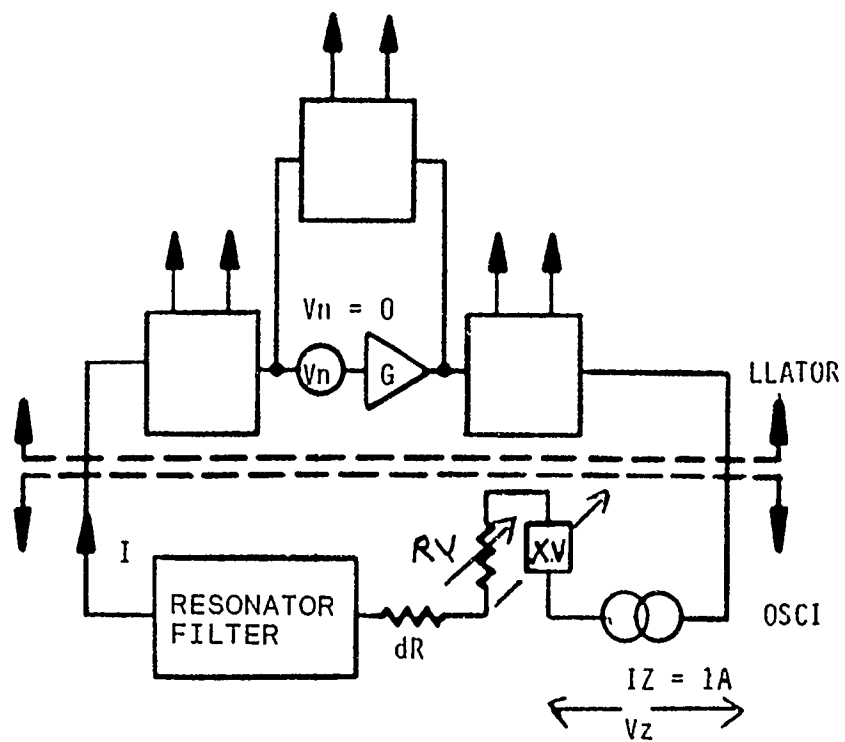


Figure 3: Real Oscillator, Special Case, Z Configuration

FINAL RESULTS OF A NEW TEST OF RELATIVITY

Timothy P. Krisher, Lute Maleki, Lori E. Primas, George F. Lutes, *
Ronald T. Logan, and John D. Anderson
Jet Propulsion Laboratory
California Institute of Technology
Pasadena, California

and

Clifford M. Will
McDonnell Center for the Space Sciences
Department of Physics, Washington University
St. Louis, Missouri

Abstract

We report on the final results of an analysis of data obtained in a recent experiment to test the isotropy of the one-way velocity of light using instrumentation of the Deep Space Network (DSN). The data consisted of measurements of the relative phase versus time of the 100 MHz output of two hydrogen maser frequency standards separated by 29 kilometers which were compared by propagating signals one-way over an ultra-stable fiber optics cable. Uninterrupted phase records spanning nearly five days were generated simultaneously at each site, thereby providing us with the capability to subtract out errors due to either a frequency offset between the masers or a temperature-dependent delay along the fiber optics cable. Adding the records removed the maser frequency offset error, while differencing the records removed the cable delay error. It was not possible to subtract out both errors simultaneously.

By taking 1000 second samples and low-pass filtering the phase records for periodicities of 12 hours or longer, we observed daily phase variations of less than 20 degrees in the differenced data and of less than 1 degree in the added data. Both spectral analysis and linear regression techniques were used to infer from the phase records limits on two possible anisotropic variations in the one-way velocity of light which could arise from the motion of the earth with respect to the cosmic microwave background. The differenced record permits a limit to be set on an anisotropy which is linear in this velocity, while the added record can be used to limit a quadratic dependence. A theoretical interpretation of the resulting limits is given in terms of the test theory of relativity proposed by Mansouri and Sexl.

*This work represents the results of one phase of research carried out at the Jet Propulsion Laboratory, California Institute of Technology, under a contract with the National Aeronautics and Space Administration

I. INTRODUCTION

At the last PTTI meeting we reported on the results of a preliminary analysis of data recently obtained in an experiment to test the isotropy of the one-way velocity of light^[1]. A more complete analysis of the data that has been performed since then is the subject of this report. The data consists of measurements of the relative phase versus time of two hydrogen maser frequency standards separated by a baseline of 21 kilometers that were compared by propagating the 100 Mhz output signals of the masers over a highly stable fiber optics link. Because the phase measurements were made continuously over several days, the data can be used to test for a possible variation in the velocity of light that could arise from the motion of the Earth through a cosmological reference frame. Although daily phase variations were apparent in the data, it is not possible to claim to have detected such an effect because of other possible causes. Nevertheless, we have been able to infer from the data an interesting limit on the size of this effect.

This report is organized as follows. A brief review of the most important features of the instrumentation and procedures which were used in the experiment is given in Section II (see Reference [1] for further details). In Section III it is shown how the data can be used to limit the size of $\delta c/c$. An interpretation of this limit within the "test theory" of relativity of Mansouri and Sexl is presented in Section IV. Concluding remarks are given in Section V.

II. REVIEW OF INSTRUMENTATION AND PROCEDURE

The experiment was conducted at the Deep Space Network (DSN) Deep Space Communications Complex located in the Mojave desert at Goldstone, California during November of 1988. Two hydrogen masers were located, respectively, at Deep Space Station 13 (DSS 13) and DSS 14, which are separated by a baseline of 21 kilometers. A 29 kilometer fiber optic link that is buried five feet underground is used to propagate the 100 Mhz output signals between the masers. Relative phase measurements were performed once per minute using Hewlett-Packard 8753A Network Analyzers located at each station. IBM personal computers were used to store the measurements onto 3.5 inch micro disks. Dual phase measurements were performed simultaneously at each station. In addition, it was possible to propagate both maser signals along a single optical fiber. Thus dual phase records were generated which could later be added or subtracted for the purpose of calibrating the data.

III. ANALYSIS

For a possible violation of the theory of special relativity, there could occur an observed variation in the velocity of light of the form

$$\delta c/c_0 = c_1 \cos \theta + c_2 \cos^2 \theta, \quad (1)$$

where θ is the angle between the propagation path and a preferred direction in space. This direction will be taken to be along the velocity vector of the Earth through the cosmic microwave background, which has been determined by observations of the dipole anisotropy of the background^[2]. The coefficients c_1 and c_2 are dimensionless, both having the value of exactly zero in special relativity, while c_0 represents a fiducial value for the speed of light (nominally equal to 3×10^5 km/sec). For convenience, we will

define $c_0 \equiv 1$. Because the measured phase difference between the two masers is related to c by the definition $\phi = 2\pi\nu L/c$, where $\nu = 100$ MHz and $L = 21$ km, equation (1) yields

$$\delta\phi/\phi_0 = \phi_1 \cos \theta + \phi_2 \cos^2 \theta, \quad (2)$$

where $\phi_1 = -c_1$ and $\phi_2 = c_1^2 - c_2$.

The two limiting sources of error in the experiment are 1) the maser stability, and 2) the temperature dependence of the fiber optics link. By differencing the dual phase records, the link error can be eliminated, yielding

$$(\delta\phi/\phi)_{DSS\ 13} - (\delta\phi/\phi)_{DSS\ 14} = 2\phi_1 \cos \theta + (\text{maser error}), \quad (3)$$

while by adding the phase records the maser error can be eliminated, so that

$$(\delta\phi/\phi)_{DSS\ 13} + (\delta\phi/\phi)_{DSS\ 14} = 2\phi_2 \cos^2 \theta + (\text{link error}). \quad (4)$$

These differenced and added phase records are shown in Figures 1 and 2, respectively. In order to remove unwanted high frequency noise from the data, the records have been low-pass filtered for periodicities of 12 hours or longer^[3]. In addition, the data has been sampled at 1000 second intervals in order to take advantage of the high frequency stability of the hydrogen maser at this integration time and also to reduce the size of the data records. It was necessary to truncate the differenced data after 72 hours because of an anomalously large phase excursion that occurred.

Daily phase variations are clearly apparent in these plots. In the case of the differenced data these variations could be due to the effects on the masers of changes in barometric pressure (see, for example, Reference [4]), while the smaller variations seen in the added data are consistent with temperature-dependent variations in the delay of the fiber optics link. The size of these systematic errors determines the limits which can be set for the anisotropy coefficients c_1 and c_2 . In order to determine these limits, equations (3) and (4) have been evaluated for the particular geometry of the experiment at the times of the phase measurements (see Figure 3). From least-squares fits of each equation to the corresponding phase record, there resulted the limits

$$c_1 < 3.5 \times 10^{-7}, \quad (5a)$$

$$c_2 < 2 \times 10^{-8}. \quad (5b)$$

The limit in equation (5a) resulted from a simple fit of the predicted cosine variation to the differenced data, where the number quoted is the fitted amplitude. Equation (5b) resulted from modeling in addition to the predicted cosine-squared variation a twenty-four hour cosine of arbitrary amplitude and phase to account for a possible diurnal variation in the link delay. In the next section the meaning of these limits will be discussed.

IV. THEORY

Great care must be taken in determining the theoretical consequences of these experimentally derived limits. Their expected values for a possible violation of special relativity can be determined only by a detailed application of the theory in question to the particular instrumentation and procedures which were used in the experiment. A complete dynamical theory would account for all physical forces which could arise from motion through a preferred reference frame. This kind of a framework has been adopted by Will and Haugan, for example, in analyzing the outcomes of relativity experiments^[5]. In our experiment, these forces could directly affect the hyperfine transition of the hydrogen atoms in the maser or perhaps change the length of the fiber optics link. A more simplified approach to understand the possible consequences of the experiment is provided by the formalism of Mansouri and Sexl, in which only the kinematics of the motion is considered^[6]. We will adopt this approach and assume that it is consistent with the actual dynamics that could be involved. Whether there exists a more interesting interpretation of the experiment remains an open question for the present.

In the formalism of Mansouri and Sexl, the Lorentz transformations of special relativity are parameterized according to:

$$t = aT + \vec{\epsilon} \cdot \vec{x}, \quad (6a)$$

$$\vec{x} = d\vec{X} - b\vec{v}T + \frac{b-d}{v^2}\vec{v}(\vec{v} \cdot \vec{x}), \quad (6b)$$

where (t, \vec{x}) are the space-time coordinates for a frame moving with a velocity \vec{v} with respect to the preferred frame (T, \vec{X}) . In special relativity the parameters $(a, b, d, \vec{\epsilon})$ have the values of $a = b^{-1} = (1 - v^2)^{1/2}$, $d = 1$, and $\vec{\epsilon} = -\vec{v}$. For light propagating isotropically with respect to the preferred frame, these transformation equations predict a relative variation in the phases of two frequency standards in the moving frame given by [7]

$$\delta\phi/\phi_0 = v(1 + 2\alpha)\cos\theta + v^2\left(\frac{1}{2} + \delta - \beta\right)\cos^2\theta, \quad (7)$$

where θ is the angle of propagation with respect to \vec{v} and the parameters (α, β, δ) result from the expansion of (a, b, d) , respectively, in powers of v^2 . In special relativity, their values are $\alpha = -1/2$, $\beta = 1/2$, and $\delta = 0$. Because the phase is related to the speed of light c according to the definition $\phi = 2\pi\nu L/c$, the observed values of the anisotropy coefficients c_1 and c_2 are:

$$c_1 = -(1 + 2\alpha)v, \quad (8a)$$

$$c_2 = [(1 + 2\alpha)^2 - (\frac{1}{2} + \delta - \beta)]v^2. \quad (8b)$$

Taking $v = 10^{-3}$ (300 km/sec) and comparing equations (5a) and (8a), the "time-dilation" parameter α is thus seen to be limited by

$$|\alpha + \frac{1}{2}| < 1.75 \times 10^{-4}. \quad (9)$$

The parameters (β , δ) are not significantly constrained because of the small value of v^2/c_0^2 .

i

V. CONCLUSIONS

By exploiting the existing time and frequency instrumentation of the Deep Space Network we have been able to limit a fundamental variation in the one-way velocity of light to a level of $\delta c/c < 3.5 \times 10^{-7}$. This result is compared to the results of related tests in Figure 4. The GPS common-view time-transfer method has the capability to provide a precise test over a long baseline. Accuracies of 10 ns which have been obtained over intercontinental baselines implies the limit given in Figure 4^[8], assuming that there are no significant correlations with spacecraft position error. A rigorous analysis of the GPS data could verify this limit, which is seen to be comparable to our result. For comparison, the results of two precise laboratory experiments have also been quoted in Figure 4. While these two limits appear to be more stringent, they are possibly not because the light propagation delay (or its variation) was not directly measurable in the experiments^[9,10]. Instead, the limits were inferred from frequency comparisons. Furthermore, the propagation paths were limited to short baselines defined by the size of the apparatus. These possible shortcomings were avoided in our experiment by the direct comparison of the maser signal phases over a long baseline.

The equipment and procedures which were used in the experiment did not exceed operational DSN requirements. Several improvements could be made in the future for the special purposes of this experiment. In particular, the maser environments could be controlled and monitored much more stringently, which could lead to a reduction of the limiting phase variations seen in Figures 1 and 2.

ACKNOWLEDGEMENTS

We are especially indebted to Dr. N. A. Renzetti, without whose continued support and encouragement this research would not have been possible. We deeply appreciate the support and helpful advice given by various members of the Advanced Time and Frequency Systems Research Group. The research described in this report was carried out by the Jet Propulsion Laboratory, California Institute of Technology, under a contract with the National Aeronautics and Space Administration and was funded through the Caltech President's Fund.

REFERENCES

1. T. P. Krisher, L. Maleki, L. E. Primas, R. T. Logan, G. F. Lutes, J. D. Anderson, and C. M. Will, in Proceedings of the Twentieth Annual Precise Time and Time Interval (PTTI) Applications and Planning Meeting, November 29 — December 1, 1988, pp. 251-260.
2. P. M. Lubin, G. L. Epstein, and G. F. Smoot, Phys. Rev. Lett. 50, 616 (1983); D. J. Fixsen, E. S. Cheng, and D. T. Wilkinson, Phys. Rev. Lett. 50, 620 (1983).
3. The high-frequency sinusoidal variation apparent in the figures of Reference [1] has been attributed to signal leakage in the fiber optics instrumentation. This signature was removed by

low-pass filtering. It should also be noted that Figure 6 of Reference [1] corresponds to adding the data records and not differencing them, as was mistakenly stated in the text.

4. J. P. Turneaure, C. M. Will, B. F. Farrell, E. M. Mattison, and R. F. C. Vessot, Phys. Rev. D 27, 1705 (1983).
5. M. P. Haugan and C. M. Will, Physics Today 40, 69 (1987).
6. R. Mansouri and R. U. Sexl, Gen. Relativ. and Gravit. 8, 497 (1977); 8, 515 (1977); 8, 809 (1977).
7. C. M. Will, in preparation.
8. M. A. Weiss and D. W. Allan, IEEE Trans. on Instr. and Meas. IM-36, 572 (1987).
9. E. Riis, L.- U. A. Andersen, N. Bjerre, O. Poulsen, S. A. Lee, and J. L. Hall, Phys. Rev. Lett. 60, 81 (1988).
10. G. R. Isaak, Phys. Bull. 21, 255 (1970).

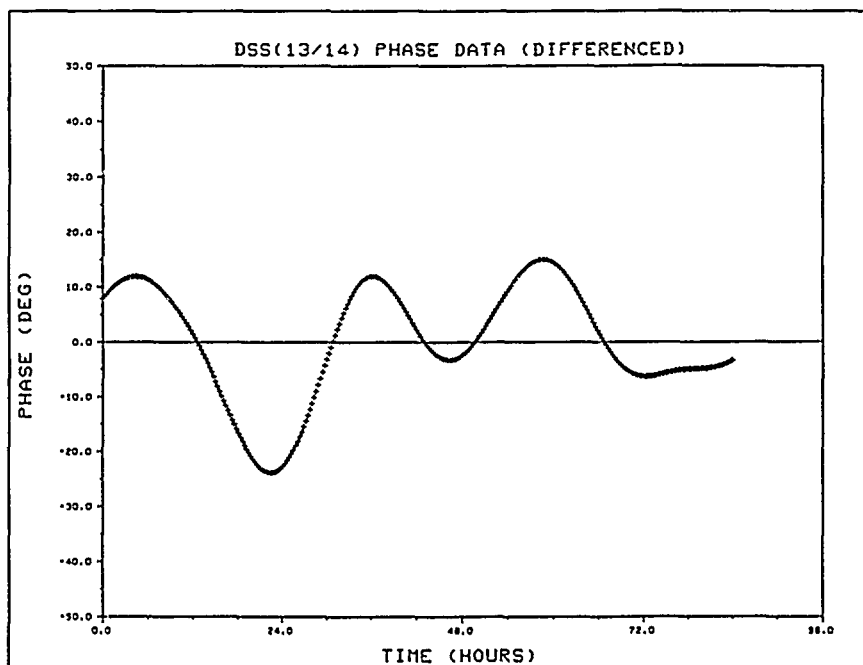


Figure 1.

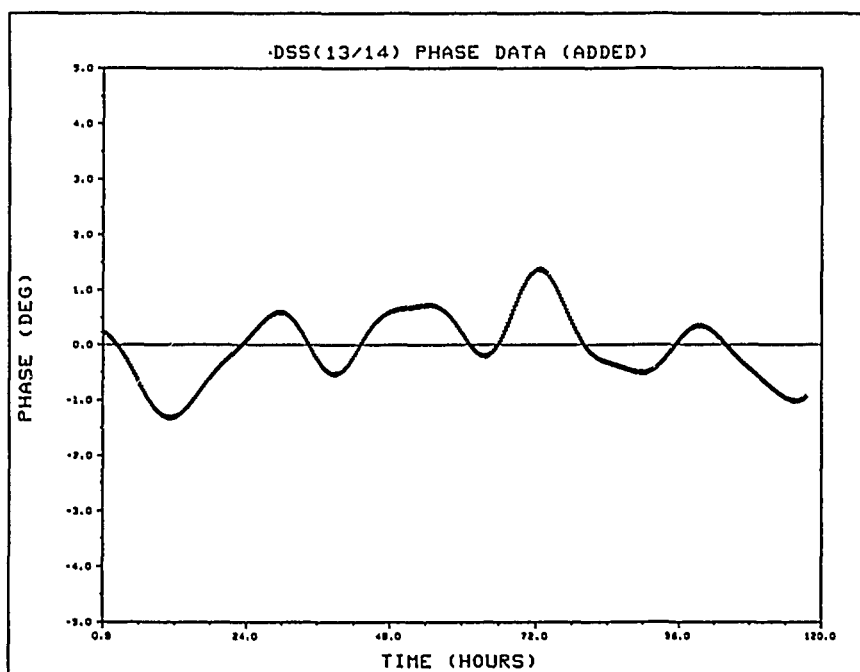


Figure 2.

TESTING FOR A COSMOLOGICAL REFERENCE FRAME

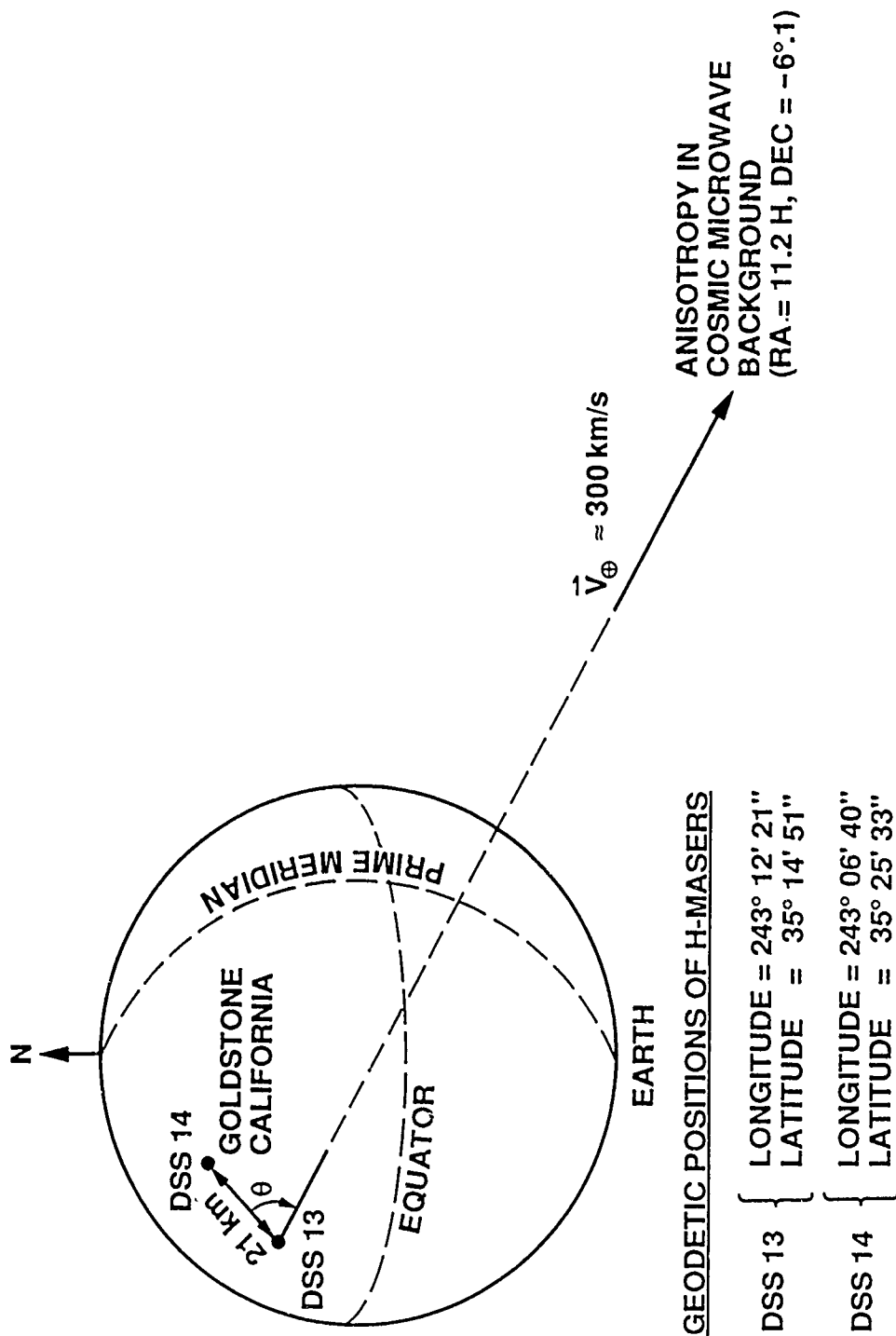


Figure 3.

TESTS OF THE ISOTROPY OF THE ONE-WAY VELOCITY OF LIGHT (ca 1989)

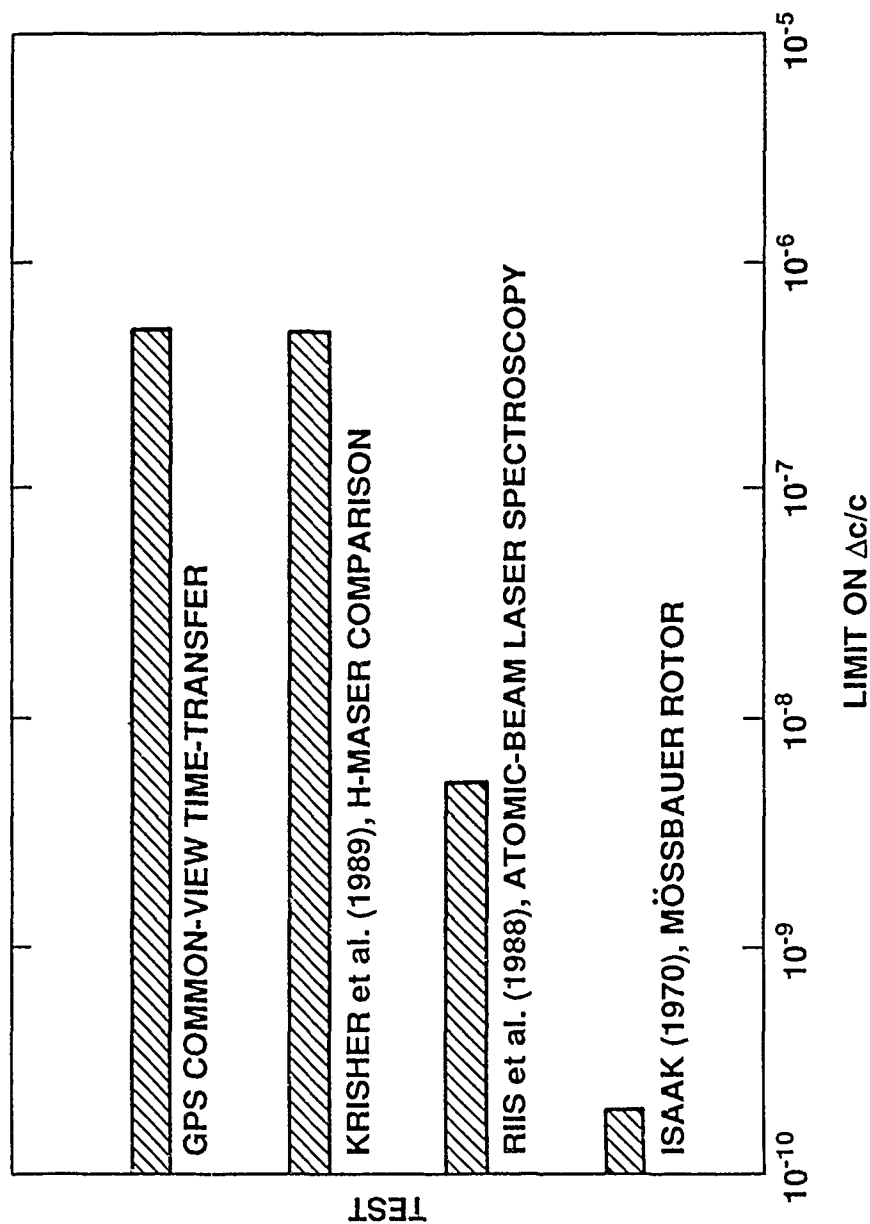


Figure 4.

THE NIST DIGITAL TIME SERVICE

J. Levine, M. Weiss, D.D. Davis, D.W. Allan, and D.B. Sullivan
Time and Frequency Division
National Institute of Standards and Technology
Boulder, Colorado 80303

Abstract

The NIST Digital Time Service is designed to provide computers with telephone access to time generated by the National Institute of Standards and Technology (NIST, formerly the National Bureau of Standards) at accuracies approaching 1 ms. Features of the service include automated estimation by the transmitter of the telephone-line delay, advanced alert for changes to and from daylight saving time and advanced notice of insertion of leap seconds. The ASCII-character time code operates with most standard modems and computer systems. The system can be used to set computer clocks and simple hardware can also be developed to set non-computer clock systems.

INTRODUCTION

The principal limitation to the accuracy of most methods of time dissemination is the uncertainty in the velocity of propagation of the information through the medium separating the transmitter and receiver. The delay, which is typically on the order of milliseconds, depends both on the physical length of the path and on the group velocity of the signal, and neither of these is well known in general. Either the path length or the group velocity is likely to change with time, so that real-time measurements of the transit time are generally required if the highest accuracy is to be realized. The telephone system provides a unique environment in this respect, since such measurements can be made using simple hardware. Using the telephone system for time dissemination is also desirable since telephone service is already widely available.

If a passive receiver is replaced by an active transponder, the time delay along the path can be determined from the transmission end by sending a pulse to the user and measuring the delay until the echoed pulse returns. Half of this round-trip delay is the time for the signal to reach the user assuming that the communication medium is reciprocal (i.e., that the delay is the same in both directions). This is not always the case for atmospheric paths because of fluctuating multi-path effects and asymmetries in the antennas, and it was not always the case in the past for telephone circuits. The telephone carriers now prefer to route both directions of transmission along the same path. As will be seen later in this paper, tests indicate that the telephone path is highly reciprocal.

With this as background and with growing interest in millisecond-level synchronization of computers, NIST has developed a simple telephone system for automated setting of clocks in digital systems. This service is called the Automated Computer Time Service (ACTS). The system makes no demands on the receiver and will function with both passive receivers and active transponders. A passive receiver consists of a modem and a terminal, computer or other display device. An active transponder consists of the same hardware with the additional capability of being able to echo the received messages back to NIST using either hardware or software methods. For either type of system, the modem must conform

to either the Bell 103A standard for frequency-shift keying at 300 bits/s or the Bell v212a standard for phase-shift keying at 1200 bits/s. The terminal, computer or display device must recognize the standard ASCII code transmitted with 7 data bits, space parity and 1 stop bit.

The current telephone number for the service is (303) 494-4774. This is not a toll-free number. The following sections describe the service in more detail including discussion of

1. the operation of the service,
2. the reliability of the transmission system and
3. software and hardware which have been developed for the user end.

OPERATION OF ACTS

Transmission Formats

The transmission format at 1200 bits/s is shown in Fig. 1.

- a. The column labeled MJD is the Modified Julian Day number, which advances by 1 at 0000 Coordinated Universal Time (UTC) every day. The MJD corresponding to 1 January 1989 was 47527.
- b. The next six numbers give the Coordinated Universal time as: years since 1900, month, day, hour, minute and second. Coordinated Universal Time is the official international time and was formerly called Greenwich mean time.
- c. The column labeled DST is a flag used to specify if a correction for daylight saving time is required now or is imminent. This flag is valid for most of the continental United States. If DST is 00 then standard time is in effect. If DST is 50 then daylight saving time is in effect. If DST is between 99 and 51 then a transition to daylight saving time is approaching. Daylight saving time will be in effect at 2:00 (2:00 a.m.) local time on the day when the count reaches 51. If DST is between 49 and 01 then a transition from daylight saving time back to standard time is approaching. It will arrive at 2:00 (2:00 a.m.) local time on the day when the counter is 01. In either transition situation, the counter is decremented at 00:00:00 (midnight) UTC every day.
- d. LS is the leap-second flag and is normally 0. It will be set to 1 to indicate that a leap second is to be added following 23:59:59 UTC on the last day of the current month. This second will be named 23:59:60 UTC, and the second following it will be 00:00:00 of the following day. The LS flag will be set to 2 to indicate that a second is to be dropped at end of the last day of the current month. The second following 23:59:58 UTC will be 00:00:00 UTC of the next day. Added leap seconds are generally required about every 18 months to maintain the coordination of UTC; it is unlikely that seconds will be dropped in the foreseeable future.
- e. DUT1 is the approximate difference between a time scale defined in terms of the rotation rate of the earth (UT1) and UTC. That is, $DUT1 = UT1 - UTC$. The difference is given to the nearest tenth of a second.
- f. msADV is the advance of the on-time marker in milliseconds. The center of the stop-bit of the on-time marker leaves the transmitter early by this amount so as to arrive at the user on-time.

- g. OTM is the on-time marker. It is either '*' or '#' as discussed below. The center of the stop-bit of this character is intended to arrive at the user at the time specified by the previous characters on the same line.

A help message is available if the user sends a question mark early in the transmission. This, however, preempts the transmission of time information for the rest of that call.

The transmission format at 300 bits/s is similar, but there is not enough time to send the entire message. The transmission consists of the UTC time in hours, minutes and seconds, the current advance in milliseconds and the on-time marker. In the future, alternating halves of the full message may be sent every second together with an on-time marker, so that the full date can be decoded every two seconds.

Modes of Operation of the Service

Depending on the user equipment, the ACTS service provides three modes for checking and/or setting computer clocks.

- In the simplest form of the service, a passive user receives the time code and the on-time marker/character but does not echo the received message.

In this case, an advance of 45 ms is used for all transmissions. The OTM should arrive at the user within 100 ms of the correct time unless the connection is routed through a satellite.

- If the user echoes all characters back to NIST, the round-trip line delay of the on-time marker will be used to adjust the advance of subsequent transmissions. The accuracy in this mode should be better than 10 ms and the repeatability is about 1 ms.
- If 300 bit/s modems are used and the user echoes all characters back to NIST, the slower transmission speed means that the full time code is not transmitted, but the measured delay is likely to be more accurate. Our experience indicates that the accuracy will be approximately 1 ms.

In any of these modes, the maximum connection time is 55 s. If all of the lines are busy at any time, the oldest call will be terminated if it has been on line more than 15 s, otherwise the call that first reaches 15 s is disconnected.

Reliability

To help ensure that ACTS never sends the wrong time, the system has triple redundancy and special self checking to enhance reliability and to increase the volume of calls that can be handled. The basic unit (see Fig. 2) consists of three time-code generators, each with a complete system for generating the time code and disseminating it through a separate modem to one of the telephone lines. Each of the time-code generators receives an independent time signal from a different clock in the NIST time scale. The time code needs to be initialized by an operator, but is automatically updated by the hardware after that. The power supply for the system is backed up by batteries so that the internal clocks do not lose time during a power failure.

Each time-code generator constantly compares its own time code with the codes of the other two, and participates in majority voting on the correctness of these codes. The time code is transmitted at 100 bits/s from each generator to the other two. This code contains all of the information transmitted through the telephone line. Each generator compares the bits of the two incoming codes with its own code and flags a generator as bad if any one disagrees with the other two. The flag of one generator declaring another bad is passed to a central control module as a vote against the offending generator. If any two of the generators vote against any single generator, the loser is taken off line. If all three disagree with one another, all three are disabled.

Each time-code generator receives a timing signal from the other two and compares these signals with its own internal time. If either time difference is larger than $15\mu\text{s}$, this is reported to the control module. Again, the votes are counted by the control module. A vote of two to one takes the loser off line and disagreement among all three disables all of them.

If an individual time-code generator finds either a code or a time error it sounds an audible alarm. If there is total disagreement among the three generators, all three generators are taken off line and the lines to these generators are set so that a caller will receive a busy signal. The system is also connected to a special alarm at the Boulder NIST security office and signals that office if problems develop. This office then contacts one of the system operators, either at work or at home. To facilitate operations and service, the system can be operated remotely using extensive control and diagnostic functions.

The ACTS system can be expanded in three-line units, each operating independently in the manner described above. If an entire three-generator unit is taken off-line, then the effect is to reduce the number of available lines by three. The desired effect is that the system transmits nothing rather than transmitting a code or time marker which is in error.

USER SOFTWARE AND HARDWARE

Software

We have developed some example ACTS software which runs on a number of popular computers.¹ There has been no attempt to be comprehensive in coverage of different computers, but rather to focus on a few example packages which can then be adapted to other machines. The NIST software provides for automated dialing, selection of time zone, selection of mode of operation, echoing of the OTM, setting of the computer clock, archiving of clock offset, and transmission to the port of the computer of a signal which can be used to produce an external time pulse coincident with the OTM. The program is written in a modular fashion so that additional features, such as a graphical presentation of the time-difference data or a more comprehensive statistical analysis of the performance of the local clock, can be added easily. This example software (which includes source code) is available on a 5.25-inch, 360 kbyte MSDOS diskette along with instructions for \$35.00. To order this software contact:

¹Example software is available for IBM PC/XT/AT and compatible systems, for the DEC PDP-11, and for Sun systems. (These trade-names are used for identification purposes only and no endorsement is implied.)

NIST Office of Standard Reference Materials
B311 - Chemistry Building
Gaithersburg, MD 20899
(301) 975-6776

Specify that you want RM 8101, software for Automated Computer Time Service.

Hardware

Using software developed by NIST, the PC/XT/AT compatibles will deliver a signal coincident with the OTM to the parallel printer port. The very simple circuit shown in Fig. 3 can be used to convert this to a positive pulse. This might be useful for synchronizing an external system or for starting or stopping a counter in a precise measurement of frequency (see Section 5). A second circuit which we have tested (see Fig. 4) echoes all characters from the user and provides an external pulse when the OTM is received. This circuit, which allows ACTS to calibrate the phone line and advance the OTM accordingly, requires an external modem, but does not require a computer. To use this circuit, the user must first manually establish the telephone connection with NIST.

TIMING ACCURACY

We have evaluated the performance of the ACTS system using both satellite and ground-based telephone circuits. The satellite test was performed between the NIST radio station WWVH in Hawaii and our laboratory in Boulder, Colorado; the ground-based test used a local telephone call in Boulder.

In both tests, we use either the circuit of Fig. 4 or a personal computer running our software to produce a pulse each time the on-time marker arrives at the receiver. We measure the time differences between these pulses and the ticks of a local time standard. These tests are repeated at different times of the day and using different brands of modems.

Consecutive measurements over both the satellite and local telephone connections showed a repeatability of $\pm 1\text{ms}$ at both 300 and 1200 bits/s. It suggests that both satellite and local telephone connections are reciprocal to a very high degree.

The accuracy of the arrival time of the on-time marker was measured using several different brands of modems. All of the tests used local telephone connections. At 300 bits/s, the offset of the on-time marker was not more than $\pm 2\text{ms}$ for any modem tested. At 1200 bits/s, different brands of modems resulted in offsets of up to $\pm 7\text{ms}$, which is significantly larger than the repeatability using any one modem. These offsets result from the difference in the group delay between the transmit and receive portions of the modem.

The accuracy of the satellite connection to Hawaii was measured using a single modem at both speeds. We measured an accuracy of 1 ms using 300 bits/s and 6 ms using the 1200 bit/s protocol. These values were stable from day to day to within the repeatability quoted above, and suggest that the satellite path is also reciprocal to a very high degree.

A more detailed discussion of the error budget for the system can be found in Levine et al.^[1]

APPLICATIONS

One of the most important applications for ACTS is the maintenance of accurate time within a digital computer or some digital hardware with a microprocessor. This may be especially important in a network where a number of computers independently tag events with the date and time and then share their information.

A second application is the measurement of frequency. Here pulses coincident with the OTM are used to start and then stop a counter which counts the output of the oscillator under test. If the start and the stop pulses are separated by one day, then the system can yield a frequency-measurement accuracy of about 0.01 ppm.

DISCUSSION AND CONCLUSIONS

NIST is now committed to long-term operation of a new Automated Computer Time Service. The format is now fixed, except for a change which will modify the 300 bit/s format to transmit the entire time/date message every 2 s. The system will be expanded as the number of calls increases. The telephone number for the service is (303) 494-4774. All of the lines will be connected to a telephone rotary switch so that they can be reached by dialing this number. This number is not toll-free.

The system was designed to make operation at the user's end particularly simple. With telephone-line delay measured at the NIST end, the user needs only a modem and a computer or some other digital system to access NIST time at accuracies of up to 1 ms. Example software and hardware has been developed by NIST, and the software is available for a small charge.

The system can be used to set digital clocks, or to perform frequency calibration at an accuracy of 0.01 ppm for a one day measurement.

REFERENCES

- [1] J. Levine, M. Weiss D. D. Davis, D. W. Allan and D. B. Sullivan, The NIST Automated Computer Time Service, J. Res. of NIST, 94, 311 - 321 (1989).

? = HELP

National Institute of Standards and Technology
Telephone Time Service

(1 second pause here)

								D	L	D						
MJD	YR	MO	DA	H	M	S	ST	S	UT1	msADV						OTM
47222	88	03	02	21	39	15	83	0	+.3	045.0	UTC(NIST)	*				
47222	88	03	02	21	39	16	83	0	+.3	045.0	UTC(NIST)	*				
47222	88	03	02	21	39	17	83	0	+.3	045.0	UTC(NIST)	*				
47222	88	03	02	21	39	18	83	0	+.3	045.0	UTC(NIST)	*				
47222	88	03	02	21	39	19	83	0	+.3	037.6	UTC(NIST)	#				
47222	88	03	02	21	39	20	83	0	+.3	037.6	UTC(NIST)	#				
etc.	etc.	etc.	etc.	etc.	etc.	etc.	etc.	etc.	etc.	etc.	etc.	etc.	etc.	etc.	etc.	etc.

Figure 1. Time code and time marker transmitted by ACTS at 1200 bits/s. The abbreviations are as follows: MJD = Modified Julian Date, YR = Year, MO = month, DA = Day, H = Hour, M = Minute, S = Second, DST = Daylight Saving Time (a flag meaning that a change is coming), LS = Leap Second (a flag meaning a leap second is to be added), DUT1 = UT1 - UTC (earth rotation time minus coordinated universal time), msADV = milliseconds of advance of the time marker, OTM = On-Time Marker.

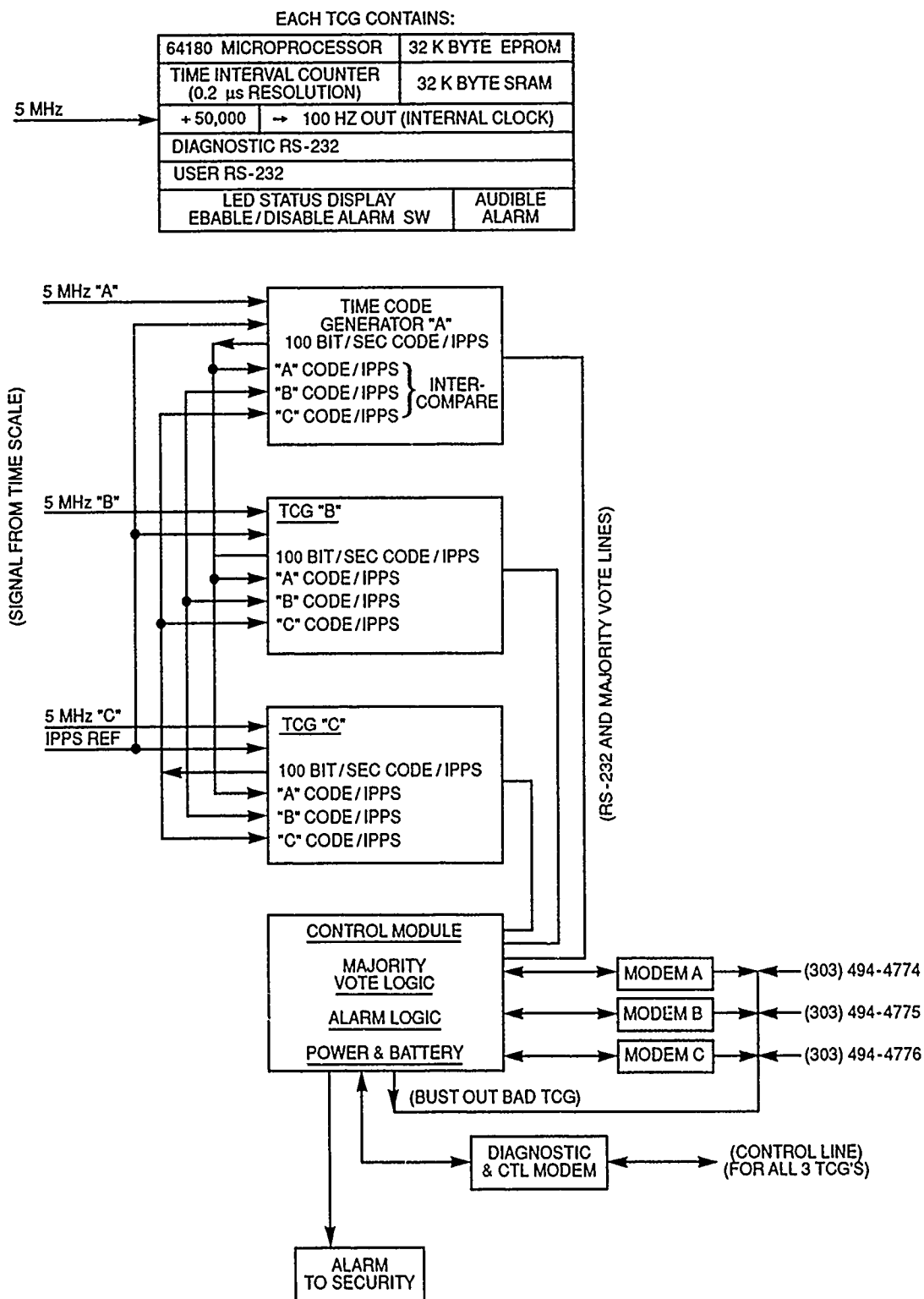


Figure 2. Block diagram of the ACTS transmitter including time-code generators and control module.

PC. INTERFACE TO PRINTER PORT FOR IPPS OUT

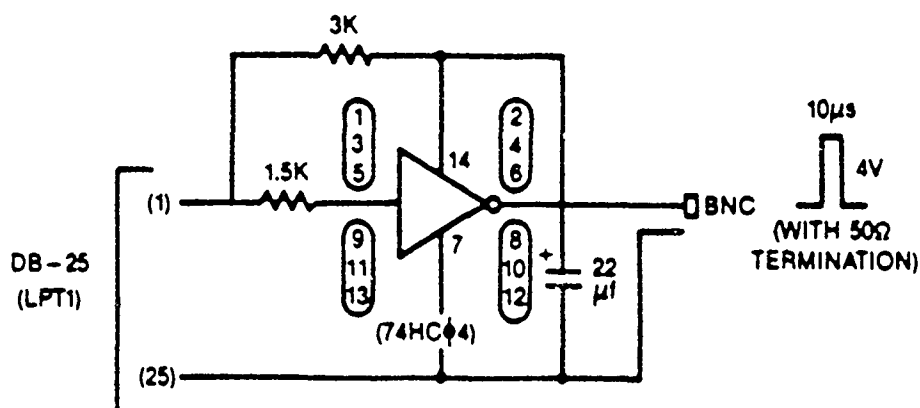
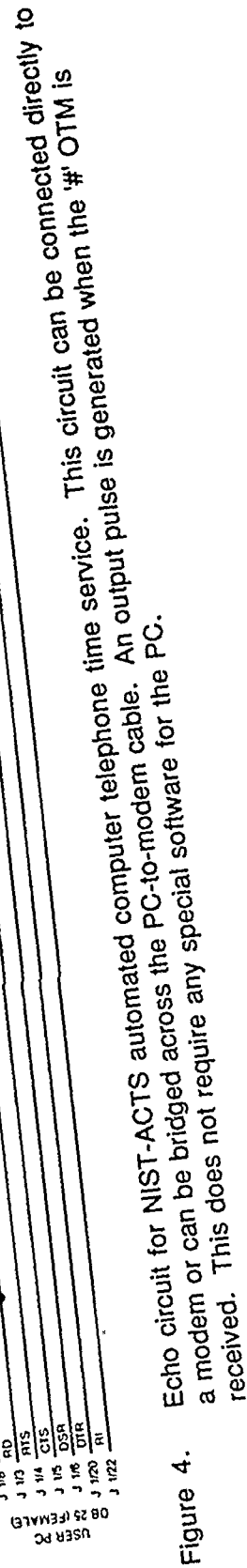


Figure 3. Simple circuit used to obtain a positive pulse coincident with the OTM from any PC/XT/AT compatible computer using the NIST software. The HCMOS inverter can be built directly into a DB-25 male connector.



Echo circuit to a modem or can be bridged across the line. This does not require any special software for the PC to receive. This does not require any special software for the PC to receive.

A NEW HYDROGEN-MASER TIME AND FREQUENCY
STANDARD AT SHESHAN VLBI STATION OF SHANGHAI OBSERVATORY

Z.C.Zhai, H.X.Huang, C.F.Lin, G.X.Jiang

W.H.Luo and J.F.Lu

Shanghai Observatory, Academia Sinica, Shanghai 200030

Abstract

A new kind of hydrogen-maser time and frequency Standard was installed this September at sheshan 25-meter radio telescope in Shanghai, for very long baseline interferometry (VLBI) experiments. This standard is a readily transportable, rugged and completely integrated frequency standard. The entire system is engineered as a unit, and all electronics were mechanically and electrically integrated with the physical portion into the overall design. This paper describes its design feature and structure as well as the measured results of its performance. Its applications and data in VLBI experiment are also included.

INTRODUCTION

The hydrogen maser is generally regarded as the ideal time and frequency standard for VLBI. It has a unique combination of superior short-term and long-term stability. Further, the maser is a primary standard with unsurpassed resettability of frequency.

In the past, the size, weight, and general awkwardness of the equipment have limited the use of the maser to fixed installations. The masers which have been used for several years in Sheshan VLBI station are this kind of hydrogen masers, which were made earlier by Shanghai Observatory⁽¹⁻³⁾.

A hydrogen maser described in this paper is a new kind of maser, designed to be easily transportable and rugged enough to withstand the normal rigors of being moved from one station to another. It was transported by truck from Zi-Ka-Wei section to SheShan VLBI station, for VLBI experiments. In the new design, we absorbed many design ideas of masers developed by Dr.R.F.C.Vessot at the SAO⁽⁴⁾.

DESIGN FEATURE OF THE NEW MASER

The design philosophy for new maser developed from several basic aspects. First, the maser design emphasizes good intrinsically stability with respect to both mechanical and thermal perturbations. It is enclosed in a very carefully controlled thermal and mechanical environment to minimize maser detuning by variations in ambient conditions, and thus to permit stable maser operation over long periods of time without requiring autotuning or other adjustments.

Second, the new maser is a compact, relatively light-weight, rugged, and easily transportable standard. The entire standard was to be self-contained in a single standard-sized rack cabinet. All electronics including the phase lock receiver were to be mechanically and electrically integrated into the overall design. It is a relatively small instrument weighing 250kg and requiring a source of only 28 volts DC at 200 watts to operate. The third feature is that there is a circulating air system in the rack cabinet. The system, which controls the temperature of the pump, the dissociator, and the upper maser electronics, is an entirely independent system with self-contained sensors and electronics. In addition, the new maser incorporates an extensive monitoring capability. Four front panel mounted meters, each with an eight-position selector switch are located on the monitor panel to provide quick-look monitoring of 32 functions. These include all main power-supply voltages, all heater voltages, hydrogen dissociator operating conditions, receiver/synthesizer signal level, and phase-lock control voltages. The monitor panel also includes a small four-digit counter and LED readout for displaying the output frequency of the synthesizer.

Fig. 1 shows the photograph of the complete maser system with the side panel removed.

NEW MASER OSCILLATOR AND CLOCK SYSTEM

The design features of the Shanghai Observatory new hydrogen maser were described in detail in earlier paper⁽¹⁾. Fig.2 is a diagram of the major structure of the maser. The cavity resonator is an extremely rugged CERVIT structure. Longitudinal stresses produced by the thermal expansion

coefficient of the resonator hold-down can be absorbed by a large Bellville spring washer. Thermally induced radial stress in the resonator base is relieved by a 40-glass balls quasi-kinematic mount. Barometrically induced stresses on the vacuum tank are isolated from the cavity resonator by a double-base structure. It should be noted that the design philosophy of the maser emphasizes good Long-term frequency stability without the necessity for continuous automatic tuning. The tuning procedure is usually required only when the maser is moved to a new location or before VLBI observations.

The entire maser clock system is shown in block diagram in Figure 3. A 100MHz crystal oscillator is phase locked to the maser signal to provide standard frequencies at levels useful to the clock system. A simple dual-conversion receiver is used to generate the phase locking signals; a synthesizer is also used to set the time scale. 1MHz and 5MHz signals, derived from internal dividers in the crystal oscillator, is used to drive the VLBI timing system.

THE PERFORMANCES OF NEW MASER

A comprehensive series of environmental and short-term stability tests on the new maser has been evaluated before the new maser was moved to Sheshan VLBI station. Figure 4 shows the short-term frequency stability of the new maser. It can be seen from the Fig.4, the stability data keeps 10^{-15} levels for the periods of time beyond 100 seconds.

The new maser has been working continuously for more than a year before it was moved to Sheshan VLBI station. Figure 5, as an example, shows the comparison data measured between the new maser and the master Cs clock of AT(SO).

In the environmental tests, the output frequency was carefully monitored while one of the environmental conditions was varied. The results of each of these environmental tests is itemized below:

1. Output frequency vs temperature tests - The new maser was placed individually in the test chamber and the chamber temperature was cycled between 22° to 31°C , the resultant variation in output frequency was plotted.
2. Barometric pressure tests - No output frequency variations were observed as the maser was individually subjected to barometric pressures of 25 mmHg above and below ambient pressure with a two-hour dwell at each extreme.

3. Magnetic field Sensitivity tests - It was measured by placing the maser under test within a 2.4-meter diameter set of Helmholtz coils and varying the current through the coils. A about 0.4 gauss axial field was used in the tests.

A summary of the environmental sensitivities of the new maser is presented in table 1.

Table 1. Environmental sensitivities^{6,7}

conditions	Sensitivities		
Temperature (22°C ~ 31°C)	slow coefficient		fast coefficient
	ΔT up	$2.9 \times 10^{-11}/^\circ\text{C}$	$1.2 \times 10^{-11}/^\circ\text{C}$
	ΔT down	$3.0 \times 10^{-11}/^\circ\text{C}$	$1.3 \times 10^{-11}/^\circ\text{C}$
Barometric pressure ($\pm 25\text{mmHg}$)	$< 1 \times 10^{-11}$		
Magnetic Field ($\pm 0.4\text{G}$)	$1.1 \times 10^{-11}/\text{G}$		

APPLICATION

1. Tuning the hydrogen maser

The oscillation frequency of a hydrogen maser is "pulled" by the maser cavity resonator. The amount of pulling is a function of cavity detuning and the line width of the atomic resonance:

$$\nu = \nu_{\text{H}} + [(\nu_{\text{c}} - \nu_{\text{H}})/\nu_{\text{c}} \cdot Q - (0.29 \nu_{\text{H}} a_0^2 h V_{\text{c}})/(Q \mu_0^2 \eta V_{\text{L}})] \Delta \nu_{\text{L}} \quad (1)$$

If the cavity is tuned to a frequency ν_{c_0} such that

$$\nu_{\text{c}_0} = \nu_{\text{H}} [1 - (0.29 \nu_{\text{H}} a_0^2 h V_{\text{c}}/Q^2 \mu_0^2 \eta V_{\text{L}})]^{-1} \quad (2)$$

then the term in brackets in equation(1) vanishes and

$$\nu = \nu_{\text{H}}$$

The maser oscillates at the centre of the atomic resonance line.

The cavity is tuned to ν_{H} by modulating the flux of atoms entering the storage bulb. It can be shown that the spin exchange contribution to the

line width is directly proportional to the flux, and when the cavity is at the tuning point ν_{co} , then ν is independent of line width and therefore also independent of the total hydrogen flux.

The maser can be tuned by using another hydrogen maser as a reference or a frequency reference less stable than that of the maser itself. At the Sheshan VLBI station, hydrogen maser is tuned by using a microcomputer system. The end results for tuning point and line Q are displayed on the screen.

2. VLBI data

During VLBI experiments, hydrogen maser performances are monitored by a microcomputer real-time measuring system. The stability data is shown not only by Allan Variance, but also in a form that might be more useful for VLBI experimenters. Fig. 6 shows phase difference in seconds with only a frequency offset term removed from the data. Notice that the data has the quadratic behavior associated with uniform frequency drift. Fig. 7 shows the same data with a uniform frequency drift term also removed.

CONCLUSION

For VLBI observations, the hydrogen maser is the suitable satisfactory frequency standard. Shanghai Observatory new hydrogen maser has demonstrated that it can be used routinely and reliably for VLBI. Doubtlessly, the features of ease transportation and convenient to operate make the maser to be also a ideal time and frequency standard for other fields.

REFERENCES

- [1]. Z.C.Zhai, JIETE, 27.11, 1981;
- [2]. Z.C.Zhai, etc, proc of 38th annual symposium on Frequency control, 1984;
- [3]. Z.C.Zhai etc, proc of 18th PTI meeting, 1986;
- [4]. R.F.C.Vessot, M.M.Levine, E.M.Mattison etc, proc. of 8th PTI meeting, 1976;
- [5]. Z.C.Zhai, H.X.Huang etc, proc, of 41st Annual symposium on Frequency control, 1987;
- [6]. Z.C.Zhai, H.X.Huang etc, "Electromagnetic metrology", International Academic Publishers, 1989.

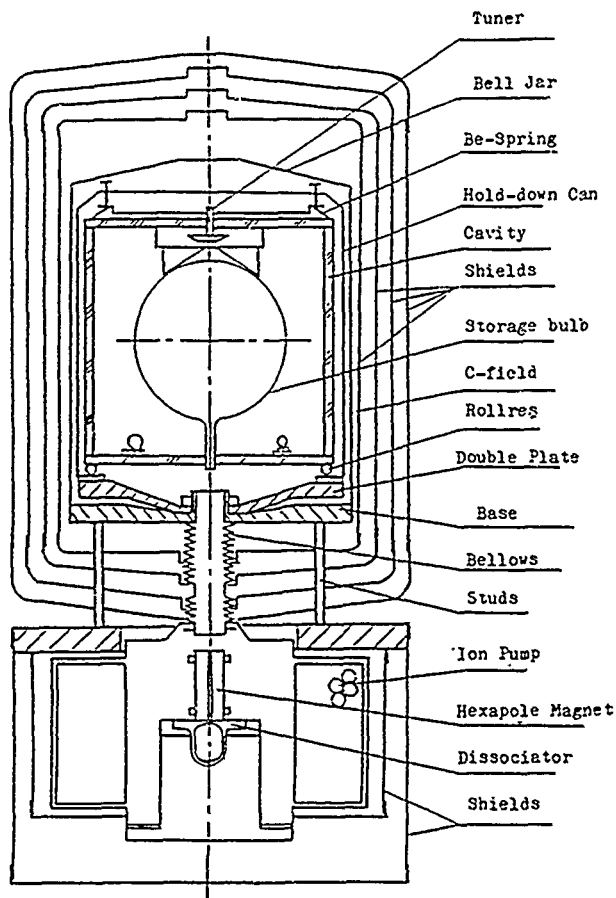


Fig 2 Major Structure of the maser oscillator

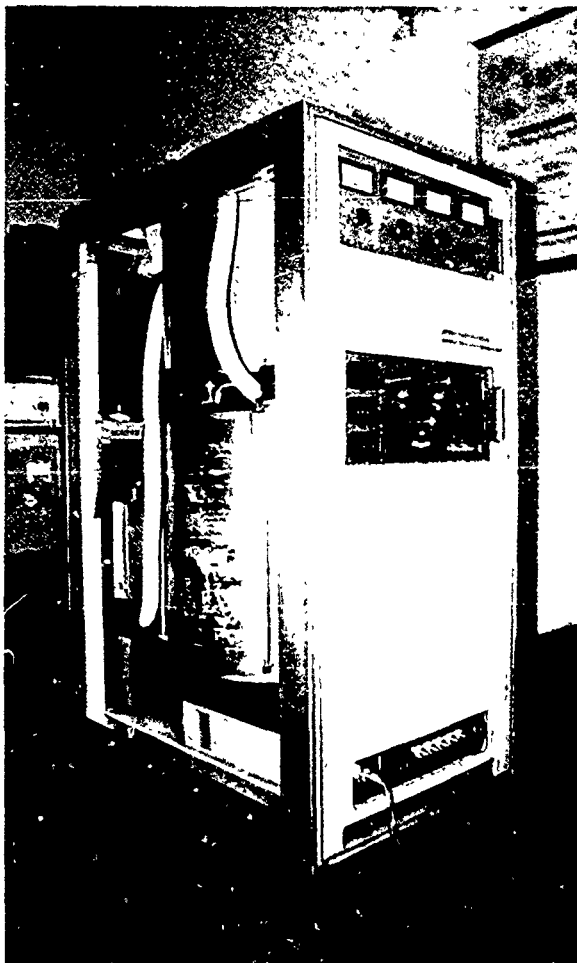


Fig 1 New Hydrogen Maser

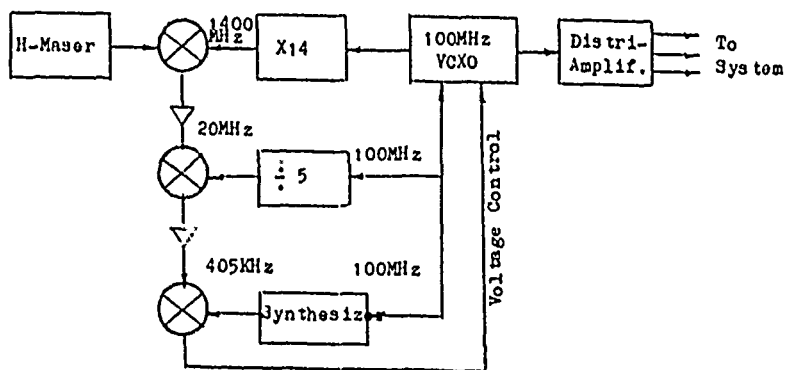


Fig 3 Maser clock system block diagram

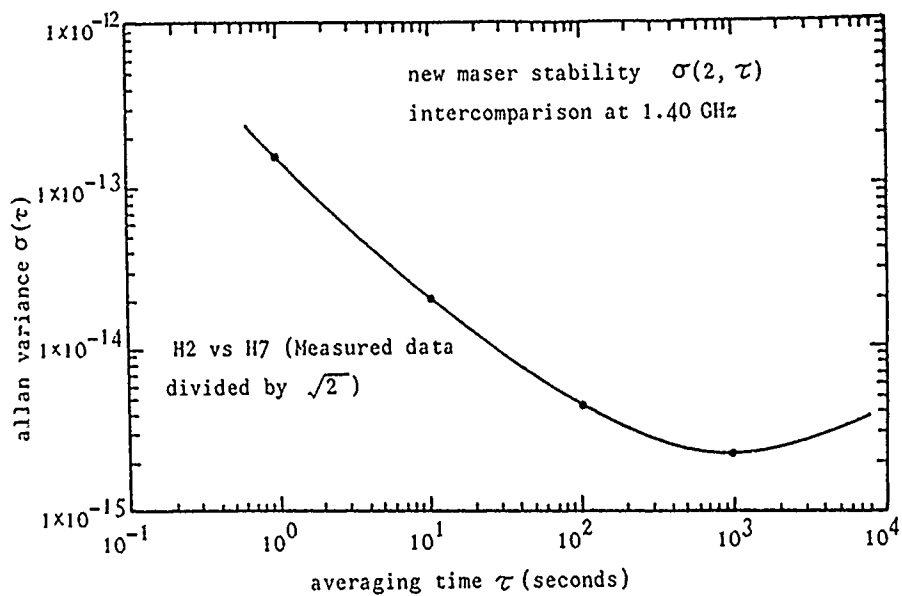


Fig.4 New maser stability data

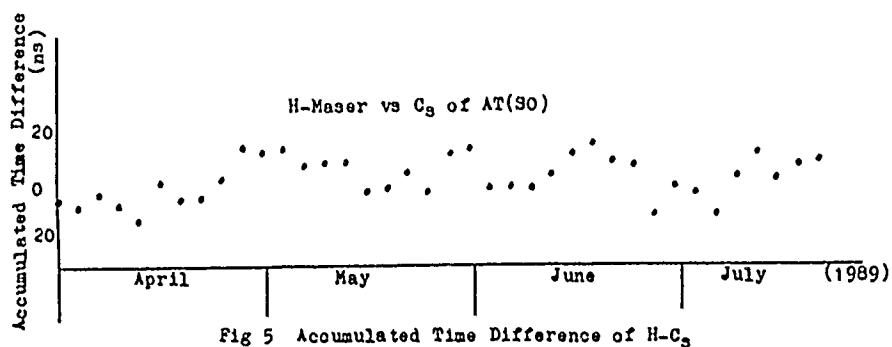


Fig 5 Accumulated Time Difference of H- C_3

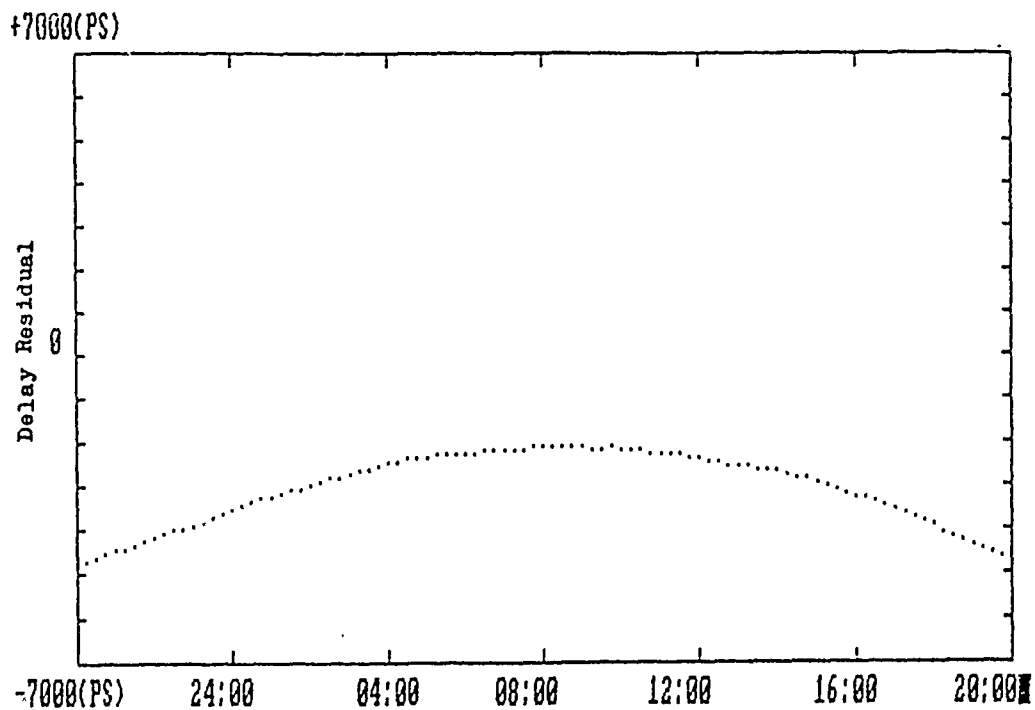


Fig.6 VLBI Phase Comparison With Frequency Offset Removed

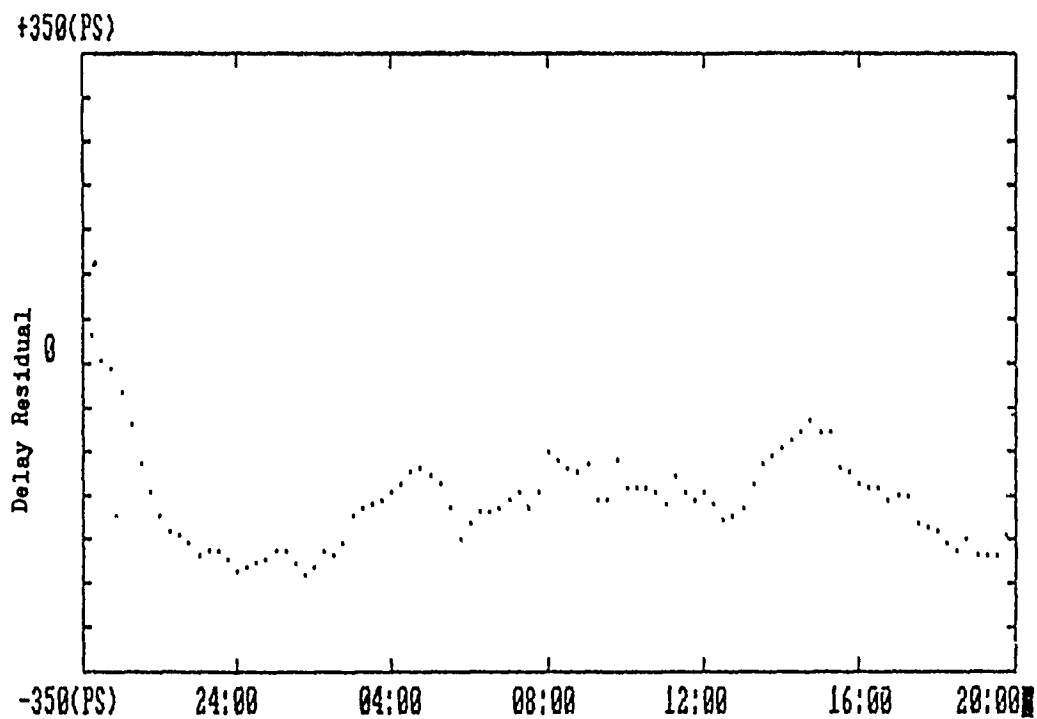


Fig.7 VLBI Phase Comparison With Frequency Drift Removed

Improvement of Time Comparison Results by using
GPS Dual Frequency Codeless Receivers
Measuring Ionospheric Delay

M. Imae and C. Miki
Communications Research Laboratory
Hirai Kashima-machi Ibaraki-ken
314, Japan

C. Thomas
Bureau International des Poids et Mesures
Pavillon de Breteuil
F92312 Sevres Cedex, France

ABSTRACT

A dual frequency GPS receiver measuring ionospheric delay or TEC (Total Electron Content) named GTR-2 was constructed in BIPM (Bureau International des Poids et Mesures)[1], and operates in regular base since October 1988. CRL (Communications Research Laboratory) also has completed a development of the same equipment this year. It has almost same performances as GTR-2 in BIPM. By using these two receivers, we have begun to compensate the time transfer results obtained from the conventional GPS time transfer receivers between Japan and Europe under the cooperation of CRL and BIPM for a construction of a tight time-transfer link by using GPS satellite. This paper shows the improvement of GPS time transfer results by using the ionospheric delays measured by GTR-2.

For a highly transportable geodetic purpose VLBI (Very Long Baseline Interferometer) station, CRL has another application program of GTR-2. For this compact VLBI station, we are making a study of ionospheric compensation of the signal from radio stars by using the TEC data obtained from GTR-2.

CRL also have a plan of an improved version of GTR-2 which uses the phase informations of reconstructed continuous signals obtained by making cross correlation of the received L1(1575.42 MHz) and L2(1227.6 MHz) signals from the GPS satellites. By using this method, it can be estimated that this equipment can make more than one order of precise measurement of the TEC than GTR-2.

INTRODUCTION

The ionospheric delay is one of the largest sources of error for the time comparison and the positioning by using GPS satellites. The activity of the ionosphere depends largely on solar activity which has a long term cycle of about 11 years. The solar activity will be maximum around 1991, the effects of the ionosphere will be very large in coming few years. And as this solar maximum is estimated as a one of the largest one, then it is expected that the ionospheric activity will have large effects not only on the time comparison and the positioning but also on the communication links via communication satellites.

MEASUREMENTS RESULTS OF TEC BY GTR-2

The construction of GTR-2 in CRL has completed in the beginning of May,

1989, and we started its continuous operation since that time. It uses a directional antenna which has a gain of about 10 dBi for L1 and L2 signals of GPS satellite. It has a measurement precision of about 2×10^{16} electrons/m² of TEC and about 1 ns of L1 signal group delay.

Figure 1 shows the measurement results of TEC for July, 1989 obtained by the GTR-2 in CRL. This figure shows the estimated vertical TEC from the measured TEC along the line of sight to the GPS satellites by using a simple ionosphere model. From this figure L1 signal has more the 10 ns of daily variation caused by the ionosphere. Therefore it can be said that one must make ionospheric compensation by using actual ionospheric delay to perform a precise time comparison or positioning.

APPLICATION TO TIME COMPARISON RESULTS

The major time keeping laboratories make the daily time comparison by using GPS time transfer receivers under the common view[2] schedule calculated by BIPM. They use the conventional GPS time transfer receivers which receive the L1 C/A code signal of the GPS satellites, and they make ionospheric delay correction by the ionospheric delay model transmitted from GPS satellites. This ionospheric correction model[3] is very useful for the single frequency GPS users, but it has not enough precision to make a precise time comparison or positioning.

Between OP (Paris Observatory) and CRL, we made the ionospheric delay correction by the ionospheric delays measured by GTR-2 on both sites instead of the correction model. Figure 2 shows its schematic concept. GTR-2 on both sites are programmed to make simultaneous measurements with time transfer receivers.

Under the common-view time transfer schedule No.13 calculated by BIPM, we have 8 common-view tracks for each day between Japan and Europe. Figure 3 shows the time comparison results for three months between OP and CRL. In this figure two curves are plotted, one is UTC(OP)-UTC(CRL) by using raw data obtained from commercial GPS time transfer receivers which use the ionospheric correction model and the other is UTC(OP)-UTC(CRL) corrected by the ionospheric delay measured by GTR-2 on both sites, and 100 ns of offset are given to divide them. Figure 4 shows the zoomed plots of the time comparison results of figure 3 (11 days of the beginning of July), and we can see that the time comparison is performed with much higher precision when the measured ionospheric delays are involved.

APPLICATION TO SINGLE FREQUENCY VLBI OBSERVATION

For the geodetical application of GTR-2, CRL is planning to apply GTR-2 to VLBI experiments.

In order to realize a compact and high cost-performance system, a highly transportable VLBI station with 3m antenna is now under development in CRL[4]. For the conventional geodetic VLBI experiments, each VLBI station makes the observations by dual frequency (X-band and S-band) to compensate the relative ionospheric delay between both sites. Therefore each station should be equipped the facilities for these two receiving bands, such as feeds, low noise amplifiers, local signals, backend equipments and so on.

On the other hand, if one can estimate the ionospheric delay by using other method, each VLBI station has no need to make the dual frequency measurement. This means that the one can realize the maximum antenna efficiency for the X-band which is the main frequency band for the geodetic VLBI measurement, and can

reduce the VLBI facilities. These merits are very effective for small mobile VLBI stations.

For this purpose we are planing single frequency VLBI experiments by using our highly transportable VLBI station and GTR-2. The key subject in this experiment is how to estimate the ionospheric delay of the line of sight to the radio stars from that of the GPS satellite. To study this subject we are making simultaneous observations of the normal two frequency VLBI experiments and GTR-2 observation. The shematic concept is denoted in figure 5.

MORE PRECISE MEASUREMENT

As the GTR-2 uses a technique of the amplitude measurement of the cross-correlated signal between received L1 and L2 P-code of the GPS satellite, then the measurement precision of TEC is limited by the S/N ratio of the received signals and the period of the P-code clock rate (about 100 ns). Namely the precision is proportional to the period of signal and square-root of inverse of S/N ratio. Therefore, to make precise measurement of TEC, we should use a high gain antenna to increase S/N ratio or a long integration time to increase the number of samples.

For the other solution to improve the measurement precision, we are planning a more precise device, named GTR-3, which uses the phase measurement technique of the reconstructed continuous signals which have the frequency of L1-L2 and L1+L2. By using this method, we can use the period of about 2.8 ns (for L1-L2 signal) and about 0.36 ns (for L1+L2 signal). By using this method we can improve the measurement precision of TEC by more then one order compared to the GTR-2 method. In this method we should use the coherent local signals in the receiver for the signal processing to keep the phase informations. Figure 6 shows the block diagram of this receiver.

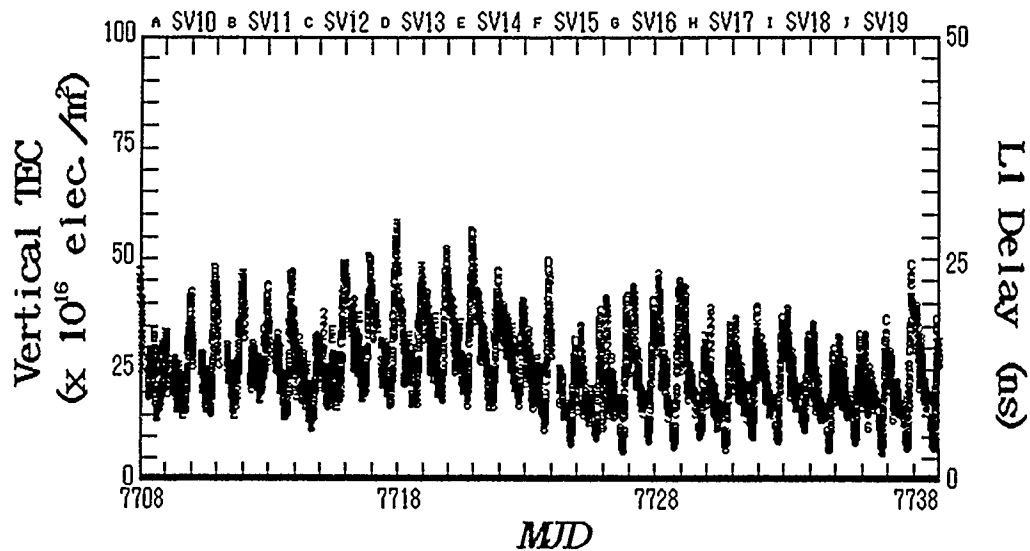
Normally, the ambiguity of period of the measurement signal is one of the largest problems to be solved, but the method mentioned above has an advantage for this problem compared to other methods. The detailed discussion will be made in the other occasion.

CONCLUSION

Using GTR-2 on both sites of time comparison stations, the improvement of the precision of time comparison were obtained. In the case of long distance time comparison between OP and CRL, we can get the rms variation of less than 10 ns by using the ionospheric delay obtained by GTR-2. This experiment is continuously made under the cooperation between CRL and BIPM. As GTR-2 has a simple structure and easily make a TEC measurement, then it can use in wide domains of science and technology not only in time comparison or geodesy.

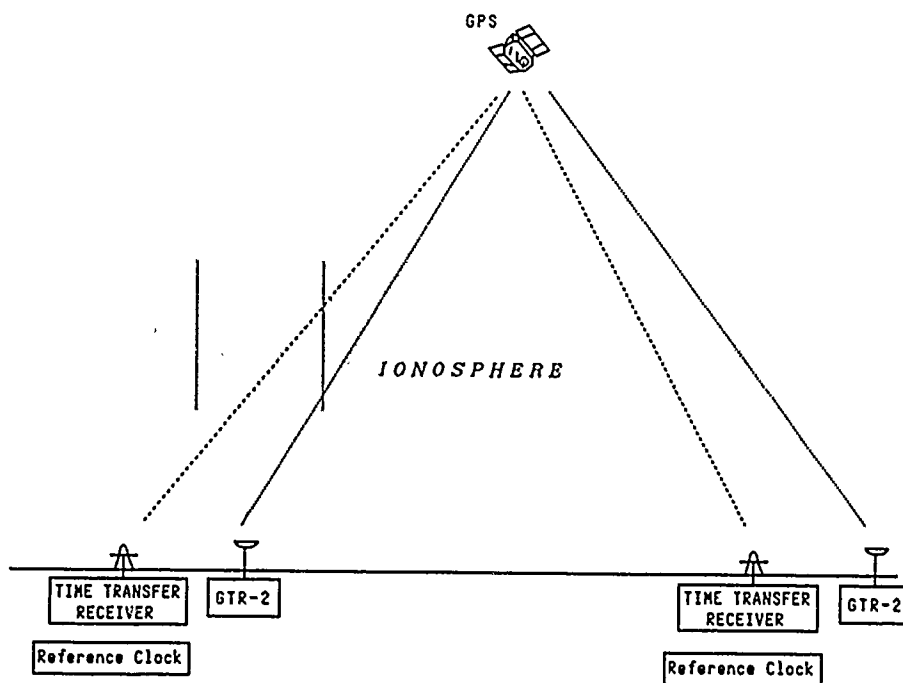
REFERENCES

1. Imae M., Lewandowski W, Thomas C., and Miki C., "A dual frequency GPS receiver measuring ionospheric effects without code demodulation and its application to time comparison", Proc. of 20th PTTI meeting, 1988.
2. Kloubucher J.A., "Ionospheric Correction for the Single Frequency User of the Global Positioning System", IEEE Trans. on NTS, 1982.
3. Allan D.W. and Weiss M.A., "Accurate time and frequency transfer duaring common view of GPS satellite", Proc. of 34th AFCS, 1980.
4. Amagai J., Kiuchi H., and Kawaguchi N., "Short Baseline Experiments Using Highly Transportable VLBI station", IEEE Trans. on IM, April 1989.



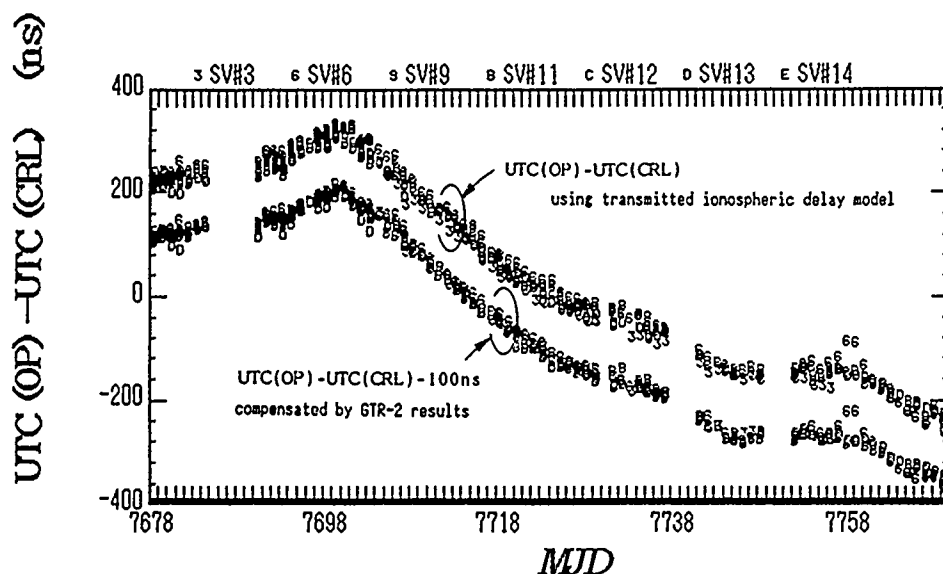
*Measurement Results of TEC by GTR-2
(July 1989 measured from CRL)*

Figure 1



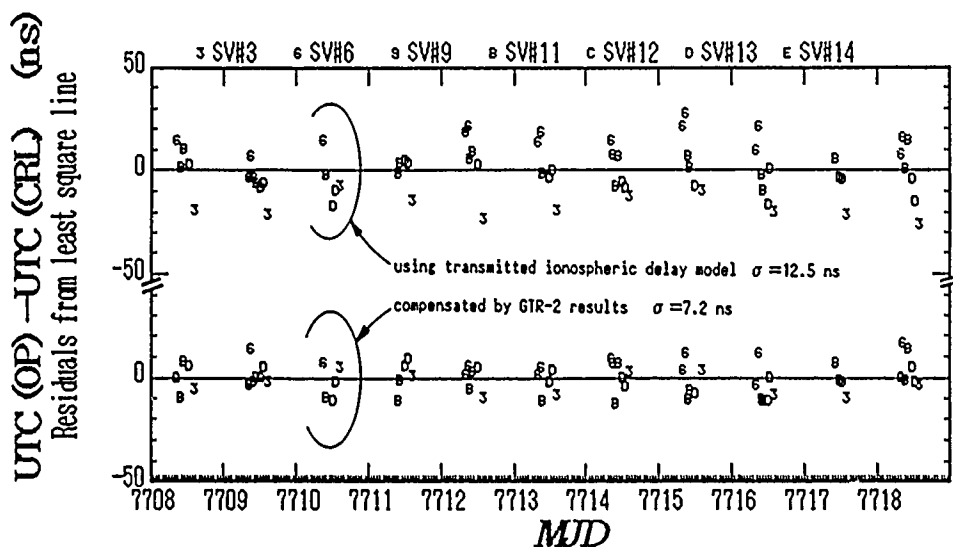
Application to Time Transfer

Figure 2



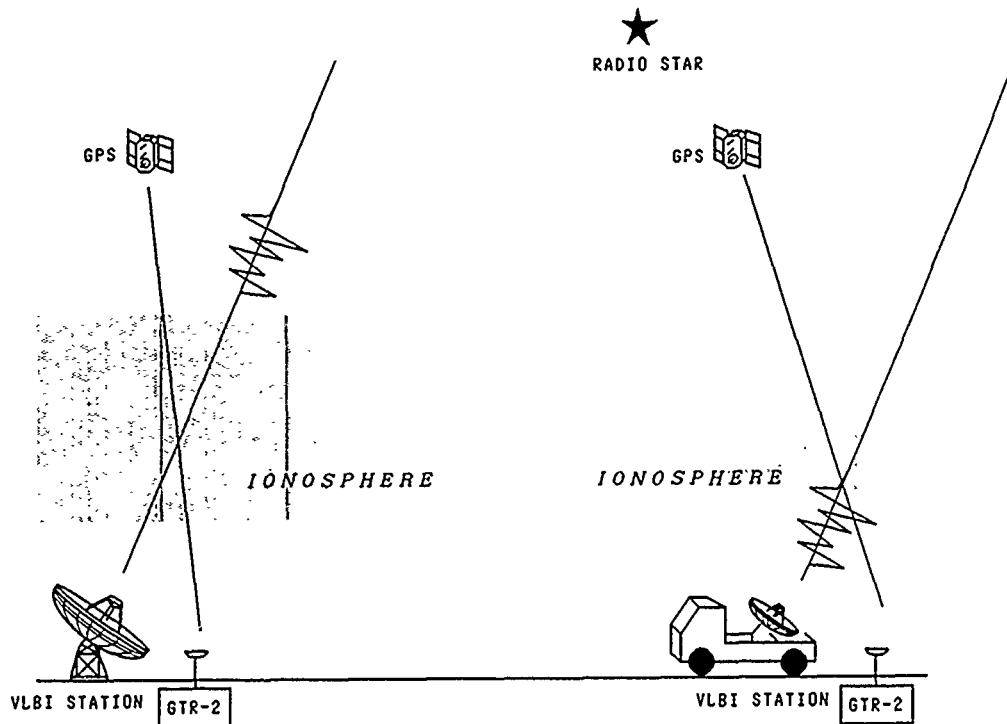
*Application results of measured TEC
to the time comparison results between OP and CRL
(June-August, 1989)*

Figure 3



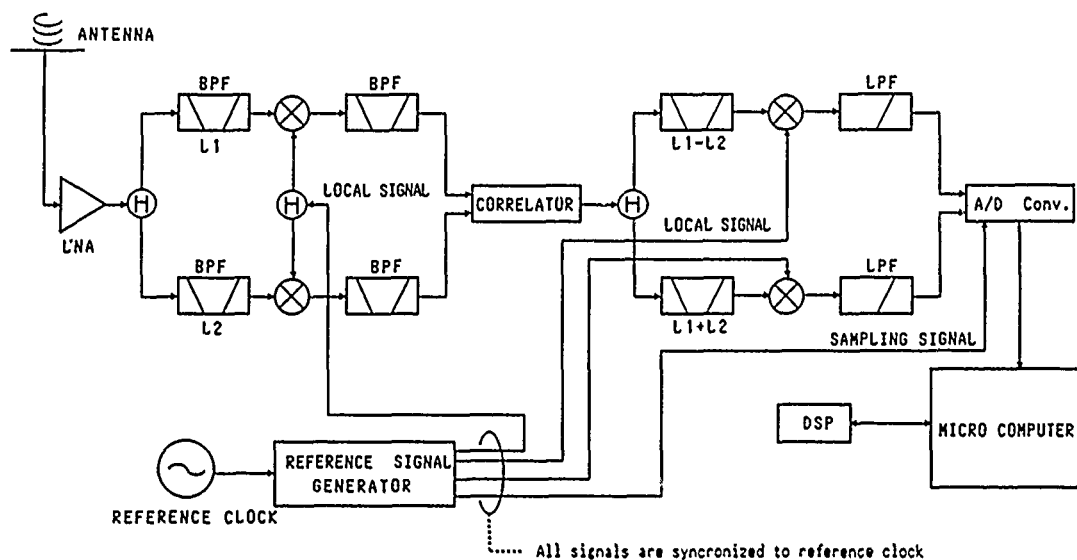
*Application results of measured TEC
to the time comparison results between OP and CRL
(July 1st ~ July 11, 1989)*

Figure 4



Application to single frequency VLBI observation

Figure 5



Block diagram of high-precision TEC reciever plan (GTR-3) (using reconstructed continuous signal phases by cross-correlation)

Figure 6

ALTERNATIVE TIMING NETWORKS WITH GPS

G.P. Landis, S. Stebbins, and R.L. Beard

Naval Research Laboratory

Washington, D.C.

and

H.F. Fliegel

The Aerospace Corporation

El Segundo, California

Abstract

An approach to determining accurate time from GPS with an independent network of receiving stations has been investigated. The methods of using the Global Positioning System (GPS) for transferring time in previous work has been by the "common view" and "melting pot" methods. Both of these techniques have used simplified single frequency receivers operating on the clear/acquisition (C/A) GPS codes and assumes that the satellite transmissions are quality observables producing "GPS time", accurately traceable to UTC(USNO). In the case of "common view", the position of the satellite is assumed to be accurately known from the satellite transmissions. Then the time delays due to position at the two common view sites may be accurately measured for time comparisons. In the "melting pot" method, an individual site measures "GPS Time" as determined from observing all GPS satellites in view resulting in an accurate over-solution of the GPS system time. The satellite broadcasts then provide the UTC - GPS time correction. The investigation into an independent network was performed on the basis of using the simplified C/A receiving equipment to produce accurate timing information regardless of the GPS broadcast information accuracy. The technique can be used to improve the inherent capabilities of these single frequency receivers or maintain accuracy with degraded GPS signals. The similarities with geodetic positioning using GPS will be described. A proof-of-concept experiment will be discussed and data presented to verify the technique.

INTRODUCTION

Two closely related techniques have been developed over the past twenty years to obtain time and/or position information from range or range-like data between ground stations and satellite positions, with no need to model the satellite orbits dynamically. The more recent is the common view technique. International synchronization of clocks in widely separated timing laboratories has been achieved using GPS space vehicles (SVs) in common view of the laboratories. Two or more stations receive almost simultaneously the same pulse from one SV. They record the times of arrival against their clocks, and correct for the differences in propagation times from the SV to the two different stations by knowing the SV position. The behavior of the SV clock is immaterial, since the data is differenced and the SV clock contribution, being the same at both sites, is eliminated. The radial distance of the SV from

the Earth's center is a common factor, and only a small component of the SV along-track and cross-track error corrupts the determination of the time offset between the two ground clocks. Common view was developed by the Time and Frequency Division of the National Bureau of Standards (NBS), now the National Institute of Standards and Technology (NIST)^[1,2]. Since 1986, the responsibility of scheduling and coordinating common view observations between international timing observatories has been assumed by the Bureau International des Poids et Mesures (BIPM) in Paris^[3].

The other, older technique for using ranging data for positioning is multilateration. A number of ground stations (M) simultaneously range to N SVs, that is, either to several SVs or to several points on the orbit of one SV. The ranges determine the coordinates of all the points, on the ground and in the sky, relative to one another. A relative reference frame is then established with the coordinates of three stations. Station 1 will be the origin of the relative coordinates and the reference planes established by the positions of the other stations used to range to six SV's. In this coordinate system the number of observations (24) will equal the number of unknowns (also 24, namely the 30 spatial coordinates of the 10 points, minus the 6 coordinates which are fixed). It has been shown in the extensive literature on multilateration^[4-9], that good solutions can be obtained for all the relative spatial coordinates, if certain singular geometric configurations of the points are avoided, e.g., in this case, if the ground stations do not lie all on one plane. Common view is a variant of multilateration, in which the spatial coordinates have been held fixed, and time coordinates are added and solved for. The theory of multilateration developed for geodesy can therefore be applied to the practical problems of time transfer.

DYNAMIC VS GEOMETRIC METHODS OF MEASUREMENT

The two basic methods of using artificial satellites for geodesy are the dynamic and the geometric. Dynamic modeling is often the more practical. A model of all the forces known to be acting on the SVs is used to develop a theory or a numerical model of their motion, and the parameters of the model are fitted to the range data. For GPS, this is done routinely by the National Geodetic Survey, the Jet Propulsion Laboratory, and the Center for Space Research of the University of Texas^[10-12]. Dynamic modeling is the method of choice when, (i) the force model is well known, or (ii) anomalous forces acting on the SVs are themselves of primary interest, and (iii) data are non-simultaneous and from widely separated locations. Conversely, geometric methods are better when (i) the force model is incomplete, (ii) improving the force model is not the task at hand, and (iii) when observations can be made simultaneously from stations of suitable number and distribution. Multilateration is the technique of measuring ranges to targets in unknown positions from several locations simultaneously. It treats every SV point location as independent of every other, uses no dynamic modeling, and therefore requires no force model or software for trajectory integration. Computer programs for multilateration tend to be very simple. Of course, hybrid dynamic/geometric systems are also used, e.g., short-arc solutions^[9].

Common view has two special advantages for international timekeeping. First, the necessary software can be kept very simple. Second, one need not handle precise ephemerides of GPS satellites which may not be readily available. A simple modification of the common view technique retains these advantages, even when the broadcast ephemeris is not sufficiently accurate to be useful. In geodesy, there are at most three unknowns per point, the three space coordinates. Using GPS, we have clock offsets to determine, so the number of unknowns increases from three to four. Nevertheless, using enough stations, solutions can always be found for all the unknowns. The basic reason could be called

"the fundamental theorem of multilateration". Given any values of A (station unknowns), B (SV point unknowns), and C (unknowns defined as reference knowns), there always exists a pair of numbers (M, N), (M stations, N SV points) such that,

$$MN \geq AM + BN - C$$

so that the number of measurements exceeds the number of unknowns. But will the normal equation matrix be well conditioned? Every application of multilateration gives rise to a particular mathematical case, which must be specially examined.

FIVE CASES OF MULTILATERATION/Common View

Designing a common view time transfer experiment addresses three questions:

1. Do we solve for time offsets only, or also correct SV and/or station coordinates?
2. If we solve for spatial coordinates, then do we correct SV coordinates only, or station locations as well?
3. Do we solve for three dimensions, or only for two?

For, if all stations are in a common plane and an SV passes nearly through that plane, good solutions can be obtained by estimating only two spatial coordinates of each point^[13-14].

Logically, these three questions give rise to five possible cases. For each case, there is a minimum number of stations and SVs which will give a solution.

CASE A: Stations in known locations measure pseudo-ranges to SVs in known locations and estimate time offsets only.

This is the classical common view case. Take station 1 as the reference station, whose time is known by definition. The remaining M-1 stations contribute M-1 unknowns, their clock offsets at the moment of measurement. Each SV contributes one unknown, its clock offset from station 1. Two stations ranging to one SV are sufficient.

CASE B: Stations in known locations measure pseudo-ranges to SVs in poorly known positions. Corrections to SV coordinates (X, Y, and Z) must be estimated as well as all time offsets relative to station 1. Five stations ranging to four SV points suffice. There are 20 unknowns (4 station clocks relative to station 1, 4 SV clocks, and 12 SV coordinates) and 20 measurements.

CASE C: Stations in poorly known locations measure pseudo-ranges to SVs in poorly known positions. Corrections to the coordinates (x, y, and z) of all stations and SV points must be determined in the reference frame of the first three stations, as well as all clock offsets relative to Station 1. Five stations ranging to thirteen SV points suffice. There are 65 unknowns (9 station coordinates, 4 station clocks relative to station 1, 13 SV clocks, and 39 SV coordinates of position) and 65 measurements. Six stations ranging to nine SV points also suffice.

CASE D: Nearly co-planar stations, that is, stations nearly on a great circle on the surface of the Earth, in known locations measure pseudo-ranges to an SV passing through the plane and correct the

along-track and radial components of SV positions. Four stations ranging to three SV points suffice. There are 12 unknowns (3 station clocks relative to station 1, 3 SV clocks and 6 SV coordinates) and 12 measurements.

CASE E: Nearly co-planar stations in poorly known locations measure pseudo-range to an SV passing through the plane, and estimate time offsets and all relevant coordinates. Four stations ranging to eight SV points suffice. There are 32 unknowns (5 station coordinates, 3 station clocks relative to station 1, 8 SV clocks, and 16 SV coordinates of position) and 32 measurements. Five stations ranging to six SV points also suffice.

The cases above are based on a minimum number of measurements. Taking additional points from the SVs as individual measurements increases the data from a clock comparison point of view but also increases the number of unknowns. The minimum number of measurements for each case to provide a solution is given by the geometric arrangement of the stations in accordance with the formulas in Table 1.

Table 1. Case Definitions
(M = stations, N = SV points)

Case A	$M + N - 1$
B	$M + 4N - 1$
C	$4M + 4N - 7$
D	$M + 3N - 1$
E	$3M + 3N - 4$

Numerical simulations seem to show that the accuracy with which the ground clock time offsets are determined increases roughly with the square root of N, even though the accuracy of the SV coordinate corrections may remain small. The reason is probably that those time offsets are common to the whole solution, and so the accuracy with which they are determined increases steadily with N, whereas each SV point is independent of every other in multilateration, and increasing N cannot increase the accuracy of any particular point. To increase accuracy of the SV points they would need to be connected dynamically, which would introduce the complexity we are attempting to avoid, determination of highly precise GPS orbits. To accomplish synchronization of ground clocks, the accuracy of simple correction of independent clock SV points appears adequate.

However, it is not enough to count unknown quantities. The configuration of the ground stations is critical to this geometric approach to avoid what Killian and Meissl called "gefährlichen Oerter" [5], "dangerous regions" or "critical configurations" [6]. Geometrical arrangements of stations and/or SV points for which the solution matrix is singular and no unique solution for coordinates can be obtained.

Using GPS, we measure pseudo-range which includes a time offset error (t). If $t[r]$ is the offset of the station i clock with respect to some reference standard, T is the offset of SV number j with respect to the same standard and c is the speed of light, then we measure t where

$$t(ij) = t[r](i) + T(j) - R(ij)/c$$

The general form of the differential equation for the corrections to all these quantities is therefore,

$$dt(ij) = dt[r](i) + dT(j) - (1/cR(ij))[(X(j) - x(i))(dX(j) - dx(i)) \dots$$

In our Case C, in which one solves for corrections to clocks and to both station and SV coordinates, the above is the observational equation. In the other cases, one or more of the terms in the unknowns dx , dy , dz , and/or dX , dY , dZ , are omitted. To anchor the coordinate frame, however, one must impose reference conditions. Set $dt[r](1) = 0$, and $dx(1)$, $dy(1)$, $dz(1)$, $dy(2)$, $dz(2)$, and $dz(3) = 0$. This establishes the station 1 clock as the reference clock, and fixes the coordinate system.

In Case A, all the space coordinate terms are omitted, and the solution is always straightforward. In Case B the normal equations will contain terms linear in time and linear in space coordinates. Generally speaking, the case will be singular only if all stations lie in a straight line, a circumstance easy to avoid. However, our Case C falls under all the restrictions discussed by George Blaha^[6]. In Case C, the normal matrix contains parallel columns of quadratic terms in the space coordinates. No solution can be obtained for both station and SV coordinates if all stations lie on a second-degree plane curve (e.g., an ellipse), or if all stations and SV points lie on a second-degree surface (e.g., an ellipsoid). That implies that the five stations cannot lie all in one plane, because fewer than six points on a plane can always be fitted by a second-degree plane curve. Therefore, Case C requires either that the five stations be spread over an area large compared to the Earth's radius, or that we use at least six stations. Likewise, the stations must not lie on two intersecting straight lines which would be the asymptotes of a family of hyperbolas. Case E (the co-planar case, adjusting stations and SV points) is subject to a similar but less troublesome restriction. All points, ground and sky, must not lie on a second-degree curve, but they seldom will. Case D (adjusting stations only) presents no singularities apt to arise in actual practice.

SIMULATING REALISTIC TIME TRANSFER EXPERIMENTS

In practice, GPS pseudo-range measurements cannot be made in an instant of time. Each measurement is an integration over a short time interval. Then will it be necessary to estimate corrections to SV velocity as well as range? Over short observing times such as those now used in common view comparisons (90 to 790 seconds), the SV positional correction could act as a mean correction to the X, Y, and Z coordinates of the SV over that time interval. Estimation of the time comparison errors involved with varying error contributions, such as velocity, will need further simulation.

The simulations discussed here are preliminary results of investigating the technique. They will ultimately be used to design an experiment to compare actual results with other time transfer techniques. The receiver locations were restricted to the continental United States and, for the most part, represent receivers at precisely known locations. Five stations were assumed to be located at Seattle, Washington (1), Los Angeles, California (2), the Naval Observatory (3), Colorado Springs (4), and Richmond, Florida (5).

For the simulation, the Block I GPS constellation on day 120 (30 April) 1989 was chosen for the SV points, since the precise trajectory data was available for NAVSTARs 3, 6, 8, 9, 10, and 11. The data selection was restricted to the times when four or more satellites were in simultaneous view at all receiver sites. Figures 1 and 2 depict the SV points at 02:45 and 05:15. These are the times of the best and worst solution results from the cases examined. The dashed lines represent the limits of coverage using a 10 degree elevation mask angle for the stations shown. The solid lines are the satellite ground tracks and the symbols represent the SVs at the specified times.

DATA GENERATION

Two methods of data processing were used. Method one made independent time transfer calculations for Case A and Case B every fifteen minutes. Method two made a single time transfer calculation based on eleven time samples of data taken every fifteen minutes. Earlier simulation results using method one are discussed in Reference 15. The uncertainties associated with the different measurements were generated with random noise. The statistics on each were set independently and the range of values is shown in Table 2. The selection of a one-meter sigma for the range measurement is based on the typical values observed in the operation of timing receivers. The values for SV point uncertainties ranged from 1.0 meters for precision SV points to 100,000 meters, five times the value of five-week-old almanac data. Station position may be known to 0.1 meters but 100 meters is used as a reasonably high limit. These noise uncertainties were considered to be spherical values. The time offsets and clock errors were not critical to this simulation, therefore the uncertainties were fixed at the equivalent of 10,000 meters. For simplicity in the simulation the calculations were performed in meters, and at least 10 trials were run to generate more information on performance. New values for the random terms were used for each trial. Method two was necessary for Case C to give a sufficient number of SV points, and the data was used to compute solutions for Case A and B for comparison.

Table 2. Measurement Uncertainties
1 sigma Values (meters)

A(SV,S)	Both considered known
B(SV)	1.5, 10, 10^3 , 10^4 , 10^5

Table 3 is a comparison of Cases A, B and C using Method Two. Case A calculations were done for two receiver position uncertainties and two SV point uncertainties. Case B calculations were on done for two receiver position uncertainties because Case B results are independent of SV point uncertainties. Case C calculations are independent of both uncertainties.

The multilateration method can improve the results of time transfer. In the case of a minimum amount of data, 4 satellites for Case B or 13 SV points for Case C, improvement is found only when there is a large uncertainty on the positions. With a larger data base, greater than 60 sky points, improvements were obtained even when position errors were in the order of a 100 meters for either the SV point or receiver.

With Method Two there is a significant increase in the number of unknowns. In Method One the number of unknowns for Case B with 5 receivers and 5 SV points was 24, but with Method Two and 62 SV points the number of unknowns increase to 252 for Case B, and 261 for Case C. For the same number of SV points and five receivers Case C requires only nine more unknowns.

FUTURE WORK

An experiment will be designed using the stations simulated in this study. A new refined simulation that is optimized and accounts for propagation and other effects will be used to guide the experiment. Work on the data generation algorithm will include ionosphere, troposphere, receiver clock frequency offsets and aging, position bias and velocity terms. In the present approach, no solution constraints

TABLE 3. Method Two Simulation Results
(Uncertainties in Meters)

CASE	A	A	A	B	B	C
Station Position	1	1	100	1	100	1000
SV Position	10	100	100	10000	10000	10000
Unknowns	66	66	66	252	252	261
Station Pairs						
1-2	0.35	0.46	31.70	2.37	195.66	9.14
1-3	0.32	0.68	26.48	2.20	217.77	11.49
1-4	0.24	0.40	24.14	1.69	123.06	10.59
1-5	0.39	0.78	33.24	3.11	262.39	13.80
2-3	0.40	0.60	40.43	2.69	292.74	12.63
2-4	0.31	0.33	28.69	1.14	116.59	3.67
2-5	0.39	0.57	39.86	2.01	215.12	10.76
3-4	0.41	0.53	41.88	1.64	182.12	10.86
3-5	0.20	0.31	20.00	1.72	158.80	5.92
4-5	0.44	0.58	44.49	1.62	154.49	8.44
Ranging Noise	1 meter					
Station Clock Uncertainty	10000 meters					
SV Clock Uncertainty	10000 meters					
Start/Stop Time of Day	1:45 / 5:15 GMT					
Stations = 5	SV Positions = 62					

have been placed on the uncertainty in position of the satellites or receivers. Statistical knowledge of these uncertainties should be included in the processing. Additional terms for the receiver clock frequency offset and aging may be appropriate if satellite motion is significant.

An international experiment will also be examined. The simplest is one which requires the fewest stations and where the stations lie nearly in the orbital plane of a GPS satellite (Cases D and E).

REFERENCES

1. D. W. Allan and M. A. Weiss, "Accurate Time and Frequency Transfer During Common View of a GPS Satellite", Proceedings of the 34th Annual Symposium on Frequency Control, pp334-346 [1980]
2. M. A. Weiss and D. W. Allan, "An NBS Calibration Procedure For Providing Time and Frequency at a Remote Site By Weighting and Smoothing of GPS Common View Data", IEEE

3. B. Guinot and W. Lewandowski, "Use of the GPS Time Transfer at the Bureau International des Poids et Mesures (BIPM)", Proceedings of the Nineteenth Annual Precise Time and Time Interval (PTTI) Applications and Planning Meeting, pp 3-12, [December 1987]
4. K. Rinner, Systematic Investigations of Geodetic Networks In Space, Report of the US Army Research and Development Group, Munich, Germany, 1966
5. Karl Killian and Peter Meissl, "Einige Grundaufgaben der Raeumlichen Trilateration und Ihre Gefaehrlichen Oerter", in Beitrage zur Theorie der Geodaetischen Netze im Raum, Deutsche Geodaetische Kommission, Reihe A, 61 [1969].
6. G. Blaha, "Investigations of Critical Configurations For Fundamental Range Networks", Report No. 150 of the Department of Geodetic Science, The Ohio State University, Columbus, Ohio [1971], NTIS N71 - 33310, NASA CR 121 - 445
7. E. Tsimis, "Critical Configurations (Determinantal Loci) for Range and Range Difference Satellite Networks", Report No. 191 of the Department of Geodetic Science, The Ohio State University, Columbus, Ohio [1973]
8. E. Grafarend and K. Heinz, "Rank Defect Analysis of Satellite Geodetic Networks (I) — Geometric and Semi-Dynamic Mode", Manuscripta Geodaetica, 3, no. 2/3, pp 107-134 [1974]
9. E. C. Pavlis, "On the Geodetic Applications of Simultaneous Range Differencing to LAGEOS", Report No. 338 of the Department of Geodetic Science, The Ohio State University, Columbus, Ohio [1982]
10. CSTG (International Coordination of Space Techniques for Geodesy and Geodynamics), GPS Bulletin, Vol. 2, No. 1, published by the National Geodetic Survey, Jan-Feb 1989
11. S. M. Lichten and J. S. Border, "Strategies for High-Precision Global Positioning System Orbit Determination", Journal of Geophysical Research, vol 92, no. B12, pp 12751-12762 [1987]
12. B.E. Schutz, B.D. Tapley, C.S. Ho, H.J. Rim, and P.A.M. Abusali, "GPS Orbit Determination: Experiments and Results", Proceedings of the Fifth International Geodetic Symposium on Satellite Positioning, Las Cruces, New Mexico, March 1989, Vol. 1, pp. 201-209 [1989]
13. P. R. Escobal, et al, "3-D Multilateration: A Precision Geodetic Measurement System", Technical Memorandum 33-605, Jet Propulsion Laboratory, Pasadena, Calif., Section XIII [1973]
14. H. F. Fliegel, M. Gantsweg, P. S. Callahan, "LIBRA: An Inexpensive Network Densification System", Technical Memorandum 33-725, Jet Propulsion Laboratory, Pasadena, Calif., pp52-54 [1975] NTIS N75- 31179
15. H.F. Fliegel, R.L. Beard, G.P. Landis, and S.B. Stebbins, "An Alternative Common View Method For Time Transfer With GPS", ION GPS-89 The Institute of Navigation Satellite Division Second International Technical Meeting Colorado Springs, 25-29 September 1989

Figure 1, GPS Coverage, Time = 02:45

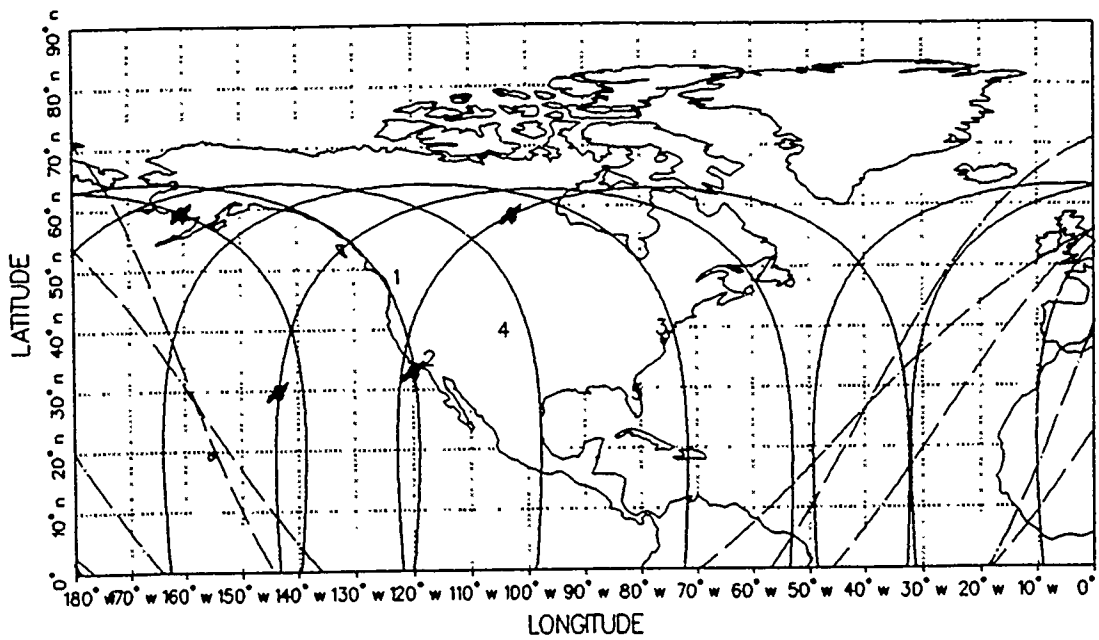
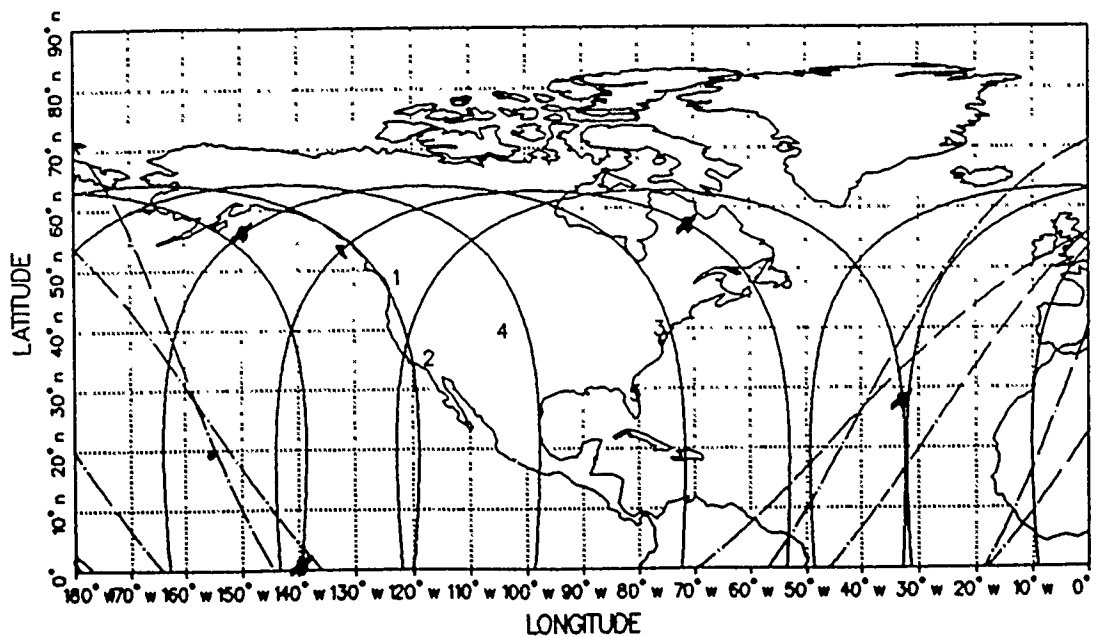


Figure 2, GPS Coverage, Time = 05:15



A COMPARISON OF TIME TRANSFER TECHNIQUES

S. Stebbins, A. Gifford, and R. L. Beard
Naval Research Laboratory
4555 Overlook Avenue
Washington, DC 20375-5000

Abstract

In the development of timing systems for the Global Positioning System (GPS), a clock ensemble has been installed at the Master Control Station for GPS at Falcon Air Force Station, Colorado Springs, Colorado. A single-frequency, Clear/Acquisition (C/A) GPS receiver is integrated into that system to perform time comparisons with the U. S. Naval Observatory (USNO). Having data from these two sites provided an opportunity to compare different techniques for time transfer and to examine their relative merits and performance. Three basic techniques were examined: common-view, melting-pot, and non-simultaneous common-view. The results and a comparison of the different techniques will be presented.

INTRODUCTION

The NAVSTAR Global Positioning System (GPS), currently being deployed for operational use, is to provide accurate positioning capability for the Department of Defense and civilian use. One aspect of the system is its ability to disseminate accurate time for military and scientific users. The NAVSTAR developmental satellites, commonly known as Block I satellites, are being used for time comparisons between timing centers and other groups interested in maintaining very accurate time synchronization. The methods used to gather the data and perform time comparison have evolved into two basic types, the first typified by the user being passive, using only the information transmitted by the satellites, and the second being an active user. The active user incorporates data gathered at other sites communicated separately, or other external data, such as independent knowledge of accurate position. These two user types are the foundation for these two widely used methods of time transfer, known as the "Common View" and the "Melting Pot" techniques.

TIME TRANSFER TECHNIQUES

The basis for time transfer is the same as for navigation with GPS, that is, pseudo-ranging to the satellites. The pseudo-ranges are essentially time comparisons between the satellite clock and the clock in the receiver on the ground. The pseudo-ranging errors are either minimized through the data collection technique or through the system design features for satellite position, ionospheric and tropospheric delays and other contributing error sources. Experiments with GPS to determine absolute

range accuracy from a single pseudo-range measurement, using the single frequency clear/acquisition signal have resulted in approximately a 15 meter uncertainty, including all system error sources. The overall behavior of the system, however, shows very consistent long term behavior resulting in quite repeatable measurements. Each of the different techniques takes advantages of the repeatability of the measurements to compare clocks.

The Common View technique, developed by the National Institute of Science and Technology^[1,2] (NIST) involves two or more ground stations simultaneously observing a single GPS satellite and compiling the observed data at a central point or interchanging the data for the final time transfer determination. This technique is similar to interferometric observation of a single source by widely separated observers. By knowing the positions of the satellite from the broadcast message, and positions of the ground stations, from prior data or independent survey, the times-of-arrival of the satellite signals can be corrected for the transmission travel times and the two clock measurements differenced for the time transfer value. This technique attempts to eliminate the effect of the satellite clocks so that a direct comparison between the two remote clocks can be made.

Another method, the melting-pot technique, is currently in use by the U.S. Naval Observatory (USNO)^[3]. In this technique, observations recorded from all satellite passes during a two-day period are combined to produce one time transfer value at the midpoint. The set of one-point-per-day data is then used to estimate the ground station time difference. This technique solves for an estimate of GPS Time, the GPS internal time reference, for each site taking observations. Another site can then difference its estimate of GPS Time, over a simultaneous observation time span, with that at USNO resulting in a time transfer between the two sites. For sites observing at non-simultaneous times, an estimate of GPS Time can be used to connect the two sites. This technique is also used to monitor GPS Time relative to UTC(USNO) as the mechanism for providing correction terms for the GPS broadcast message.

A third method under investigation is a non-simultaneous common view approach, by which a curve fit is made to the recorded data at each station for each satellite pass. Time transfer values are then calculated from data values estimated at selected regular times on the two curves. These time transfer values for all satellite passes can then be combined to estimate the clock difference for a specified time period.

DATA COLLECTION

The data used for analysis was collected from Day 86 (27 March) to Day 170 (19 June), 1989 at USNO and the Consolidated Space Operations Center (CSOC), Colorado Springs. The receivers employed were single frequency C/A and produced a corrected and smoothed pseudo-range value every 13 minutes. The largest source of error was expected to be from ionospheric correction since the broadcast correction model was used. These data from both CSOC and USNO have been referenced to GPS time ((CSOC - GPS) and (USNO - GPS)). Data was analyzed from all GPS satellites active during the time period: NAVSTAR's 3, 6, 8, 9, 10, and 11. A total of 4,199 points from USNO and 5,050 points from CSOC were used in the melting-pot approach, and 1,347 points were matched and used in the common view technique.

GPS systematic noise can introduce large biases in both USNO and CSOC data. Figures 1 through 3 show the biases on the data obtained via NAVSTAR 11 from USNO and CSOC, and on the resulting common view time transfer (USNO - CSOC) for an eight-day time span. Table 1 contains the

statistics of the curve fits to these data sets.

Table 1. Statistics of Curve Fits for Eight-Day Data Sets

Day 148 Calculated Clock Difference (Microseconds)	Frequency (pp10 ⁻¹³)	Aging (pp10 ⁻¹⁴)	RMS (ns)	No. Points Used	
Fig 1.	-0.144	0.18	-1.2	8	58
Fig 2.	-2.544	-0.58	-1.1	15	155
(1-2)	2.400	—	—	—	—
Fig 3.	2.389	0.73	-0.5	11	56

ANALYSIS

Exactly simultaneous observations were not necessarily available for this study; therefore, a five-minute tolerance was used to select "matched" observations for the common view method. A time transfer value was calculated for each match in the 83-day span, for each satellite. A second-degree curve was fit to the set of time transfer values of each satellite, and a single value was estimated at the midpoint of the time span, Day 128. In addition, a second-degree curve fit was performed on the composite set of all satellite matches, and a single time transfer was calculated for Day 128.

Figures 4 and 5 represent partial sets of data (USNO - GPS Time), and (CSOC - GPS Time) used for the melting pot method before correlating for common view. Figure 6 presents all the common view time transfer values, (USNO - CSOC), for matched observations from the entire data set. Table 2 contains the statistics of the curve fits to these data sets.

Table 2. Statistics of Second Degree Fits to 83-Day Data Sets

Day 128 Calculated Clock Difference (Microseconds)	Frequency (pp10 ¹³)	Aging (pp10 ¹⁴)	RMS (ns)	No. Points Used	
Fig 4.	-0.186	0.08	0.0	21	4149
Fig 5.	-2.449	-0.79	0.1	29	5040
(4-5)	2.263	—	—	--	—
Fig 6.	2.254	0.88	0.0	20	1347
Fig 7.	2.265	0.87	0.0	10	76 *

* First degree curves were fit to each of the two-day data sets to produce the 76 points used here.

For the time transfer calculations using the melting pot technique, a curve was fit to the two-day span of data centered on each day in the 83-day set for each station. Due to the data spread, a first-degree fit produced a more consistent calculation of the daily points. The daily points were differenced to produce daily time transfer values as shown in Figure 7. A second-degree curve was fit to the set of daily values to estimate the time transfer for Day 128, shown in Table 2.

CONCLUSIONS

The common view technique, using simultaneous observations, accurate satellite positions, and common receiver algorithms, provides time transfer values almost independent of the system and very stable day-to-day results. However, an estimated time transfer for a time span is only a function of a subset of the entire data base — the “matched” times. Communication of the gathered data determines the frequency of performing the time transfers, and can be done on demand as needed.

The melting pot technique uses all available data to estimate GPS Time as a basis for transferring time. The use of all the data should provide a more robust estimation of the state of the system. Since this technique actually correlates GPS Time to UTC(USNO), it provides a more general database for transferring time, rather than minimizing or eliminating the system from the time comparisons. It can also be used without a large transfer of data between sites, and by those who may have limited or no common observation times.

A comparison of the results of the two methods is shown in Table 2. The common view method produced a time transfer value of 2.254 microseconds with a 20 ns RMS, and the melting pot 2.265 microseconds with a 10 ns RMS. These values are roughly comparable although the melting pot solution should merit a higher confidence.

REFERENCES

1. D. W. Allan and M. A. Weiss, “Accurate Time and Frequency Transfer During Common View of a GPS Satellite”, Proceedings of the 34th Annual Symposium on Frequency Control, pp334-346 [1980]
2. M. A. Weiss and D. W. Allan, “An NBS Calibration Procedure For Providing Time and Frequency at a Remote Site By Weighting and Smoothing of GPS Common View Data”, IEEE Transactions on Instrumentation and Measurement, vol. 36, no. 2, pp571-578 [June 1987]
3. G.M.R. Winkler, private communication.

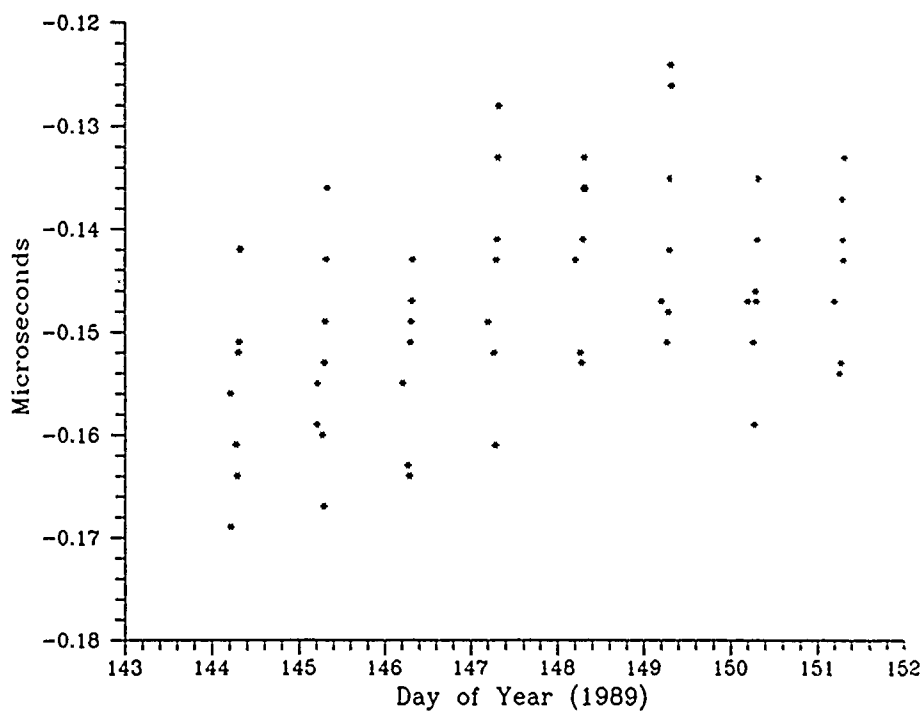
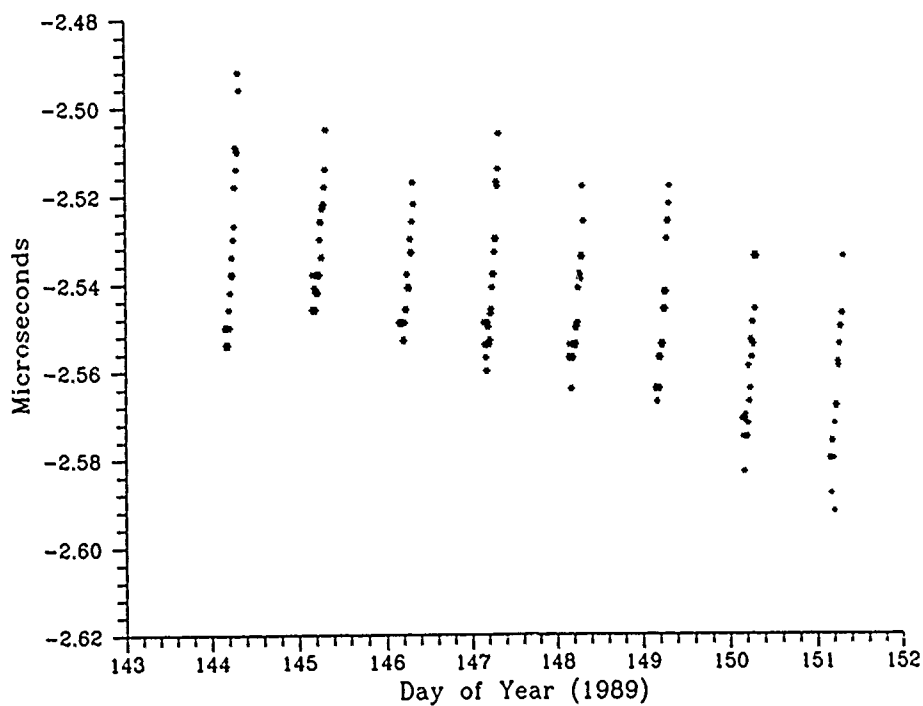


Figure 1. Clock Difference (USNO - NAVSTAR 11)



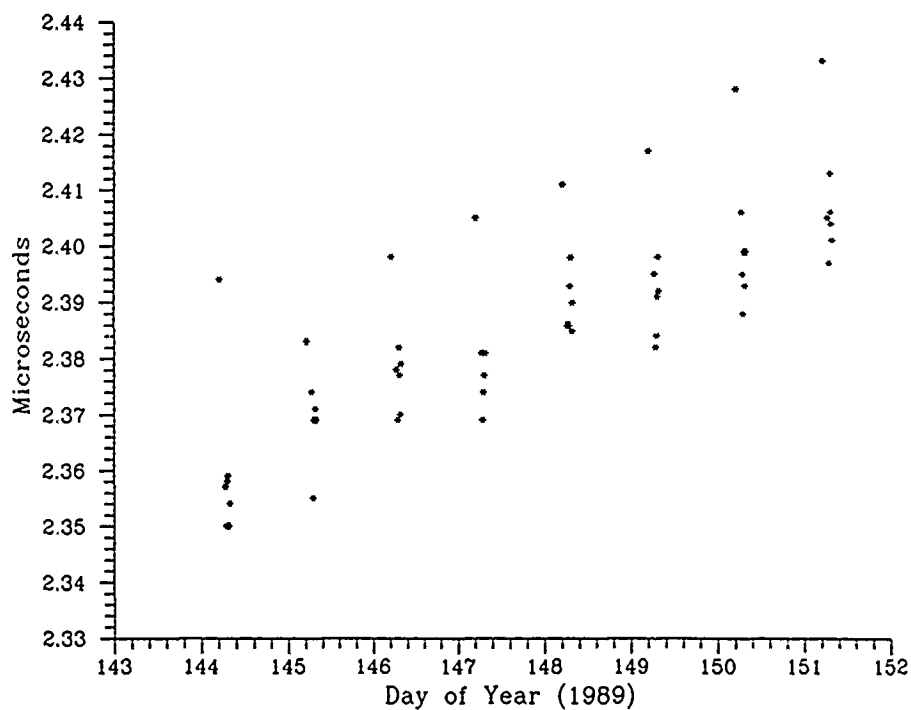


Figure 3. Common View via NAVSTAR 11 (USNO - CSOC)

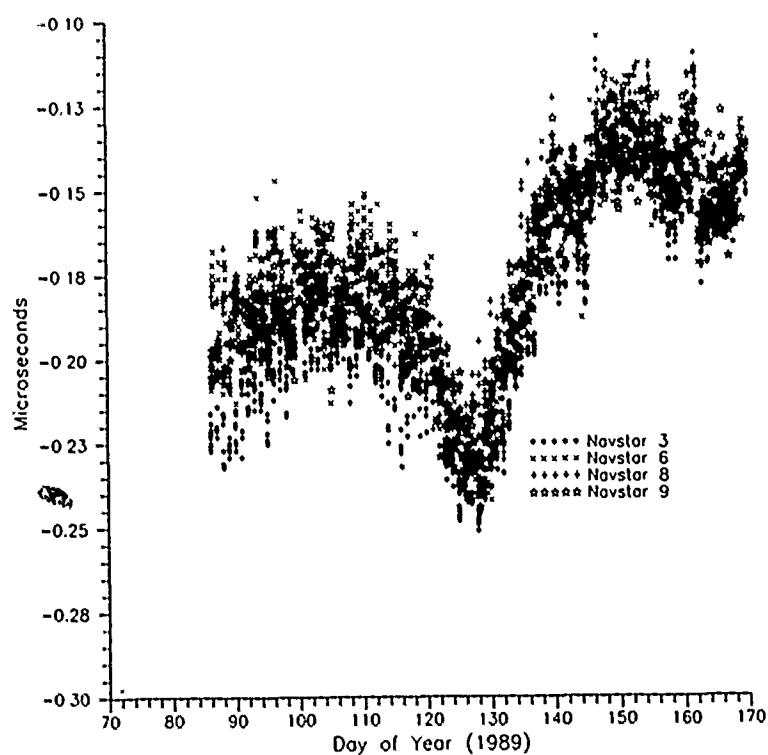


Figure 4 Clock Difference (USNO-GPS Time)

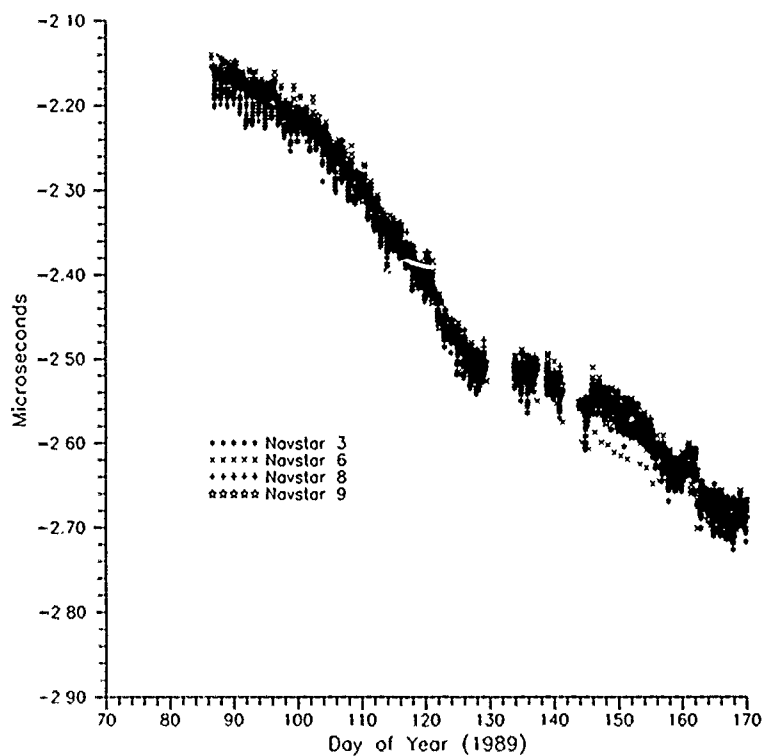


Figure 5 Clock Difference (CSOC-GPS Time)

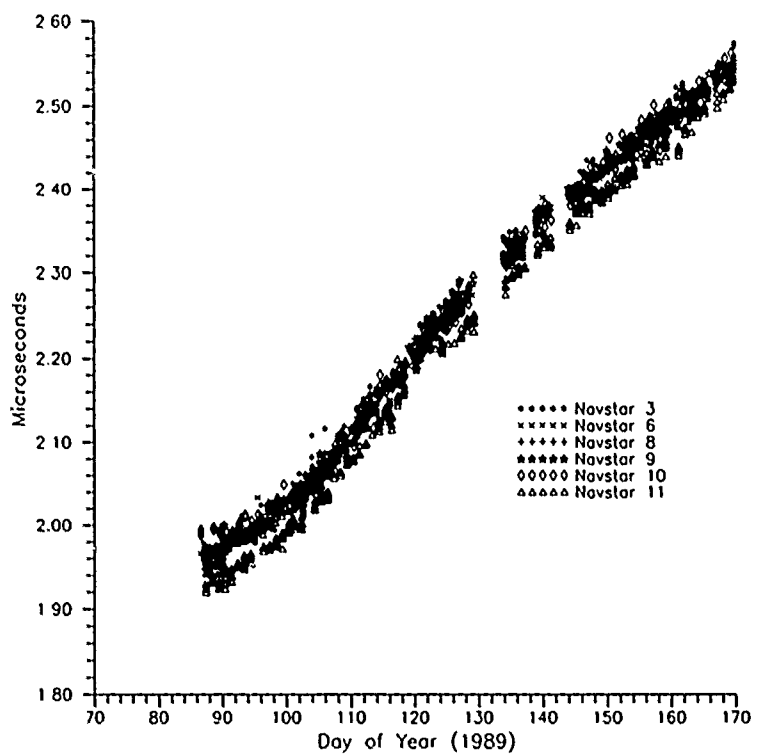


Figure 6 Common View via All NAVSTARS (USNO-CSOC)

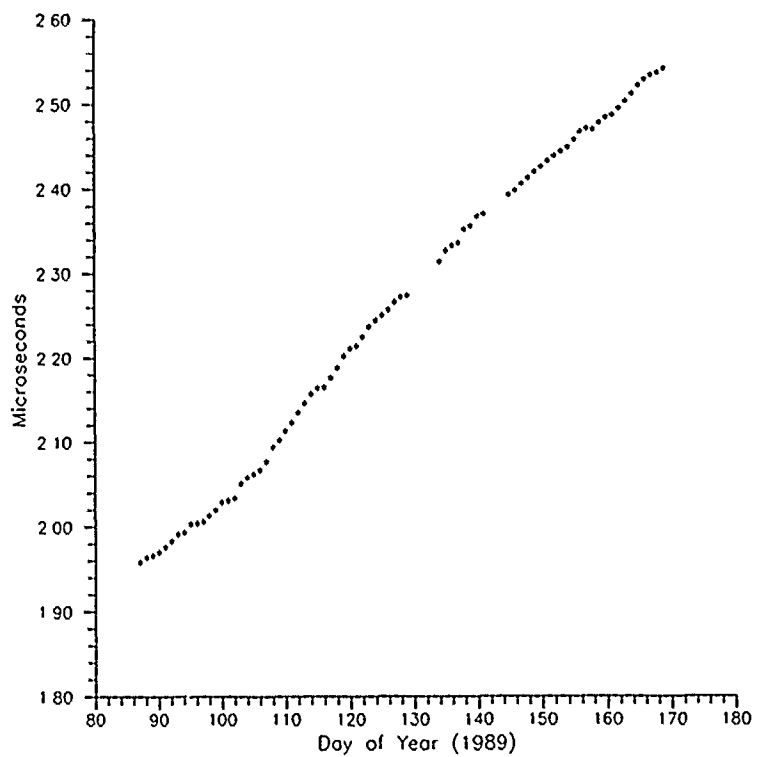


Figure 7 Melting Pot Time Transfer (USNO-CSOC)

ATOMIC VELOCITY DISTRIBUTIONS OUT OF HYDROGEN MASER DISSOCIATORS

Bernardo Jaduszliwer and Yat C. Chan
Chemistry and Physics Laboratory
The Aerospace Corporation
P.O. Box 92957, Los Angeles, CA 90009

Abstract

We have determined velocity distributions of atoms effusing out of RF discharge hydrogen dissociators, of the type used in hydrogen masers. This work was motivated by long-term reliability issues related to the possible use of masers as frequency standards on board satellites. Chief amongst these issues is the maser's hydrogen budget, since many of the common failure modes of a maser involve either the hydrogen source or sink. Since the focussing properties of the state-selecting magnets are velocity-dependent, the overall hydrogen budget will depend not only on the dissociation efficiency, but also the velocity distribution of the hydrogen atoms leaving the dissociator. Many times, that distribution has been tacitly assumed to be Maxwellian at wall temperature, but that assumption is not necessarily valid. Our measurements show the distributions to be much narrower than Maxwellian, and to broaden as the hydrogen pressure in the dissociator increases. Operating the dissociator to yield a relatively narrow velocity distribution and using a state-selecting magnet well matched to that distribution may significantly improve the efficiency of hydrogen use by the maser.

INTRODUCTION

The use of hydrogen masers as frequency standards on board spacecraft requires careful consideration of long-term reliability issues. Chief amongst them is the maser's hydrogen budget, since many of the common failure modes of a hydrogen maser involve either the hydrogen source (storage or dissociator) or sink (ion pump or getters). An excess of hydrogen atoms in the $F = 1$, $M = 0$ state must be continuously fed into the maser bulb. The ratio of the rates at which atoms in the proper hyperfine state enter the bulb and molecules are fed into the dissociator will impact strongly the maser's long-term reliability. This ratio will be determined mainly by the dissociator's efficiency and the properties of the state-selecting magnet. Atomic state-selection is performed in hydrogen masers by a quadrupole or hexapole magnet which focuses atoms in the $F = 1$, $M = 0$ state at the bulb's entrance orifice, and defocuses the $F = 0$, $M = 0$ ones. The focal length of those magnets depends strongly on atomic speed, and typically only a narrow range of atomic velocities will be focussed. Clearly, dissociators yielding narrower velocity distributions could make more efficient use of the hydrogen supply.

Relatively little is known of the velocity distribution of atoms effusing out of RF discharge hydrogen dissociators. In many cases the tacit assumption is made that the atoms will be in thermal equilibrium with the dissociator wall, but that is not necessarily the case. The threshold for molecular dissociation by collisions with discharge electrons is about 8.5 eV; since the molecular binding energy

is approximately 4.7 eV, each atom carries away an excess energy of about 2 eV^[1]. Depending on dissociator geometry and gas density, the hydrogen atoms may, or may not, undergo enough gas and wall collisions to thermalize fully. Walraven and Silvera^[2] have studied the characteristics of a beam of hydrogen atoms produced in a microwave discharge followed by a thermal accommodator and found the velocity distributions to be Maxwellian at the accommodator temperature. Hershcovitch et al.^[3] studied a similar dissociator-and-accommodator combination, operated at higher pressures and flow rates, and measured velocity distributions in reasonable agreement with the calculated supersonic-flow ones. Since thermal accommodators are not commonly used in maser dissociators, these results are not directly applicable to our problem. Miller^[4] investigated a helium-cooled microwave discharge dissociator at relatively high pressure (3.3 Torr) and measured a velocity distribution which was slightly narrower than the Maxwellian at the estimated discharge temperature. We are studying the velocity distributions of atomic hydrogen produced in an RF discharge dissociator having a geometry and operating parameters resembling those of a maser dissociator. This paper discusses the experimental technique and presents our preliminary results.

EXPERIMENTAL APPARATUS

Atomic hydrogen velocity distributions have been determined using a magnetic deflection technique. Figure 1 shows the experimental arrangement. Hydrogen is fed through a standard, temperature-controlled Pd-Ag alloy leak^[5] into a cylindrical double-walled Pyrex bulb, 15 cm long, 1.9 cm internal diameter and 3.8 cm outside diameter. Compressed air flows between the walls to provide cooling, and RF power is inductively coupled to the discharge through an external 25-turn coil. The hydrogen beam exits the dissociator through a 0.1 cm long, 0.025 cm wide slit, is collimated by a second slit, 0.025 cm wide, set at $d = 63.7$ cm away from the source slit, and then travels between the polepieces of an $L = 11.4$ cm long electromagnet configured in the "two-wire" geometry described by Rabi et al.^[6]. After additional travel through a $D = 71.3$ cm drift tube, the beam is detected by a quadrupole mass analyzer.

Molecular hydrogen, having no magnetic dipole moment, will travel through the magnet without deflection, but the hydrogen atoms will be deflected by the inhomogeneous magnetic field. The dissociator is attached to the rest of the apparatus by flexible vacuum bellows, and can be displaced transversally by micrometer screws; in this way, the angular distribution of atoms deflected by the field can be measured.

ATOMIC DEFLECTION IN A "TWO-WIRE" MAGNETIC FIELD

An atom having magnetic moment $\vec{\mu}$, immersed in a magnetic field \vec{H} , has an energy $E = -\vec{\mu} \cdot \vec{H}$. The force acting on the atom is $\vec{F} = \text{grad}(\vec{\mu} \cdot \vec{H}) \approx \mu_{eff} \text{grad}(H)$, where μ_{eff} is the component of the atomic magnetic moment along the field direction. In general, μ_{eff} will depend on the atomic ground state quantum numbers and the magnetic field strength. If an atom has total electron angular momentum $J = 1/2$ and nuclear spin I , both in units of $\hbar/2\pi$ then its effective magnetic moment is given by Breit-Rabi's formula^[7],

$$\mu_{eff} = \pm \frac{\epsilon + 2M/(2I + 1)}{[1 + 4M\epsilon/(2I + 1) + \epsilon^2]^{1/2}} \mu_0, \quad (1)$$

where the (+) sign corresponds to total angular momentum $F = I - 1/2$, the (-) sign to $F = I + 1/2$ and M is the total azimuthal quantum number. ϵ is proportional to the ratio of magnetic-to-hyperfine

energy, $\epsilon = g\mu_0 H/W$, where g is the Lande factor for the atom, μ_0 is the Bohr magneton and W the atomic hyperfine splitting.

Figure 2 shows the cross section of the "two-wire" magnet; 2α is the separation between the "equivalent wires"^[8]. If a narrow atomic beam enters the magnet at $X = 1 \cdot 2\alpha$ (as determined by the collimating slit) and the atomic transversal displacements within the magnet are small, then the force acting on the atoms remains approximately constant^[9], and so does the acceleration:

$$a \approx \frac{0.984}{\alpha} \frac{\mu_{eff}}{m} H \hat{i}, \quad (2)$$

where H is the magnetic field intensity at the atomic beam, m is the atomic mass and \hat{i} a unit vector pointing along the x -axis. Under these conditions, the trajectory equations for the atoms traveling from source to detector can be solved easily. With no magnetic field, an atom of magnetic moment μ_{eff} and speed V leaving the source slit at X_S will be detected at $X_D = -X_S(L + D)/d$. If now the field is set at H and the detector is not moved, an identical atom will have to leave the plane of the source slit at X'_S , given by

$$X'_S \approx X_S + \frac{a}{V^2} \frac{Ld}{2} \left(1 + \frac{D}{L+D}\right) \quad (3)$$

in order to be detected. If $f_0(X_S)$ is the distribution of detected atoms as a function of source slit position at zero magnetic field, and $g(V)$ the speed distribution of atoms leaving the source slit, then the distribution of detected atoms at non-zero field, $f(X_S)$, will be given by

$$f(X_S) \approx \sum_{F,M} \int_0^\infty f_0(X_S - K_{FM}/V^2) g(V) dV, \quad (4)$$

where

$$K_{FM} = \frac{0.492}{\alpha} \frac{\mu_{eff}}{m} H L d \left(1 + \frac{d}{L+D}\right). \quad (5)$$

Both $f_0(X_S)$ and $f(X_S)$ can be measured, and then Eq. (4) can be used to verify whether a given velocity distribution is consistent with these measured distributions.

CALIBRATION AND PROOF-OF-CONCEPT EXPERIMENT

A preliminary experiment to study the deflection of a rubidium beam was performed in order to calibrate the electromagnet and test the use of Eq. (4) to verify an assumed velocity distribution.

Equation (1) shows that for an atom having nuclear spin I , $\mu_{eff} = 0$ if $\epsilon = -2M/(2I + 1)$. At field intensities determined by

$$H = \frac{-M}{2I + 1} \frac{W}{\mu_0}, \quad (6)$$

atoms with $M < 0$ will not be deflected by the field. Natural rubidium is a mixture of 72.2% Rb_{85} ($I = 5/2$) and 27.8% Rb_{87} ($I = 3/2$). Rb_{85} will have zero effective moments at $H = 361$ G ($M = -1$) and $H = 722$ G ($M = -2$). Rb_{87} will have a zero effective moment at $H = 1221$ G ($M = -1$). Figure 3 shows the detected atomic signal as a function of magnet coil current, with the rubidium beam source and detector on the apparatus axis. At the field values listed above, atoms in the zero effective moment states will travel through the magnet without deflection, leading to an increased signal. The effect of the zero effective moment states can be made more apparent on the figure by subtracting from each one of the marked features the local sloping background. The peaks labeled A and B can then

be identified with the zero effective moments at 722 *G* and 1221 *G*, respectively, yielding a calibration of 66.3 *G/A* for the magnet.

The rubidium source for these measurements was a two-chambered oven designed and operated to insure effusive flow; under those conditions, the atomic beam speed distribution should be beam-Maxwellian,

$$g(V) = (2/\beta)(V/\beta)^3 \exp[-(V/\beta)^2], \quad (7)$$

where $\beta = \sqrt{(2kT/m)}$, and *T* is the oven temperature. We measured $f(X_S)$ for *H* = 1061 *G*, 1220 *G* and 1525 *G*, as well as $f_0(X_S)$, and then used Eq. (4), with the speed distribution given by Eq. (7), to calculate the expected $f(X_S)$ at those field values. The results are presented on Figure 4. For $x < 0$ the agreement between calculated and measured detected atom distributions is somewhat poor; this is the convex polepiece side of the magnet, and the constant-force approximation made to derive Eq. (3) breaks down for atoms traveling too close to the polepiece. For $x > 0$, the agreement between calculated and measured $f(X_S)$ is excellent; these results fully validate our experimental technique.

ATOMIC HYDROGEN VELOCITY DISTRIBUTIONS

Figure 5 shows the atomic hydrogen beam fraction as a function of total pressure in the dissociator bulb, and discharge RF power. These data were obtained at 205 MHz; the discharge power was corrected for reflection, and the atomic fraction, measured with the quadrupole mass analyzer, was corrected for the H^+ background when detecting H_2 .

We have taken preliminary atomic hydrogen deflection data at total dissociator pressures of 0.2, 0.4 and 0.7 Torr, and at 995 and 1326 *G* magnetic fields. Zero field detected atom distributions have also been measured at each operating pressure. We then used Eq. (4) with the beam-Maxwellian distribution given by Eq. (7) to test the validity of the hypothesis of a thermal beam; the source temperature *T* was treated as a free parameter. Figure 6 shows, as an example, the deflection data at 995 *G* and 0.4 Torr, together with the expected detected atom distributions for Maxwellian beams at 300 *K* and 500 *K*. Bearing in mind that, as shown by Eq. (3), the transversal atomic displacement by the field is inversely proportional to V^2 , it is clear that the distribution at 300 *K* contains a large excess of slow atoms (large deflections), while the distribution at 500 *K* contains a correspondingly large excess of fast atoms (small deflections). Similar problems were encountered when analyzing the rest of the deflection data. These results show that the atomic velocity distribution in the beam must be significantly narrower than the beam-Maxwellian.

In order to estimate qualitatively the characteristics of the actual velocity distribution in our atomic hydrogen beam, we decided to model it by a Gaussian distribution of peak speed V_0 and standard deviation σ ,

$$g(V) = \frac{1}{\sigma\sqrt{2\pi}} \exp[-(V - V_0)^2/2\sigma^2]. \quad (8)$$

V_0 and σ were treated as free parameters and adjusted to provide a reasonable approximation to the measured deflection data. Given the preliminary nature of the deflection data and model velocity distribution, no attempt was made to obtain a "best fit". Figures 7, 8 and 9 show the deflection data at 995 *G* for dissociator total pressures of 0.2, 0.4 and 0.7 Torr, with the corresponding results calculated using the velocity distributions given by Eq. (8). A much closer agreement with the measured data is obtained than when using Maxwellians. Similar results were obtained for the data at 1326 *G*.

DISCUSSION AND CONCLUSIONS

The Gaussian velocity distributions used to calculate the results presented in Figures 7-9 are presented in Figures 10, 11 and 12, together with the corresponding Maxwellians having the same peak velocity. They show that the atomic beam velocity distributions are indeed non-thermal, and much narrower than Maxwellians. Since the distribution at 0.7 Torr is broader than the distributions at 0.2 and 0.4 Torr, it is also clear that we are not measuring distributions narrowed by gas-dynamics effects. Instead, incomplete thermalization of the hydrogen atoms must be the cause; this interpretation is consistent with the width of the distribution becoming closer to the Maxwellian width as the discharge pressure increases.

The peak velocities correspond to kinetic energies of about 0.06 eV, much smaller than the approximately 2 eV of kinetic energy available per atom immediately after dissociation. Since the atoms must lose the excess energy without broadening significantly their energy distribution, the main energy-loss mechanism must be an inelastic process with a relatively large energy loss per collision; vibrational excitation of the background hydrogen molecules, (0.546 eV/collision) seems to be a good candidate. Further studies in this area are required.

It is well known that the velocity passband of the hexapole or quadrupole magnets used as state selectors in hydrogen masers is rather narrow (about 25% FWHM). Our findings indicate that it should be possible to design the state-selecting magnet having a velocity passband which matches as closely as possible the fairly narrow velocity distribution of the hydrogen atoms effusing out of the dissociator, thus greatly enhancing the efficiency with which the maser uses its hydrogen supply.

REFERENCES

1. S. J. B. Corrigan and A. von Engel, "Excitation and Dissociation of Hydrogen by an Electron Swarm", *Proc. Roy. Soc. A*, 245, 335 (1958).
2. J.T. M. Walraven and I. F. Silvera, "Helium-Temperature Beam Source of Atomic Hydrogen", *Rev. Sci. Instrum.* 53, 1167 (1982).
3. A. Hershcovitch, A. Kponou and T. O. Niinikoski, "Cold High-Intensity Atomic Hydrogen Beam Source", *Rev. Sci. Instrum.* 58, 547 (1987).
4. T. M. Miller, "Atomic Beam Velocity Distributions with a Cooled Discharge Source", *J. Appl. Phys.* 45, 1713 (1973).
5. J. Viennet, P. Petit and C. Audoin, "Regulateur de Debit d'Hydrogene a Reponse Rapide", *J. Phys. E* 6, 261 (1973).
6. I. I. Rabi, J. M. B. Kellogg and J. R. Zacharias, "The Magnetic Moment of the Proton", *Phys. Rev.* 46, 157 (1934).
7. G. Breit and I. I. Rabi, "Measurement of Nuclear Spin", *Phys. Rev.* 38, 2082 (1931).
8. N. F. Ramsey, "Molecular Beams" (Oxford University Press, New York, 1956), p. 400.
9. N. F. Ramsey, *ibid.*, p. 398.

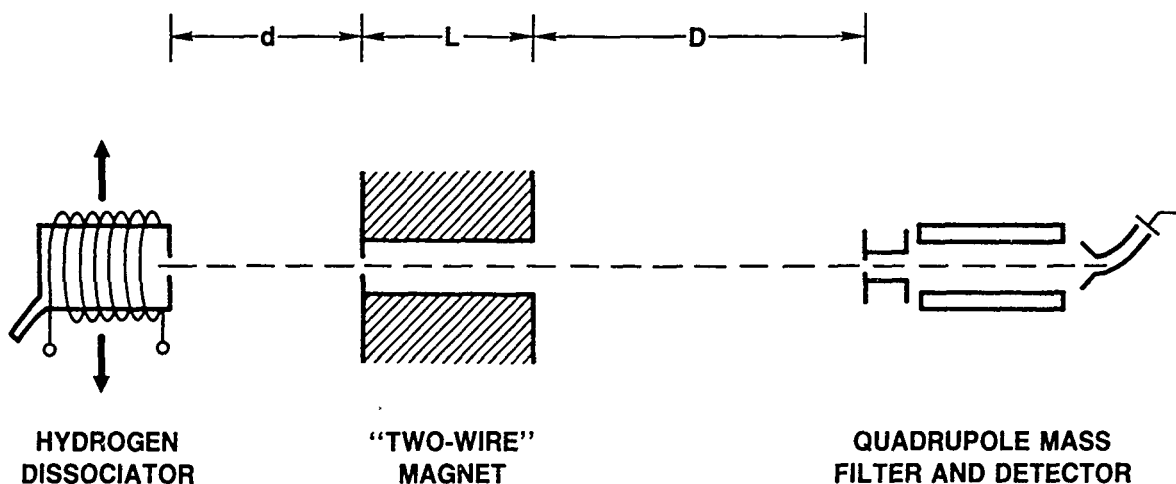


Fig.1: Schematic view of the experimental arrangement. The hydrogen dissociator can be displaced transversally.

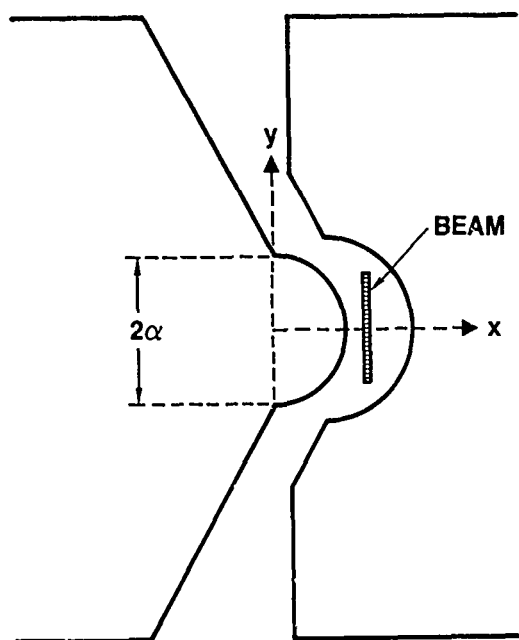
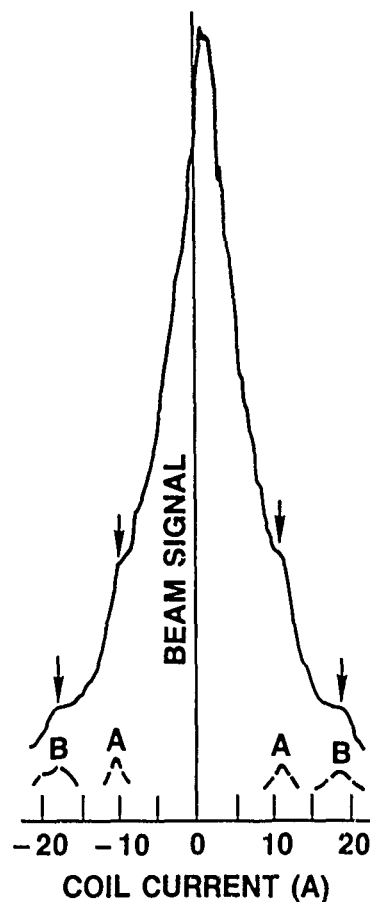


Fig.2: Cross section of the "two-wire" field magnet. 2α is the separation of the "equivalent wires".

Fig. 3: Rubidium atomic beam signal (detector and oven on axis) vs. magnet coil current. Arrows show features due to zero effective moment states. Dashed lines were obtained by subtracting the local constant-slope background from each feature. A: Rb_{85} , $M=-2$; B: Rb_{87} , $M=-1$.



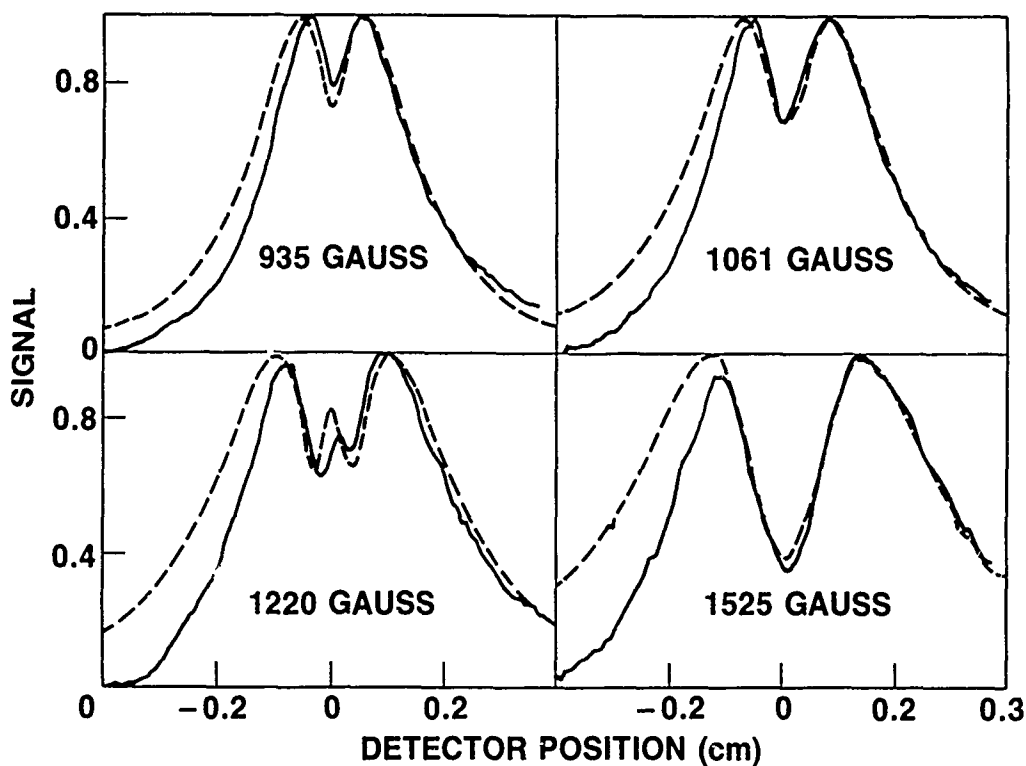


Fig.4: Detected rubidium atom distributions at indicated magnetic fields. Oven temperature: 484 K. Full line: measured. Dotted line: calculated for a Maxwellian beam.

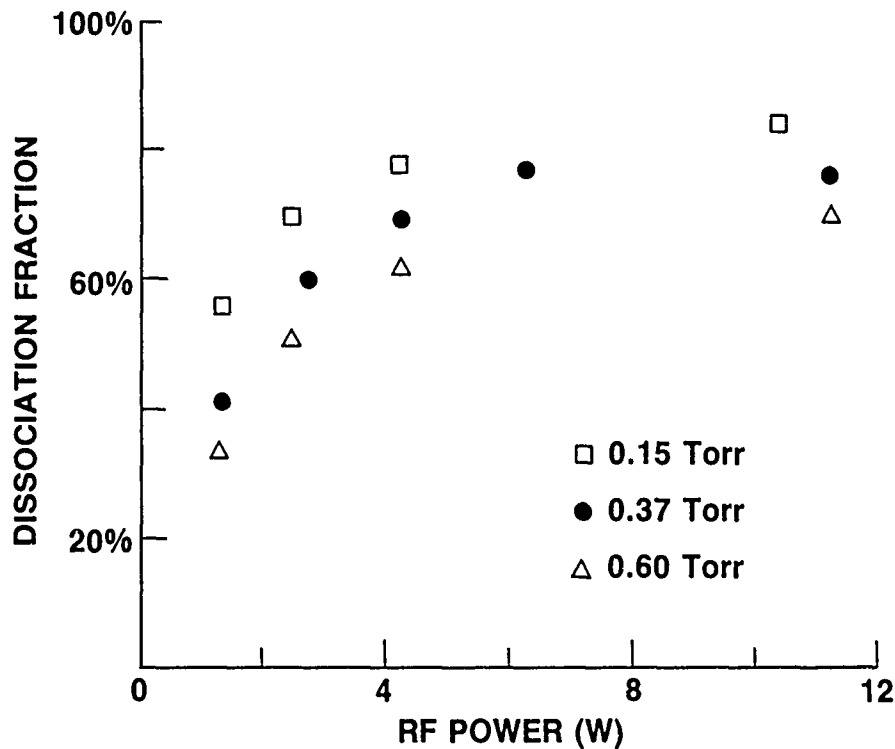


Fig.5: Atomic hydrogen beam fraction vs. rf discharge power. Total dissociator bulb pressures are indicated.

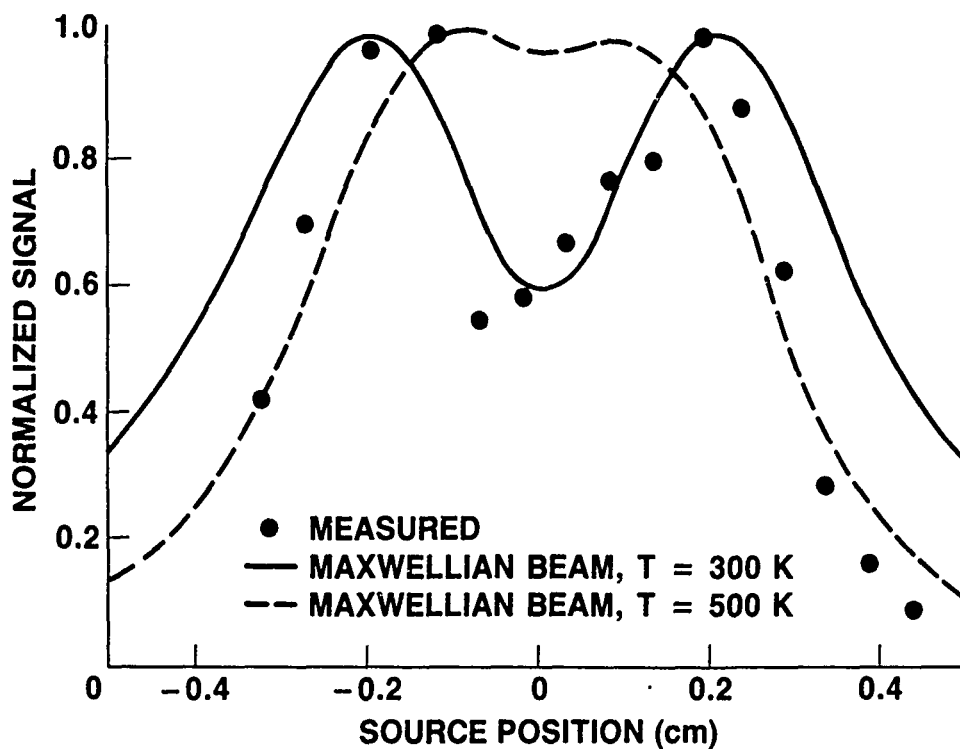


Fig.6: Detected hydrogen atom distribution, at 995 G and 0.40 Torr. Dots: measured. Curves: calculated.

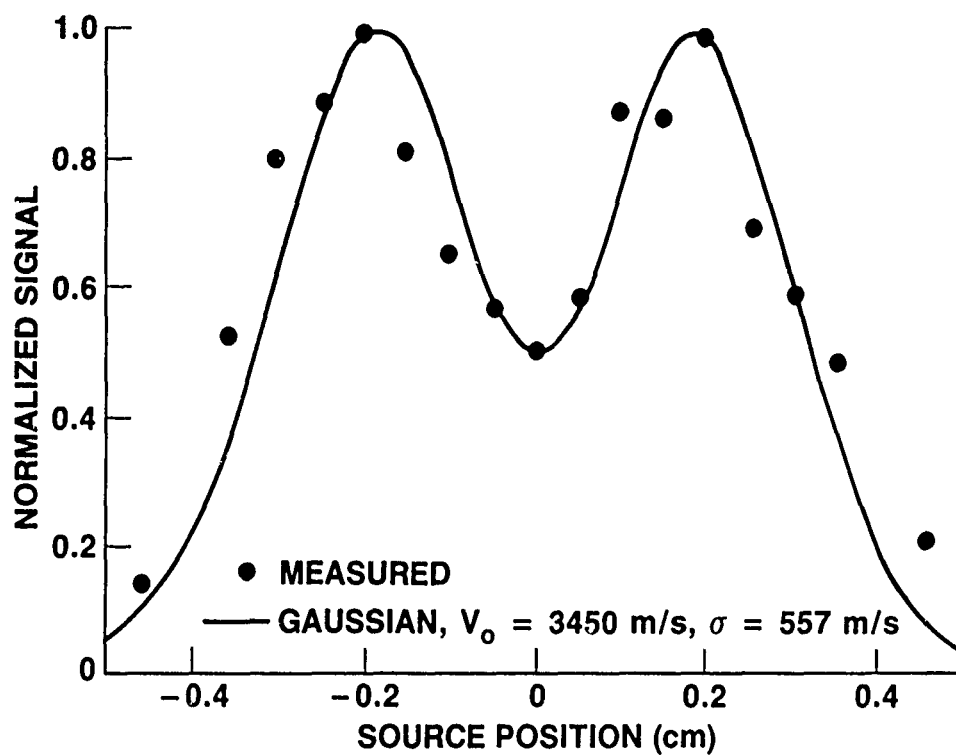


Fig.7: Detected hydrogen atom distribution, at 995 G and 0.20 Torr. Dots: measured. Curve: calculated.

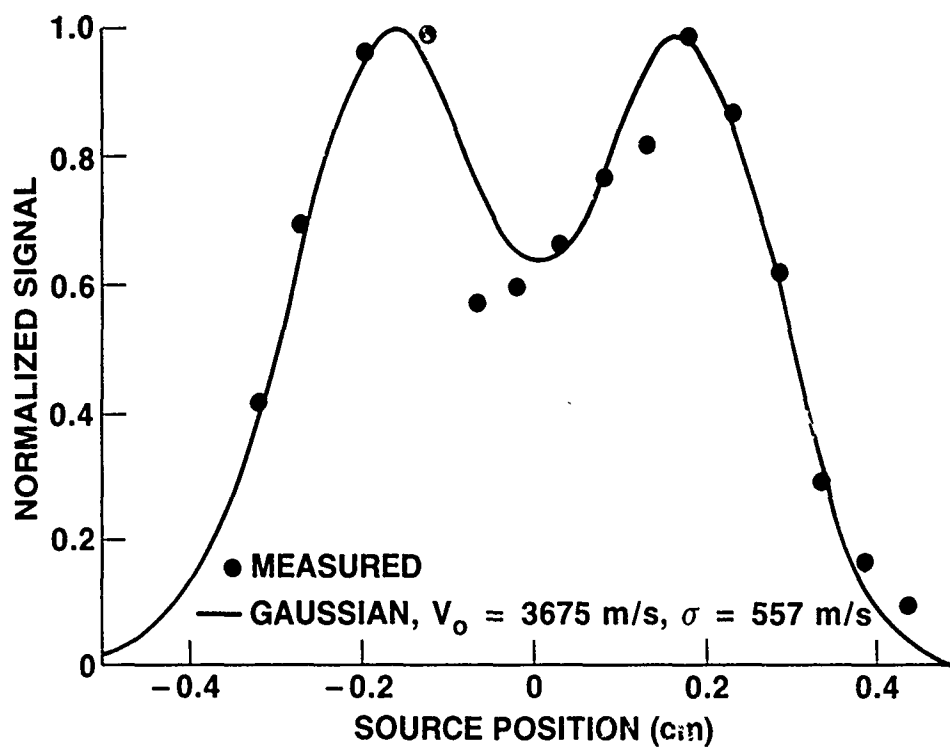


Fig.8: Detected hydrogen atom distribution, at 995 G and 0.40 Torr. Dots: measured. Curve: calculated.

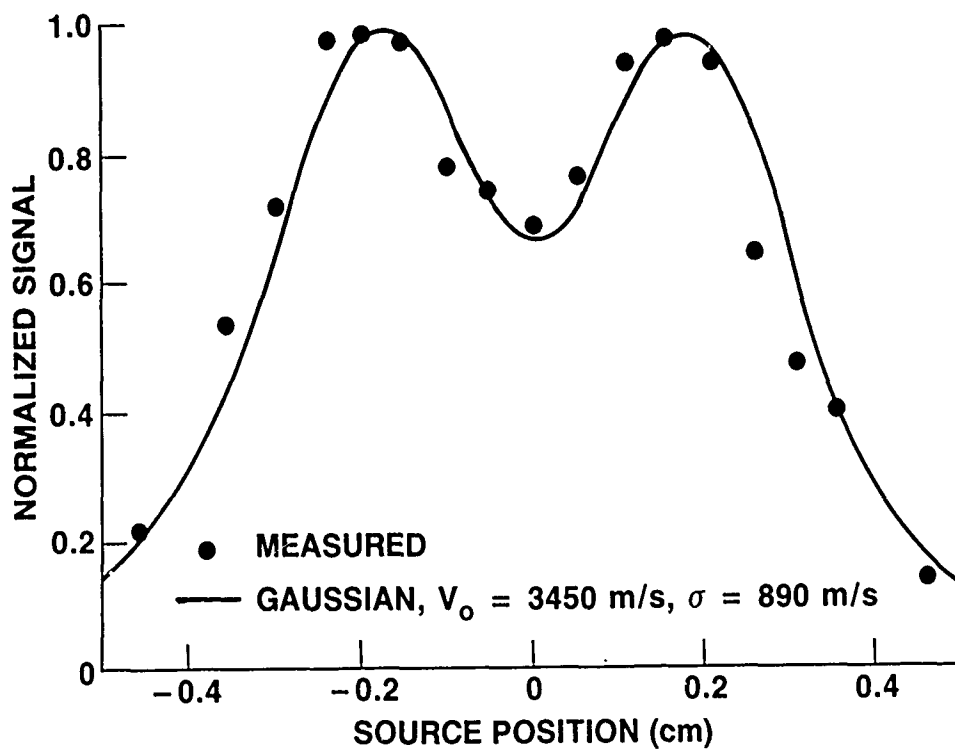


Fig.9: Detected hydrogen atom distribution, at 995 G and 0.70 Torr. Dots: measured. Curve: calculated.

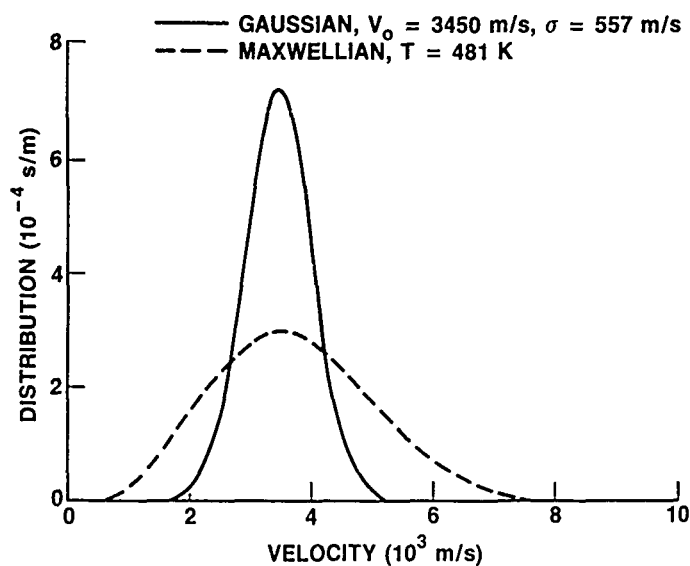


Fig. 10: Full line: Gaussian velocity distribution used for Fig. 7. Dashed line: beam-Maxwellian distribution having the same peak velocity.

Fig. 11: Full line: Gaussian velocity distribution used for Fig. 8. Dashed line: beam-Maxwellian distribution having the same peak velocity.

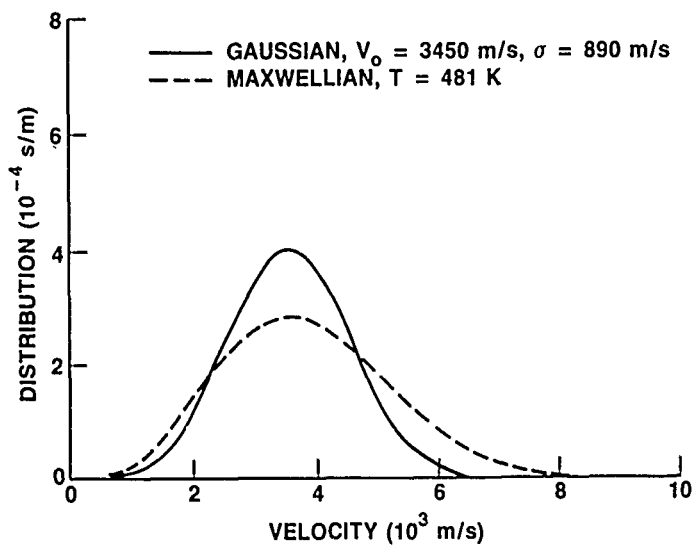
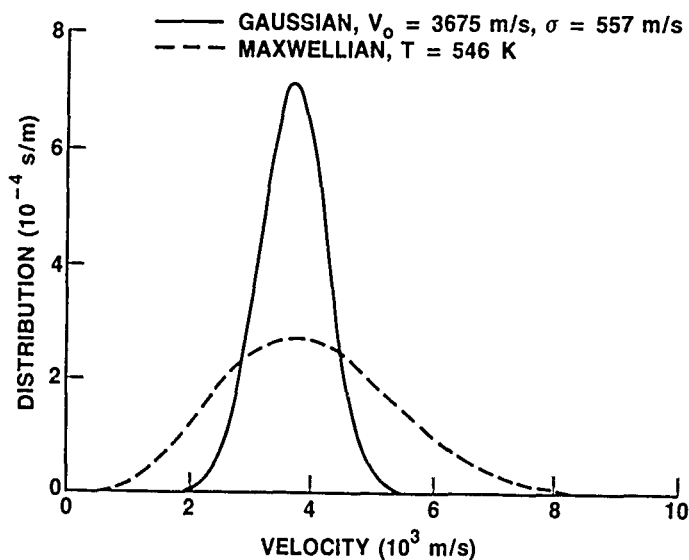


Fig. 12: Full line: Gaussian velocity distribution used for Fig. 9. Dashed line: beam-Maxwellian distribution having the same peak velocity.

TROPOSPHERIC LIMITATIONS TO THE STABILITY OF RADIO METRIC DELAY MEASUREMENTS

Dr. R. N. Treuhaft
Jet Propulsion Laboratory
California Institute of Technology
Pasadena, California

Abstract

Fluctuations in the index of refraction in both the wet and dry components of the troposphere induce timing instabilities in radio metric data in excess of that of modern frequency standards. At zenith, the wet and dry tropospheres cause fluctuations of the order of 2×10^{-14} s/s and 7×10^{-15} s/s at 1000 seconds, respectively. A description of the temporal and spatial characteristics of the wet and dry troposphere is given based on frozen flow modelling. The level of the fluctuations at various time scales and elevations is presented along with calibration strategies being investigated for both the wet and dry components.

CHARACTERIZING TROPOSPHERIC FLUCTUATIONS

Wet and dry tropospheric fluctuations, of the order of 2×10^{-14} s/s and 7×10^{-15} s/s at 1000 seconds respectively, far exceed the temporal fluctuations of modern time standards in radio metric data. The tropospheric fluctuations can be characterized as a spatial pattern obeying Kolmogorov statistics^[1], which is transported across a site by the wind. The results presented in this paper are based on a model which follows from that assumption^[2]. The fluctuation modelling results show good agreement with wet tropospheric levels and spectral shapes. Dry fluctuation results presented here are an extension of the wet fluctuation model, with the parameters of wind speed, atmospheric height, and turbulence scale factor changed. The model has not yet been extensively compared to dry fluctuation data. Wet statistics were normalized by water vapor radiometer data from Goldstone, California^[2] and dry statistics were normalized by barometric pressure fluctuation data also taken at Goldstone.

Viewing tropospheric fluctuations as arising from a frozen spatial pattern, which is blown across a site by the wind, allows an important connection between spatial and temporal fluctuation scales. For example, for a wind vector \vec{V} , a fluctuation lasting for T seconds corresponds to a spatial fluctuation of approximate dimension VT . Similarly, if radio metric delay is averaged over a time T , then only spatial features of the order of VT contribute to the observed average delay. Features much shorter than this scale average to zero, and features much larger than VT tend to vary slowly over the time interval T . For an interferometer of length L , tropospheric fluctuations on time scales smaller than L/V will not be correlated between the two ends of the interferometer; while fluctuations on time scales much greater than L/V will cause similar signatures at each end of the interferometer and

will therefore largely cancel. Applications of the relation between spatial and temporal scales will be discussed in the section on calibration techniques.

THE LEVEL OF WET AND DRY FLUCTUATIONS

Figure 1 shows the Allan standard deviation of zenith wet and dry fluctuations, based on the frozen flow modelling mentioned above. At 1000 seconds, the wet and dry Allan standard deviations are approximately 2×10^{-14} s/s and 7×10^{-15} s/s respectively. These levels of instability are of the order of or exceed those of modern timing standards. Most statistics of the troposphere have the characteristic rollover seen around 100 seconds in Figure 1. This is typically referred to as the transition from three dimensional to two dimensional turbulence. This nomenclature arises from the fact that at short time periods, or high frequencies, turbulent cells smaller than the tropospheric scale height (1–2 km wet, 4–8 km dry) dominate. These cells can be equally large in any dimension, and can be regarded as statistically spherical. Moving to the right on the abscissa of Figure 1 is equivalent to sampling larger and larger spherical cells. At a time equal to about the tropospheric scale height over the wind speed, taken to be 8 m/s for the wet and 15 m/s for the dry, moving to the right on the abscissa no longer samples spherical features. The cells must become oblate as they "hit" the top of the troposphere. A qualitative explanation of the rollover is that, as the time interval increases, the oblate cells can no longer grow in the height dimension, and therefore the statistical fluctuation trend with time decreases slightly relative to that describing the spherical cells.

The elevation dependence of fluctuation statistics can also be qualitatively deduced from similar arguments. At short time scales, as the elevation angle decreases from zenith, more small fluctuation cells will be seen along the line of sight. Some cells will have an index of refraction higher than the mean, and some less. The net effect is to increase the fluctuation level proportional to the square root of the length of the raypath, or approximately proportional to $\frac{1}{\sqrt{\sin \theta}}$ where θ is the elevation angle. At time scales long compared to the scale height over the wind speed, as elevation decreases, one large feature is being sampled and the long-term statistics vary approximately as $\frac{1}{\sin \theta}$. The quantitative details supporting these arguments are in reference [2].

CALIBRATION STRATEGIES FOR WET AND DRY FLUCTUATIONS

The most promising means for reducing the effects of delay fluctuations due to water vapor is by the use of water vapor radiometers (WVR). While comparisons of WVR delays with radio metric delays have shown systematic differences over many-hour time scales^[3], there is also data which suggest a high correlation between WVR and radio metric data over 1000-second time scales^[4]. If the long-period systematics persist, it is possible that they can be removed by estimating tropospheric parameters from the radio metric data themselves. Because of the relation between spatial and temporal fluctuations, WVR's must be a distance no greater than VT from the antenna taking the radio metric data, in order to calibrate fluctuations over times greater than T . This is probably one of the reasons why direct WVR calibration has had mixed results, as the WVR's are usually within a few hundred meters of the primary antenna.

As indicated in Figure 1, if WVR's are successful at reducing the wet fluctuation level, the dry

fluctuations, which are about $1/3$ as strong, will be the next tropospheric stability limitation. Three approaches are proposed here which could reduce the dry fluctuation level: 1) Global Positioning System (GPS) observations, 2) antenna arrays, 3) barometric arrays. The first two approaches could also be used to calibrate the wet component in the absence of WVR's. If all GPS errors besides the tropospheric contributions can be reduced on the time scale of interest, then GPS measurements near the line of sight of interest can be used to reduce the tropospheric contribution in other radio metric data. This technique could be used to calibrate both the wet and dry components, but, in the exercise that follows, it will be assumed that WVR's have completely removed the wet contribution from both the line of sight of interest and the lines of sight to the GPS satellites. A calculation has been done to determine the impact of the difference between the GPS and radio metric lines of sight. For both the primary line of sight of interest and the GPS raypath, assume an elevation angle of 20° . A single GPS satellite is assumed to be 20° away in azimuth from the line of sight of interest. Figure 2 shows the delay rate standard deviation for the uncalibrated dry delay along a line of sight at 20° elevation. The figure also shows the delay rate standard deviation for the difference between the uncalibrated line of sight and the delay measured along the GPS line of sight, 20° away in azimuth. The delay rate standard deviation is within about 30% of the Allan standard deviation and has the same approximate shape. A 4000-km scale height was assumed along with a wind speed of 15 m/s. It can be seen from the figure that the GPS calibration reduces the dry fluctuation level for time scales greater than about 200 seconds. Inferring the level of correlation of the two raypaths using the methods of described in the first section of this report yields a similar time scale. Naturally this result is based on a simplification of the real situation in which several GPS satellites are in view simultaneously with the line of sight of interest. This calculation is meant only to illustrate the potential of reducing the dry fluctuation level by observing a well-known beacon, such as the GPS, near the raypath of interest.

A second possible means of calibrating both wet and dry tropospheres is the use of antenna arrays. The frozen flow modelling again can be used to infer the utility of this approach. If a time scale T is of interest in a radio metric experiment, a second antenna located at a distance greater than VT away will experience tropospheric fluctuations which are uncorrelated with the first. The two signals from the antennas can later be averaged to reduce the effect of the fluctuation by a factor of $\sqrt{2}$. This argument can be extended to more than two antennas, and would therefore be applicable to experiments with the Very Large Array or arrays of GPS receivers. For time scales less than 40 minutes, multiple antennas within the Goldstone Deep Space Network complex could also be used to reduce the tropospheric fluctuation effects.

A possible approach for calibrating the dry delay is the use of barometric arrays. The dry zenith delay can be inferred from barometric pressure measurements. At lower elevations, atmospheric features as far as 20 kilometers from the antenna are being sampled due to the height of the troposphere. Using barometric arrays which sample the dry zenith delay at locations up to approximately 20 kilometers away may be useful in determining the dry fluctuations at low elevations. The measurement accuracy, modelling techniques, and spatial deployment necessary for barometric arraying to be effect have not been studied at the time of this report.

SUMMARY

Tropospheric fluctuations, both wet and dry, cause zenith delay fluctuations in radio metric measurements of the order 2×10^{-14} and 7×10^{-15} respectively at 1000 seconds. These fluctuations have been described in terms of a frozen flow model in which spatial index of refraction patterns are blown

across a site by the wind. For short time scales, fluctuation statistics are approximately proportional to $\frac{1}{\sqrt{\sin \theta}}$ where θ is the elevation angle. For long time scales, the statistics are approximately proportional to $\frac{1}{\sin \theta}$. The transition between "short" and "long" time scales takes place at about $\frac{h}{v}$, where v is the wind speed and h is the height of the troposphere. The most direct method for calibrating wet tropospheric delay fluctuations appears to be water vapor radiometry. Both the wet and dry delay could be calibrated by using a nearby GPS satellite raypath which, for sufficiently long time scales, will share the tropospheric signature of the raypath of interest. Results of a calculation were shown in which 20° elevation dry signatures could be reduced from 2×10^{-14} to 8×10^{-15} at 1000 seconds by a GPS raypath 20° from the raypath to be calibrated. Signals from additional receiving antennas located at distances greater than VT from the primary antenna can be used to calibrate wet and dry tropospheres for time scales less than T . Obtaining barometric pressure readings at multiple sites surrounding the receiving antenna is another proposed method for reducing dry fluctuation effects.

REFERENCES

1. Tatarskii, V. I., Wave Propagation in a Turbulent Medium, Dover, New York, 1961.
2. Treuhaft, R. N. and Lanyi, G. E., The Effect of the Dynamic Wet Troposphere on Radio Interferometric Measurements, Radio Science, 22, March 1987.
3. Lichten, S. L. and Kornreich, S., Stochastic GPS Estimation of Tropospheric Path Delays, EOS, Transactions of the American Geophysical Union, 70, October 1989.
4. Ray, J. R. and Edwards, C. D., Observations of Rapid Atmospheric Fluctuations in VLBI and WVR Data, EOS, Transactions of the American Geophysical Union, 70, October 1989.

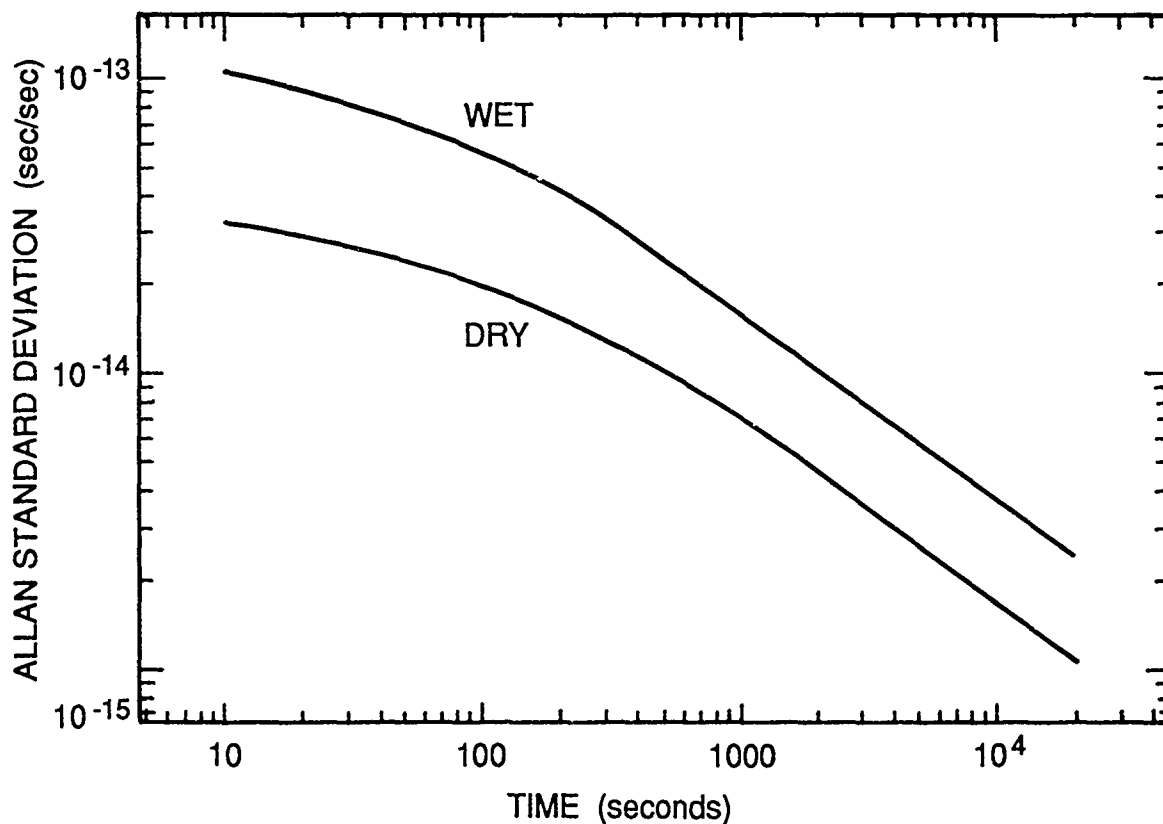


Figure 1: The calculated Allan standard deviation of the zenith wet and dry tropospheric delay.

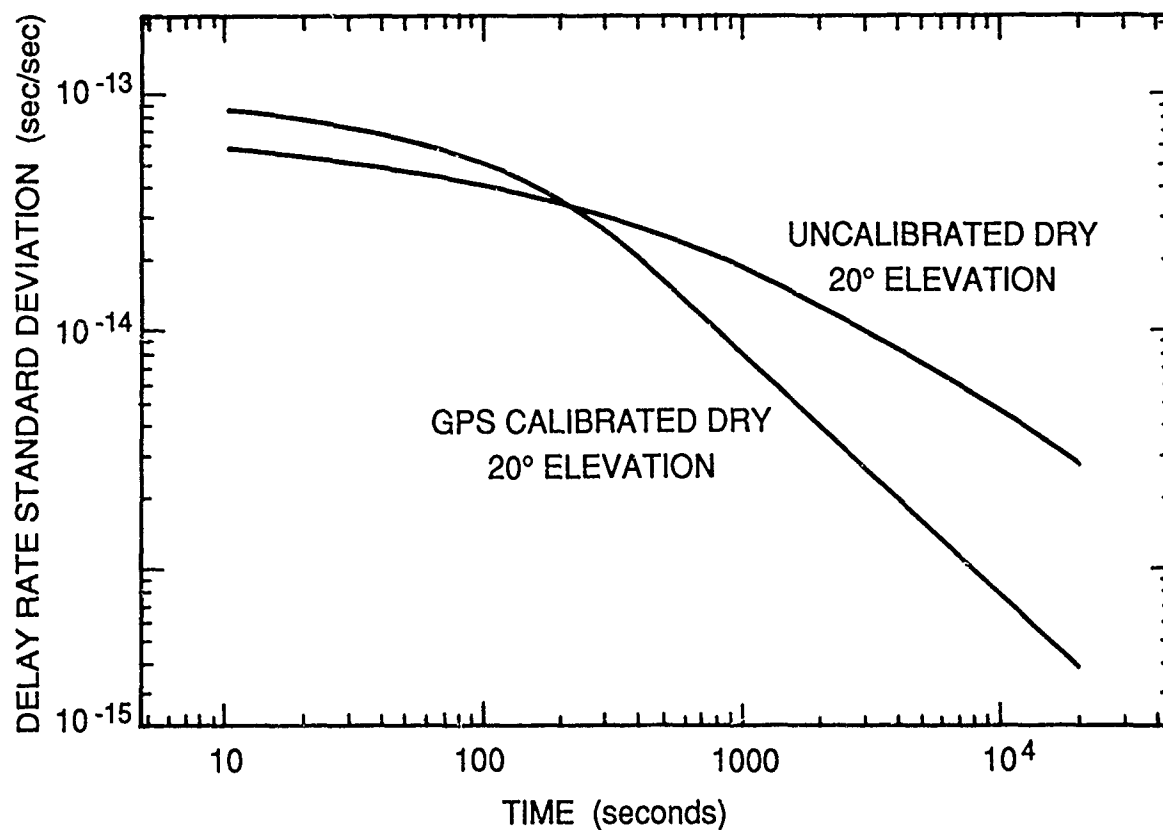


Figure 2: The calculated delay rate standard deviation of the 20-degree elevation dry troposphere. Also shown is the delay rate standard deviation for the difference between a 20-degree elevation raypath and a GPS raypath, also at 20 degrees elevation, and 20 degrees away in azimuth.

QUESTIONS AND ANSWERS

GERNOT WINKLER, USNO: In your first view graph, you showed the decreasing variation as a function of integration time. This cannot continue forever, do you have an idea where the turn-over point is?

MR. TREUHART: It is not so clear from the data the I have shown you here, but there is even a bit of a turn-over point in this plot. That is due to hitting the top of the atmosphere. There is another turn-over point which we base on a time series of WVR data as well as what people have said in the literature, and there is great debate on this. We believe that this turn-over point is of the order of thousands of kilometers, which means, in time, a good part of a day. Then it flattens out completely and is white from then on. That is of the order of 20,000 seconds.

HENRY FLIEGEL, AEROSPACE: I liked your paper very much and I have a very minor comment. You say that the solar hydrometer, in the traditional form, works only when aimed at the sun. There is no good reason, however, that it couldn't be made to work against the blue sky. Most of the blue sky light is, after all, coming from the oxygen and nitrogen in the atmosphere and the scale height of that is 18,000 feet, much higher than the scale height of water vapor. In principal at least you should be able to see the water vapor against the blue sky. Its just a question of engineering the hardware.

MR. TREUHART: It is just a matter of signal-to-noise at that point then?

MR. FLIEGEL: Perhaps so, but with photomultipliers there should be no difficulty with signal-to-noise. I am very happy that JPL is looking into the solar hydrometer, but maybe we should get rid of the word 'solar'. It is indeed a promising technique.

ON-ORBIT FREQUENCY STABILITY ANALYSIS OF GPS NAVSTAR CESIUM AND RUBIDIUM CLOCKS

Thomas B. McCaskill
James A. Buisson
U.S. Naval Research Laboratory

Tammy J. Hogan
SFA, Inc.

Washington D.C., 20375

Abstract

Naval Research Laboratory (NRL) on-orbit analysis of GPS NAVSTAR cesium and rubidium clocks has been performed using a three-year database that extended from 1 Jan., 1986 to 31 Dec., 1988. The NAVSTAR clock offset measurements were computed from pseudo-range data observed using a single frequency GPS receiver. Time and frequency inputs were derived from the U.S. Naval Observatory (USNO) time ensemble. Orbital data was obtained from the NAVSTAR broadcast ephemeris.

A key feature of the NRL NAVSTAR clock analysis is the capability to analyze phase and frequency discontinuities, solve for the discontinuity, and correct the clock data. This feature was developed primarily as a means to solve and correct for the NAVSTAR time or frequency adjustments that are required to keep NAVSTAR clock time close to GPS time. Discontinuities are analyzed to find both the amount and the probable cause for the break. This feature makes possible the use of sample times of 100-days or more, and the analysis of data to identify and model long term clock, system, and environmental effects.

Results for this NAVSTAR clock analysis will include the presentation of clock offset, frequency offset, and aging as a function of time. The NAVSTAR eclipse cycles will be superimposed on selected plots to demonstrate temperature sensitivity on several rubidium clocks. Clock performance in the time domain will be characterized using frequency stability profiles with sample times that vary from 1 to 100-days. Included in this analysis is the impact of clock aging on NAVSTAR frequency stability performance. It is demonstrated that uncorrected aging on the order of 1×10^{-13} /day has a measurable effect on NAVSTAR one-day frequency stability. It is further demonstrated that uncorrected aging on the order of 1×10^{-15} /day has negligible impact on one-day frequency stability and only a small effect on 100-day frequency stability.

The NAVSTAR rubidium clocks varied considerably in frequency stability results. The earlier NAVSTAR rubidium clocks have significant temperature coefficients. The four NAVSTAR cesium clocks demonstrated excellent and consistent performance for all sample times that were evaluated. Composite NAVSTAR frequency stability and time-prediction uncertainty plots are included that summarize clock analysis results for NAVSTAR clocks using sample times that vary from one-day to 100-days. All of the NAVSTAR clocks analyzed in this report meet the GPS one-day specification for frequency stability performance.

INTRODUCTION

The NAVSTAR Global Positioning System (GPS) is a space-based navigation satellite system which, when operational in the early 1990's, will provide accurate navigation and time information to users anywhere on the Earth's surface, or in near-Earth orbit. A constellation of 21 satellites, with three on-orbit spares, will be tracked by a network of GPS Monitor Stations (MS) and controlled from the Master Control Station (MCS). GPS will provide a near-instantaneous navigation capability because each NAVSTAR Spacecraft Vehicle (SV) clock is synchronized to a common GPS time. Each NAVSTAR clock must then maintain GPS time until the next update by the MCS, therefore NAVSTAR clock performance is critical to the GPS mission.

The Naval Research Laboratory (NRL) determines on-orbit NAVSTAR GPS clock performance using a procedure as depicted by the Figure 1. The goal of the NRL NAVSTAR clock analysis is to separate the clock offset from the orbit and other system effects that are present in the GPS signal. Outputs from the clock analysis include frequency and aging histories, frequency-stability profiles, time-prediction uncertainty profiles, time-domain noise process analysis, spectral analysis, and anomaly detection. Events that perturb normal NAVSTAR or MS clock operation are of particular interest in the clock analysis.

The NRL on-orbit analysis^[1] represents total system errors super-imposed on the NAVSTAR clock results. GPS system influences may either enhance or detract from actual clock performance. Therefore, deviations from a typical frequency-stability profile will be further analyzed to identify GPS clock, ephemeris, or other factors.

The following table presents the NAVSTAR number, SV number, clock identification, clock type and data span for each of the NAVSTAR clocks included in this analysis.

NAVSTAR CLOCK DATA						
DATA SPAN: 1 Jan 1986 to 31 December, 1988						
NAV #	SV #	CLOCK ID	CLOCK TYPE	DATA SPAN		
				t1 MJD	t2 MJD	t2-t1 days
3	6	19	Rb	6431	7526	1095
4	8	18	Rb	6431	6678	247
6	9	14	Rb	6431	7526	1095
8	11	33	Rb	6431	6563	132
8	11	2	Cs	6569	7526	957
9	13	4	Cs	6431	7526	1095
10	12	5	Cs	6431	7526	1095
11	3	3	Cs	6431	7515	1084

The NAVSTARs are referenced by both NAVSTAR numbers (column #1) and NAVSTAR SV numbers (column #2). Column #3 presents the NAVSTAR clock identification number. The clock type is abbreviated by Cs for a cesium clock and by Rb for a rubidium clock. The starting and stop dates for the data span are expressed in Modified Julian Days (MJD), and the data span is expressed in days.

Reference to the table shows that six of the eight NAVSTAR clocks have data spans that are close to

1000 days. The longer data spans will be used to evaluate clock performance with sample times of up to 100 days.

The NAVSTAR SVs included in this analysis are Block I models that do not have any degradation in the ephemeris or broadcast signal due to Selective Availability (SA). Three of the four NAVSTAR rubidium clocks are of the early models that have significant temperature coefficients; the fourth rubidium has additional temperature compensation. The four NAVSTAR cesium clocks are expected to have performance that is close to the Block II NAVSTAR cesium clocks.

PSEUDO-RANGE MEASUREMENT MODEL

Measurements of pseudo-range (PR) are taken between signals derived from the NAVSTAR SV clock and the MS reference clock using a single-frequency, spread-spectrum receiver. Each measurement is corrected for equipment delay, ionospheric and tropospheric delay, earth rotation, relativistic effects, and the ephemeris offset is computed from the broadcast NAVSTAR ephemeris. The clock offset measurements are then aggregated and smoothed once per 13 minutes.

The equation that relates the pseudo-range measurement to the time difference between the NAVSTAR clock and the reference MS clock is

$$PR = R + c(t_{SV} - t_{MS}) + ct_A + e$$

where

- PR is the measured pseudo-range,
- R is the slant range (also known as the geometric range) from the NAVSTAR at the time of transmission to the MS at the time of reception,
- c is the speed of light,
- t_{MS} is the reference MS clock time,
- t_{SV} is the NAVSTAR clock time,
- t_A is ionospheric, tropospheric, and relativistic delay, with corrections for antenna and equipment delays, and
- e is the PR measurement error.

The NAVSTAR clock and the MS clock (or other reference clock) enters the PR measurement as the difference between NAVSTAR clock time t_{SV} and MS clock time t_{MS} . Because the reference MS clock t_{MS} enters directly into the measurement the stability of the MS reference clock must be considered in the NAVSTAR clock analysis. For the measurements that are referenced to the USNO Master Clock #2 the stability of the USNO time-scale is significantly better than that of an individual NAVSTAR clock for sample times of 1 to 100-days.

It should be noted that NAVSTAR clock time is used with the clock coefficients that are broadcast as part of each NAVSTAR navigation message to compute GPS time. The NAVSTAR clock time (for each NAVSTAR) is measured and controlled by the GPS MCS to be within plus or minus one millisecond of GPS time.

NAVSTAR CLOCK MODEL

The pseudo-range measurements that are taken between a NAVSTAR SV and a GPS monitor site (or by any GPS user) are normally sampled by the reference MS clock (or the user reference clock)

at the discrete times $t_{MS} = t_k$. The *clock phase offset* between a NAVSTAR clock and the reference MS clock is obtained by solving the pseudo-range equation for the quantity $(t_{SV} - t_{MS})$, which is the difference between the NAVSTAR clock time and the MS clock time.

$$(t_{SV} - t_{MS}) = (R/c + t_A + e/c) - PR/c$$

The time difference between the NAVSTAR clock and the MS clock, $(t_{SV} - t_{MS})$, is usually expressed in microseconds; the pseudo-range is a measure of distance expressed in kilometers or meters, and c is the speed of light expressed in a consistent set of units.

The pseudo-range measurements are normally sampled at a uniform rate, therefore another variable $x(t_k)$ may be defined to denote the *clock offset*, sampled at time $t_{MS} = t_k$ by the MS clock.

$$x(t_k) = (t_{SV} - t_{MS})$$

where $k = 0, 1, 2, 3, \dots, N$ (the number of clock measurements)

Given two clock measurements, $x(t_j)$ and $x(t_k)$, which were sampled at times t_j and t_k , the *sample time* τ is defined as

$$\tau = (t_k - t_j)$$

In *time-domain analysis*, the performance of a NAVSTAR clock will be analyzed as a function of τ , the sample time. In *frequency-domain analysis*, the independent variable is the Fourier frequency.

The average clock rate can now be computed using a variable known as the average *fractional-frequency offset*, as defined by the following equation.

$$\bar{y}(t) = \frac{x(t_k) - x(t_j)}{\tau}$$

The fractional-frequency offset $\bar{y}(t)$ will be analyzed as a function of time to determine NAVSTAR clock coefficients, and anomalies such as frequency discontinuities or environmentally induced frequency fluctuations.

TIME-DOMAIN STABILITY ANALYSIS

NAVSTAR clock performance in the time-domain is characterized through the use of a frequency-stability profile^[2]. The time-domain measure of frequency-stability used in this analysis is the Allan variance^[3]. Time-domain clock performance parameters can be related to the Allan variance by the following equation.

$$\sigma_y^2(\tau) = a\tau^\mu$$

In this equation, τ is the sample time, σ_y is the square root of the variance of the fractional-frequency measurements $\bar{y}(t)$, the coefficient a varies with each type of clock and the random noise process type, μ depends on the random noise process type. The variance $\sigma_y^2(\tau)$ is defined as an infinite average which is estimated using successive triplets of clock phase measurements or pairs of fractional frequency offset measurements separated by the sample time τ . Confidence intervals are then computed for each stability measurement according to the random noise process type and the number of samples.

The random clock phase or frequency fluctuations for quartz, rubidium, cesium, and hydrogen clocks can be modeled by an appropriate combination of five types of random noise processes. A typical

frequency-stability profile is presented in the Figure 2. The dependent variable presented is $\sigma_y(\tau)$ (the square root of the Allan variance) as a function of sample time, τ .

Once a clock has been characterized through a frequency-stability analysis, the frequency-stability profile may then be used to estimate a clock's time-prediction performance. The time-prediction uncertainty is computed using optimal two-point prediction that can be related to the frequency-stability by the following equation.

$$\sigma_x(\tau) = \sqrt{2\tau}\sigma_y(\tau)$$

In this equation $\sigma_x(\tau)$ represents the NAVSTAR clock phase time-prediction uncertainty, $\sigma_y(\tau)$ represents the NAVSTAR frequency-stability, and τ represents the sample time or the NAVSTAR clock update time.

This time-prediction model indicates that the long-term time-prediction performance is driven by the product of the clock update time and the frequency-stability. Therefore, the frequency-stability is also related to time-prediction uncertainty. The length of time between NAVSTAR clock updates is determined by GPS performance requirements, hence improved frequency-stability is the parameter that will improve GPS time-prediction performance.

Sets of clock measurements may now be analyzed to determine both deterministic and random components of NAVSTAR clock performance. These clock measurements also contain residual ephemeris, environmental, and system effects.

NAVSTAR PHASE/FREQUENCY DISCONTINUITY ANALYSIS

The primary reason for applying the phase or frequency discontinuity corrections is so that sample times from 1 day up to 100 days, or more, may be used in the stability analysis. Otherwise the clock data would have to be partitioned at every discontinuity, which would in turn reduce the longest possible sample time that could be computed.

Clock phase offset measurements computed from smoothed pseudo-range measurements taken between the NAVSTAR-03 and USNO are presented in Figure 3. Each measurement is time-tagged using three related time scales which are:

- (a) Modified Julian day (MJD) for the lower time axis
- (b) the day-of-year is on the upper time axis
- (c) the calendar month and year are on the upper time axis

The clock data is nominally sampled at a rate of once per sidereal day at the point of closest approach of the NAVSTAR to the ground MS. This choice results in sampling the NAVSTAR-SV clock offset at the same place in the 12-sidereal hour GPS orbit. This procedure also insures that the NAVSTAR-SV clock parameters and stability are determined, except for missing observations, using a uniformly sampled database.

Analysis of the NAVSTAR-03 phase data indicates piecewise continuous clock data with three phase discontinuities and a negative slope for each segment. These discontinuities in the clock data can be caused by normal GPS operations such as NAVSTAR time or frequency adjustments or MS clock resets, therefore these discontinuities do not represent the normal unperturbed clock behavior. As part of the NAVSTAR clock analysis the amount of each discontinuity is estimated and a search is

made to find a reason for each discontinuity in the clock data. The phase discontinuity correction procedure will now be presented for a typical phase discontinuity that was present in the (USNO vs NAVSTAR-03) clock data.

The NAVSTAR-03 vs USNO clock data in the neighborhood of one phase discontinuity that was detected is presented by the Figure 4. The time of the phase discontinuity was estimated to be MJD 6525.483 (5 April, 1986). The clock phase data was partitioned into subsets delineated by the discontinuity. The clock phase offset was then predicted at the time of the discontinuity using the two subsets; the difference between these two predictions yields the clock phase discontinuity. The corrected clock phase data is presented by the Figure 5. The time of the discontinuity is indicated on the figure with an arrow. The values of the phase correction (0.444E03 microseconds) and frequency correction which in this case is zero, are plotted adjacent to the arrow. The clock phase data is now continuous within the interval analyzed.

All data prior to the discontinuity has been corrected, which can be seen by comparing the NAVSTAR-03 clock data before and after the discontinuity correction. This discontinuity correction procedure is repeated until all significant phase discontinuities have been detected and corrected. The error in the clock phase discontinuity correction procedure can be related to the clock prediction performance at a sample time of $\tau/2$ days.

The fractional-frequency offset was computed using pairs of clock phase measurements separated in time by one sidereal day. Figure 6 presents the NAVSTAR-03 fractional-frequency as a function of time.

Analysis of the NAVSTAR-03 frequency offset data indicates an overall negative slope with large frequency fluctuations that appear to be periodic. Previous NRL analyses have determined that the NAVSTAR-03 rubidium clock frequency was sensitive to temperature changes that occur in the NAVSTAR spacecraft. The temperature coefficient was determined to be 1.96×10^{-12} per degree Celsius. The onset and departure of each NAVSTAR-03 eclipse cycle has been plotted using two vertical lines with a shaded fill during the eclipse season. A total of six eclipse cycles occurred during the three year data span. Analysis of the frequency data that ended in May, 1986 and the following eclipse cycle (beginning in late September, 1986) indicated that a frequency discontinuity occurred on MJD 6613. The observation that a frequency discontinuity had occurred was determined by extracting subsets of data during 1986, 1987, and 1988 that are partitioned using a nominal one-year partition size.

The amount of the NAVSTAR-03 frequency discontinuity was determined by iteratively analyzing the frequency offset data for the value of the discontinuity, applying the correction, and then analyzing the corrected frequency offset data. The total amount of the frequency discontinuity determined was -1.75×10^{-12} .

Closer examination of the NAVSTAR-03 frequency data indicates rapid changes in frequency offset occurs at the onset of the NAVSTAR-03 eclipse season. Rapid changes in frequency also occur at the end of the eclipse seasons. The observed frequency changes are on the order of 1.0×10^{-12} to 3.5×10^{-12} . Because of the correlation with the eclipse season and the temperature sensitivity of the NAVSTAR-03 rubidium clock, these data are treated as normal behavior and will be included in the subsequent NAVSTAR-03 stability analysis.

Additional frequency corrections were made for a series of small rate corrections that were made by the USNO to coordinate their Universal Time Coordinated (UTC) time scale with an international time scale. These rate corrections affect all NAVSTAR clock measurements made by USNO. The

NAVSTAR-03 versus USNO clock data that includes the USNO rate corrections is presented by Figure 7.

The NAVSTAR-03 versus USNO clock offset with all corrections applied is presented by Figure 8 and the fractional frequency offset presented by Figure 9. The corrected data will be used to compute long term clock coefficients and frequency-stability.

The NAVSTAR-10 versus USNO raw phase offsets is presented by Figure 10. No phase or frequency discontinuities were detected in this data during the entire three year data span. The USNO rate corrections were the only corrections that were made to the NAVSTAR-10 versus USNO data. The NAVSTAR-10 frequency offset data is presented by Figure 11 with the eclipse cycles highlighted. It is clear that a significant improvement exists between the earlier NAVSTAR rubidium clocks and the NAVSTAR-10 cesium clock. The corrected NAVSTAR-10 versus USNO clock is presented by Figure 12. Comparison of the data without the USNO rate corrections (Figure 10) and with the USNO rate corrections indicates no detectable difference for this scale factor. The corrected NAVSTAR-10 versus USNO clock data was used to compute the long term clock parameters, frequency-stability, and time-prediction uncertainty results.

NAVSTAR LONG TERM AGING RATE ANALYSIS

Each NAVSTAR spacecraft carries atomic clocks that are used as time and frequency references for GPS and to determine the epochs of the transmitted waveforms. The physics of atomic clocks indicates that the frequency of these clocks should remain invariant, ie, not change with time. The clock aging parameter gives a measure of how quickly a NAVSTAR clock departs from a reference clock.

The departure of a NAVSTAR clock from an initial frequency that is within GPS specifications impacts GPS operation in at least two ways.

The first way NAVSTAR clock aging impacts GPS operation depends on how well the aging rate parameter has been estimated. Stability results indicate that an uncorrected aging rate term on the order of 1×10^{-13} /day can have a measurable impact of clock performance. This can be seen by comparing (Figure 13) the NAVSTAR-08 rubidium frequency-stability results with and without an aging rate correction. The uncorrected aging rate of -1.3×10^{-13} /day results in a measured stability of 1.4×10^{-13} for a 1-day sample time. The aging-rate corrected stability is 8.9×10^{-14} for a 1-day sample time. It follows that an uncorrected aging rate on the order of 3×10^{-13} /day would drive the stability over the GPS 1-day specification and cause unacceptable performance.

For an uncorrected aging rate term on the order of 1×10^{-15} /day the impact of aging rate on stability is significantly reduced. This can be demonstrated using the NAVSTAR-10 cesium frequency-stability results with and without an aging rate correction (Figure 14). There is no measurable difference up to a sample time of 15-days between the measured 1-day stability without an aging rate correction and with an aging rate correction for the NAVSTAR-10 long term aging rate of -1.1×10^{-15} /day. The impact of the -1.1×10^{-15} /day aging rate is so small that the frequency-stability values are still less than 1×10^{-13} for a 100-day sample time.

The second way aging impacts GPS operation is that a relatively large aging rate causes any initial frequency offset to drift away from the GPS time and frequency limits. Furthermore each NAVSTAR clock reset by a Z-adjust or C-field tune requires a re-estimation of the all clock parameters. The amount of time required to accurately determine the NAVSTAR aging rate parameter is on the order of one week or more.

The NAVSTAR long-term aging performance was further analyzed by computing the aging as a function of sample length. The NAVSTAR 30-day sample length aging results will be presented using the same scale factor for the NAVSTAR-08 rubidium clock and the NAVSTAR-10 cesium clock.

The NAVSTAR-03 rubidium clocks shows significant periodic changes in aging that are presented by the Figure 15. The amplitudes of the 30-day aging for this rubidium clock are on the order of 1.3×10^{-13} /day. The periodic changes in aging are (probably) driven by the rubidium clock's sensitivity to temperature as has been previously noted.

The NAVSTAR-10 one-day corrected frequency offset data is presented in Figure 16. The slope of this frequency data is the long term aging.

The NAVSTAR-10 cesium 30-day aging results without the eclipse cycles highlighted are presented by Figure 17. By comparison with the NAVSTAR-03 data it is clear that there is a significant improvement in temperature changes that occur during the NAVSTAR eclipse cycles.

Comparison between the NAVSTAR rubidium results and the NAVSTAR cesium results indicates a significant improvement in aging performance for the cesium clocks.

NAVSTAR STABILITY ANALYSIS

The frequency-stability was computed using sample times that varied according to the amount of clock data available during the three year data span. Six of the (USNO vs NAVSTAR) clock pairs had close to 1000 days of data. The remaining two clock pairs had a limited amount of data that restricted the sample times that could be computed with high confidence.

The composite frequency-stability profile plot (Figure 18) includes stability results for eight clocks pairs. All of the eight clock pairs had frequency-stabilities that are better than the GPS Block I one-day frequency-stability specification limit of 2×10^{-13} .

Time-prediction uncertainty results were computed using the aging-corrected frequency stability profile for each clock pair. The clock times evaluated are the same as the sample times used for each clock pair.

All clock pairs evaluated indicate a time prediction uncertainty that was in the 11 to 21 nanoseconds range for a 1 day clock update time. The time-prediction uncertainty for longer clock update times indicated significant differences between the NAVSTAR cesium and rubidium clocks.

Ensemble cesium frequency-stability and time-prediction uncertainty results were computed for the NAVSTAR cesium clocks by averaging the individual stability-variances and the time-prediction results. The ensemble NAVSTAR cesium frequency-stability and time-prediction uncertainty results are as follows.

- * 1.6×10^{-13} for a 1-day sample time
- * 4.0×10^{-14} for a 10-day sample time
- * 6.0×10^{-14} for a 100-day sample time

- * 19 nanoseconds for a 1-day sample time
- * 52 nanoseconds for a 10-day sample time
- * 577 nanoseconds for a 100-day sample time

NAVSTAR CLOCK ANALYSIS CONCLUSIONS

On-orbit (USNO vs NAVSTAR) clock analysis results were obtained using a three year database of clock data that covers from 1 Jan, 1986 through 31 December, 1988. The results are summarized by the following table.

NAVSTAR ON-ORBIT RESULTS DATA SPAN: 1 Jan, 1986 to 31 December, 1988

NAV ID	CLOCK TYPE	frequency stability			time-prediction			data span days
		$\times 10^{-13}$	$\times 10^{-14}$	$\times 10^{-14}$	ns	ns	ns	
		1 day	10 days	100 days	1 day	10 days	100 days	
3	Rb	1.5	34.0	74.0	19	417	8982	1095
4	Rb	1.6	54.0	-	19	655	-	247
6	Rb	1.7	34.0	160.0	19	414	20072	1095
8	Rb	0.9	4.8	-	11	58	-	132
8	Cs	1.4	4.0	6.0	18	49	658	957
9	Cs	1.7	4.5	5.0	20	55	555	1095
10	Cs	1.6	4.4	4.0	20	53	543	1095
11	Cs	1.6	4.7	3.0	19	51	360	1084

- * All NAVSTAR clocks are better than the GPS Block I frequency-stability specification of 2×10^{-13} for a 1-day sample time.
- * The NAVSTAR-08 rubidium clock shows a significant improvement over earlier model rubidium clocks with respect to stability and reduced temperature sensitivity.
- * All NAVSTAR cesium clocks show excellent frequency-stability performance that varies from 1.7×10^{-13} for a one-day sample time to 6.0×10^{-14} or less for a 100-day sample time. The ensemble cesium time-prediction uncertainty results are from 19 nanoseconds for a 1-day clock update to 577 nanoseconds for a 100-day clock update.

REFERENCES

1. McCaskill, T.B., Buisson, J.A., and Stebbins, S.B., "On-Orbit Frequency-Stability Analysis of the GPS NAVSTARs 3 and 4 Rubidium Clocks and NAVSTARs 5 and 6 Cesium Clocks", Proceedings of the Fifteenth Annual Precise Time and Time Interval(PTTI) Applications and Planning Meeting, December 6-8, 1983.
2. Luck, J.Mc., "Construction and Comparison of Atomic Time Scale Algorithms", TR 32, Division of National Mapping, Canberra, Australia, 1983.
3. Allan, D.W., "Clock Characterization Tutorial", Proceedings of the Fifteenth Annual Precise Time and Time Interval(PTTI) Applications and Planning Meeting, December 6-8, 1983.

NAVAL RESEARCH LAB (NRL)

CLOCK ANALYSIS FLOW CHART FOR NAVSTAR GPS

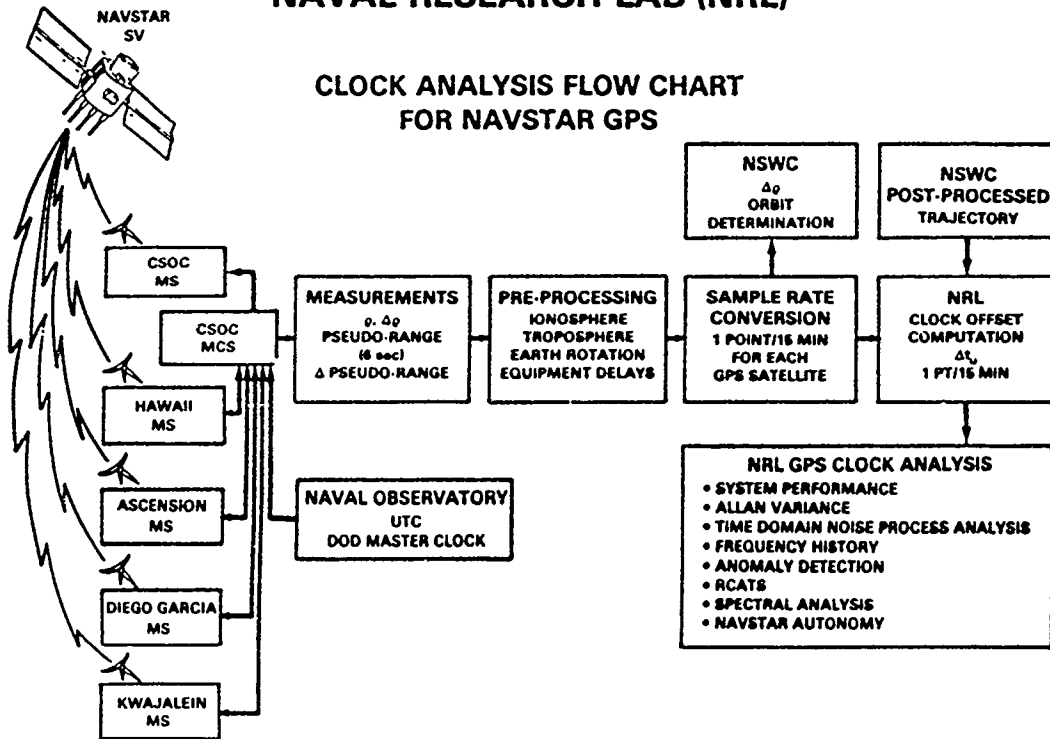


FIGURE 1

TIME DOMAIN FREQUENCY STABILITY PROFILE

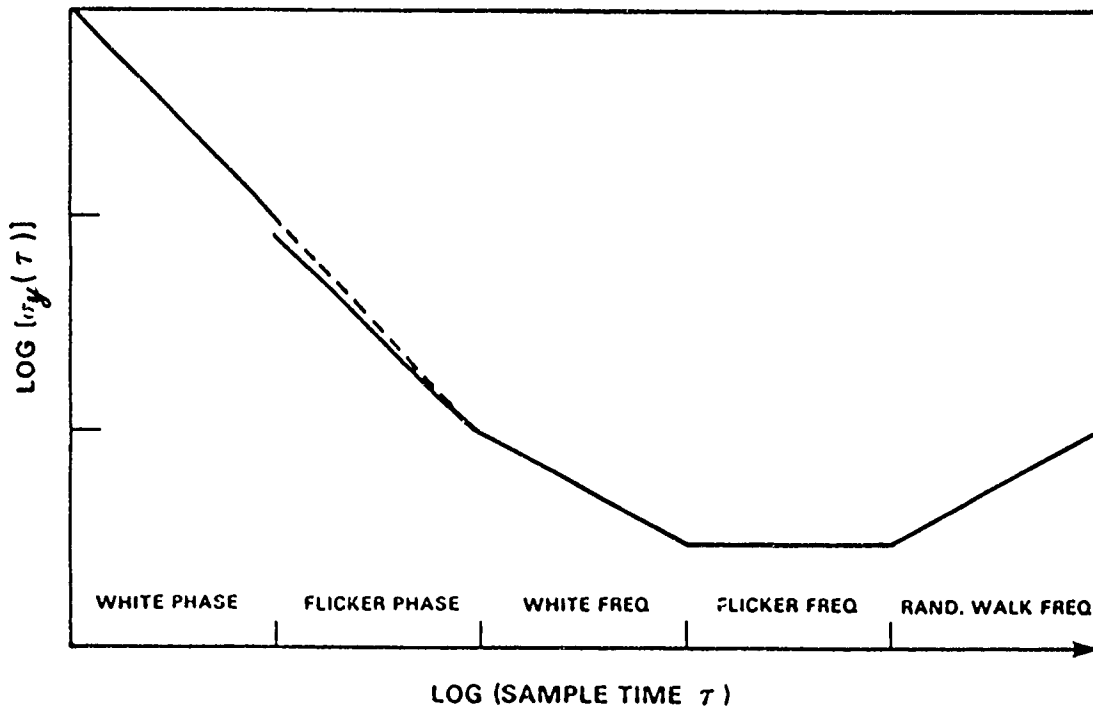


FIGURE 2

RUBIDIUM OSCILLATOR (NO.19) RAW PHASE OFFSET
NAVSTAR 3 versus
United States Naval Observatory MC #2

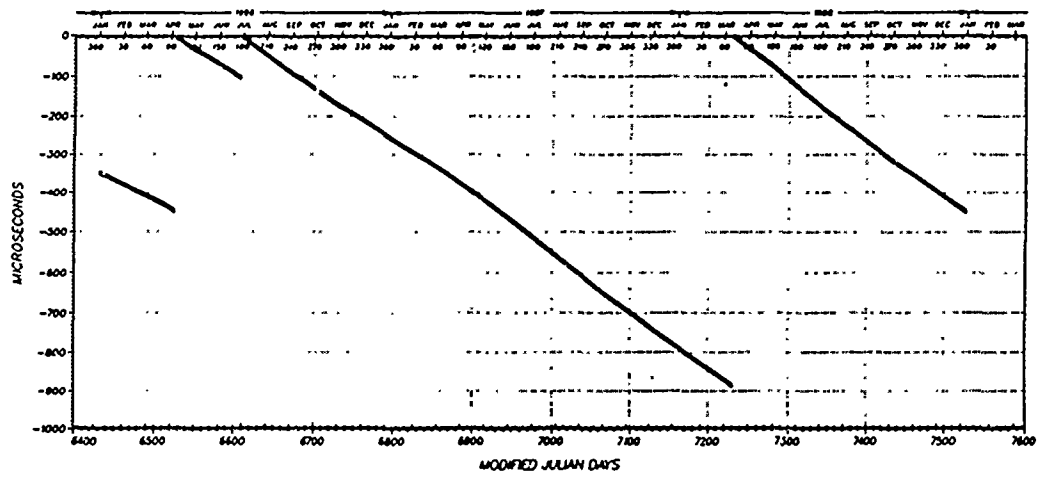


FIGURE 3

RUBIDIUM OSCILLATOR (NO.19) RAW PHASE OFFSET
NAVSTAR 3 versus
United States Naval Observatory MC #2
CLOCK PHASE DISCONTINUITY on MJD 6525 (5 Apr. 1986)

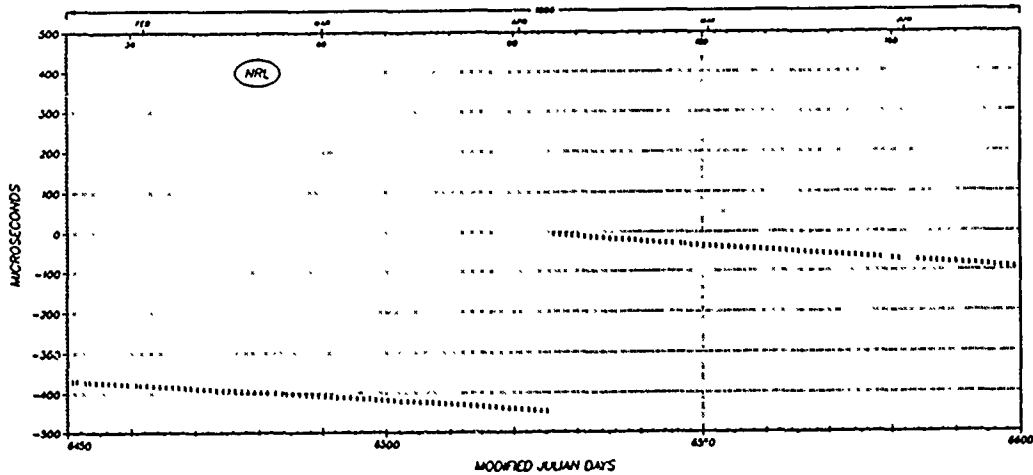


FIGURE 4

RUBIDIUM OSCILLATOR (NO 19) CORRECTED PHASE OFFSET
 NAVSTAR 3 versus
 United States Naval Observatory MC #2
 CORRECTED PHASE DISCONTINUITY @ MJD 6625 (5 Apr. 1986)

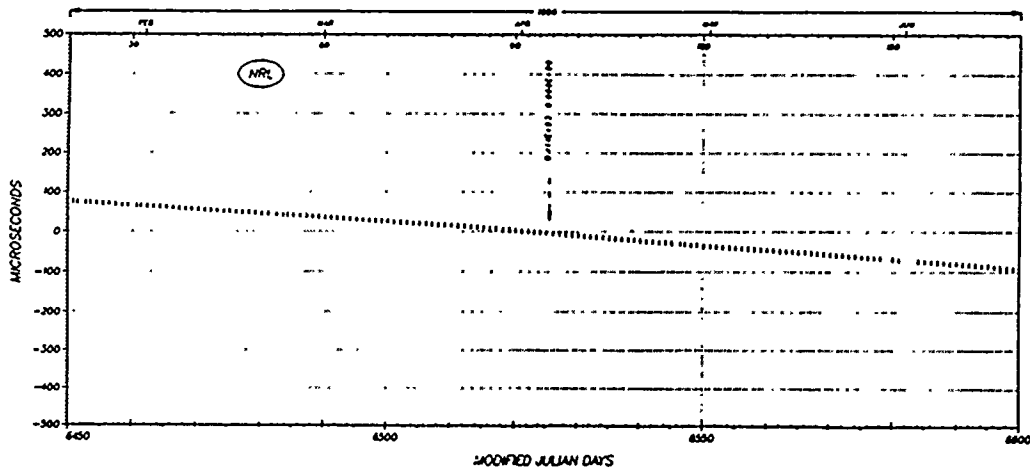


FIGURE 5

RUBIDIUM OSCILLATOR (NO 19) FREQUENCY OFFSET
 NAVSTAR 3 versus
 United States Naval Observatory MC #2
 -175 pp10(14) FREQUENCY BREAK @ MJD 6613

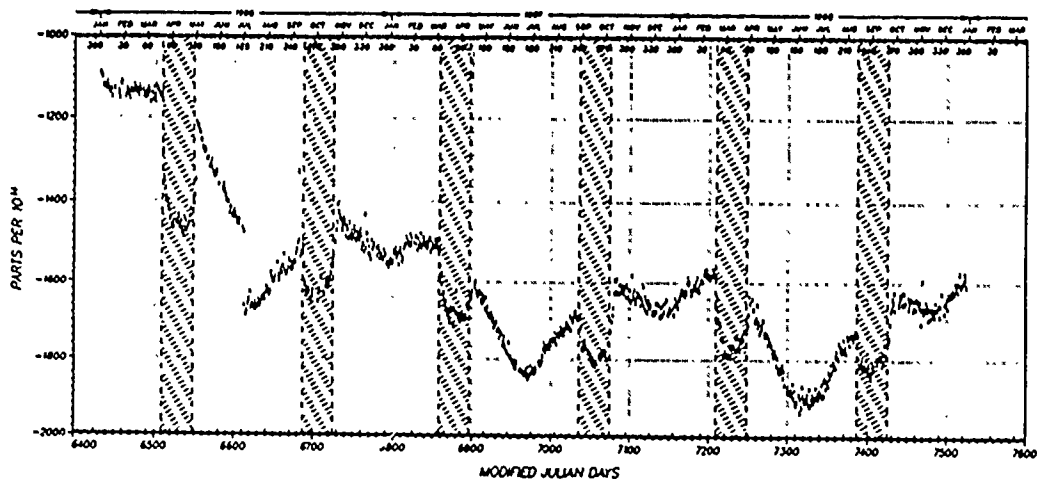


FIGURE 6

RUBIDIUM OSCILLATOR (NO.19) CORRECTED PHASE OFFSET
 NAVSTAR 3 versus
 United States Naval Observatory MC #2

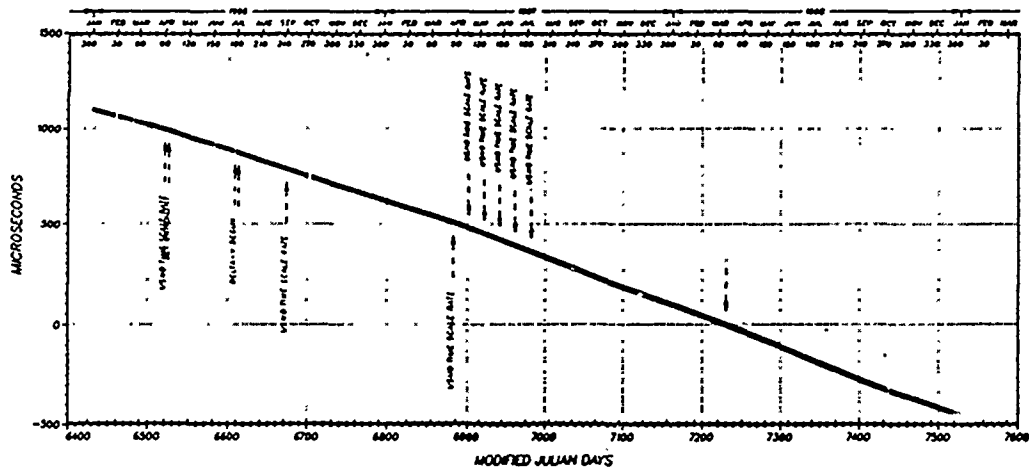


FIGURE 7

RUBIDIUM OSCILLATOR (NO.19) CORRECTED PHASE OFFSET
 NAVSTAR 3 versus
 United States Naval Observatory MC #2

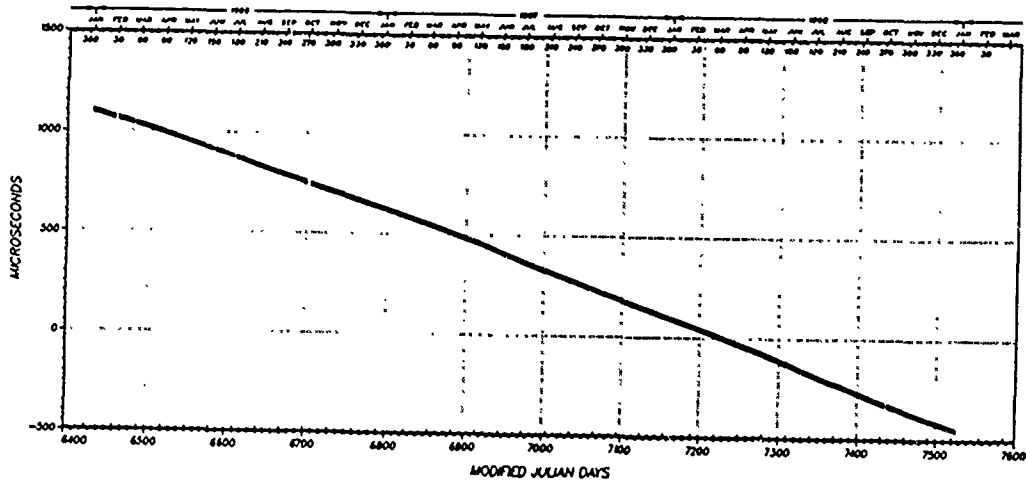


FIGURE 8

RUBIDIUM OSCILLATOR (NO. 19) CORRECTED FREQUENCY OFFSET
 NAVSTAR 3
 U.S. Naval Observatory MC #2
 ECLIPSE SEASONS HIGHLIGHTED

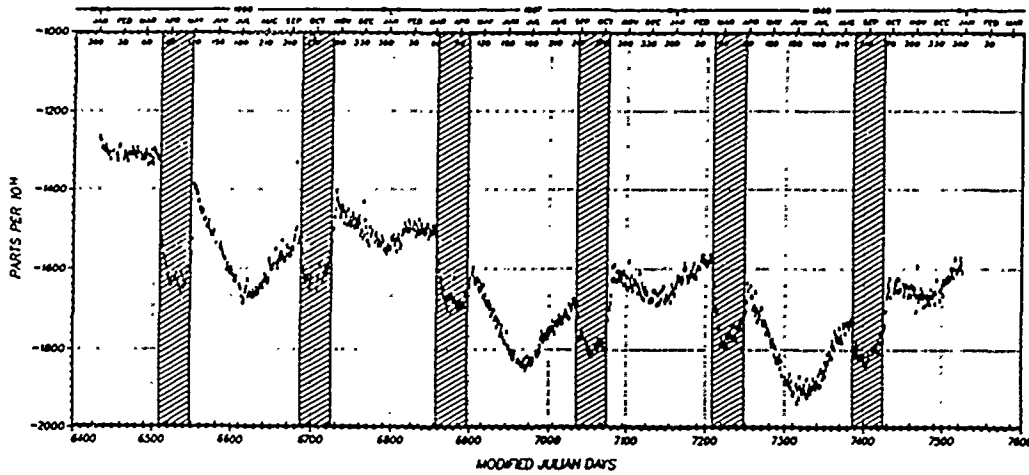


FIGURE 9

CESIUM OSCILLATOR (NO. 5) RAW PHASE OFFSET
 NAVSTAR 10 versus
 U.S. Naval Observatory MC #2

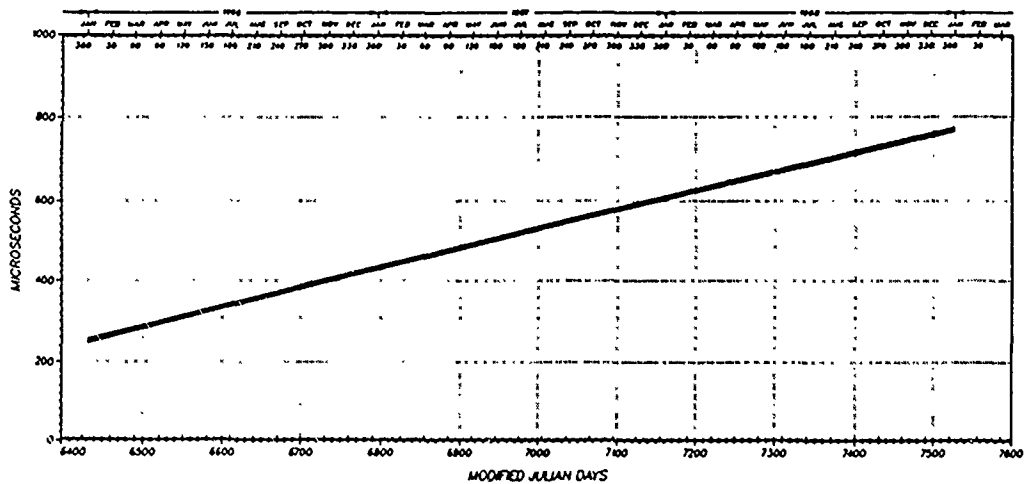


FIGURE 10

CESIUM OSCILLATOR (NO 5) CORRECTED PHASE OFFSET
NAVSTAR 10 versus
U.S. Naval Observatory MC # 2

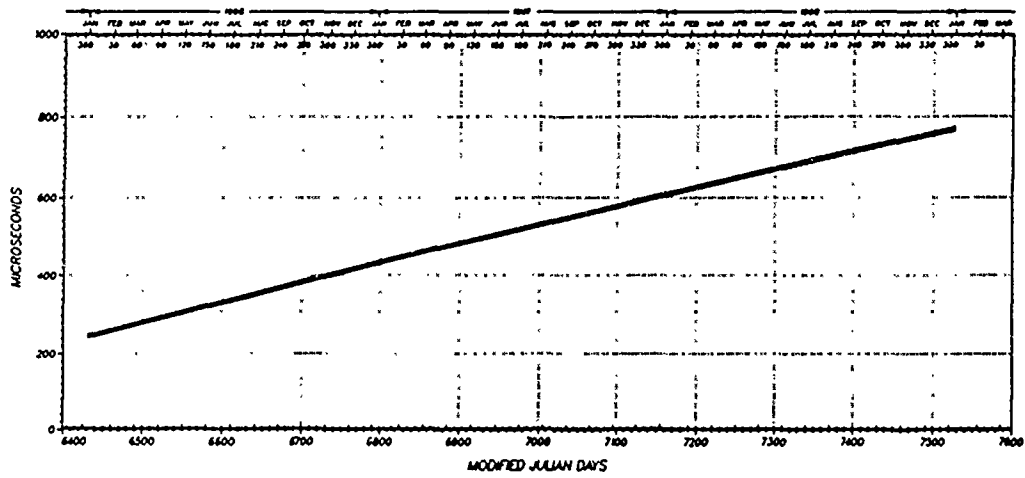


FIGURE 11

CESIUM OSCILLATOR (NO 5) CORRECTED FREQUENCY OFFSET
NAVSTAR 10 versus
U.S. Naval Observatory MC # 2
ECLIPSE SEASONS HIGHLIGHTED

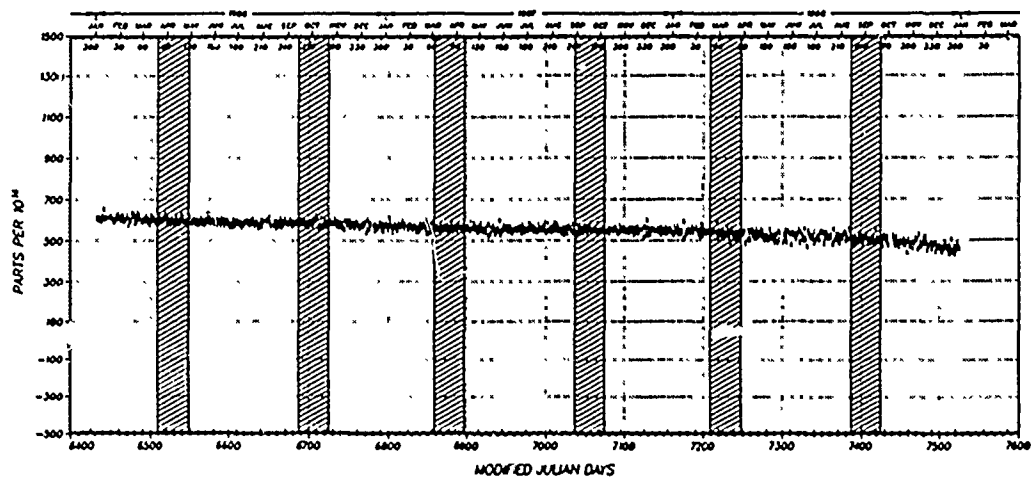


FIGURE 12

FREQUENCY STABILITY OF
NAVSTAR-SV-08 RUBIDIUM versus
U.S. Naval Observatory MC #2
PRESENTS EFFECT OF AGING vs NO-AGING CORRECTION

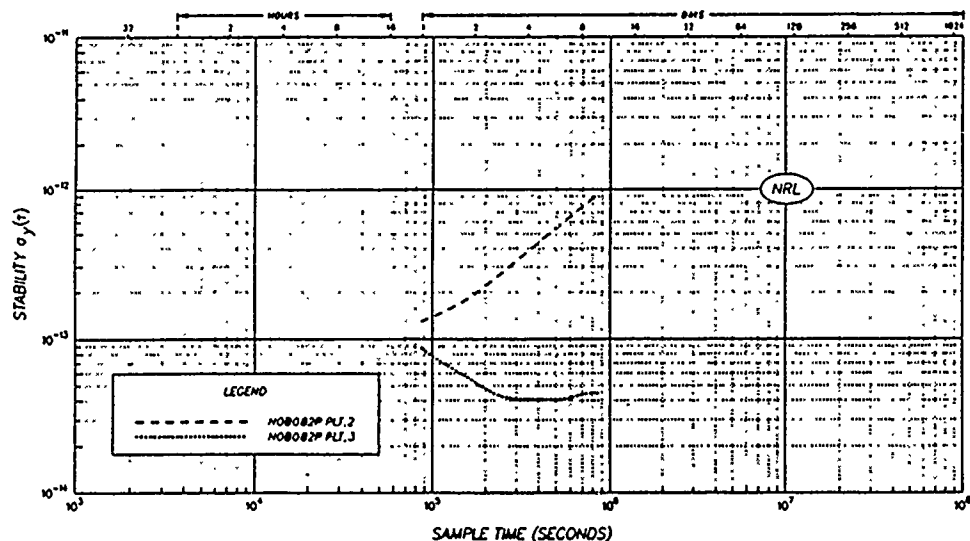


FIGURE 13

FREQUENCY STABILITY OF
NAVSTAR-SV-10 CESIUM CLOCK versus
U.S. Naval Observatory MC #2
PRESENTS EFFECT OF AGING vs NO-AGING CORRECTION

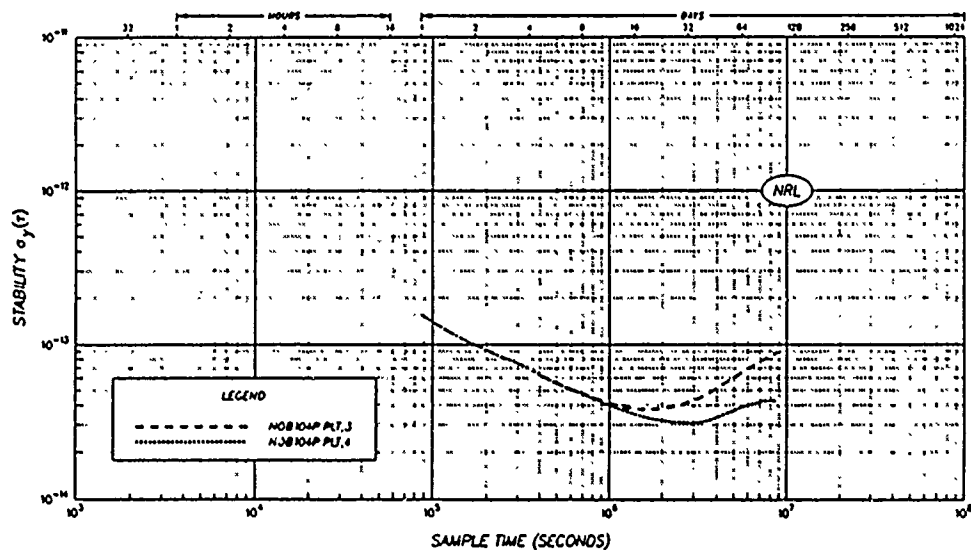


FIGURE 14

RUBIDIUM OSCILLATOR (NO.19) SAMPLE AGING RATE
NAVSTAR 3 versus
United States Naval Observatory MC #2

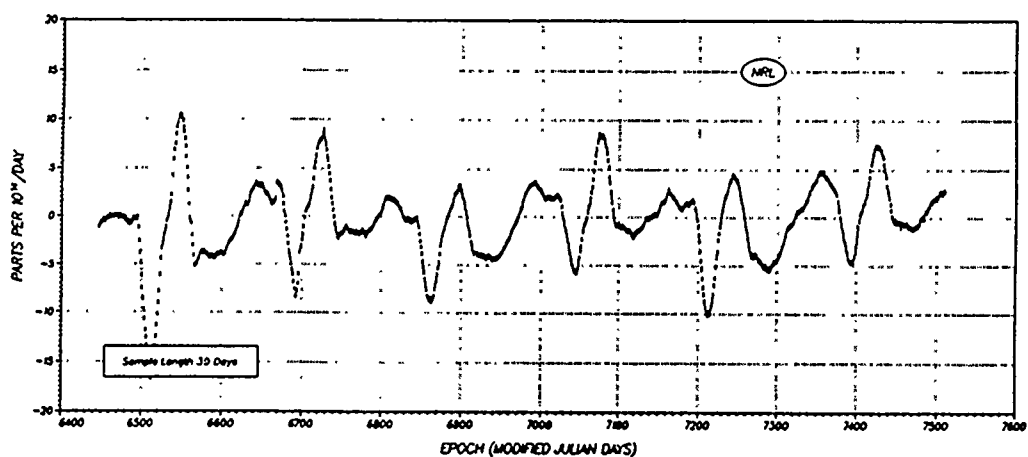


FIGURE 15

CESIUM OSCILLATOR (NO. 5) CORRECTED FREQUENCY OFFSET
NAVSTAR 10 versus
United States Naval Observatory MC #2
ECLIPSE SEASONS HIGHLIGHTED

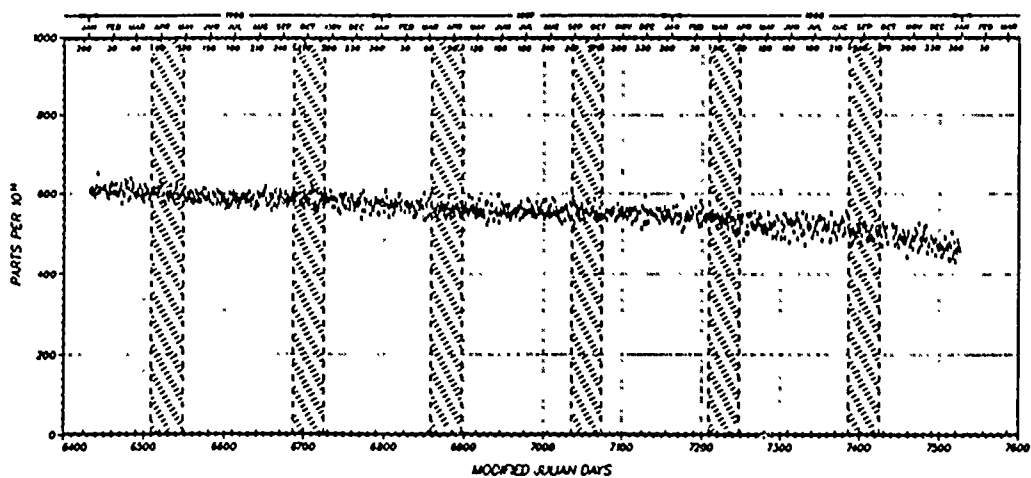


FIGURE 16

CESIUM OSCILLATOR (NO. 5) SAMPLE AGING RATE
NAVSTAR 10 versus
United States Naval Observatory MC #2

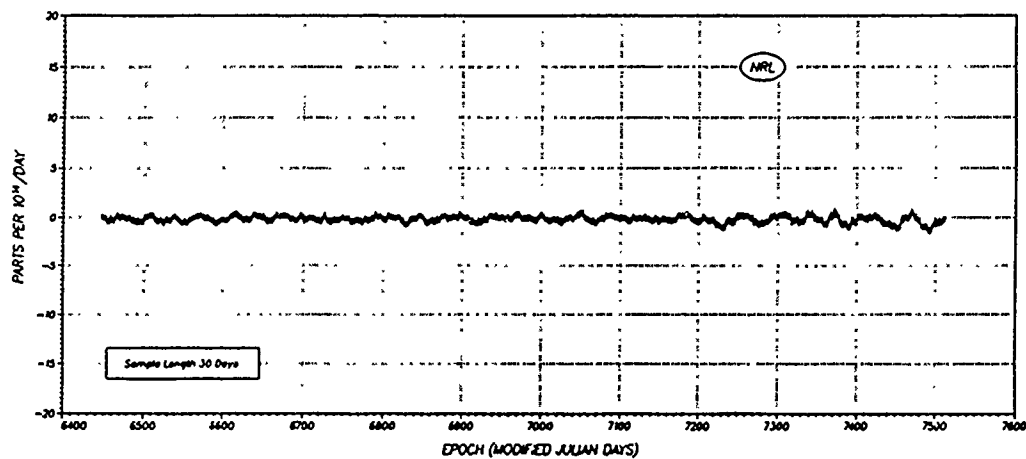


FIGURE 17

NRL NAVSTAR FREQUENCY STABILITY ANALYSIS
REFERENCE GROUND CLOCK: USNO
AGING CORRECTED

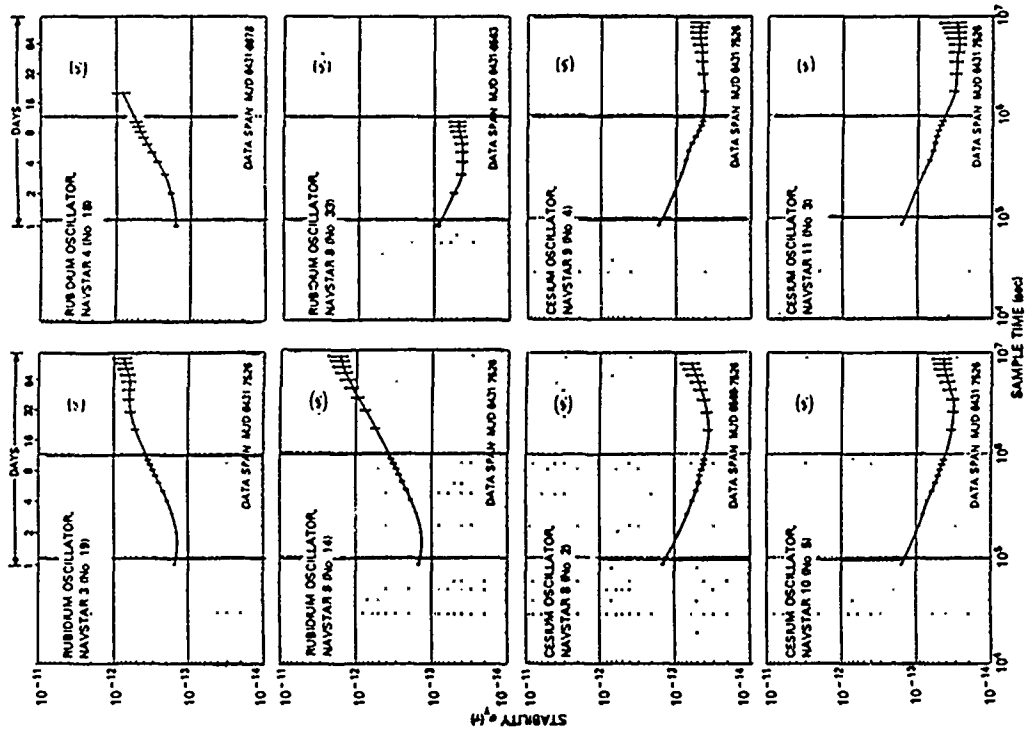


FIGURE 18

NRL NAVSTAR TIME PREDICTION UNCERTAINTY ANALYSIS
REFERENCE GROUND CLOCK: USNO

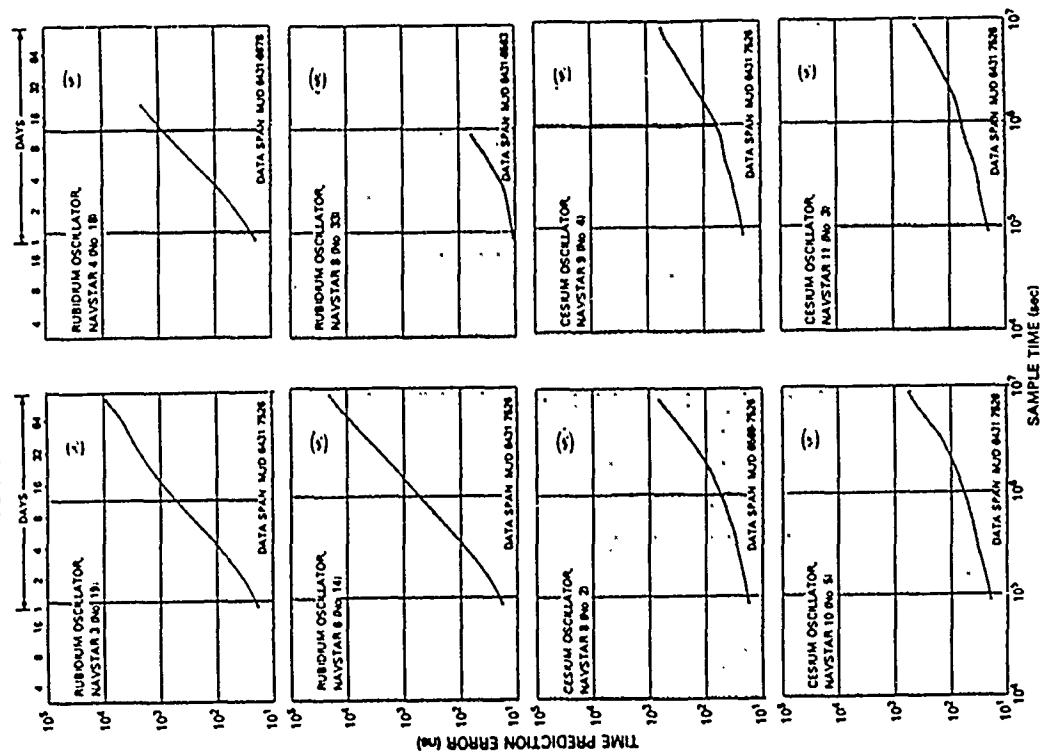


FIGURE 19

APPLICATION OF HYDROGEN-MASER TECHNOLOGY TO THE SEARCH FOR GRAVITATIONAL RADIATION

John D. Anderson, John W. Armstrong, and Eunice L. Lau*
Jet Propulsion Laboratory
California Institute of Technology
Pasadena, California 91109

Abstract

The Deep Space Network (DSN) is currently able to track distant spacecraft with a worldwide network of 70 m stations located near Goldstone, California; Tidbinbilla, Australia and Madrid, Spain. Hydrogen-maser timekeeping at all three sites makes possible a search for gravitational radiation at useful levels of sensitivity. We report on 10.5 days of data from the December 1988 opportunity with the Pioneer 10 spacecraft at a distance of 44.2 astronomical units (22052 s). A microwave link near 2.3 GHz was established with the spacecraft using one station of the DSN on the uplink and another on the downlink. The utilization of hydrogen masers at each station, plus the spacecraft transponder, effectively provided a one-arm interferometer for detecting gravitational radiation with a phase-coherent pathlength of 12.25 hr.

Starting with integrated cycle count of the Doppler shift as raw data, we sequentially differenced the data at a sample interval of 60 s and thereby generated a Doppler frequency record. Next, we removed trends caused by the relative motions of the spacecraft and the DSN stations in inertial space. The resulting residual frequency record was dominated by refraction of the 2.3 GHz signal in the Earth's atmosphere and ionosphere. By applying a regression analysis to a stratified atmospheric model, we reduced these refraction effects by more than an order of magnitude.

We show plots of the detrended Doppler residuals at the 60 second sample interval. The overall RMS residual is on the order of 2 mHz (10^{-12} in fractional frequency), but the major contributor to the noise at this level is the high-frequency component caused by the poor signal to noise ratio in the received signal from the distant Pioneer spacecraft. We illustrate this property by displaying the power spectral density of the reduced data. As expected, the high-frequency end of the spectrum is typical of thermal noise in the microwave receiver. On the other hand, the low frequency end is dominated by refraction of the signal by interplanetary plasma. The lowest noise is achieved for a period range from 200 s to 2000 s where the advantage of hydrogen-maser timekeeping is most apparent. In this region, the local mean amplitude of the noise is on the order of 10^{-14} in fractional frequency. This implies that any sinusoidal gravitational waves in the bandwidth are limited to a strain amplitude of 4×10^{-14} .

*This work was performed at the Jet Propulsion Laboratory, California Institute of Technology, under contract with the National Aeronautics and Space Administration

INTRODUCTION

From 1 December to 10 December 1988 the Deep Space Network (DSN), using three 70 m stations in California, Australia, and Spain respectively, provided nearly continuous radio tracking of the Pioneer 10 spacecraft at a single S-band frequency near 2.3 GHz. Each December Pioneer 10 is nearest solar opposition, an optimum location for minimizing the effects of the solar wind on the telecommunication link. Being a spinning spacecraft with a minimum of nongravitational forces, at a distance from Earth of 44.2 astronomical units (6 hr 7.5 min), it is uniquely suited for a search for gravitational radiation. In principle, gravitational waves (GW) crossing the solar system can be detected by a one-arm interferometer consisting of a phase-coherent radio link between Earth and a distant spacecraft. Such a link can be established with the Pioneer spacecraft by transmitting an S-band signal from one 70 m station and receiving the transponded signal at another station separated by intercontinental distances. Coherency is maintained by means of hydrogen masers at both stations.

As a GW detector, the one-arm interferometer at the distance of Pioneer 10 in 1988 has an effective pathlength of 12.25 hr, the round-trip light time (RTLTL) of the radio signal. Ideally it has a broad-band response and a sensitivity of parts in 10^{15} in the very-low-frequency (VLF) region of the GW spectrum from about 7×10^{-5} Hz (period \approx RTLTL/3) to 5×10^{-3} Hz, where the upper frequency limit is set by thermal noise in the microwave receiver, and the lower limit by the response function to gravitational radiation. But in fact the inherent stability provided by the hydrogen masers (parts in 10^{15}) does not determine the sensitivity limit for the radio link to the Pioneer spacecraft. Instead the useful level of sensitivity is limited by the propagation of the radio signal through both neutral and ionized media. Nevertheless by computing the power spectral density and Allan variance of the reduced data, we can show that the current experiments approach a level of sensitivity to spatial strain of 10^{-14} in a 10^{-6} Hz bandwidth over a limited GW band of 3×10^{-3} to 5×10^{-4} Hz. Even better sensitivities, by at least a factor of 10, are expected for future missions in the mid to late 1990's, at which time the experiments may approach the limiting accuracy of the DSN's frequency and timing system.

BACKGROUND

The idea of using the Doppler tracking of distant spacecraft to detect gravitational radiation originated with A. J. Anderson^[1] about 20 years ago. In that early period Anderson looked into the feasibility of the technique^[2] and concluded that it was worth pursuing. In the meantime, the theory of the interaction of gravitational radiation with a Doppler link was developed in 1975 by Estabrook and Wahlquist^[3]. Over the next few years the theory was developed further^[4,5,6,7] and over the last few years some experimental results have appeared^[8,9,10,11]. No detection has been reported, but some interesting limits have been set on a stochastic cosmic background of radiation^[8,10], burst sources^[8,11], and sinusoidal sources^[9,11]. The December 1988 opportunity with the Pioneer 10 spacecraft resulted in the best set of GW Doppler data to date. The distance to the spacecraft ranged from 22051 s on 1 December 1988 to 22087 s on 10 December 1988.

DATA

The raw Doppler data, delivered to us by the DSN on magnetic tape, consist of records of cumulative cycle count at a sample interval of 1 s. Before these data can be filtered for GW signals, some data reduction is required. First we use software of the Navigation Subsystem (NAV) at JPL to convert cycle count (phase) to a finite differenced record of frequency at a sample interval of 60 s. Because

the spatial strain of gravitational radiation is directly proportional to the Doppler frequency shift^[3], it is this differenced record that is most useful for GW analysis. Next, again using NAV software, we remove the Doppler motion effects from the data with the best Pioneer 10 orbit available, and with the best available models for the station locations, Earth rotation, and Earth polar motion. These geodynamic models are provided to the users of NAV software by the DSN as part of their multimission support.

During the initial data reduction with NAV software, we also introduce a bias into the frequency data to account for the rotation of the Pioneer spacecraft and its parabolic high-gain antenna. The rotating antenna introduces a Doppler shift of one cycle per rotation period. For the 1988 data, the spin period, as determined by the Pioneer Project from onboard photopolarimeter data, varies approximately linearly from 13.365123 s on 1 December to 13.366524 s on 10 December. Because the spacecraft spin also affects the physical motion of the antenna feed in space, a time-varying periodicity appears in the reduced data. However this small signal can easily be identified and removed, if necessary. In fact, because we know such a signal is present, it can be used to advantage in testing filtering algorithms for unknown small signals whose periods vary slowly with time. Such signals, with period decreasing with time, are expected from coalescing binary stars in the final stages of their radiation of gravitational waves^[12].

After we have reduced the data with NAV software, the dominant colored noise that remains is generated by refraction of the radio beam in the Earth's atmosphere and ionosphere. Though the DSN provides a seasonal tropospheric model to NAV, we find that over just ten days of data we can remove more of the effects of atmospheric refraction by applying a regression analysis to a parameterized stratified model of the atmosphere. Stratification assures that the stationary component of both the troposphere and ionosphere are accounted for. The resulting reduced data record, which is the starting point for a search for gravitational waves, is shown in Figure 1. The residual Doppler shift is plotted against time from 1 December, 1988. The average of the 60 s data at an averaging interval of 300 s is shown in Figure 2. The obvious reduction in data noise in Figure 2 results from an effective integration of the received signal beyond the point where high-frequency thermal noise dominates.

LIMITING NOISE SOURCES

The power spectrum of the reduced data of Figure 1 is shown in Figure 3, and the corresponding Allan variance is plotted in Figure 4. It is apparent that at high Fourier frequencies the noise is dominated by f^2 white phase noise. However the magnitude of the Allan variance is much too big to be attributable to the hydrogen masers, and it probably exceeds reasonable limits on the performance of the 70 meter stations. The thermal noise extrapolates to 5.3×10^{-14} at 1000 s. We suggest that this rather high level of thermal noise is caused by a very weak received signal from Pioneer 10 transmitting at 8 W into a 3 m parabolic antenna at a distance of 44.2 AU.

From the viewpoint of the search for gravitational radiation, the most serious limiting noise source is not the thermal component, but instead the $1/f$ flicker-frequency fluctuations. This component dominates beginning at about a 300 s integration time and continues indefinitely for longer integration times. The Allan variance is constant in this region with a limiting value of 2.8×10^{-13} . The source of the noise can be traced to random fluctuations in the solar wind^[11]. The effect of these plasma fluctuations on the Doppler data is proportional to the inverse square of the frequency of the radio transmission. Fortunately future gravitational wave searches will be conducted at higher frequency.

Two recent missions, Galileo to Jupiter and Magellan to Venus, have the capability of transmitting in

the X band on both the up and down links. The higher frequency, by a factor of $11/3$ over previous S-band experiments, would suggest an Allan variance of 2×10^{-14} for the equivalent plasma noise experienced by Pioneer 10 in 1988. Indeed early examination of Doppler data from Magellan at X band suggests a noise floor at this level. Being close to the Earth, Magellan has been tracked by the new 34 m High Efficiency (HEF) stations of the DSN. The Magellan data demonstrate that the overall HEF tracking system, including the hydrogen masers, is at least as good as 2×10^{-14} . On the other hand, if the noise in the Magellan data is dominated by plasma fluctuations near Earth, then the HEF system may perform even better, perhaps to parts in 10^{15} . Future X-band tracking of Galileo, after deployment of its high-gain antenna in May 1991, may reach this improved level of sensitivity, particularly in a more benign plasma environment.

CONCLUSIONS

We have shown that current GW Doppler experiments at S band are not limited by hydrogen-maser stability, nor even by the overall frequency and timing system of the DSN. Instead noise introduced on the tracking link by random fluctuations in the solar wind limit current experiments. In the future when similar experiments can be performed in the X band, using the Galileo orbiter for example, the noise from the solar wind may be reduced to a level where the limiting accuracy of the frequency and timing system will be important.

Though limited by plasma noise, the current GW search with the Pioneer 10 spacecraft should continue for as long as coherent tracking is possible. The Galileo spacecraft will not venture beyond the orbit of Jupiter, so its phase-coherent pathlength (maximum RTLTL of 8.5 AU) will severely limit its response to GW radiation in regions of the spectrum where Pioneer 10 is particularly sensitive (RTLTL ≈ 100 AU). The Pioneer 10/11 spacecraft are unique in their potential for detecting and characterizing broad-band gravitational radiation bursts with duration of a few hours.

By accumulating several days of phase-coherent data from Pioneer 10 near solar opposition, a limiting sensitivity of 2.8×10^{-13} in the Allan variance is not as bad as one might suppose. In Figure 5 we show the limiting sensitivity to spatial strain for sinusoidal signals within about 6800 independent spectral bins. These amplitudes, obtained by taking the square root of the power multiplied by the appropriate resolution bandwidth in Hz, represents our best estimate of the amplitudes of sinusoidal signals in the reduced data record of Figure 1. The RMS sensitivity to strain amplitude is about 1×10^{-14} . The corresponding 90% confidence limit for a real signal in these exponentially distributed spectral estimates is $4.1\sigma = 4 \times 10^{-14}$. A discussion of the relationship between the upper limit on the strain amplitude determined from the Doppler data and the corresponding upper limits on the GW excitation can be found elsewhere^[11].

Finally we point out that clock technology probably has important applications to other space experiments designed to detect gravitational radiation. In particular, spaceborne clocks could be used to establish multilink radio tracking between the Earth and one or more spacecraft, or very large microwave GW antennas utilizing several freeflying spacecraft could be entirely spaceborne^[13]. Though we have not addressed these issues here, we encourage the support of studies that do.

ACKNOWLEDGEMENTS

Reduction and analysis of the data are being supported by the Pioneer Project, NASA/Ames Research Center, as part of the Pioneer 10/11 Heliospheric Mission. We acknowledge essential assistance and

cooperation by the DSN at all phases of the experiment.

REFERENCES

1. A.J. Anderson, *Nature* 229, 547 (1971).
2. A.J. Anderson, in *Gravitazione Sperimentale*, Proceedings of the International Symposium, ed. B. Bertotti, Accademia Nazionale dei Lincei, Rome, 1977, p. 235.
3. F.B. Estabrook and H.D. Wahlquist, *GRG* 6, 439 (1975).
4. R.W. Hellings, *Phys. Rev. D* 17, 3158 (1978).
5. B. Bertotti and B.J. Carr, *Astrophys. Jour.* 236, 1000 (1980).
6. B. Mashhoon and L.P. Grishchuk, *Astrophys. Jour.* 236, 990 (1980).
7. R.W. Hellings, *Phys. Rev. D* 23, 832 (1981).
8. R.W. Hellings et al., *Phys. Rev. D* 23, 844 (1981).
9. J.D. Anderson et al., *Nature* 308, 158 (1984).
10. J.D. Anderson and B. Mashhoon, *Astrophys. Jour.* 290, 445 (1985).
11. J.W. Armstrong, F.B. Estabrook, and H.D. Wahlquist, *Astrophys. Jour.* 318, 536 (1987).
12. H.D. Wahlquist, *Gen. Rel. Grav.* 19, 1101 (1987).
13. R.F.C. Vessot, Proceedings of the XXVII COSPAR Plenary Meeting, Helsinki, Finland July 18-29, 1988, Symposium S.15, "Relativistic Gravitation," in the press.

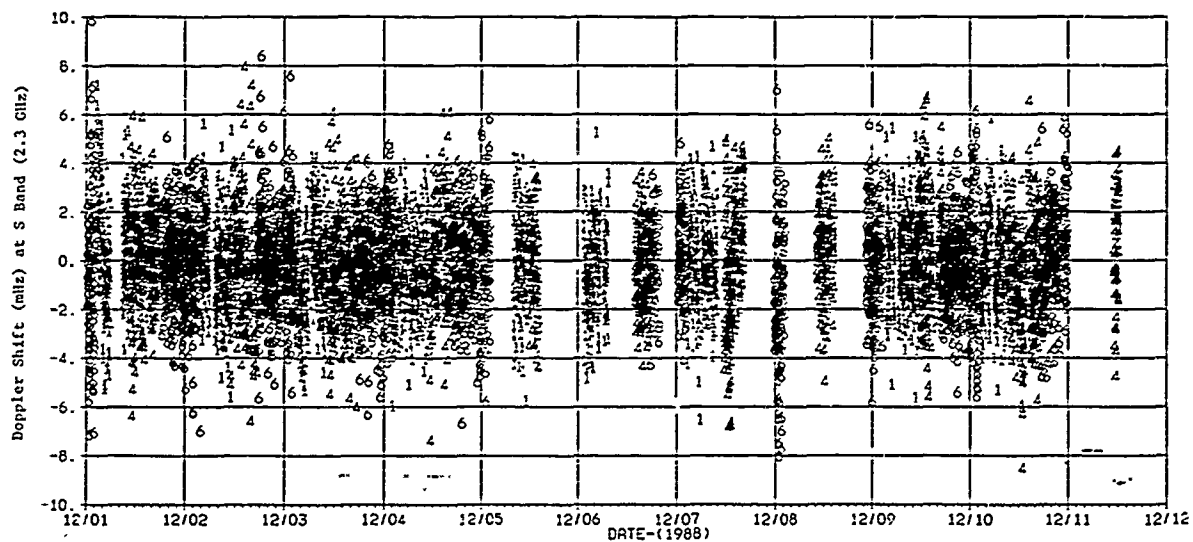


Figure 1: Reduced Data at a Doppler Integration Time of 60 Seconds

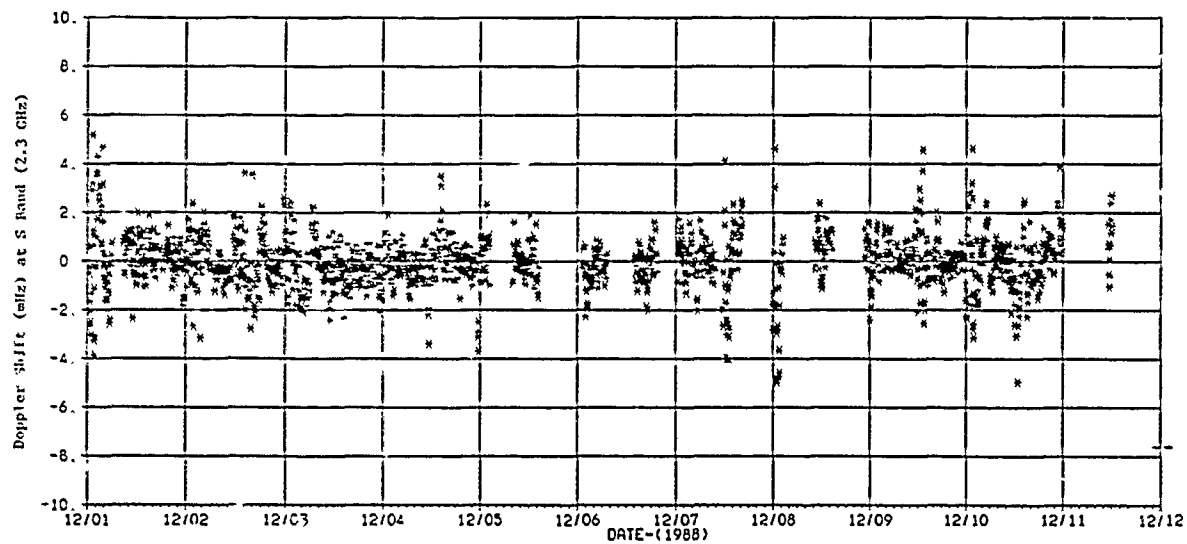


Figure 2: Reduced Data at a Doppler Integration Time of 300 Seconds

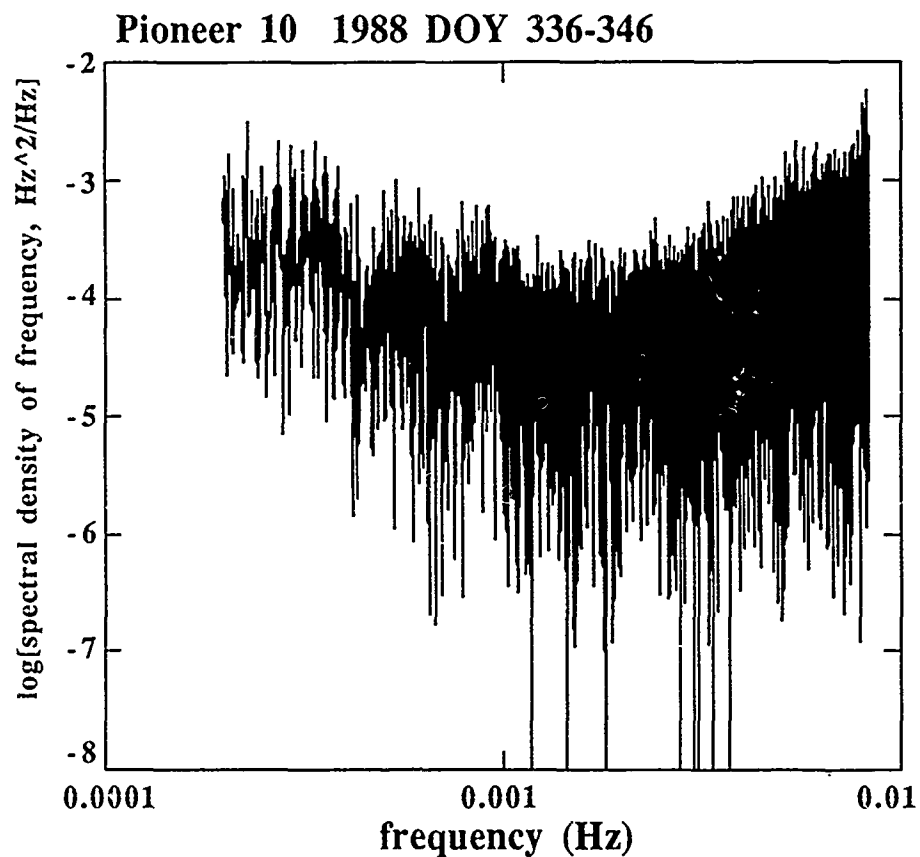


Figure 3: Power spectrum of frequency residuals.

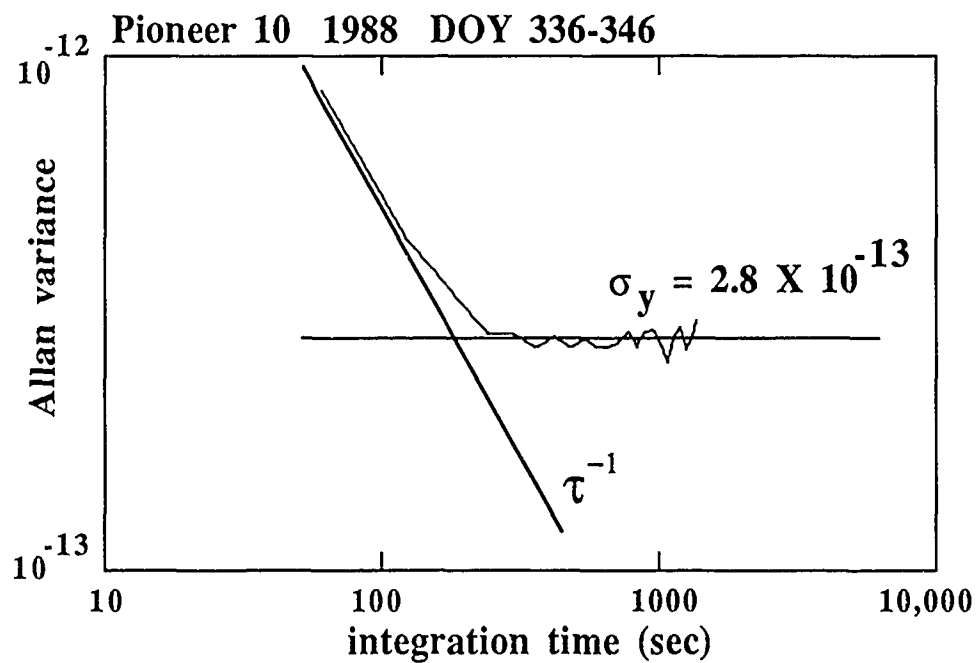


Figure 4: Allan variance of frequency residuals.

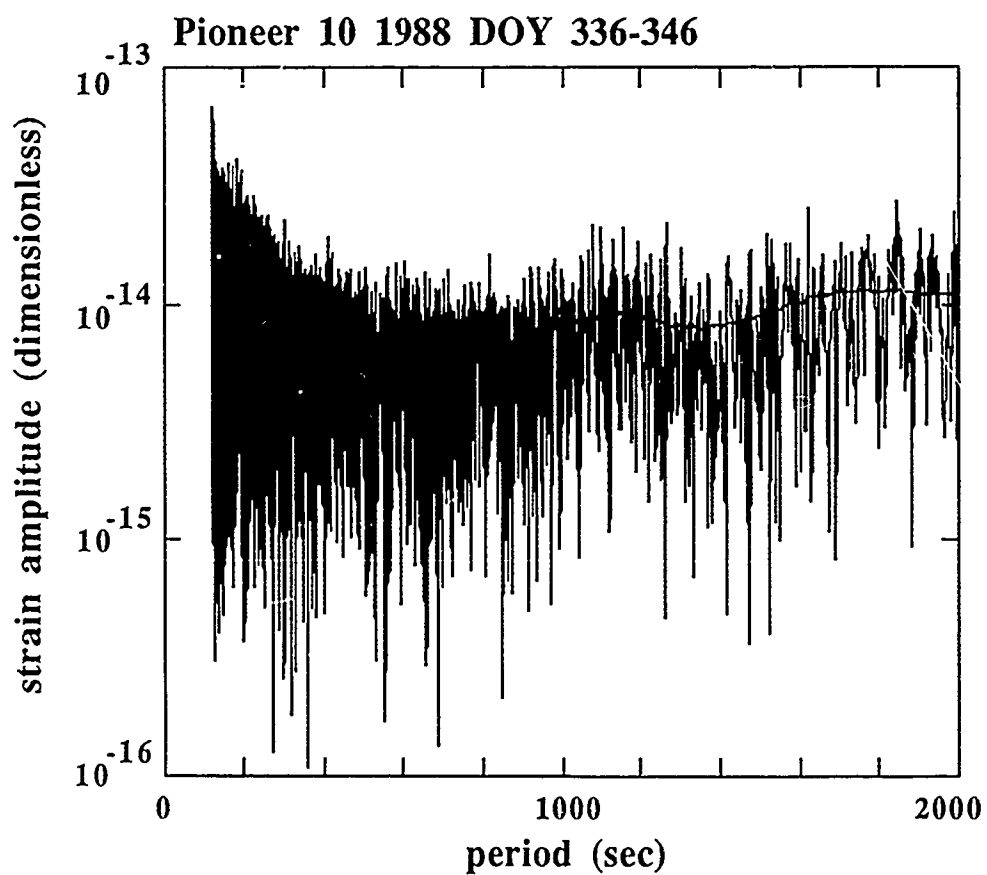


Figure 5: Equivalent sinusoidal strain amplitude versus Fourier period for the frequency residuals.

QUESTIONS AND ANSWERS

UNIDENTIFIED QUESTIONER: The gravitational radiation that you are looking for, is that from supernovas, black holes—what in particular are you looking for?

MR. ANDERSON: That is a good question. There are some predictions by the theorists about what we might see at these frequencies. The black hole is a possibility, the coalescing binary black hole is something that we might see, supernovas are at the higher frequencies, in the kilohertz region, while, as you see here, we are in the lower frequency range from 300 seconds out to thousands of seconds. The resonant bar detectors on the earth are better for detecting the supernova collapse that occur on the order of milliseconds. We would be looking for cataclysmic events, either galactic or extra-galactic. One of the things that we are considering is coalescing binaries. There would be a sinusoid of gravity radiation with the frequency of the sinusoid slowly changing as the binaries gradually coalesce. Those are the kinds of sources that we are examining.

SAME QUESTIONER: Can you derive vectors as to where the radiation is coming from?

MR. ANDERSON: Yes, in that cartoon there is a directional dependence on the shift. It affects both where the third pulse occurs, and the amplitudes of the three pulses because they have to sum to zero. That is, after the wave passes, there is no memory left in the Doppler link, you have to observe it as it passes. You might think of this as a single arm interferometer detecting a gravitational wave. You can make a determination of this angle, Θ , with some precision when you make a detection, which will determine a small circle on the sky. You can't get an unambiguous direction from a single arm interferometer. You need multi-arm interferometers for that. We might think of using space-borne Hydrogen Masers in the future for multi-arm interferometers, but for now we will be just able to describe the small circle on the sky.

REPORT ON THE TIMESCALE ALGORITHM TEST BED AT USNO

S. R. Stein *

Ball Communication Systems Division
Broomfield, CO 80038-1235

G. A. Gifford

Naval Research Laboratory
Washington, DC 20375-5000

L. A. Breakiron

U. S. Naval Observatory
Washington, DC 20392-5100

Abstract

A test bed is described for the evaluation of timescale algorithms. Test results for two algorithms (AT1 and KAS-1) using simulated data are presented. Both algorithms are optimum in the sense that, with the appropriate selection of clock weights, they are able to produce an output with minimum squared time prediction error in steady state for ensembles of clocks whose noises are all proportional to the noise of one of the members. The KAS-1 algorithm is also optimum during known transients such as startup, utilizes robust outlier detection, and has the property of time continuity. As a result of these improvements, KAS-1 is more suited to automated operation. Neither algorithm is optimum at all sampling times for ensembles of clocks having radically different noise processes. The KAS-1 algorithm and a clock simulator, both representing a new Kalman-filter approach, are documented herein.

INTRODUCTION

The Master Clock Upgrade Program at USNO is a SPAWAR- and USNO-funded project which tasks NRL and USNO to procure, monitor, and evaluate advanced frequency standards (trapped mercury ion devices and hydrogen masers) currently under development by others, devise and test a low-noise time-difference measurement system for all the cesium clocks and hydrogen masers at USNO; and develop a test bed for algorithms designed to generate an optimum timescale^[1]. In order to accomplish the latter, a software package is being developed by NRL that will be an integral part of the data collection and management system at USNO. The current version of the software that comprises the test bed is written in "Rocky Mountain Basic" for the IIP (Hewlett Packard) series 300 computer. The next version of the test bed package will be in the standard "C" language and will be less machine dependent. In addition to the standard clock analysis tools, the test bed will allow two algorithms to run simultaneously using the same data, which may be real or simulated. In the case of the latter, the output of an algorithm is compared to truth, where truth is known by definition.

As a joint project, USNO and NRL are making complementary contributions to the algorithm test bed. NRL's contribution is the experience in developing automated clock systems. USNO's contribution is the experience of and knowledge about maintaining a timescale.

*Work supported in part by Naval Research Laboratory, Contract Nos. N00173-87-M-J780, N00173-88-M-0031, N00173-88-M-5999, and N00173-88-M-G568

NRL is developing a number of automated clock systems for field use designed to have the following features:

1. the systems are fully automated clock ensembles with real-time output;
2. they can be steered to UTC (USNO) automatically via GPS;
3. their timescale algorithms permit the easy addition or deletion of clocks; and
4. the algorithms generate a timescale more uniform than any single clock in the ensemble.

For our purposes, we will define a timescale as a multifaceted procedure defining the scale of time by means of an algorithm that usually entails filtering or smoothing the data from two or more clocks or clock ensembles, and possibly steering one or more of the clocks toward the ensemble or steering them or the ensemble itself toward a more stable reference. We define a clock ensemble to be a procedure by which a single output is obtained from two or more clocks. Generally an ensemble performs better than its individual members. For a set of N clocks with equal noise processes, an output can be obtained that is \sqrt{N} more stable than a single clock, assuming the absence of intercorrelations and systematic errors. For a set of clocks whose noises are not proportional, the output is more complicated, as we shall see.

RESOURCES

As mentioned above, the test bed uses both simulated and real data. One source of the latter is the 2-picosecond-noise time measurement system developed by NRL for USNO that is connected to at least twenty high-performance cesium clocks, twelve hydrogen masers, and three mercury stored-ion devices (SIDs). The measurement system incorporates a phase-difference measurement subsystem developed by the first author while at NBS^[2]. The cesiums and masers provide phase-difference measurements, while the SIDs give frequency measurements. This mix of measurement types, a challenge to most ensembling procedures, is handled quite naturally by a Kalman-filter approach. In addition to these new data, there is available the old USNO database of several years from two masers and about fifty cesiums.

NRL has available for this effort a database of phase measurements from three masers, at least ten (some high-performance and some GPS-type) cesiums, and several rubidium clocks. In addition, NRL has a means of measuring the USNO Master Clock to the 50-picosecond level via the carrier frequency of a local television station using a system similar to one devised in France^[3]. This precise method of remote measurement will permit clocks several miles apart to be compared and allow the potential ensembling of clocks at both NRL and USNO.

The clock simulator employed in this test bed is a Kalman-filter type introduced in the next section. Simulated data have several advantages over real data:

1. any amount of data over any length of time can be generated;
2. data free of systematic errors or containing specific types of errors can be produced;
3. any number of clocks or combination of clock types can be modelled; and
4. most importantly, truth is known by definition.

To illustrate the latter, consider the simulation of a single clock, which involves the generation of a series of numbers that represent the accumulation of phase, usually over equal time intervals. The

numbers are produced with a clock model in mind and against which they may be verified statistically. To generate phase-difference data, two or more clocks are simulated simultaneously; one clock is then selected as the reference and its phase value at each measurement step is subtracted from the other clocks.

THE ALGORITHMS

The first algorithm tested was AT1, developed at NIST^[4,5]. The source code was provided by NBS (now NIST) in 1987. It is an ad hoc procedure designed for a steady-state ensemble of clocks manifesting the types of noise typical of cesium clocks. Exponential filters are used in the frequency estimation and weight calculation.

The second algorithm, called the Kalman Aiding Sources Algorithm (KAS-1), developed in 1987 by Ball Aerospace for NRL, uses Kalman-filter methodology. The KAS-1 algorithm was first employed in an automated clock ensemble at the Master Control Station of the Global Positioning System (GPS) at the Consolidated Space Operations Center (CSOC), Falcon AFB and was presented at the Third International Time Scale Algorithm Symposium held in Torino in 1988^[6]. This paper provides a more complete description as well as operational and simulated performance data. The KAS-1 approach is now being tested by NIST for use with AT1 and their results are described in the paper by Weiss and Weissert in these same proceedings. The KAS-1 algorithm was the first successful use of a Kalman filter in connection with clock ensembles, and this approach has been enhanced for use at USNO.

KALMAN APPROACH TO SIMULATING AND ENSEMBLING CLOCKS

Background

The ensembling method employed in KAS-1 uses one clock to form an initial estimate of time and uses each additional clock to improve or 'aid' the initial estimate. The same approach is used in the NIST AT1 timescale. The work described here improves and extends the AT1 algorithm in several areas: optimum filtering of all clock types, automatic startup and clock addition, robust outlier processing, time and frequency step detection, real time clock parameter estimation, and adaptive modelling.

The KAS-1 algorithm utilizes Kalman filters to provide the necessary state estimation and forecasting functions, resulting in estimates which are optimum in the minimum squared-error sense both in steady state and during transient conditions such as turn-on. Any mix of clocks can be included provided that the correct models and covariances are used. The use of the Kalman filter is a computational device and any other method of minimum squared-error state estimation based on the same assumptions and system dynamics would produce an identical result.

In contrast, the NIST AT1 algorithm uses fixed length exponential filters to perform frequency estimation. It is optimum only in steady state and requires external clock calibration for startup and addition of clocks to the ensemble.

Definition of the KAS-1 Ensemble

Each of the N clocks provides an independent forecast of the time of clock r , the reference clock, with respect to the ensemble at time $t + \delta$. These individual forecasts are called 'primitive' forecasts of the reference clock time. The primitive forecast of the time of the reference clock at $t + \delta$ using clock i is

$$u_{re}^i(t + \delta | t + \delta) = u_{ie}(t + \delta | t) + u_{ri}(t + \delta) \quad (1)$$

where $u_{ie}(t + \delta|t)$ is the forecast of the time of clock i with respect to the ensemble at time $t + \delta$ based upon the true state of clock i with respect to the ensemble at time t and $u_{ri}(t + \delta)$ is the clock r vs. clock i time difference.

The KAS-1 algorithm utilizes the natural definition

$$u_{re}(t + \delta) \equiv \sum_{i=1}^N a_i(t + \delta) u_{re}^i(t + \delta, t + \delta). \quad (2)$$

The weights, $a_i(t)$, may be chosen in any way subject only to the restriction that the sum of the weights is one. In the absence of noise, the ensemble definition is deterministic. However, in the presence of clock and measurement noise, the computational problem is to find the minimum squared-error estimate of the time of the reference clock with respect to the ensemble.

Computational Methodology for the KAS-1 Algorithm

One method of estimating ensemble time is to use the definition of Eq. 2 directly. Taking the estimate of both sides, one obtains

$$\hat{u}_{re}(t + \delta|t + \delta) = \sum_{i=1}^N a_i(t + \delta) [\hat{u}_{ie}(t + \delta|t) + \hat{u}_{ri}(t + \delta)]. \quad (3)$$

The estimate of the time of clock i with respect to the ensemble at time $t + \delta$ based on measurements through time t , the first term in the square brackets on the right side of Eq. 3, is calculated from the results of the last computation of the ensemble. Thus

$$\hat{u}_{ie}(t + \delta|t) = \hat{x}_{ie}(t|t) + \delta \hat{y}_{ie}(t|t) + \frac{\delta^2}{2} \hat{w}_{ie}(t|t) \quad (4)$$

where x is the phase before perturbation by white phase noise, y is the frequency and w is the frequency aging. The second term in the square brackets on the right side of Eq. 3 is the minimum square-error estimate of the clock pair difference state. This estimate is easily computed using the appropriate Kalman filter.

Kalman Filter for Computing Clock Difference States

The n parameters which are to be estimated are formed into an n dimensional state vector $\vec{x}(t)$. The system evolves from time t to time $t + \delta$ according to

$$\vec{x}(t + \delta) = \Phi(\delta) \vec{x}(t) + \Gamma \vec{s}(t + \delta|t) + \Phi(\delta) \vec{p}(t), \quad (5)$$

where the $n \times n$ dimensional state transition matrix $\Phi(\delta)$ embodies the system model, the n dimensional vector $\Gamma \vec{s}(t + \delta|t)$ contains the noise inputs to the system during the interval from t to $t + \delta$, and the n dimensional vector $\vec{p}(t)$ contains the control inputs made at time t . The state transition matrix is assumed to depend on the length of the interval, but not on the origin. Each element of $\vec{s}(t + \delta|t)$ is Normally distributed with zero mean and is uncorrelated in time, thereby generating a random walk in the elements of the state vector. The observation vector $\vec{z}(t)$ is described by the measurement equation

$$\vec{z}(t) = \mathbf{H}(t) \vec{x}(t) + \vec{v}(t). \quad (6)$$

The r observations made at time t are related linearly to the n elements of the state vector by the $r \times n$ dimensional measurement matrix $\mathbf{H}(t)$ and the r dimensional white noise vector $\vec{v}(t)$. Kalman and

Bucy defined a recursive procedure for estimating the next state, which requires the mean squared-error of the estimates from the true state to be minimum.

The error in the estimate of the state vector after the measurement at time t is $\hat{\mathbf{x}}(t|t) - \bar{\mathbf{x}}(t)$ and the error covariance matrix is defined to be

$$\mathbf{P}(t|t) = E \left\{ \left[\hat{\mathbf{x}}(t|t) - \bar{\mathbf{x}}(t) \right] \left[\hat{\mathbf{x}}(t|t) - \bar{\mathbf{x}}(t) \right]^T \right\}. \quad (7)$$

The diagonal elements of this $n \times n$ matrix are the variances of the estimates of the components of $\bar{\mathbf{x}}(t)$ after the measurement at time t . Next, the error covariance matrix just prior to the measurement at time $t + \delta$ is defined as

$$\mathbf{P}(t + \delta|t) = E \left\{ \left[\hat{\mathbf{x}}(t + \delta|t) - \bar{\mathbf{x}}(t + \delta) \right] \left[\hat{\mathbf{x}}(t + \delta|t) - \bar{\mathbf{x}}(t + \delta) \right]^T \right\}. \quad (8)$$

Finally, $\mathbf{R}(t)$ is the covariance matrix of the measurement noise and $\mathbf{Q}(t + \delta|t)$ is the covariance matrix of the system noise generated during the interval from t to $t + \delta$

$$\mathbf{R}(t) = E \left[\bar{\mathbf{v}}(t) \bar{\mathbf{v}}(t)^T \right] \quad (9)$$

$$\mathbf{Q}(t + \delta|t) = E \left[\bar{\mathbf{s}}(t + \delta|t) \bar{\mathbf{s}}(t + \delta|t)^T \right]. \quad (10)$$

The error covariance matrix evolves according to the system model

$$\mathbf{P}(t + \delta|t) = \Phi(\delta) \mathbf{P}(t|t) \Phi(\delta)^T + \Gamma \mathbf{Q}(t + \delta|t) \Gamma^T. \quad (11)$$

The new estimate of the state vector depends on the previous estimate and the current measurement

$$\begin{aligned} \hat{\mathbf{x}}(t + \delta|t + \delta) &= \Phi(\delta) \hat{\mathbf{x}}(t|t) + \Phi(\delta) \bar{\mathbf{p}}(t) \\ &+ \mathbf{K}(t + \delta) \left[\bar{\mathbf{z}}(t + \delta) - \mathbf{H}(t + \delta) \Phi(\delta) \hat{\mathbf{x}}(t|t) - \mathbf{H}(t + \delta) \Phi(\delta) \bar{\mathbf{p}}(t) \right], \end{aligned} \quad (12)$$

where the gain matrix, $\mathbf{K}(t + \delta)$, determines how heavily the new measurements are weighted. The optimum or Kalman gain, \mathbf{K}_{opt} , is determined by minimizing the "square of the length of the error vector," i.e., the sum of the diagonal elements (the trace) of the error covariance matrix

$$\mathbf{K}_{opt}(t + \delta) = \mathbf{P}(t + \delta|t) \mathbf{H}(t + \delta)^T \left[\mathbf{H}(t + \delta) \mathbf{P}(t + \delta|t) \mathbf{H}(t + \delta)^T + \mathbf{R}(t + \delta) \right]^{-1}. \quad (13)$$

Finally, the updated error covariance matrix is

$$\begin{aligned} \mathbf{P}(t + \delta|t + \delta) &= [\mathbf{I} - \mathbf{K}(t + \delta) \mathbf{H}(t + \delta)] \mathbf{P}(t + \delta|t) [\mathbf{I} - \mathbf{K}(t + \delta) \mathbf{H}(t + \delta)]^T \\ &+ \mathbf{K}(t + \delta) \mathbf{R}(t + \delta) \mathbf{K}(t + \delta)^T \end{aligned} \quad (14)$$

where \mathbf{I} is the identity matrix. If the optimum filter gain is used, Eq. 14 reduces to a simpler form:

$$\mathbf{P}(t + \delta|t + \delta) = [\mathbf{I} - \mathbf{K}_{opt}(t + \delta) \mathbf{H}(t + \delta)] \mathbf{P}(t + \delta|t). \quad (15)$$

Equations 11 through 15 define the Kalman filter, and so defined it is an optimal estimator in the minimum squared error sense. Each application of the Kalman recursion yields an estimate of the state of the system which is a function of the elapsed time since the last filter update. Updates may occur at any time. In the absence of observations, the updates are called forecasts. Simultaneous observations may be processed in parallel or serially, in any order, if the measurement noise is uncorrelated with

the process noise. The interval between updates, δ , is arbitrary and is specifically not assumed to be constant.

The estimates of the clock states relative to clock r are obtained from $N - 1$ independent Kalman filters. The four dimensional state vectors are:

$$\bar{x}_{ri}(t) = \begin{bmatrix} u_{ri}(t) \\ x_{ri}(t) \\ y_{ri}(t) \\ w_{ri}(t) \end{bmatrix}. \quad (16)$$

Every clock pair has the same state transition matrix

$$\Phi(\delta) = \begin{bmatrix} 0 & 1 & \delta & \delta^2/2 \\ 0 & 1 & \delta & \delta^2/2 \\ 0 & 0 & 1 & \delta \\ 0 & 0 & 0 & 1 \end{bmatrix} \quad (17)$$

and Γ matrix

$$\Gamma(\delta) = \begin{bmatrix} 1 & 1 & 0 & 0 \\ 0 & 1 & 0 & 0 \\ 0 & 0 & 1 & 0 \\ 0 & 0 & 0 & 1 \end{bmatrix}. \quad (18)$$

The system covariance matrices are:

$$Q^{ir}(t + \delta|t) = \quad (19)$$

$$\begin{bmatrix} S_{\beta}^{ir}(t)f_h & 0 & 0 & 0 \\ 0 & S_{\xi}^{ir}(t)\delta + S_{\mu}^{ir}(t)\delta^3/3 + S_{\zeta}^{ir}(t)\delta^5/20 & S_{\mu}^{ir}(t)\delta^2/2 + S_{\zeta}^{ir}(t)\delta^4/8 & S_{\zeta}^{ir}(t)\delta^3/6 \\ 0 & S_{\mu}^{ir}(t)\delta^2/2 + S_{\zeta}^{ir}(t)\delta^4/8 & S_{\mu}^{ir}(t)\delta + S_{\zeta}^{ir}(t)\delta^3/3 & S_{\zeta}^{ir}(t)\delta^2/2 \\ 0 & S_{\zeta}^{ir}(t)\delta^3/6 & S_{\zeta}^{ir}(t)\delta^2/2 & S_{\zeta}^{ir}(t)\delta \end{bmatrix}$$

where the clock pair spectral densities are the sum of the individual contributions from each of the clocks:

$$S^{ir} = S^i + S^r. \quad (20)$$

The white phase measurement noise is given by the measurement model:

$$\bar{z}_{ri} = H\bar{x}_{ri} + \bar{v}_{ri}, \quad (21)$$

where each time measurement is described by the same 4×1 row matrix

$$H_{ri} = (1 \ 0 \ 0 \ 0). \quad (22)$$

The updated difference states are given by Eq. 12, but only the time state is used in the following steps of the ensemble calculation.

Calculation of the Weighted Average of the Times of the Clocks

Although it is not necessary, a Kalman filter is used to calculate the 'weighted average' of the N primitive estimates of the time of clock r . Kalman filters are normally applied to dynamic systems, but they are equally relevant to the static problem of 'averaging' the N estimates of the time of clock

r at sample time t . The choice of the Kalman filter methodology is motivated by the fact that it deals with the clock weights in an easy and natural manner and automatically provides scale factors for use in outlier deweighting. The deweighting scheme is similar to one developed by Percival^[7] for maximum likelihood estimation, but it has been adapted for use with the Kalman methodology. It is desirable for the resulting estimator (with outlier deweighting) to be both efficient and robust. For certain types of outliers, the method used here is both more efficient and more robust than rejection rule methods.

The state transition matrix is a scalar and is equal to one since the system does not evolve between 'observations'. The 'measurement' model is

$$u_{re}(t) = u_{re}^i(t|t) + v_i(t) \quad (23)$$

where the random shocks $v_i(t)$ have variances $\sigma_i^2(t)$ and are used to set the weights of the clocks. For example, $v_i(t) = v(t)$ independent of the clock number produces equal weighting. On the other hand, setting $v_i(t)$ equal to the estimated time prediction error of clock i since the last ensemble calculation produces an ensemble with minimum time prediction error. Note that the latter operating condition is not necessarily the best since the clocks may not be perfectly modeled.

It is possible to solve for the Kalman gain in closed form:

$$K_i(t) = \frac{\frac{1}{\sigma_i^2(t)}}{\sum_{j=1}^i \frac{1}{\sigma_j^2(t)}} \quad (24)$$

However, the full Kalman recursion is more suited to the deweighting of outliers. Since a scalar is being estimated, $\Phi = H = 1$, $Q = 0$, and $R = \sigma_j^2(t)$. In order to deweight outliers, a robust initial guess is required for the time of clock r with respect to the ensemble after the measurement at time $t + \delta$. The median¹ of the available estimates is a good choice since it is not unduly affected by outliers.

$$\hat{u}_{re}(t + \delta|t + \delta)_1 = \text{median} \{ u_{re}^i(t + \delta|t + \delta) \} \quad (25)$$

This estimate is subsequently refined by using the information in the remaining primitive estimates. The primitive estimates are sorted according to their deviation from the median so that clock $I(k)$ is the k^{th} nearest the median and $I(1)$ is the median. To start the Kalman recursion one needs to initialize the state and the covariance matrices. Having just completed the estimate of the ensemble time for the measurements taken at time t , the ensemble calculation for time $t + \delta$ commences by setting the initial estimate of the time of clock r vs. the ensemble equal to the 'primitive estimate' using clock $I(1)$. The starting point is important only for outlier deweighting. A 'robust' initial estimate for the time of clock r is required and using one of the primitive estimates avoids biasing the final estimate. The first estimate must be robust because it cannot be deweighted. This implies no loss of generality since it is not possible to detect an outlier with only one clock and it is not possible to assign responsibility for an outlier time difference measurement with only two clocks. That is, there is one more cycle in the Kalman recursion than is needed for outlier deweighting. The recursion begins by setting the initial state estimate:

$$\hat{u}_{re}(t + \delta|t + \delta)_1 = \hat{u}_{re}^{I(1)}(t + \delta|t + \delta).$$

¹When the number of points is odd, the number of observations larger than the median equals the number of observations smaller than the median. When the number of observations is even, the median is one of the two central observations. Other definitions of the median are sometimes used.

The covariance matrix prior to processing the measurement of clock $I(2)$ is

$$P(I(2)|I(1)) = \sigma_{I(1)}^2$$

and the optimum Kalman gain is

$$K_{I(2)} = \frac{P(I(2)|I(1))}{P(I(2)|I(1)) + \sigma_{I(2)}^2}.$$

At this point in the calculation, the standard Kalman methodology must be modified to account for the possible presence of outlier observations. If primitive estimate $I(2)$ does not come from the distribution included in the physical model, then it should not be used to determine the Kalman state estimate. In order to preserve the continuity of the state estimates, measurements should not be rejected precipitously, rather the Kalman gain should be reduced as the measurement departs from expectation. A non-optimum Kalman gain is calculated from

$$K'_{I(2)} = \frac{\psi_{HA}[q_{I(2)}]}{q_{I(2)}} K_{I(2)} \quad (26)$$

where

$$\psi_{HA}(q) = \begin{cases} q & \text{if } |q| \leq a \\ \frac{a}{b-a} \left[\frac{bq}{|q|} - q \right] & \text{if } a < |q| \leq b \\ 0 & \text{if } |q| > b \end{cases} \quad (27)$$

is Hampel's ψ function and

$$q_{I(2)} = \frac{\hat{u}_{rc}^{I(2)}(t + \delta|t + \delta) - \hat{u}_{rc}(t + \delta|t + \delta)_1}{s_2}. \quad (28)$$

The scale factor, s_2 , is discussed later. The second step in the Kalman recursion is completed by using the modified Kalman gain to calculate the updated covariance matrix according to the formula for non-optimum Kalman gain

$$P[I(2)|I(2)] = [1 - K'_{I(2)}]^2 P[I(2)|I(1)] + [K'_{I(2)}]^2 \sigma_{I(2)}^2 \quad (29)$$

and to calculate the new estimate of the time of clock 1 with respect to the ensemble

$$\hat{u}_{rc}(t + \delta|t + \delta)_2 = (1 - K'_{I(2)}) \hat{u}_{rc}(t + \delta|t + \delta)_1 + K'_{I(2)} \hat{u}_{rc}^{I(2)}(t + \delta|t + \delta). \quad (30)$$

The recursion continues in this way until all the measurements are processed. The computation for clock $I(j)$ starts by setting

$$P[I(j)|I(j-1)] = P[I(j-1)|I(j-1)].$$

The first time the recursion is performed, each of the constants s_j is set equal to the maximum of the σ_j . This prevents the high noise level of the median from causing a very quiet clock to be downweighted. Next, the computation is repeated setting the initial estimate of the time of the reference with respect to the ensemble equal to the primitive estimate closest to the result of the previous computation and setting s_j equal to the second largest σ_j or its own prediction error, whichever is larger. The recursion is repeated until each estimate is processed using the σ_j of the corresponding clock. If any of the clocks were downweighted in this process, then the new estimate of the time of clock r with respect

to the ensemble is compared with the previous estimate and the process is repeated until the change in the estimate between iterations is negligible. When there are no outliers, this recursive solution is identical to Eq. 3. In the presence of outliers, it is still a weighted average of the estimates from the individual clocks. The weights of the clocks are given by

$$a_{I(j)} = K'_{I(j)} \prod_{i=j+1}^N (1 - K'_{I(i)}) \quad (31)$$

where $K'_{I(1)} \equiv 1$. To preserve the reliability of the ensemble, one usually limits the weights of each of the clocks to some maximum value, a_{max} . A deweighting factor, κ , may be calculated to accomplish this goal by starting at index $I(N)$ and proceeding to index $I(1)$ so that $\kappa K'$ are new weights which do not exceed the limit. Each time the Kalman recursion is used to estimate the time of clock r , the previously calculated κ is used. The process rapidly converges to a stable value.

Finally, the times of the remaining clocks are computed from the time of clock r and the estimated time differences. Thus

$$\hat{u}_{ie}(t + \delta|t + \delta) = \hat{u}_{re}(t + \delta|t + \delta) - \hat{u}_{ri}(t + \delta|t + \delta). \quad (32)$$

Calculation of the Frequency and Frequency Aging States

The time of clock i relative to the ensemble is used as input to a Kalman filter that estimates the frequency and frequency aging of clock i relative to the ensemble. This filter uses the state transition matrix of Eq. 17. It is assumed that the ensemble is so large that its contribution to the noise can be accounted for to first order only. Based on this assumption of a large ensemble, the system covariance matrix is:

$$Q^{ie}(t + \delta|t) = Q^i(t + \delta|t). \quad (33)$$

and

$$\Gamma(t)^{ie} = \begin{bmatrix} 1 - a_i(t) & 1 - a_i(t) & 0 & 0 \\ 0 & 1 - a_i(t) & 0 & 0 \\ 0 & 0 & 1 & 0 \\ 0 & 0 & 0 & 1 \end{bmatrix} \quad (34)$$

The change in Γ from the case of a single clock or clock pair reflects the fact that each clock is a member of the ensemble with respect to which it is measured.

The measurement model is noiseless since the calculated times of the N clocks are used as pseudomeasurements. This procedure guarantees that the Kalman filter reproduces the phase estimates obtained directly from the ensemble definition while simultaneously estimating consistent values of the frequency and frequency aging.

Adaptive Modelling Parameter Estimation

A variance analysis technique compatible with irregular observations has been developed^[8]. The variance of the innovation sequence of the Kalman filter is analyzed to provide estimates of the parameters of the filter. The result is

$$E [\bar{v}(t + \delta)\bar{v}(t + \delta)^T] = H(t + \delta)P(t + \delta|t)H(t + \delta)^T + R(t + \delta). \quad (35)$$

Like the Allan variance analysis, which is performed on the unprocessed measurements, the innovation variance analysis requires only a limited memory of past data. However, the forecasts provided by the Kalman filter allow the computation to be performed at arbitrary intervals once the algebraic form of the innovation variance has been calculated. Adaptive modelling begins with an approximate Kalman gain, $\hat{\mathbf{K}}$. As the state estimates are computed, the variance of the innovations on the left side of Eq. 35 is also computed. The right-hand side of this equation is written in terms of the actual filter element values (covariance matrix elements) and the theoretical parameters. Finally, the equations are inverted to produce improved estimates for the parameters.

Using the autocovariance function to solve for the parameters is inappropriate here, because the autocovariance function is highly correlated from one lag to the next and the efficiency of data utilization is therefore small. Instead, only the autocovariance of the innovations for zero lags, *i.e.*, the variance of the innovations, is used. The variance is given by

$$\begin{aligned} E [\tilde{\nu}_{ie}(t+\delta)\tilde{\nu}_{ie}(t+\delta)^T] = & \mathbf{P}_{11}^i(t|t) + 2\delta\mathbf{P}_{12}^i(t|t) + \delta^2\mathbf{P}_{13}^i(t|t) \\ & + \delta^3\mathbf{P}_{23}^i(t|t) + \delta^2\mathbf{P}_{22}^i(t|t) + \frac{\delta^4}{4}\mathbf{P}_{33}^i(t|t) \\ & + [S_{\xi}^i(t)\delta + S_{\beta'}^i(t)f_h][1 - a_i(t)]^2 + S_{\mu}^i(t)\frac{\delta^3}{3} + S_{\zeta}^i(t)\frac{\delta^5}{20} + \sigma_{v_{xi}}^2(t). \end{aligned} \quad (36)$$

It is assumed that the oscillator model contains no hidden noise processes. This means that each noise in the model is dominant over some region of Fourier frequency space. The principle of parsimony encourages this approach to modelling. Inspection of Eq. 36 leads to the conclusion that each of the parameters dominates the variance of the innovations in a unique region of prediction time interval, δ , making it possible to obtain high-quality estimates for each of the parameters through a process of bootstrapping.

For each parameter to be estimated, a Kalman filter is computed using a subset of the data chosen to maximize the number of predictions in the interval for which that parameter makes the dominant contribution to the innovations. The filters are designated 0 through 4, starting with 0 for the main state estimation filter which runs as often as possible. Each innovation is used to compute a single-point estimate of the variance of the innovations for the corresponding δ . Substituting the estimated values of the remaining parameters, Eq. 36 is solved for the dominant parameter, and the estimate of that parameter is updated in an exponential filter of appropriate length. If the minimum sampling interval is too long, it may not be possible to estimate one or more of the parameters. However, there is no deleterious consequence of this situation, since a parameter that cannot be estimated is not contributing appreciably to the prediction errors. It is not necessary to use separation of variances to estimate individual clock parameters since the Γ matrix takes into account the first order clock-ensemble correlations.

The KAS-1 algorithm is adaptive in two ways. First, the clock noise parameters are updated after each cycle of the recursion and used during the next cycle of the recursion. Second, the clock weights are updated after each cycle based on the real time parameter estimates or the measured time prediction errors. For minimum time prediction errors, the variances (inverse weights) needed for the calculation of the time of the reference clock with respect to the ensemble are

$$\sigma_i^2 = S_{\beta'}^i(t)f_h + S_{\xi}^i(t)\delta + S_{\mu}^i(t)\delta^3/3 + S_{\zeta}^i(t)\delta^5/20. \quad (37)$$

Kalman Clock Simulation Algorithm

The algorithm presented here may be used to compute the simulated state of a precision clock at any time in the future based on the current state of the clock and appropriate noise inputs. White phase measurement noise, white phase additive noise, white frequency noise, random walk frequency noise, and random walk frequency aging noise may all be included. Although the algorithm is quite simple, it has several advantages over the ARIMA technique described by Barnes^[9]. The time interval between observations is included explicitly so that a time series of observations separated by varying intervals may be created. In addition, the parameters are easily calculated from the power spectral densities of the noise. These physical parameters are the same ones required for the Kalman analysis of the clock. The final advantage is that the simulated clock noise for each state is appropriately correlated with the noise on other states, as should be the case since the physical model for a clock is an integrator.

The simulator is based on the same equation of motion for a clock, Eq. 5, used in Kalman filter analysis. Each element of $\bar{s}(t + \delta|t)$ is Normally distributed with zero mean and is uncorrelated in time. The problem is to generate simulated noise vectors, $\bar{s}(t + \delta|t)$, having the desired covariance, given in Eq. 19. The spectral densities which appear in the system covariance matrix may be written in terms of the standard oscillator noise coefficients. The values and units are shown in Table 1.

Table 1: Relationship between spectral densities and h coefficients

Spectral density	h coefficient	units
$S_{\beta'}(t)$	$(2\pi)^{-2}h_2(t)$	seconds ³
$S_{\xi}(t)$	$h_0(t)$	seconds
$S_{\mu}(t)$	$(2\pi)^2h_{-2}(t)$	seconds ⁻¹
$S_{\zeta}(t)$	$(2\pi)^4h_{-4}(t)$	seconds ⁻³

The goal is to derive a solution for the noise vector, \bar{s} , in the form

$$\bar{s} = \Lambda \bar{r}, \quad (38)$$

where \bar{r} is a four dimensional vector of Normal deviates with unity variance whose elements are uncorrelated with each other and uncorrelated in time. Multiplying this equation by its transpose and taking the expectation value, one finds

$$Q(t + \delta|t) = \Lambda \Lambda^T. \quad (39)$$

Since the elements of the state vector are successive integrals, Λ is an upper right half triangular matrix. Equating the corresponding elements of the previous equation, one finds

$$\Lambda(t + \delta|t) = \quad (40)$$

$$\begin{bmatrix} \sqrt{S_{\beta'}(t)}f_h & 0 & 0 & 0 \\ 0 & \sqrt{S_{\xi}(t)\delta + \frac{S_{\mu}(t)\delta^3}{12} + \frac{S_{\zeta}(t)\delta^5}{720}} & \frac{\delta}{2}\sqrt{S_{\mu}(t)\delta + \frac{S_{\zeta}(t)\delta^3}{12}} & \frac{\delta^2}{6}\sqrt{S_{\zeta}(t)\delta} \\ 0 & 0 & \sqrt{S_{\mu}(t)\delta + \frac{S_{\zeta}(t)\delta^3}{12}} & \frac{\delta}{2}\sqrt{S_{\zeta}(t)\delta} \\ 0 & 0 & 0 & \sqrt{S_{\zeta}(t)\delta} \end{bmatrix}.$$

The algorithm is easily mechanized. A random number generator function normally produces deviates uniformly distributed over the unit interval. They may be converted to Normally distributed deviates using one of the standard procedures. Four Normal deviates are then combined to form the noise vector \vec{r} and multiplied by Λ to produce the \vec{s} vector needed to evaluate Eq. 5 for the next clock state. The element $u(t)$ is the desired simulated clock time state. The simulated clock measurement is obtained by adding white measurement noise, $v(t)$, to $u(t)$.

$$z(t) = u(t) + v(t) \quad (41)$$

TEST RESULTS

The two algorithms were run simultaneously in order to intercompare them. Only the 1987 version of the KAS-1 algorithm (i.e. without automatic parameter estimation and mixed-mode measurement capability) was available for testing.

Figure 1 displays the difference between the two algorithms, in the sense AT1 - KAS-1, for an ensemble of eleven equally weighted clocks with no data rejection. The two algorithms are seen to be essentially identical in steady state on the long term. However, as mentioned above, AT1 is not designed for the natural handling of transients, while KAS-1 is still optimal in such situations.

In Figure 2, AT1 was allowed to exercise its 3-standard-deviation rejection criterion, while the KAS-1 algorithm was forced to accept all the data. As a result, on the short term AT1 is shown to suffer from small discontinuities. This effect is avoided with the KAS-1 algorithm (in its usual form) by its use of progressive deweighting of outlying data based on Hampel's ψ function^[7].

Figure 3 is a plot of Allan deviation vs. sampling time τ for one of the eleven clocks (no data rejection), assuming it to have the white FM and random-walk FM noises characteristic of a conventional (HP5061A model) high-performance cesium.

Figure 4 is a similar plot for the ensemble when the KAS-1 algorithm and its rejection criterion are employed. Each of the clocks has equal white FM and equal random-walk FM noises; hence, they are equally weighted. There is a \sqrt{N} improvement in the ensemble's collective stability, and the τ of minimum Allan variance is constant.

Figures 5 and 6 show simulated data of contrasting clock types. Figure 5 shows the frequency stability of VLG11-type hydrogen maser without a long-term frequency drift and fig. 6 is a similar plot of a SID or very stable (e.g. a De Marchi-tuned) cesium (no random walk of frequency). The clock types represented in figs. 3, 5, and 6 are used in an ensemble of unequal clocks similar to that which will soon comprise the USNO ensemble (60 percent cesiums, 30 percent masers, 10 percent SID's). This unequal clock set is used as the input to two algorithms with contrasting weighting philosophies.

Figure 7 is the Allan deviation of an algorithm (either AT1 or KAS-1) which automatically determines the weights of individual clocks in the ensemble according to the inverse time prediction errors at the sampling time; whereas fig. 8 is the deviation of an algorithm that forces all clocks to be weighted equally. Comparing the two figures, representing eight years of data, the weighted algorithm is significantly better in the short-term, whereas the equally weighted algorithm is better in the long-term. Future versions of the KAS algorithm will produce optimum results at all sampling times by completely accounting for the clock-ensemble correlations.

Figures 9 and 10 are analogous to Figs. 7 and 8, respectively, but display 25 years of data. The same

effects are noted, with the long-term degradation of the weighted algorithm being even more evident. Clearly, neither the AT1 nor the KAS-1 algorithm when using a weighting scheme is optimal for sets of dissimilar clocks. A new algorithm, KAS-2, has been developed by Ball Aerospace that is optimum for all clock types and all sample times. It will be tested in the Algorithm Test Bed in 1990.

CONCLUSION

The use of simulated data is shown to be a powerful method of comparing different clock models and ensembling algorithms. A Kalman filter-based algorithm, such as KAS-1, can use unequally spaced data and can handle transients well, unlike an ad hoc procedure like the AT1 (1987) algorithm. The KAS-1 algorithm is able to handle a mix of time and frequency measurements quite naturally.

Data rejection with AT1 leads to small discontinuities in the timescale, unlike the case for KAS-1. While both algorithms are optimal in steady state for clocks having proportional noises, they are not optimal for sets of significantly different clocks. The stability of a real clock ensemble would be further degraded by clock intercorrelations and systematic errors, so that, if the clock weights are based only on Allan variances, the results may not be as good as those employed simply using equal weights^[10].

As the project continues, more study will be made of simulated data; real clock data will be analyzed; and the improvements to the KAS-1 algorithm suggested herein will be implemented and tested.

References

- [1] Gifford, G. A. and Wheeler, P., "Report on the master clock upgrade program at USNO," Proceedings of the 43rd Annual Symposium on Frequency Control, 31 May-2 June, 1989, Denver, CO, pp. 158-161.
- [2] Stein, S. R., Glaze, D., Levine, J., Gray, J., Hilliard, D., Howe, D., and Erb, L., "Performance of an automated high accuracy phase measurement system," Proceedings of the 36th Annual Symposium on Frequency Control, 2-4 June, 1982, Philadelphia, PA, pp. 314-320.
- [3] Gabry, A., Faucheron, G., and Dubois, B., "Distant comparison of stable frequency standards by means of the transmission of a beat note between the carrier of a TV broadcast signal and a frequency synthesized from the frequency standards," Proceedings of the 31st Annual Symposium on Frequency Control, 1-3 June, 1977, Atlantic City, NJ, pp. 499-502.
- [4] Allan, D. W., Gray, J. E., and Machlan, H. E., "The National Bureau of Standards Atomic Time Scale: Generation, Stability, Accuracy, and Accessibility," chap. 9, Time and Frequency: Theory and Fundamentals (B. E. Blair, ed.), 1974, National Bureau of Standards Monograph No.140, pp. 214-229.
- [5] Varnum, F. B., Brown, D. B., Allan, D. W., and Peppler, T. K., "Comparison of Time Scales Generated with the NBS Ensembling Algorithm," Proceedings of the 19th Annual Precise Time and Time Interval (PTTI) Applications and Planning Meeting, 1-3 December, 1987, Redondo Beach, CA, pp. 13-23.
- [6] Stein, S. R., "Kalman Ensembling Algorithm: Aiding Sources Approach," Proceedings of the Third International Time Scale Algorithm Symposium, 12-13 September, 1988, Turin, Italy, pp. 345-357.
- [7] Percival, D. B., "Use of robust statistical techniques in time scale formulation," presented at the Second International Time Scale Algorithm Symposium, 23-25 June, 1982, Boulder, CO, report

on USNO contract N70092-82-M-0579.

- [8] Stein, S. R., "Kalman Filter Analysis of Precision Clocks with Real-Time Parameter Estimation," Proceedings of the 43rd Annual Symposium on Frequency Control, 31 May -2 June, 1989, Denver, CO, pp. 232-236.
- [9] Barnes, J. A., "Simulation of Oscillator Noise," Proceedings of the 38th Annual Symposium on Frequency Control, 29 May - 1 June, 1984, Philadelphia, PA, pp. 319-326.
- [10] Breakiron, L. A., "The effects of data processing and environmental conditions on the accuracy of the USNO timescale," Proceedings of the 20th Annual Precise Time and Time Interval (PTTI) Applications and Planning Meeting, 29 November-1 December, 1988, Tysons Corner/Vienna, VA, pp. 221-236.

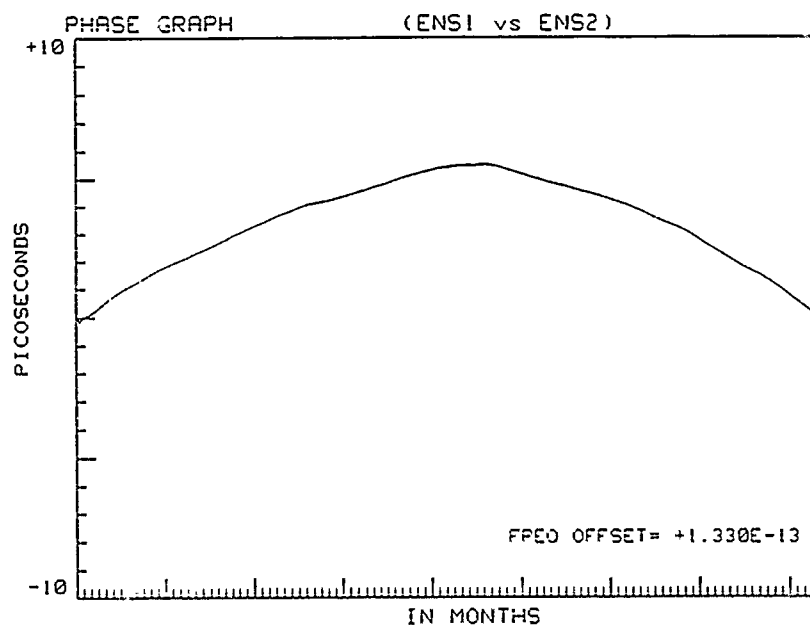


Figure 1: AT1 and KAS-1 are essentially identical in steady state.

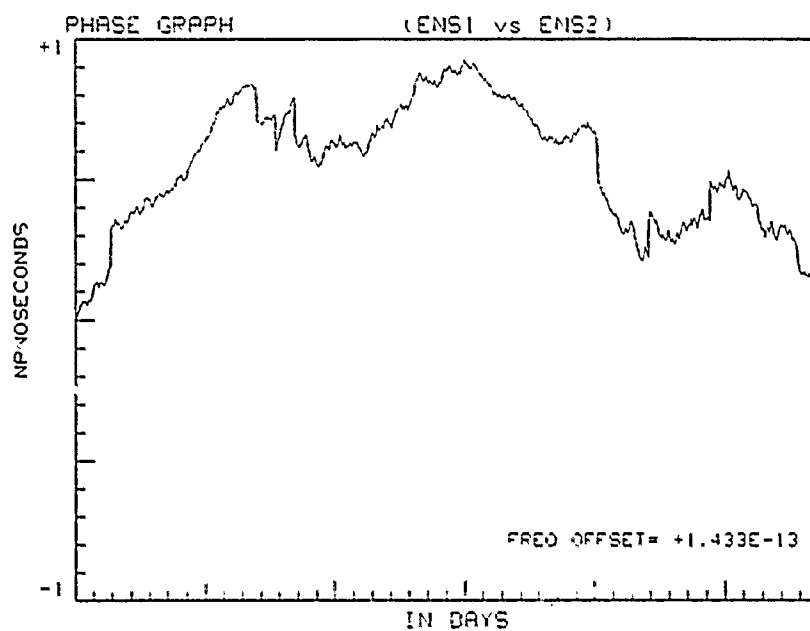


Figure 2: Small discontinuities in AT1 rejection method.

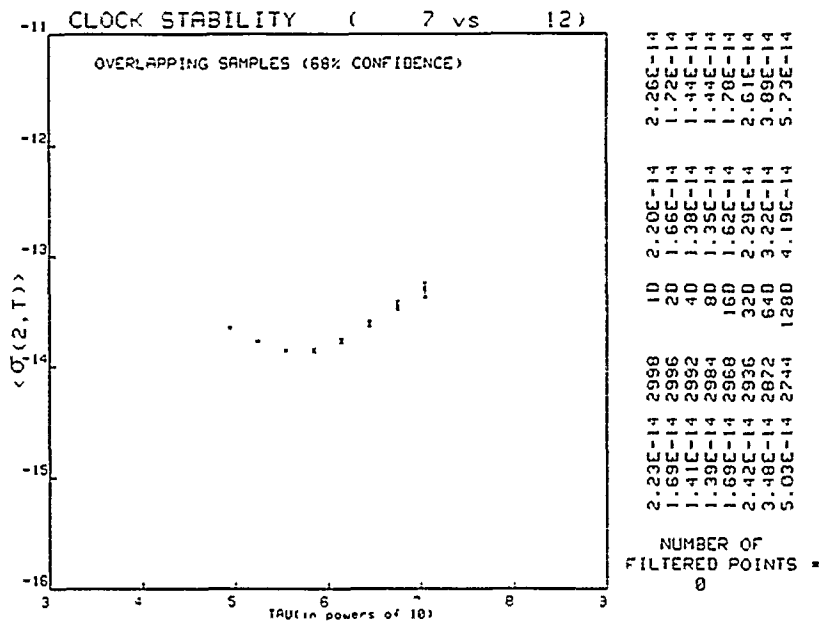


Figure 3: Simulated cesium clock data.

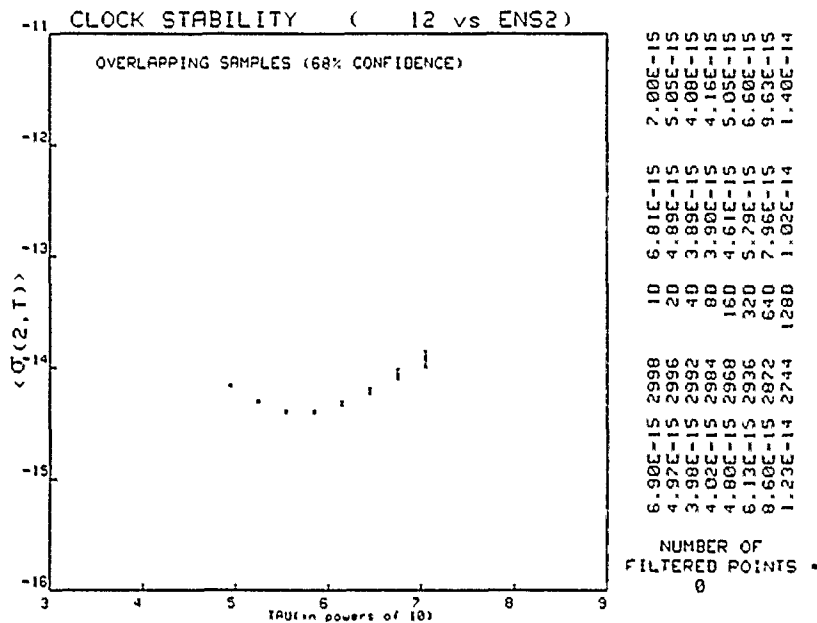


Figure 4: Square-root of N improvement with 11 equal clocks.

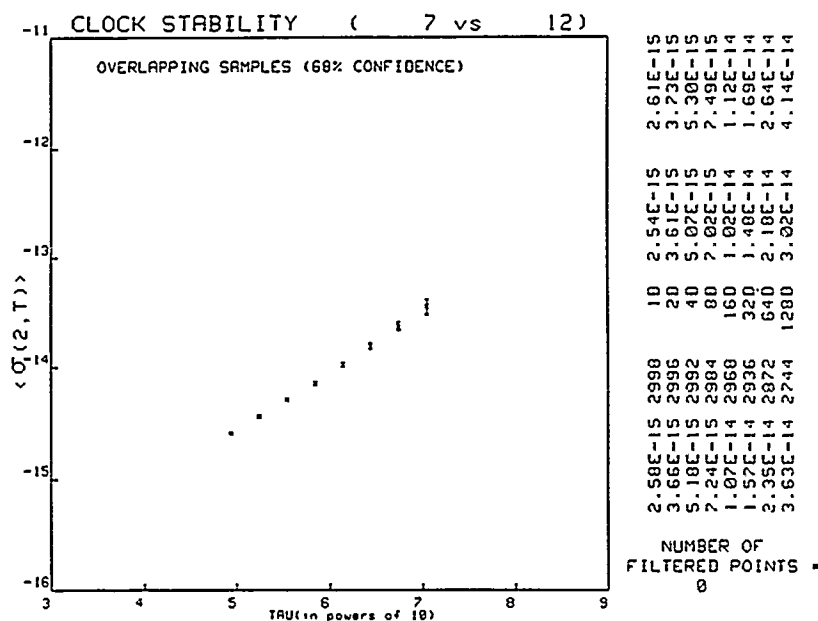


Figure 5: Simulated hydrogen maser data.

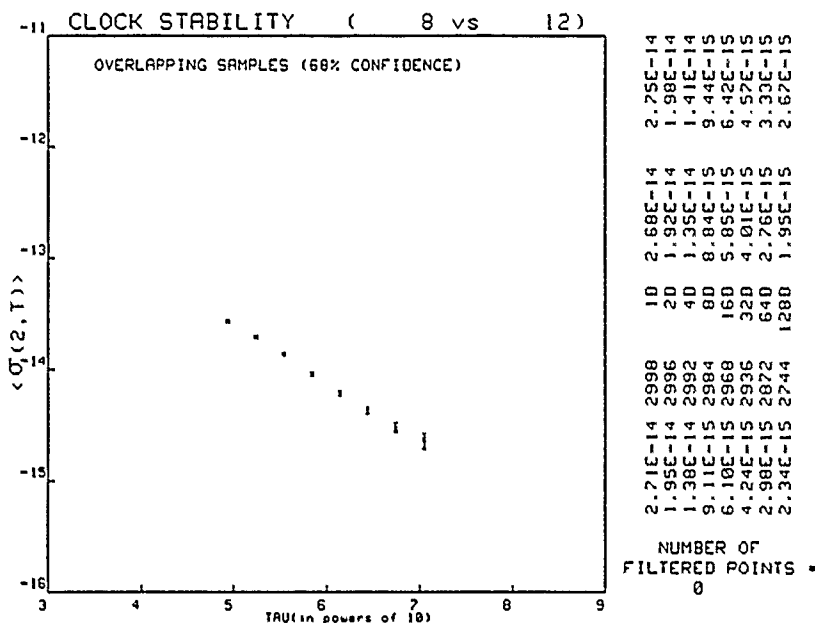


Figure 6: Simulated clock with no random walk of frequency.

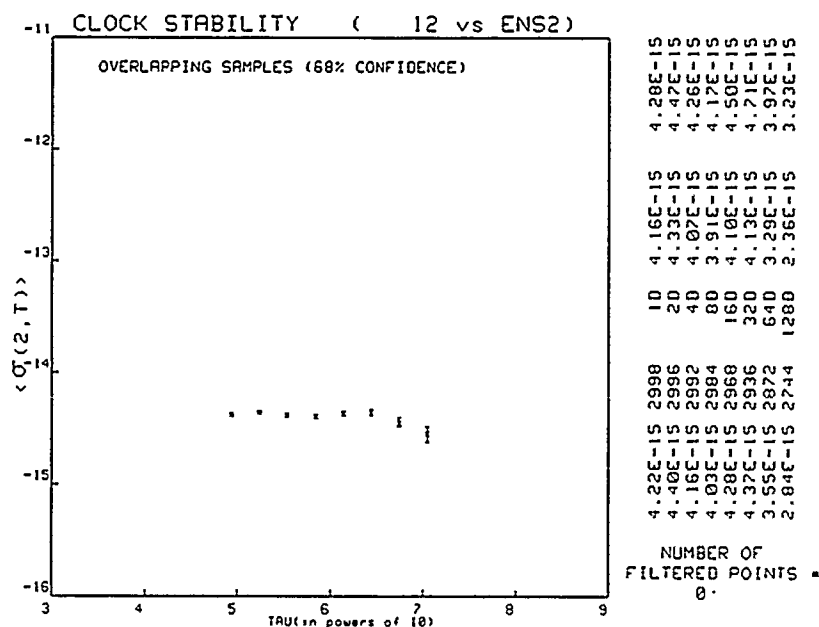


Figure 7: Output of algorithm using inverse variance weighting (8 years of simulated data).

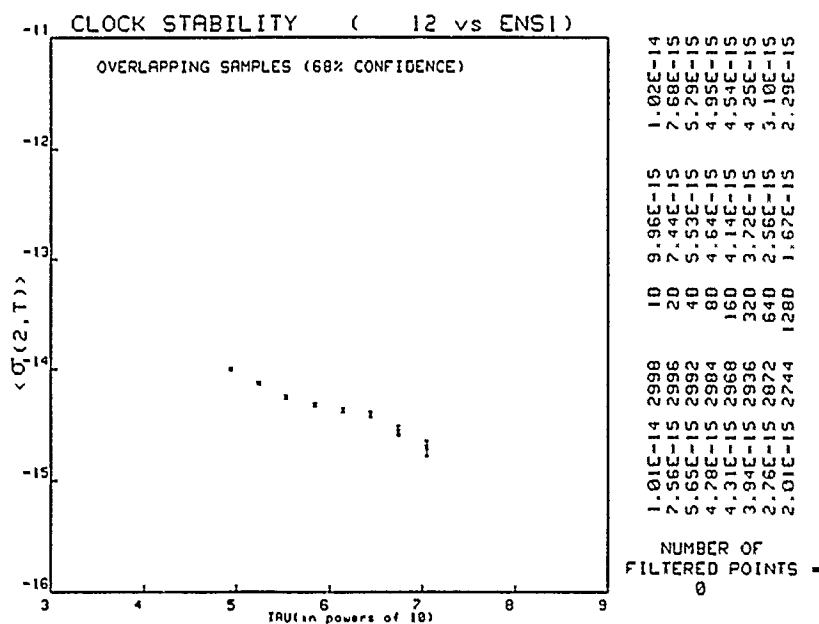


Figure 8: Output of algorithm using equal weights for all clocks (8 years of simulated data).

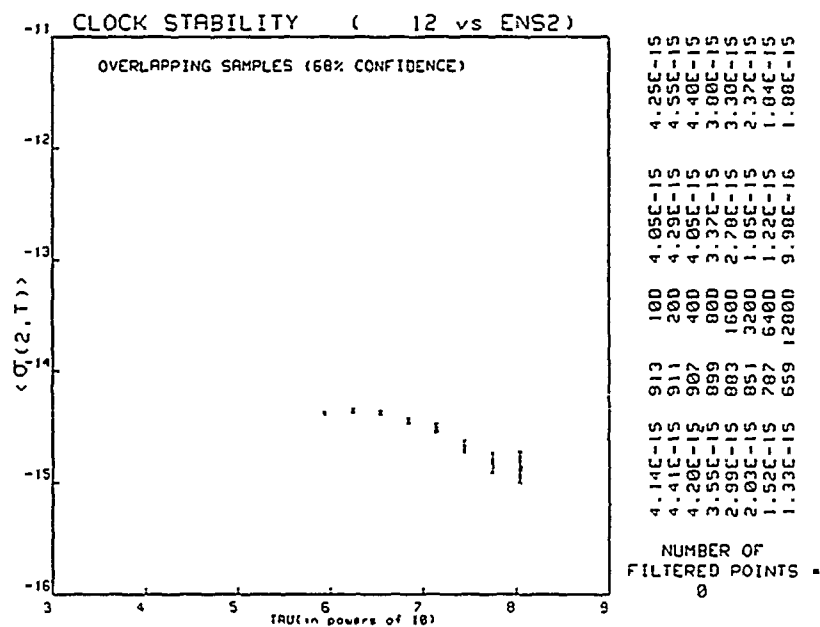


Figure 9: Output of algorithm using inverse variance weighting (25 years of simulated data).

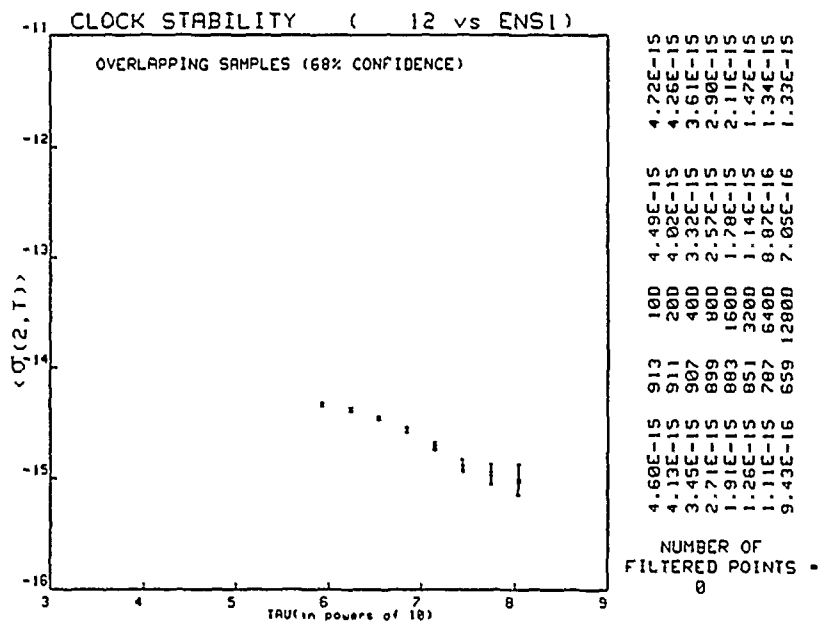


Figure 10: Output of algorithm using equal weights for all clocks (25 years of simulated data).

Observation Plan of High-stable Pulsars in CRL

Shin'ichi Hama, Michito Imae, Hitoshi Kiuchi, Hiroshi Takaba,
Fujinobu Takahashi
Communications Research Laboratory
893 Hirai Kashima-cho Ibaraki-ken 314 Japan

ABSTRACT

We implemented a new parabolic antenna for VLBI experiments in Kashima Space Communication Center, CRL. The receivers for 330M, 610M, 1.5G, 2.2G, 5G, 8.3G, 10G, 15G, 22G, and 43GHz (with a receiver for 49GHz also under preparation) enable us to carry out not only VLBI but also various other tasks.

CRL is now making a system for observing milli-second pulsars such as PSR1937+21, which are well-known for their extreme stability. We plan to obtain very precise timings of pulses by compensating the dispersion in frequency domain with high-speed and wideband sampling. We also plan to survey other highly stable pulsars using the VLBI backend.

This report outlines the status quo of pulsar observation in CRL, and VLBI of pulsars.

Introduction

As our laboratory is responsible for time keeping in Japan, we intend to observe the milli-second pulsars for precise time keeping. We also have potential in radio astronomy and earth rotation measurement through VLBI experiments.

The characteristics of Pulsars

Pulsars radiate pulses with very stable timing, with so-called milli second pulsars such as PSR1937+21 having especially stable periods and period derivatives. Table 1 shows the profile of the PSR1937+21⁽¹⁾. Since dispersion broadens the pulse width, observation using a higher frequency is preferable. But pulsars usually have a spectral index of -1 thru -2. For example the compact flux density measured in Westerbork is 0.13Jy for 609MHz and 0.017Jy for 1415MHz⁽²⁾. Therefore, less dispersion with higher frequency means fainter flux, and stronger flux with lower frequency means larger dispersion.

Fig.1 shows the Allan variance of various frequency standards, and the timing of PSR1937+21 observed in the Arecibo Observatory⁽³⁾. The slope of PSR1937+21 gives the precision of the timing observation, which is around 1

micro second. The long-term stability of PSR1937+21 reached 10^{-13} , based on the data until 1984. With the improvement of the backend and the adoption of a GPS receiver for time transfer, precision in timing measurement is now around 300 ns, and long-term stability reaches 10^{-14} .⁽⁴⁾ As we assume that this pulsar is much more stable than any other artificial frequency standard, we anticipate the adoption of milli-second pulsars as a new time standard.

Present research activity in CRL

A new 34m ϕ antenna has been constructed in Kashima, the specifications of which are shown in Table 2. It receives frequencies between 300 MHz and 43 GHz, although there is no receiver for 49 GHz yet. The feeds and receivers are switchable by remote control. The receivers for 300 and 600 MHz are at room temperature, with all others cooled with gas helium.

We have just started observing a strong pulsar by taking a hundred samples with low frequencies between 300 MHz and 2 GHz. Although we could detect PSR0329+54 with 300 MHz and 1.5 GHz, observation was not possible with 600 MHz because of strong and dense interferences.

Fig.2 shows the waveform of PSR0329+54 observed with 1.4GHz. The bandwidth was 2MHz. 139 periods were averaged using a digital oscilloscope.

System to be made by CRL

We are now making a one channel system for pulsar observation as shown in Fig.3. The signal is received by the 34m ϕ antenna and converted to the video band with a K-3 video converter, which has filters from 125 kHz to 4MHz. This video signal is sampled with an 8-bit A/D converter. After conversion to digital, the signal is averaged by triggers coming from the programmed signal generator. It is then stored on a hard disc or laser disc. The whole system is controlled with an NEC PC9801 personal computer. This system will be expanded to handle up to 16 channels. Our clock system, consisting of one Cesium and two hydrogen masers, is linked with UTC(CRL) by GPS.

VLBI of pulsars

We intend to conduct VLBI experiments of pulsars to determine their precise positions and the proper motions. With the new 34m ϕ antenna, we can make VLBI experiments from 300 MHz to high frequency.

A problem that the expected fringe amplitude is very small even for the strongest pulsars exists. There are two reasons for this. One is that particularly at higher frequencies pulsars are not very strong. Another reason is that the pulse width occupies say only about 1% out of the whole period. In this case a correlation processor must close its gate and accumulator when no pulse comes.

Our K-3 correlation processor for VLBI has this function. The correlator opens the gate from a certain point during certain bits according to the parameters which are sent from a computer every 2 or 3 seconds.

The pulsar PSR0329+54 was included in the VLBI experiment conducted this November between Kashima 34m, Kashima 26m, and Nobeyama 6m. The observing frequency was 2.3 GHz and the bandwidth was 2 MHz. The fringe amplitude for the baseline between Kashima 26m and 34m can be estimated with Equation (1).

$$\rho = \frac{\pi D_1 D_2 S}{8 k} \sqrt{\frac{\eta_1 \eta_2}{T_1 T_2}} \quad \text{Eq. (1)}$$

In the case where the "pulsar gate" is not used, the equivalent flux density is one percent of the peak value. As the peak value of PSR1937+21 is 1Jy, the effective flux turns out to be only 10mJy. Considering other parameters shown in Fig.4, we can get a fringe amplitude of only 1.88×10^{-5} . This means that it is not possible to distinguish this fringe from noise even with 800 second integration, which is the total length of the standard VLBI tape. Therefore, we are now attempting to detect a fringe by making use of the "pulsar gate".

Summary

We have recently started observing pulsars for precise time keeping. The first step was detection of the strong pulsar PSR0329+54.

A problem with compensation for dispersion has been encountered, and one possible solution is increasing the number of channels. The output of each channel has different timing, therefore we must accumulate the data after time-shifting according to each dispersion.

Furthermore VLBI of pulsars is also an attractive method to determine the position and proper motion of pulsars.

References

- (1) Rawley, L.A. et al. "Millisecond pulsar PSR1937+21: A high stable clock" Science Vol.238 '87 Nov.
- (2) Backer, D.C. et al. "A milli-second pulsar" Nature Vol.300, '82 Dec.
- (3) Davis, M.M. et al. "High-precision timing observations of the milli-second pulsar PSR1937+21" Nature Vol.315 '85
- (4) Allan, D. et al. "In search of best clock" IEEE-IM '89 Apr.

Table 1 Profile of PSR1937+21

Period (msec)	1.55780644887275 ± 3
Period derivative (10^{-20} sec sec $^{-1}$)	10.51054 ± 0.00008
Right ascension (1950.0)	$19^h37^m28^s.74601 \pm 0.00002$
Declination (1950.0)	$21^\circ28'01''.4588 \pm 0.0003$
Epoch (Julian ephemeris date)	2445303.2940
Proper motion in right ascension (year $^{-1}$)	$-0''.0003 \pm 0''.0002$
Proper motion in declination (year $^{-1}$)	$-0''.0005 \pm 0''.0003$
Dispersion constant (10^{16} sec $^{-1}$)	29.479 ± 0.001

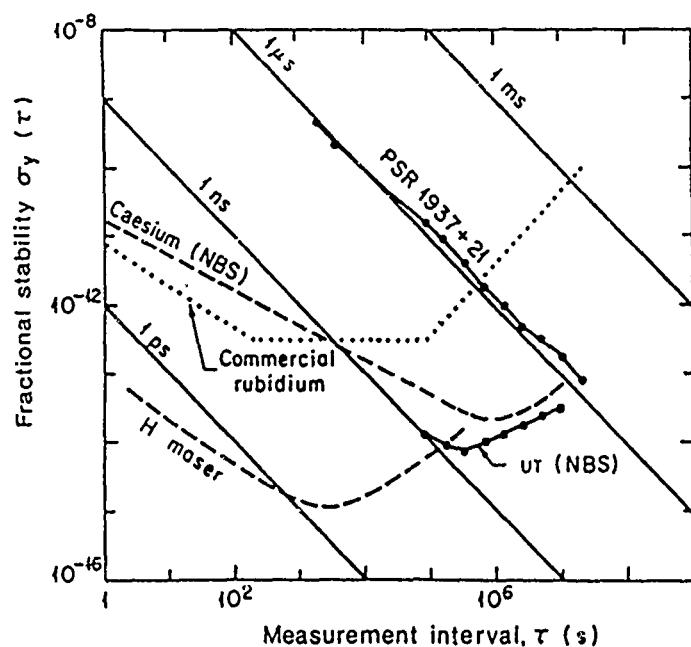


Fig.1 Allan variance of various frequency standards and the timing of PSR1937+21 (observed in Arecibo)

Table 2 Performance of the new 34-m antenna

Receivers	RF band		T_{LNA} (K)	T_{SYS} (K)	G/T (dB/K)
300MHz	312 -	342MHz	43	199	15
600MHz	580 -	640MHz	(Data Not Available)		
1.5GHz	1.35 -	1.75GHz	10	33	37
2GHz	2.15 -	2.35GHz	11	71	38
5GHz	4.60 -	5.10GHz	25	60	45
8GHz	7.86 -	8.60GHz	12	53	50
10GHz	10.2 -	10.7GHz	44	71	51
15GHz	14.4 -	15.4GHz	42	106	51
22GHz	21.98 -	22.48GHz	101	189	52
22GHz	23.58 -	24.08GHz	158	223	52
43GHz	42.8 -	43.3GHz	400	1200	

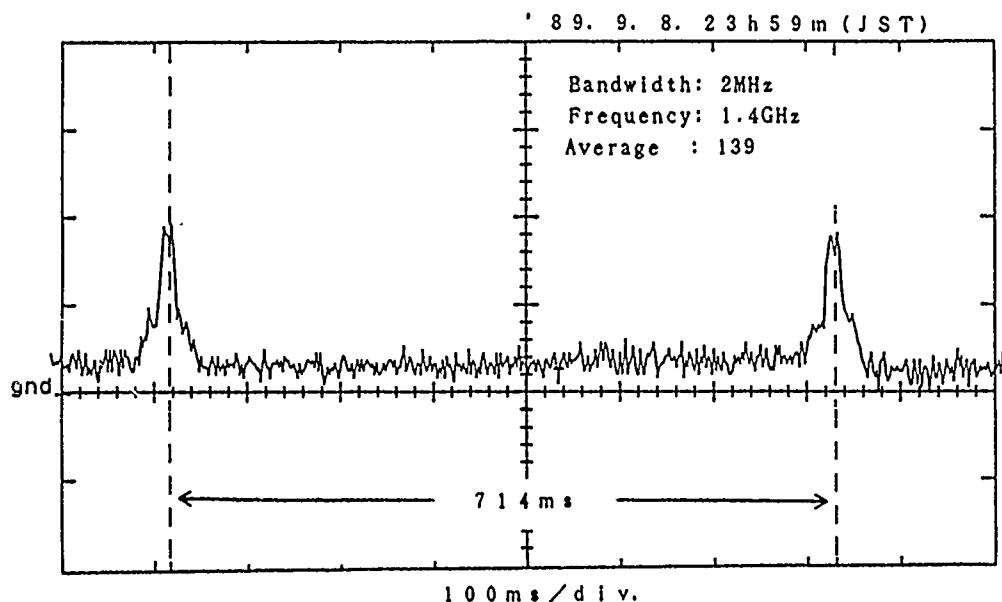


Fig.2 Waveform of PSR0329+54 observed by the Kashima 34m antenna

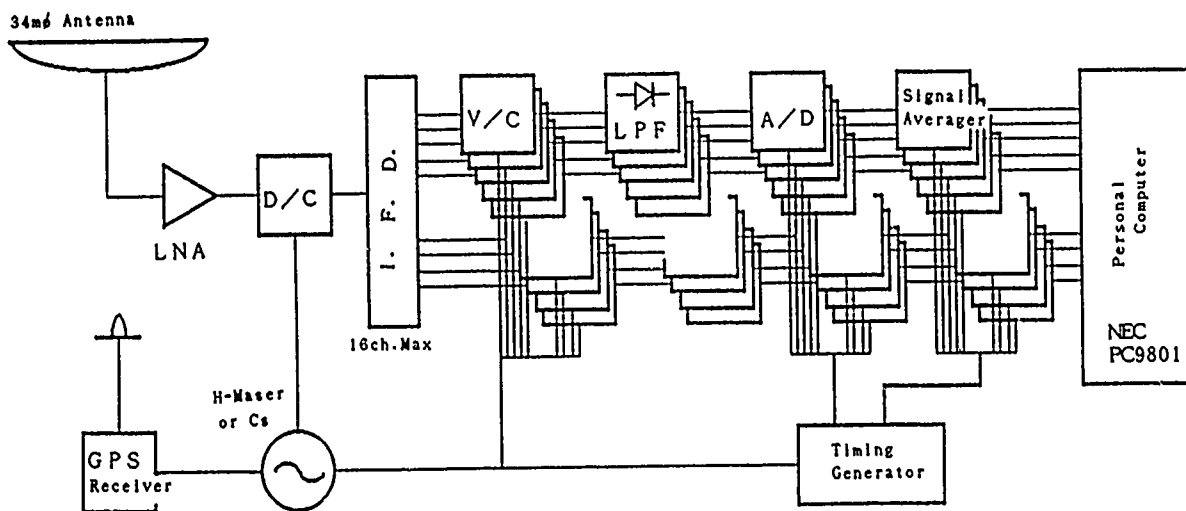


Fig.3 Pulsar observing system of CRL Kashima

ρ : Fringe Amplitude
 D : Diameter
 S : Flux Density
 k : Boltzman constant
 η : Antenna Efficiency
 T : System Temp.

$D_1=34$ [m]
 $D_2=26$ [m]
 $S=0.01$ [Jy]^{*}
 $\eta_1=0.68$
 $\eta_2=0.52$
 $T_1=70$ [K]
 $T_2=90$ [K]

Suffix --- 1=34m, 2=26m

* (Jy = 10^{-26} W/Hz/m²)

Fig.4 Parameters for estimation of fringe amplitude of PSR0329+54
(between Kashima 34m & 26m)

ACCURACY MODEL FOR PHASE NOISE MEASUREMENTS*

F. L. Walls, C.M. Felton, A.J.D. Clements
National Institute of Standards and Technology
Boulder, CO 80303
and
T.D. Martin
Gravity Research Institute
Boulder, CO

Abstract

We have recently completed a new modular system for accurate measurements of phase noise in oscillators, amplifiers, frequency synthesizers, and passive components. This new system is capable of measuring the phase noise at carrier frequencies from 5 MHz to 1.5 GHz, 1.5 to 26 GHz, and 33 to 50 GHz. Other frequency ranges can be measured using external mixers to convert the signals into one of the above frequency ranges. The analysis bandwidths vary from 0.1 Hz to 10% of the carrier frequency up to a maximum of about 1 GHz. Extensive internal calibration of the system is used to correct for all gain variations with analysis frequency including phase-locked-loop and cable-loss effects. We have also included a precision noise source to calibrate the spectral density functions of the spectrum analyzers. As a part of this program we have developed a method for determining the biases in the various spectrum analyzers as a function of noise type and the confidence of the spectral density estimates. We also investigate the effect of amplitude noise and phase delays on phase noise measurements. The combination of all these features makes it possible, under favorable conditions, to measure phase noise in various signal handling components and sources to an accuracy of 1 dB over very wide analysis bandwidths. Detailed descriptions of the new calibration procedures, including a sample table of uncertainties, are given. High accuracy determinations of phase noise can be used to compute accurate values of short-term, time-domain frequency stability.

I. INTRODUCTION

We have developed a new concept for the measurement of phase noise offering much higher accuracy and bandwidth than was possible using previous approaches^[1-4]. This new approach makes it possible to measure phase noise over bandwidths that approach 10% of the carrier frequency (up to a maximum frequency of about 1 GHz) with an accuracy that exceeds 1 dB under most conditions. The wide bandwidths and the higher accuracy are necessary to adequately characterize new equipment used in

*Contribution of the U.S. Government; not subject to copyright.

very wide bandwidth communication, navigation, and measurement systems. To achieve these new goals, it was necessary to develop a method to calibrate virtually every aspect of the measurement process, to reconsider the effects of residual amplitude noise, and to examine the confidence of spectral estimates for non-white noise.

II. MODEL OF A NOISY SIGNAL

Equation 1 shows the simple model of the signal of a source where the frequency fluctuations are very small compared to the average frequency, ν_0 and the fluctuations in the amplitude are very small compared to the average amplitude, V_0 . The amplitude variations are incorporated into $\epsilon(t)$ and the phase or frequency fluctuations are incorporated into $\phi(t)$ ^[5,6]:

$$V(t) = [V_0 + \epsilon(t)]\cos[2\pi\nu_0 t + \phi(t)]. \quad (1)$$

The phase noise of such a source is often expressed in terms of $S_\phi(f)$, the spectral density of phase fluctuations. $S_\phi(f)$ can be understood as the one-sided, mean-squared phase fluctuation, $\delta\phi^2(f)$, measured at a Fourier frequency separation, f , from the carrier in a measurement bandwidth BW.

$$S_\phi(f) = \frac{\delta\phi^2(f)}{\text{BW}} \quad (\text{rad}^2/\text{Hz}) \quad 0 < f < \infty. \quad (2)$$

Equations 3 and 4 show the relationship between $S_\phi(f)$ and several commonly used expressions for frequency or phase fluctuation. $\mathcal{L}(\nu_0 - f)$ is the single-sideband phase noise at a frequency, f , below the carrier while $\mathcal{L}(\nu_0 + f)$ is the single sideband noise at a frequency, f , above the carrier. There may be conditions under which the upper sideband is not equal to the lower sideband. $S_y(f)$ is the spectral density of fractional frequency fluctuations.

$$S_\phi(f) = \mathcal{L}(\nu_0 - f) + \mathcal{L}(\nu_0 + f) \quad (3)$$

$$S_y(f) = \frac{f^2}{\nu_0^2} S_\phi(f) \quad 0 < f < \infty \quad (4)$$

These measures fully characterize the random variations of the phase of a precision source. The time domain characterization of the frequency fluctuations are usually expressed in terms of the Allan variance, $\sigma_y^2(\tau)$, or the modified Allan variance, $\text{Mod } \sigma_y^2(\tau)$. Both variances can be accurately determined by an integration of $S_y(f)$ or equivalently $S_\phi(f)$ as shown below, where the measurement time is n times the minimum measurement time, τ_0 , and f_h is the measurement bandwidth. An accuracy of 1 dB in determining $S_\phi(f)$ corresponds to about 10% accuracy in determining $\sigma_y(\tau)$ or $\text{Mod } \sigma_y(\tau)$. Numerical integration techniques have been used to extend earlier work and calculate the ratio of $\text{Mod } \sigma_y^2(\tau)$ to $\sigma_y^2(\tau)$ for all the common noise types found in oscillators and measurement systems as shown in Figure 1^[7-11]. This makes it possible to transform from $\sigma_y(\tau)$ to $\text{Mod } \sigma_y(\tau)$ and back for virtually any value of n . $\text{Mod } \sigma_y(\tau)$ averages the high-frequency-phase-noise components of white-phase and flicker-phase noise faster than $\sigma_y(\tau)$. This can be very useful in measuring the long-term performance of a source which has high frequency noise components^[4-9]. The inversion of $\sigma_y(\tau)$ or $\text{Mod } \sigma_y(\tau)$ to obtain $S_\phi(f)$ has relatively poor precision due to the integral nature of the time domain measures. These inversions are

$$\sigma_v(n\tau_0) = \left[2 \int_0^{f_h} S_v(f) \frac{\sin^4(\pi f n\tau_0)}{(\pi f n\tau_0)^2} df \right]^{1/2} \quad \text{and} \quad (5)$$

$$\begin{aligned} \text{Mod}\sigma_v(n\tau_0) = & \left[\frac{2}{n^4 \pi^2 \tau_0^2} \left[n \int_0^{f_h} \frac{S_v(f)}{f^2} \sin^4(\pi f n\tau_0) df \right. \right. \\ & \left. \left. + 2 \int_0^{f_h} \sum_{k=1}^{n-1} (n-k) \frac{S_v(f)}{f^2} \cos(2\pi f k\tau_0) \sin^4(\pi f n\tau_0) df \right] \right]^{1/2}. \end{aligned} \quad (6)$$

Equation (6) can be simplified^[7] to:

$$\text{Mod}\sigma_v(n\tau_0) = \left[\frac{2}{n^2 (\pi n\tau_0)^2} \int_0^{f_h} S_v(f) \frac{\sin^6(\pi f n\tau_0)}{f^2 \sin^2(\pi f n\tau_0)} df \right]^{1/2}. \quad (7)$$

Generally, the effect of the time variations on the signal amplitude, $V(t)$, as characterized by the power spectral density of amplitude fluctuations, $S_v(f)$, are ignored in the measurement of $S_\phi(f)$. However, $S_v(f)$ often sets the lower limits for the measurement of added noise in devices and in determining the noise floor of measurement systems. $S_v(f)$ is given by

$$S_v(f) = \frac{\delta\epsilon^2(f)}{V_0^2 \text{BW}} \quad (\text{rel to carrier/Hz}) \quad \text{or} \quad (8)$$

$$10 \log S_v(f) \quad (\text{dBc/Hz})$$

where $\delta\epsilon^2(f)$ is the mean-squared amplitude fluctuation measured at a Fourier frequency separation, f , from the carrier in a measurement bandwidth, BW.

III. PHASE NOISE MEASUREMENT SYSTEM

Figure 2 shows a block diagram of our new modular phase-noise-measurement system for measuring phase noise in oscillators, amplifiers, frequency synthesizers and other devices. As presently configured, three front end units cover the bands of 5 to 1500 MHz, 1.5 to 26 GHz, and 33 to 50 GHz. Other frequency ranges can be easily added by the installation of cables which carry the appropriate reference frequencies as discussed below, or by using external mixers to heterodyne the frequencies into the range of one of the three present front ends. Using this latter approach makes it possible to extend the range to cover the entire millimeter range and most laser frequencies as well.

All three front ends feature directional couplers for continuous monitoring of the frequency or power of the input signals. They also have internal phase shifters for use in making measurements of the noise floor or the phase added by signal handling components. The power meter covers 100 kHz to 50 GHz while the counter covers 0.001 Hz to 26 GHz. The modulation reference source covers 0.1 Hz to 1 GHz. The low-phase-noise frequency reference has outputs at 5, 10, 100, $N \times 500$ MHz ($1 \leq N \leq 30$), 10.6 GHz, 21.2, GHz and 42.4 GHz. There is also a low-noise frequency synthesizer which cover 10 kHz to 1.28 GHz.

The system can be run manually from the front panels of the various instruments or run from an AT-compatible microprocessor. The microprocessor makes it easy to perform a wide variety of calibrations, to correct for variations in the various instruments over the frequency range of interest. As with previous systems, a mixer is used to transform phase variations to voltage variations that are measured by various spectrum analyzers^[1-4]. The signal from the mixer in each of the front ends is switched to a common amplifier that has several output channels. Each is optimized to drive a particular measurement instrument. There are three spectrum analyzers, a 100 MHz digital oscilloscope and a multipurpose counter. By far the most difficult task is to determine, with an accuracy of 0.5 dB, the sensitivity of the mixer for converting small phase variations to voltage variations for Fourier frequencies from dc to about 1 GHz. In previous approaches the mixer calibration was accomplished with amplifiers that were very flat with frequency and by calibrating the mixer conversion sensitivity using the beat frequency method^[1,2]. This is possible for Fourier frequencies which are very small compared to the carrier, but extremely difficult at higher Fourier frequencies due to the dependence of the reactive impedance of the mixers on termination and source characteristics^[2]. Our new method overcomes this difficulty.

IV. BASIC MEASUREMENT PROCESS

The first step in the measurement of phase noise between two oscillators is to adjust the input drive levels of the signal and reference channels to between +13 and +23 dBm. Next we use the beat frequency method to calibrate the absolute sensitivity for transforming small variations in phase to voltage variations at the output of the scope channel shown in Figure 3. The period of one beat cycle (2π rad) is determined using the digital oscilloscope. The oscilloscope is then used to digitize the beat signal and determine the average slope at approximately ± 0.05 radians of the zero crossing. The oscilloscope channel uses a relatively low-gain (22 dB) operational amplifier with high slewing rate and dynamic range. This measurement is done at a low beat frequency where the frequency response of both the mixer and the amplifier is constant. The sensitivity at the output of the oscilloscope channel is just

$$k_d = \text{slope (V/s) T(s)} / (2\pi) \quad (\text{volts/rad}). \quad (9)$$

We measure both the positive-going and the negative-going zero crossings to verify that they are equal to better than 10%. If they are not the same the mixer may be damaged or there may be significant injection pulling which would invalidate the slope measurements. The injection pulling can be reduced by increasing the beat frequency. When the beat signal is noisy, it is averaged with the digital oscilloscope to improve the precision of the measurement. Typically, this measurement is accurate to better than 1%, which corresponds to ± 0.09 dB in the determination of $S_\phi(f)$.

The tuning sensitivity of one of the oscillators is then determined using the counter and a programmable, voltage-bias source. This measurement, along with the determination of k_d , is used to calculate the appropriate gain and integration times to close the phase lock loop (PLL). The dc output voltage from the mixer, divided by k_d , yields the phase deviation from quadrature. This phase offset is continuously monitored to verify that it does not exceed 0.1 rad. If this limit is exceeded, an error message is sent to the operator. The phase noise data are also tagged with the peak phase deviation during the entire run. This is intended to help in the detection of large phase excursions during the measurements which would invalidate the data.

Once the phase lock is executed and the phase deviations from quadrature are verified to be less than ± 0.1 rad, a special phase modulator is used to determine the relative gains of all the amplifiers over the entire range of Fourier frequencies of interest. A schematic diagram of the phase modulator, which is used in each front end to generate phase modulation on the reference carrier signal, is shown in Figure 4. A small portion of the input carrier signal is coupled into a processing channel using a directional coupler. This signal is phase shifted, bi-phase amplitude-modulated using a double balanced mixer, and reinserted into the carrier. If the phase shift is such that the reinserted signal is at precisely 90° to the carrier, the resulting modulation is phase modulation with negligible amplitude modulation. This is illustrated by the vector diagram in Figure 2. This special condition of nearly pure phase modulation is obtained in practice by monitoring the signal after the phase modulator and actively adjusting the phase shift until the amplitude modulation is minimized. This eliminates the need to actually measure the phase shift. The adjustment need only be made at the beginning of a measurement, since it is very stable.

Figure 5 shows the variation in the amplitude of the phase modulation tones introduced by three phase modulators of the type shown in Figure 4 as a function of the frequency of the modulation. This figure shows that it is possible to insert phase modulation tones (on the carrier) that are constant in amplitude to ± 0.5 dB from dc up to 5 to 40% of the carrier frequency. The difference in performance is evidently related to the standing-wave ratio introduced by the components.

To calibrate the relative gains of the various measurement channels, the frequency of the modulation is swept over the range of Fourier frequencies of interest, and the response of the various measurement instruments is recorded. The ratio of the response of the instruments is then the relative gain. This corrects for frequency-dependent effects in the mixer and amplifiers, the effect of the PLL on the low frequency gains, cable losses, and even errors in the internal-voltage references of the instruments. Since the absolute response of the oscilloscope channel was determined above, using the beat frequency method, the sensitivity of all the other channels can be calculated. The repeatability of the measurement of the relative gains of the amplifiers and their measurement instruments is typically better than ± 0.02 dB up to 32 MHz and about ± 0.2 dB up to 0.5 GHz.

The spectral density function of the low-frequency spectrum analyzer is verified using the noise source shown in Figure 6 where the output is proportional to the Johnson noise from a metal-film resistor. The gains of the amplifiers are determined to 0.05 dB from the ratios of resistors. The noise density output is known to ± 0.14 dB from 20 Hz to 20 kHz. At higher frequencies the noise gain of the amplifiers becomes important and is compensated to 0.2 dB out to 100 kHz. Figure 7 shows a calibration of the spectral density function of the low-frequency spectrum analyzer for several different window functions^[12]. The Hanning window has proven to be the most suitable for measuring noise while the "Flattened-Peak window" is best suited for the measurement of discrete peaks^[12]. The primary uncertainty in the 20 Hz to 20 kHz region is the temperature; ± 10 K corresponds to ± 0.14 dB in the noise density. The effect of the input-noise current and added-noise voltage of the amplifier is determined by measuring the output-noise density for input terminations of 10^5 ohms, 220 pF in parallel with 44×10^6 ohms and a short. This noise source can be injected into the output of the mixer and used with the relative gains to verify the measurement bandwidths of the other two spectrum analyzers.

The next step in the process is to measure the noise voltage on the three spectrum analyzers. This data is stored and later scaled by the relative gains and measurement bandwidths to obtain $S_\phi(f)$. The statistical confidence of the data is calculated using the method outlined previously^[12]. For the low-frequency spectrum analyzer, which is a fast-Fourier-transform (FFT) device, the confidence

interval is virtually independent of the noise type (if the first few channels are neglected), and is given by

$$S = S_m(1 \pm \frac{1}{\sqrt{N}}), \quad (10)$$

where S is the true spectral density, S_m the measured spectral density, and N the number of independent samples averaged together. For the other spectrum analyzers, which use sweeping techniques, the confidence interval is roughly the square root of the ratio of the measurement bandwidth, before the detector, to the smoothing bandwidth. Accurate determinations of the confidence intervals for specific instruments can be obtained using^[12].

V. CORRECTIONS FOR NOISE FLOOR, 3-CORNER HAT

The above procedure determines only the phase noise BETWEEN the two oscillators plus the noise floor of the measurement system, and does not, by itself, determine the noise of either oscillator. All we can say with certainty is that the phase noise of both oscillators is less than the measured value. To determine the phase noise of each unit, it is necessary to evaluate several additional terms which contribute to the apparent phase noise as shown in equation [11] and to measure both of the oscillators against another source of nearly equal noise performance.

$$S_\phi(f)_{|AB} = \frac{[\Delta\phi_A(f) - \Delta\phi_B(f)]^2}{BW} + \frac{V_n^2(f)_{|mixer} + V_n^2(f)_{|Amp} + [(V_n^2(f)_{|SA})/G^2]}{k_d^2} + S_{VA}(f)\beta_A^2 + S_{VB}(f)\beta_B^2, \quad (11)$$

where $[\Delta\phi_A(f) - \Delta\phi_B(f)]^2$ is the mean-squared phase fluctuations between the two ports of the mixer and the three V_n terms represent the amplitude noise of the mixer, the amplifier, and low pass filter, and the noise of the spectrum analyzer scaled by the amplifier gain. $S_{VA}(f)$ is the amplitude noise of source A and β_A^2 is the sensitivity of the mixer for converting amplitude noise into voltage noise at the output of the mixer. $S_{VB}(f)$ represents similar terms for source B . For simple oscillators the amplitude noise of a source is generally no worse than the phase noise. This condition does not necessarily hold true for complex systems with automatic leveling circuits. Equation [11] can be simplified to

$$S_\phi(f)_{|AB} = S_{\phi A}(f) + S_{\phi B}(f) + \frac{V_n^2(f)}{k_d^2} + S_{VA}(f)\beta_A^2 + S_{VB}(f)\beta_B^2. \quad (12)$$

The noise floor of the measurement system when driven by source A alone ($A \equiv B$) is given by

$$S_\phi(f)_{|Noise Floor} = S_{\phi A}(2\pi f\tau_{delay})^2 + \frac{V_n^2(f)}{k_d^2} + S_{VA}(f)\beta_A^2 + S_\phi(f)_{|ps} \quad (13)$$

where $S_\phi(f)_{|ps}$ is the added phase noise of the power splitter.

The term resulting from the phase difference between the two ports of the mixer drop out except for a new term which results from the 90° phase difference (between the ports) that is necessary for the

mixer to operate properly. This results in a dephasing of the phase noise of the source between the two ports of the mixer. The portion of the source appearing across the mixer increases as f^2 and has the character of a delay-line, phase-noise-measurement system. This term is very important in wide-band, phase-noise-measurement systems, and is only 16 dB below the source noise for $f = \nu_0/10$, and $\tau = 1/(4\nu_0)$. The noise floor is also dependent on the amplitude noise of the delay source scaled by the conversion sensitivity of mixer.

Figure 8 shows one approach to measuring amplitude noise. The conversion sensitivity of the diode detector and the amplifier gain can be determined at a specific carrier frequency and power level using a substitute source that can be amplitude modulated. If the amplitude modulation signal is of the form,

$$V = V_0[1 + A_0 \cos \alpha t] \cos \omega t,$$

where the relative power at the modulation frequency α is $A_0^2/2$ assuming $A_0 \ll 1$ and a linear detector. The signal detected at the spectrum analyzer is

$$\text{Output} = \frac{A_0^2}{2} G^2(\alpha) K_{AM}^2(\nu_0, V_0, \alpha),$$

where $G^2(\alpha)$ is the square of the voltage gain of the amplifier at frequency α , and $K_{AM}^2(\nu_0, V_0, \alpha)$ is the conversion sensitivity of the diode. $S_v(f)$ of the source of interest is then determined using the same $G^2(f)$ and K_{AM}^2 . The value of $S_{VA}(f)$ determined by this approach is an upper limit since it does not directly determine the noise contribution of the diode or the amplifier.

The noise contribution of the amplifier can be determined by measuring the noise with no input signal. The measurements of the diode noise can sometimes be determined by comparing the results of several low-noise sources. These measurements are used to determine $S_{VA}(f)$, $S_{VB}(f)$ and estimate $V_n(f)$.

Table 1 shows the pair measurement of the phase noise of a frequency synthesizer against a low-noise quartz oscillator at 5 MHz. The amplitude noise was measured using the scheme shown in Figure 8. At low Fourier frequencies the amplitude noise is lower than the phase noise. However, at higher Fourier frequencies, the amplitude noise is higher than the phase noise. When the noise floor of the measurement system was measured, the noise floor was relatively high. By determining the mixer sensitivity for converting amplitude noise into output-voltage noise we could approximate the noise floor from the measured amplitude noise by $S_v(f)|_A \beta_A^2$. This shows that, in some circumstances, it is the amplitude noise and not the phase noise of the source that limits differential measurements such as the system noise floor or the phase noise added by a component.

The relative contributions of sources A and B to the pair measurement of equation 12 is determined by measuring both sources against another source, C . The phase noise of C should be roughly comparable or lower in phase noise than those of A or B . Equation 16 shows how these measurements can be combined with measurements of the noise floor and the amplitude noise to yield an unbiased estimate of $S_\phi(f)$ for source A .

$$S_\phi(f)|_{AB} + S_\phi(f)|_{AC} + S_\phi(f)|_{BC} = 2S_{\phi A} + \frac{V_n^2(f)}{k_d^2} + 2S_{VA}(f)\beta_A^2. \quad (14)$$

Table 2 shows the results of a precise calibration of the phase noise of a 100 MHz frequency synthesizer against a low-noise quartz oscillator. The analysis covers the range from 32 Hz to 10 MHz or 10% of

the carrier frequency. The column showing modulation level indicates the modulation level detected on the two spectrum analyzers used for this calibration. The absolute sensitivity of the mixer multiplied by the gain of the oscilloscope channel at 100 Hz was 12.8 dB. The difference between the gain of the oscilloscope channel and the FFT channel was 14.3 dB. Combining these calibrations yields the values for the pair measurements of $S_{\phi}(f)$. Also listed is the amplitude noise of the frequency synthesizer (source A). The sensitivity of the mixer for converting the amplitude noise into output noise was -25.3 dB. When this is combined with the measured amplitude noise, the result is much below the measured phase noise. This result indicates that amplitude noise has negligible effect on the phase noise of these measurements. Direct measurements of the noise floor of the system, using the synthesizer as the driving source, indicate that the noise floor of the system also has negligible effect on the measured phase noise. Measurements of the phase noise against another source show that the phase noise of the synthesizer is 20 to 30 dB above the noise of the crystal oscillator (source B). The last column shows the final result of calibration. The uncertainties in the various steps of the calibration are listed in Table 3. The combination of these uncertainties is approximately ± 1 dB. The differences between columns 4 and 7 for Fourier frequencies of 50, 70, and 100 kHz are indicative of the statistical uncertainties of the noise spectral density measurements from the two channels.

VI. CONCLUSION

We have outlined a new concept for the measurement of phase noise which features an accuracy of 1 dB under most conditions, and analysis bandwidths of approximately 10% of the carrier frequency up to a maximum of 1 GHz. A model which contains all the known contributions to the uncertainties in the measurement of phase noise is presented. This new approach uses a new type of ultra-flat phase modulator to determine all of the frequency dependent changes in the response of the mixer, the various amplifiers, cable losses, and even the internal calibration of the spectrum analyzers. The role of amplitude noise in the sources is also examined. It is shown that under some circumstances (especially differential measurements such as the noise floor of a system or the phase noise added by a signal processing component) the amplitude noise of the sources limits the ability to measure phase noise. It was also shown that when measuring the added phase noise of signal-handling components, the dephasing due to the 90° phase shift needed to operate the mixer in a linear region, limits the cancellation of the phase noise of the source. Combining all of these features, we are able, under most conditions, to determine the phase noise of signal sources and signal handling components to an accuracy of ± 1 dB.

Acknowledgments

The authors wish to thank their many colleagues for helpful discussions on this topic, especially Dr. Tom Parker, Charles Stone, David Howe, Bob Temple, Michael Driscoll, Andrea DeMarchi, and David Allan. We also thank the Calibration Coordination Group of JCTG/CMT-JLC for support of this work.

REFERENCES:

1. F.L. Walls, S.R. Stein, J.E. Gray, and D.J. Glaze, Design Considerations in State-of-the-Art Signal Processing and Phase Noise Measurement Systems, Proc. 30th Ann. SFC, 269-274 (1976). (Available from National Technical Information Service, Sills Building, 5285 Port Royal Road, Springfield, VA 22161.)
2. F.L. Walls and S.R. Stein Accurate Measurements of Spectral Density of Phase Noise in Devices, Proc. of 31st SFC, 335-343 (1977). (Available from National Technical Information Service, Sills Building, 5285 Port Royal Road, Springfield, VA 22161.)
3. A.L. Lance and W.D. Seal, Phase Noise and AM Noise Measurements in the Frequency Domain at Millimeter Wave Frequencies, from Infrared and Millimeter Waves, Ken Button Ed., Academic Press, NY 1985.
4. F.L. Walls, A.J.D. Clements, C.M. Felton, M.A. Lombardi, and M.D. Vanek, Extending the Range and Accuracy of Phase Noise Measurements, Proc. of the 42nd Ann. SFC, 432-441 (1988.)
5. J.A. Barnes, A.R. Chi, L.S. Cutler, D.J. Healey, D.B. Leeson, T.E. McGunigal, J.A. Mullen, Jr., W.L. Smith, R.L. Sydnor, R.F.C. Vessot, G.M. Winkler, Characterization of Frequency Stability, Proc. IEEE Trans. on I&M 20, 105-120 (1971.)
6. D.W. Allan, H. Hellwig, P. Kartaschoff, J. Vanier, J. Vig, G.M.R. Winkler, and N.F. Yannoni, Standard Terminology for Fundamental Frequency and Time Metrology, Proc. of the 42nd Ann. SFC, 419-425 (1988.)
7. F.L. Walls, J. Gary, A. O'Gallagher, R. Sweet and L. Sweet, Time Domain Frequency Stability Calculated from the Frequency Domain Description: Use of the SIGINT Software Package to Calculate Time Domain Frequency Stability from the Frequency Domain, NISTIR 89-3916.
8. D.W. Allan and J.A. Barnes, A Modified "Allan Variance" with Increased Oscillator Characterization Ability, Proc. of the 35th Ann. SFC, 470-475 (1981.)
9. P. Lesage and T. Ayi, Characterization of Frequency Stability: Analysis of the Modified Allan Variance and Properties of Its Estimate, IEEE Trans. on I&M, 1984, IM-33, 332-337.
10. V.P. Kroupa and L. Sojar, "Modified Allan Variance: Transfer Function and Practical Applications," CPEM 1984 Digest (Delft, the Netherlands.)
11. P. Tremblay in "Étude de l'Effet du Filage du Signal sur la Caractérisation de la Stabilité de Fréquence," Thèse Université Laval, Quebec 1985.
12. F.L. Walls, D.B. Percival, and W.R. Ireland, Biases and Variances of Several FFT Spectral Estimators as a Function of Noise Type and Number of Samples, Proc. of 43rd Ann. SFC, 336-341 (1989.)

Table 1.

MEASUREMENTS OF $S_{\phi}(f)$ @ 5 MHz

SYNTHESIZER VS OSCILLATOR

f (Hz)	$S_{\phi}(f) _{AB}$ (dB Rel Rad ² /Hz)	$S_v(f) _{AB}$ (dBc/Hz)	$S_v(f) _A \beta^2_A$ (dBc/Hz)	Measured Noise Floor (dBc/Hz)
32	-119.8	-126.0	\approx -151.0	-154.0
100	-124.2	-127.0	\approx -152.0	-154.0
1 K	-132.1	-132.0	\approx -157.0	-158.0
10 K	-137.3	-133.0	\approx -158.0	-158.0
100 K	-136.8	-133.0	\approx -158.0	-158.0

Table 2.

MEASUREMENTS OF $S_{\phi}(f)$ @ 100 MHz SYNTHESIZER VS OSCILLATOR

0.050 to 32 MHz SA			0.1 Hz to 100 kHz SA			AM	NOISE	NOISE FLOOR	RESULT	
f (Hz)	Noise (dBV/Hz)	Mod level (dBV)	$S_{\phi}(f)_{AB}$ (rad ² /Hz)	Mod		$S_{VA}(f)$ (dBc/Hz)	β_A^2 (dB)	$S_{VA}(f) \beta_A^2$ (dBV/Hz)	$S_{\phi}(f)_{AB}$ (Rad ² /Hz)	
				Noise level (dBV/Hz)	Noise level (dBV)					
10 M	-99.1	-11.48	-148.0			-164			-148.0	
5 M	-96.0	-10.85	-145.6			-160			-145.6	
2 M	-94.8	-10.86	-144.3			-152			-144.3	
1 M	-92.0	-11.33	-141.1			-150			-141.1	
300 k	-84.7	-11.93	-133.2			-147			-133.2	
100 k	-85.6	-14.63	-131.4	-107.2	-36.07	-131.5	-141	-25.3	-166	-131.4
70 K	-88.4	-17.01	-131.8	-106.7	-34.94	-132.2				-132.0
50 k	-91.5	-20.10	-131.9	-105.8	-34.22	-132.0				-132.0
30 k				-105.5	-33.76	-132.1	-142		-167	-132.1
10 k				-106.4	-33.38	-133.4	-147		-172	-133.4
3 k				-105.8	-33.34	-132.9	-143		-168	-132.9
1 k				-102.5	-33.49	-129.4	-144		-169	-129.4
300				-102.4	-35.24	-127.6	-144		-169	-127.6
100				-102.7	-41.79	-121.3	-139		-164	-121.1
32				-102.0	-47.47	-114.9	-135		-160	-114.8

Table 3. Table of Uncertainties

EFFECT	OFFSET	UNCERTAINTY (dB)
Spectral density function of 100 kHz Spect. Analy.	0	0.2
Spectral density function of 32 MHz Spect. Analy.	0	0.2
Determination of mixer sensitivity	See Table 2	0.1
Relative gains of amplifiers	See Table 2	0.02
Linearity of 100 kHz Spect. Analy.	0	0.15
Linearity of 32 Mhz Spect. Analy.	0	0.2
Statistical confidence of data	0	$\pm 1/(200)^{1/2}$
Contribution of system noise floor	0	0.05
unfolding 3 corner hat	0	0.1
Contribution of residual AM	0	0.05

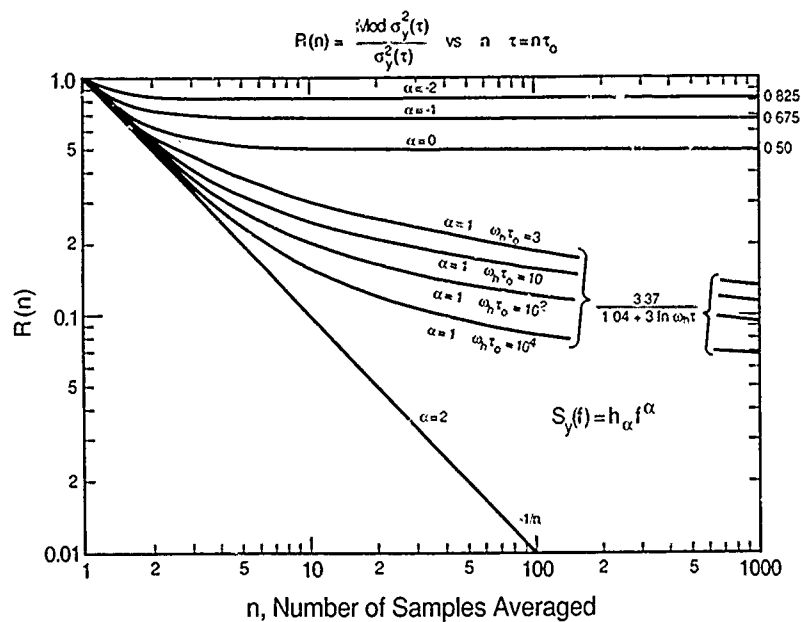


Figure 1. Ratio of $\text{Mod } \sigma_y^2(\tau)$ to $\sigma_y^2(\tau)$ as a function of n , the number of samples averaged together to obtain $\text{Mod } \sigma_y(\tau)$ and the power-law noise type.

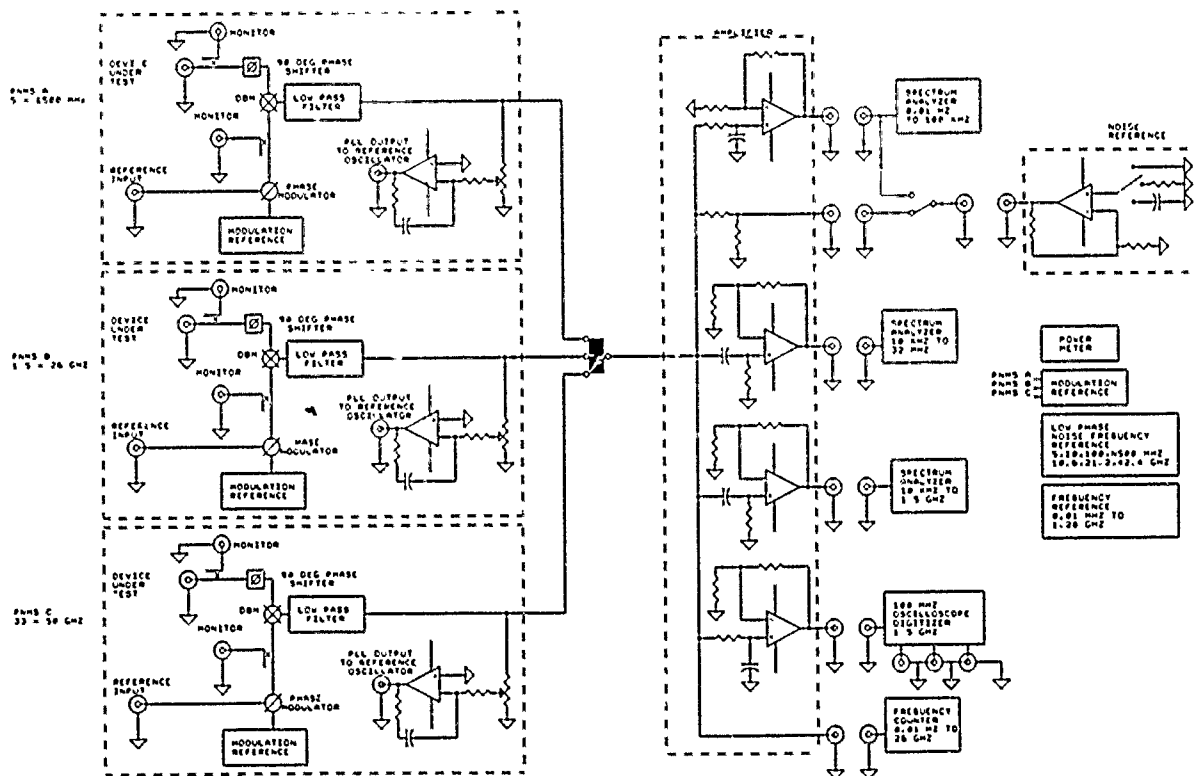


Figure 2. Overall block diagram of our new phase-noise-measurement system.

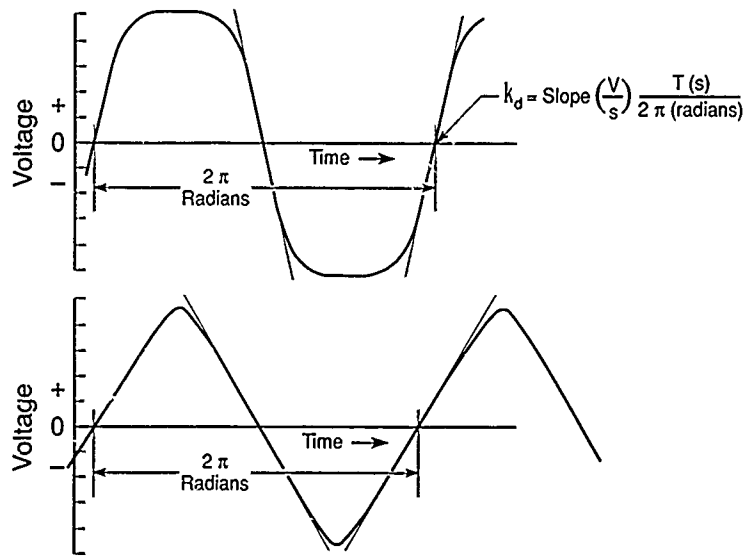


Figure 3. Typical beat-frequency waveforms seen at the output of the scope channel. This channel has high dynamic range and low gain so that it does not saturate or experience slewing rate limitation for beat frequencies from dc to 50 kHz.

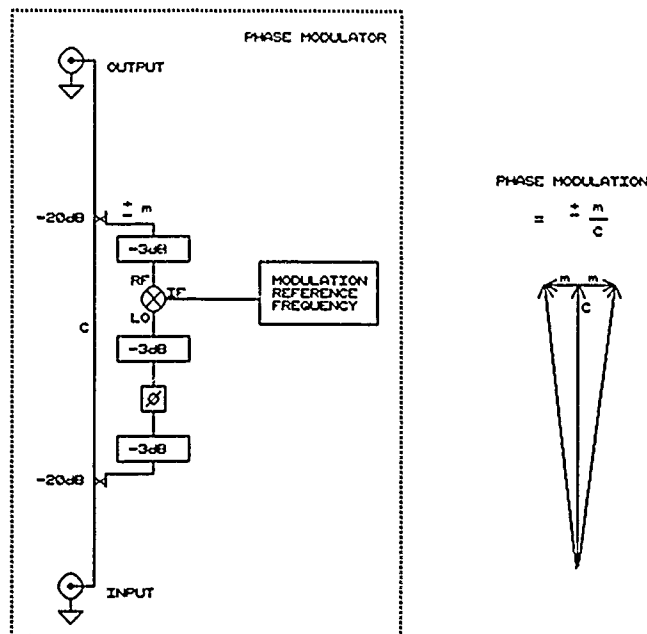


Figure 4. Block diagram of our new phase modulator. The phase modulation is given by $\pm m/C$ where m is the amplitude of the signal coupled back into the carrier and C is the amplitude of the carrier. This assumes that m/C is small compared to 1. The phase shift, ϕ , is adjusted to minimize the amplitude modulation detected on the output signal.

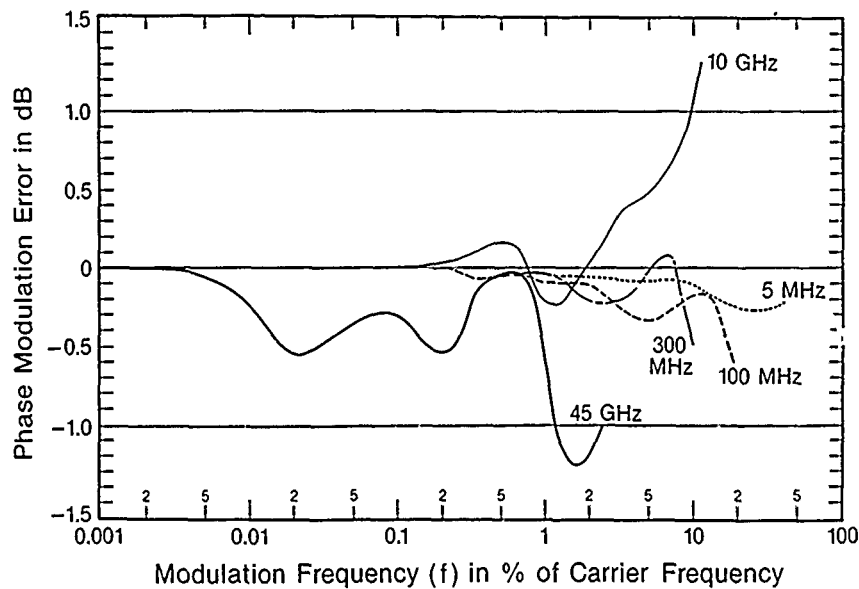


Figure 5. Error in the amplitude of the phase modulation as a function of the modulation frequency expressed as a percentage of the carrier frequency. The curves labeled, 5, 100, and 300 MHz refer to results measured on the modulator for the 5-1500 MHz front end. The phase shift, ϕ , was adjusted for each frequency. The curve labeled 10 GHz refers to results measured on the modulator for the 1.5 to 26 GHz front end. The curve labeled 45 GHz refers to the results measured with the 33 to 50 GHz front end.

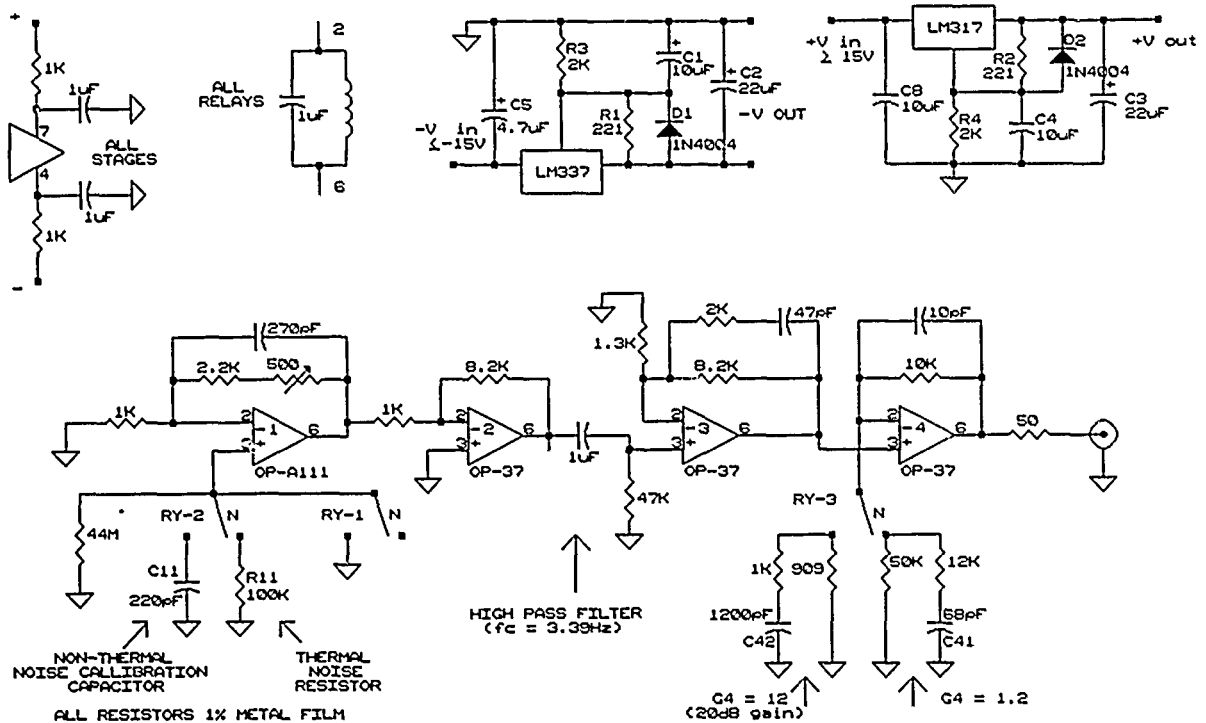


Figure 6. Schematic diagram of the precision noise source used to verify the spectral density function of the spectrum analyzers.

CALIBRATION OF FFT SPECTRUM ANALYZER

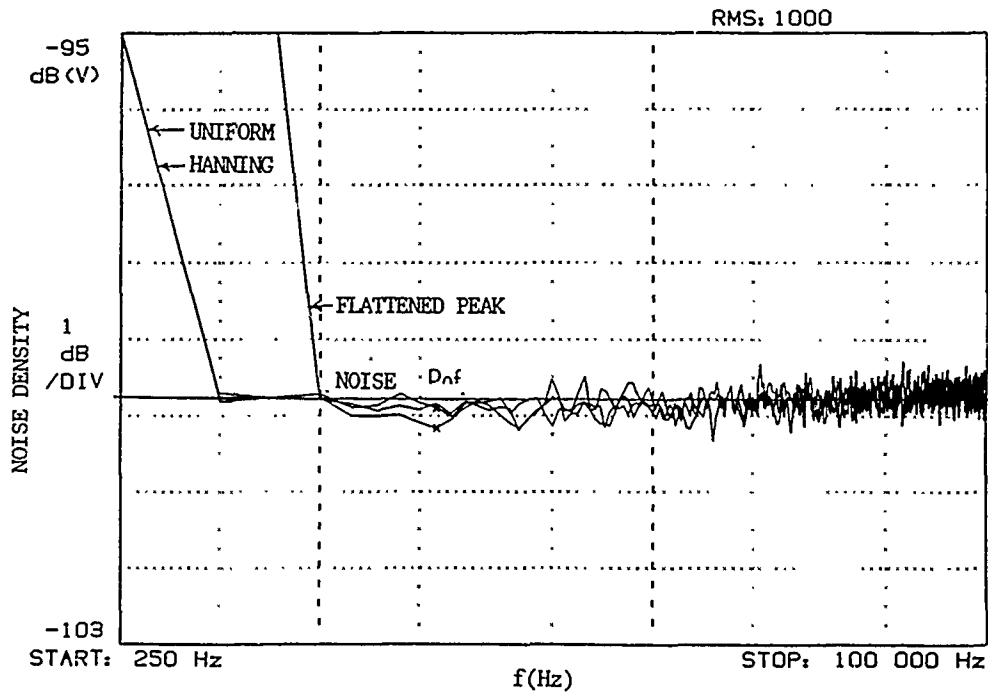
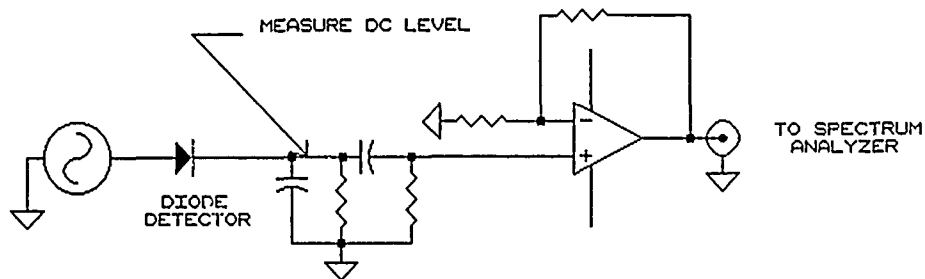


Figure 7. Calibration of the spectral density function of an FFT spectrum analyzer using the noise source of figure 6. The Hanning window yields the best overall performance for noise. The Uniform window is not accurate for noise that falls faster than f^{-2} . The first 15 channels are inaccurate for the flattened-peak window if the noise falls as f^{-2} or faster.



$$V(t) = V_0(1 + \alpha t)(\cos \omega t)$$

Figure 8. Block diagram of one possible method for measuring amplitude noise in sources. The conversion sensitivity of the diode $K_{AM}^2(\nu_0, V_0, \alpha)$ is calibrated using a source that can be modulated. The amplitude of the modulated source is adjusted so that the detected dc level is the same as the source to be measured.

QUESTIONS AND ANSWERS

DAVID ALLAN, NIST: Maybe I am missing something here, I am not sure—once before you showed the biases caused by the different windowing functions in the spectrum analyzer for $1/f$ noise and so forth. Is that also in your error budget?

MR. WALLS: That has been taken care of by using the appropriate window function and controlling the range over which it is used.

MR. STEIN: The question that I have is related to the decorrelation when you measure the noise floor with two signals coming in. You used a time delay between the two paths that was related to the 90° phase shift at the mixer. Is it possible to get, other than delay lines, to operate the mixer in quadrature and still get the same group delay? By using two phase shifts instead of delay?

MR. WALLS: I have thought about it. I am not sure. When you are trying to go out to 10% of the carrier it will absolutely limit your capability.

NEW HYDROGEN MASERS AT THE NATIONAL RESEARCH COUNCIL OF CANADA

D. Morris and J. Vanier
Laboratory for Basic Standards
Physics Division, National Research Council
Ottawa, Ontario, Canada K1A 0R6

Abstract

Two active hydrogen masers for laboratory use have been constructed recently at the National Research Council of Canada (NRC). These have been designed to be operated as clocks and as contributors to the NRC time scale. Details of their design are presented. Although the masers have not yet been operated under full temperature control and with the complete electronics package, some preliminary measurements of line-Q and frequency stability have been made, and will be discussed.

INTRODUCTION

The National Research Council of Canada has been involved in research in the PTTI field for over 40 years. A number of designs of primary cesium beam frequency standards and clocks have been built and, currently, three are in operation. These are designated CsV, CsVIA, and CsVIC. In addition, two hydrogen masers, H1 and H2, have been operated as frequency standards for over 20 years. At present, one of these (H1) is still in use. Recently, two new active hydrogen masers, designated H3 and H4, have been designed and constructed. They form the subject of this paper. Details of their design will be presented, together with some preliminary operating characteristics.

GENERAL DESIGN DETAILS

The design of these masers has been based partly on experience gained at NRC^[1] and at Laval University in Quebec City where hydrogen masers have also been built. Details of the Laval masers were presented at an earlier PTTI meeting^[2].

Eventually, it is planned to operate the masers H3 and H4 as clocks and as contributors to the NRC time scale. This requires that they exhibit good reliability and good long-term frequency stability. To this end, considerable care has been taken to isolate the resonant cavity mechanically and thermally. Also, a number of improvements have been made over the earlier masers constructed at NRC. For example, only metal seals are used on the vacuum system. Improved magnetic shielding and improved temperature control systems are also employed.

The masers are housed in cabinets 71 cm wide, 120 cm long and 155 cm high. They can be moved to different locations in the building, if desired, but are not designed for complete portability. The electronic circuits are contained in the maser cabinets. DC power for the masers is obtained from float-charged storage batteries, and AC power from the line with back-up diesel generator protection.

The design of the masers is shown in Fig. 1. Many of the features are quite conventional and only certain points of interest will be referred to. To reduce the effect of ambient magnetic field fluctuations five layers of magnetic shielding are used. The dimensions and spacing of these shields are similar to those used on the Laval University masers^[2] for which a longitudinal shielding factor of 100,000 was measured^[3]. A similar value is expected in this case. This means that a 10% fluctuation in the earth's field should cause a frequency change of less than 1 part in 10^{15} .

Three concentric ovens are used outside the vacuum system for temperature control and, inside the vacuum system, two thermal shields consisting of aluminum cylinders and end plates enclose the resonant cavity. They are thermally insulated from each other and from the vacuum enclosure by means of ceramic spacers. This arrangement should result in high isolation of the cavity from external temperature changes.

CAVITY SUPPORT STRUCTURE

The structure used for supporting the cavity inside the thermal shields and the vacuum enclosure has been designed to give good mechanical decoupling from outside vibration and barometric pressure changes. The bases of the thermal shields are supported on kinematic mounts employing the ceramic spacers already mentioned and pyrex balls. The quartz baseplate of the cavity is supported on three titanium pins with rounded tips which fit into conical holes in the quartz. Flexing of the pins will take up the difference in dimensions due to relative thermal expansion of the quartz and aluminum. The top plates of the cavity and the thermal shields are lightly loaded mechanically by beryllium copper leaf springs which are thermally isolated by pyrex balls. Details of the cavity region are shown in Fig. 2.

The resonant cavity is made of fused quartz. It is thermally compensated by means of a re-entrant aluminum disk attached by three aluminum posts to the quartz ring at the top. The quartz is silvered internally using fired-on silver paint. The loaded Q of the cavity is 38 000. There are two coupling loops, one with a coupling coefficient of about 0.15 and the other with a much lower value. A spherical storage bulb 18 cm in diameter is symmetrically located in the cavity. It is coated internally with FEP-120 Teflon and the neck of it is fitted with a collimator consisting of a bundle of seven thin-walled quartz tubes inside a quartz sleeve. The tubes are also coated with Teflon. The theoretical storage time is 3 seconds.

VACUUM SYSTEM AND HYDROGEN SOURCE

All vacuum seals on the masers use metal wires or rings: either copper or indium. Pumping is performed by a single 270 L/s ion pump. A successful sealing arrangement for the pyrex source bulb is shown in Fig. 3. It uses a double indium wire seal. Two stainless steel rings are clamped to a flange on the source bulb using one indium seal. The assembly, consisting of the bulb plus the rings, is then inserted into the housing and clamped against the second indium seal.

The hydrogen pressure in the source bulb is stabilized by using a servo system controlling the temperature of a thin-walled tube of palladium-silver alloy closed at one end and heated by passing a current directly through it. This system has a response time of a few seconds, making it very useful for rapid beam flux changes required when cavity tuning by spin exchange broadening is used.

MASER ELECTRONICS

The masers have been designed with the option of operating either free-running, with stand-alone cavity frequency servos employing injected square wave FM signals^[4], or with an external spin-exchange auto-tuner which uses each maser in succession as a stable frequency reference^[5]. A simplified block diagram of the receiver is shown in Fig. 4. A 5 MHz BVA quartz crystal oscillator is locked to each maser. The signal injection cavity control servo shown can be disabled quite simply if free-running operation of the maser is desired.

When the masers are used as time standards, it is necessary to run the 5 MHz crystal oscillators at their nominal values by adjustment of the 5751 Hz synthesizers. These can be adjusted in steps of 0.1 mHz, resulting in minimum relative frequency changes in the maser output of steps of 7 parts in 10^{14} .

If an external spin-exchange auto-tuner is used there must be a frequency offset between the signals from the two masers so that suitable beat periods can be measured. It is preferable to do this without adjusting the settings either of the 5751 Hz synthesizers or of the magnetic fields of the masers. One way of accomplishing this is to use the system shown in Fig. 5. The 5 MHz output from maser H4 is multiplied to 1400 MHz and that from H3 is multiplied to 1440 MHz. These are mixed and filtered to give the 40 MHz component, which is again mixed with a signal derived from H3. This signal is produced by mixing the outputs of a multiplier and a synthesizer, to give a frequency of $40 \text{ MHz} + \delta$, where δ is the desired beat frequency (typically 1 Hz). The beat frequency may be changed by adjustment of the synthesizer frequency. Although it is not obvious from Fig. 5, the circuitry is designed so that it is a simple matter to switch from the signal injection cavity servo mode to the external auto-tuner mode.

PRELIMINARY PERFORMANCE DATA

Masers H3 and H4 are not yet in full operation. However, mechanical construction is complete and preliminary testing has been carried out. Both masers have oscillated at low magnetic fields, and preliminary measurements have been made using a temporary receiver. A line-Q value of 4×10^9 at a reasonable operating flux level has been measured. This compares favorably with the value of 1.9×10^9 at normal operating flux for maser H1. Fig. 6 shows a plot of maser power as a function of linewidth for H4. The experimental values of linewidth at the extremes of the oscillation curve correspond to line-Q values of 6.1×10^9 and 1.3×10^9 respectively. The accuracy to which the maser can be tuned when the spin-exchange method^[6] is used depends on the relative linewidth broadening between operation at a low beam flux setting and a higher one. With the range of linewidths available at reasonable flux levels in this case the accuracy of tuning can be made high. Crampton and Wang^[7] have shown that by fitting a quadratic to the power vs linewidth data it is possible to derive the value of several maser parameters and, in particular, the quality factor q ^[8,9]. From the data shown in Fig. 6 a value of q of 0.08 was derived.

The receivers and cavity control circuits have now been completed and installed on the masers. However, they have not yet been completely checked out. Earlier this year, preliminary frequency stability measurements were made using a temporary receiver. In this test the magnetic field of one maser was increased in order to obtain a frequency offset of the masers of about 0.1 Hz. The measured frequency stability is shown in Fig. 7. This preliminary measurement shows a minimum value of $\sigma(2, \tau)$ of 5.0×10^{-15} (3.5×10^{-15} on a per maser basis) at 1000 s. In view of the lack of temperature control on the masers and the use of temporary electronic circuits, it is felt that this is a satisfactory result.

FUTURE PLANS

This paper is essentially a progress report on the development of the two new hydrogen masers. More comprehensive results will be reported at a later date, when all the final electronic circuits are in use. It is planned to obtain frequency stability data under free-running conditions and with the two different tuning systems before deciding which system gives rise to the best long term frequency stability. After this decision is made the masers will be incorporated into the NRC time scale as clocks.

ACKNOWLEDGEMENTS

We would like to thank Mr. R. Cote and Mr. G.J. Trudeau for the mechanical construction of the masers, Mr. M. Kotler for assistance with the mechanical design, and Mr. W. Cazemier and Mr. J. Belanger for technical assistance with electronic circuits and mechanical assembly, respectively.

REFERENCES

1. A. G. Mungall, D. Morris, H. Daams, and R. Bailey, *Metrologia* 4, 87-94 (1968).
2. J. Vanier, G. Racine, R. Kunski, and M. Picard, *Proc. 12th Annual PTTI Applications & Planning Meeting*, 807-824 (1980).
3. R. Kunski and J. Vanier, *J. Phys. E. Scientific Instr.* 15, 1207-1209 (1982).
4. C. Audoin, *Rev. Phys. Appl.* 16, 125-130 (1981).
5. D. Morris and K. Nakagiri, *Metrologia* 12, 1-6 (1976).
6. J. Vanier and R.F.C. Vessot, *Appl. Phys. Lett.*, 4, 122-123 (1964).
7. S.B. Crampton and H.T.M. Wang, *Phys. Rev. A* 12, 1305-1312 (1975).
8. D. Kleppner, H.C. Berg, S.B. Crampton, N.F. Ramsey, R.F.C. Vessot, H.E. Peters, and J. Vanier, *Phys. Rev.* 138, A972-A983 (1965).
9. J. Vanier and C. Audoin, "The Quantum Physics of Atomic Frequency Standards", Adam Hilger, Bristol, U.K. (1989)

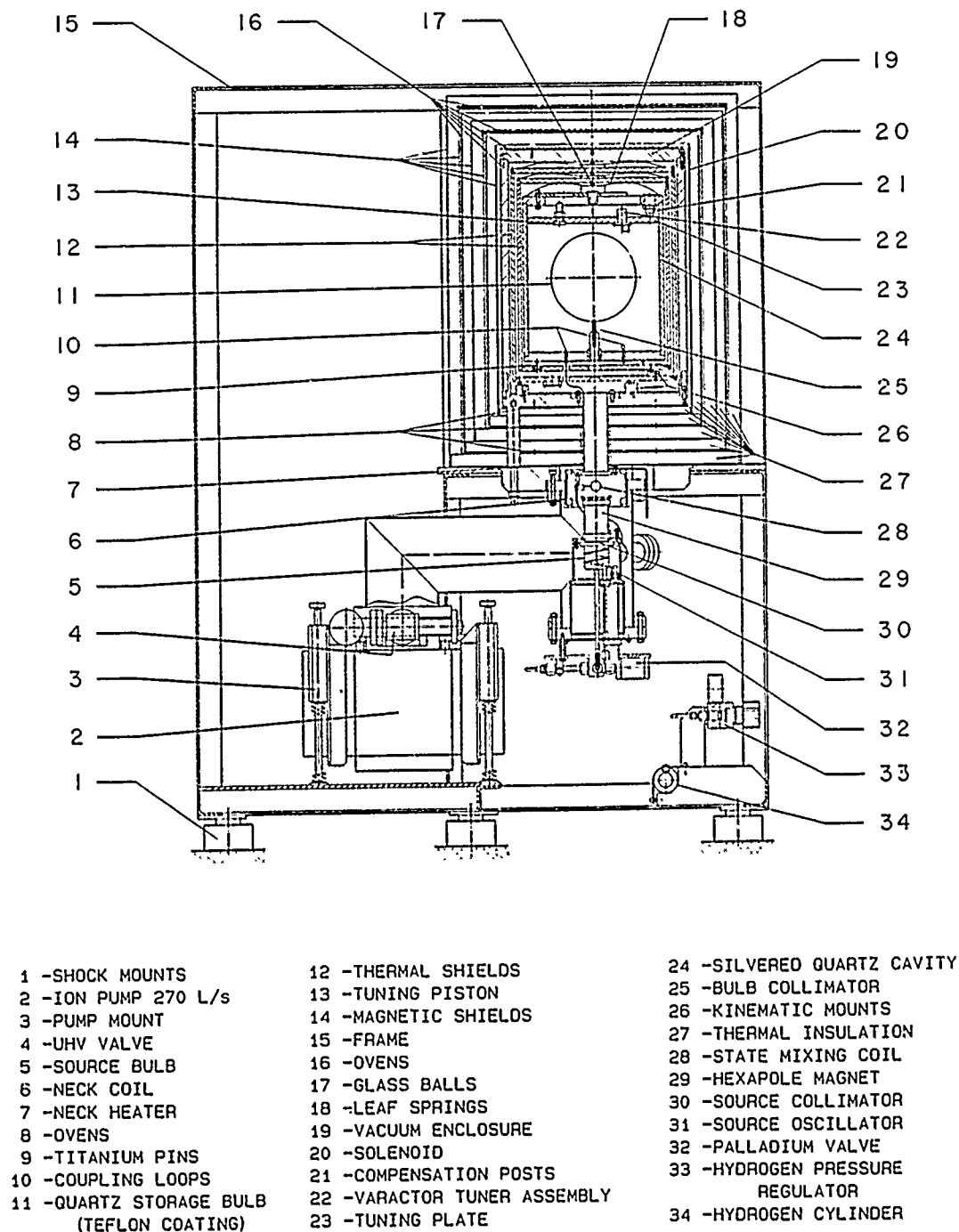


Fig. 1. Drawing showing the design features of the masers.

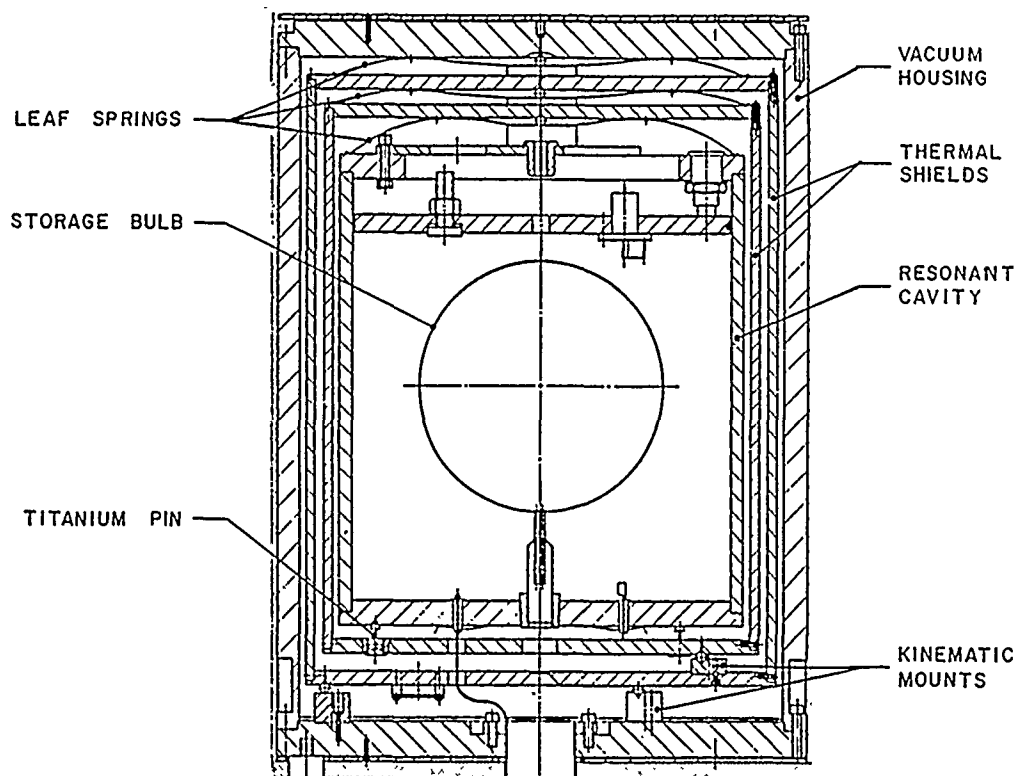


Fig. 2. Detail of cavity region showing thermal shields and kinematic supports.

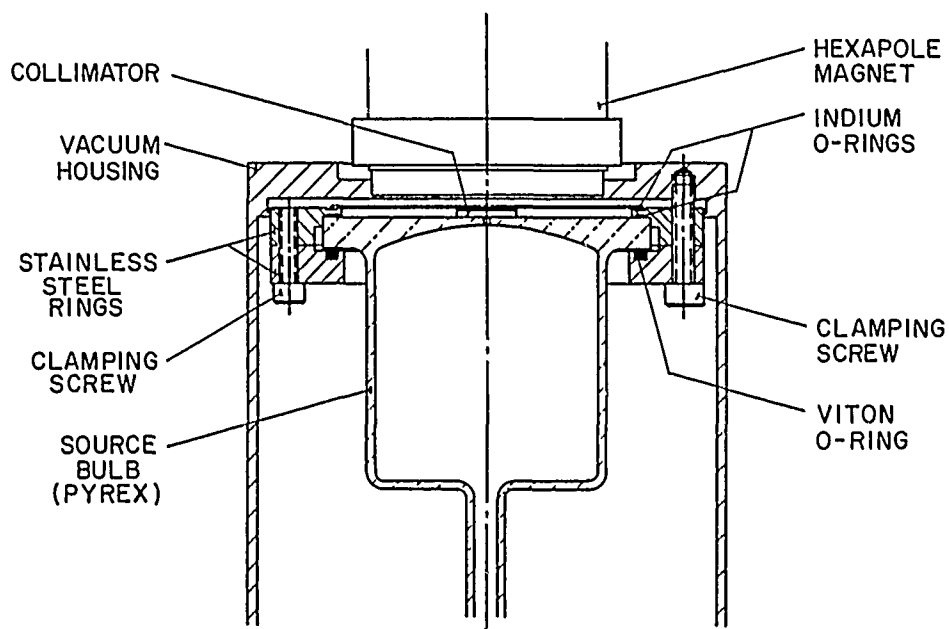


Fig. 3. Detail of vacuum seal to the hydrogen source. The seal is shown in process of assembly.

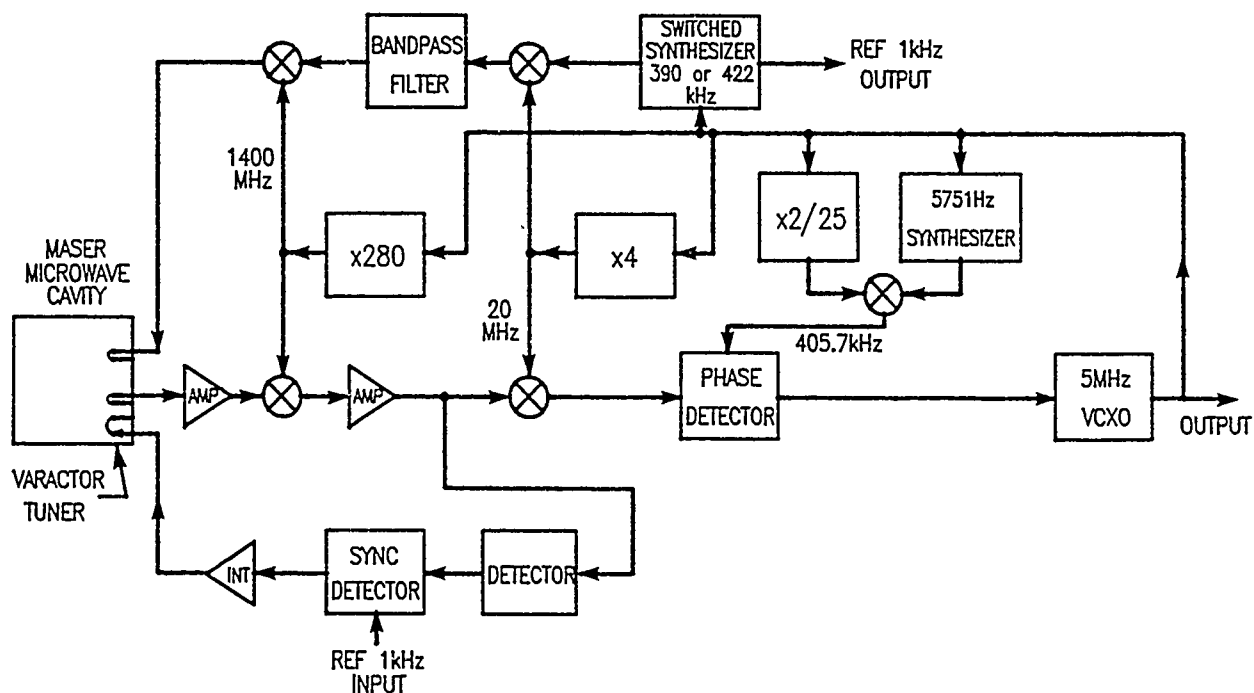


Fig. 4. Simplified block diagram of the maser receiver.

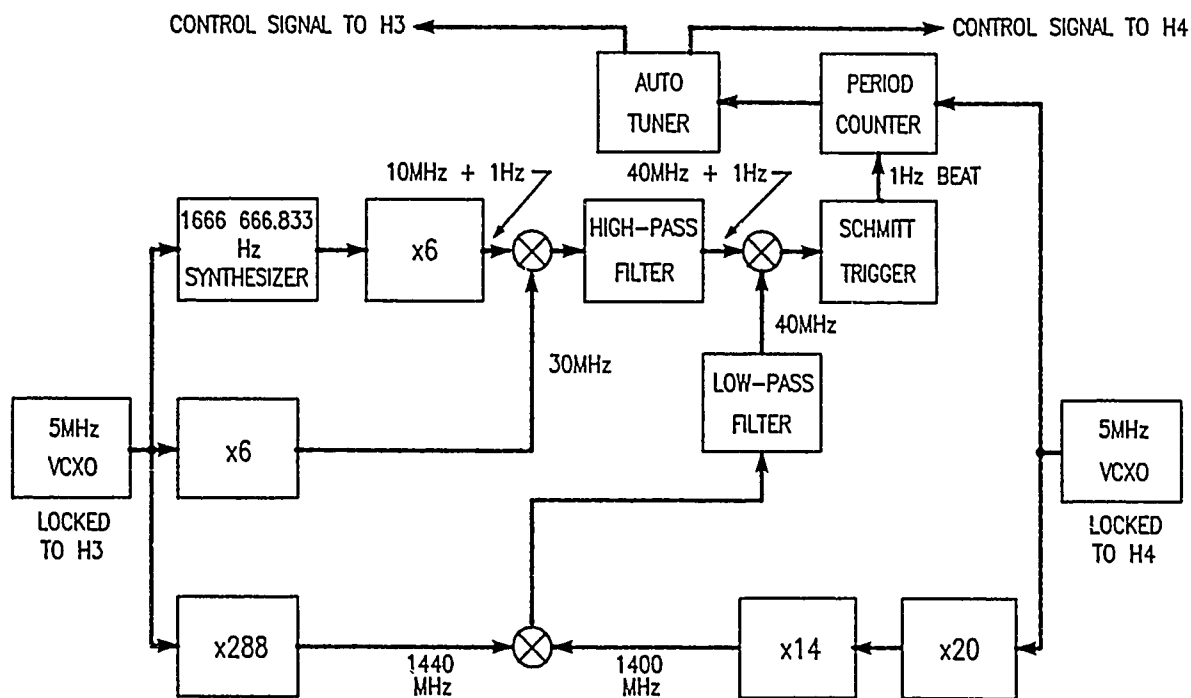


Fig. 5. Block diagram of system designed to produce beats between the masers.

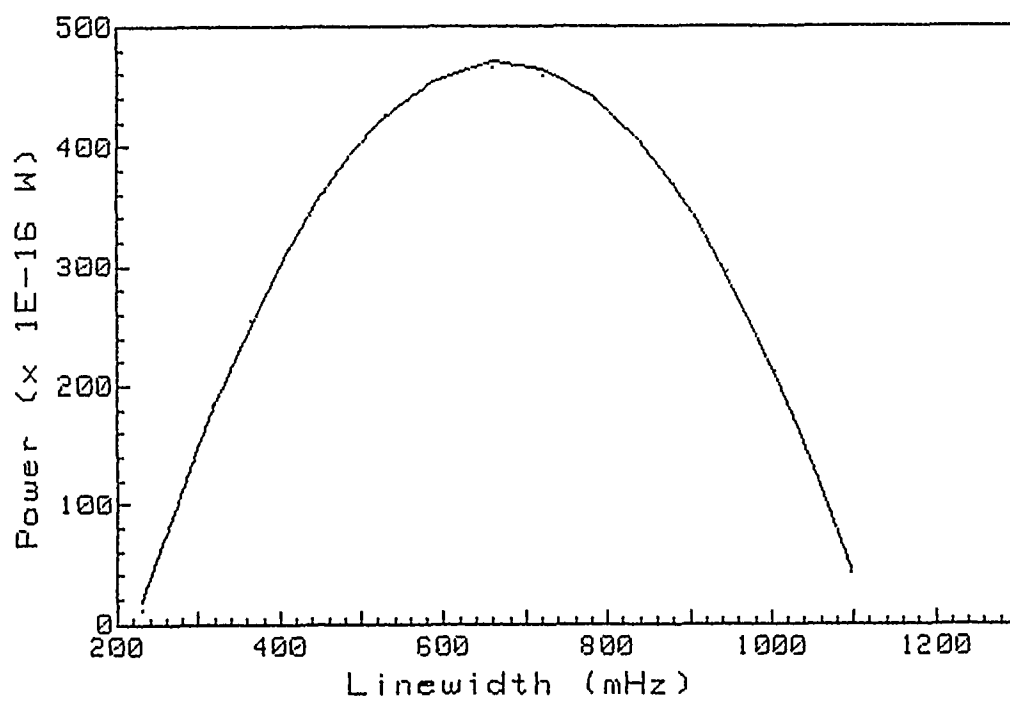


Fig. 6. Output power of maser H4 as a function of linewidth.

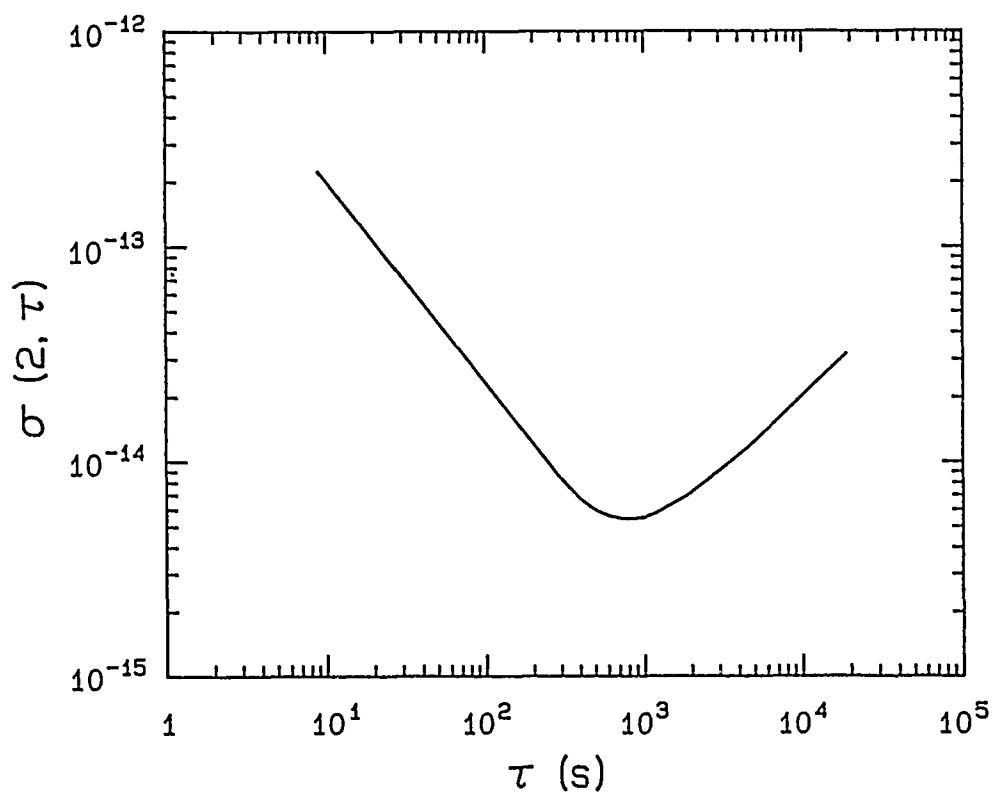


Fig. 7. Preliminary frequency stability data.

QUESTIONS AND ANSWERS

ALBERT KIRK, JPL: How do you introduce the hydrogen into the dissociator bulb and what kind of seal do you use there?

MR. MORRIS: We use a palladium leak which is brazed on and then copper seals are used.

MR. KIRK: Copper seals between the palladium and the glassware?

MR. MORRIS: There is a metal-glass seal and then the stainless steel tubing seal with copper rings seal to the palladium leak.

FRED WALLS, NIST: Do you have any magnetic shielding between the source and the state selector and the entrance to the magnetic shields around the cavity?

MR. MORRIS: No, we don't. We have a coil that can be activated if necessary in the region between the source and the underside of the magnetic shields. We haven't really had a chance to look at any effects yet, but a quick look at, applying reasonable currents, seemed to show no change in oscillation level.

DAVID ALLAN, NIST: The turn up in the σ vs. τ curve, was that cavity pulling or do you know what be the cause?

MR. MORRIS: We had no temperature control on the masers, there were cables all over the place. It was just to get an initial look at how they were working. We don't have the proper receivers in operation yet, either.

STATUS REPORT ON A SYNCHRONIZATION EXPERIMENT BETWEEN EUROPEAN TIME SCALES USING ECS GEOSTATIONARY SATELLITE

V. Pettiti, F. Cordara, P.G. Galliano
Istituto Elettrotecnico Nazionale Galileo Ferraris
Torino (Italy)

This work has been done in the frame of a scientific cooperation program
between Czechoslovakia and Italy

Abstract

To test the capabilities of a synchronization system based on the use of the passive television method applied to the signals broadcasted by a geostationary satellite, namely ECS telecommunication satellites, a time synchronization experiment between the time scales of the Istituto Elettrotecnico Nazionale (IEN) and other European laboratories (URE - Czechoslovakia, TUG - Austria, AOS - Poland, ASMW - Democratic Rep. of Germany, VSL - Netherlands, STA - Sweden), was started in July 1988 and is still in progress.

The results obtained in the first year of comparisons are presented and possible solutions to the satellite position determination problem are considered together with the measurement results of the receiving station delay performed at IEN.

1.- Introduction

The synchronization of time scales by means of the television passive method using the ground TV networks, has been experienced during the last twenty years by most of the laboratories involved in time and frequency metrology. It is known that, within the view of a common TV transmitter, this simple and inexpensive method can yield a timing precision of about 10 ns (1 σ). Over extended geographical areas, where different transmitters interconnected by microwave links have to be used, the precision is lowered by at least one order [1] due mainly to the differential propagation delay variations between the measuring sites. Nowadays there seems to be a chance to overcome these problems by using the TV method with the signal received from geostationary telecommunication satellites that covers nearly continental areas with different TV programs.

Some synchronization experiments between time scales using this kind of technique were already performed in some countries [2,3,4,5,6], but no attempt has been made to elaborate the method, both technically and organizationally, to a degree that it could serve on a routine basis to various users.

This paper will give a status report about a synchronization experiment, which started in July 1988 and is still continuing, between some European laboratories, aiming to establish a system based on the reception of television signals from a geostationary satellite which would allow for high precision time and frequency comparisons at moderate costs all over Europe.

2.- Estimation of Timing Accuracy

The use of the television signals broadcasted by a geostationary satellite for the synchronization of clocks has some advantages but also one major drawback. If it is evident in fact that the measurements are performed on signals coming from a unique source and that the propagation effects on their carrier frequency (11 GHz) are negligible, the key question that has to be solved is how to determine the satellite instantaneous position to evaluate the differential delays with sufficient accuracy. Obviously, the differential delay error will be equal to the timing error. The problem is that the satellite in the geostationary orbit is not fixed with respect to its observers; due to the natural forces it is in a permanent motion maintained within a so called "parking box" by occasional corrective manoeuvres initiated by the control tracking center on the Earth. Generally the satellite position may not deviate by more than 0.1° from its nominal position, both in longitude and latitude [7]. Though small the deviation seems, it may still cause unacceptable changes of the differential delay depending, for a given satellite, on the position of the observers.

The geostationary satellites chosen for this synchronization experiment belong to the family of European Communication Satellites (ECS) of the European Space Agency (ESA). In the followings we will deal in particular with ECS 5 satellite, that is positioned at 10 degrees East to estimate the time synchronization error that one can expect over the European continent if the satellite coordinates are affected by unpredictable variations. The zone covered by the ECS satellites is shown in Fig. 1 where is outlined also the area served by the spotbeam west that has been used in our experiment.

Let us consider two receiving sites A and B and a geostationary satellite S, whose positions relative to a rotating equatorial geocentric reference frame can be expressed with the following vectors:

$$\begin{aligned}\vec{r}_A &= \vec{r}_A(\theta_A, \lambda_A, r_A) \\ \vec{r}_B &= \vec{r}_B(\theta_B, \lambda_B, r_B) \\ \vec{S} &= \vec{S}(\theta_S, \lambda_S, r_S)\end{aligned}\tag{1}$$

where: $\theta_{A,B,S}$ is the geodetic latitude
 $\lambda_{A,B,S}$ is the longitude referred to Greenwich
 $r_{A,B,S}$ is the distance from the center of the Earth

The differential propagation delay of the signals transmitted by the satellite and received at stations A and B, can be expressed as:

$$t_p = \frac{1}{c} [|\vec{S}-\vec{r}_A| - |\vec{S}-\vec{r}_B|] = \frac{1}{c} [\rho_A - \rho_B] \quad (2)$$

where ρ_A and ρ_B are the distances of the receiving stations from the satellite and c is the mean value of the speed of light along the propagation path.

To compute the variation of the differential propagation delay t_p , between the two stations, that affect the synchronization results, we have considered the satellite movements both in longitude $\Delta\lambda$ and latitude $\Delta\theta$ neglecting any change in its range. This assumption is justified as a first approximation because in our case, as can be verified in the followings, the variation in range is nearly one fifth compared with the variations in latitude and longitude.

Differentiating the term $(\rho_A^2 - \rho_B^2)$ versus $\Delta\theta$ and $\Delta\lambda$, assuming that the variations of $(\rho_A + \rho_B)$ due to the satellite motion are negligible with respect to those of the term $(\rho_A - \rho_B)$ and, being the latitude of the satellite θ_s very close to 0 degrees, we can write the approximate expression:

$$\Delta(\rho_A - \rho_B) = \frac{2Sr_A}{\rho_A + \rho_B} [\cos\theta_A \sin(\lambda_S - \lambda_A) \Delta\lambda_S - \sin\theta_A \Delta\theta_S] - \frac{2Sr_B}{\rho_A + \rho_B} [\cos\theta_B \sin(\lambda_S - \lambda_B) \Delta\lambda_S - \sin\theta_B \Delta\theta_S] \quad (3)$$

Solving this equation for different "B" sites in Europe after having fixed station A at IEN - Torino, several values of $\Delta t_p = \Delta(\rho_A - \rho_B)/c$ have been found assuming the worst case of 0.1° of variation both in latitude ($\Delta\theta$) and longitude ($\Delta\lambda$) of ECS 5. In Fig. 2 are reported the contours of the time errors that can affect the synchronization values as obtained from equation (3).

3.- Experiment Description

To test the potentiality of a synchronization system based on a geostationary satellite using the passive television method, four European laboratories began on July 1988 an experiment that is still in progress and were joined later on by other three in the frame of a Euromet project. The participating laboratories at November 1989 are the following ones:

- Astronomical Latitude Observatory (AOS) - Borowiec, Poland
- Amt für Standardisierung, Messwesen und Warenprüfung (ASMW) - Berlin, Dem. Rep. of Germany
- Istituto Elettrotecnico Nazionale (IEN) - Torino, Italy
- Ústav Radiotechniky a Elektroniky (ÚRE) - Praha, Czechoslovakia
- Swedish Telecommunications Administration (STA) - Stockholm, Sweden
- Technische Universität (TUG) - Graz, Austria
- Van Swinden Laboratorium (VSL) - Delft, Netherlands

In Table 1 are reported the baselines between the laboratories involved in the experiment.

Table 1 - Baselines between the laboratories

IEN							
AOS	1064						
ASMW	937	236					
STA	1726	769	797				
URE	765	301	266	1033			
TUG	649	590	614	1356	348		
VSL	813	869	634	635	736	525	
	IEN	AOS	ASMW	STA	URE	TUG	VSL

ECS satellites of Eutelsat and in particular, since mid-October 1988, ECS-5 placed in a geostationary orbit at 10° East longitude, were chosen for the experiment.

Among the television channels available from these satellites, RAI UNO program broadcasted at 11.009 GHz in horizontal polarization by a 20 w transponder has been used. At each site was arranged a measurement setup of the kind shown in Fig. 3. Some technical details about the receiving stations are reported in Table 2 together with the antennas coordinates.

Table 2 - Ground stations specifications

Laboratory	PARAMETER						
	Latitude	Longitude	Height	Antenna Ø	LNA	IF BWT	Time ref.
AOS	52°16'37.0" N	17°04'23.7" E	129 m	2 m	1.4 dB	40 MHz	UTC(AOS)
ASMW	52°27'14" N	13°37'01" E	50 m	0.9 m	1.4 dB	30 MHz	UTC(ASMW)
IEN	45°00'53.6" N	07°38'20.1" E	297 m	3 m	1.9 dB	40 MHz	UTC(IEN)
URE(TP)	50°07'53" N	14°27'09" E	300 m	3 m	2 dB	-	UTC(TP)
TUG	47°04'01.5" N	15°29'35.5" E	534 m	1.5 m	1.4 dB	30 MHz	UTC(TUG)
VSL	51°59'58.9" N	04°22'50.7" E	60 m	3 m	4.5 dB	40 MHz	UTC(VSL)
STA	59°09'54.2" N	18°08'13.5" E	109 m	-	-	-	UTC(STA)

Every day two sets of 20 time interval measurements between the local 1 PPS reference and the trailing edge of the first field synchronizing pulse of the RAI UNO video signal were measured starting at 08:15:01 UTC and 20:15:01 UTC in each laboratory.

In two sites, namely IEN and TUG, time differences between the local 1 PPS and the satellite TV signal were also measured every ten minutes from November 1988 to March 1989 to get information about the satellite movement.

All the participating laboratories collaborate to the international atomic time scale and are linked to BIPM using either the GPS time link (IEN, TUG, VSL, STA) or the television link (AOS, ASMW, TP).

Satellite position data for November and December 1988 have been supplied by the ESA satellite control station at Redu (Belgium) that is charged of ECS satellites tracking. These data have been used to investigate the satellite movement and to correct the synchronization data.

4.- Measurement results

The evaluation of the results obtained in the ECS synchronization experiment, has been focused on the period for which ESA-Redu orbital elements data were available. From these data, the variations of ECS 5 in latitude, longitude and range from the origin of the rotating reference frame have been computed and reported in Figure 4 where it can be seen that the variations around their mean values are within ± 16 km (range), $\pm 0.07^\circ$ (long.), $\pm 0.08^\circ$ (lat.). Some discontinuities due to orbital manoeuvres can also be observed.

In Fig. 5 are reported the differences between the ECS measurements performed every ten minutes at IEN and TUG relative to the beginning of November 1988 where the diurnal variations due to the satellite movement are clearly recognizable. Each point in this figure represents in microseconds, with a constant value subtracted, the difference of the distances of the satellite from IEN - Torino and from TUG - Graz versus time. The interruptions in the curve are due to the lack of TV transmissions.

For all the computations performed on the measured data whose results are reported in all the next graphs, the linear regression parameters, computed at every laboratory for each series of 20 time interval readings, were used. This solution was chosen to reduce the amount of information to be exchanged among the laboratories. Together with the linear fit parameters, the standard deviation of the residuals was computed after the rejection of the outliers by means of a statistical filter.

In Fig. 6 have been reported the time differences between UTC(IEN) and UTC(TP) obtained from ECS 4 and ECS 5 (*) synchronization measurements from

(*) The following ECS satellites were used in the course of this experiment:

ECS 4 from mid-Sep. 88 to mid-Oct. 88 (10°E)

ECS 5 from mid-Oct. 88 onward (10°E)

mid-September 1988 up to June 1989. Two curves have been traced to distinguish the two daily sets of measurements (08:15 and 20:15 UTC). The peak-to-peak variation of each curve, if the mean rate between the two time scales is removed, is of the order of 5 microseconds that is well within the time error estimated previously and reported in Fig. 2.

The results of the time comparisons performed between IEN and the other metrological laboratories (AOS, ASMW, TP-URE by means of ECS 5 in November-December 1988 together with those corrected for the ESA satellite position data and the BIPM data, from Circular-T, have been plotted in Fig. 7.

From these graphs it can be seen that the peak-to-peak time excursions are reduced to some hundreds of nanoseconds, if one corrects for the differential propagation delay variations, and that the mean rates of the time scales compared are in good agreement with those obtained from BIPM data. As regards to the uncertainty of these comparisons, worst-case residuals at the microsecond level have been found.

As a sample of the dependence of the peak-to-peak fluctuations from the baselines between the laboratories, in Fig. 8-a are reported the differences between UTC(TP) and UTC(ASMW) having a baseline of 266 km, and in Fig. 8-b those obtained in the case of UTC(IEN) and UTC(STA) that have a baseline of 1726 km. The time step of the order of 1 μ s that can be noticed in the graphs of UTC (ASMW) is probably due to instrumental changes in the ECS measurement system of this laboratory.

The differences between the synchronization results obtained with ECS 5 and the BIPM data are mainly due to the following factors: the uncertainties in the satellite position data supplied by ESA, of the order of 0.004° in latitude (~ 3 km in the North-South direction), 0.007° in longitude (~ 5 km in the East-West direction), in the receiving antennas coordinates that were given in different reference systems and the differential delays of the receiving stations which have not been entirely accounted for.

In the case of the time comparisons between IEN and TUG, reported in Fig. 9, the curves obtained from ECS 5 (corrected for the satellite position) and the BIPM data are in closer agreement because the antenna coordinates are expressed in the same reference system with a better uncertainty. The differential propagation delays corrections, about 1 ns in the case of the ionosphere and about 5 ns in that of the troposphere, have been neglected. Viceversa the relativistic correction due to Earth rotation (Sagnac effect), amounting to about 20 ns, has been applied to the IEN/TUG results.

In Fig. 10 are reported the residuals of UTC(IEN)-UTC(TUG) obtained subtracting the ECS synchronization data from the GPS ones; the mean value of the differences is 180 ns and the standard deviation is 44 ns. In this particular case, if we compute the error budget due to the uncertainties of the satellite position and stations coordinates we obtain as a result about 160 ns. Considering that in the computation of the synchronization results, the differential delay of the equipment set up has been taken into account, apart

from that of the satellite receivers, we can estimate that the above mentioned residuals are comparable with the error budget.

5.- Correction of the ECS synchronization results using GPS measurements

To substitute the ESA position data to correct the synchronization results, it has been studied and tested a correction procedure that uses both the ECS and GPS measurements performed in two stations.

If we assume that the variation of the differential delay between two stations due to the satellite motion follows a sinusoidal law of period T equal to a sidereal day, as a first approximation and for short observation times, the mean value of the differential delay computed at $T/2$ intervals is constant. Therefore performing ECS synchronizations at $T/2$ intervals and computing the mean between two adjacent values it is possible to remove the diurnal variation. Nevertheless, this procedure cannot compensate for the drift of longitude that yields to a long term variation in the mean differential delay which is left superimposed on the time differences between the reference clocks.

In the case of two laboratories performing also GPS time comparisons, the difference between the reference clocks can be subtracted and the residuals used to correct the averaged synchronization data of the laboratories performing only ECS comparisons.

This procedure has been tested using the ECS and GPS data of IEN and TUG to correct the synchronization results of IEN vs. TP and IEN vs. ASMW. The curves obtained are reported in Fig. 11 where, if one removes the mean rates, peak fluctuations of the order of 0.4 us can be observed and the differences between the time scales, compared with those computed by BIPM, can range from 0.5 us to 1.5 us. Comparing these results with those of Fig. 7, it is evident that this approach improves the precision of the ECS synchronization results, as do the ESA data, but is not satisfactory as regards to the measurement uncertainty.

Further tests using this method will concern the use of ECS synchronization measurements taken at exactly half-sidereal day (up to October 1989 it has been used a half solar day interval), and the determination of the longitude variation corrections by means of a polynomial fit over several days instead of computing the correction for each couple of consecutive data.

6.- Delay measurement of the satellite receiving station at IEN

In the computation of the time difference between two laboratories also the differential time delay of the stations must be taken into account. If the same transmitting equipment is used to perform the measurement of the delay at each station, the systematic uncertainty affecting the single test will be

deleted. To this purpose, a microwave transmitter, named "satellite simulator", has been built and tested.

6.1.- Satellite simulator description

The satellite simulator is a microwave generator (Gunn oscillator), tuned at $f = 10.945$ GHz, with an output signal level of 0 dBm, which can be frequency modulated by a standard video signal.

The test setup used to perform the satellite simulator delay measurement is shown in Fig. 12. A pulse generator with a 5 ns risetime, instead of a video signal generator, was used to modulate the satellite simulator. The simulator output frequency was down converted to about 100 MHz by means of a microwave generator, used as local oscillator, and a diode mixer.

The measurement was performed evaluating on an oscilloscope the delay between the leading edge of the modulation pulse and the output signal from the mixer taking as a reference the point where an abrupt frequency change was evident. The simulator delay was estimated to be 10 ± 5 ns, the delays introduced by the coaxial cables on both oscilloscope channels being equivalent.

6.2.- Receiving station delay measurement procedure

The block diagram of the equipment used is shown in Fig. 13. A horn antenna, connected to the satellite simulator by means of a coaxial cable 4 m long, is placed in front of the parabolic antenna in such a way that the beam length, from the transmitting antenna to the illuminator, is about 2 m. The satellite simulator is modulated by a test video signal in order to measure the overall delay of the station, pulse extractor included. The frequency $f = 10.945$ GHz was chosen because free from any other emission.

To obtain the station delay T_r , from the illuminator input to the STOP input of the counter, the following measurements were performed:

- the total delay T_t , from the START to the STOP inputs;
- the delay T_g , from the START to the simulator video input, using a calibrated cable to connect this last to the STOP.

The following results were obtained:

$$T_t = 1090 \text{ ns}, T_g = 198 \text{ ns}$$

$$T_r = T_t - T_g - T_a = 851 \text{ ns}$$

where $T_a = 41$ ns is the delay of the satellite simulator with the addition of the delays of a 4 m cable to the horn antenna and a 2 m free-space beam to the illuminator input. During the measurement of T_r the trigger level of the counter STOP input was regulated to a value equal to $\frac{1}{2}$ 50% of the synchronization pulse amplitude, the same value of the pulse extractor threshold. The uncertainty of

the measurement of T_r was evaluated to be 30 ns (1σ), having taken into account that the rise time of the television synchronization pulses is about 200 ns.

To determine the long-term stability of the station delay, it is planned to perform a series of measurements lasting some months, after having controlled in temperature the satellite simulator to eliminate frequency variations already observed in the Gunn oscillator.

7.- Conclusions

The results obtained in the synchronization experiment between some European laboratories, based on the television signals received from ECS5 geostationary satellite, have shown that an uncertainty ranging from some hundreds of nanoseconds up to one microsecond is achievable over a very large area, provided that the measurements are corrected for the satellite position parameters as determined by an ESA tracking station.

As a first attempt to reduce the diurnal effects on the time comparisons, since November 1989 a new measurement schedule, that allows to compute the synchronization results at a half-sidereal day, was adopted.

Future developments will concern the satellite position determination investigated both with four laboratories performing ECS and GPS measurements and establishing a range measurement equipment at the Fucino ground station of Telespazio, where the television signals are transmitted to the satellite. Furthermore, the station delay measurements, actually performed at IEN, could be extended to the other laboratories to improve the accuracy of the time synchronization.

8.- Acknowledgments

The authors would like to thank all the participating laboratories, and particularly O. Buzek and J. Čermák of ÚRE, and B. Demellenne and G. Desiderio of ESA - Redu for the indispensable cooperation.

References

- [1] Ptacek V.: The Long-Term Stability of Time Comparisons using the TV Method, Bull. Astron. Inst. Czechosl. 29/1978, pp. 372-375, No.6, June 1978.
- [2] Kirchner D., Ressler H., Cordara F., Galliano P.G., Pettiti V.: A comparison of Time and Frequency measurements via OTS-2 with results obtained by NAVSTAR/GPS and Loran-C, IEEE Trans. Instr. vol. IM-34, No.2, June 1985.

- |3| De Jong G., Kaarls R.: Time Synchronization via OTS-2, BCR Information, Applied Metrology, Report EUR 10554 EN, 1986.
- |4| Kawase S.: Closed dynamical One-Way Time-Synchronization using geostationary Satellite, Journal of Radio Research Laboratory, vol. 34, No.142, pp. 43-53, June 1987.
- |5| Banerjee P., Mithlesh Saxena, and Mathur B.S.: Passive TV Technique for Time Transfer via Indian Satellite INSAT-1B, IEEE Trans. Instr. and Meas. vol. IM-36, No.2, June 1987, pp. 579-583.
- |6| McK Luck J., Harvey J.K., Harris R.W., Harvey G.G.: Status of Activities and Plans for precise time comparisons in Australia, Proc. 18th PTTI, Washington, Dec. 1986.
- |7| Kovacevic B.Z., Dimitrijevic B.R., Arsic M.Z., Kovacevic N.S.: Precise Real time signal dissemination over the TV broadcasting satellite, Radio Science, vol. 14, No.4, July-August 1979.

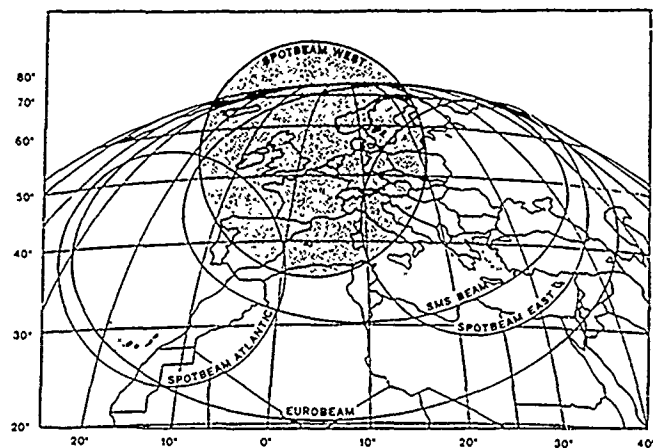


Fig. 1 - ECS satellite coverages.

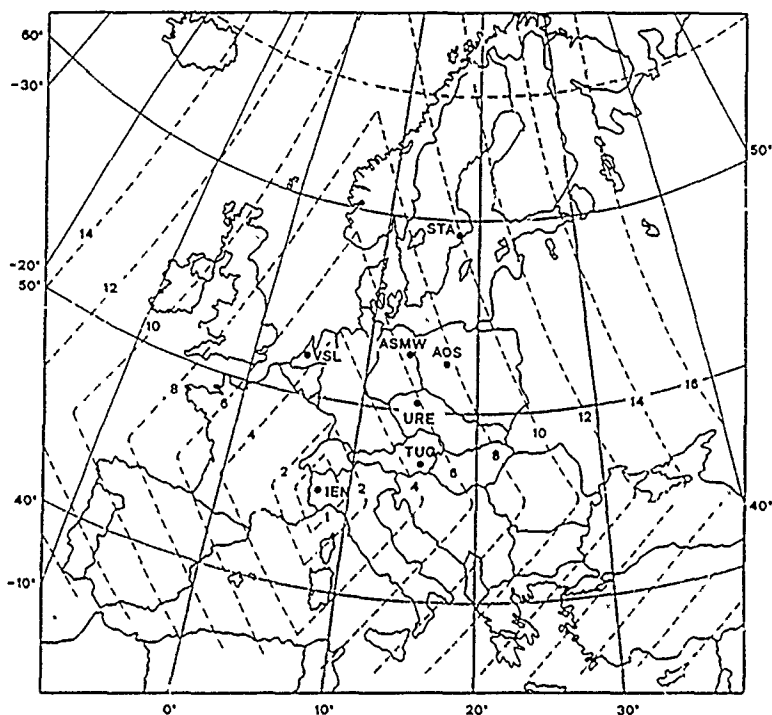


Fig. 2 - Map of the time error contours (in microseconds).

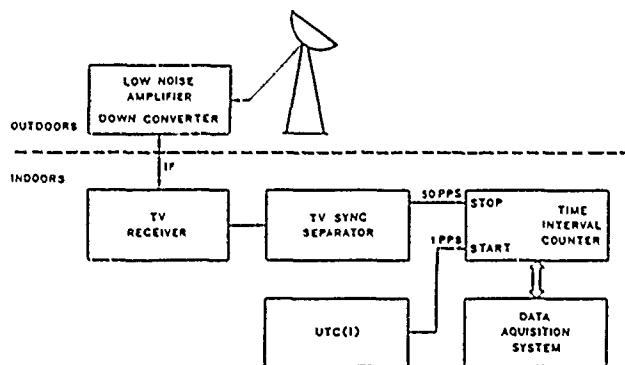


Fig. 3 - Measurement setup.

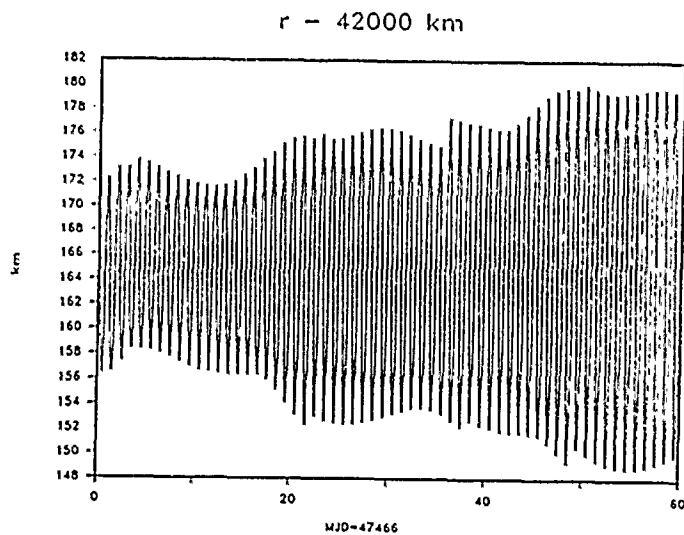
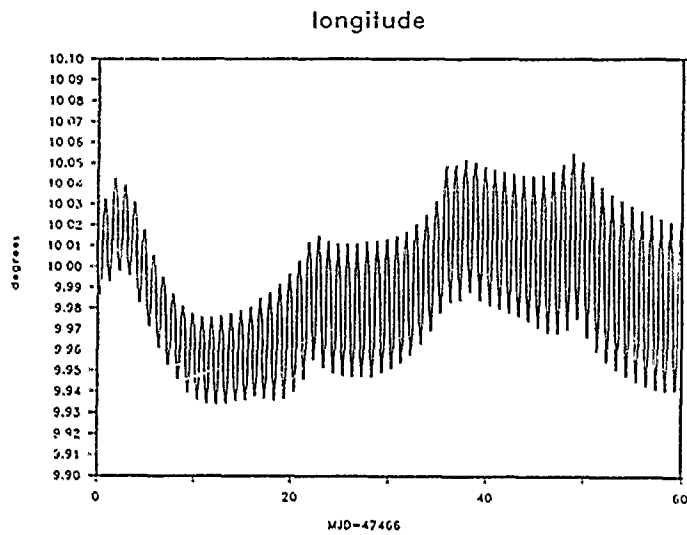
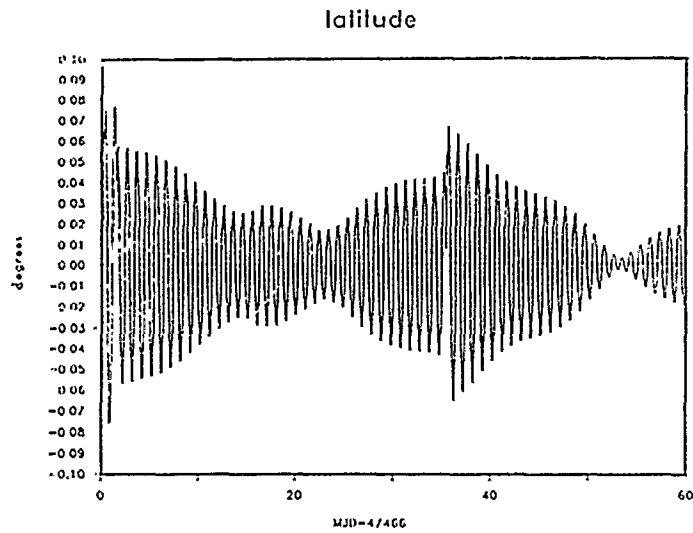


Fig. 4 - ECS 5 position from ESA-Redu data (November-December 1988).

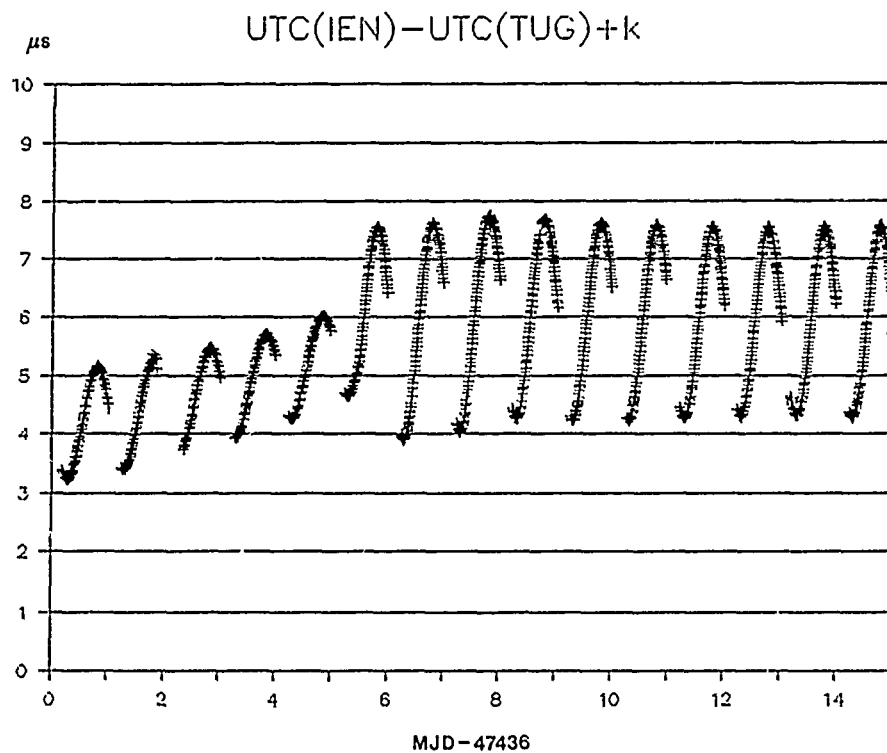


Fig. 5 - Ten minutes time differences between IEN and TUG via ECS TV signal.

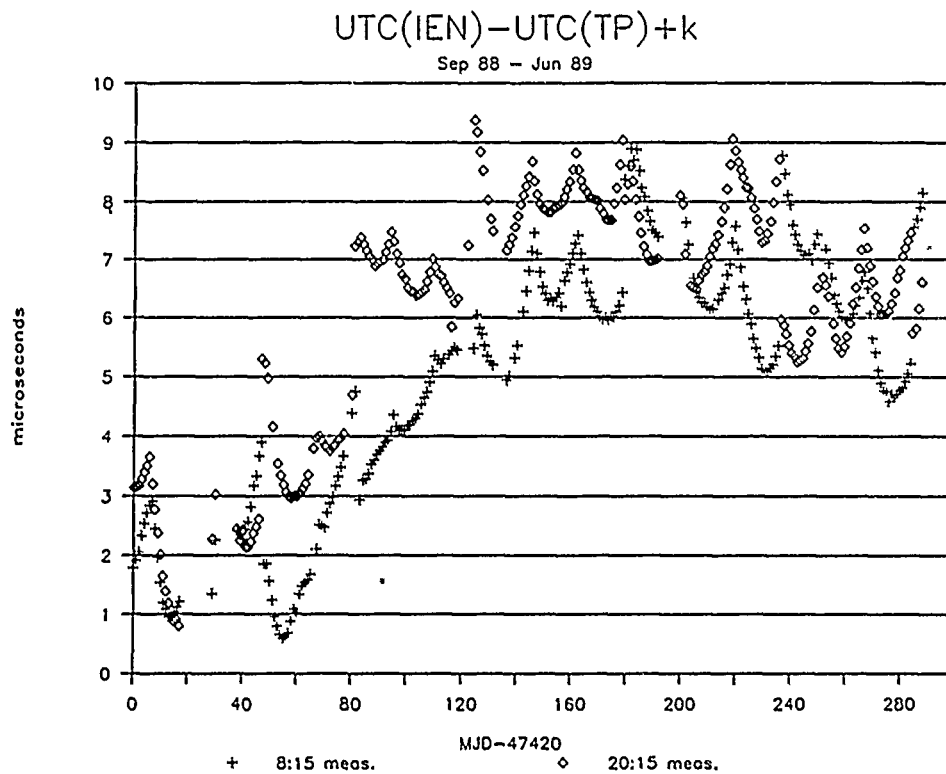


Fig. 6 - Time differences between IEN and URE from ECS 5 satellite.

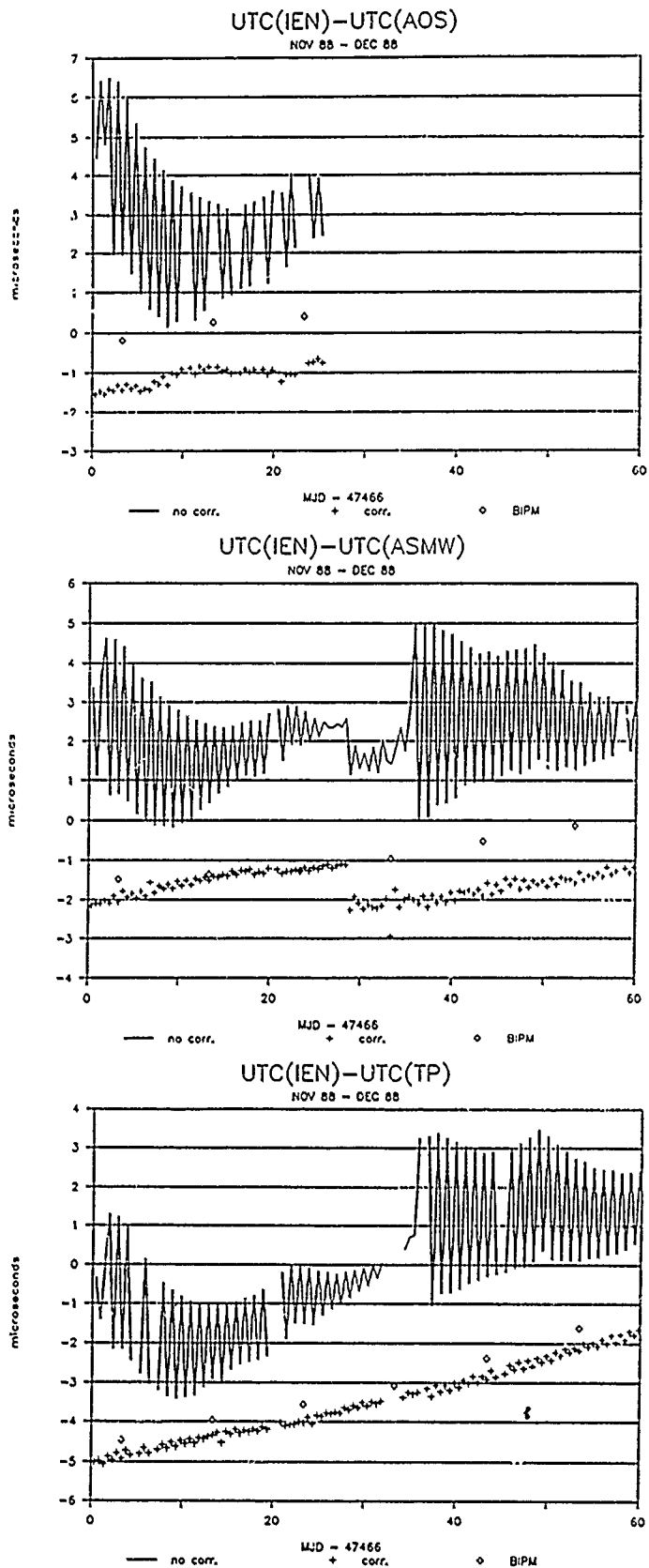


Fig. 7 - Time scales comparisons by means of ECS 5 satellite and BIPM Circular T.

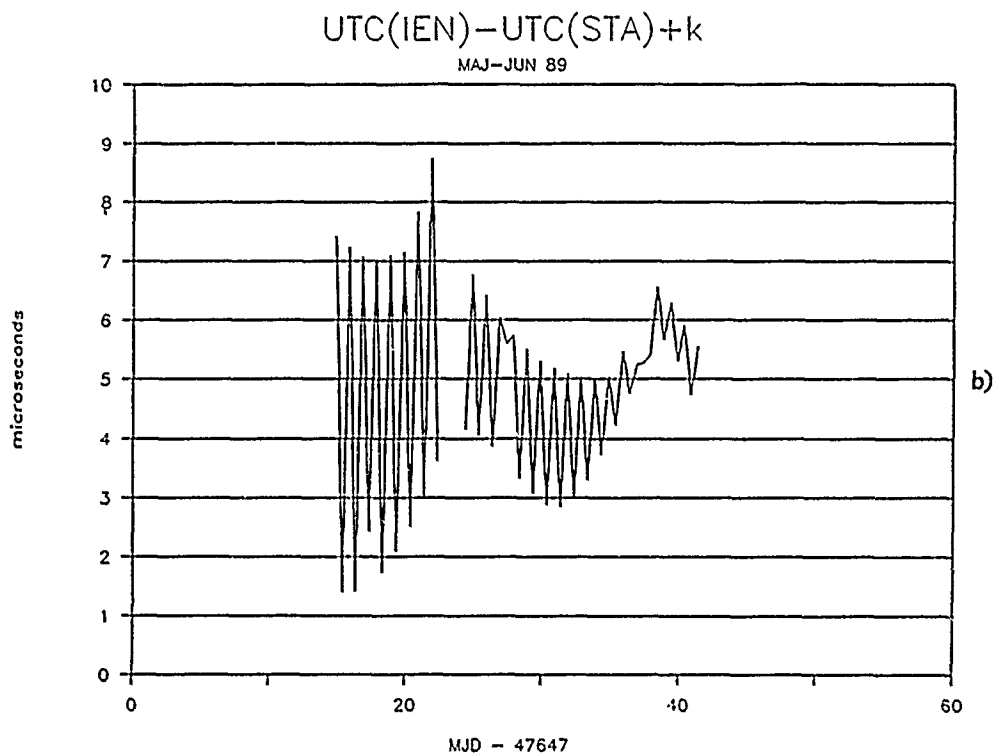
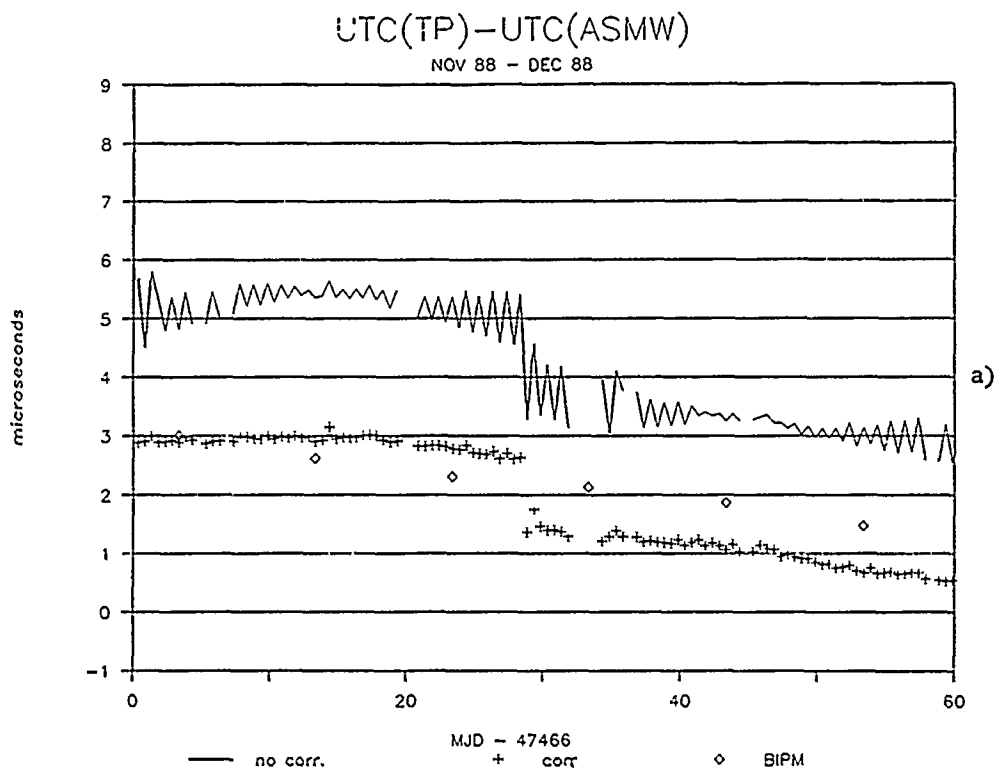


Fig. 8 - Time scales comparisons by means of ECS 5 satellite.

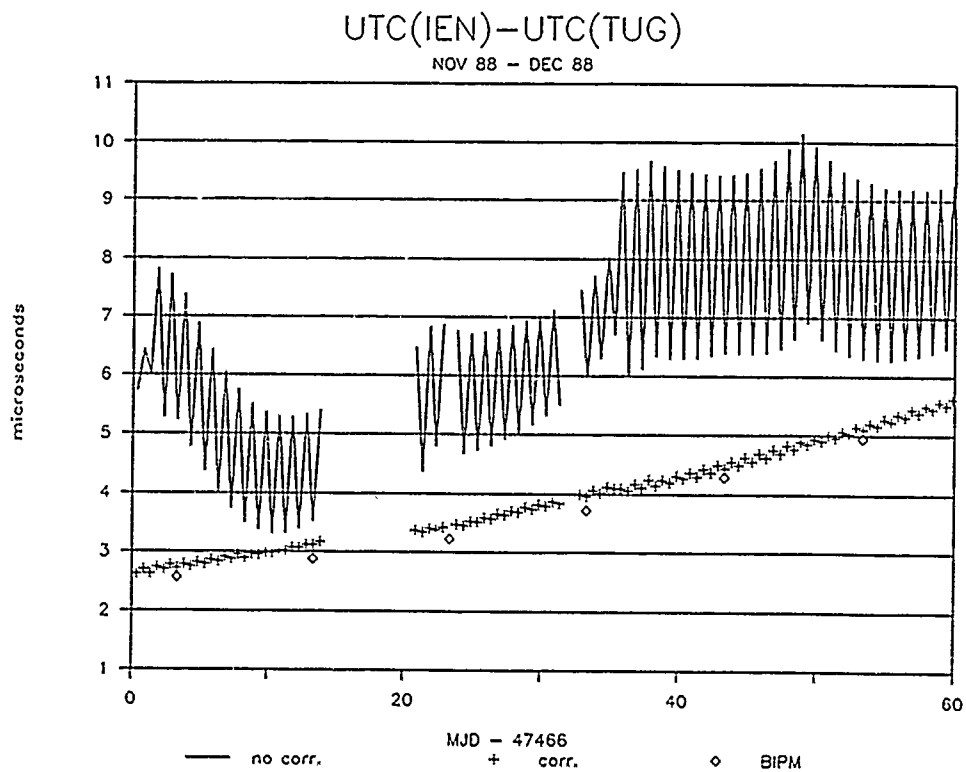


Fig. 9 - UTC(IEN vs. UTC(TUG) from ECS 5 and BIPM Circular T
(TUG time scale step compensated).

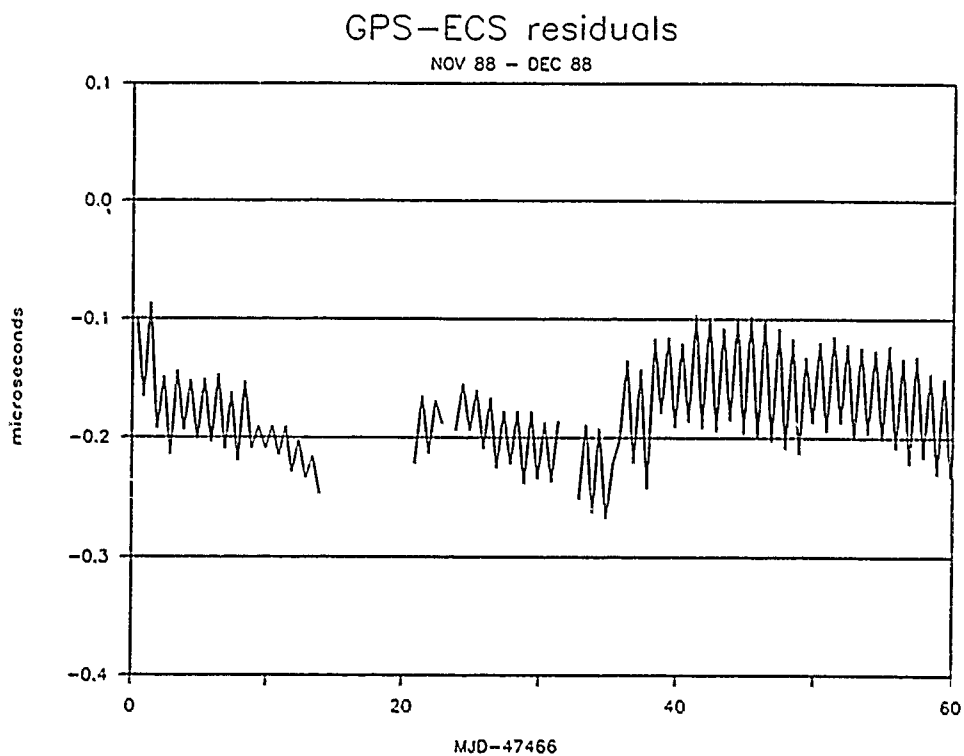


Fig. 10 - Residuals of UTC(IEN) - UTC(TUG) via GPS and ECS.

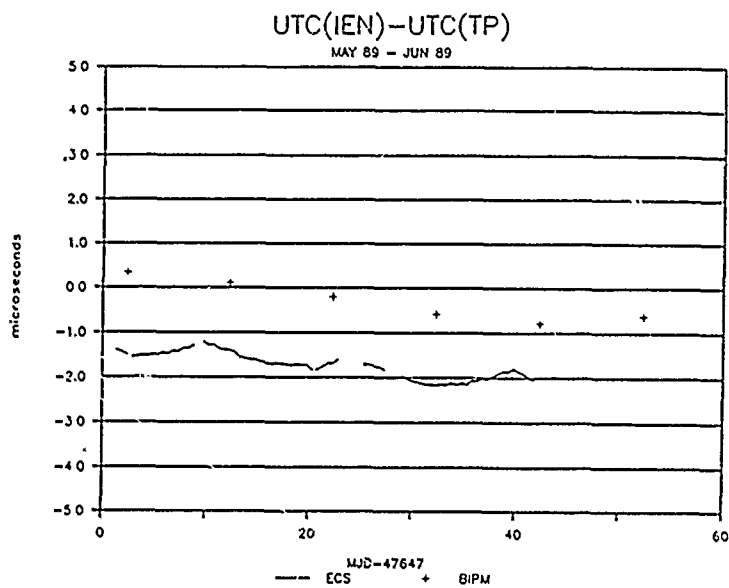
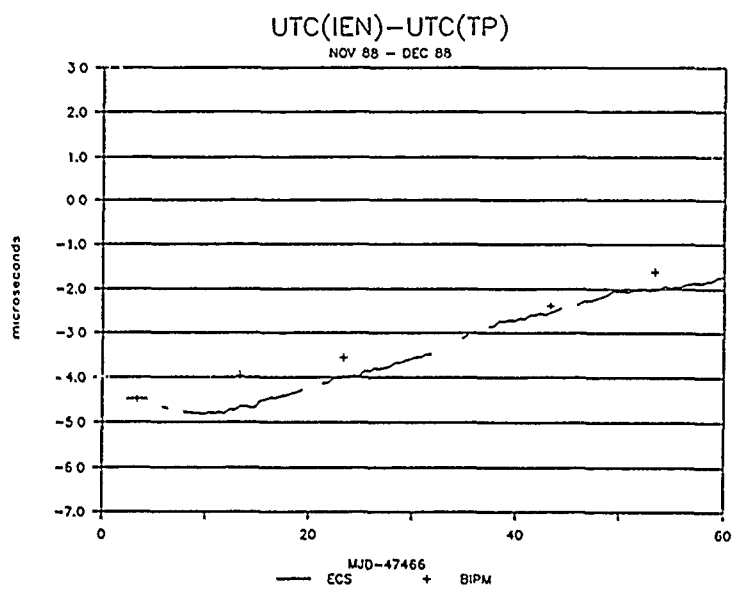
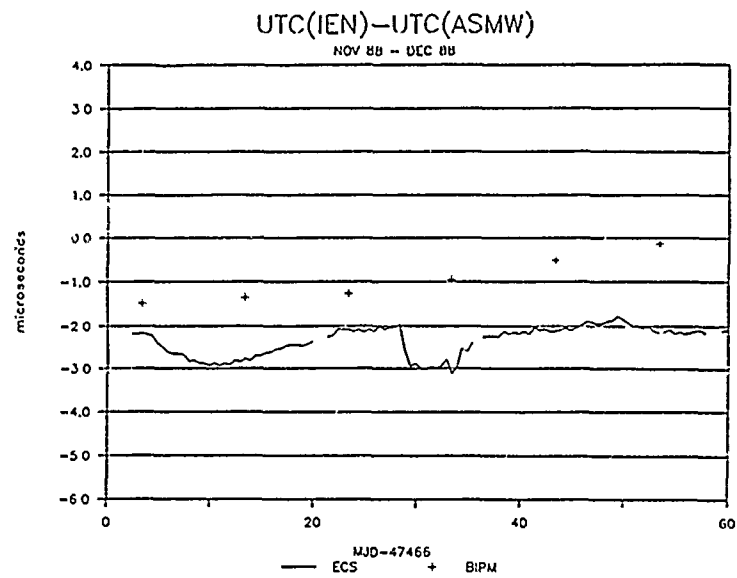


Fig. 11 - ECS 5 time scale comparisons corrected with IEN-TUG GPS data.

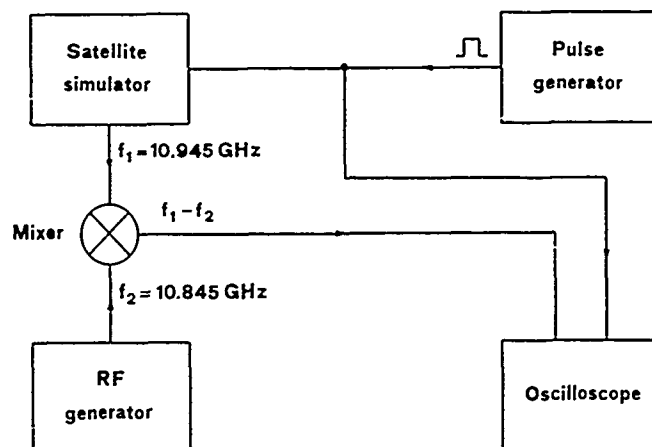


Fig. 12 - Block diagram of satellite simulator delay measurement.

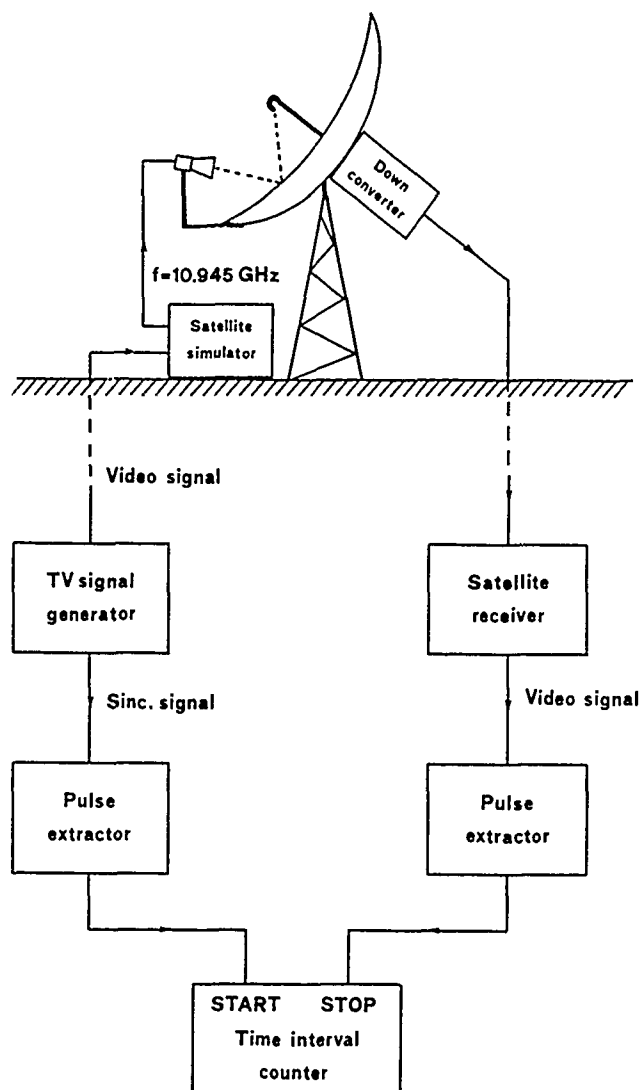


Fig. 13 - Receiving station delay measurement setup.

QUESTIONS AND ANSWERS

GERNOT WINKLER, USNO: In one of your view graphs you could see a very significant break in the daily variation to a much more regular performance. Is that due to a station-keeping change in the satellite, or what happened at that moment?

MR. PETTITI: It was about the satellite position information. Unfortunately, it is not easy to get information from the tracking station about what is happening. This is why we are trying to eliminate this input. It was certainly due to something in the satellite control, because in the corrected data there is no sign of this behavior. It is not, however, easy to determine *a priori* what they are doing there.

A NEW TIME SCALE ALGORITHM: AT1 PLUS FREQUENCY VARIANCE

M. Weiss, T. Weissert
NIST, 576
325 Broadway, CO 80303

Abstract

The algorithm which generates the AT1 time scale at the National Institute of Standards and Technology (NIST) has generated a scale with many desirable properties since 1968. Five of these are as follows:

1. The fractional frequency variation of the scale is smaller than any clock in the scale for all integration times.
2. The algorithm adaptively estimates the weights of clocks in real time.
3. The scale is much more reliable than any individual clock.
4. One can add or remove clocks from the scale easily, with a minimum impact on the scale.
5. One can correct the ensemble for calibrations against a primary reference.

There are three other properties we would like to obtain:

1. Automatic frequency step detection.
2. A scale optimized for post-processing, including running both forwards and backwards in time.
3. A scale that can run with minimal supervision for use in non-technical environments.

It turns out that simply estimating a variance of the frequency state of the clocks facilitates all three of these new properties. We report here a new algorithm which uses techniques from Kalman filtering to estimate this variance. Results from simulation and applications to real clocks are presented also.

INTRODUCTION

Ideally, a time scale algorithm samples an ensemble of clocks to generate time and frequency with more reliability, stability, and frequency accuracy than any of the individual clocks in the ensemble. In this paper we study an approach to this ideal.

A time scale algorithm calculates the time offset of each of the ensemble clocks at a given reference time. Ensemble time, the time of the scale, is realized by applying the appropriate correction to any one clock. If there is no measurement noise this value is independent of which clock is used. The input to the algorithm at a given reference time is the time difference between each clock and a particular

clock. The algorithm also requires estimates of the deterministic and stochastic parameters which characterize each clock's frequency offsets.

It is important to notice that the time of a clock is not measured. One measures only time differences between clocks. Thus the ensemble time which the algorithm generates is not observable. For this reason it is inappropriate to use an accuracy algorithm, such as a Kalman filter, to generate time by minimizing time error. We can, and do in the algorithms discussed here, optimize time and time interval stability.

It is also important to realize that a clock as a physical system produces a frequency. The time of a clock is artificially derived from the frequency, which is the true physical quantity. Because of this, all the parameters which characterize clock performance describe aspects of the frequency. One can use these parameters to optimize time uniformity and frequency accuracy. An algorithm that optimizes time accuracy should simply allow the clock with the best long term stability to dominate the scale, thus sacrificing much of the performance of other clocks, especially in short term. We will look at these things further as we go along.

The AT1 time scale algorithm at the National Institute of Standards and Technology (NIST) has generated a scale with many desirable properties since 1967. Five of these are as follows:

1. The fractional frequency variation of the scale generally appears smaller than any clock in the scale for all integration times.
2. The algorithm adaptively estimates the weights of clocks in real time.
3. The scale is much more reliable than any individual clock.
4. We can add or remove clocks from the scale easily, with a minimum impact on the scale.
5. We can correct the ensemble for calibrations against a primary reference.

There are three other properties we would like to obtain:

1. Automatic frequency step detection.
2. A scale optimized for post-processing, including running both forwards and backwards in time.
3. A scale that can run with minimal supervision for use in non-technical environments.

The new algorithm we report here combines aspects of the NIST AT1 algorithm with techniques from Kalman filtering to estimate clock states representing the random walk plus drift of the frequency offsets of each clock, as well as the variance of these states. For a given clock, this state, which we call "Y", is not a physical state, but a mathematical estimate of the frequency offset in the presence of white noise modulating the frequency. The variance of this state gives us a confidence of this estimate. Having this estimate facilitates attainment of all three of our goals.

Frequency step detection always requires examining the data over some time period. In nearly real time operation it is possible to compare the estimate of average frequency offset over an interval with the filtered estimate from the beginning of that interval. Using the estimate of frequency deviation as a test for outliers, we can determine if a frequency step occurred in the recent past.

We can also smooth our estimates of "Y" in post-processing by combining the forward and backward filters. The proper way to combine these is well-defined in Kalman filter theory. Essentially, we use the reciprocal of the forward and backward filter variances as weights to combine their respective state estimates at a given reference time. We must be careful not to incorporate the data at that time in both filters before combining them, else they will not be independent estimates. Thus, at a given reference time, we use the extrapolated estimates of state and variance from one direction, the backward filter for example, and combines this state estimate with the one from the forward direction which has been updated with the data.

The AT1 time scale is adaptive once we know the clock parameters characterizing the short and long term behavior of the clocks. Since our new scale uses the Kalman formalism, we can enter a new clock and the algorithm will optimally adapt its estimate of frequency offset variance. This allows us to enter new clocks without perturbing the scale.

Both results from simulation and applications to real clocks are presented.

THEORY: AT1

We first present the AT1 algorithm and then show how we have modified it. In the AT1 algorithm each clock has two states which are estimated: the time and frequency offsets of the clock from ensemble time. Frequency drift can be entered and used, but it is not estimated adaptively by the algorithm. The AT1 algorithm is a three-tiered process: the time update, the update of the variance of the time offset, and the frequency update. The weight of a clock is proportional to the reciprocal of the variance. Each of these updates can be broken down into two steps: an initial estimate and the update.

1. Time Prediction:

$$\hat{X}_i(t + \tau) = X_i(t) + (Y_i(t) + D_i\tau/2)\tau \quad (1)$$

We predict the time offset from ensemble time, \hat{X}_i , of clock i for the current measurement time $(t + \tau)$ based on the previous estimates at time t of time offset, X_i , and filtered frequency, Y_i , and the entered frequency drift, D_i .

2. Time Update:

$$X_j(t + \tau) = \sum_{i=1}^n w_i [\hat{X}_i(t + \tau) - X_{ij}(t + \tau)] \quad (2)$$

We update the time offset of each clock j against the scale at time $t + \tau$ given the measurements $X_{ij}(t + \tau)$. Clock j 's offset is estimated using the measurement and prediction of each other clock, i , then these estimates are combined in a weighted average. The weights w_i are determined adaptively in equations 6 - 10. This is the maximum likelihood estimate of X_j if the w_i 's are proportional to the reciprocal of the variances of the time residuals, and the residuals have a gaussian normal distribution.^[1]

3. Frequency Estimate:

$$\hat{Y}_i(t + \tau) = \frac{X_i(t + \tau) - X_i(t)}{\tau} \quad (3)$$

\hat{Y}_i is the estimate at time $t + \tau$ of the average frequency of clock i over the interval τ based on the latest two time updates, X_i .

4. Frequency Update:

$$Y_i(t + \tau) = \frac{1}{m_i + 1} [\hat{Y}_i(t + \tau) + m_i Y_i(t)] \quad (4)$$

We incorporate the previous frequency update into an exponentially filtered estimate of the current average frequency offset of clock i . The exponential frequency-weighting time constant (m_i) is determined from the relative levels of white noise FM and random walk (or flicker) FM for clock i (equation 5).

5. Frequency Update, Exponential Time Constant:

$$m_i = 1/2 \left[-1 + \left[\frac{1}{3} + \frac{4\tau_{Mini}^2}{3\tau_0^2} \right]^{1/2} \right] \quad (5)$$

We determine m_i used in equation 4 to form the filtered estimate of the frequency of clock i . Here, τ_{Mini} is the integration time which gives the minimum value on a $\sigma_y(\tau)$ plot given that the clock's stochastic deviations are characterized by white and random walk FM. τ_0 is the minimum τ value used for computing $\sigma_y(\tau)$. This value of m_i can be shown to optimize the stability in predicting time (equation 1) given these two kinds of noise in the clock (white and random walk FM)^[1]. If white FM and flicker FM are more suitable models, then m_i can be approximated as τ_z/τ_0 , where τ_z is the intercept value of τ on a $\sigma_y(\tau)$ plot for the white and flicker FM.

6. Variance Estimate:

$$\hat{\epsilon}_i(\tau) = \left| \hat{X}_i(t + \tau) - X_i(t + \tau) \right| + K_i \quad (6)$$

$\hat{\epsilon}_i$ is the lack of predictability of clock i over the interval τ , being the difference between the prediction and the update. Thus it is an estimate of the deviation (square root of variance) of the clock based on the current measurement cycle. The additive term K_i accounts for the fact that the term in brackets on the right-hand side of equation 6 is biased because clock i is part of the ensemble. See equation 10 to calculate K_i .

7. Variance Update:

$$\epsilon_i^2(\tau)|_{t+\tau} = \frac{1}{N_\tau + 1} \left[\hat{\epsilon}_i^2(\tau) + N_\tau \epsilon_i^2(\tau)|_t \right] \quad (7)$$

$\epsilon_i^2(\tau)$ estimates the mean squared time error of clock i by filtering exponentially the estimate of clock i 's deviation from the current measurement cycle. Since the noise characteristics of a clock may not be stationary, past measurements are de-weighted in the filtering process. The time constant for the filter is typically chosen to be $N_\tau = 20$ days for cesium clocks, representing the time one expects the white FM level to be constant. The initial value of $\epsilon_i^2(\tau)$ can be estimated as $\tau^2 \sigma_y^2(\tau)$.

8. Ensemble Variance:

$$\epsilon_x^2(\tau) = \left[\sum_{i=1}^n \frac{1}{\epsilon_i^2(\tau)} \right]^{-1} \quad (8)$$

$\epsilon_x^2(\tau)$ forms an estimate of ensemble time error. Any clock can only improve this number - a poorly performing clock cannot harm the stability of the ensemble.

9. Adaptive Clock Weights:

$$w_i = \frac{\epsilon_x^2(\tau)}{\epsilon_i^2(\tau)} \quad (9)$$

w_i is the weight to be used in equation 2 for clock i . When calculated this way, the resulting ensemble time stability can be shown to be optimized in a maximum likelihood sense, assuming a normal distribution of the noise of clock i with variance $\epsilon_i^2(\tau)$.

10. Bias of the Error Estimate:

$$K_i = \frac{.8\epsilon_x^2}{(\epsilon_i^2)^{1/2}} \quad (10)$$

K_i estimates the bias in the error estimate from the first term on the right of equation 6. This error estimate is biased small, on the average, because each clock is a member of the ensemble and sees itself through its weighting factor. The larger a clock's weight, the larger is the bias. Under the assumption of a normal distribution of clock noise the size of the bias can be estimated as given by equation 10, which is added to equation 5 in order to remove the bias, on the average^[1].

THEORY: AT1-PLUS-VARIANCE

What is missing here is an estimate of the variance of the residuals of the frequency offset from the ensemble, Y . In our approach, we interpret X_i as a measurement of the time of clock i against the

scale. Thus the first difference, \hat{Y}_i of X_i , as in equation 3, is a measurement of the frequency offset of clock i from the scale. We use a simple Kalman formalism to filter this measurement to estimate Y , where we use $\epsilon_i(\tau)$ as noise of the measurement. We model Y as having a random-walk noise and a fixed drift. Thus, Y is not the physical frequency as produced by the clock, but since we are filtering down the white frequency modulation (FM), it is only the random-walk component of the frequency of the clock, plus any drift.

The X terms do reflect the physical time offset of the clock from the scale, thus incorporating the white FM. The Y term is used to better predict the X values. We substitute equations 4 and 5 with the Kalman equations:

11. System Model:

$$Y_i(t + \tau) = Y_i(t) + D_i\tau + \eta(\tau). \quad (11)$$

Y_i is the random walk component of the frequency offset of clock i from the scale plus the drift offset. The random walk is driven by the white noise process $\eta(\tau)$.

12. Measurement Model:

$$\hat{Y}_i = Y_i + \epsilon_i(\tau) \quad (12)$$

The measurement \hat{Y}_i is a direct measurement of Y_i , plus white noise.

The actual equations used for update are:

13. Variance Prediction:

$$\hat{P}(t + \tau) = P(t) + \sigma_\eta^2 * \tau. \quad (13)$$

\hat{P} is the prediction of variance of the residuals of Y which grows with τ according to σ_η^2 , the variance of the white noise process, η , driving the random-walk FM.

14. Frequency Update:

$$Y(t + \tau) = \frac{\epsilon_i^2(\tau) * Y(t) + \hat{P} * \hat{Y}}{\epsilon_i^2(\tau) + \hat{P}} \quad (14)$$

We see that the Kalman formalism also gives us an exponential filter on Y . Thus in steady state this algorithm reduces to AT1 if the weights are chosen properly. This implies that this algorithm inherits the ability that AT1 has to model flicker frequency.

15. Variance Update:

$$P = \frac{\epsilon_i^2(\tau) \star \hat{P}}{\epsilon_i^2(\tau) + \hat{P}} \quad (15)$$

In the Kalman formalism the system parameters are known in advance. This system is a modification, an adaptive Kalman filter, where we estimate the "measurement noise," $\epsilon_i^2(\tau)$. This allows the variance of the residuals of Y to evolve both from an initial value, as is normal for the Kalman filter, and if $\epsilon_i^2(\tau)$ changes. This allows the exponential filter parameters on Y , as expressed in 14, to change with time, both after entering a new clock, and if the white FM level of the clock changes.

It is possible to solve for the steady state form of these equations and make identifications between the AT1 algorithm and our new algorithm. We find that the steady state value of P is:

16.

$$P = \frac{\eta^2}{2} \left(\sqrt{1 + 4 \cdot \frac{\epsilon_i^2(\tau)}{\eta^2}} - 1 \right) \quad (16)$$

Making the appropriate identifications between equations 4 and 14 we find:

17.

$$m = \frac{\epsilon^2(\tau)}{P + \eta^2} \quad (17)$$

Using 16 in addition yields:

18.

$$m(m+1) = \frac{\epsilon^2(\tau)}{\eta^2} \quad (18)$$

These equations allow us to compare the performance of the two algorithms with the parameters m and η set consistently.

We close this theoretical section mentioning results from elsewhere. Jones and Tryon^[2] have designed a time scale algorithm which is purely a Kalman filter. This scale, called TA(NIST), has been run at NIST in parallel with AT1 since about 1983. That filter is mathematically identical with the AT1 algorithm for the time and frequency predictions and updates^[3]. The difference among these algorithms is the weighting of clocks in the time update and the exponential filter parameters in the frequency update. These differences effect the ensemble time they generate, which is realized as the time offsets, X_i , of the clocks against ensemble time.

We will show in simulation and with real clocks that the pure Kalman filter time scale sacrifices short term performance, and simply follows the clock with the best long term performance. This is consistent with the design of Kalman filters in general which minimize error. The Jones Tryon filter attempts to estimate and minimize both time and frequency error. An additional problem with this is

that since time is unobservable, elements of the covariance matrix grow without bound. In practice, with a good ensemble of clocks, this growth is not large enough to cause computer overflow errors in any reasonable amount of time, though it is suggestive of an undesirable situation.

SIMULATION

In simulation we show the following:

1. Both algorithms AT1 and AT1 plus frequency variance produce a time scale apparently better than the best clock in the scale at all integration times.
2. The TA(NIST) algorithm is dominated by the clock with the best long term performance at all integration times.
3. The AT1-plus-frequency- variance estimate of the confidence on the frequency offset estimate appears to be a reasonable estimate.
4. The use of this confidence estimate to determine frequency steps improves long term performance of the time scale.

Figure 1 illustrates item (1). Here we have generated data simulating clocks with various levels of white FM and random-walk FM. We have treated the problem as we would with real clocks where we only measure clock differences. We have computed the stability of each clock using an N-cornered hat technique^[4]. The stability of the scale we have determined by taking the output value of clock minus scale and subtracting the generated value of clock minus truth. If we look directly at the variances of the generated data, we see significant differences between the variances computed directly, and those estimated from N-cornered hat (Figure 2). These differences must be due to apparent correlations in the data. This should come either from the finite data length, or from real correlations in the pseudo-random number generator. If the generated clocks are truly correlated, then the algorithm can only produce a variance better than the uncorrelated part. We notice that the scale seems to follow the shape of the variances from the N-corner hat. This suggests correlation in the generated data.

Figure 3 shows a comparison of the output of a version of the Kalman filter which defines TA(NIST) with the simulated input data. We see that the Kalman algorithm has the stability of the clock with the best long term variations.

Figures 4 and 5 show the residuals from the AT1-plus-variance algorithm compared with the estimated confidence, from the estimated variance of frequency residuals. The algorithm estimates the random-walk component of a clock's frequency offset from the ensemble time. Since these are generated clocks we know the true value of the random-walk component of frequency of that clock versus the true value of the time scale. The differences of these two, the estimate minus truth, are the residuals plotted. The sigma value used in the plot is the root-mean-square of the estimated deviation of the clock plus the estimated deviation of the scale. The line plotted is the three-sigma value. This should be a 99.8 percentile. Over the 700 points plotted we should get 1 or 2 residuals crossing the lines of the sigmas. This seems to be the case.

Last, we inserted frequency steps in the simulated clocks. Figure 6 shows the frequency offset from the scale of the simulated clock 9, with a frequency step of 1×10^{-12} on MJD 46500. This clock

was given a white FM level of 30 ns, and a random walk FM level of 0.5 ns, both at 1 d. Figure 7 shows the estimate from the AT1-plus-variance scale of the random-walk component of frequency. The reduction in the white FM is apparent. The scale was able to detect the frequency step, with the step detector set at 4 sigma, with sigma defined as above. When such a step is detected, we re-run the scale, removing the clock with the step until the scale can learn the new frequency value. Figure 8 shows the frequency offset from the scale of the simulated clock 1, with a frequency step of 2×10^{-12} on MJD 46100. The noise of this clock is almost all random walk FM as compared to its level of white FM. The estimate from the scale shows very little smoothing. Yet, even in this case, the frequency step detector automatically found the step and removed the clock from the scale. In Figure 9 we see the benefit from having detected the frequency steps. There is a significant improvement at an integration time of 128 d and longer.

REAL DATA

Last, we took data from real clocks at NIST over the period from December 31, 1988, to October 30, 1989. We ran our AT1-plus-variance algorithm on this data, including automatic frequency step detection and recalculation. We also took data using GPS common view measurements^[5] with other laboratories: PTB, USNO, TUG, and NRC. Using an N-cornered hat technique, we were able to determine the variance of each of these. We compared these results with a similar analysis using the official NIST AT1 time scale. The results for the two scales run on NIST clocks as well as USNO and PTB are plotted in Figure 10. We find that the official AT1 and the new AT1-plus-variance scale are similar, though in long term the official scale is somewhat better. The official AT1 scale is watched carefully and administratively checked for time and frequency steps, as well as changes in clock performance in general. We find that human care adds much to a time scale.

BIBLIOGRAPHY

1. Allan, D. W., Weiss, M. A., The NBS Atomic Time Scale Algorithm: AT1, NBS Technical Note 1316, 1989.
2. Jones, R. H., and Tryon, P. V., "Continuous Time Series Models for Unequally Spaced Data Applied to Modeling Atomic Clocks," SIAM J. Sci. Stat. Comput., vol 8, no. 1, Jan 87, pp 71-81.
3. Weiss, M. A., Allan, D. W., Peppler, T. K., "A Study of the NBS Time Scale Algorithm," IEEE I&M, vol. 38, no. 2, April 89, pp 631-635.
4. Barnes, J., "Time Scale Algorithms Using Kalman Filters - Insights from simulation," Proceedings of the 2nd Symposium on Atomic Time Scale Algorithms, NBS, Boulder, CO.
5. Allan, D.W., Weiss, M.A., 1980, "Accurate time and frequency transfer during common view of a GPS satellite", Proc. 34th Ann. Freq. Control Symp., Ft Monmouth, pp 334-346.

AT1 + Variance on Simulated Clocks

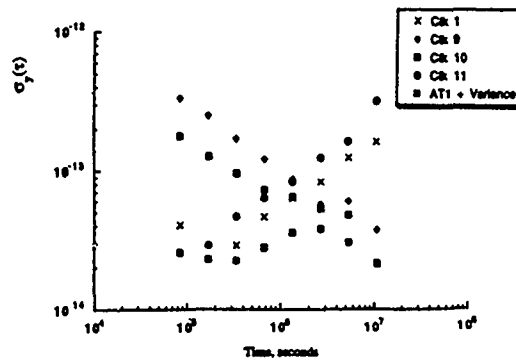


Figure 1: We have computed the stability of each simulated clock using an N-cornered hat technique. The stability of the scale we have determined by taking the output value of clock minus scale and subtracting the generated value of clock minus truth. The AT1 scale outperforms all clocks at all integration times.

Truth vs N-Corner Hat

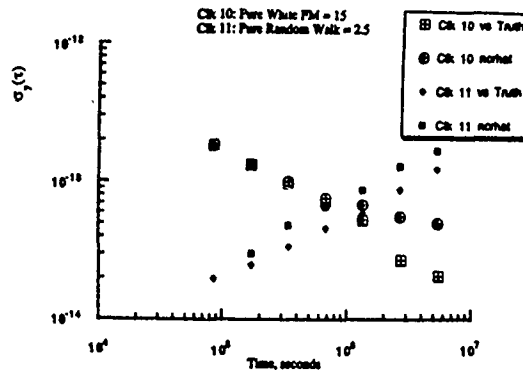


Figure 2: If we look directly at the variances of the generated data, we see significant differences between the variances computed directly, and those estimated from N-cornered hat. These differences must be due to apparent correlations in the data.

Kalman on Simulated Clocks

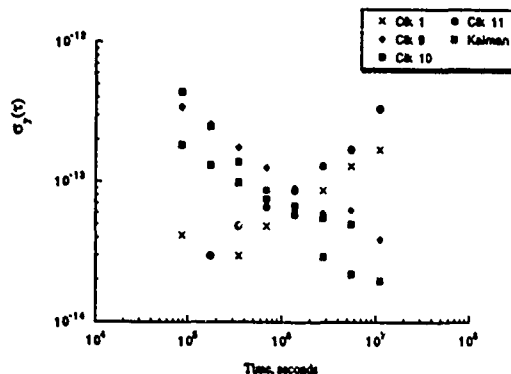


Figure 3: A comparison of the output of a version of the Kalman filter which defines TA(NIST) with the simulated input data. We see that the Kalman algorithm has the stability of the clock with the best long term variations.

Simulation Clk 1: Residuals vs. Estimated Confidence

White FM = 1 ns, Random Walk FM = 15 ns, both @ 1 day

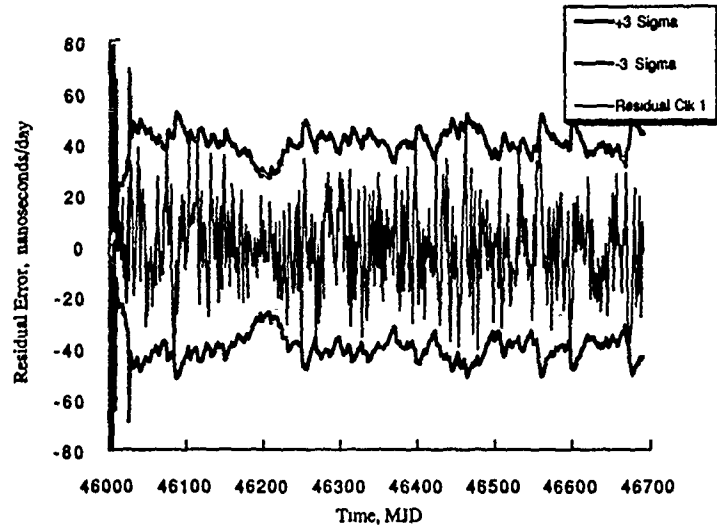


Figure 4: The residuals from the AT1-plus-variance algorithm compared with the estimated confidence, from the estimated variance of frequency residuals. The line plotted is the three-sigma value.

Simulation Clk 9: Residuals vs. Estimated Confidence

White FM = 30 ns, Random Walk FM = 0.5 ns, both @ 1 day

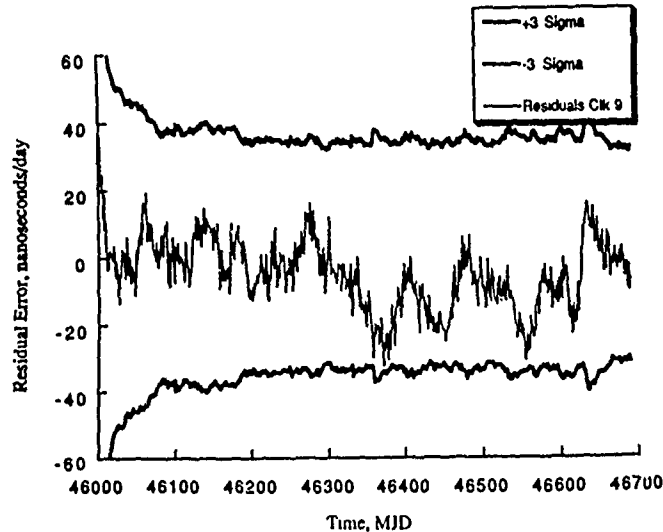


Figure 5: The residuals from the AT1-plus-variance algorithm compared with the estimated confidence, from the estimated variance of frequency residuals. The line plotted is the three-sigma value.

Frequency-Step Detection Improves Long-Term Stability Simulated Clocks

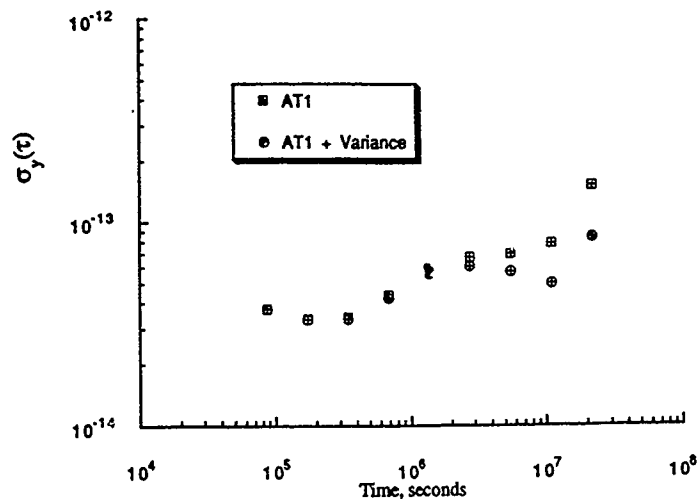


Figure 6: The frequency offset from the scale of the simulated clock 9, with a frequency step of 1×10^{-12} on MJD 46500.

Comparison of Ensembles

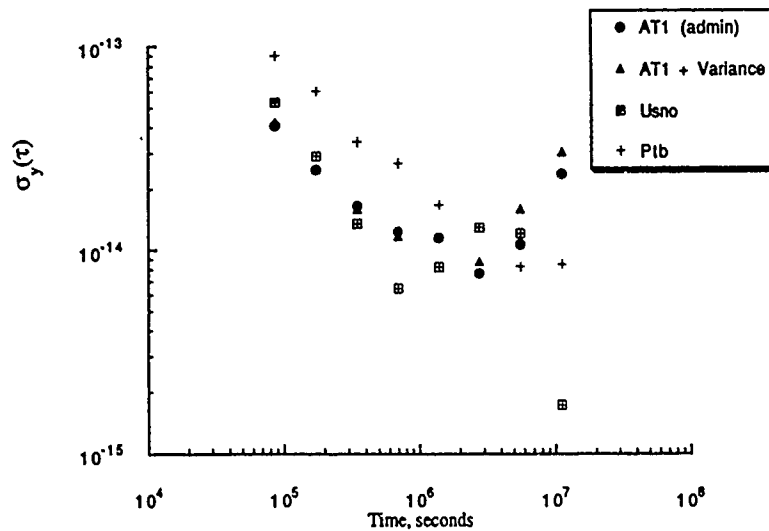


Figure 7: The estimate from the AT1-plus-variance scale of the random-walk component of frequency for clock 9. The scale was able to detect the frequency step, with the step detector set at 4 sigma.

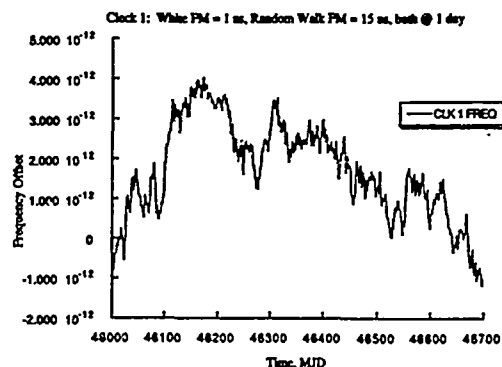


Figure 8: The frequency offset from the scale of the simulated clock 1, with a frequency step of 2×10^{-12} on MJD 46100. The estimate from the scale shows very little smoothing, yet the frequency step detector automatically found the step and removed the clock from the scale.

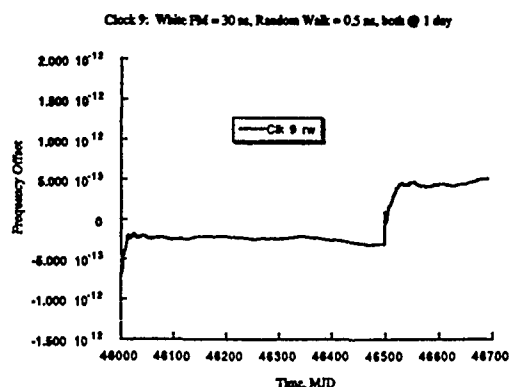


Figure 9: The benefit from having detected the frequency steps is seen in this diagram. There is a significant improvement at an integration time of 128 d and longer.

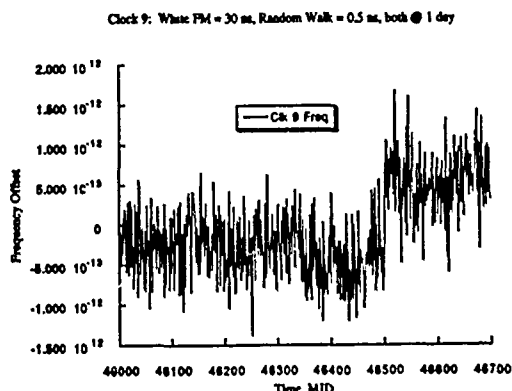


Figure 10: The results for the two scales, the official AT1 and the new AT1-plus-variance, run on NIST clocks as well as USNO and PTB.

QUESTIONS AND ANSWERS

GERNOT WINKLER, USNO: There are quite a few things that I didn't understand, but there is one thing that bothers me—at the beginning you said that, since you don't measure your time scale, but generate it, the use of a Kalman filter is inappropriate. Then you turn around and use it. Could you elaborate on that?

MR. WEISS: The use of a pure Kalman filter is inappropriate. Using Kalman techniques in part of the time scale is very useful. This is not a criticism of Sam Stein's algorithm which does a very similar thing. Kalman techniques have very important places. But to use the Kalman to generate the time itself is inappropriate. The result of that is what I have shown. You lock onto the clock with the best long term stability and you lose the short term.

MR. STEIN: I think that I would like to make a comment on that myself. The Kalman filter is merely a computational technique. It doesn't define a time scale, in the sense that we use the word. Whether or not you can use a Kalman filter, I strongly disagree with your statement, is simply whether or not you can formulate an appropriate definition of the time scale, definition of the ensemble in a way that is compatible with requirements. In fact, troubles that you pointed out, which are real, in some of the past Kalman filters were a result of the incorrect identification of the system noise covariance. An identification that did not agree with what the people that did those time scales really wanted to get out of the system. Other noise models produce different results.

JAMES BARNES, How often do you see frequency steps?

MR. WEISS: Dave Allan can probably answer that.

MR. ALLAN: It is a fairly difficult question because we don't really understand the mechanism. We do know that they occur. I have seen some clocks where they occur maybe once a year, several times a year and some clocks that seem not to have step problems. They can be fairly large and fairly significant.

MR. WEISS: We have recently discovered a possible source of the steps which was humidity, and we had never realized that before. Tracking and controlling humidity may remove some steps that we didn't understand the cause of before. As we do more research, we may understand the causes of other frequency steps.

UNIDENTIFIED QUESTIONER: How do you define 'truth'?

MR. WEISS: I don't define truth. When I generate a clock, I know what I have put into it. I generate a clock as being an offset against zero, zero being truth. If I make it up, I know what truth is.

SAME PERSON: Is it related to the Planck time?

MR. STEIN: No. You can relate it to what Einstein said, 'Time is what a clock reads'.

UNIDENTIFIED QUESTIONER: I have a question for you, Sam. You said that your model differed from the others in the process noise. As far as I can tell, the problem is one of observability. You can't change the observability of the model by changing process noise. If your H matrix is the same as everyone else's, then you have the same observability problem they do and all you are doing is de-weighting somewhat past data. I think that I know how you are doing that and I can tell you.

MR. STEIN: The problem, as Mark pointed out, is not a problem of observability. We can discuss it further off-line.

DONALD PERCIVAL, U OF WASHINGTON: I just had a question to clarify what you are doing here. You are not using the (indcipherable)-Jones Kalman filtering model, is that correct? What you are doing then is taking one component of that model, the random walk component, and then using a Kalman filter by itself, a very simple one, to estimate that.

MR. WEISS: Exactly. I am using the output of AT1 time estimate against the scale as if it were a

measurement of frequency against the scale. Then I filter that to obtain only the random walk component plus the variance, or confidence, on that estimate.

MR. PERCIVAL: Is there any problem, do you feel, with the observability. For example, in the time model, the random walk component is only one component of what the thing is actually doing. To separate that out, you are saying that it can be filtered out in a certain fashion.

MR. WEISS: I think that that is a subtle question, because the scale is a mathematical construct. It is something that, mathematically you are making up. The only observability of that is within the scale, there is no physical measurement of the clock against the scale. The closest that we can get to it is what the scale says is the estimate. There is no question of observability because I am looking at something that is defined.

GERNOT WINKLER, USNO: I would like to go back to the frequency step detection thing. It seems to me that it is intrinsically related to the question of post-processing or not. You can readily make a decision as to whether or not there was a frequency step, after the fact. You define as a frequency step as a systematic change in the average frequency. Whether it is systematic or random can only be decided with any kind of confidence only after the fact for small frequency steps. It is a question of the size of the frequency steps that you want to estimate *vs.* the question of post-processing or immediate detection. Here you have to solve the problem of whether you can tolerate post-processing or not. That will determine whether you can reliably detect frequency steps and account for them.

MR. WEISS: That's true. But, if you can detect that a step happened, in real time, that is, you detect now that a step happened yesterday—and the step is large enough, you can get some benefit from that now, in real time. You get the most benefit in post-processing, because then you go back over the last day as well. If the step is large enough that it is pulling the scale now, you can readjust that. You can also re-compute the scale for the last day and, even if you can't use that in real time, you can say that the frequency of the scale is now off, somewhat, from what I am actually outputting, and steer back to what the frequency should be.

THE CRYOGENIC HYDROGEN MASER: PROJECTED PERFORMANCE AND RECENT PROGRESS TOWARDS SPACEBORNE APPLICATIONS

Ronald L. Walsworth and Isaac F. Silvera
Lyman Laboratory of Physics
Harvard University
Cambridge, MA 02138

Robert F.C. Vessot and Edward M. Mattison
Smithsonian Astrophysical Observatory
Cambridge, MA 02138

Michael L. Dings
Alabama Cryogenic Engineering
Huntsville, AL 35804

ABSTRACT

The possibility of significant improvement in the frequency stability of hydrogen masers by operation at cryogenic temperatures (< 1 K) is discussed. The results of the Harvard/SAO collaboration to build and operate a cryogenic hydrogen maser are summarized, and ongoing work to include space-qualified technology in the cryogenic system is described. Finally, a short list is given of scientific applications (on Earth and in space) of a cryogenic hydrogen maser of superior frequency stability.

1. INTRODUCTION

Currently, room temperature hydrogen masers can provide fractional frequency stability close to 10^{-16} for averaging intervals of about 10^4 seconds. Hydrogen maser operation at cryogenic temperatures (≈ 0.5 K) may bring this stability into the 10^{-18} region, as both thermal noise and the line-broadening effect of interatomic hydrogen collisions would be reduced by more than two orders of magnitude^[1]. Phenomena exist, however, that may prevent a substantial improvement in frequency stability. In a cryogenic hydrogen maser (CHM) a liquid helium film replaces Teflon as the storage chamber wall coating; superior frequency stability will require proper control of the temperature dependent frequency shift associated with this helium wall. Also, recent quantum mechanically exact calculations^[2] of hydrogen atom-atom collisions predict low temperature behavior that may mitigate any frequency stability improvement. The projected performance of cryogenic masers in general,

and the Harvard/SAO (Smithsonian Astrophysical Observatory) CHM in particular, will be discussed in section 2, below.

Section 3 includes an overview of the design of the Harvard/SAO CHM, a summary of the results achieved to date with this system, and a discussion of ongoing work to incorporate space-qualified cryogenic technology with the CHM. The National Aeronautics and Space Administration has provided support for the construction of a compact $^3\text{Helium}$ refrigerator for use with the Harvard/SAO CHM. Many of the cryogenic technical problems involved in this project have already been addressed by the recent NASA-sponsored development of a space-worthy recirculating $^3\text{Helium}$ refrigerator. If a CHM proves to be significantly more stable than a room temperature maser, then our system could easily be modified into a fully space-qualified CHM. Such a spaceborne clock would permit both improved and new tests of relativistic gravitation, and would be useful in space-based radio astronomy. Some of the possibilities for new science to be done with a CHM, in space as well as in the laboratory on Earth, will be presented in section 4.

2. PROJECTED PERFORMANCE OF A CHM

The two sources of noise that limit the performance of room temperature hydrogen masers, for averaging time intervals $< 10^4$ seconds, are the added white phase noise of the first stage of amplification of the maser signal (the "preamp"), and thermal noise within the atomic hydrogen's transition linewidth (causing a random walk in phase). The added white phase noise leads to a τ^{-1} dependence of the maser's Allan deviation^[3] (or two-sample deviation) $\sigma_y(\tau)$, where τ is the averaging time interval; this effect typically is the dominant source of maser frequency instability for $\tau < 20$ to 100 seconds. The thermal noise within the atomic line gives a $\tau^{-1/2}$ dependence to $\sigma_y(\tau)$, and typically dominates observed maser performance for $\tau > 100$ seconds. For $\tau > 10^4$ seconds, systematic frequency variations usually dominate.

As is shown in Figure 1, the performance of room temperature H masers is optimum for averaging time intervals $\sim 10^3 - 10^4$ seconds, with $\sigma_y(\tau)$ reaching a minimum $\approx 5 \times 10^{-16}$. A maser optimized for operation ≈ 0.5 K could reach $\sigma_y(\tau) \approx 10^{-18}$ for similar averaging times, assuming that the added white phase noise of the preamp and the thermal noise within the atomic line remain the dominant sources of frequency instability. For both these noise sources the great gain in frequency stability comes from the reduction of the system's temperature (including the preamp noise temperature for the added white phase noise) by a factor of about 500, and the reduction of the line broadening effect of hydrogen-hydrogen collisions by nearly three orders of magnitude^[1]. These results follow from an application of the system parameters for a typical room temperature (SAO) H maser, and for the Harvard/SAO CHM, to the expressions given in Figure 1 for the $\sigma_y(\tau)$ of the two aforemen-

tioned noise sources; straightforward derivations of the $\sigma_y(\tau)$ expressions can be found in references 4 and 5, for the thermal noise within the atomic line and the added white phase noise, respectively. The qualitative reasons that a CHM may exhibit such a significant improvement in frequency stability are: it should be possible to operate a CHM at much higher output power levels than a room temperature maser, with the same linewidth (i.e. line Q), due to the greatly reduced interatomic collisional broadening; in addition thermal noise effects are greatly reduced. Thus both the *signal* and the *noise* of a CHM should be improved over a room temperature maser, yielding a more stable frequency source.

Systematic effects will inevitably limit the frequency stability of a CHM, but at what level and from what sources? Many of the causes of systematic frequency drift in room temperature masers are related to slow, long-term changes ("creep") in the maser cavity materials, or to sensitivity to external influences such as local temperature and magnetic field. These effects may be greatly reduced in a CHM, as materials are in general much more stable mechanically and thermally at low temperatures, and since significantly improved magnetic shielding is possible at low temperatures with the use of superconducting materials. Thus it is reasonable that the conventional sources of systematic frequency drift may be reduced sufficiently in a CHM to allow substantial improvements in frequency stability to be realized. Nevertheless, there are two sources of frequency instability in a CHM that may limit such achievements. The first is the temperature dependence of the frequency shift due to hydrogen atom collisions with the liquid helium film that serves as the storage chamber wall coating in a CHM, and with the helium vapor associated with the film⁽¹⁾. As shown in Figure 2, the frequency shift due to collisions with the helium wall is negative, and increases in magnitude as the temperature of the system is lowered (the hydrogen atoms remain on the wall longer during collisions, since they are moving slower). The frequency shift due to collisions with the helium gas in the storage chamber is also negative, but it increases in magnitude as the temperature is raised (as the vapor pressure of the helium rises). Thus a minimum in the magnitude of the H-He frequency shift occurs for $T \sim 0.5 - 0.6$ K; the exact temperature of the minimum depends on the geometry of the CHM, for the Harvard/SAO CHM it is 0.53 K. This minimum provides a point of operation where the frequency is insensitive to temperature deviations and fluctuations to first order. Nonetheless, temperature control and homogeneity at the level of $10 \mu\text{K}$ will be required to keep fractional frequency deviations $< 10^{-18}$. This level of temperature control can be achieved in cryogenic systems, but remains challenging, especially for a device of the physical size of a maser.

The second source of frequency instability that may be important in a CHM is the nature of the hydrogen-hydrogen collisions at low temperatures. In Figure 3 the effects of these collisions (normalized with respect to H density) are plotted against temperature, as determined by a complete, quantum

mechanical calculation^[2] of the problem (results that have been verified experimentally^[1] are given by solid lines). As discussed above, the linewidth broadening effect of H-H collisions decreases by almost three orders of magnitude as the temperature is reduced from ~ 300 K to ~ 0.5 K. The H-H collisional frequency shift is compensated at room temperature by an appropriate tuning of the maser cavity; the result being that the maser frequency is effectively insensitive to variations in the input H flux, and to any variations in the linewidth (thus the maser performance is limited by the added white phase noise and the thermal noise within the atomic line). The calculation of the H-H collisional interaction reveals, however, that there is an additional component to the collisional frequency shift that cannot be compensated for in the manner just described. At the frequency stability level of a room temperature maser ($\sim 10^{-15}$) this additional frequency shift effect is not observed, but as one attempts to reach stabilities of 10^{-17} to 10^{-18} (with a CHM) the effect becomes important. A determination of the veracity of this H-H interaction calculation, at low temperatures, is one of the major short-term goals of the Harvard/SAO CHM research effort.

3. THE HARVARD/SAO CHM

Figure 4 shows a cutaway, schematic view of the CHM built and operated by the Harvard/SAO collaboration^[6]. The system was designed to be accommodated in a pre-existing dilution refrigerator facility (capable of reaching 0.005 K), in rough analogy with room temperature H maser designs. A room temperature microwave discharge outside of the refrigerator provides atomic hydrogen. The H beam is piped into the refrigerator and thermalized at ~ 10 K, where the desired atomic hydrogen states are focussed by a hexapole magnet into the H storage chamber, located inside a sapphire resonant cavity. A sapphire cavity is used in the CHM because of its smaller size for the same resonant frequency (due to the large dielectric constant of sapphire): the dilution refrigerator could not hold an object as large as a conventional room temperature maser cavity. Also, sapphire resonant cavities are mechanically stable and can have high Q's at low temperatures. The cavity frequency can be externally controlled over a range of ~ 1 MHz. A nested set of four magnetic shields, currently made out of a conventional high permeability alloy, surrounds the isothermal vacuum vessel housing the resonant cavity. There are longitudinal solenoids around the beam tube (between the hexapole magnet and the cavity) and the cavity to provide a static magnetic field (~ 1 mG in the H storage chamber). Also, transverse rf fields can be applied to the H storage chamber region and to the beam tube region, for determination of the static magnetic field strength and for the mixing of the Zeeman levels. Liquid helium flows continuously into the CHM; at temperatures < 1 K it forms a superfluid film that uniformly coats all surfaces, including the walls of the H storage chamber. The helium flows down towards the warmer regions of the CHM, evaporates, and is differentially pumped by a large sorption

pump (this also pumps away the "spent" hydrogen leaving the resonant cavity). The lifetime of the sorption pump in the current design is about 3 weeks.

The Harvard/SAO CHM was first oscillated in 1986^[6], one of three CHM's operated, independently, for the first time that year^[7,8]. Measurements were made of the H-He frequency shift and the line Q, as a function of temperature, for thin liquid helium film wall coatings, and much was learned of the limitations of the cryogenic design. The system was operated again in 1988, after modifications. It was learned that it is important to have a relatively thick and benign wall coating (e.g. 20 μm of teflon) between the sapphire and the liquid helium film (thickness < 0.02 μm) to prevent sapphire paramagnetic sites from rapidly flipping the H atom spins (thereby severely broadening the atomic line and preventing oscillation).

Limited access to the dilution refrigerator for which the Harvard/SAO CHM was first built has led us to begin a program to design and construct a closed cycle $^3\text{Helium}$ refrigerator dedicated to housing the CHM. In addition, it was decided to use space-worthy cryogenic technology in the new refrigerator, when feasible, with an eye towards the long-term goal of operating a CHM of superior frequency stability in space. This effort has broadened our collaboration to include Alabama Cryogenic Engineering (ACE), Inc., experts in space-worthy cryogenic technology. Specifically, the new $^3\text{Helium}$ refrigerator may include the following elements (see Figure 5): a lightweight, compact, sealed $^3\text{Helium}$ pump that can operate in any orientation relative to the Earth's gravitational field; and a $^3\text{Helium}$ evaporation chamber containing a porous silver sinter plug to act as a "sponge" to hold the liquid $^3\text{Helium}$ in place in weightless conditions. In the recent past, ACE has developed functioning cryogenic systems employing these technologies. The new $^3\text{Helium}$ refrigerator is expected to be working by the end of next summer, at which point the CHM will be installed and operated. We hope to make frequency stability measurements of the CHM soon thereafter, using a "three-cornered hat" method to simultaneously intercompare the CHM with two room temperature SAO masers.

4. SCIENTIFIC USES OF A CHM

A spaceborne clock of superior frequency stability (such as may be provided by a CHM) could be employed in the improvement of several scientific tests of relativity, in the important effort to detect long wavelength gravitational radiation, and as a component in a space-based radio astronomy observatory. The verification of the gravitational redshift (a consequence of the Weak Equivalence Principle of relativity) could be improved by more than an order of magnitude with a clock in an eccentric Earth orbit, and by nearly five orders of magnitude with a clock sent over a pole of the Sun^[9]. Also, a space-based clock would allow a test of the isotropy of the speed of light at a level

approaching one part in a trillion^[9]; the best Earth-based tests are at the level of 100 parts in a trillion^[10]. The largest amplitude gravitational waves are believed to be generated by rare, large-scale cataclysmic events, and to have long wavelengths ($> 10^8$ km) and hence long periods (> 1000 seconds)^[11]. Detection of this long wavelength gravitational radiation would require a network of clocks of superior frequency stability located in deep space (over a range $> 10^8$ km)^[9]. A radio astronomy observatory in space would employ VLBI (Very Long Baseline Interferometry) techniques, and the associated synchronization of distant radio antennas. Improved, space-based clocks would allow greater measurement sensitivity by permitting an increased observation baseline to be used, and would eliminate the problem of tropospheric noise that would arise with the use of ground-based clocks^[12].

Prior to any use in space, a great deal of atomic and low temperature physics may be done with the CHM on Earth. As discussed above, the various hydrogen-helium and hydrogen-hydrogen interactions need to be studied, both to understand the details of the low energy atomic physics involved (entering the "quantum mechanical regime" of slow moving atoms), and to determine the practical feasibility of the CHM as a clock. In addition, the CHM could be used to study interesting "collective phenomena" such as: spin (or magnetization) waves that can propagate in a low temperature (< 1 K) atomic hydrogen gas a quantum mechanical effect^[13]; and "chaos" in the CHM's output signal amplitude for high maser cavity Q's ($> 300,000$), a result of the nonlinearity of the equations of motion (the "Maxwell-Bloch" equations) governing the maser's radiative transitions^[14]. Finally, the CHM could be exploited as an effective two-level oscillator of great frequency stability to make an improved test of the linear superposition of quantum mechanics. A failure of the linear superposition principle would result in a dependence of the H maser output frequency on the relative population of the two masing states (energy levels)^[15]. Recent measurements with room temperature H masers set "state-of-the-art" limits on this effect^[16]. The measurements are limited by the maser frequency stability; thus a CHM of superior frequency stability would allow an improved test to be performed.

5. CONCLUSION

In this paper the possibility of significantly improving H maser frequency stability by operation at temperatures ≈ 0.5 K has been examined, and the Harvard/SAO cryogenic H maser (CHM) research program has been reviewed. It was found that the noise sources that limit room temperature H maser stability for $\tau < 10^4$ seconds are greatly reduced at low temperature, such that an Allan deviation approaching 10^{-18} can become feasible. Nevertheless, new sources of frequency deviation may emerge at low temperature (involving the hydrogen-helium and hydrogen-hydrogen collisional frequency shifts) to mitigate any stability improvement. The determination of

the nature and importance of these effects is one of the main short-term goals of the Harvard/SAO effort, described above. In addition, a discussion was given of recent progress to include space-worthy cryogenic technology in the Harvard/SAO CHM, and the science that could be performed (in space and on Earth) with a CHM of superior frequency stability.

ACKNOWLEDGEMENTS

The Harvard/SAO cryogenic hydrogen maser research program has benefitted from support from the following sources: NASA's Science Coordinating Committee for Experimental Gravitation; NASA's Graduate Student Researchers Program; the Smithsonian Institution Scholarly Studies Program; and the Department of Energy. We are grateful to Charles Agosta and Herman Godfried for their close collaboration in the early stage of the research effort.

REFERENCES

1. W.N. Hardy and M. Morrow, *J. Phys. (Paris) Colloq.* **42**, C8-171 (1981).
2. J.M.V.A. Koelmann, S.B. Crampton, H.T.R. Stoof, O.J. Luiten and B.J. Verhaar, *Phys. Rev. A* **35**, 3825 (1987).
3. D.W. Allan, *Proc. I.E.E.E.* **54**, 221 (1966).
4. D. Kleppner, H.C. Berg, S.B. Crampton, N.F. Ramsey, R.F.C. Vessot, H.E. Peters and J. Vanier, *Phys. Rev. A* **138**, 972 (1965).
5. R.F.C. Vessot, L. Mueller and J. Vanier, *Proc. I.E.E.E.* **54**, 199 (1966).
6. R.L. Walsworth, I.F. Silvera, H.P. Godfried, C.C. Agosta, R.F.C. Vessot and E.M. Mattison, *Phys. Rev. A* **34**, 2550 (1986).
7. H.F. Hess, G.P. Kochanski, J.M. Doyle, T.J. Greytak, and D. Kleppner, *Phys. Rev. A* **34**, 1602 (1986).
8. M.D. Hurlimann, W.N. Hardy, A.J. Berlinsky, and R.W. Cline, *Phys. Rev. A* **34**, 1605 (1986).
9. L.L. Smarr, R.F.C. Vessot, C.A. Lundquist, R. Decher, and T. Piran, *General Relativity and Gravitation* **15**, 129 (1983).

10. C.O. Alley, et al., In Proceedings of the 20th Annual Precise Time and Time Interval Applications and Planning Meeting, Vienna, VA, Nov. 29 - Dec. 1, 1988.
11. L.L. Smarr, Ed., *Sources of Gravitational Radiation, Proceedings of the Battelle Seattle Workshop* (Cambridge University Press, Cambridge, 1978).
12. R. Decher, D.W. Allan, R.F.C. Vessot, G.M.R. Winkler, and C.O. Alley, *I.E.E.E. Trans. on Geoscience and Remote Sensing* GE-20, 321 (1982).
13. J.P. Bouchaud, thesis, Ecole Normale Supérieure (Paris, unpublished).
14. A. Mann and B.J. Verhaar, to be published.
15. S. Weinberg, *Phys. Rev. Lett.* 62, 485 (1989).
16. R.L. Walsworth, to be published.

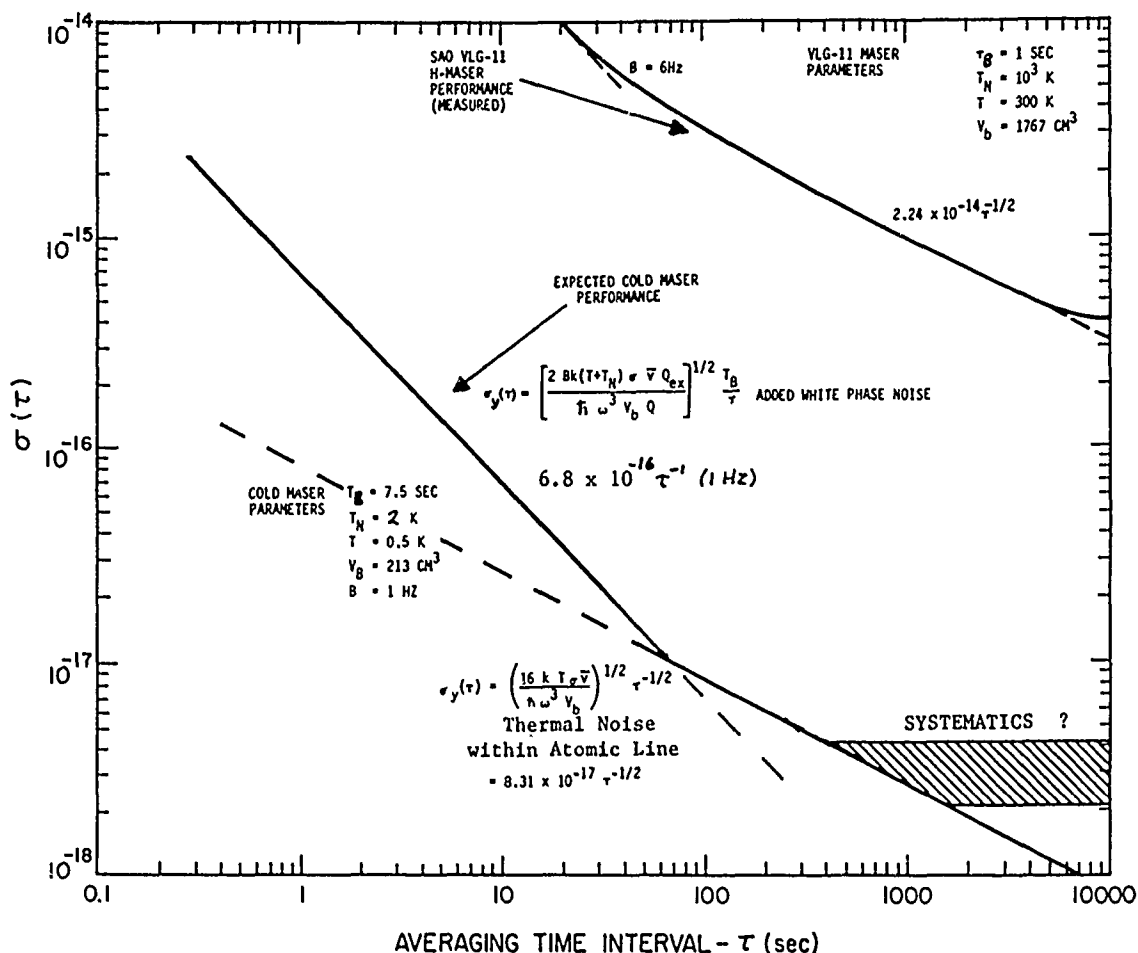


Figure 1. Comparison of Frequency Stability of Room Temperature H Maser (Measured) and Cryogenic H Maser (Projected)

Figure 2
Frequency Shifts due to
Hydrogen-Helium Collisions

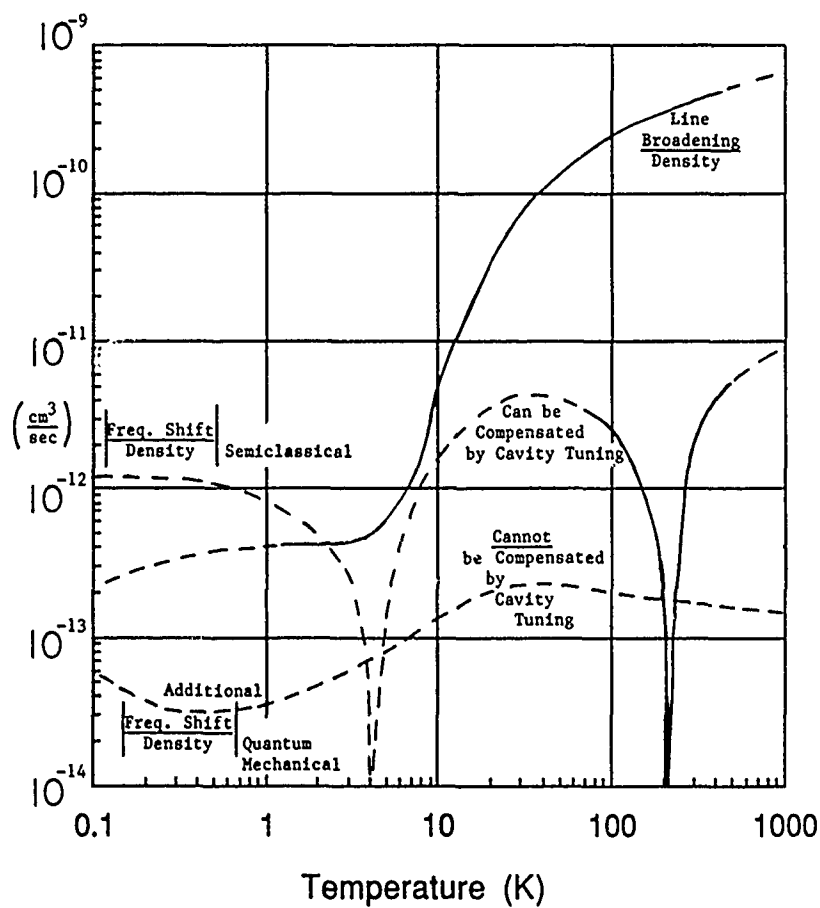
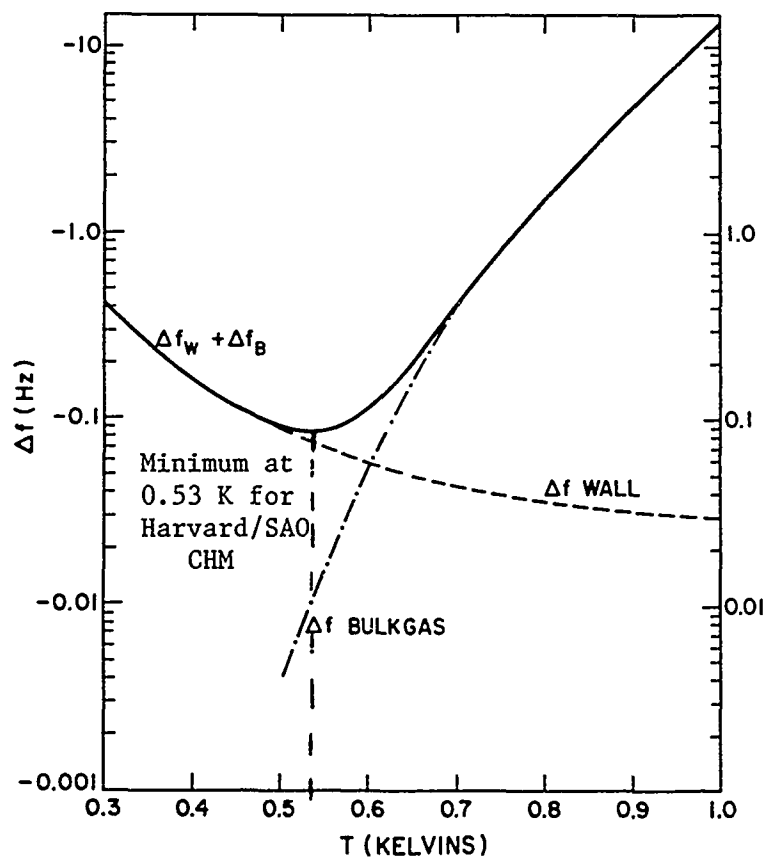


Figure 3
Linewidth Broadening and
Frequency Shifts due to
H-H Collisions

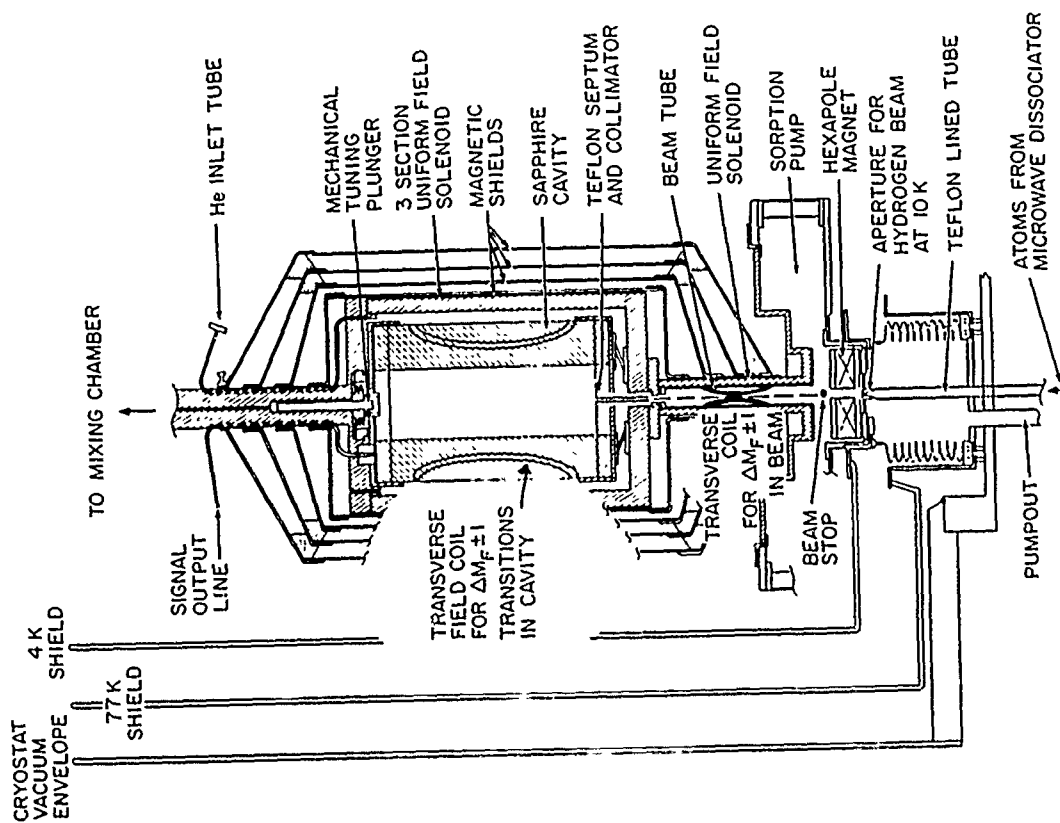


Figure 4.
Cutaway schematic view of Harvard/SAO
CHM (as configured in dilution refrig.)

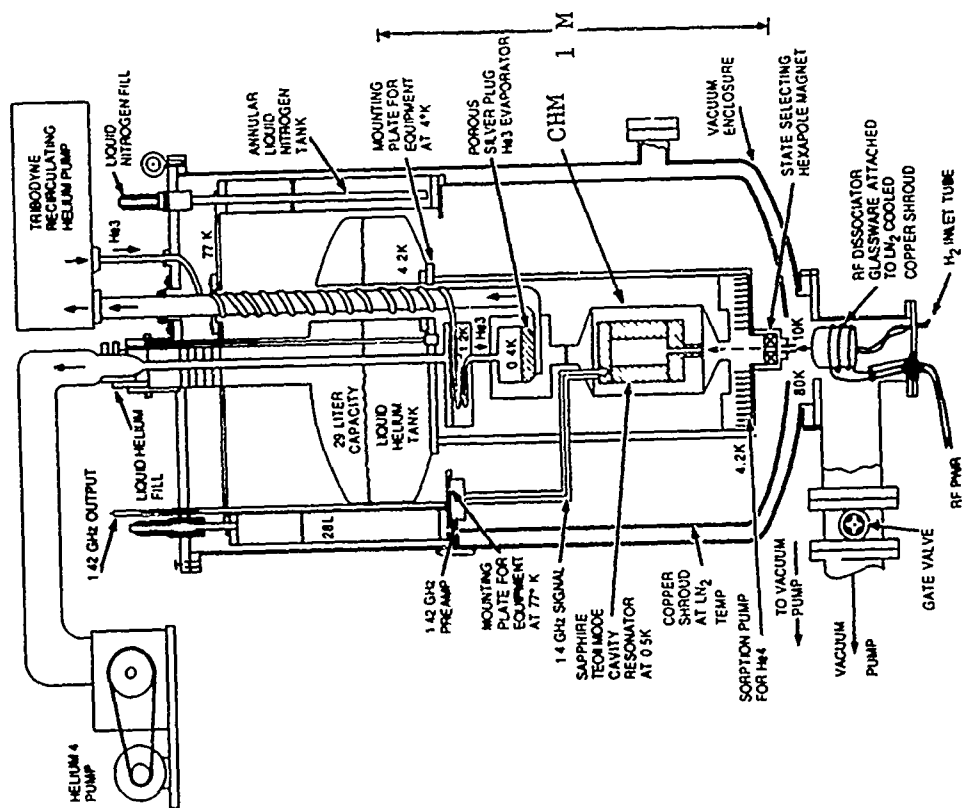


Figure 5.
Cutaway schematic view of CHM installed
in new 3Helium refrigerator

QUESTIONS AND ANSWERS

CARROLL ALLEY, U OF MARYLAND: There are some here who are interested in quantum mechanics. Could you elaborate a little more on the planned studies.

MR. WALSWORTH: I have been performing experiments this fall with the room temperature masers, testing the linearity of quantum mechanics. This is a relatively new thing that was started by Steven Weinberg, about a year ago, doing some theoretical analysis, looking into whether or not one could develop a quantum mechanics that was not necessarily linear. One could generalize quantum mechanics and generalize the linearity that was involved in the superposition principle. He found in the detailed analysis, looking at the group algebra and other things, that he could, in a general way, for the internal degrees of freedom, the spin degrees of freedom, generalize the superposition principle by letting go of the distributive property in the superposition principle and holding on to the homogeneity properties. The result of this, experimentally, is that this predicts a output frequency of a spin system depends on their state distribution. This is opposed to an NMR or hydrogen maser or other spin system where the output frequency, the transition between two levels, does not depend on the distribution of the ensemble between these two levels, the tipping angle if you will, this theory predicts that the output frequency will depend on this distribution, much like a pendulum, a simple harmonic motion, the period of the pendulum is independent of the angle swung by the pendulum, non-linear terms in the equation of motion cause the period to depend on the angle. Quantum mechanics has been assumed since the 20's and 30's to be linear, but you might as well test it to see how well verify that, and maybe discover some new and interesting physics. Dave Weinland's group at NIST has made some very good measurements in nucleus spin systems and we are trying to do one in atomic spin systems with room temperature masers. Cryogenic masers would allow us to make a much better test because we are limited in the accuracy that we can measure frequency by the short term frequency stability right now.

JOHN DICK, JPL: I wonder if you could talk a little bit about the temperature coefficient, considering that this is a long term frequency standard. About 10^{-8} per $^{\circ}\text{C}^2$ looks a little worrisome and I wonder if you could also say a little about the gradient due to the hydrogen flow.

MR. WALSWORTH: That is the temperature shift of the Helium? Some straightforward calculations that were done back in 1982 by Walter Hardy at the University of British Columbia, who is also working on cryogenic hydrogen masers, showed that for the typical curvature that you need something like $10\ \mu\text{K}$ temperature control. I don't know if that corresponds to the number that you just quoted, but if it is true, it is not easy, but it is not impossible in this temperature regime. As far as the gradients of the hydrogen, the heating effect of the hydrogen as opposed to the helium, the helium is the major effect and I don't think there will be big gradients due to the hydrogen. The sapphire dielectric in our system is surrounded by copper shims outside the silver coating. This helps thermalize the sapphire.

DIELECTRIC RESONATOR OSCILLATORS THEORY AND STATE-OF-THE-ART*

A.P.S.Khan^{na}
AVANTEK INC.
481 Cottonwood Drive
Milpitas CA. 95035

INTRODUCTION

With the advent of high-Q temperature-stable dielectric material, the transistor dielectric resonator oscillator (DRO) is fast becoming the most desirable choice in a vast number of fixed-frequency microwave signal source applications. A DRO clearly fills the gap between a free-running oscillator and a synthesized source, and represents a good compromise of cost, size and performance compared to alternative signal sources such as high-Q cavity oscillators, microstrip oscillators or multiplied crystal oscillators. Dielectric resonators, due to their excellent integrability in MIC circuits, can directly be used as the frequency-determining element for realizing a stable microwave frequency source. The primary characteristics of the ceramic material to be used for dielectric resonators are:

- The quality factor, Q , which is approximately equal to the inverse of the loss tangent.
- The temperature coefficient of the resonant frequency, τ_f which includes the combined effects of the temperature coefficient of the dielectric constant and the thermal expansion of the dielectric resonator and the shielding package.
- The dielectric constant, ϵ_r .

The Q , τ_f , and ϵ_r values required for various applications differ and, in general, satisfactory oscillator operation under most conditions can be achieved by choosing an appropriate material composition. Until several years ago, the lack of suitable materials (i.e., materials possessing acceptable combinations of Q , τ_f , and ϵ_r) severely limited dielectric resonator applications. Materials such as rutile-phase TiO_2 , which has an unloaded Q of about 10000 at 4 GHz and ϵ_r of 100, were most often used. However, TiO_2 has a τ_f value of 400 ppm/°C which makes it impractical for most applications.

The development of temperature-stable dielectric resonators dates back about a decade. A number of material compositions have been explored in attempts to develop suitable dielectric materials, including ceramic mixtures containing TiO_2 , various Titanates and Zirconates, glass, ceramic systems and alumina-based ceramics. At present, several ceramic compositions have been developed offering excellent dielectric properties. Complex perovskite compounds with the general formula $A(B'_{1/3}B''_{2/3})O_3$

*©Avantek, Inc.

(where $A = Ba, Sr$; $B' = Zn, Mg, Co, Ni$; $B'' = Ta, Nb$) have proved to possess acceptable properties for dielectric resonators. These compounds have dielectric constants between 20 and 40, a high quality factor, some greater than 10000 at 10 GHz, and a temperature coefficient which is variable through modification of the composition. Table 1 compares the important properties of different materials developed commercially^[1].

It is impossible to say that any of the dielectric compositions shown in Table 1 is "better" than any other, since other factors, such as the ease of ceramic processing and the ability of a manufacturer to hold tolerances on the dielectric properties must also be considered. Performance limitations, if any, of the lower dielectric constant materials remain to be determined, since most component work reported thus far has used dielectric resonators with ϵ_r in the range of 37-100. The lower dielectric constant material is likely to be more sensitive to shielding, due to the increase in fields outside the resonator.

RESONANT FREQUENCY

A dielectric resonator, made of low-loss, high-permittivity ceramic material, resonates in various modes at frequencies determined both by its dimensions and its surroundings^[1]. Although the geometrical form of a dielectric resonator is extremely simple, an exact solution of the Maxwell equations is considerably more difficult than for the hollow metallic cavity. For this reason, the exact resonant frequency of a particular resonant mode, such as the most commonly used $TE_{01\delta}$, can only be computed by rigorous numerical procedures.

A number of mathematical techniques which can predict resonant frequency to an accuracy of $\pm 1\%$ for specific configurations appear in the literature. Unfortunately, these methods call for the use of high-powered computers. Kajfez^[2] has presented an approximate solution of the equations for both the case of an isolated dielectric resonator and for a resonator coupled into a MIC microstrip circuit. This method is typically accurate to $\pm 2\%$. Practical dielectric resonators available today cover the frequency range of 2 to 100 GHz. However, with the recent development of conveniently-sized coaxial tubular dielectric resonators, the usable frequency range has been extended to 500 MHz. The lower frequency limit is imposed by the large resulting dimensions of the resonator, while the upper frequency is limited by the reduced Q of small resonators, as well as by resonator dimensions that become too small to effectively couple to a transmission line.

To a first approximation, a dielectric resonator is the dual of a metallic cavity. The radiation losses of the dielectric resonators with commonly-available permittivities, however, are generally much greater than the energy losses in the metallic cavities, which makes proper shielding of the dielectric resonator a necessity. Dimensions of a dielectric resonator are also considerably smaller than those of an empty metallic cavity resonant at the same frequency - by a factor of approximately $\sqrt{\epsilon_r}$. If ϵ_r is high, the electric and magnetic fields are confined in the region near the resonator, which results in small radiation losses. The unloaded quality factor is thus limited by the losses in the dielectric resonator. The shape of a dielectric resonator is usually a solid cylinder, but tubular, spherical and parallelepiped shapes are also used.

In the $TE_{01\delta}$ mode, the most commonly used mode, magnetic field lines are contained in the meridian plane while the electric field lines are concentric circles around z-axis as shown in Fig. 1. For a distant observer, this mode appears as a magnetic dipole, and for this reason it is sometimes referred-to as the "magnetic dipole mode." When the relative dielectric constant is around 40, more than 95% of

the stored electric energy, and more than 60% of the stored magnetic energy is located within the cylinder. The remaining energy is distributed in the air around the resonator, decaying rapidly with distance away from the resonator surface.

COUPLING TO THE RESONATOR IS CRITICAL

To effectively use dielectric resonators in microwave circuits, it is necessary to accurately understand the coupling between the resonator and transmission lines. The $TE_{01\delta}$ mode of the cylindrical resonator can be easily coupled to a microstrip line, fin line, magnetic loop, or to a metallic or dielectric waveguide^[1]. Figure 2 shows the magnetic coupling between a dielectric resonator and microstrip line. The resonator is placed on top of the microstrip substrate, with the lateral distance between the resonator and the microstrip conductor primarily determining the amount of coupling between the resonator and transmission line^[3]. The degree of coupling has a direct effect upon output power, frequency stability, and harmonic content, as well as resonant frequency of a dielectric resonator oscillator. Proper metallic shielding, required to minimize the radiation losses (hence to increase Q), also affects the resonant frequency of the $TE_{01\delta}$ mode. Figure 3 & 4 show the equivalent circuit of the dielectric resonator coupled to a microstrip line.

ACTIVE DEVICES FOR DRO'S

Transistors are most commonly used to build today's DROs up to 40 GHz. Transistor DROs can be realized using either silicon bipolar or GaAs FET devices. The maximum oscillation frequency for silicon bipolar transistor oscillators is lower than that of the GaAs FET oscillators. Reasonable power outputs have been obtained up to 40 GHz and 20 GHz using GaAs FET and silicon bipolar devices respectively. Figure 5 shows the present power and frequency coverage capabilities of the dielectric resonator oscillators. The silicon bipolar transistor, however, offers lower phase noise close to the carrier and faster frequency settling characteristics compared to a GaAs FET oscillator. Other devices usable in DROs are Gunn and Impatt diodes. Gunn oscillators offer lower AM and FM noise characteristics at the cost of poor DC to RF efficiency (<1%) and reliability problems over the wide range of temperature operation. Impatts have poor noise performance, but offer medium powers at reasonable efficiencies (>30%). Transistors, on the other hand, offer medium noise with medium efficiencies (>20%). Both Gunn and Impatt diode sources are commonly used at millimeter frequencies (30-100 GHz).

DRO CIRCUITS

There are two means of incorporating a dielectric resonator in a MIC oscillator: as a passive stabilization element (stabilized DRO) or as a circuit element in a frequency-determining network (stable DRO).

A stabilized DRO is an oscillator which uses a dielectric resonator in the output plane of the circuit to stabilize an otherwise free-running oscillator (Fig. 6). This approach has several disadvantages, including a tendency toward mode jumping, frequency hysteresis problems, higher insertion loss due to the resonator being coupled to the output circuitry and increased output power variation.

The stable DRO configuration, which uses the dielectric resonator as a feedback/frequency determining element, is the most commonly used. It provides greater efficiency, simpler construction and more resistance to mode jumping and hysteresis effects than the stabilized DRO.

To realize a stable DRO, the resonator may be used as either a series or parallel feedback element in the frequency determining circuit. Figure 7 shows two common configurations of each type.

Series feedback configurations are based on the ability of the active device to produce a negative resistance (reflection coefficient greater than 1) at at least one of the three terminals, in the frequency range of interest^{[1][10]}. The small signal oscillation conditions in this case are reduced to:

$$\begin{aligned} |S'_{11}| \cdot |\Gamma_1| &> 1 \quad \text{and} \\ \angle S'_{11} + \angle \Gamma_1 &= 2\pi n \quad n = 0, 1, 2, \dots \end{aligned}$$

where S'_{11} and Γ_1 are the reflection coefficients of the transistor and the resonator at any plane between the device and the resonator (Fig. 7a). Since Γ_1 is always less than 1, this condition implies that $|S'_{11}|$ looking into the device should be greater than 1. A distributed capacitance in the source for the configuration of Fig. 7a and inductance in the gate for the configuration shown in Fig. 7b is commonly required to generate a high value of $|S'_{11}|$ (> 1). Position of the dielectric resonator with respect to the device is now determined to satisfy the oscillation condition completely.

The parallel feedback configuration is based on the use of the forward gain of a device (transmission coefficient greater than 1). In such a design, a dielectric resonator is used as a bandpass filter, and connected across the two terminals of an active device possessing transmission gain greater than the insertion loss of the dielectric resonator. To oscillate, the electrical line length between the device input and output must provide a phase shift around the feedback loop equal to an integer multiple of 2π radians at the oscillation frequency.

An advantage of the series feedback design is the relative ease of coupling to a single line, compared to the parallel circuit's requirement for coupling to two lines. In addition, the two coupling coefficients in the parallel case are not independent, increasing the difficulty of alignment. With the parallel feedback circuit, however, the use of a high-gain amplifier can allow significant decoupling of the resonator from the microstrip lines, resulting in a higher loaded Q factor with associated reduction in phase noise.

ELECTRICAL PERFORMANCE

The transistor DROs are available spanning the frequency range of 3 GHz to 40 GHz with power outputs ranging to greater than +23 dBm at X-band (Fig. 5). As noted earlier, the oscillator can use either a silicon bipolar or GaAs FET device, each device having associated tradeoffs in performance, and the oscillator can be followed by one or more buffer amplifier stages as required to meet power output specifications. The center frequency is usually specified in MHz with an associated frequency accuracy (temperature, pulling and pushing dependant) specification. The DRO frequency can be fixed, mechanically or electrically tunable over a narrow band. Important aspects of the salient characteristics of a DRO are discussed next.

TEMPERATURE STABILITY

The principal cause of DRO frequency drift with temperature is the phase deviation between the resonant circuit and the active circuit including device, feedback and output circuitry. Using the oscillation condition in the reflection coefficient form,^[4] it can be easily proved that the temperature coefficient of DRO frequency is a function of the following parameters:

- The temperature coefficient, τ_f , of the dielectric resonator placed in a shielded MIC configuration.
- The unloaded Q of the dielectric resonator.
- The coupling coefficient of the dielectric resonator with the microstrip line.
- The temperature coefficient, $\tau_{\rho\eta}$, of the device (transistor) input reflection coefficient phase that is known to decrease linearly with temperature.

In order to achieve a temperature-compensated DRO, a resonator with a temperature coefficient of +1 to +4 ppm/°C is generally required to offset the negative temperature coefficient of the device phase temperature coefficient. Figure 8 shows some of the typical frequency drift curves over temperature for free-running DROs.

With present technology it is now possible to repeatably produce free-running DROs with frequency drift of less than ± 100 ppm over the -55 to +85°C military temperature range, at frequencies up to 18 GHz. However, as shown in Fig. 8, results reported in the R & D environment are significantly better (± 10 ppm over temperature)^[4].

FREQUENCY TEMPERATURE COMPENSATION

Certain system applications require greater temperature stabilities than are achievable using free running DROs, even with temperature compensation. A number of techniques are used to improve the temperature stability of a DRO.

The Digitally Compensated DRO (DC-DRO) uses a sensor mounted in the oscillator to detect temperature changes. The output of the sensor goes through an A/D converter to produce a digital word corresponding to the particular temperature. EPROMs, programmed with the temperature characteristics of the DRO and a correction look-up table, drive a D/A converter to provide the correction signal, which is applied to the varactor of an electronically-tuned DRO. Using this technique frequency stability of ± 15 ppm can be obtained over temperature^[5].

The Analog-Compensated DRO (AC-DRO) uses an analog compensator circuit in conjunction with a temperature sensor to achieve up to ± 20 ppm frequency stability. In analog compensation the individual oscillator is tested to produce a custom tuning voltage vs. temperature curve required to maintain a constant frequency. The compensation circuit is then aligned to fit the curve of the specific oscillator^[5].

Ovenization may also be used to enhance the temperature stability of a DRO. To achieve temperature stability, the oscillator package is inserted in a temperature-stabilized oven. Using a heater element, a quick-response thermistor and associated control circuitry, the package temperature can be maintained

within $\pm 5^{\circ}\text{C}$ at 5 to 10 degrees above the maximum ambient temperature. A total frequency stability of better than ± 10 ppm can be obtained using this approach.

Ovenized DROs offer lower phase noise than analog—or digitally—compensated DROs because the oscillator does not need to incorporate electrical tuning circuitry. Analog- and digitally-compensated DROs, however, are smaller in size and do not need the substantial amount of heater power required by the ovenized DRO.

LOCKED DRO'S

Phase Locked DROs (PL-DRO) and Injection Locked DROs (IL-DRO) are used when the requisite frequency stability and phase noise cannot be achieved using stabilization techniques. A PL-DRO or IL-DRO approach also becomes necessary when multiple oscillators are required to be phase- or frequency-coherent or both. For locked systems, a highly stable crystal-controlled signal source operating at HF or VHF is used as a reference oscillator.

In injection (frequency) locking, a VHF power amplifier driving a step-recovery diode is used to generate a wideband harmonic comb, which includes the required locking frequency. A bandpass filter is used to select the desired harmonic, and a free-running DRO is locked to the harmonic through the circuit shown in Fig. 9a^[6]. The main requirement in this case is to make sure that the DRO frequency drift under all operating conditions is less than the injection locking bandwidth, Δf . This bandwidth is a function of the injection power, oscillator output power, and external Q .

Injection locking is simpler and less expensive than phase locking, but the RF output is more likely to contain spurious signals at the harmonics of the reference oscillator frequency.

Figure 9b shows a typical phase-locked DRO circuit. A DC-coupled sampler/phase detector is used to mix the desired harmonic of the amplified crystal oscillator with the incoming frequency from the DRO. If the difference frequency is small enough, the loop will be driven towards a point where the difference frequency out of the sampler becomes zero. The loop then drives the DRO towards a zero phase error condition.

A search mechanism is generally included in the system so that the loop will be forced to tune through a stable lock point if the initial difference frequency is too large for capture to occur. An AC-coupled phase-locked DRO circuit is used when the output frequency of the DRO is not harmonically related to the reference oscillator frequency.

PHASE NOISE

Phase noise, related to short-term frequency stability, is characterized by variations in the output frequency which appear, in the frequency domain, as FM energy around the carrier frequency. This is shown graphically in Fig. 10. Phase noise is specified in dBc/Hz measured at specified offsets from the carrier frequency: typical offsets are 10 and 100 kHz. In a DRO, phase noise is primarily dependent on the following factors:

1. The low-frequency noise sources inherent in the active device,

2. The upconversion factor, a measure of the efficiency in the conversion of the low frequency noise to the phase noise of the microwave oscillator,
3. The loaded Q factor of the dielectric resonator,
4. The output power and external Q of the oscillator.

Optimization of phase noise performance calls for the use of a high- Q dielectric resonator and a low-noise device combined with specific design considerations in the oscillator circuit.

It has been proven that the low-frequency noise in a GaAs FET is inversely proportional to the gate length and width of the device. Both biasing conditions and the processing of the GaAs FET also play vital roles in achieving low noise oscillators. Figure 11 compares the phase noise performance of a number of different oscillators.

As noted earlier, silicon bipolar transistors are known to produce lower levels of low-frequency noise compared to GaAs FETs. Silicon bipolar DROs typically offer 6 to 10 dB improvement in the phase noise close to the carrier (up to at least 100 kHz off the carrier) compared to FET versions. Figure 11 compares the phase noise of a bipolar and GaAs FET DRO at different frequencies. Fortunately, bipolar transistors are now available for use in fundamental-output oscillator circuits at up to Ku band.

Some of the newer design techniques that can be used to further reduce phase noise include:

- Low frequency feedback, using a parallel feedback circuit designed at low frequencies (up to 1 MHz) to reduce upconversion of the low frequency noise. Phase noise improvement of up to 20 dB has been reported using this technique^[7]. This method is sometimes referred to as bias feedback.
- Noise degeneration, using the same dielectric resonator both as the frequency-determining element of the oscillator and the dispersive element of a frequency discriminator. The DC output of the discriminator is applied to the frequency control port of the DRO. This technique has been reported to achieve phase noise as low as -120 dBc at 10 kHz from the carrier at 10 GHz^[8].

MECHANICAL TUNING

The frequency of oscillation of the dielectric resonator is dependant on a number of factors, not the least of which is its proximity to the ground plane. To take advantage of this, a tuning screw can be installed in the top cover directly above the resonator which, by reducing the distance between the resonator and the apparent ground plane, will provide for a certain amount of change in the resonant frequency (Fig. 12).

The reason for such behavior can be found in the cavity perturbation theory. Namely, when a metal wall of a resonant cavity is moved inward, the resonant frequency will decrease if the stored energy is predominantly in the electric field. Otherwise, when the stored energy close to the walls is mostly magnetic, as is the case for the shielded $TE_{01\delta}$ dielectric resonator, the resonant frequency will increase when the wall moves inward.

Current designs allow for up to 0.2% tuning range without significant degradation of other performance parameters. A properly-designed mechanical tuning option will provide a maximum of tuning range while still maintaining hermeticity and reliability, and will not appreciably affect the resonator Q factor (apparent as a degradation in noise and power performance) or temperature stability.

ELECTRONIC TUNING

Some applications, such as FMCW radar sources, narrowband-modulated communication systems or PLL systems, need electronic tuning bandwidths on the order of 0.1% to 1%. These applications require sources with low phase noise, high tuning speed and low tuning power. Electronically tunable DROs (ET-DRO) can now meet the requirements for many such applications.

ET-DROs are also commonly used for analog or digital temperature compensation of the oscillator. This application requires that the frequency tuning range of the DRO exceeds the frequency drift of the oscillator under any combination of operating conditions (temperature, load and bias variations). Various means are used to electrically tune the DRO^[1], including ferrite tuning, optical tuning, and the more popular varactor and bias tuning.

Varactor tuning (a typical scheme is shown in Fig. 13) can provide up to 1% frequency adjustment. To permit varactor tuning, the dielectric resonator is coupled to another microstrip line connected to a varactor, resulting in mutually-coupled resonant circuits. The bias-voltage-dependant capacitance of the varactor varies the resonant frequency of the low-Q resonant circuit with the tuning voltage.

The amount of frequency tuning range can be controlled by varying the coupling between the low-Q microstripline/varactor circuit and the dielectric resonator circuit. Tighter coupling permits greater tuning range, however the attendant degradation in the Q factor manifests itself primarily as an increase in phase noise. Varactor tuning is by far the most common means of incorporating electronic tuning.

Bias voltage tuning takes advantage of the frequency sensitivity to changes in the supply voltage of the oscillating device. By not using an internal voltage regulator, the oscillator can be designed to provide the necessary tuning range by varying the bias voltage, typically within 0.1% of the center frequency. This is sufficient frequency variation to compensate for the frequency drift of the oscillator over load and temperature variations, as well as the long-term drift due to component aging.

Better phase noise performance can be achieved with the bias-tuned DRO than the varactor tuned DRO. The latter requires the dielectric resonator to be simultaneously coupled to two microstrip lines, thus lowering the loaded quality factor of the resonator[9]. However, as the output power is often a function of the supply voltage, care must be exercised to maintain suitable output power variation characteristics for the bias-tuned DRO.

MECHANICAL CONSIDERATIONS

The minimum size of a practical DRO is primarily limited by the cavity required by the particular resonator. Normal design procedure calls for a separation of more than one resonator diameter between the resonator and its surrounding walls in order to properly excite the $TE_{01\delta}$ resonant mode. Also, the separation between the resonator and the housing lid should be more than one resonator thickness to

minimize the effects of the lid on the resonator performance. Too-small a cavity can prevent oscillation in the preferred mode, as well as causing Q-factor degradation^[3].

Hermeticity is an important consideration when defining DRO requirements. Oscillators which are backfilled with a dry inert gas and then welded closed, have less of a tendency to be susceptible to degradation due to long-term environmental effects. Hermetically-sealed oscillators are, of course, much more readily incorporated in a military system with the attendant performance and qualification requirements. Hermetic sealing is normally characterized by the helium leak rate of the DRO enclosure after it has seen a saturated helium environment. Typical leak rates of hermetically-sealed DROs are better than 10^{-7} cc(He)/second.

When a mechanical tuner is required, tuner construction, expected lifetime, over-travel protection and ease of operation are also important considerations. A properly-designed mechanical tuner should provide the desired tuning range, be simple to adjust, have an acceptable number of operations, incorporate stops to limit travel and still maintain case integrity and hermeticity.

LIMITATIONS OF TRANSISTOR DROS

Free-running DROs presently do not have the low phase noise and temperature stabilities required for certain high-performance applications. This limitation necessitates the use of phase locking, injection locking, ovenizing or analog or digital compensation circuits when necessary. Another important limitation of the DRO is the phase noise degradation under vibration due to the variation of the distance between the resonator and the outer shield. Significant deterioration of the phase noise at offsets up to the highest frequency of vibration can be expected under vibration. Ruggedization of the oscillator, injection locking or phase locking are typically used to minimize these effects.

FUTURE TRENDS

The dielectric resonator oscillator technology is developing exceedingly rapidly. Emphasis will continue to develop higher performing DROs. The following aspects are likely to be dealt with in the near future:

- Lower phase noise and higher temperature stability oscillators.
- Reduction in cost and size
- Wider mechanical and electrical tuning bandwidths
- Improvement in DRO performance under vibration
- Development of new materials for dielectric resonators for linear temperature coefficient and higher quality factor.
- Use of higher-order modes in resonators.

REFERENCES:

1. R. Soares, "GaAs MESFET Circuit Design," Artech House, 1988, Chapter 7.
2. D. Kajfez and P. Guillon, Dielectric Resonators, Artech House 1986.
3. A.P.S. Khanna, "Q Measurements of Microstrip Coupled Dielectric Resonators," *Microwaves & RF*, vol. 23, pp. 81-86, January 1984.
4. C. Tsironis and V. Pauker, "Temperature Stabilization of GaAs MESFET Oscillators Using Dielectric Resonators," *IEEE Trans. MTT*, Vol. MTT-31, pp. 312-314, March 1983.
5. J. Lee et al, "Digital and Analog Frequency-Temperature Compensation of Dielectric Resonator Oscillators," *IEEE MTT-S Int. Microwave Symposium Digest.*, pp.277-279, San Francisco, 1984.
6. A.P.S. Khanna and Ed Gane, "A Fast Locking Transmission Injection Locked X-band DRO," *IEEE MTT-S Int. Microwave Symposium Digest*, pp. 601-606, New York, 1988.
7. M. Prigent & J. Obregon, "Phase Noise Reduction in FET Oscillators by Low-Frequency Loading and Feedback Circuitry Optimization," *IEEE Trans. MTT*, Vol. MTT-5, No.3, pp. 349-352, March 1987.
8. Z. Galani et al, "Analysis and Design of a Single-resonator GaAs FET Oscillator with Noise Degeneration," *IEEE Trans. MTT*, Vol. MTT-32, pp. 1556-1565, December 1984.
9. A.P.S. Khanna and E. Topacio, "A Highly-Stable 36 GHz GaAs FET DRO with Phase-Lock Capability," *Microwave Journal*, Vol. 32, pp. 117-122, July 1989.
10. A.P.S. Khanna et al, "Efficient, Low Noise Three Port X-Band FET Oscillator Using Two Dielectric Resonators," *IEEE MTT-S Int. Microwave Symposium Digest.*, pp.277-279, Dallas, 1982

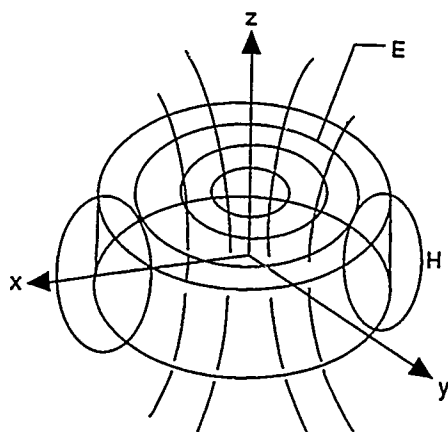


Figure 1. Field Distribution of $TE_{01\delta}$ Mode in a Dielectric Resonator

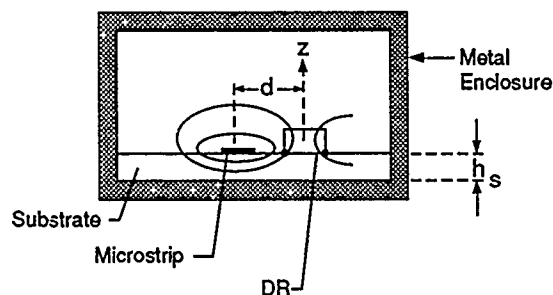


Figure 2. Dielectric Resonator Coupled to a Microstrip Line

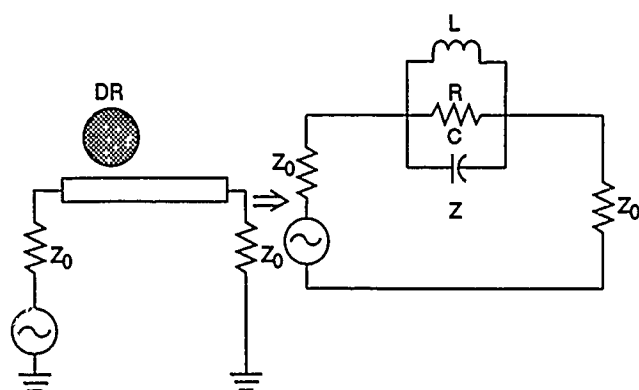


Figure 3. Equivalent Circuit of D.R. Coupled to a Microstrip Line

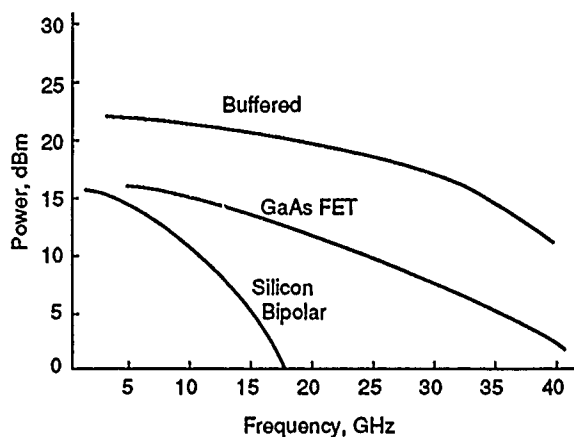


Figure 5. Power vs. Frequency for Transistor DROs

Table 1. Dielectric Resonator Materials

Composition	Dielectric constant	Q	Temperature coefficient of frequency (ppm)	Frequency range (GHz)	Manufacturer
Ba_2TiO_{20}	40	10 000 at 4 GHz	+2	1-100	Bell Labs
$(Zr-Sn)TiO_4$	38	10 000 at 4 GHz	-4 to +10 ^a	1-100	Trans Tech Thomson-CSF Murata
$Ba(0.33Zn0.67Ta)O_2$	30	10 000 at 10 GHz	0-10 ^a	4-100	Murata
$Ba(0.33Mg0.67Ta)O_2$	25	25 000 at 10 GHz	4	4-100	Sumimoto
$BaO-PbO-Nd_2O_3-TiO_2$	88	5000 at 1 GHz	0-6 ^a	<4	Murata-Trans Tech
Al_2O_3	11	50 000 at 10 GHz	0-6 ^a	>18	NTK-Trans Tech

^a Adjustable with composition.

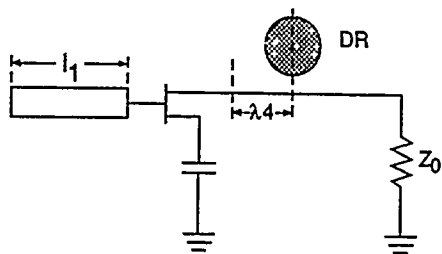


Figure 6. Stabilized GaAs FET DRO

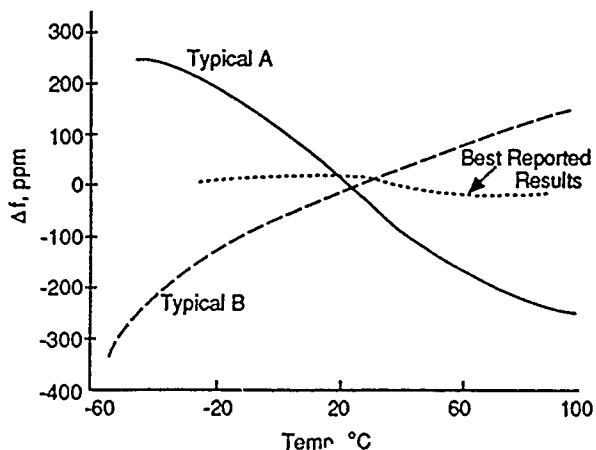
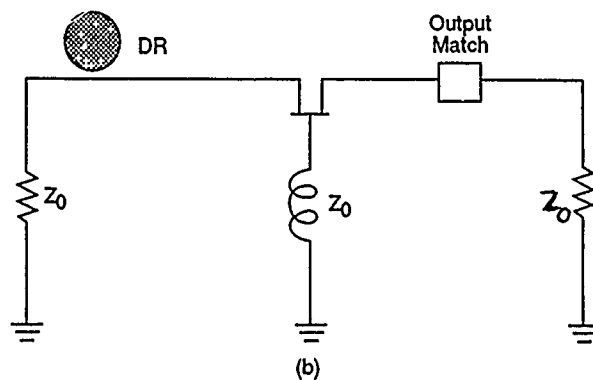
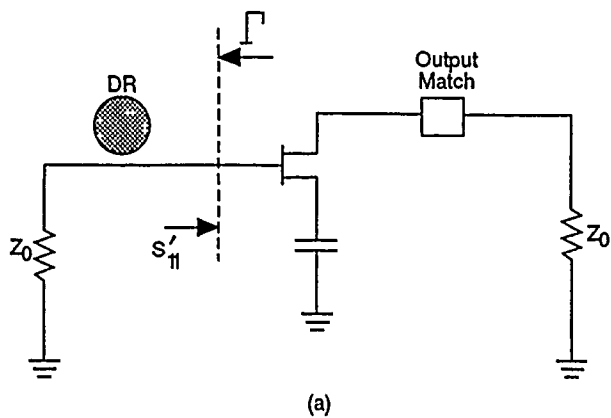


Figure 8. Frequency Drift vs. Temperature for a Free Running 12 GHz GaAs FET DRO

Series Feedback



Parallel Feedback

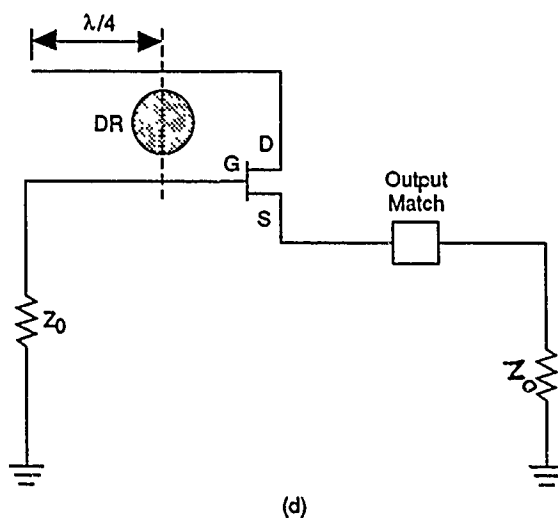
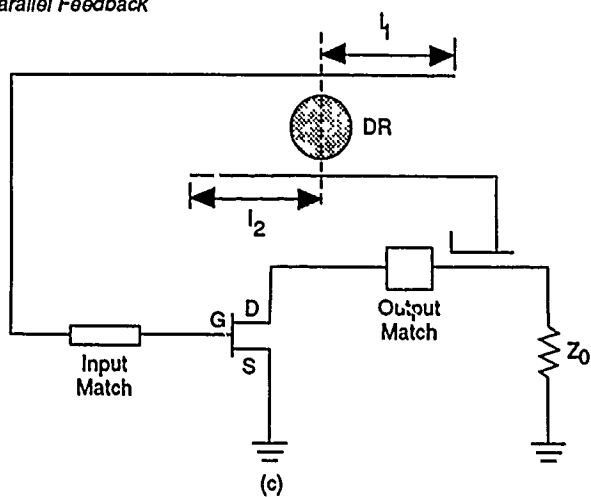


Figure 7. Stable DRO Configurations

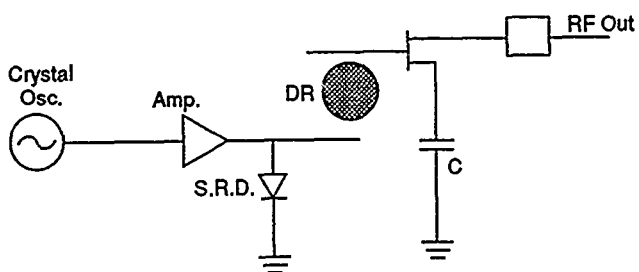


Figure 9a. Injection Locked DRO

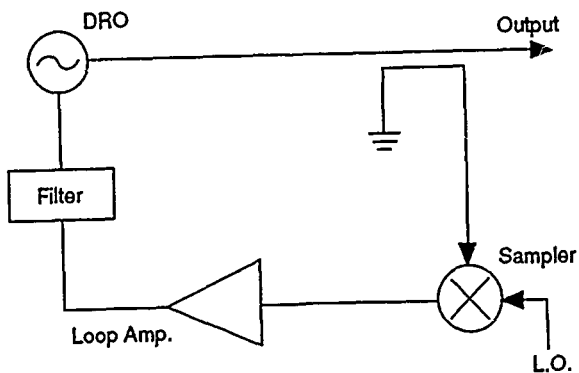


Figure 9b. Phase Locked DRO

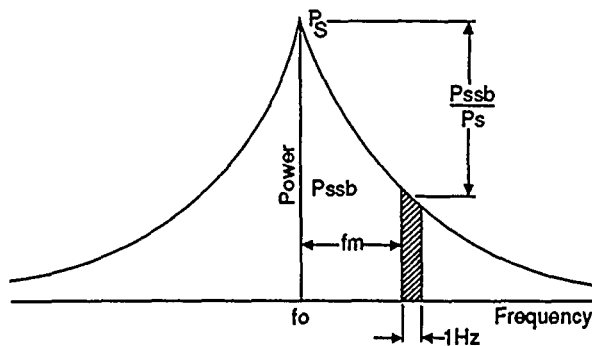


Figure 10. Oscillator Phase Noise

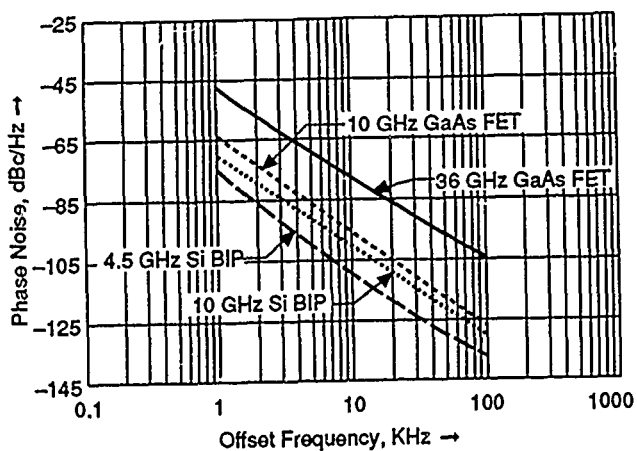


Figure 11. DRO Phase Noise: GaAs FET & Bipolar

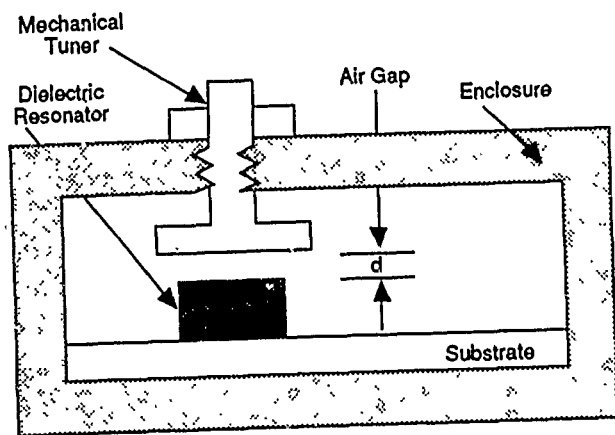


Figure 12. DRO Mechanical Tuning

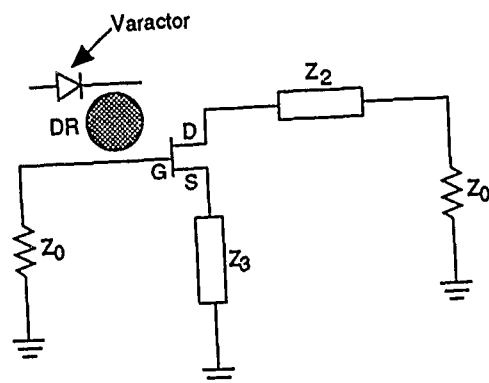


Figure 13. Varactor Tuned DRO

QUESTIONS AND ANSWERS

JACQUES VANIER, NRC: Could you comment on the variation of Q with frequency?

MR. KHANNA: In the dielectric resonator, the $Q \times f$ product tends to be constant.

DETERMINING OPTIMUM C-FIELD SETTINGS THAT MINIMIZE OUTPUT FREQUENCY VARIATIONS IN CESIUM ATOMIC FREQUENCY STANDARDS

S. K. Karuza, W. A. Johnson, J. P. Hurrell, and F. J. Voit
Electronics Research Laboratory
The Aerospace Corporation
El Segundo, CA 90245

Abstract

De Marchi at the National Institute of Standards and Technology (NIST) performed an experiment on Hewlett-Packard cesium (Cs) frequency standards, in which he showed that there exist optimum values of the C-field that make the output frequency insensitive to variations in microwave power. Moreover, and most important, De Marchi demonstrated that the long-term stability of the Cs standard was improved at these optimum values of the C-field.

To see if these results could be obtained with standards made by different manufacturers and having different modulation schemes and Cs tube designs, we performed a similar study using a completely automated measurement system on four Cs standards made by two other manufacturers. Our results, similar to those of De Marchi, showed that there are similar optimum C-field settings in these standards; furthermore, they showed that it may be more important to tune the microwave cavity precisely to the center Cs resonance frequency (f_0) than it is to set the C-field at an optimum value. The best procedure of course is to do both, i.e., to tune the cavity to the Cs resonance frequency as well as set an optimum C-field.

INTRODUCTION

De Marchi has presented experimental evidence^[1,2] on five Hewlett-Packard (HP) model 1650 dual-beam cesium (Cs) frequency standards that confirms that Rabi pulling and cavity pulling are the major transducing effects that turn microwave power variations into frequency changes. It was found that there are C-field values for which the output frequency of the Cs standards is insensitive to changes in microwave power (P).

In Fig. 1 is a plot, calculated from De Marchi's data^[1], of the fractional frequency change for a +1-dB change in microwave power as a function of the Zeeman frequency (f_z), after the Cs beam tube's microwave cavity is carefully tuned by maximizing the Cs beam current. It can be seen that there are four Zeeman frequencies (corresponding to four C-field settings) where the change in frequency will be zero for a change in microwave power of +1 dB. The peak-to-peak change in fractional frequency over the range of C-fields plotted is about 5×10^{-12} . The Zeeman frequency difference between adjacent C-field zero crossings of the Rabi-pulling curve is about 8.9 kHz. The frequency sensitivity at the 39-kHz zero crossing is 0.62×10^{-12} /kHz for a +1-dB microwave power change. De Marchi^[1] showed that

long-term frequency stability was improved by about an order of magnitude if the Zeeman frequency was set at 39 kHz (optimum frequency), rather than at a nonoptimum Zeeman frequency of 53 kHz.

De Marchi stated^[1] that the results he had obtained on the HP Cs standards should be "... at least typical for all Cs standards ...". He cautioned, however, that results obtained on Cs frequency standards that used different servo-loop schemes other than sine wave or slow square-wave frequency modulation might be somewhat different. Consequently, considerable interest developed to determine if the stability of other Cs frequency standards using different modulation schemes could be improved by this technique of optimum C-field setting. Measurements similar to those of De Marchi were made in our own laboratory on four Cs standards, from two different manufacturers, that used single-beam optics and different modulation schemes. Because the measurements are very time-consuming, it was decided to automate them completely in order to maximize the data-taking time available. An additional advantage of this automation is that one never has to make and remake microwave power connections.

MEASUREMENT SYSTEM

The C-field experiment was performed in our laboratory on four Cs frequency standards. These standards were modified to allow access to the C-field coil wires and the microwave power source. Figure 2 shows the block diagram of the complete measurement system. Both of the parameters that are varied, namely the C-field current and the microwave power, are computer controlled; the current is set by a precision constant-current generator and the microwave power is changed by a calibrated PIN diode attenuator. The entire system is controlled by an HP series 300 computer, which also acquires and processes the data.

Figure 3 is a block diagram of the frequency measurement system. The frequency reference for both the Fluke synthesizer and the HP counter is an HP model 5061A-004 Cs frequency standard. Before the data are taken, the microwave cavity of the Cs tube must be tuned. Figure 4 shows the block diagram of the microwave-cavity tuning measurement system, which measures the return loss of the Cs tube's microwave cavity. The microwave tuning is adjusted to obtain a maximum return loss at the resonant frequency (f_0) of 9.192631770 GHz. The microwave power is then adjusted to maximize the output current from the beam tube. The resulting microwave power is called the optimum power (P_0).

A typical data-taking sequence consisted of the following steps:

1. Set the C-field current at some low value (typically 6 to 8 mA) and the microwave power at some value (e.g. at the optimum value P_0).
2. Measure the beat frequency over some long averaging time T (typically 7000 sec).
3. Change the microwave power level (e.g. to $P_0 + 1$ dB).
4. Measure the beat frequency over T again.
5. Increase the C-field current by some programmed amount (typically 0.5 mA).
6. Measure the beat frequency over T again.
7. Change the microwave power back to the initial value.
8. Repeat steps 2 through 7 until the final C-field current (typically 20 to 25 mA) is reached.

MEASUREMENT RESULTS

Figure 5 shows the results of measurements made on the first of four Cs frequency standards after the tube's microwave cavity was tuned to f_0 for changes in the microwave power level of -1, +1, and +3 dB. For the -1-dB data, each point represents the difference between two 7000-sec samples; for the +1-dB data, each point represents the difference between two 14,000-sec samples; and for the +3-dB data, each point represents the difference between two 21,000-sec samples. Each data point is calculated as the difference in output frequency between the frequency at the higher power and the lower power, both of which are normalized to the nominal output. In other words,

$$\text{ordinate} = (\bar{f}_H - \bar{f}_L)/5 \text{ MHz} \quad (1)$$

where \bar{f}_H is the average output frequency for the higher microwave power and \bar{f}_L is the average output frequency for the lower microwave power. As Fig. 5 shows, for the +1-dB and -1-dB data there is a zero crossing at about 26 kHz, but it is difficult to see if there are any other zero crossings. For the +3-dB data it is clear that there are two zero crossings, at about 25 and 37 kHz.

Because De Marchi, using the HP Cs frequency standard, had found multiple zero crossings for a +1-dB power change (Fig. 1), it was decided to spend the time to make a statistically significant measurement on this first Cs frequency standard for the same +1-dB change. Figure 6 shows the results of this measurement, with each data point representing the difference between two long samples (the error bars represent +2 standard deviations). The sample lengths varied from 30,000 to 210,000 sec. These data show distinct zero crossings at about 25 and 37 kHz, in agreement with the earlier results for the larger power change of +3 dB. Thus, by using data for the 3-dB change, it may be possible to shorten greatly the amount of time it takes to determine the location of the 1-dB zero crossing. This could reduce the data-taking time to as few as two or three days.

As Fig. 6 shows, the slope at the 37-kHz zero crossing is $0.11 \times 10^{-12}/\text{kHz}$, compared to the slope of $0.62 \times 10^{-12}/\text{kHz}$ for the HP standard (Fig. 1). Thus, for a given departure from the optimum Zeeman frequency, the frequency of the first Cs frequency standard would be from five to six times less sensitive to power changes than would be that of the HP standard.

The first Cs frequency standard was taken to the National Institute of Standards and Technology (NIST) at Boulder, Colorado, for an evaluation of the standard's long-term frequency stability at C-field settings of Zeeman frequencies of 37 kHz (optimum setting) and 44 kHz (nonoptimum setting). Figure 7 shows the Allan standard deviation of the frequency standard at 44 kHz and Fig. 8 at 37 kHz. From these results we can say only that there was no obvious improvement in the long-term frequency stability for this standard when it was set at an optimum C-field setting.

The second Cs frequency standard was also a single-beam type, with the same type of modulation scheme as the first. It was decided that on this standard we would also measure the effect of the cavity pulling on the C-field curve. The tube cavity's return loss was measured by means of the measurement system shown in Fig. 4. Tuning was accomplished by varying two tuning screws on the microwave transition piece at the input of the Cs tube. The plot of the return loss of the tuner and tube is shown in Fig. 9. Also shown are return losses for a short-circuit reference and a matched termination. The cavity was tuned first to the Cs resonance at f_0 (9.192631770 GHz). Changes in output frequency for changes in microwave power of 3 dB were then measured as a function of the C-field. The cavity was then retuned to 12 MHz above f_0 and the measurements were repeated, after which the cavity was tuned to 12 MHz below f_0 and the measurements were repeated once more. Figure 10 shows the results of the three measurements. This clock is especially interesting because it demonstrated the effect of the cavity pulling. It appears that if the cavity is tuned precisely to f_0 , the Rabi pulling is

minimized and there are no clear multiple zero crossings. Also, the slope of the curves is very small for Zeeman frequencies above about 35 kHz. The maximum frequency change was about 3.2×10^{-12} per +3-dB change in microwave power at a Zeeman frequency of about 42 kHz. For this particular Cs clock we can say that, in order to minimize the frequency sensitivity to microwave power variations it may be just as important to tune the microwave cavity properly, perhaps more important than it is to set the C-field at an optimum value.

The third Cs frequency standard measured used a single-beam tube having a different modulation scheme from the first and second Cs frequency standards that we measured. In this third Cs standard we measured the changes in output frequency for a +1 dB microwave power change above P_0 for the cavity tuned at f_0 as well as 40 MHz above and below f_0 . Figure 11 shows the results of the cavity tuning on the C-field curves. We note here that the maximum frequency offset was about 8×10^{-11} per +1-dB power change at a Zeeman frequency of 27 kHz. It is hard to distinguish the effect of cavity pulling, because the Rabi pulling dominates the frequency offset for the +1-dB microwave power change. In this particular frequency standard, we can see clear zero crossings of the C-field curve at about 24, 47, 68, and 83 kHz. The Zeeman frequency difference between adjacent C-field zero crossings of the Rabi-pulling curve is about 23 kHz. The slope at the 47-kHz zero crossing is 0.53×10^{-11} /kHz for a +1-dB microwave power change. Because of this high slope, the long-term frequency stability should improve if one sets the C-field at a zero crossing of the C-field curve. This slope compares to slopes of 0.62×10^{-12} /kHz and 0.11×10^{-12} /kHz for a 1-dB power change for the HP standard and the first standard we measured (see Figures 1 and 6). We caution, however, that this clock was of a very old design, and thus the results presented here should not be considered as typical of that manufacturer's present product.

The fourth Cs frequency standard was sent to us by one of the manufacturers to determine its C-field characteristics; this was a new off-the-shelf production unit. Measurements were made to determine the effect of microwave cavity tuning on the C-field curve for 20 MHz above and below f_0 , as well as at f_0 , for a +3-dB microwave power change above P_0 . Figure 12 shows the plot of the three C-field curves. For the C-field curve tuned at f_0 , the maximum frequency change was about 3.2×10^{-12} at a Zeeman frequency of 39 kHz per 3-dB microwave power change. There were zero crossings at approximately 30, 64, and 74 kHz. The C-field at f_0 had a shape similar to that found earlier on Cs standard number two. The same conclusion can be drawn for this standard as for the second one. The factor perhaps more important than the actual C-field zero crossing is the cavity tuning. The Rabi pulling is minimal in this particular Cs frequency standard. Also, there is no obvious periodicity in the curve, which is in contrast to that found in the HP Cs standard reported on by De Marchi^[1], or in the third Cs standard that we measured (see Fig. 11) earlier. The cavity pulling dominates the frequency changes in this Cs standard.

INACCURACIES IN THE MEASUREMENT SYSTEM

Our measurement system introduces three sources of error or uncertainty: (1) frequency measurement errors, (2) C-field current setting errors, and (3) power setting errors. The first error (Fig. 6) has been shown to be almost two orders of magnitude below the measurement data. The uncertainty in the C-field current setting is probably on the order of parts in 10^4 in our laboratory environment over the three months during which data were taken; this stability is largely set by the stability of a precision film resistor. The third source of uncertainty, the measurement of the microwave power, is the most difficult of the three to assess. Figure 13 shows the measured power at two levels over 21 days of the C-field measurement time. Over a period of about two weeks, separate stability measurements were

made on the power meter and its sensor. It was found that the noise in the measurement system, as measured by the standard deviation, was more than two orders of magnitude below the noise in the power measurements, as shown in Fig. 13. The data in this figure were analyzed statistically and, in conjunction with the data in Fig. 6, were used to calculate the effects of these power variations on the noise floor of the clock.

Using the power data from both power levels in Fig. 13, we computed the Allan standard deviation of the power as a function of time. We then multiplied this statistic by a power sensitivity coefficient to determine the Allan standard deviation of the frequency that would result from these power changes. The power sensitivity coefficient used was $8 \times 10^{13}/\text{dB}$, which was approximately the largest value measured (see Fig. 6).

Table 1 presents the results of this analysis. Column 3 is the Allan standard deviation of the power for time τ , τ being listed in column 1 with the number of data points being listed in column 2. The resulting Allan standard deviation of the clock's frequency is given in column 4 for an assumed $\sqrt{\tau}$ dependency of $3.55 \times 10^{-11}/\sqrt{\tau}$ and a C-field setting resulting in the sensitivity of an $8 \times 10^{-13}/\text{dB}$.

It was concluded from this analysis of the power data (Fig. 13) that, even if the C-field is not set close to an optimum setting, the effect of microwave power changes on the Allan standard deviations will be small for periods of less than a few days. At 2.5 days, the Allan standard frequency deviation that is due to the beam tube noise is still about twice what could result from power variations. Thus, if the Allan standard deviation of the power stayed about constant, the Allan standard frequency deviation due to the beam tube noise and that due to microwave power variations would be about equal at 10 days. Figure 14 is a plot of the data in Table 1.

CONCLUSIONS

In this paper we have presented experimental results of the C-field experiment of De Marchi on four cesium (Cs) frequency standards from two different manufacturers. The results showed that in some Cs frequency standards, there were unique zero crossings that minimized the variations in output frequency caused by changes in microwave power. In one Cs frequency standard, the long-term frequency stability was measured at one of these zero crossings; however, the data did not clearly show a significant stability improvement as had been previously demonstrated on HP Cs standards. None of the other Cs frequency standards clearly had more than one zero crossing, but they all showed that the cavity tuning was effective in minimizing the output frequency variations that were microwave due to power changes. Therefore, to minimize the effects of microwave power changes on output frequency, one should first carefully tune the microwave cavity to the Cs resonance frequency and then set the C-field to a minimum or zero crossing of the C-field tuning curve.

ACKNOWLEDGMENTS

The authors are grateful to David W. Allan and Andrea De Marchi of the National Institute of Standards and Technology, and to Ronald L. Beard and Frederick Danzy of the Naval Research Laboratory, for their helpful and stimulating discussions and assistance in supplying some of the hardware and long-term frequency-stability measurements.

This work was supported, in part, by the U.S. Air Force Space Systems Division under Contract No. FO4701-88-C-0089.

REFERENCES

1. A. De Marchi, "New Insights into Causes and Cures of Frequency Instabilities (Drift and Long-Term Noise) in Cesium Beam Frequency Standards," Proc. 41st Frequency Control Symposium, Philadelphia, Pa. (1987), pp. 54-58.
2. A. De Marchi, "Rabi Pulling and Long-Term Stability in Cesium Beam Frequency Standards," IEEE Trans. Ultrasonics, Ferroelectronics, and Frequency Control UFFC-34 [6], 598-601 (November 1987).

Table 1. Measurement Data

Power Data			Frequency Data	
Time (τ), days	No. of Points	Allan Std. Dev. $[\sigma_p(\tau)],$ dBm	Allan Std. Dev. $[\sigma_y(\tau) \equiv \sigma_p(\tau) \times 8 \times 10^{-13}]$	$\frac{3.55 \times 10^{-11}}{\sqrt{\tau}}$
0.14	128	0.04390	0.3512×10^{-13}	3.228×10^{-13}
0.41	64	0.05794	0.4635×10^{-13}	1.886×10^{-13}
0.82	26	0.03719	0.2975×10^{-13}	1.334×10^{-13}
2.5	12	0.04807	0.3846×10^{-13}	0.7638×10^{-13}

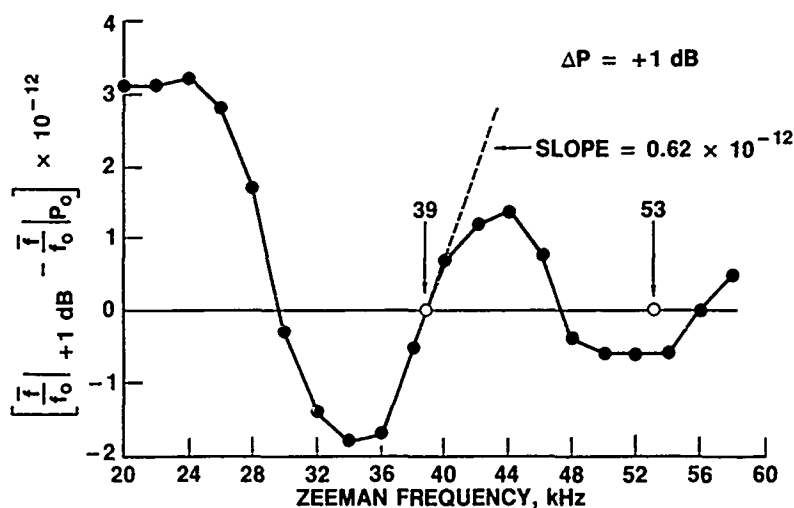


Fig. 1. The Difference in the Average Frequencies for Two Power Levels (P_0 and $P_0 + 1$ dB) as a Function of C-Field in an HP 1653 Cs Frequency Standard.

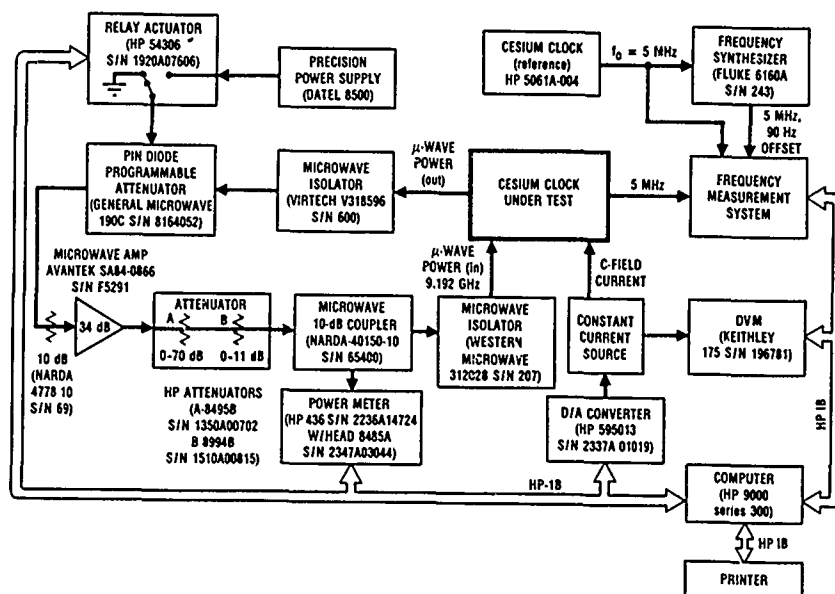


Fig. 2. Block Diagram of the C-Field Measurement System for a Cs Frequency Standard.

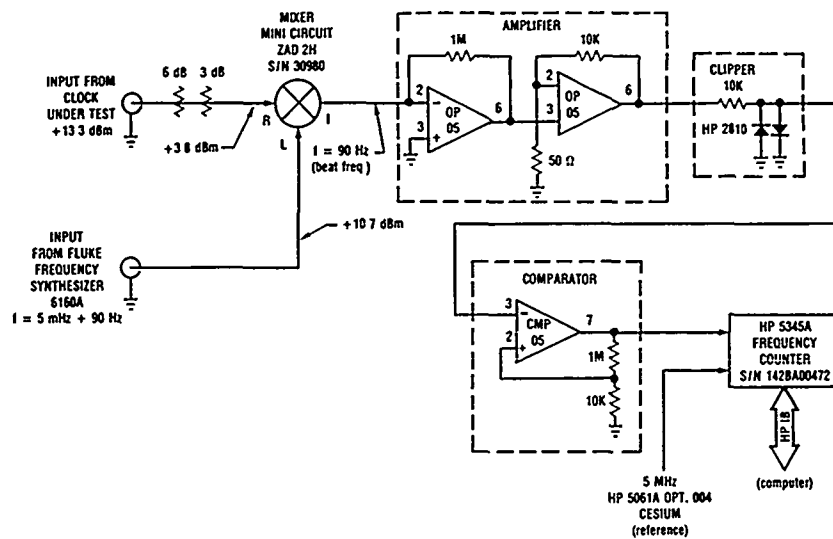


Fig. 3. Circuit Diagram of the Single-Mixer Frequency Measurement System Used to Determine the Fractional Frequency Changes at Different C-Field Settings.

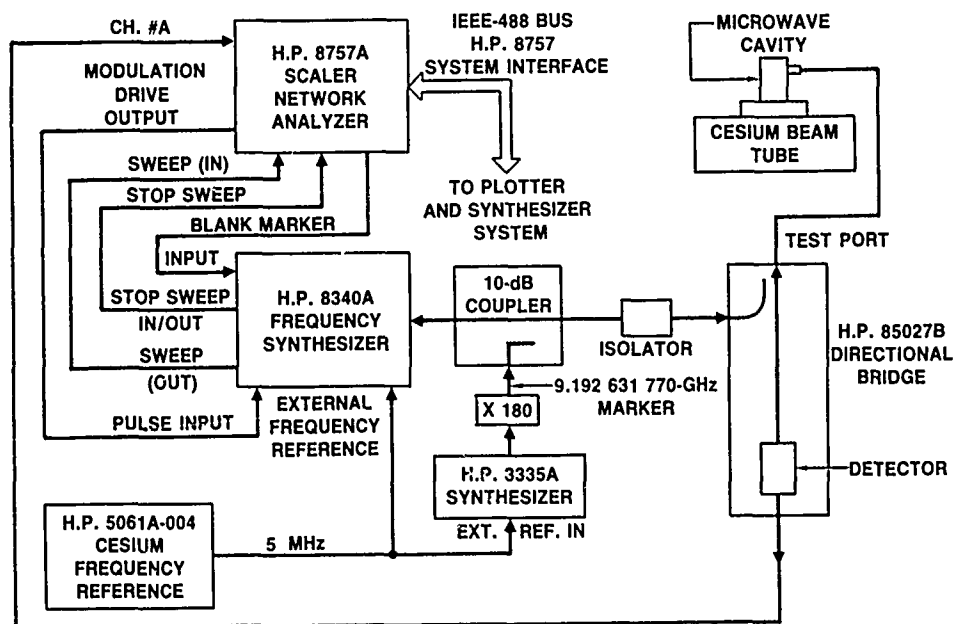


Fig. 4. Block Diagram of the Cs Beam Tube Microwave Cavity Measurement System.

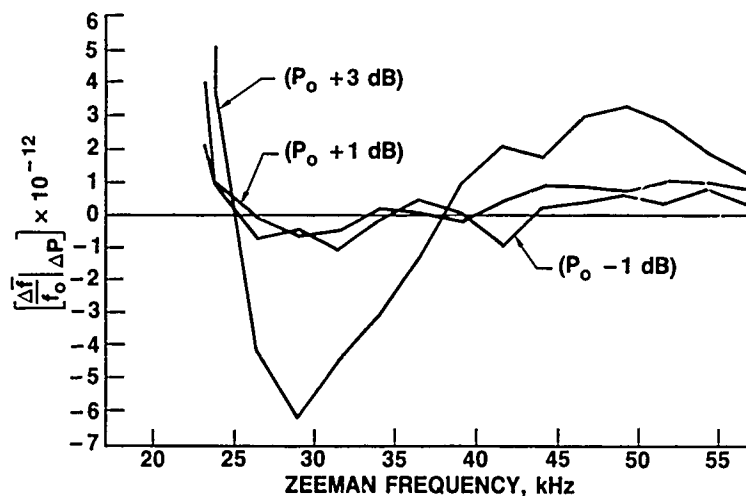


Fig. 5. A Plot of the Difference of the Average Frequencies as a Function of the C-Field of the First Cs Frequency Standard for Three Microwave Power Changes (-1, +1, and +3 dB) with Respect to the Optimum Power Level P_0 .

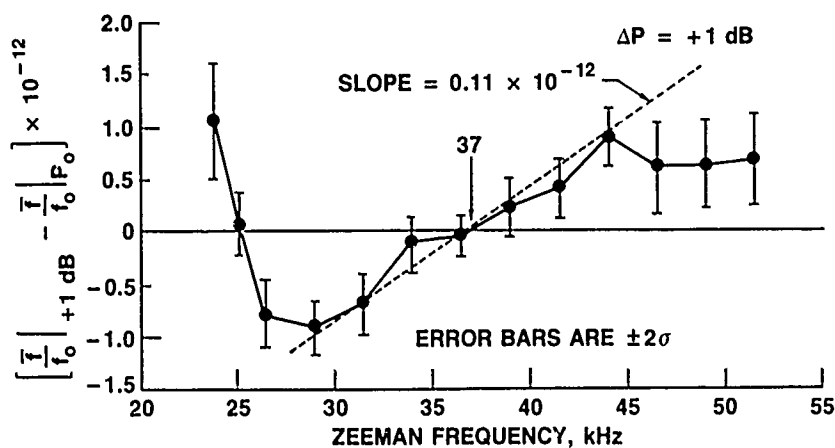


Fig. 6. Average of Final Data of the First Cs Frequency Standard on the Difference of the Average Frequencies as a Function of C-Field for a Microwave Power Change of +1 dB above the Optimum Power level P_0 .

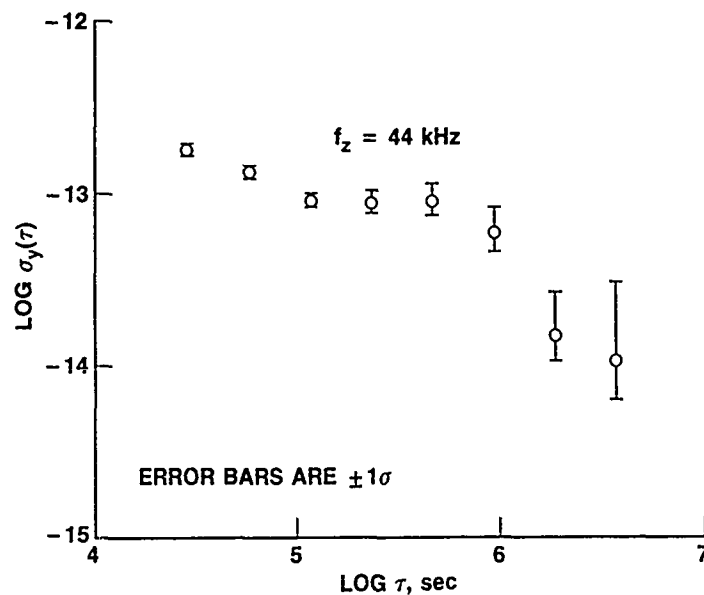


Fig. 7. The Measured Allan Standard Deviation of the First Cs Frequency Standard at the Nonoptimum (Power-Sensitive) Zeeman Frequency Setting of 44 kHz. The confidence intervals are 95%. (Data taken by NIST.)

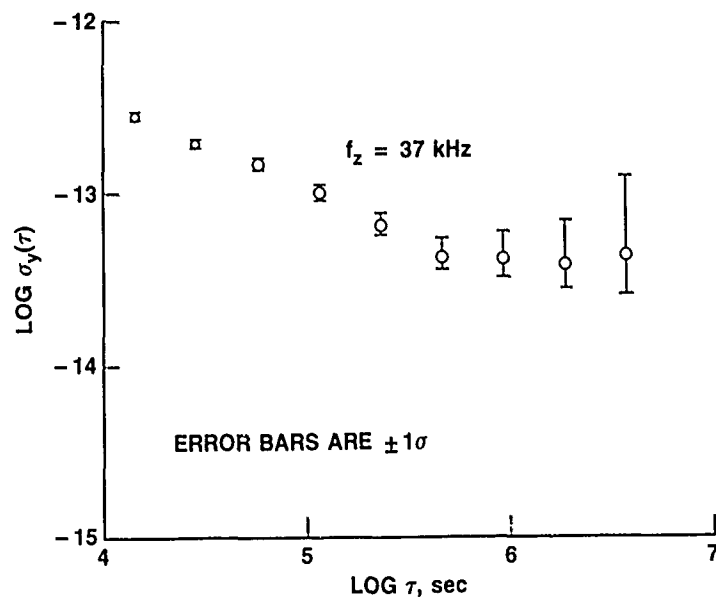


Fig. 8. The Measured Allan Standard Deviation of the First Cs Frequency Standard at the Optimum (Power-Insensitive) Zeeman Frequency Setting of 37 kHz. The confidence intervals are 95%. (Data taken by NIST.)

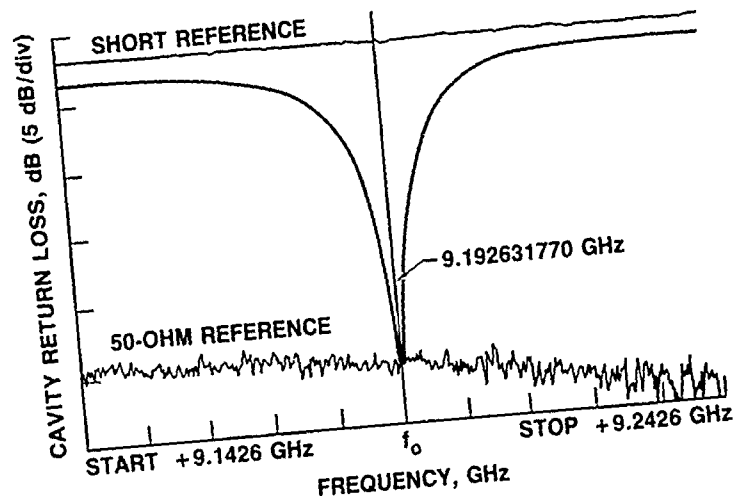


Fig. 9. Plot of the Microwave Cavity Return Loss of the Second Cs Frequency Standard Tuned to a Cs Resonance Frequency.

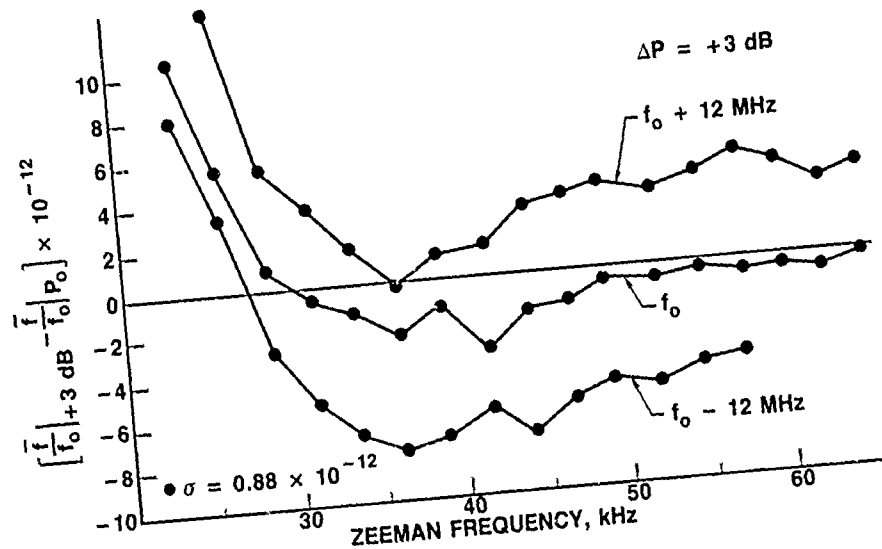


Fig. 10. A Plot of the Difference of the Average Frequencies as a Function of the C-Field of the Second Cs Frequency Standard for Three Microwave-Cavity Tuned Frequencies (f_0 and ± 12 MHz) for a Microwave Power Change of +3 dB above the Optimum Power Level P_0 .

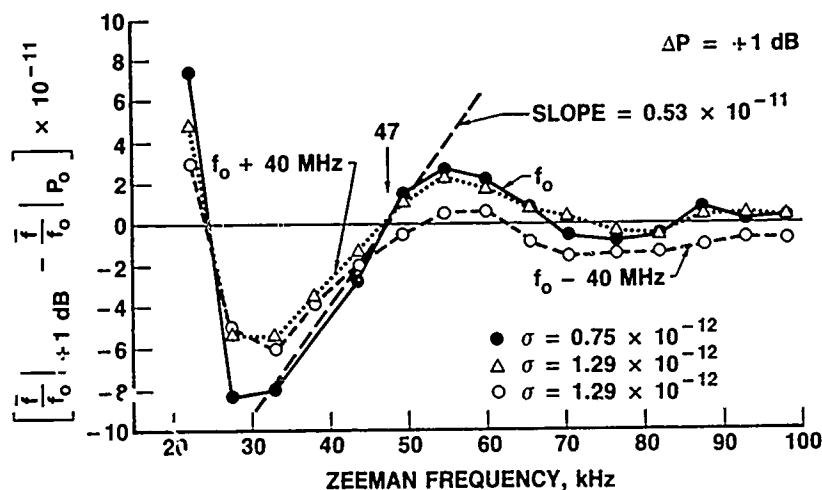


Fig. 11. A Plot of the Difference of the Average Frequencies as a Function of the C-Field of the Third Cs Frequency Standard for Three Microwave-Cavity Tuned Frequencies (f_0 and $\pm 40 \text{ MHz}$) for a Microwave Power Change of $+1 \text{ dB}$ above the Optimum Power Level P_0 .

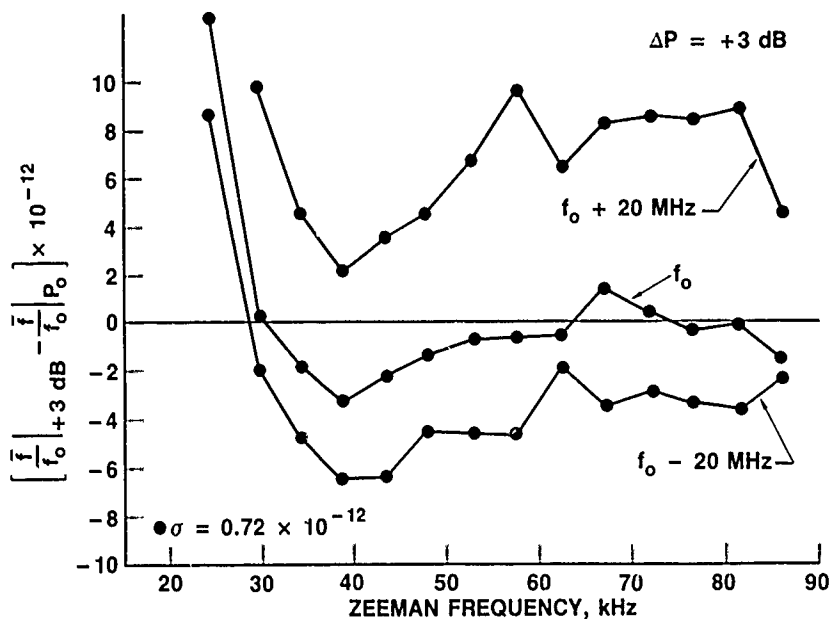


Fig. 12. A Plot of the Difference of the Average Frequencies as a Function of the C-Field of the Fourth Cs Frequency Standard for Three Microwave-Cavity Tuned Frequencies (f_0 and $\pm 20 \text{ MHz}$) for a Microwave Power Change of $+3 \text{ dB}$ above the Optimum Power Level P_0 .

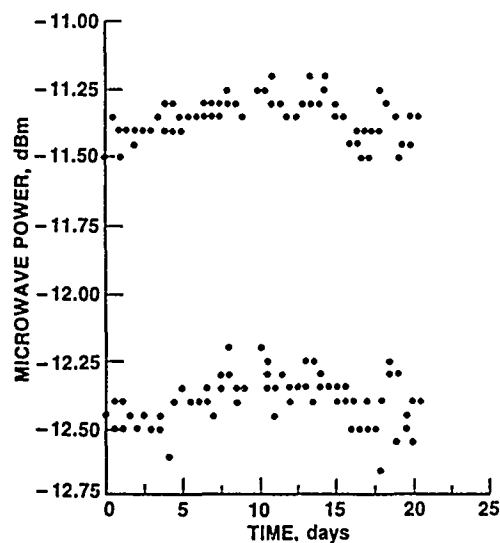


Fig. 13. A Plot of Power Measurements Made during the C-Field Experiment. Power was switched between the two nominal levels of -11.35 and -12.35 dBm approximately every 0.4 days.

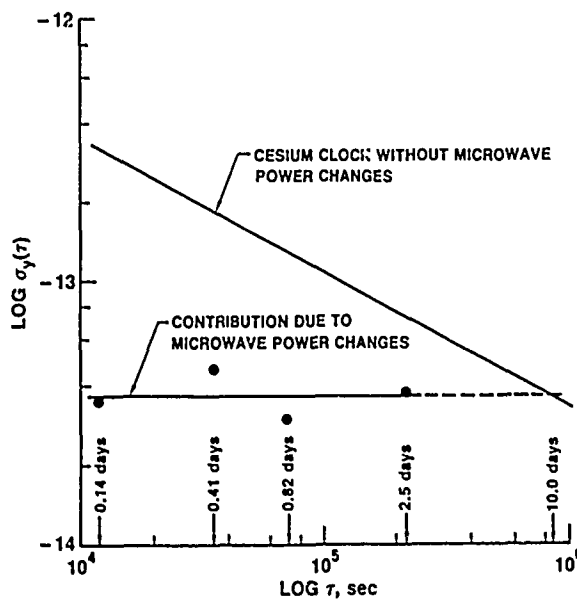


Fig. 14. A Plot of the Calculated Contribution of Microwave Power Changes to the Allan Standard Deviation for Cesium Clock No. 1.

QUESTIONS AND ANSWERS

GERNOT WINKLER, USNO: When you tune the cavity, how did you make sure that the phase difference stayed constant between the two cavities?

MR. KARUZA: We tuned it for the best match, we didn't do anything with the phase.

LEN CUTLER, HP: The tuning pretty much has to be done externally. In the usual U-type Ramsey cavity the phase shift end-to-end is not affected by the tuning.

MODELING FAST MODULATION EFFECTS IN CESIUM ATOMIC CLOCKS

J. P. Hurrell, W. A. Johnson, S. K. Karuza, and F. J. Voit
Electronics Research Laboratory
The Aerospace Corporation
P.O. Box 92957
Los Angeles, CA 90009

Abstract

A theory for fast modulation effects in cesium frequency standards has been developed and expressions derived for frequency offsets produced by Rabi and cavity pulling with square-wave phase modulation. These are compared with equivalent expressions for sine-wave phase modulation. Ratios of the amplitudes of the frequency offsets in the two modulation schemes are calculated for a mono-velocity beam and shown to be in agreement with measurements performed on a commercial standard. This analysis allows a more complete evaluation and comparison of different modulation schemes for cesium atomic beam standards.

INTRODUCTION

A number of different modulation schemes are used to implement the servo loop in cesium atomic clocks. They include sine-wave phase (frequency) modulation, square-wave phase modulation and square-wave frequency modulation. The choice of modulation scheme is based on a number of considerations, e.g., ease of implementation, optimization of cesium flux usage and Allan variance, minimized frequency offsets. Analysis of servo loop gain has been performed for all these schemes and expressions exist to model the gain dependence upon loop parameters. However, the analysis of the effects of modulation scheme on accuracy and long term stability are less complete. Sine-wave and square-wave frequency modulation effects have been considered^[1] within the context of slow modulation^[2], but fast modulation transients have not been modeled because of the lack of an atomic description of those atoms that experience the step change in microwave phase or frequency. A theory for square-wave phase modulation is outlined in this paper.

In the analysis of servo loop gain, it can be assumed that the cesium atoms experience a constant microwave frequency and the effects of phase modulation only perturb the relative phase of the precessing atoms and the microwave field in the second arm of the Ramsey cavity^[3]. In particular, the transient effects in square-wave phase modulation can be safely omitted, and the contribution neglected from those atoms which experience the step change in phase during their resonant interaction with the microwave field. The error incurred in the calculation of servo gain slope is only of order $\omega_m \tau$ where τ is the interaction time and ω_m is the modulation frequency. Similarly, by neglecting the frequency variation of the microwave field, small errors of order $\Delta\omega \tau$ are incurred in the frequency modulation calculations. $\pm\Delta\omega$ represents the depth of frequency modulation.

Spurious servo signals are introduced by neighboring transitions (Rabi pulling) and cavity mistuning (cavity pulling) and affect the performance of cesium frequency standards. Differences in the velocity

distributions of $|+m\rangle$ and $|-m\rangle$ have the potential to generate a frequency offset by causing a sloping background to the $|0\rangle \rightarrow |0\rangle$ transition. Both σ -transitions ($\Delta m = 0$) and weak π -transitions ($\Delta m = \pm 1$) may contribute to this background. Since the background and the servo gain slope have different microwave power dependencies, the resulting offset provides a means for transforming power changes to frequency changes^[4]. Cavity pulling can render cesium clocks sensitive to both microwave power level and temperature changes. Both offsets are mediated by exactly those contributions which could be safely neglected above.

Apart from transient effects in frequency modulation schemes, the unwanted signals can be calculated by allowing the atoms to experience a constant microwave frequency during resonance, but one that changes in time before succeeding atoms arrive. This preserves the conditions for standard microwave resonance. The transient conditions, on the other hand, require a different description. This paper describes an approach to include the transient contributions to both Rabi and cavity pulling. The results comparing sine-wave and square-wave phase modulation offsets are compared with experiments performed on a commercial frequency standard.

RABI PULLING

First order time-dependent perturbation theory is used to calculate the background signal resulting from transitions which are far off-resonance. This approach can be easily applied to any modulation scheme because it allows the phase modulation to be addressed by Fourier decomposition. Writing

$$\langle F=4, m | \mathcal{H} | F=3, m' \rangle = \sum_n 2\hbar c_n \cos(\omega t + n\omega_m t + \theta_n) \quad (1)$$

for a particular $|m\rangle \rightarrow |m'\rangle$ transition leads to a general first order transition probability, W , for a single velocity given by

$$W = \sum_n \sum_m c_n c_m \left\{ \frac{\sin(\Delta + n\omega_m/2)\tau \sin(\Delta + m\omega_m/2)\tau}{(\Delta + n\omega_m/2)(\Delta + m\omega_m/2)} \right\} \\ \times \left\{ \cos[(m-n)\omega_m(t - T(1 + D/L)) + \theta_m - \theta_n] + \cos[(m-n)\omega_m(t - TD/L) + \theta_m - \theta_n] \right\}. \quad (2)$$

The notation follows [2] where 2Δ represents how far the microwave frequency is above resonance, τ is the transit time through one arm of the Ramsey cavity, T is the transit time between arms distance L apart, and D is the detector distance from the second arm. Velocity averaging has been presumed in order to average to zero the interference term between interaction regions (there are no Ramsey oscillations in the wings of a transition!). The $\sin x/x$ terms arise from assuming perfect square-wave amplitude variation of the microwave field on passing through a cavity arm^[4]. The expression can be simplified by linearizing these terms with respect to frequency over the small n, m values of interest. Then it can be applied to a particular modulation scheme to predict the fundamental Fourier signal component appropriate to narrow-band amplification and detection.

a) Sine-wave modulation: $\omega(t) = \omega + \Delta\omega \cos\omega_m t$ with $C_n = cJ_n(\frac{\Delta\omega}{\omega_m})$ and $\theta_n = 0$,

$$W \rightarrow \frac{\Delta\omega}{2} \frac{\partial}{\partial \Delta} \left\{ \frac{c^2 \sin^2 \Delta \tau}{\Delta^2} \right\} \left\{ \cos\omega_m [t - T(1 + D/L)] + \cos\omega_m [t - TD/L] \right\}. \quad (3)$$

This result has been derived previously by De Marchi^[4].

- b) Square-wave modulation: $\cos[\omega t + \theta(t)]$, with $\theta(t)$ alternating between 0 and θ at frequency ω_m and for which

$$c_0 = c \cos \theta/2, \theta_0 = \theta/2; C_n = (2c/n\pi) \sin \theta/2, \theta_n = \theta/2 \quad \text{for } n \text{ odd.}$$

Only terms with $n = 0, \pm 1$ contribute and

$$W \rightarrow \left(\frac{\omega_m \sin \theta}{\pi} \right) \frac{\partial}{\partial \Delta} \left\{ \frac{c^2 \sin^2 \Delta \tau}{\Delta^2} \right\} \left\{ \cos \omega_m [t - T(1 + D/L)] + \cos \omega_m [t - D/L] \right\}. \quad (4)$$

$\Delta\omega$ times the phase factors in Eq.(3) may be interpreted as the instantaneous frequency in the two arms of the Ramsey cavity. $(2\omega_m/\pi)$ times the similar phase factors in Eq.(4) are the Fourier components of delta function responses from atoms residing in the two interaction regions at the time when the step changes in phase occur. These expressions for W have to be averaged over velocity distributions and summed over separate $|m \rightarrow m' >$ transitions to complete the calculation.

These signals are nullified by a servo loop error signal, with the resulting offset determined by the servo gain slope. The gain slopes are determined for the usual mono-velocity expressions^[3] which must also be separately averaged over the velocity distribution for the $|0 \rightarrow 0 >$ transition. All the averaging procedures have been suppressed for the sake of clarity in the following expressions. The procedures have been discussed elsewhere^[1].

$$(\omega - \omega_c)_s = \frac{\left(\frac{\Delta\omega}{\partial \Delta} \right) \left\{ \frac{c^2 \sin^2 \Delta \tau}{\Delta^2} \right\} \cos \omega_m T/2 \cos \omega_m [t - T(1/2 + D/L)]}{T \sin^2 2cr J_1(\beta) \cos \omega_m [t - T(1/2 + D/L)]} \quad (5)$$

$$\text{with } \beta = 2 \left(\frac{\Delta\omega}{\omega_m} \right) \sin \omega_m T/2.$$

$$(\omega - \omega_c)_{sq} = \frac{\left(\frac{2\omega_m \sin \theta}{\pi} \right) \frac{\partial}{\partial \Delta} \left\{ \frac{c^2 \sin^2 \Delta \tau}{\Delta^2} \right\} \cos \omega_m T/2 \cos \omega_m [t - T(1/2 - D/L)]}{T \left(\frac{2 \sin \theta}{\pi} \right) \sin^2 2cr \sin \omega_m T/2 \cos \omega_m [t - T(1/2 + D/L)]} \quad (6)$$

In the limit of small modulation index, $\Delta\omega \rightarrow 0$ and $(\omega - \omega_c)_s = (\omega - \omega_c)_{sq}$. At finite values for $\Delta\omega$, $(\omega - \omega_c)_s > (\omega - \omega_c)_{sq}$. Exact values for this inequality will depend upon the velocity averages and the specific values chosen for servo parameters. However, the magnitudes of the offsets will remain very similar.

The perturbation expansion developed for W is in powers of (c/Δ) . The ratio of second order to first order terms is $(c/\Delta)^2$. Noting that $c \approx 2.5$ kHz and $\Delta \approx 20$ kHz, it is apparent that the series is rapidly convergent.

CAVITY PULLING

Cavity pulling is caused by the asymmetry of the microwave spectrum about its unperturbed frequency, induced by a difference between that frequency and the cavity resonant frequency. The fact that square-wave phase modulation leaves the frequency unchanged except during the step changes in phase leads to a natural modeling approach in which the atomic resonance is treated exactly before and after the step change, while the transition itself is treated by perturbation theory. Only those atoms residing in the separate arms of the Ramsey cavity at the time of the step changes are affected.

If the transition occurs infinitely fast, i.e. in a time short compared to the precession period of the atoms in the microwave field, the sudden approximation can be invoked to predict that the transient itself will not induce any atomic response. Of course, the step change in phase will result in a servo signal from those atoms, which will merely be added to the usual servo signal arising from the greater number of atoms in flight between the two arms of the cavity. However, the finite bandwidth of the microwave cavity prevents infinitely fast changes in phase from occurring and causes a breakdown of the sudden approximation. Now the transient frequency changes are finite. Moreover, the positive and negative frequency transients remain symmetric only if the microwave frequency is located at cavity resonance. It is this asymmetry which records the cavity offset and induces a cesium beam signal at the modulation frequency. This signal is derived from fast responses at the beginning and end of each half-cycle of the servo error signal and may be written as

$$- \left(\frac{2 \sin \theta}{\pi} \right) \left(\frac{8Q_L^2 \omega_m}{\omega_0} \right) \sin^2 2c\tau \left\{ (2c\tau)/\tan(2c\tau) \right\} \cos \omega_m T/2 \cos \omega_m [t - T(1/2 + D/L)] \left(\frac{\omega - \omega_0}{\omega_0} \right). \quad (7)$$

When this is combined as before with the servo gain slope, the offset $(\omega - \omega_c)$ can be calculated. For a mono-velocity beam, it reduces to

$$\left(\frac{\omega - \omega_0}{\omega_0} \right)_{sq} = \frac{-8Q_L^2 \omega_m}{\omega_0^2 T} \frac{\cos \omega_m T/2}{\sin \omega_m T/2} \left\{ (2c\tau)/\tan(2c\tau) \right\} \left(\frac{\omega - \omega_0}{\omega_0} \right) \quad (8)$$

The similar result for sine-wave modulation^[1] may be written

$$\left(\frac{\omega - \omega_c}{\omega_0} \right)_s = \frac{-4Q_L^2 \Delta\omega}{\omega_0^2 T} \frac{\cos \omega_m T/2}{J_1(\beta)} \left\{ 1 + J_0(\beta) - J_2(\beta) \right\} \left\{ (2c\tau)/\tan(2c\tau) \right\} \left(\frac{\omega - \omega_0}{\omega_0} \right) \quad (9)$$

In the limit $\Delta\omega \rightarrow 0$, the two expressions become equal, and cavity pulling effects are the same for sine-wave and square-wave modulation. The sine-wave frequency offset is reduced as $\Delta\omega$ increases from zero.

EXPERIMENTAL RESULTS

Sine-wave and square-wave modulation were compared by measuring the frequency of an atomic standard for both modulation schemes, under as identical conditions as possible. This allows the differences in modulation schemes to become apparent but does not attempt to optimize performance. The square-wave modulation depth θ was held close to 90 degrees and the modulator drive signal was passed through a narrow band, unity gain filter and phase shifter to generate the sine-wave modulation. This produced a modulation index $(\Delta\omega/\omega_m)$ of unity and allowed phase adjustment to maximize the signal. The modulation frequency was close to maximizing the gain slope of the servo loop with $\omega_m T \approx \pi$ and $\beta \approx 2$.

Rabi pulling was separately identified by measuring the frequency as a function of C-field at two microwave power levels; the optimum power maximized the average beam current, and the higher power was 3 dB above optimum. Figure 1 shows the resulting fractional change in frequency with power level for both modulation schemes. Cavity pulling was determined by measuring the frequency for cavity tuning on resonance and ± 12 MHz off-resonance. In the data reduction, it was assumed that the Rabi pulling was independent of cavity tuning, and the cavity pulling was independent of C-field. Three cavity settings, two power levels and two modulation schemes lead to a total of twelve curves of frequency versus C-field. The Rabi pulling could be reduced to a single curve at optimum power by the following relationships:

$$(\omega - \omega_c)_{sq} = 0.94(\omega - \omega_c)_s \text{ for both power levels,} \quad (10)$$

$$\text{and } (\omega - \omega_c)(P + 3\text{dB}) = 1.85(\omega - \omega_c)(P) \text{ for both modulation schemes.} \quad (11)$$

This curve is shown in Fig.2 and illustrates that Rabi pulling effects are small in this standard. Zero frequency offset may be arbitrarily chosen for the highest C-field, but is truly zero only at even higher fields. The ratio 0.94 between square-wave and sine-wave amplitudes is closer to 1 than predicted from Eqs.(5) and (6). In the absence of velocity averaging, this ratio is predicted to be $J_1(2) = 0.58$. Also, the ratio between high power and optimum power is predicted to be 2.5, slightly higher than the measured value of 1.85. It is reasonable to anticipate that velocity averaging will improve the agreement between theory and experiment. The approximately linear dependence on power arises because the off-resonance transition probabilities increase linearly with power, whereas the resonant transitions are already optimized.

Table I lists the measured offset frequencies versus cavity tuning. Systematic errors of unknown origin exceed the standard deviation (2×10^{-13}) in the frequency measurements. Zero offset was arbitrarily chosen to be that for the sine-wave modulation case at optimum power and cavity tuned on resonance. Eqs.(8) and (9) would predict a mono-velocity offset ratio

$$\frac{(\omega - \omega_c)_{sq}}{(\omega - \omega_c)_s} = \frac{2J_1(2)}{1 + J_0(2) - J_2(2)} = 1.32 \quad (12)$$

The measured ratio, obtained by taking the difference of the offsets at $\pm 12\text{MHz}$, is 1.3 at both power levels. The power dependence of the offsets is contained in the usual expression $(2cr)/\tan(2cr)$ which is zero for $4cr = \pi$ and rises to -1.7 as the power is raised 3 dB. Clearly, the optimum power did not produce zero cavity pulling, but the increase by a factor 2.7 on raising the power 3 dB would imply that the nominal power was within 1.6 dB of that necessary for zero offset.

CONCLUSIONS

Our measurements show that sine-wave and square-wave phase modulation yield similar values for Rabi and cavity pulling effects in cesium frequency standards. The result is consistent with the theory presented in this paper. It predicts that, in the limit of small frequency modulation depth, sine-wave modulation produces the same frequency offsets as square-wave modulation. At higher modulation depth, however, Rabi pulling tends to be larger and cavity pulling smaller for the sine-wave modulation scheme. Exact predictions will require knowledge of specific servo parameters and averaging over beam velocities.

ACKNOWLEDGEMENT

This work was supported by the U. S. Air Force under contract FO4701-88-C-0089.

REFERENCES

1. A. De Marchi, G. D. Rovera, and A. Premoli, IEEE Trans. on Ultrasonics, Ferroelectrics, and Frequency Control, UFFC-34,582 (1987).
2. J. H. Shirley, J. Appl. Phys. 34, 789 (1963).
3. C. Audoin, V. Candelier, and J. Vanier, IEEE Trans. on Ultrasonics, Ferroelectrics, and Frequency Control, UFFC-34,573 (1987).
4. A De Marchi, G. D. Rovera, and A. Premoli, Metrologia 20, 37 (1984).

TABLE I.				
Fractional frequency offsets (parts in 10^{12}) determined from measurements at two microwave power levels for both sine-wave and square-wave modulation. The cavity was tuned to the cesium frequency F_0 and to $F_0 \pm 12$ MHz. The cavity pulling is normalized to the frequency for sine-wave modulation at optimum power (maximum dc signal) and cavity tuned to F_0 . Standard deviation = 3×10^{-13} .				
		$F_0 + 12$ MHz	F_0	$F_0 - 12$ MHz
optimum power	sine-wave	-0.9	0	3.6
	square-wave	-3.6	-1.2	2.2
optimum + 3dB	sine-wave	-3.6	-0.2	8.5
	square-wave	-8.2	-1.0	6.9

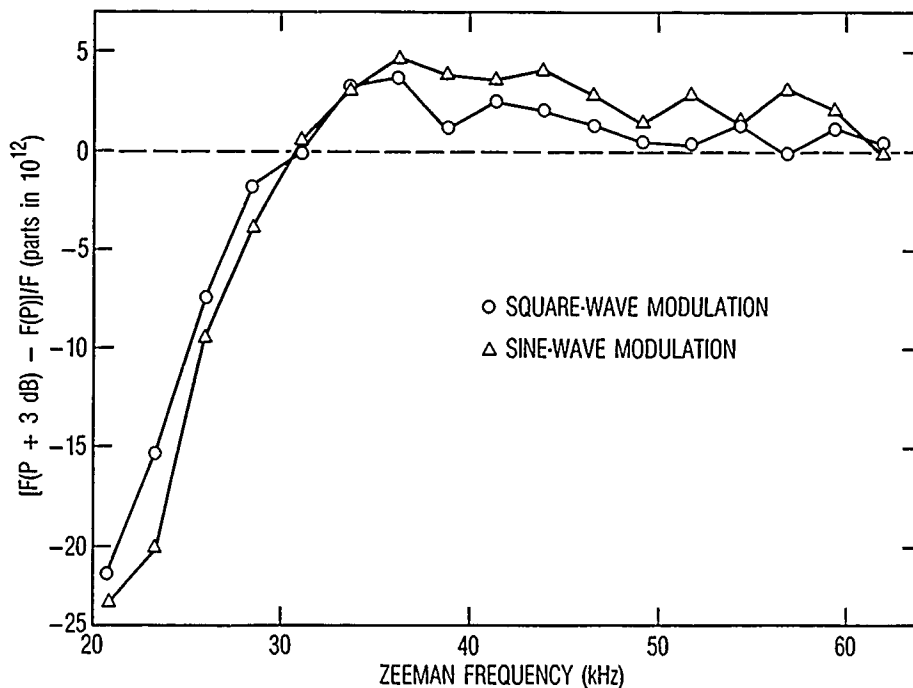


Figure 1. C-field dependence of the fractional change in frequency caused by a 3 dB increase in microwave power above optimum (maximum dc signal) for sine-wave and square-wave phase modulation.

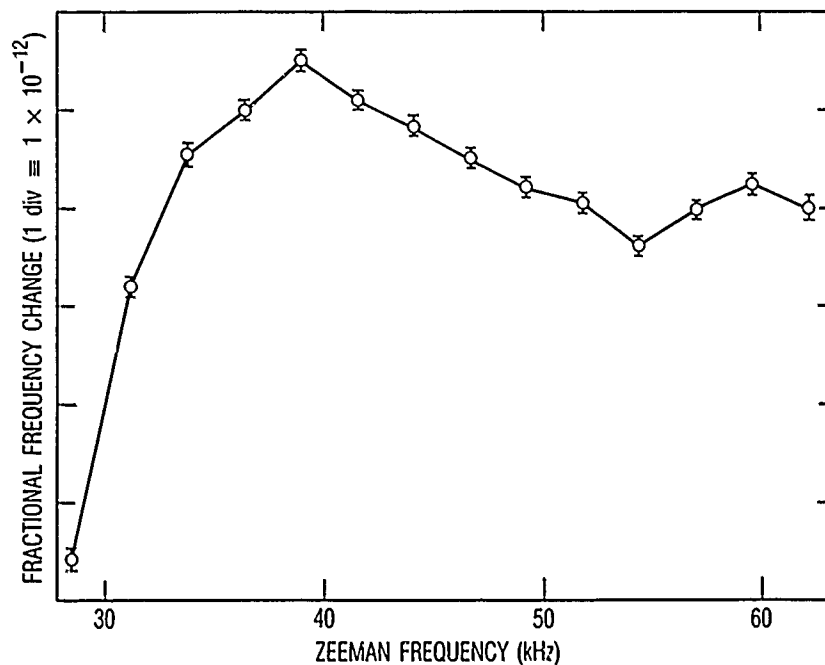


Figure 2. C-field dependence of Rabi pulling measured on a cesium frequency standard with sine-wave modulation. Rabi pulling is assumed to be those changes in frequency which depend upon C-field.

ENVIRONMENTAL TESTS OF CESIUM BEAM FREQUENCY STANDARDS AT THE FREQUENCY STANDARDS LABORATORY OF THE JET PROPULSION LABORATORY*

Richard L. Sydnor, Thomas K. Tucker,
Charles A. Greenhall, William A. Diener, and Lute Maleki
California Institute of Technology
Jet Propulsion Laboratory
4800 Oak Grove Drive
Pasadena, California 91109

Abstract

Tests of the effect of various environmental parameters on HP 5061B, option 004, cesium beam frequency standards have been made at the test facilities of the Frequency Standards Laboratory at JPL. These standards were on loan from the United States Naval Observatory for these tests as a part of a larger cooperative program of testing and adjustment of cesium beam frequency standards between the United States Naval Observatory, National Institute of Standards and Technology, Jet Propulsion Laboratory and the University of Ancona. The environmental parameters of interest include humidity, ambient pressure and temperature. Marked sensitivity to humidity was found in all the standards, but the sign of frequency change vs relative humidity was not the same in all standards. The results of all the tests will be given and plans for future work under this program will be discussed.

INTRODUCTION

Purpose:

The tests described herein were performed by the Jet Propulsion Laboratory (JPL) in cooperation with the United States Naval Observatory (USNO) JPL was chosen for this evaluation because of its unique testing capability and facilities. They were conducted at JPL in the Frequency Standards Laboratory Test Facility (FSL) in Pasadena, California, between June and September 1989.

*This work represents the results of one phase of research carried out at the Jet Propulsion Laboratory, California Institute of Technology, under contract with the National Aeronautics and Space Administration.

Test Facilities:

The JPL Frequency Standards Laboratory is responsible for the research, development and implementation of a wide variety of state-of-the-art frequency generation and distribution equipment used within the Deep Space Network (DSN). In order to achieve the demanding performance and reliability requirements, a substantial amount of assembly and subassembly testing is required. Toward this end, an extensive testing capability has been developed which includes special equipment, facilities, procedures and personnel skilled in the testing and characterization of precision oscillators and other signal sources and signal processing equipment. This facility has previously described in the literature^[1].

The stability and environmental tests which are routinely performed in this facility are as follows:

1. Allan Variance
2. Spectral Density of Phase
3. Temperature Sensitivity
4. Humidity Sensitivity
5. Barometric Pressure Sensitivity
6. Magnetic Field Sensitivity (both AC and DC)
7. Vibration Sensitivity (0.1 to 30 Hz, small items).

The instrumentation and test area has approximately 2,700 square feet of floor space, and houses the necessary instrumentation and test equipment. Additionally, two or more active hydrogen maser frequency references are conveniently located in this area. Several cesium standards and clocks are used for calibration to NIST and/or USNO. A GPS receiver is used to maintain these standards and clock calibrations. All critical equipment as well as the units under test are powered by an uninterruptable power source. The entire test area, as well as the environmental control system is backed up by an automatically switched motor generator. Temperature control is maintained to within ± 0.05 degrees Centigrade through the use of a doubly redundant air conditioning system. Magnetic field variations are minimized by the use of non-magnetic construction materials throughout the facility. As an additional precaution, one of the reference hydrogen masers is housed in a magnetically shielded enclosure.

Table 2. Environmental Test Capability	
Parameter	Range
Temperature	15 to 35 deg. C ± 0.05 deg.
Pressure	± 24 inches of water ± 0.5 inches.
Relative Humidity	11% to 90% RH $\pm 5\%$
Magnetic Field	± 0.5 Gauss



Figure 1: Environmental Test Chambers

Environmental testing capability is provided by the three custom-built Tenny Corporation environmental test chambers shown in Figure 1. Each chamber has 64 square feet of floor space and is approximately 10 feet high, providing adequate space for the equipment under test as well as required cables and peripherals. The capability of these chambers is shown in Table 2:

Measurement System

Figure 2 is a block diagram of the measurement system used to determine frequency stability and the Allan deviation between the units under test and the laboratory reference masers.

TEST SCHEDULE

Preliminary Tests

Prior to performance and environmental testing, and after several days of stabilization, each of the cesium standards was degaussed and aligned in accordance with the manufacturers operating procedures. The critical operating parameters of each of the standards was measured and determined to be within the manufacturers specifications. Shortly after the tests were begun, Cesium Standard Number 1 failed. The tests were continued with Standards Numbers 2, 3 and 4.

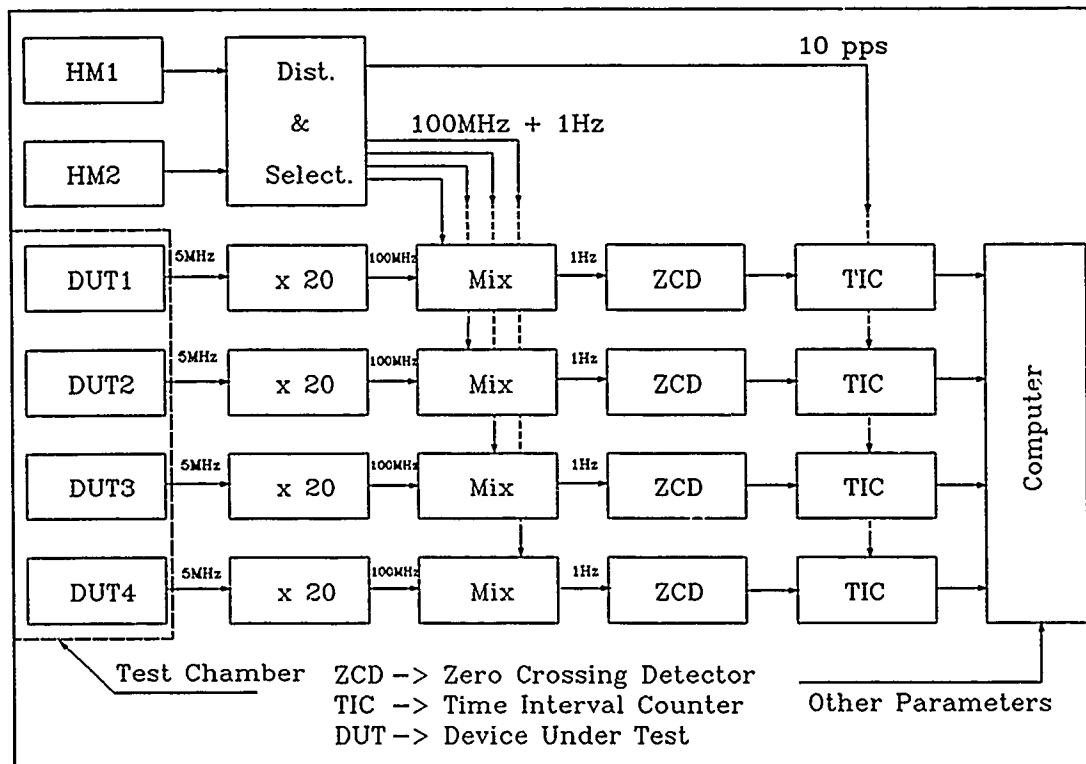


Figure 2: Block Diagram of Measuring System

Sequence of Tests:

The test schedule and test limits are shown Table 3 and Figure 3:

Table 3. Test Ranges	
Parameter	Range
Temperature	17 to 33 Deg. C
Humidity	15% to 85% RH
Barometric Pressure	±24 inches of water

Environmental Tests:

The purpose of these tests was to characterize each cesium beam frequency standard in terms of frequency shift for a given change in environmental condition. In each test, the output frequency was carefully monitored while one of the environmental parameters was varied as specified in Table 3 and Figure 3. The results of each of these environmental tests are shown in Figures 4, 5, 6, 7, 8, 9, 10, 11 and 12.

Figures 4, 5, and 6 show the changes in frequency from standards number 2, 3, and 4 respectively *vs* changes in relative humidity at four constant temperatures; 17, 22, 27 and 33 °C. The four humidity

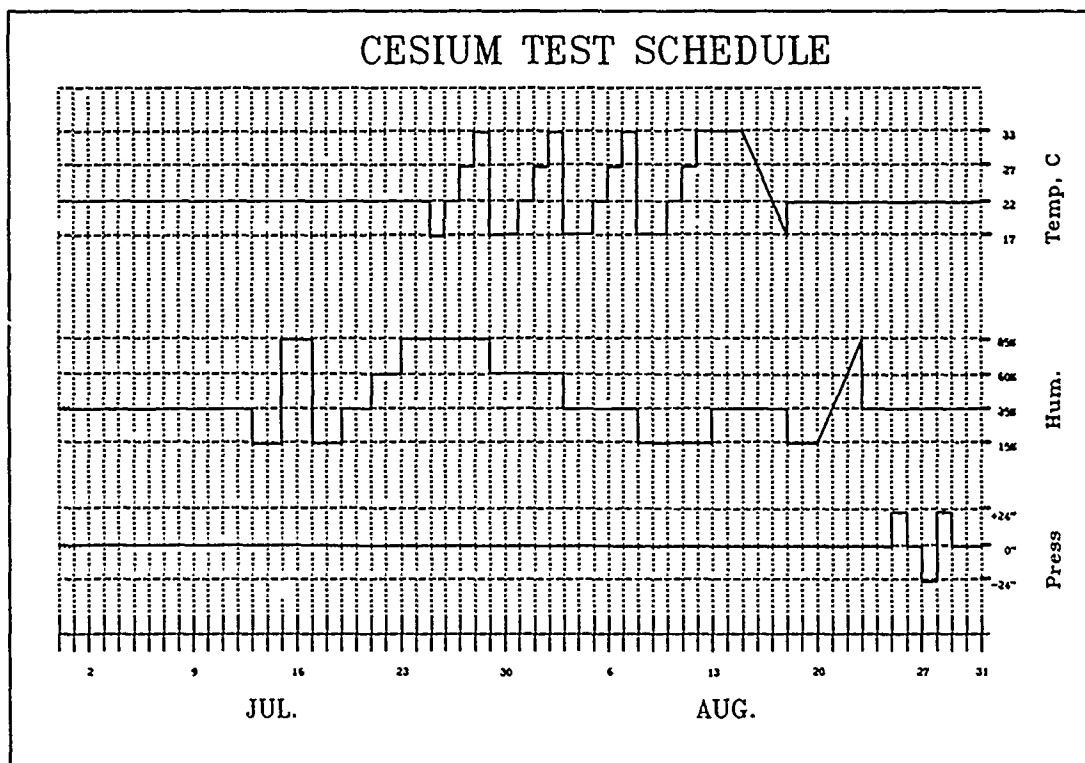


Figure 3: Schedule of Tests

levels which were used were 15%, 35%, 60% and 85%. We note that the changes in frequency are as large as 4×10^{-13} for standard number 2 and somewhat smaller for the other two standards. We also note that the changes in frequency were much smaller at the lower temperatures for the same change in relative humidity. This led us to believe that the important parameter might be the total water content of the ambient air, so the data was re-plotted in Figures 7, 8 and 9.

The results of Figures 7, 8 and 9 are much more readily interpreted than those of Figures 4, 5 and 6. For Cesium Standards numbers 2 and 3, a clear trend is seen in the frequency vs water content, with the frequency decreasing with increasing water content. Cesium standards number 4 has a much more anomalous behavior which also depends on temperature, with a turn-over temperature of approximately 30 °C.

The tests shown in Figures 10, 11 and 12 are taken by varying the temperature while the relative humidity was held constant. Again, we see that the lower humidity produces less frequency change over the temperature range than higher humidity does. The frequency changes can be as high as 4×10^{-13} for the standards.

The frequency changes vs pressure produced no significant changes, and were below the level of uncertainty of these tests.

CONCLUSIONS

These data demonstrate that, if the ultimate stability is to be obtained from this type of cesium frequency standards, not only must the temperature be controlled to a level of $\approx \pm 0.1^\circ\text{C}$, but control of humidity is essential. It appears that, at a nominal relative humidity of 35%, the humidity control must maintain a stability of $\approx \pm 5\%$.

FUTURE PLANS

The second and third phases of this test program, i.e. the adjustment for minimum power dependence and re-testing, have not been scheduled yet. Scheduling any series of tests entailing this length of time among three different bureaucracies are, at the best, difficult. It appears that a better sequence of tests might be arranged, based upon what was learned from this preliminary experiment. The variation of frequency *vs* temperature at constant relative humidity should have been performed at constant water content to give more meaningful results.

ACKNOWLEDGEMENTS

The authors wish to acknowledge the cooperation of G. M. R. Winkler and L. Charon of the U. S. N. O. for the use of the Cesium Standards for use in this test. The encouragement of Andea Di Marchi was the spark that caused the fruition of this experiment.

REFERENCES

- [1] Sydnor, R. L., "Environmental Testing at the Jet Propulsion Laboratory's Frequency Standards Laboratory", Proc. of the 43rd Annual Symposium on Frequency Control, IEEE 89CH2690-6, 31 May-2 June, 1989, pp 289-295

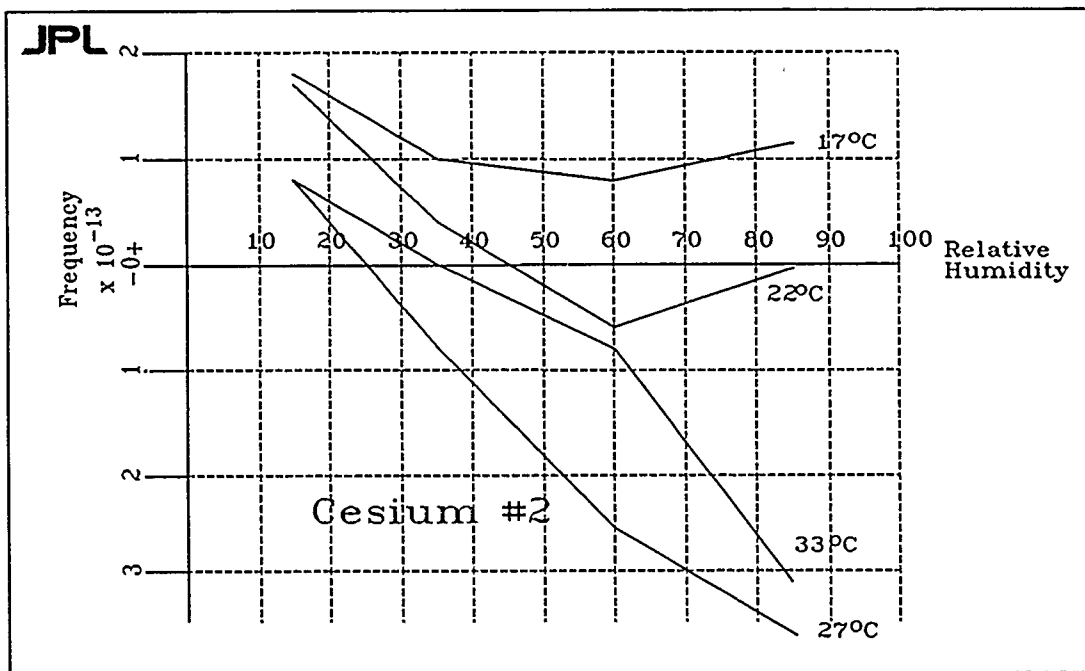


Figure 4: Frequency vs Relative Humidity, Constant Temperature, Cesium # 2

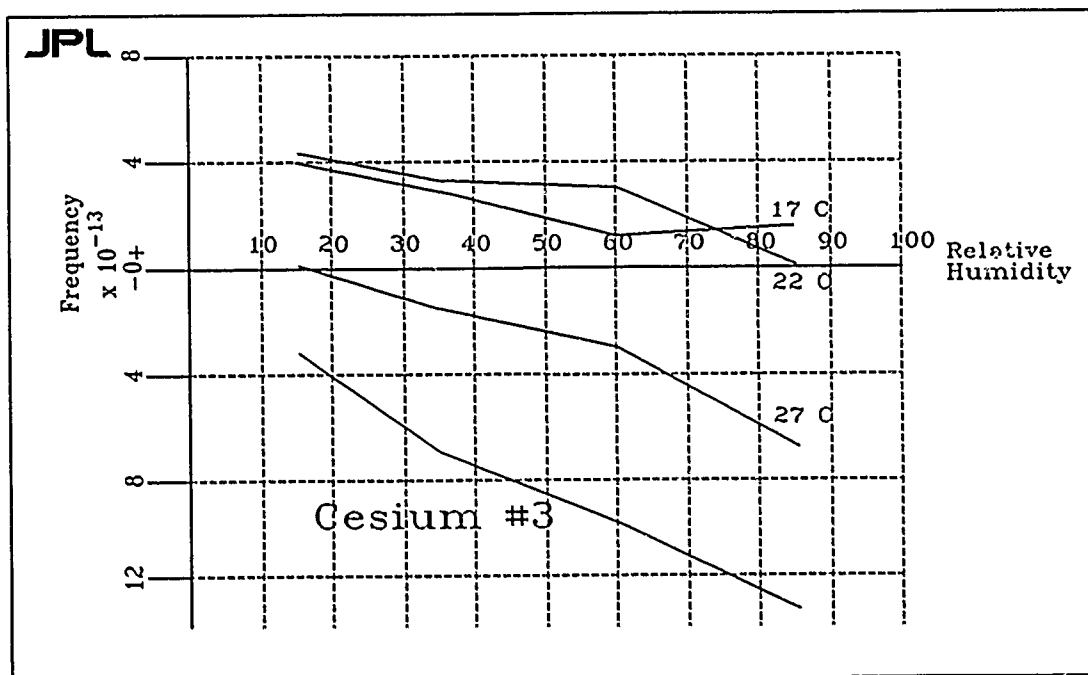


Figure 5: Frequency vs Relative Humidity, Constant Temperature, Cesium # 3

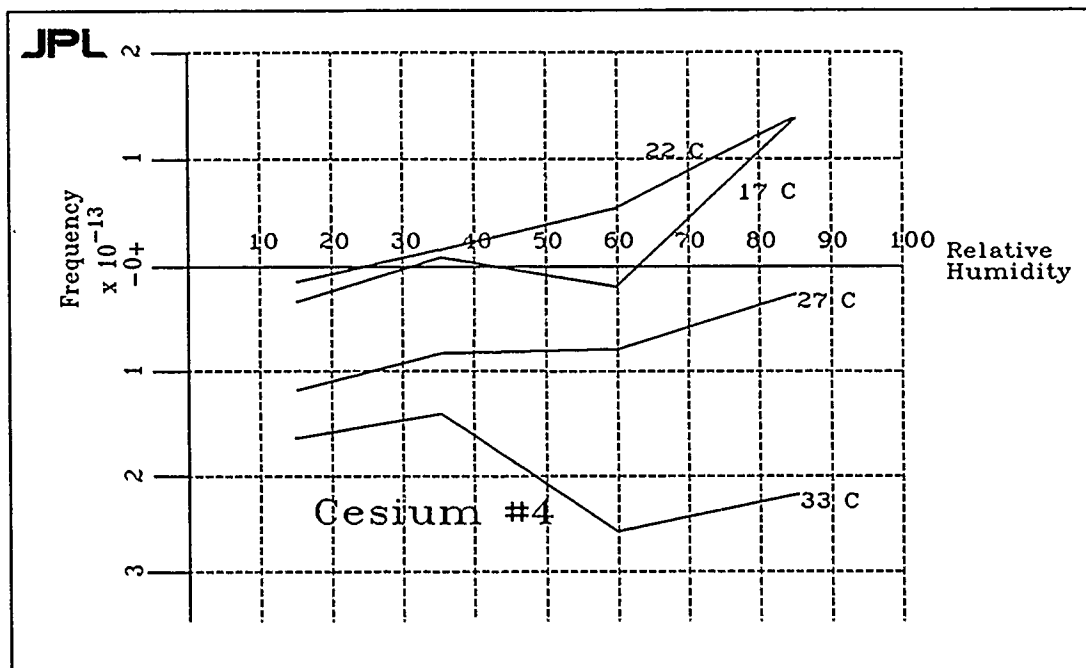


Figure 6: Frequency vs Relative Humidity, Constant Temperature, Cesium # 4

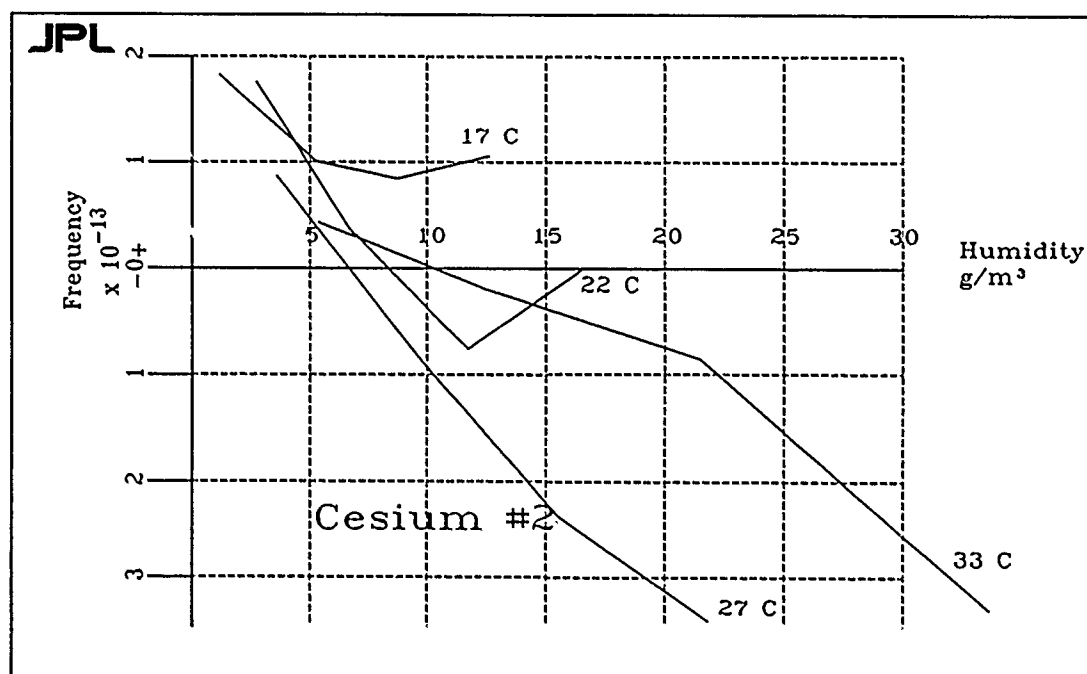


Figure 7: Frequency vs Absolute Humidity, Constant Temperature, Cesium # 2

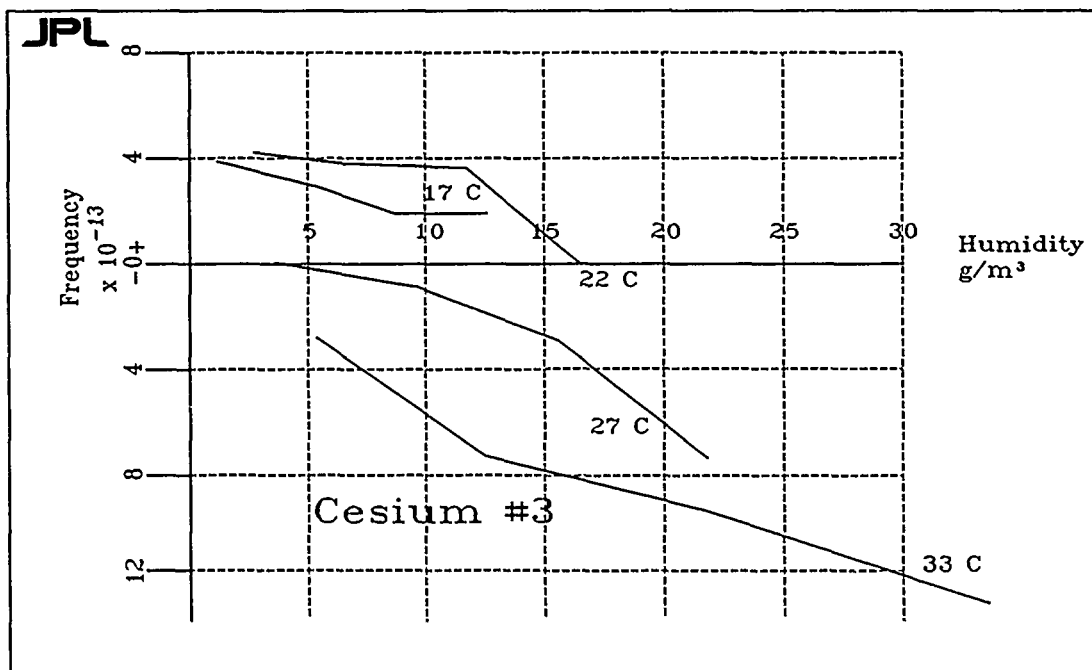


Figure 8: Frequency vs Absolute Humidity, Constant Temperature, Cesium # 3

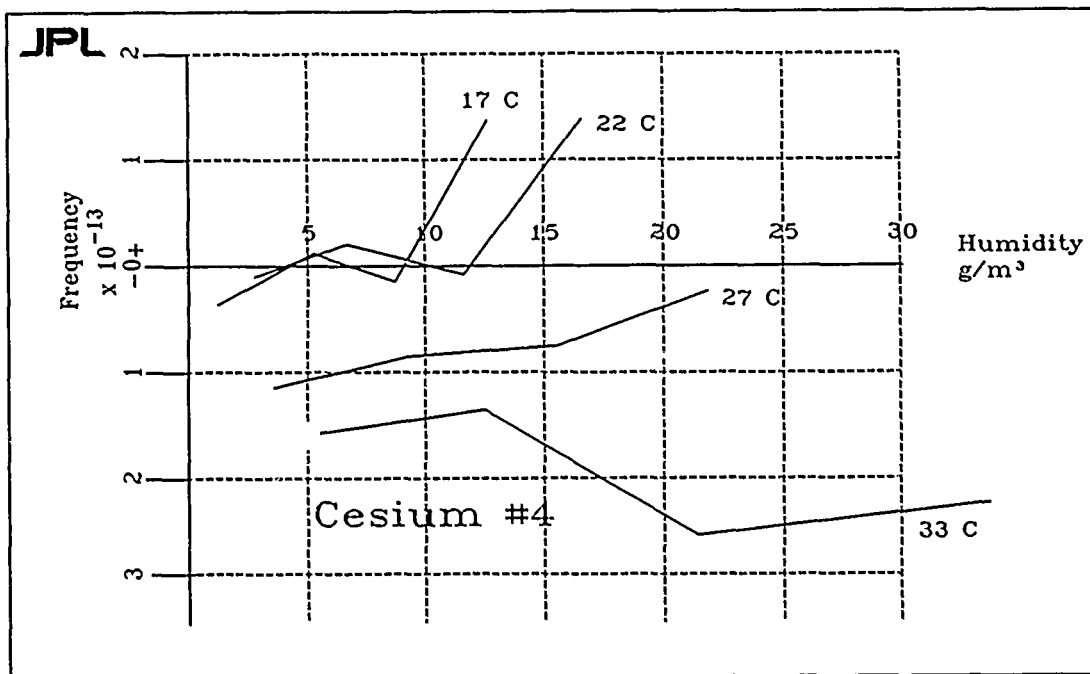


Figure 9: Frequency vs Absolute Humidity, Constant Temperature, Cesium # 4

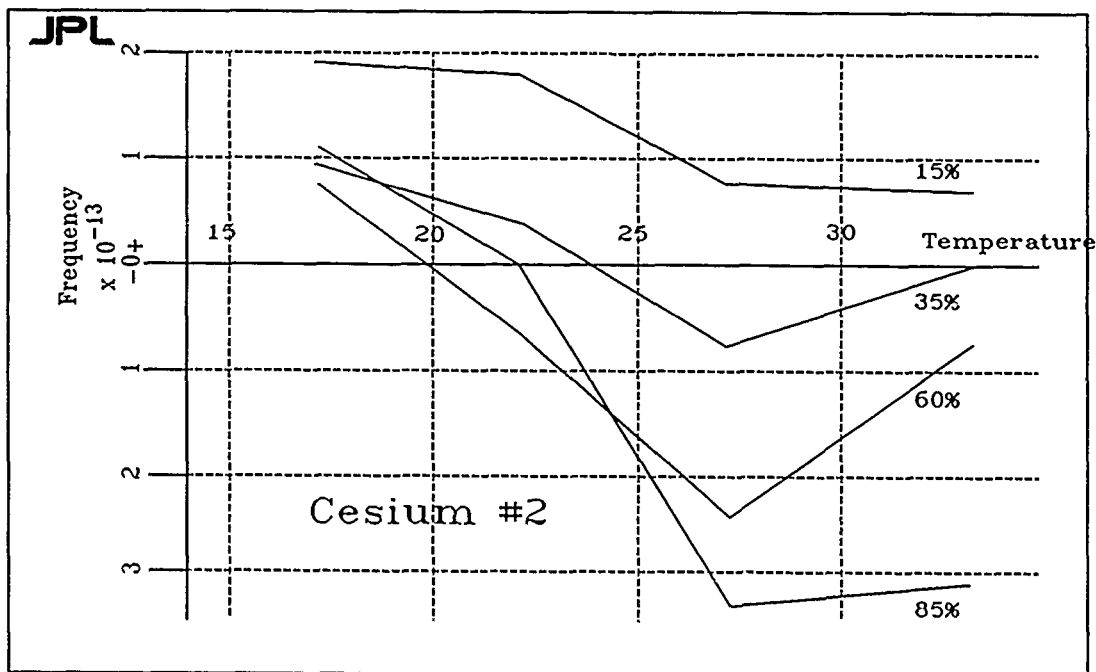


Figure 10: Frequency vs Temperature, Constant Relative Humidity, Cesium # 2

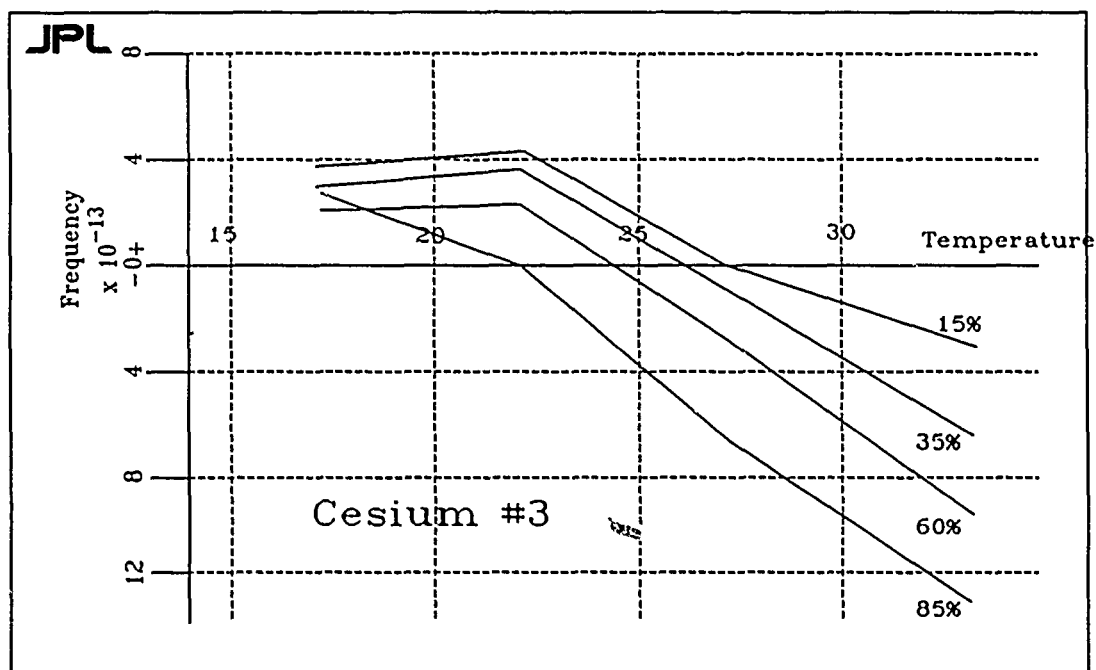


Figure 11: Frequency vs Temperature, Constant Relative Humidity, Cesium # 3

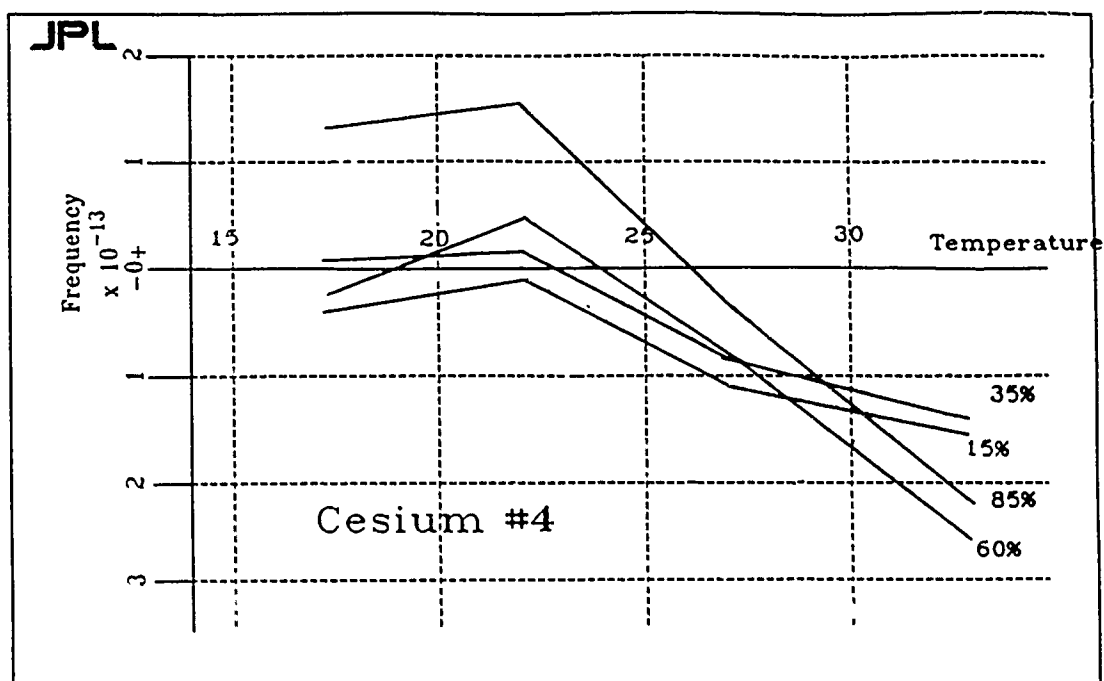


Figure 12: Frequency vs Temperature, Constant Relative Humidity, Cesium # 4

QUESTIONS AND ANSWERS

ROBERT VESSOT, SAO: It is easy to put these in a plastic bag with a bag of silica gel, I suppose. That would get rid of the bulk of the problem, but it would be interesting to know what you think is going on in there.

LEN CUTLER, HP: Two things, probably. Power shift and resonance affects on the cavity tuning.

MR. SYDNOR: Professor Leschiutta took some data and he got an indication that the integrator board was sensitive, also.

MR. REINHARDT: We have seen similar effects in other standards. The very high impedances in servo boards can be affected.

MR. CUTLER: That is certainly possible. It is hard for me to say, but in the original designs, those circuits were all guarded. They should have been very resistant to humidity changes.

MR. SYDNOR: There is another interesting bit of information—if you look at humidity effects in hydrogen masers, there is along time constant associated with them. It may take several days for the effect to take place. The effect on these cesiums was nearly instantaneous. It doesn't appear to be absorption of moisture into a circuit board.

JACQUES VANIER, NRC: This is to Len Cutler. How does the humidity affect the cavity tuning?

MR. CUTLER: It is actually an interaction between power shift and cavity tuning. If the cavity is properly tuned and doesn't change with humidity, then power shift doesn't affect things very much. If the cavity is de-tuned then power shift will affect it.

MR. VESSOT: The tuning is a result of the dielectric effect of the humidity, I assume.

MR. CUTLER: That can affect it, yes.

MR. VESSOT: Would it have made sense to change the barometric pressure? That would change the density and the dielectric constant.

MR. SYDNOR: We did change pressure at constant humidity and temperature. We couldn't see any effect, it was in the noise. Of course, the pressure change was not huge, it was ± 24 inches of water—like a big storm.

MR. REINHARDT: One thing that I would recommend is to monitor the loop stress because you have a frequency locked loop and the oscillator may be changing.

ANDREA DI MARCHI, UNIVERSITY OF ANCONA: I think that some of these questions may be answered if we set these standards at the power insensitive point and then do the tests again.

MR. SYDNOR: That was the original plan.

PERFORMANCE OF OPTICAL FIBERS FOR REFERENCE FREQUENCY AND IF SIGNAL TRANSMISSIONS IN VLBI OBSERVATION

Katsuhisa Sato and Tadayoshi Hara
Division of Earth Rotation
National Astronomical Observatory
Mizusawa, Iwate, 023 Japan

Abstract

We have constructed a 6 m antenna system in the Nobeyama Radio Observatory (NRO) complex of the National Astronomical Observatory, Japan. This system is used for the International Radio Interferometric Surveying trans-Pacific (IRIS-P VLBI) network observation of the International Earth Rotation Service with the Mark-111 VLBI Back-end and the hydrogen maser frequency standard operating at the control room of the 45 m antenna in the NRO. This 6 m antenna is located about 880 m apart from the control room. Therefore, the 10 MHz reference frequency signal and the IF signals should be transmitted over 880 m distance without signal phase fluctuations in the Mark-111 VLBI observations. The phase stabilized signal transmission should be attained by using phase stabilized optical fiber (PSOF). Prior to introduction of this system, we have made a phase stability estimation by experiments.

The PSOF is currently developed at Sumitomo Electric Industries, Ltd. of Japan. We have tested the prototype of this PSOF signal transmission system of which the length is 1000 m. The phase stability of the 1000 m PSOF system is 3.95×10^{-15} ($t=1000$ sec.) in Allan standard deviation (ASD) at the stabilized temperature of $21.4^\circ\text{C} \pm 0.5^\circ\text{C}$ and at the frequency of 20.9 MHz. The stability is about 55 times better than the ordinary coaxial cable transmission system. In the environment of temperature variation of $+30^\circ\text{C}$, the stability of this PSOF is 1.97×10^{-14} ($t=1000$ sec.) in ASD.

INTRODUCTION

A group for a 6 m antenna construction project in Division of Earth Rotation of National Astronomical Observatory has currently constructed the 6 m antenna VLBI system which uses the Mark -111 back-end in NRO complex. This system will be used for the IRIS-P VLBI network observation of an International Earth Rotation Service. The Mark-III VLBI Back-end was originally installed as the back-end of the 45 m antenna in the NRO. The location of the 6 m antenna is about 880 m apart from the control room of the 45 m antenna where the Mark-111 back-end is installed.

The correlation amplitude in a VLBI correlation observation is dependent on the antenna diameter, the system noise and coherence factor. The coherence factor of the VLBI observation is influenced from a stability of a reference frequency signal. Our 6 m antenna is small in diameter and this small

diameter is a large factor in decreasing the correlation amplitude. We could not install a preamplifiers which have sufficiently low noise due to some limitations. So, we tried to maintain the coherence due to the phase fluctuations of the reference frequency signal and IF signal transmission lines as small as possible to obtain enough correlation amplitude.

Phase stability measurement of a coaxial cable and phase stabilized optical fiber (PSOF) signal transmission systems was made to examine these systems can satisfy our requirement. In this paper, we will report the result of the measurements obtained in the laboratory at the National Astronomical Observatory (NAO) Mizusawa and in the NRO where the PSOF is actually installed in the underground tunnel for VLBI observations.

TOLERANCE OF PHASE FLUCTUATIONS

To obtain a moderately large correlation amplitude in the VLBI observation using the 6m antenna system, we have decided maintain the coherence loss due to the phase fluctuations as small as 2%. It means the limitation of the phase variation of 5 MHz reference frequency should be 0.01° rms when the noise is assumed to be white phase. In general, a phase variation $\langle \Delta\phi^2 \rangle^{1/2}$ is expressed as

$$\langle \Delta\phi^2 \rangle^{1/2} = \left[\frac{2}{3} \sigma_y^2(\tau) \right] \omega \tau \quad (1)$$

in Allan variance σ_y^2 when the noise is white phase and τ is integration time^[1]. Or, one can write

$$\sigma_y^2(\tau) = \frac{3}{2} \left[\langle \Delta\phi^2 \rangle^{1/2} / (\omega \tau) \right]^2. \quad (2)$$

In the case of $f = 5 \times 10^6$ Hz, $\tau = 0.1, 10, 1000$ seconds, $\Delta\phi = 0.01^\circ$, we have Allan standard deviation (See Table 1).

PHASE STABILIZED OPTICAL FIBER

An ordinary optical fiber has positive thermal expansion coefficient and it causes transmission time delay in proportion to a temperature when this kind of optical fiber is used for signal transmission. The normal optical fiber has a silica fiber in the center and this silica fiber is coated twice. The primary coating is a kind of an absorber for a friction between the center silica and secondary coating which is crust. Sumitomo Electric Industries has currently developed PSOF which uses liquid crystal polymer (LCP) for the secondary coating^[2]. The LCP has a negative thermal expansion coefficient and compensates the positive thermal expansion coefficient of the center silica fiber. The change of transmission delay time of this PSOF is 100ps/km in the temperature range of $-40^\circ\text{C} \rightarrow +40^\circ\text{C}$.

MEASUREMENT SYSTEM FOR PHASE STABILITY EVALUATION

Time domain measurements of frequency stability have been made to obtain the ASD. A dual mixer time domain (DMTD) system was used for these measurements^[3]. We used a delay calibrator (D-cal) of the Mark-III VLBI back-end in which both a 5 MHz reference signal and a 5 MHz test signal are

mixed down to 25 Hz and the time interval between these two 25 Hz output signals from the D-cal is measured. Two types of these DMTD system was made. One of these systems is for the measurement of the frequency for 5 MHz and the other is the double conversion system for 20.9 MHz or 150.9 MHz measurement. Figures 1, 2 and 3 show the block diagrams of these DMTD systems.

RESULTS OF THE MEASUREMENTS

The phase stability of PSOF with the length of 1 km has been measured at 5 MHz in the laboratory. And the phase stability of RG-213/U coaxial cable with the length of about 490 m which is installed most of the part in a trench is also measured at the frequency of 5 MHz. The depth of the trench is about 50 cm and the temperature fluctuation in the trench is expected as ± 0.4 °C/hour in December at this depth. The results of these measurement is shown in figure 4. From this measurement, we conclude the phase stability of PSOF is about 55 times better than that of coaxial cable. A frequency dependency of the phase stability was found out for the PSOF in this measurement as shown in figure 4. Extra measurement for an effect of a fiber distortion was made to make clear this frequency dependency. From the figure 5, it is considered that the origin of this frequency dependency is the distortion caused by the optical fiber. The distortion effect is considered to be caused by the modulation of a signal by a reflected light signal in the fiber cable. It is recommended that the use of the frequency over 10 MHz for less distortion effect from the figure 5. And an isolator in a optical fiber line will help to eliminate this frequency dependency^[4]. In our case, however, no isolator for the reflected signals was used and the optical fibers were installed without any distortion due to antenna's motion. A coaxial cable was used for the part of the inside of the antenna. The phase stability of this PSOF at various environment temperature was measured at 20.9 MHz so that the distortion effect on the fiber was smaller. The results of the measurement are shown in figure 6. The phase of the PSOF is stable enough in the environment temperature change below $+6$ °/hour. From the figures 4 and 6, we have decided to use the PSOF's for the reference frequency and IF signal transmission lines of 6 m antenna system.

The specifications of the signal transmission system (PSOF system) which uses PSOF are shown in Table 2. We have measured the phase stability of the installed PSOF system at NRO using the same component used for the laboratory measurement at the frequency of 5 MHz and 150.9 MHz. The figure 7 shows the result of this measurement. The temperature fluctuations of the tunnel which was designed for the 5 element interferometer using 10 m antennas at the NRO is considered to be very small. The PSOF systems for 6 m antenna are installed in this tunnel and very high phase stability is expected even for ordinary coaxial cable because the tunnel is designed to stabilize the phase of transmission signal in coaxial cables. So, the results of the phase stability measurement for 1760 m round trip (880 m one way) coaxial cable is very stable compared to the result of the 490m coaxial cable in the environment temperature ± 0.4 °/hour shown in figure 4. Even though, the PSOF system is more stable than coaxial cable at 5 MHz but the ratio of the stability is not 55, because the frequency dependency which mainly caused by reflection of a light in a fiber affects more strongly at lower frequency such as 5 MHz. The result of the measurement at 20.9 MHz in the laboratory is also plotted in the figure 7. These result of the measurement made at 20.9 MHz in the laboratory is considered to be almost the same as the result of the PSOF system installed for 6 m antenna because environment temperature variation for the measurement of the installed PSOF system at NRO seems to be almost the same environment as the laboratory. The plots of 5 MHz, 20.9 MHz and 150.9 MHz in figure 7 follow the characteristics of the frequency dependency shown in figures 4 and 5. The reference frequency which is transmitted through this PSOF system is 10 MHz for 6 m antenna system. Assuming that the phase stability of 10 MHz is almost the same as 20.9

MHz, we conclude that the PSOF system does not exceed the phase stability tolerance for coherence loss of 2% when introduced to the 6 m antenna system at 10 MHz for the distance over 1700m. And the stability of the PSOF system at 10 MHz is about 2.2 times lower than that of coaxial cable even in the condition of temperature stabilized environment carefully designed for the 5 element mm wave length interferometer.

CONCLUSION

The PSOF is used for 10 MHz reference frequency transmission of which the distance is over 880 m in 6 m antenna system without exceeding the tolerance of phase stability estimated for coherence loss of 2%. The PSOF is also used for wide band (100–520 MHz) IF signal transmission of which the distance is over 880 m in this 6 m antenna system without a loss of a signal power. This IF signal transmission system does not require the frequency response equalizer which usually degrades a phase stability and is required for a coaxial cable system.

ACKNOWLEDGMENT

The authors thank T. Miyaji of NRO and T. Sasao of NAO for their help in arrangement of equipments for the measurements. The authors also thank S. Tanaka and Y. Murakami of Sumitomo Electric Industries, Ltd. Japan for providing PSOF and signal transmission modules for the measurement in the laboratory.

REFERENCES

1. K. Horiai, On the frequency standards and time keeping system of the VERA, Proc. of third VERA symposium, pp344–354, 1988.
2. T. Kakuta, S. Tanaka, LCP coated optical fiber with zero thermal coefficient of transmission delay time, Sumitomo Electric Industries, Ltd., 1, Taya-cho, Sakae-ku, Yokohama, 244 Japan
3. F. L. Walls, David W. Allan, Measurements of frequency stability, Proc. of the IEEE, vol. 74, no. 1, January 1986.
4. G. Lutes, L. Primas, State-of-the-art fiber optics for short distance frequency reference distribution, TDA progress report, pp 42–97, January–March 1989.
5. Thomas A. Clark, Allan E.E. Rogers, Manual for Mark III phase and group delay calibrator, Manual of Mark III VLBI data acquisition terminal, vol. 1, pp DC-1–DC-55, January 1982.

Table 1. Tolerance of Phase Stability for VLBI Observations which has coherence loss of 2 % for X-band observation with integration time of 800 seconds.

Integration Time	Allan Standard Deviation $\langle \sigma^2 \rangle^{1/2}$
0. 1	6.8×10^{-11}
1 0	6.8×10^{-13}
1 0 0 0	6.8×10^{-15}

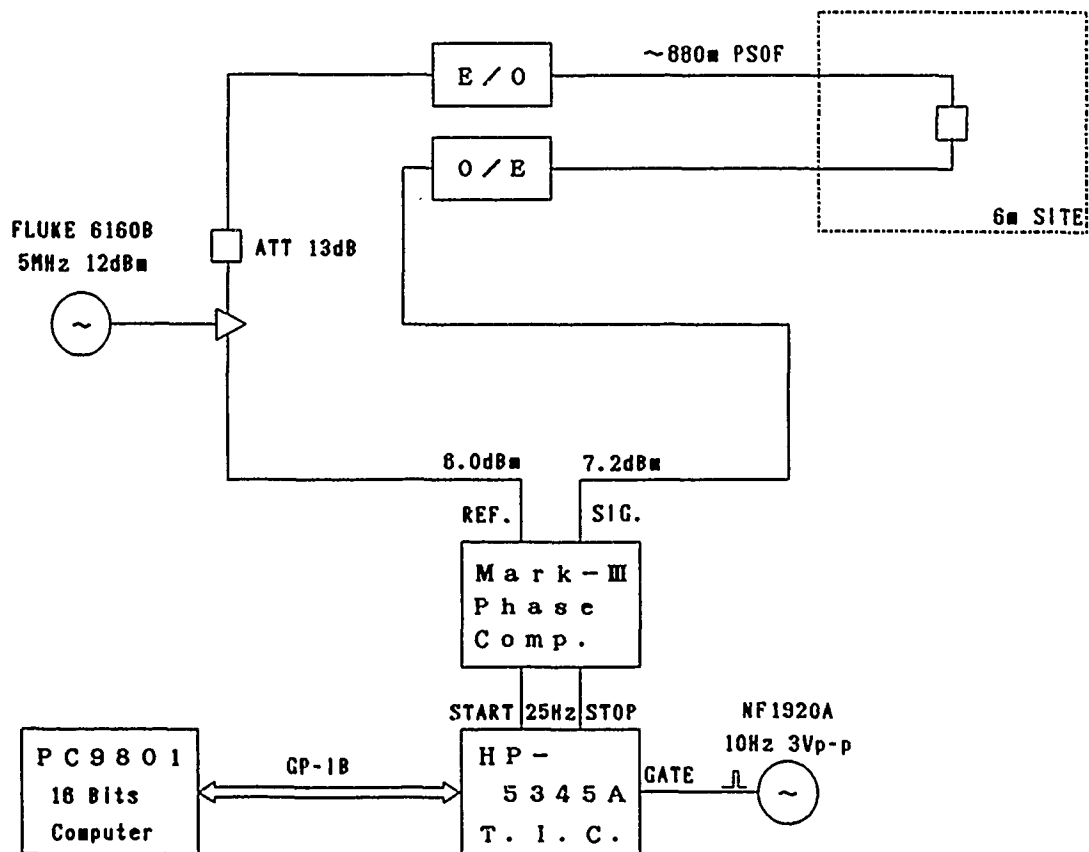


Figure 1. The block diagram of the Dual Mixer Time Domain (DMTD) system for the phase stability measurement. This system is used for the measurement of the installed PSOF at NRO. The frequency of this system is 5MHz.

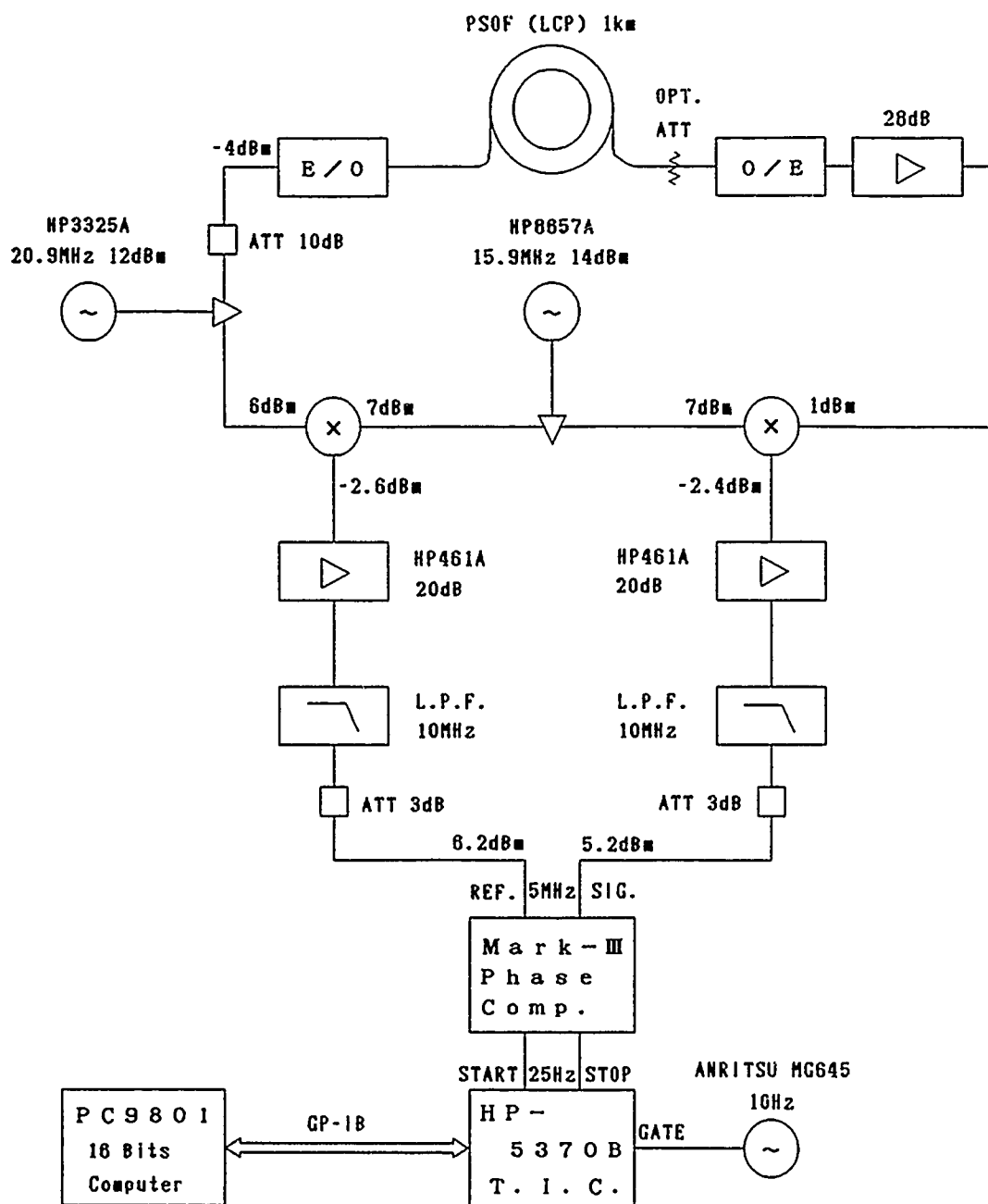


Figure 2. The block diagram of the Dual Mixer Time Domain (DMTD) system for the phase stability measurement. This system is used for the measurement of 1km PSOF in the laboratory. The frequency of this system is 20.9MHz.

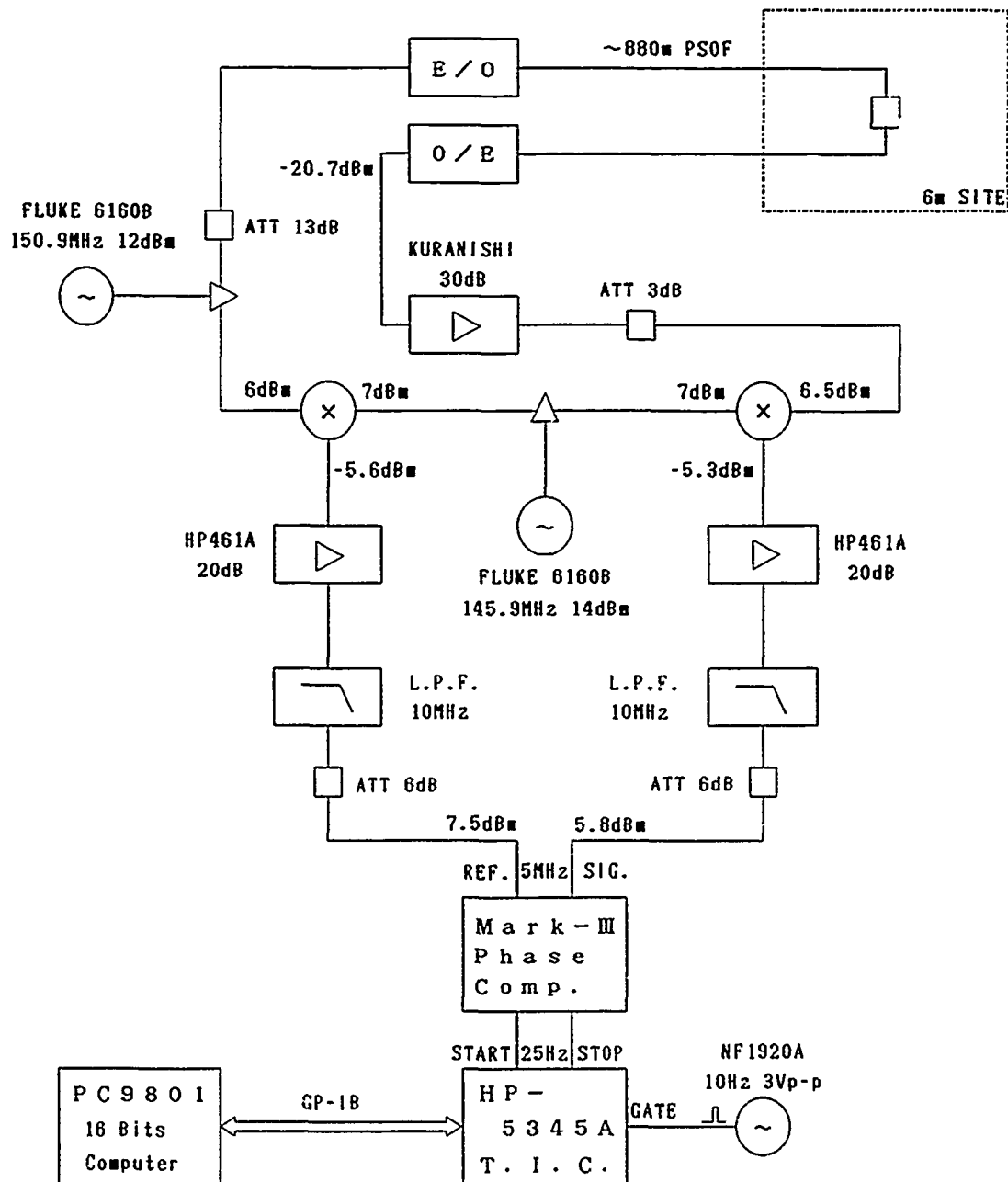


Figure 3. The block diagram of the Dual Mixer Time Domain (DMTD) system for the phase stability measurement. This system is used for the measurement of the installed PSOF at NRO. The frequency of this system is 150.9MHz.

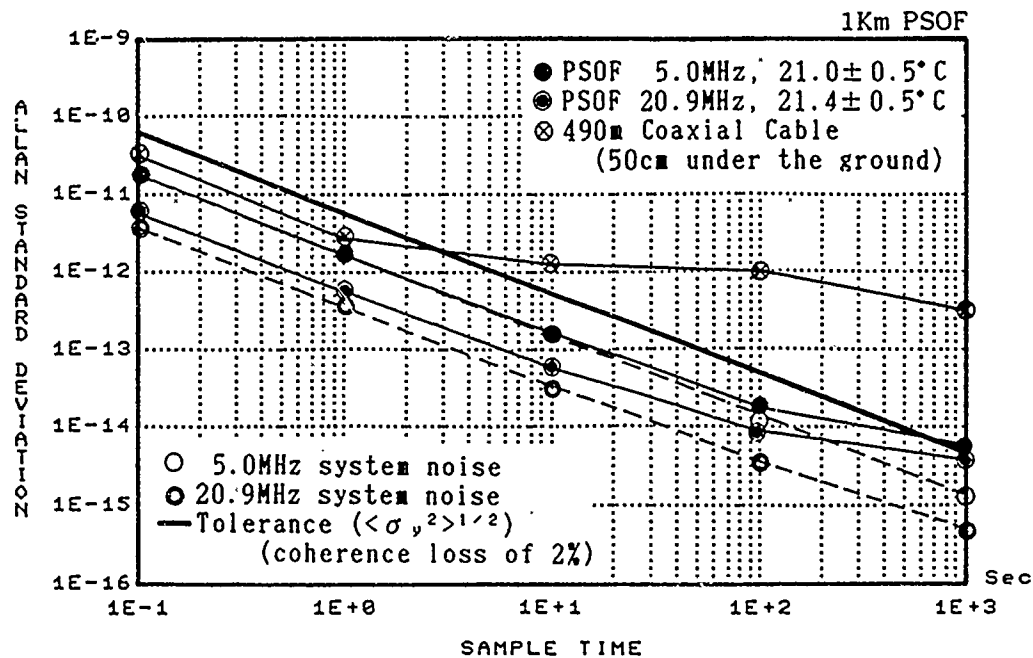


Figure 4. The Allan standard deviation of the 1km PSOF and coaxial cable laid 50cm under the ground. All these measurement had been obtained in a Laboratory

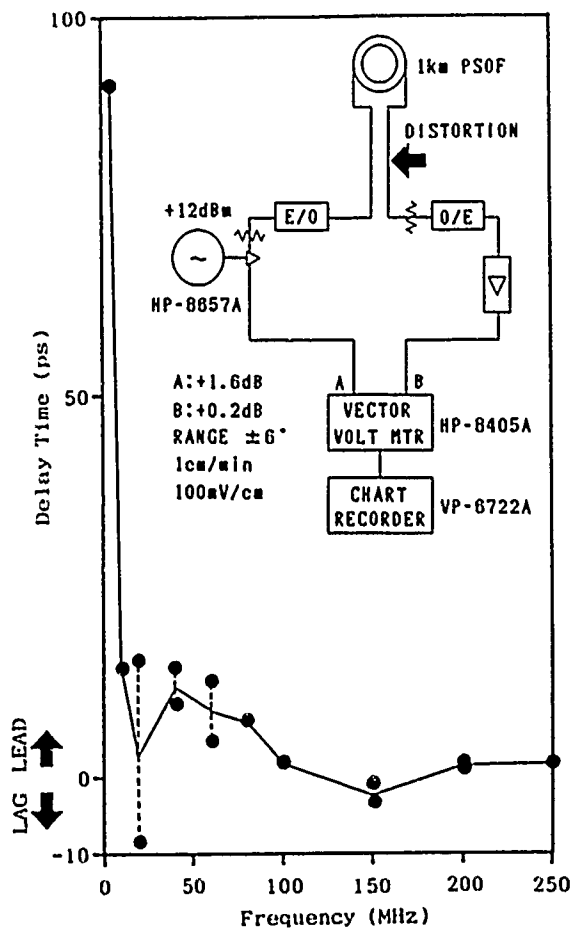


Figure 5.

The frequency dependency of transmission delay time in the condition of a distortion is inflicted to the optical fiber. The block diagram of this measurement system is also shown in this figure.

Table 2. Specifications of Optical Transmitter and Optical Receiver for PSOF

CMT-50 (1MHz~50MHz) Transmitter	
Bandwidth	1~50MHz at gain flatness $<\pm 1\text{dB}$
Optical output level	$>-2\text{dBm}$ (mean value)
Electrical input level	$-5\sim-30\text{dBm}$ at 50 ohm load
Phase noise	$<-80\text{dBc}$ at 100Hz offset
Phase stability	$<2^\circ\text{rms}$ in 10 minutes
2nd harmonics	$<-30\text{dB}$
CMR-50 (1MHz~50MHz) Receiver	
Bandwidth	1~50MHz at gain flatness $<\pm 1\text{dB}$
Optical input level	$>-10\sim-20\text{dBm}$ (mean value)
Electrical output level	$+10\sim-20\text{dBm}$ (50 ohm & opt -10dBm)
Phase noise	$<-80\text{dBc}$ at 100Hz offset
Phase stability	$<2^\circ\text{rms}$ in 10 minutes
2nd harmonics	$<-30\text{dB}$
CMT-500 (100MHz~520MHz) Transmitter	
Bandwidth	100~520MHz at gain flatness $<\pm 1\text{dB}$
Optical output level	$>-2\text{dBm}$ (mean value)
Electrical input level	$-5\sim-30\text{dBm}$ at 50 ohm load
Phase noise	$<-80\text{dBc}$ at 100Hz offset
Phase stability	$<2^\circ\text{rms}$ in 10 minutes
2nd harmonics	$<-30\text{dB}$
CMR-500 (100MHz~520MHz) Receiver	
Bandwidth	100~520MHz at gain flatness $<\pm 1\text{dB}$
Optical input level	$>-10\sim-20\text{dBm}$ (mean value)
Electrical output level	$-5\sim-35\text{dBm}$ (50 ohm & opt -10dBm)
Phase noise	$<-80\text{dBc}$ at 100Hz offset
Phase stability	$<2^\circ\text{rms}$ in 10 minutes
2nd harmonics	$<-30\text{dB}$

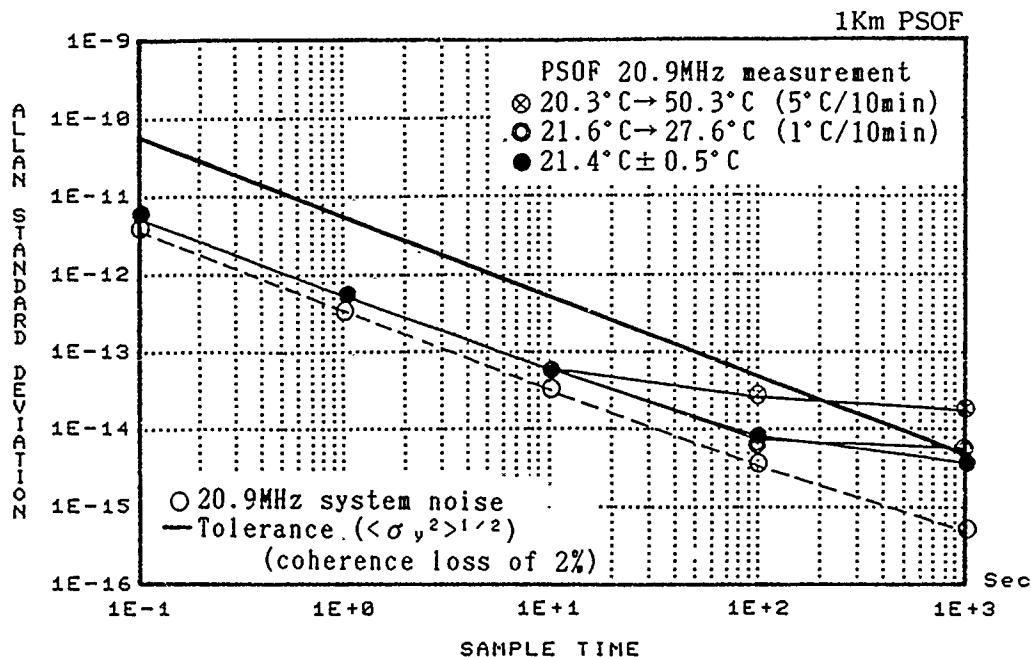


Figure 6. The Allan standard deviation of the 1km PSOF in environment temperature fluctuation. The measurement had been obtained in a laboratory.

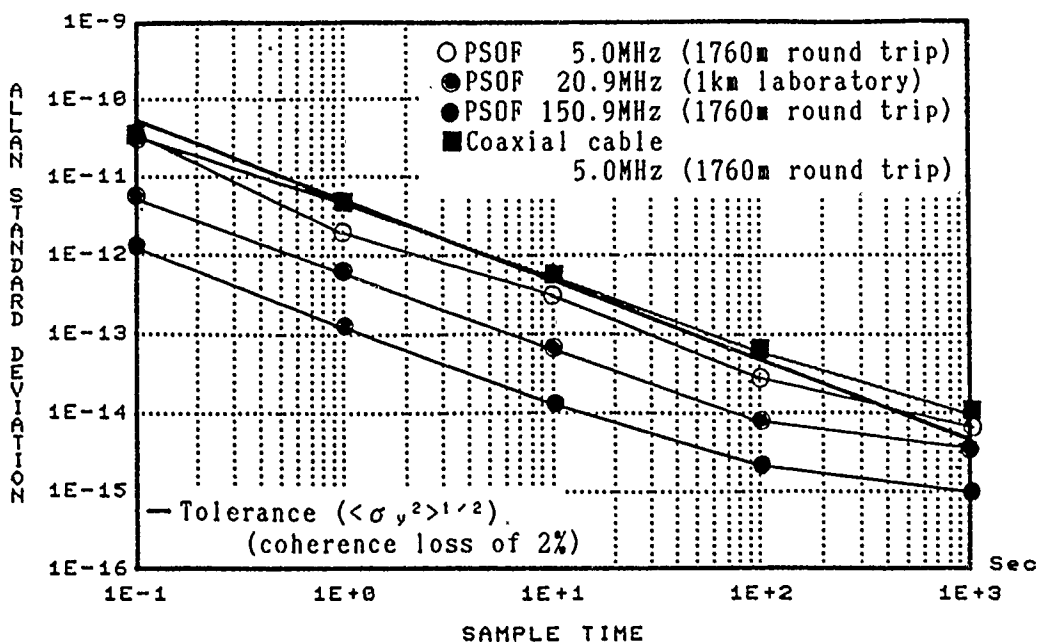


Figure 7. The Allan standard deviation of the 880m PSOF's and the coaxial cable installed in the tunnel at NRO for 6m antenna system. The temperature in the tunnel is well stabilized and even the coaxial cable has good phase stability. The phase stability of PSOF is remarkably better than the stability of the coaxial cable.

RELIABILITY STUDIES OF LAMP CELLS FOR USE IN RUBIDIUM VAPOR FREQUENCY STANDARDS

T McClelland
Frequency Electronics, Inc.
Mitchel Field, New York 11553

Abstract

Atomic vapor frequency standards, and in particular rubidium vapor frequency standards utilize electrodeless discharge lamps in order to measure the atomic hyper-fine frequency. These lamps have been isolated as a reliability problem in commercially available frequency standards, and have been associated with failures of rubidium standards on GPS satellites. For satellites systems, lifetimes of ten years or more are required.

An extensive study has been undertaken at FEI and the Aerospace Corporation to establish reliability data for rubidium lamp cells. In this study, lamp cell failures are attributed to one of two mechanisms; either random failures in which the probability of failure is constant with time but the physical mechanism of failure is unknown, or wear out failures due to consumption of Rb in the cell. An upper bound random failure rate has been established for lamp cells manufactured at FEI. In addition, Over thirty-five FEI lamp cells have been continuously operated for the last three years, with regular Rb mass measurements to determine Rb consumption. The major Rb consumption mechanisms have been clearly identified and techniques to minimize total consumption have been established.

The results of this study are reported, with special attention to the implications for future space programs. It is shown that adoption of precise lamp acceptance criteria is critical to the attainment of extended lamp life. It is concluded that 20 year continuous operation of Rb lamps can be achieved without difficulty.

This paper was presented,
but the text was not available for publication.

ANALYSIS OF FUNDAMENTAL AND SYSTEMATIC EFFECTS LIMITING HYDROGEN MASER FREQUENCY STABILITY

Edward M. Mattison
Robert F.C. Vessot

Smithsonian Astrophysical Observatory
Cambridge, Massachusetts 02138

INTRODUCTION

The hydrogen maser is currently one of the most stable frequency standards currently available, providing frequency stabilities of several parts in 10^{16} for averaging times of $10^3 - 10^4$ seconds. Further improvement to the stability of hydrogen masers requires a comprehensive understanding of the relative magnitudes of physical processes that influence frequency stability. We discuss an approach to understanding a variety of thermodynamic and systematic processes that can affect maser frequency stability.^[1] This examination enables the maser researcher and user to identify stability-limiting effects and thus to choose areas where improvements could lead to increased stability. As is true with many complex systems, overall improvements can generally be gained only by attending simultaneously to a variety of factors. Improving one aspect of the maser will not significantly increase the frequency stability if variations in another area limits the stability to a level comparable to the first.

The hydrogen maser's frequency stability is affected by fundamental thermal noise and by systematic effects. The maser frequency stability, expressed by the two-sample, or Allan, deviation^[2] $\sigma(\tau)$ typically has three approximately linear portions when displayed on a log-log plot.

For values of the averaging interval τ between approximately 1 and 100 seconds, $\sigma(\tau)$ is approximately proportional to τ^{-1} . This behavior results from thermally-induced phase noise within the bandwidth of the maser's receiver system. Between roughly 100 and 1000 seconds $\sigma(\tau)$ is proportional to $\tau^{-1/2}$; in this range of averaging interval, the frequency stability is determined by thermal noise within the hydrogen atomic linewidth. For longer averaging times $\sigma(\tau)$ is generally found to vary with τ between $\tau^{1/2}$ and τ^1 . τ^1 behavior is characteristic of linear frequency drift, while $\tau^{1/2}$ behavior is termed random walk of frequency.

FUNDAMENTAL STABILITY EFFECTS DUE to THERMAL NOISE

The Allen deviation $\sigma_A(\tau)$ due to thermal noise within the atomic linewidth is given by^[3]

$$\sigma_l(\tau) = \frac{1}{Q_l} \sqrt{\frac{kT}{2P\tau}} \quad (1)$$

Here Q_l is the atomic line Q, k is Boltzmann's constant, T is the absolute temperature within the maser's resonant cavity, and P is the power delivered by the atomic beam to the cavity.

The effect of thermal noise on the maser's receiver is given by^[4]

$$\sigma_r(\tau) = \frac{1}{\omega\tau} \sqrt{\frac{FkTB}{P_r}} = \frac{1}{\omega\tau} \sqrt{\frac{FkTB}{P} \left(\frac{1+\beta}{\beta} \right)} \quad (2)$$

Here F is the noise figure of the receiver system, B is the receiver's effective noise bandwidth, P_r is the power delivered by the maser cavity to the receiver, β is the cavity coupling factor, and $\omega = 2\pi f_m$, where f_m is the maser transition frequency, 1420.405...MHz.

It is necessary to express the frequency stability in terms of quantities that are either measurable or controllable, such as the coupling factor, cavity Q, and hydrogen flux. These parameters enter the Allan variance through the line Q and the beam power.

The power radiated by the beam can be expressed^[3] in terms of the net flux I of radiating atoms entering the storage volume, that is, the difference between the number of atoms entering in the hyperfine state "c" ($F=1, m_F=0$) and the number in the state "a" ($F=0, m_F=0$).

$$P = \frac{\hbar\omega}{2} I_{th} \left[-2q^2 \left(\frac{I}{I_{th}} \right)^2 + (1 - cq) \left(\frac{I}{I_{th}} \right) - 1 \right] \quad (3)$$

where I_{th} , the minimum flux required for oscillation in the absence of spin exchange, is given by

$$I_{th} = \frac{\hbar V_c}{4\pi\mu_o^2 Q_c \eta} \gamma_t^2 \quad (4)$$

and the parameter q is defined by

$$q = \frac{\sigma \bar{v}_r \hbar}{8\pi\mu_o^2} \frac{\gamma_t}{\gamma_d} \frac{V_c}{\eta V_b} \frac{1}{Q_c} \frac{I_{tot}}{I} \quad (5)$$

Here μ_o is the Bohr magneton, σ is the spin-exchange cross section, \bar{v}_r is the relative hydrogen velocity in the storage bulb, V_c is the resonant cavity volume, η is the storage bulb's filling factor and Q_c is the loaded cavity Q. In most masers $(I_{tot}/I) \approx 2$ because the state selection magnet focusses atoms in both states "c" and "d" ($F=1, m_F=1$) into the storage bulb. If single state selection is used, only state "c" atoms enter the bulb and $(I_{tot}/I) \approx 1$. γ_t is the total density-independent relaxation rate and γ_d is the rate at which atoms are removed from the storage bulb by escape through its entrance collimator and by recombination on the wall surface. Generally, γ_t exceeds γ_d because to magnetic inhomogeneity relaxation and to wall relaxation processes other than recombination; in a properly built maser $(\gamma_t/\gamma_d) \approx 1$. Under similar assumptions, the parameter c in Eq. 3 has the value $c = 3$.

The atomic line Q is also related to the flux and the relaxation rates:

$$Q_t = \frac{\omega}{2\gamma_2} = \frac{\omega}{2\gamma_t} \left[1 + q \left(\frac{I}{I_{th}} \right) \right]^{-1} \quad (6)$$

To find the level of flux that minimizes the Allan variance $\sigma^2(\tau)$, we can express $\sigma^2(\tau)$ as a function of flux by substituting Eqs. (3) and (6) into Eqs. (1) and (2) and finding the minimizing flux by differentiating with respect to I . It is physically reasonable that values of I exist that minimize $\sigma_t^2(\tau)$ and $\sigma_r^2(\tau)$. $\sigma_r^2(\tau)$ is proportional to P^{-1} ; since P is a quadratic function of I with a maximum (resulting from spin exchange relaxation overwhelming the increase in power with increasing flux), $\sigma_r^2(\tau)$ has a corresponding minimum. $\sigma_t^2(\tau)$ is proportional to $[Q_t^2 P]^{-1}$. At low flux levels, Q_t has a maximum value determined primarily by atomic loss mechanisms described by γ_d , and its value decreases with increasing flux. Thus the product $Q_t^2 P$ has a maximum at a smaller value of flux than does P alone, and $\sigma_t^2(\tau)$ has a corresponding minimum at a smaller value of flux than does $\sigma_r^2(\tau)$.

Minimization of $\sigma_t(\tau)$

We wish to find maser operating conditions that minimize the Allan variance $\sigma_t^2(\tau)$, and thus the Allan deviation $\sigma_t(\tau)$. For a given maser the readily variable parameters are the flux I , cavity coupling factor β , and state selection ratio I_{tot}/I . We assume that Q_o , the maser's unloaded cavity Q , is fixed, since it is determined by the dimensions and materials of the maser's resonant cavity and storage bulb. (Altering the dimensions to change the bulb filling factor, however, can affect Q_o .) Then Q_c , the loaded cavity Q , is determined by the coupling factor:

$$Q_c = \frac{Q_o}{1 + \beta} \quad (7)$$

The parameter q can be expressed as

$$q = q_o(1 + \beta) \quad (8)$$

where q_o is independent of β and is defined by

$$q_o = \frac{\sigma \bar{v}_r \hbar}{8\pi\mu_o^2} \frac{\gamma_t}{\gamma_d} \frac{V_c}{\eta V_b} \frac{1}{Q_o} \frac{I_{tot}}{I} \quad (9)$$

It is convenient to introduce the normalized flux variable

$$x = q \frac{I}{I_{th}} \equiv \frac{\gamma_{2se}}{\gamma_t} \quad (10)$$

By expressing the beam power and line Q in terms of x and β and differentiating with respect to x , one can find^[1,5,6] the condition on flux that minimizes σ_t^2 :

$$\tilde{x}_t = \frac{1 - q}{1 + q} \quad (11)$$

From Eq. 12 we can express Eq. 11 as

$$\left(\tilde{\gamma}_{2se} \right)_t = \gamma_t \left(\frac{1 - q}{1 + q} \right) \quad (13)$$

This means that for a particular value of cavity coupling, the minimum Allan variance due to thermal noise within the atomic linewidth occurs when the flux is adjusted so that the spin exchange relaxation rate γ_{2se} equals the density independent relaxation rate γ_t decreased by the factor $(1 - q)/(1 + q)$. For many masers, particularly those employing single state selection, $q \ll 1$, and $(\tilde{\gamma}_{2se})_t \approx \gamma_t$.

Minimization of $\sigma_r(\tau)$

The contribution to the Allan variance due to thermal noise at the maser receiver is given by Eq. 1. σ_r^2 is affected by the properties of the maser's receiver system through the noise figure F and noise bandwidth B , and by the maser's operating conditions through the beam power P and rf coupling factor β . One approach to reducing σ_r^2 is by reducing the noise figure and bandwidth. In practice this generally means narrowing the receiver's lock-loop bandwidth and employing a low-noise preamplifier. σ_r^2 can also be reduced by adjusting the maser's beam flux and the cavity's coupling constant β . The conditions for minimum value are established straightforwardly by setting the partial derivatives of Eq. 1 with respect to x and β equal to zero. The optimum value of flux is

$$\tilde{x}_r = \frac{1 - 3q}{4q} \quad (14)$$

For $q = 0.08$, a typical value using a traditional state selector, Eq. 14 gives $\tilde{x}_r = 2.38$, a level of flux that is difficult to achieve in practice due to limitations imposed by beam optics and scattering.

The optimizing value of β , for a value of $q_0 \sim 0.08$, is $\beta \simeq 14$. Such a large value of β would reduce the loaded cavity Q below the value required for oscillation, so that the optimizing value of β is unattainable. Then, to reduce σ_r^2 as much as possible, β should be made as large as possible consistent with the requirement for maser oscillation.

Characterization of Systematic Portion of Allan Variance

The expressions above for the Allan variance and the maser's operating conditions allow one to calculate the consequences of adjusting the various operating parameters. The mechanisms σ_r^2 and σ_t^2 contribute to the Allan variance for short ($< 10^2$ sec) and intermediate ($\sim 10^2$ to 10^5 sec) averaging times. To include the contributions of systematic effects, which dominate the stability for longer averaging times, one must model the long-term Allan variance. $\tau^{1/2}$ behavior, which has often been observed, is characteristic of random walk of frequency. As is shown in the later discussion of systematic processes, cavity pulling is a substantial source of systematic maser frequency variation. Maser frequency variations due to cavity pulling are proportional to the ratio (Q_c/Q_t) . Consequently we model the random walk component of σ by

$$\sigma_{RW}^2 = \xi \left(\frac{Q_c}{Q_t} \right)^2 \tau \quad (15)$$

Long-term measurements of a pair of VLG-11 masers give the value $\xi \left(\frac{Q_c}{Q_l} \right)^2 \sim 9 \times 10^{-36} \text{ sec}^{-1}$ for masers with $Q_c \sim 39 \times 10^3$ and $Q_l \sim 2 \times 10^9$; thus a reasonable value of ξ for comparison purposes is

$$\xi \sim 2.4 \times 10^{-26} \text{ sec}^{-1} \quad (16)$$

We shall assume that for masers with other values of Q_c and Q_l , σ_{RW}^2 scales according to Eq. 15, with the value of ξ given by Eq. 16. Improved control of systematic frequency-pulling processes would be reflected in lower values of ξ .

Effect of Maser Operating Parameters on $\sigma(\tau)$

Using the expressions derived for the maser's operation we have calculated the Allan deviation $\sigma(\tau) = [\sigma_r^2(\tau) + \sigma_l^2(\tau) + \sigma_{RW}^2(\tau)]^{1/2}$ for a variety of operating parameters. The resulting graphs illustrate the benefits and tradeoffs that result from different choices of operating conditions.

To examine the effect of state selection, we consider a maser equipped with an adiabatic fast passage (AFP) state selection system. When the AFP system is off, $I_{tot}/I = 2$, and when the AFP system is on, the $F=1$, $m_F=1$ atoms are eliminated and $I_{tot}/I = 1$. Because q is proportional to I_{tot}/I , the AFP system reduces the value of q by half. Fig. 1 shows the calculated Allan deviation with the AFP system on and off. The values assumed for q_0 are typical of those measured in VLG-12 masers. For both curves we assume the flux is adjusted to give $x = 1$, approximately the value that minimizes $\sigma_l(\tau)$. (This assumption means that the total flux I_{tot} with AFP on would have to be twice as large as when AFP is off, in order to maintain the spin exchange relaxation rate γ_{se} equal to γ_l .) The curves show that, if the assumption $x = 1$ is satisfied, use of the AFP system would increase the frequency stability by a factor of approximately 2 for averaging intervals from 1 to about 10^3 seconds. The long-term stability is unaffected because γ_{sc} , and therefore the line Q, is constant under the assumption of constant x .

The effect of varying the beam flux, as measured by the parameter x , is shown in Fig. 2. Reducing x from 1 to 0.5 increases σ_l only slightly, because Q_l increases at the same time that P decreases. The deviation σ_r increases by about 30% due to the decrease in P , while σ_{RW} decreases by about 20% because Q_l increases. Reducing the flux substantially, to $x = 0.15$, increases σ_r by a factor of about 3, and σ_l by about twice, from their value for $x = 1$. These increases are due to the decrease in beam power and to the fact that the line Q decrease with flux is limited by the fixed value of γ_l . σ_{RW} is about 40% lower for $x = 0.15$ than for $x = 1$. We can see that a reduction of flux to the level of $x \sim 0.5$ would likely increase the long-term stability without substantially degrading the intermediate term stability from its optimum value.

Increasing the cavity coupling factor β decreases the loaded cavity Q and increases the rf power to the receiver. The decrease in Q_c reduces the cavity pulling effect, thereby improving the maser's long-term frequency stability, while the increase in receiver power

improves the stability for short averaging times. Increasing β also increases q , which decreases the beam power P , degrading the intermediate-term stability slightly. However, β cannot be increased indefinitely. In order for the maser to oscillate, the flux must be in a range set by the condition $P > 0$, which results in the limiting condition on q , $q < 0.172$. Using $q = q_0(1 + \beta)$ and $q_0 \sim 0.08$, typical for non-AFP operation, the limit on β is $\beta < 1.15$. For $\beta < 1.0$, the allowable range of flux reaches values accessible to both AFP and non-AFP operation. The effect of β on maser frequency stability is shown in Fig. 3 for $q_0 = 0.04$ (AFP on) and $x = 1$. Using a large coupling factor, $\beta = 1$, instead of a smaller value, $\beta \simeq 0.2$, improves the short-term stability at $\tau=1$ second by about 9%, degrades the intermediate term stability by about 15%, and improves the long-term stability by almost 40%, under the assumptions of our model.

The maser's long-term stability is determined by systematic processes. The stability can be improved by decreasing the sensitivity of maser components to external influences and improving their inherent long-term stability. Figure 4 shows the frequency stability improvement to be gained by decreasing the systematic effects by a factor of 2, assuming our model of a random walk of frequency proportional to the ratio Q_c/Q_L . We discuss below a variety of systematic processes that can affect maser frequency stability.

SYSTEMATIC EFFECTS on HYDROGEN MASER FREQUENCY STABILITY

A great many physical effects can result in systematic maser frequency variations. It is impossible in the space available to present an analysis of more than a few; rather, it is our intention to describe a systematic approach to such an analysis, and to summarize the results of a more extensive study. A detailed analysis of identified effects is given in reference 1.

To analyze systematic effects, one must identify three levels of physical effects: (i) basic physical processes that directly determine the maser's observed output frequency; (ii) transducing factors that can affect the basic frequency-determining processes; and (iii) driving mechanisms that can vary the transducing factors. Fundamental frequency-determining processes include the cavity's resonance frequency, internal magnetic field, and collisional and wall frequency shifts. In addition, phase variations in the maser's amplifying and phase locking circuits can change the observed output frequency. Transducing factors include the cavity dimensions, the storage bulb's dielectric coefficient, the internal magnetic field strength and gradients, the beam flux, the atomic state distribution, and the properties of voltage dividers. Finally, intrinsic driving mechanisms – those independent of the environment – include the creep of material dimensions over time, long-term voltage reference aging, and aging of magnetic shield domains, while environmental driving mechanisms include temperature, humidity, barometric pressure, magnetic fields, and vibration. As an example of the three-step identification process, we note that both material dimension creep, an intrinsic mechanism, and temperature, an environmental mechanism, can affect the dimensions of the resonant cavity and, through the mechanism of cavity pulling, the maser's frequency.

Many of the three-step processes can be described analytically. The procedure is as follows:

1. Identify the frequency determining mechanisms, such as cavity pulling or internal magnetic field intensity.
2. Express the maser frequency f as a function of the relevant driving variables X_i , such as temperature, time, or external magnetic field.
3. Calculate the frequency variation δf as a differential:

$$\frac{\delta f}{f} = \sum \frac{1}{f} \frac{\partial f}{\partial X_i} \frac{\partial X_i}{\partial X_j} \delta X_j \quad (17)$$

4. Calculate or measure the sensitivities $\partial f / \partial X_i$ (e.g., $\partial f / \partial T_{\text{cavity}}$).
5. Estimate or measure the driving functions δX_j (e.g., δT_{cavity}).

As an example of this analytic approach, consider maser frequency variations due to changes in the cavity's resonance frequency that result from changes in the cavity's dimensions. Mechanisms that can affect the dimensions include bulk thermal expansion or contraction of the cavity's structural material, expansion or contraction of the cavity's metallic coating, relaxation of the coating's internal stress, and contraction of the cavity's joints with time. The driving mechanisms are time and cavity temperature. The maser frequency variation due to these mechanisms can be written as

$$\delta f_c = \left[\frac{\partial f_c}{\partial R} \frac{\partial R}{\partial T} + \frac{\partial f_c}{\partial L} \frac{\partial L}{\partial T} + \frac{\partial f_c}{\partial \sigma_s} \frac{\partial \sigma_s}{\partial T} \right] \delta T + \left[\frac{\partial f_c}{\partial \sigma_s} \frac{\partial \sigma_s}{\partial t} + \frac{\partial f_c}{\partial L} \frac{\partial L}{\partial t} \right] \delta t \quad (18)$$

Here R and L are the cavity's radius and length, σ_s is the coating's internal surface stress, T is the cavity's temperature, and t is elapsed time.

We consider those terms involving thermal expansion of the bulk cavity material. It can be shown that the fractional change in resonance frequency with temperature is given by

$$\frac{1}{f_c} \frac{df_c}{dT} = -\alpha \quad (19)$$

where α is the linear coefficient of expansion of the cavity material, assumed to be isotropic. Consequently, the maser frequency varies with temperature, due to bulk expansion, as

$$\frac{1}{f} \frac{\partial f_o(\text{bulk})}{\partial T} = -\alpha \left(\frac{Q_c}{Q_l} \right) = -\alpha \times 10^{-5} \quad (7)$$

for $(Q_c/Q_l) = 10^{-5}$, a typical value for SAO VLG-12 masers. The effect of bulk expansion on cavities made of different materials can readily be estimated. Table 1 gives the maser frequency variations expected to result from a cavity temperature variation of 10^{-5} °C for cavities made of low-expansion Cervit or Zerodur and of metals such as copper or aluminum.

Some processes that affect the maser's frequency are not amenable to calculation or measurement. An example are magnetic field effects. The maser frequency is affected by the average magnetic field intensity in the storage bulb through the quadratic hyperfine level dependence on magnetic field^[7] – the Breit-Rabi – shift, and also by magnetic field gradients through collisional (Crampton-Verhaar) shifts^[8]. While the field magnetic intensity, which drives the Breit-Rabi shift, can be measured, the internal field gradients, which affect the collisional shifts, are difficult or impossible to calculate or measure. However, the atomic state distribution in the beam, which also affects the collisional shifts, is both measurable and controllable, through single-state selection. If all atoms are in the "c" state, the collisional shifts are predicted to be zero. Fig. 5 shows measured sensitivities to external magnetic field variations with an AFP system both off and on. The solid lines represent the value of $\partial f / \partial B$ predicted by the Breit-Rabi equation from the measured change in field intensity. It is clear that use of single-state selection substantially eliminates the collisionally-induced field sensitivity.

Summary of Systematic Effects

An examination of a substantial number of systematic effects^[1] is summarized in Fig. 6. The calculations assume attainable values of environmental driving functions and maser sensitivities; for example, control of the maser cavity to 10^{-5} °C is assumed. Solid lines indicate ranges of variables that are fairly well understood, while dashed lines indicate ranges that could occur if special care is not taken. Dotted lines represent variables whose behavior is not well characterized. In particular, the long-term constancy of the wall shift is an area needing careful investigation.

It will be seen that most known effects are at the low 10^{-16} level. Thermal changes in storage bulb dielectric coefficient, possible cavity dimensional aging, and possible external magnetic field variations are predicted to predominate at that level. Improving the stability below 1 part in 10^{16} will clearly require attention to many effects simultaneously.

ACKNOWLEDGEMENT

This work was supported by the Jet Propulsion Laboratory.

References

1. The material in the present paper is discussed more extensively in work sponsored by the Jet Propulsion Laboratory and reported in: E.M. Mattison and R.F.C. Vessot, Final Report on JPL contract 958019, "A study on the feasibility of development of a state-of-the-art hydrogen maser," October, 1989.
2. Allan, D.W., "Statistics of atomic frequency standards," *Proc. I.E.E.E.* 54, 221-230 (1966).

3. D. Kleppner, H.C. Berg, S.B. Crampton, N.F. Ramsey, R.F.C. Vessot, H.E. Peters and J. Vanier, "Hydrogen maser principles and techniques," *Phys. Rev. A* **138**, 972 (1965).
4. R.F.C. Vessot, L. Mueller, and J. Vanier, "The specification of oscillator characteristics from measurements in the frequency domain." *Proc. I.E.E.E.* **54**, 199-207 (1966). See also W. A. Edson, "Noise in oscillators," *Proc. IRE* **48**, 1454-1456 (1960).
5. Berlinsky, A.J., and Hardy, W.N., in *Proc. of 19th Annl. Precise Time and Time Interval Meeting*, U.S. Naval Research Laboratory, December 1-3, 1981, pp. 542-562.
6. J. Vanier and C. Audoin, *The quantum physics of atomic frequency standards*, Adam Hilger, Philadelphia (1989).
7. N.F. Ramsey, "Molecular Beams," Clarendon Press (1956). P.86.
8. J.M.V.A. Koelmann, S.B. Crampton, H.T.R. Stoof, O.J. Luiten and B.J. Verhaar, "Spin exchange frequency shifts in cryogenic and room temperature hydrogen masers," *Phys. Rev. A*, **35**, 3825 (1987).

Cavity Material	α ($^{\circ}\text{C}^{-1}$)	$(1/f)(\partial f_0/\partial T)$ ($^{\circ}\text{C}^{-1}$)	$\delta f/f$ ($\delta T=10^{-5}$ $^{\circ}\text{C}$)
Cervit or Zerodur	-1×10^{-7}	1×10^{-12}	1×10^{-17}
Copper or Aluminum	$+2 \times 10^{-5}$	-2×10^{-10}	2×10^{-15}

Table 1. Frequency Variations Due to Cavity Bulk Expansivity

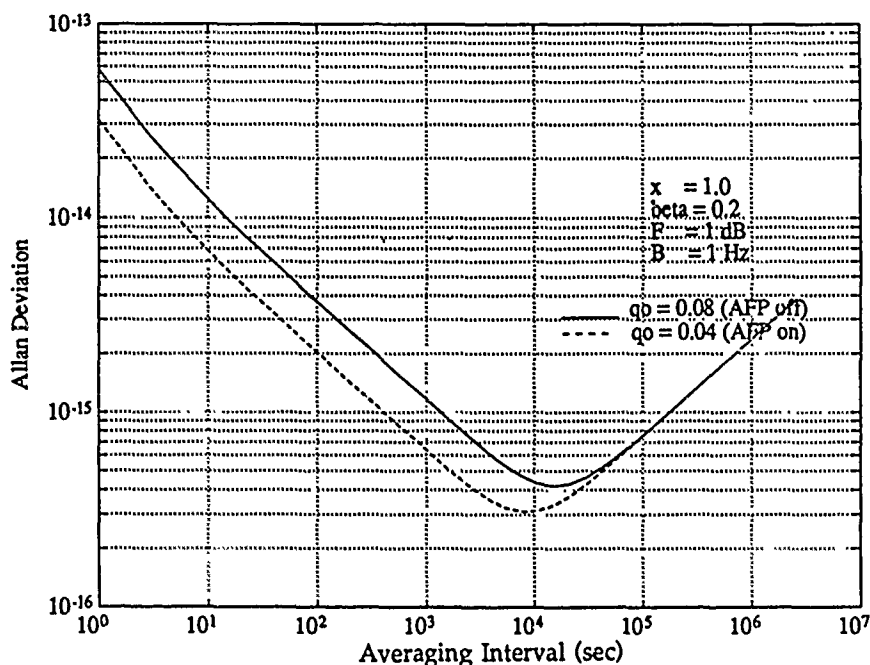


Fig. 1. Effect of State Selection on Frequency Stability

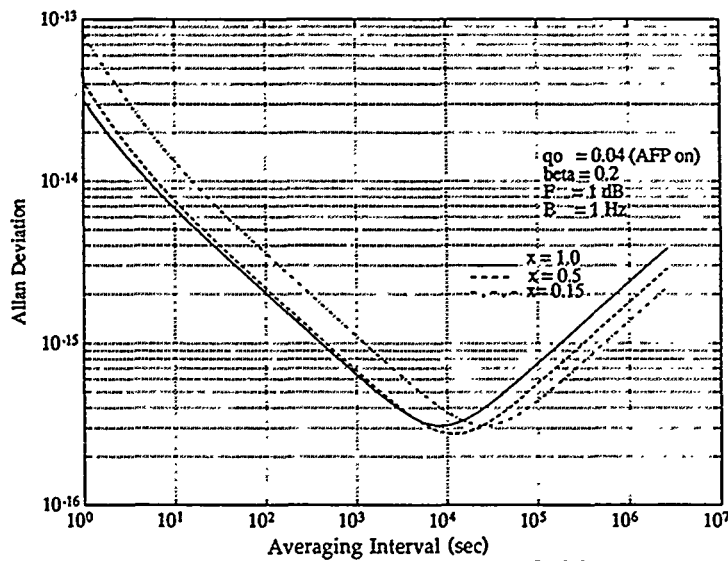


Fig. 2. Effect of Beam Flux on Frequency Stability

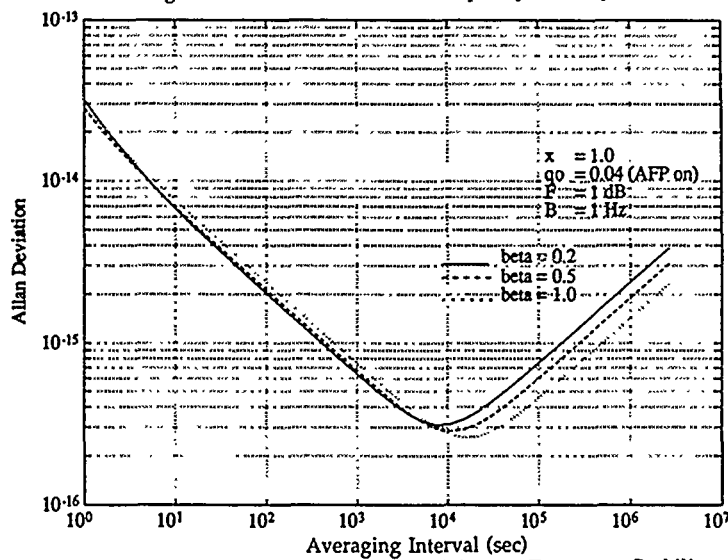


Fig. 3. Effect of RF Coupling Coefficient on Frequency Stability

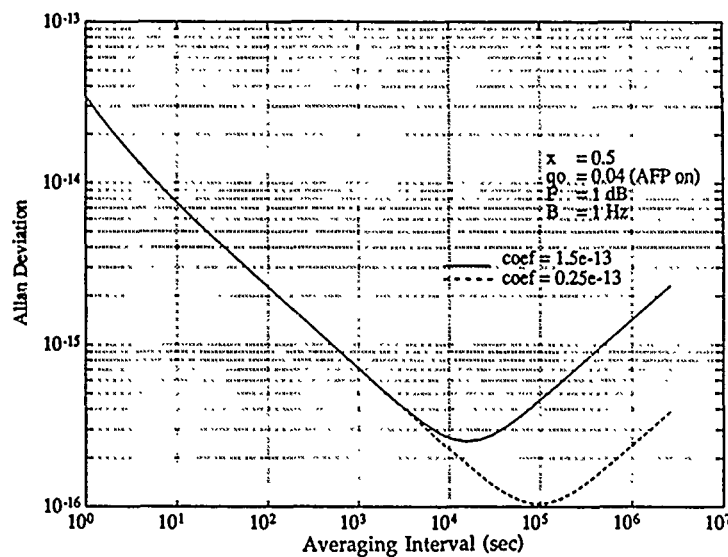


Fig. 4. Effect on Frequency Stability of Reducing Random-Walk Coefficient

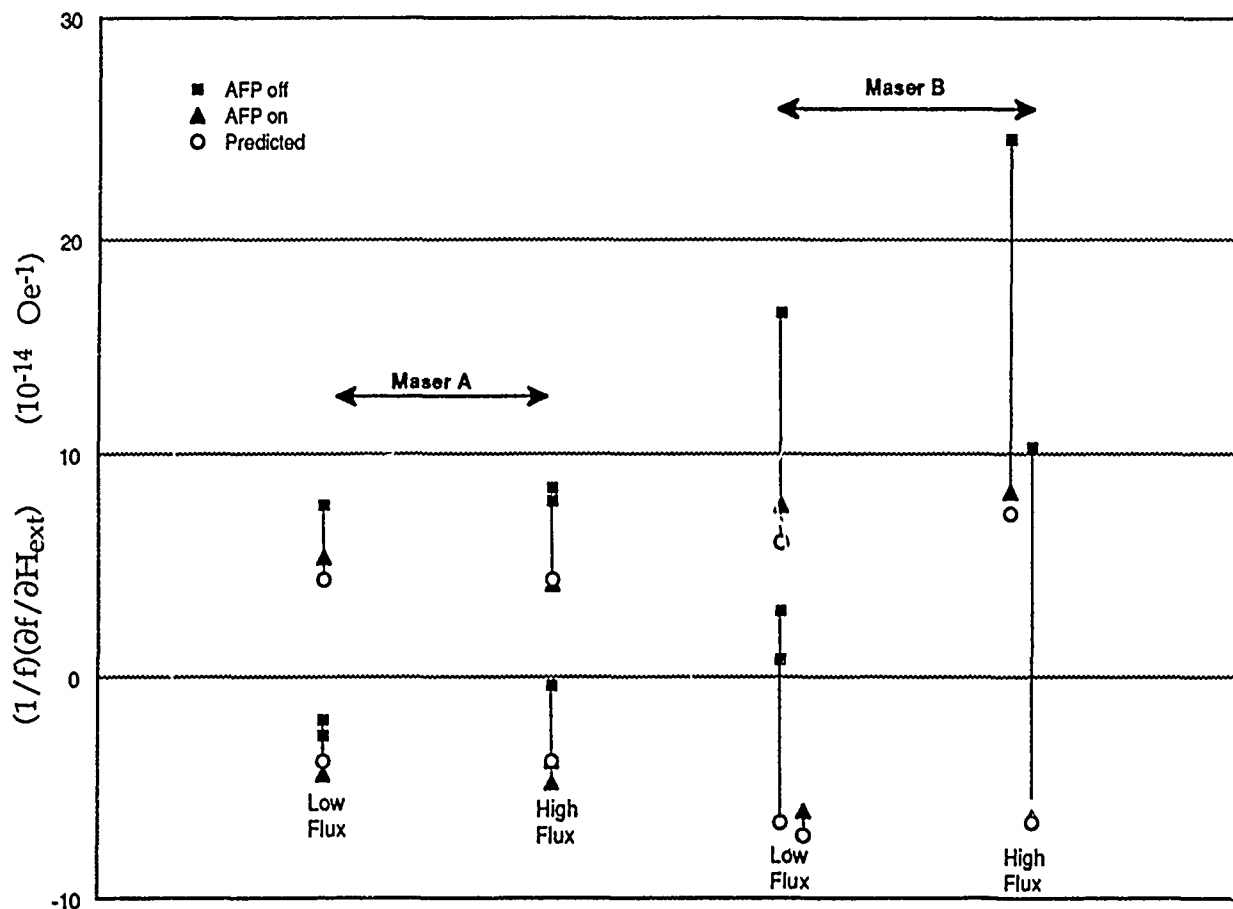


Fig. 5. Effect of State Selection on Magnetic Sensitivity

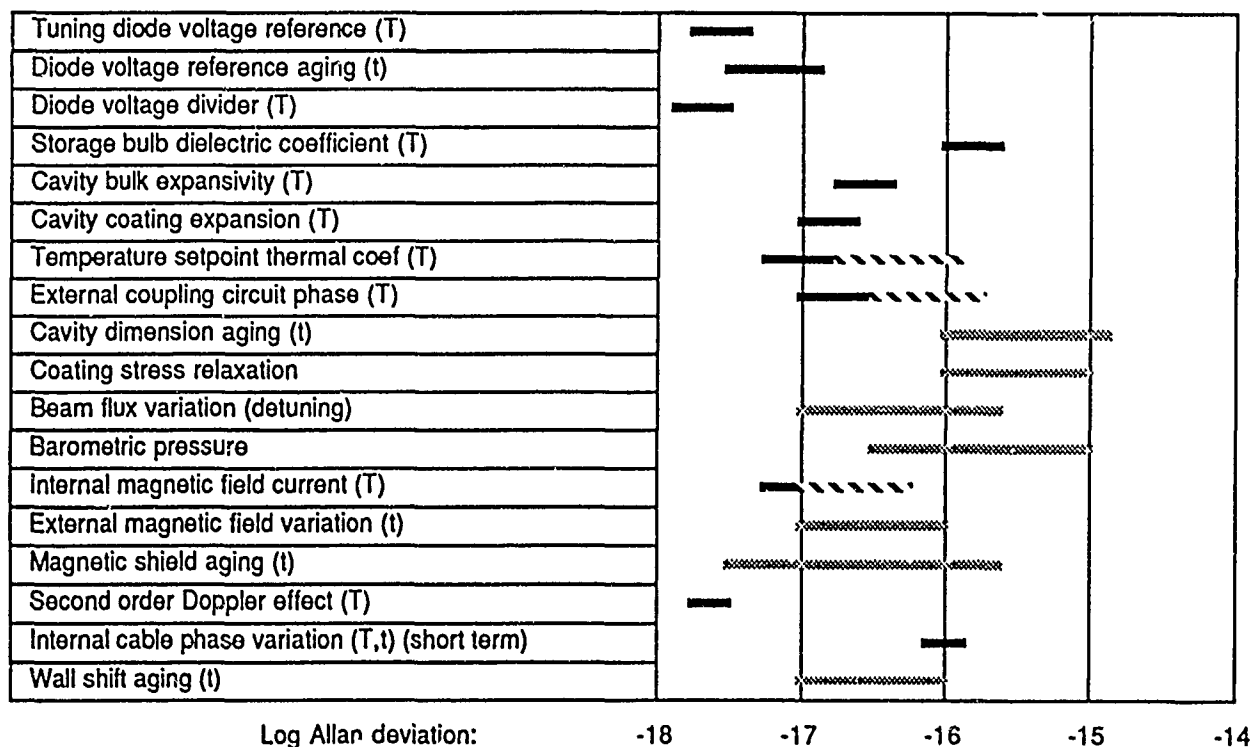


Fig. 6. Summary of Systematic Effects on Maser Frequency Stability

QUESTIONS AND ANSWERS

JACQUES VANIER, NRC: You have built several masers over the years. Different masers have different line Q's. Could you comment on the correlation between the line Q and the long term stability? Does it depend on the line Q or on all these other parameters.

MR. MATTISON: Until recently, most of our masers have had line Q's between 1 and 2 times ten to the ninth. It is only recently, with the VLG12 masers that we have had line Q's of 5 times ten to the ninth. We really don't have good measurements of the long term stability of them yet. They are now at USNO and that is where we are going to find out. I assume that Dr. Winkler will let us know about their long term stability.

TOM ENGLISH, BALL CORP.: I noticed on your last view graph that you had a mechanism called 'dielectric constant of the storage bulb'. Could you just say a few words about that?

MR. MATTISON: In the maser the storage bulb is made of quartz which acts to load the cavity. The dielectric constant of the quartz changes with temperature and therefor changes the resonant frequency of the cavity. That is quite a significant effect. **HARRY PETERS, SIGMA TAU:** I just wanted to say that some of the considerations of optimization relative to power output, cavity Q etc. do not necessarily apply to all configurations of hydrogen masers. If you have a cavity switching servo such as ours have, your signal-to-noise ratio for your servo system depends on your amplitude of oscillation and the power coupled out. Therefor, you tune more precisely with more power out and you might want to use a much higher Q cavity than if you were not tuning this way. There are a few other parameters which may differ if you are considering other automatic tuning systems.

MR. MATTISON: With any analytic approach such as this, the results depend on the model that you are using. Clearly, as you say, if tuning is another process involved, you have to include that in the calculation. It was not including here.

MICROCOMPUTER-COMPENSATED CRYSTAL OSCILLATOR FOR LOW-POWER CLOCKS

S. S. Schodowski, R. L. Filler,
J. A. Messina, V. J. Rosati and J. R. Vig
U. S. Army Electronics Technology and Devices Laboratory
Fort Monmouth, New Jersey 07703-5000

Abstract

Temperature-compensated crystal oscillators (TCXO) are widely used in applications requiring precision frequency control or timing, especially when power availability is limited and the temperature range is wide. The best overall accuracy in wide temperature range (e.g., -55°C to $+85^{\circ}\text{C}$) TCXO has remained at about 1 ppm for the past 30 years because of thermal hysteresis, the trim effect, and thermometry inaccuracies.

In this paper a microcomputer-compensated crystal oscillator (MCXO) is described. This MCXO employs external compensation, i.e., there is no frequency "pulling". It thus permits the use of a low-hysteresis, low deviation-sensitivity SC-cut crystal in a non-trimmed oscillator. Resonator self-temperature-sensing, using a dual-mode oscillator, virtually eliminates thermometry-related errors. As a consequence, all basic TCXO limitations are overcome or significantly reduced. The MCXO incorporating this technology is capable of providing at least 10- to 100-times improvement in overall frequency accuracy when compared to conventional TCXO. Milliseconds-per-day timekeeping accuracy, with an input power of less than 40 milliwatts, is now available.

INTRODUCTION

Temperature-compensated crystal oscillators (TCXO) are widely used in applications requiring precision frequency control or timing, especially when power availability is limited and the temperature range is wide. The best overall accuracy in wide temperature range (e.g., -55°C to $+85^{\circ}\text{C}$) TCXO has remained at about 1 ppm for the past 30 years because of thermal hysteresis, the trim effect, and thermometry inaccuracies.

Conventional TCXO are based on a method of "pulling" the crystal frequency, typically via a varactor, to counteract the crystal's frequency *vs* temperature (*f vs T*) deviation. This approach requires a high frequency-deviation-sensitivity resonator, i.e., a fundamental mode AT-cut, which usually possesses thermal hysteresis in the 0.2 ppm to 1.0 ppm range. The high deviation-sensitivity, however, also makes the TCXO susceptible to significant frequency error resulting from the thermal hysteresis and aging of circuit components. TCXO trim effect is the degradation (rotation) of the compensated *f vs T* characteristic when the output frequency is adjusted to correct for frequency aging. This

effect, which cannot easily be corrected by ordinary circuit means, typically produces a 0.1 to 0.5 ppm error for a frequency adjustment range of ± 3 ppm. Temperature sensing in a TCXO relies on one or more thermistors placed close to the resonator. This method suffers from inaccuracies due to thermal lag (thermal path differences and unequal crystal and thermistor thermal time constants), thermal gradients across the crystal and between the crystal and thermistor (thermistor location and self-heating), and thermistor instability.

In this paper we describe a microcomputer-compensated crystal oscillator (MCXO). This MCXO employs external compensation, i.e., there is no frequency "pulling". It thus permits the use of a low-hysteresis, low deviation-sensitivity SC-cut crystal in a non-trimmed oscillator. Resonator self-temperature-sensing, using a dual-mode oscillator, virtually eliminates thermometry-related errors. As a consequence, all basic TCXO limitations are overcome or significantly reduced. The MCXO incorporating this technology is capable of providing at least 10- to 100-times improvement in overall frequency accuracy when compared to conventional TCXO. Milliseconds-per-day timekeeping accuracy, with an input power of less than 40 milliwatts, is now available. More detailed descriptions of the MCXO can be found in references 1 to 6.

RESONATOR SELF-TEMPERATURE-SENSING

Simultaneous excitation of a resonator in two modes provides a means for the resonator to sense its own temperature. Previously, the only means available for resonator self-temperature-sensing was the b-mode of an SC-cut crystal when used in a dual b- and c-mode oscillator. However, the b-mode is not well-behaved over a wide temperature range due to a high incidence of frequency and resistance anomalies, i.e., activity dips.^[1] In the MCXO, a different resonator self-temperature-sensing method is being applied.^[2-4] This method uses a pair of c-modes of an SC-cut resonator in a dual c-mode oscillator. By employing an SC-cut, the c-modes are almost guaranteed to be free of activity dips over the full operating temperature range.^[1]

Self-temperature-sensing is based on the "harmonic effect" as illustrated in Figure 1. The harmonic effect is the change in the apparent orientation angle between harmonically related modes of a resonator. As shown, the effect progressively diminishes with increasing harmonic number M . For SC-cut resonators, the effect primarily manifests itself as a change in the first-order temperature coefficient of the polynomial

$$\frac{\Delta f_m}{f_m} = a_M \Delta T + b_M \Delta T^2 + c_M \Delta T^3 \quad (1)$$

where the normalized frequency, $\Delta f_M/f_M$, and the difference temperature, ΔT , are referenced at, e.g., 25°C, and a_M , b_M , and c_M , are the first-, second-, and third-order temperature coefficients of frequency at harmonic number M .

THE THERMOMETRIC BEAT FREQUENCY

In the illustration of Figure 2, the fundamental-mode frequency, f_1 , is multiplied by three and mixed with the third overtone frequency, f_3 , to obtain a beat frequency f_β , i.e.,

$$f_{\beta} = 3f_1 - f_3 \quad (2)$$

Alternatively, another beat frequency can be defined as

$$f'_{\beta} = f_1 - f_3/3. \quad (3)$$

Using the f vs T dependence of the two modes as given by Equation (1), the beat frequency may be described in normalized form as a function of temperature

$$\frac{\Delta f_{\beta}(T)}{f_{\beta}} = \frac{3a_1 - na_3}{3 - n} \Delta T + \frac{3b_1 - nb_3}{3 - n} \Delta T^2 + \frac{3c_1 - nc_3}{3 - n} \Delta T^3, \quad (4)$$

where a_1 , b_1 , c_1 , and a_3 , b_3 , c_3 are the temperature coefficients of frequency for the fundamental mode and third-overtone, respectively; n is the ratio of the frequencies for the harmonic pair at the reference temperature, i.e., $n = f_3/f_1$. A noninteger n is conveniently available, since the frequencies of harmonic modes of actual resonators are rarely exact multiples of each other. Values of n ranging from 2.94 to 2.98 are typical for a variety of SC-cut designs.^[1] Equation (4) then yields the temperature coefficients for the beat frequency. The first-order term dominates the higher-order terms for at least 100° above and below 25°C. Therefore, when a pair of modes is simultaneously excited in a dual-mode oscillator and combined a thermometric beat frequency is obtained, which can be used in an MCXO for compensating either of the c-mode frequencies.

A typical resonator's fundamental-mode and third-overtone frequencies are shown plotted against temperature in Figure 3. The apparent angle-of-cut change is evidenced by the shift of turning point from +5°C to approximately +45°C.

Figure 4 shows the temperature dependence of the beat frequency for the same SC-cut crystal unit. The f vs T curve is monotonic and nearly linear. For example, for a -55°C to +85°C temperature range, the maximum deviation from the best-fit straight line is about two percent of the total frequency change. The high degree of linearity permits approximating the slope by its first order temperature coefficient, which is -96 ppm/°C. Since n is usually in the range of 2.94 to 2.98, the temperature sensitivity ranges from -60 ppm/°C to -150 ppm/°C.

MCXO RESONATOR

Dual c-mode SC-cut resonators that are suitable for self temperature-sensing and MCXO application have been successfully developed.^[1] The major MCXO resonator requirements are:

- a. f vs T characteristic that is free of significant anomaly,
- b. minimum f vs T slope over the operating temperature range,
- c. high Q , and
- d. small hysteresis.

Plano-convex resonator designs of the proper contour were shown to be capable of meeting all requirements. Figure 5 shows the f vs T characteristics for an optimum-design resonator for a -55°C to +85°C operating temperature range. An optimum resonator f vs T characteristic is the one for

which the maximum f vs T slopes of the two modes are minimized. This condition is satisfied when the absolute value of the slope of the fundamental mode at the upper temperature extreme equals the slope of the third-overtone at the lower temperature extreme. For the -55°C to $+85^{\circ}\text{C}$ range, the absolute values of the maximum slopes are 2.7 ppm per $^{\circ}\text{C}$, which occur when the turnover temperature of the third-overtone is at about $+20^{\circ}\text{C}$. The exact condition for optimum f vs T is that the maximum f vs f_{β} slopes be minimized; however since f_{β} vs T is nearly linear, the difference between the two conditions is small.

FREQUENCY vs TEMPERATURE vs ANGLE OF CUT CHARACTERISTICS

It has been shown that the necessary angle-of-cut tolerances can be readily achieved with conventional cutting technology. For example, for the optimum -55°C to -85°C MCXO resonator (lower turnover temperature $\approx +20^{\circ}\text{C}$), a cutting error of 5 minutes results in an 8°C shift in the lower turnover temperature. For such an MCXO resonator, the rate of change in f vs T slope with lower turnover temperature is $0.043 \text{ ppm}/^{\circ}\text{C}^2$ at -55°C . Therefore, a -5 minute error increases the lower turnover temperature to $+28^{\circ}\text{C}$, which increases the slope at -55°C from the optimum $2.7 \text{ ppm}/^{\circ}\text{C}$ to $3.0 \text{ ppm}/^{\circ}\text{C}$. A +5 minute error causes a smaller maximum slope change at -85°C , since the rate of change in f vs T slope is $0.029 \text{ ppm}/^{\circ}\text{C}^2$ at -85°C . Therefore, in many MCXO applications, the angle-of-cut tolerance requirement may be loose enough for x-ray orientation and angle-correction to be unnecessary.

MCXO AND TCXO RESONATOR COMPARISON

Table I shows a comparison between resonators for the MCXO and for precision analog TCXO. Not only is the angle-of-cut tolerance looser for MCXO resonators, but so are the blank frequency and plating tolerances. For example, in one MCXO implementation,^[3] pulse deletion is used to generate an accurate time-corrected pulse train. The resonator target frequency during plating is chosen to ensure that the resonator frequency is above the nominal clock frequency at all temperatures. Therefore, there is no need to specify a tight plating tolerance. In fact, the accuracy achievable with "rough" plating may be sufficient; i.e., no frequency adjustment should be necessary if the rough plating is reasonably well controlled.

The hysteresis and aging are lower for MCXO resonators than for TCXO resonators because third-overtone SC-cut resonators are inherently more stable than the fundamental-mode AT-cut resonators usually used in wide-temperature-range TCXO. Another possible factor may be that the interface between the rough plating and the fine plating can be eliminated in MCXO resonators.

Hysteresis is the major limitation on the f vs T stability that is achievable with the MCXO. Although the majority of resonators exhibited hysteresis at the low 10^{-8} level, some were in the 10^{-9} range. This shows that MCXO's with an f vs T stability in the 10^{-9} , or better, range is a reasonable goal for the future. For that goal to be met, further research is needed to gain a better understanding of the mechanisms responsible for hysteresis.

THE DUAL-HARMONIC-MODE CRYSTAL OSCILLATOR (DHMXO)

Figure 6 shows one example of a dual-mode oscillator capable of generating the two c-mode frequencies. This DHMXO can be described as two separate oscillators sharing a crystal that operates at series resonance. A single section resembles that of the Butler or bridged-tee oscillator, and falls into the family of crystal oscillators characterized by the crystal current being essentially equal to the transistor emitter current. In this configuration, the crystal is grounded to facilitate design. In each gain loop, emitter degeneration provides negative feedback that is sufficient to reduce net loop gain below unity for all frequencies except the desired c-mode frequency, where the crystal branch impedance is a minimum. This condition is assured by the series tuned networks C_s , L_s , and C'_s , L'_s , which also serve to decouple the adjacent mode signal. Using this circuit, the coupled frequencies can be attenuated more than 50 dB below the primary output signal level. Positive feedback at each c-mode is provided by the phase-shifting PI-networks consisting of C_1 , C_2 , and L_3 and C'_1 , C'_2 , and L'_3 .

Simultaneous excitation of the c-modes can also be obtained with the single-gain-loop Colpitts-type DHMXO shown in Figure 7. Suppression of undesired SC-cut b-mode frequencies is accomplished by the network C_2 , L_2 , C'_2 , L'_2 , which is designed to appear capacitive, and which provides the correct phase shift for oscillation only at the two c-mode frequencies. Inherent nonlinearities in the transistor provide frequency multiplication and mixing such that the beat frequency is available at the collector output following filtering of the higher frequency components. Either the fundamental mode or third-overtone frequencies can be extracted at the emitter using a frequency selective amplifier. The single-gain-loop DHMXO offers lower parts count and lower input power than the double-gain-loop circuit. However, it does trade off the flexibility of independent control of crystal-current for each mode, and it limits stability coefficient optimization. These limitations can prevent the single-gain-loop DHMXO from achieving the high level of performance of the double-gain-loop design. However, use of the single-gain loop may be warranted in applications permitting somewhat lower temperature-sensing accuracy.

IMPLEMENTATION OF THE DUAL C-MODE METHOD

Implementation of the dual c-mode method is shown by the MCXO simplified block diagram of Figure 8. In this illustration, the thermometric beat frequency is the one defined in Equation 3. f'_β is divided by M to obtain a convenient value for gating a reciprocal counter with the third-overtone frequency as the input. The reciprocal counter produces a number, $N1$, that represents the temperature of the crystal. The divisor M serves to scale the $N1$ counter range, consistent with the required temperature-sensing resolution and the number of counter bits. This number, or temperature word, is read by the microcomputer and is used to compute a second number, $N2$, that programs the correction circuitry. Correction algorithms may consist of evaluation of a polynomial, or a look-up table using coefficients or table entries, respectively, that were stored in memory during the calibration process.

The authors' laboratory is sponsoring two contracts, using two different approaches, for implementation of the MCXO, at Frequency Electronics, Inc. (FEI), and at General Technical Services (GTS).

THE FEI MCXO

The basic MCXO in development at FEI employs pulse deletion.^[3] The SC-cut resonator frequency, f_1 or f_3 , is selected so that, at all temperatures, it is always greater than the required output frequency. This ensures that pulses can always be deleted from the pulse train to provide the required number of output pulses in each interval. If the calculated correction includes a fraction of a pulse, the remainder is stored in memory, and an additional pulse will be deleted when the remainder, which is adjusted in subsequent cycles, has reached or exceeded a full pulse.

Figure 9 is a more detailed digital control block diagram. There are two inputs, f_β (≈ 157 kHz) and f_1 ($\approx 3.3+$ MHz). At the start of each measurement interval both the 12 stage f_β counter and the 18 stage f_1 counter are reset to zero and started simultaneously. The microcomputer is set to detect 36 overflows of the f_β counter to get a 0.94 second gate time ($36 \times 2^{12}/157$ kHz = 0.94 s). The f_1 counter then contains the number N_c which is the remainder of $f_1/2^{18}$, i.e., f_1 modulo 2^{18} . The crystal resonator is manufactured to have a f vs T characteristic such that, over the intended temperature range, the number of overflows is always the same. For example, the resonator frequency can be between $12 \times 2^{18} = 3.145728$ MHz and $13 \times 2^{18} = 3.407872$ MHz which is a $\Delta f/f$ of 262 kHz (80,000 ppm, not a major manufacturing dilemma). The microcomputer uses N_c to compute N_d , the number of pulses that must be deleted during the next measurement interval. The variable-divide counter is loaded with N_d/f_1 so that a pulse is deleted each time the variable-divide counter overflows. The net result is a pulse train with average frequency f_o and missing pulses uniformly spaced in time.

Start-up time, i.e., the time interval between application of power and the first valid correction (pulse deletion), is about 3.5 seconds. The output signal, f_o , is a time-corrected pulse train that can be divided to produce a 1 pps time reference, or can be used directly to drive a clock. Because of the noise characteristics created by the pulse deletion process, additional signal processing is necessary to provide rf output useful for frequency-control applications. This can be accomplished, for example, by imparting the MCXO accuracy to a low-noise, low-cost, voltage controlled crystal oscillator via a phase-locked-loop (PLL). A prototype MCXO, with a phase-locked VCXO operating at 5 MHz, showed a phase noise of -100 dBc at 100 Hz and -140 dBc at 100 kHz.

Construction of the basic MCXO consists of an SC-cut lateral field crystal unit, custom hybrid dual-mode oscillator, CMOS microcomputer, and a 2,550-gate application specific IC (ASIC). The power consumed in each of the major assemblies for a compensated f_1 output and one-second update is:

Dual-mode oscillator	8 mW
Microcomputer	18 mW
ASIC	15 mW
	<hr/>
	41 mW

By extending the time between updates, e.g., to 60 seconds, the average input power can be made to approach the idle power of the MCXO, which is about 25 mW.

An even lower average input power, approaching 5 mW, can be obtained by combining the MCXO with a low-power clock.^[6] In this approach, illustrated in Figure 10, the MCXO is turned off, except when calibrating the low power clock. If the duty cycle is sufficiently low, the total input power will be almost independent of MCXO power. As in the previous approach, temperature variations between calibrations will affect the frequency, reducing the accuracy of the clock. Thus, there will be a trade-off between input power and accuracy, as shown in Figure 11. The low-power clock can reduce the

input power to 5 mW, but accuracy continues to decrease, reaching 70 milliseconds in 24 hours.

The FEI MCXO uses a Motorola MC1468705G2 microprocessor that has 2K of EPROM and 112 bytes of RAM.

THE GTS MCXO

In the MCXO developed at GTS^[4], f_β is used to generate a correction frequency with a direct digital synthesizer. The correction frequency is added to the third overtone frequency in a PLL to produce a temperature-stable 10 MHz output. In an alternative time-only mode, f_β is used to generate a constant 4 kHz, which is divided to produce a 1 pps clock output.

Referring to Figure 12, and assuming that the MCXO is set to the "frequency" mode, operation is as follows:

The temperature-dependent beat frequency, f_β'' , is the output of the digital mixer, with f_1 the fundamental-mode frequency and f_3 the 3rd overtone frequency. The mixer is configured such that

$$f_\beta'' = f_1/2 - f_3/6 = f_\beta'/2 \quad (5)$$

The output of the mixer, f_β'' , is divided by 2^{16} to produce a gate width of approximately 0.16 seconds for the 24 bit counter. The counter input is $f_3/2$, i.e., nominally 5 MHz. The number of f_β'' counts measured in the 0.16 seconds, N_1 , is equivalent to the period of f_β . N_1 is used by the microcomputer to determine the necessary correction from the stored calibration data. The microcomputer computes the number N_2 which sets the direct digital synthesizer (DDS). The DDS is driven by $f_3/32$ (≈ 312 kHz) and gives an output frequency of between 200 and 900 Hz. This frequency, Δf , is compared with the difference between a (10 MHz, AT-cut) VCXO and f_3 in the PLL. The error signal controls the VCXO so that the difference frequency is that computed by the microcomputer, i.e., the output is 10 MHz.

The third-overtone oscillator can operate equally well at an offset of up to -2500 Hz, so the plating target frequency of the SC-cut resonator can be 10 MHz -1500 Hz ± 100 ppm. Therefore, the resonator for the GTS MCXO can also be only rough-plated.

Since no pulse deletion is used, one would expect a clean spectrum. However, under the condition where the number N_2 is other than an integer power of 2, the DDS is likely to produce a periodic phase modulation that manifests itself as spurious sidebands on Δf . By judicious selection of the PLL bandwidth (approximately 10 Hz), the spurious sidebands will be suppressed and the VCXO output phase noise will be only slightly degraded in the region outside the loop bandwidth. Within the loop bandwidth the close-in noise is dominated by the short-term stability of the third-overtone frequency. The phase noise for the current design ($f_o = 10$ MHz) falls from -106 dBc at 10 Hz to -160 dBc at 50 kHz. The noise floor depends on the VCXO signal-to-noise ratio, i.e., a low noise floor requires a high crystal drive current. In the present VCXO, crystal current is about 1.5 mA.

To understand the operation of the "time" mode, refer again to Figure 12, with the switch set to "T". In this mode, the PLL, including the VCXO, is disabled to conserve power. Further, the third-overtone oscillator is activated only periodically, to update N_1 . In the time mode, the DDS is driven by $f_1/16$ (211 kHz, nominally), and N_2 is calculated to deliver a constant 4 kHz output. The 4 kHz is divided by 4,000 to give 1 pps. The long-term accuracy capability of the MCXO in the "time"

mode is nearly the same as in the "frequency" mode, i.e., about $\pm 1 \times 10^{-8}$. However because of the resolution of the DDS in the "time" mode, there is up to 4.7 microseconds of jitter. (The jitter in the "frequency" mode is less than 50 nanoseconds.^[7])

The GTS MCXO currently (December, 1989) uses an Intel 87C51FA microprocessor that has 8Kbytes of EPROM and 256 bytes of RAM on the chip. The internal EPROM holds the program, and the RAM is used as a scratchpad. A 128 byte EEPROM (an ICT93C46) is used to store the polynomials for the fundamental and third overtone frequencies. The aging-correction coefficient is also stored in the EEPROM, making aging correction nonvolatile.

Start-up time in either operating mode is approximately 2 seconds. In addition to the initial temperature measurement and correction computation periods, the start-up time in the frequency mode includes the acquisition time of the PLL, and in the clock mode, the period delay in providing the first 1 pps time tick in the divide by 4000 output stage.

MCXO PERFORMANCE TESTS

Four configurations of the MCXO^[5] were tested:

1. A packaged FEI MCXO consisting of a dual-mode oscillator, a microcomputer, and a gate array.^[3] We shall refer to this device as the MCXO, and report results for five samples.
2. A dual-mode oscillator design using a lateral-field resonator and hybrid circuit construction. The lateral field resonator was designed to eliminate the requirement for the b-mode suppression circuit in the oscillator. We will refer to this device as the LFR dual-mode oscillator, which is a component in the MCXO described in Configuration (1).
3. A dual-mode oscillator design using a thickness-field resonator.^[4] We will refer to this oscillator as the TFR dual-mode oscillator. We tested two samples of the TFR dual-mode oscillator. Each sample was tested with two resonators, one each from two manufacturers.
4. The dual-mode oscillator from configuration (3) with internal microprocessor compensation. Testing was performed by GTS.^[8]

F vs T PERFORMANCE

TEMPERATURE PROFILE

Details of the experimental setup and measurement methods can be found in reference no. 5.

MCXO F vs T

Figure 13 shows the results for a typical MCXO.

DUAL-MODE OSCILLATOR F vs T

It can be seen from Fig. 13 that the compensation can be improved with a simple "rotation," that is, a change in the first-order temperature coefficient in the compensation algorithm. The necessary

frequencies are available from the MCXO, so that compensation of the devices could be simulated on a desktop computer.

To perform the "simulated" compensation, we made a least-square fit of the set of data (f_β, f_1) to a 6th-order polynomial.

$$F(f_{\beta i}) = \sum_{p=0}^6 C_p(f_{\beta i})^p \quad (6)$$

We then computed the residuals R_i

$$R_i = f_{1i} - F(f_{\beta i}). \quad (7)$$

A plot of the residuals *vs* temperature is equivalent to an MCXO f *vs* T stability plot, assuming a perfect technique for applying the calculated correction, e.g., pulse deletion or numerical synthesis.

LFR DUAL-MODE OSCILLATOR F *vs* T

Figure 14 shows a typical plot of the residuals from a 6th order polynomial for the 5 LFR dual-mode oscillators. The algorithm does not take into account thermal history, therefore, it cannot eliminate hysteresis.

Even including the hysteresis, the f *vs* T stability is $\pm 2 \times 10^{-8}$. The probable cause for the difference between the MCXO results and the simulated compensation is that the MCXO was compensated midway in the manufacturing process. Subsequent manufacturing steps caused a change in the required compensation coefficients, possibly by changing circuit strays. In the future, improved manufacturing techniques should allow realization of the simulated compensation.

TFR DUAL-MODE OSCILLATOR F *vs* T

Figure 15 shows a plot of the residuals of a TFR dual-mode oscillator. The excellent results shown indicate that it is possible to obtain very low hysteresis.

AGING

All five MCXO's were placed into a temperature chamber and put through the sequence depicted in Figure 16. The duration of the aging segments was approximately 30 days. Figure 17 shows aging data for a typical MCXO. The dashed line is a linear approximation of the last several days of data. The value of the slope of the dashed line is given in the figure.

F *vs* T REPEATABILITY

Figure 18 is the superposition of 18 f *vs* T runs on MCXO 16723 taken over the course of 13 months. Two different temperature ranges (-55°C to $+85^\circ\text{C}$ and -46°C to $+68^\circ\text{C}$), two step sizes (2°C and

3°C), and three soak times (4, 12, and 30 minutes) were used. The performance of the MCXO appears to be independent of temperature range, soak time, and step size. Most important, there is no evidence of any f vs T aging, which would occur, e.g., if the aging of the two modes differed significantly.

SUMMARY AND CONCLUSIONS

A performance summary is given in Table II.

Whereas conventional TCXO accuracy has remained at about 1 ppm for the past 30 years, the MCXO now allows a temperature stability of 2×10^{-8} and an overall accuracy of $< 5 \times 10^{-8}$ for a -55°C to $+85^{\circ}\text{C}$ temperature range.

A thermometry method of using two c-modes in a dual-mode oscillator has been described. Its potential is now being realized in the development of high-performance MCXO having stabilities 10 to 100 times greater than that of analog TCXO. The method overcomes the limitations of existing temperature-compensation methods, is easy to implement, is microprocessor compatible, and makes possible a new generation of inexpensive, high-accuracy, low-power, temperature-compensated crystal oscillators.

REFERENCES

1. R. Filler and J. Vig, "Resonators for the Microcomputer Compensated Crystal Oscillator," Proc. 43rd Annual Symposium on Frequency Control, IEEE publication no. 89CH2690-6, 1989.
2. S. Schodowski, "Resonator Self-Temperature-Sensing Using a Dual-Harmonic-Mode Crystal Oscillator," Proc. 43rd Annual Symposium on Frequency Control, IEEE publication 89CH2690-6, 1989.
3. M. Bloch, M. Meirs and J. Ho, "The Microcomputer Compensated Crystal Oscillator (MCXO)," Proc. 43rd Annual Symposium on Frequency Control, IEEE publication 89CH2690-6, 1989.
4. A. Benjaminson and S. Stallings, "A Microprocessor-Compensated Crystal Oscillator Using an SC-Cut Third Overtone Resonator," Proc. 43rd Annual Symposium on Frequency Control, IEEE publication 89CH2690-6, 1989.
5. R. Filler, J. Messina and V. Rosati, "Frequency-Temperature and Aging Performance of Microcomputer-Compensated Crystal Oscillators," Proc. 43rd Annual Symposium on Frequency Control, IEEE publication no. 89CH2690-6, 1989.
6. M. Bloch, M. Meirs, J. Ho, J. Vig and S. Schodowski, "Low Power Timekeeping," Proc. 43rd Annual Symposium on Frequency Control, IEEE publication no. 89CH2690-6, 1989.
7. A. Benjaminson, private communication, October, 1989.
8. A. Benjaminson, private communication, December, 1989.

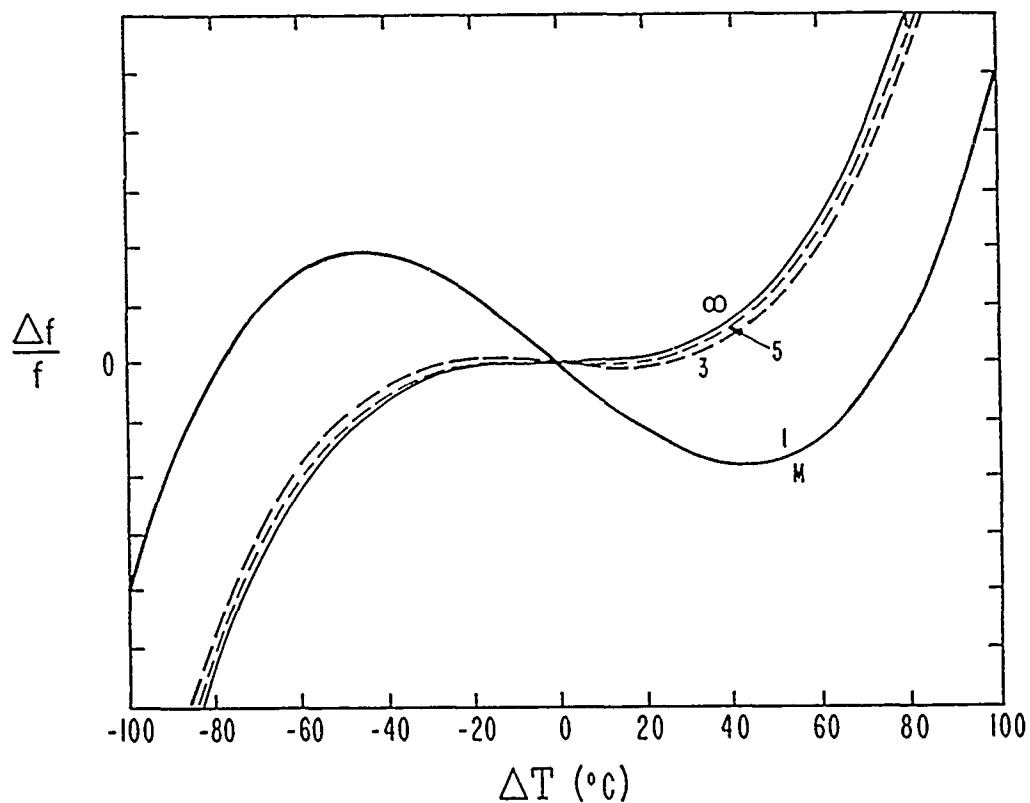


Figure 1. Frequency-temperature-harmonic characteristics of temperature-stable resonators.

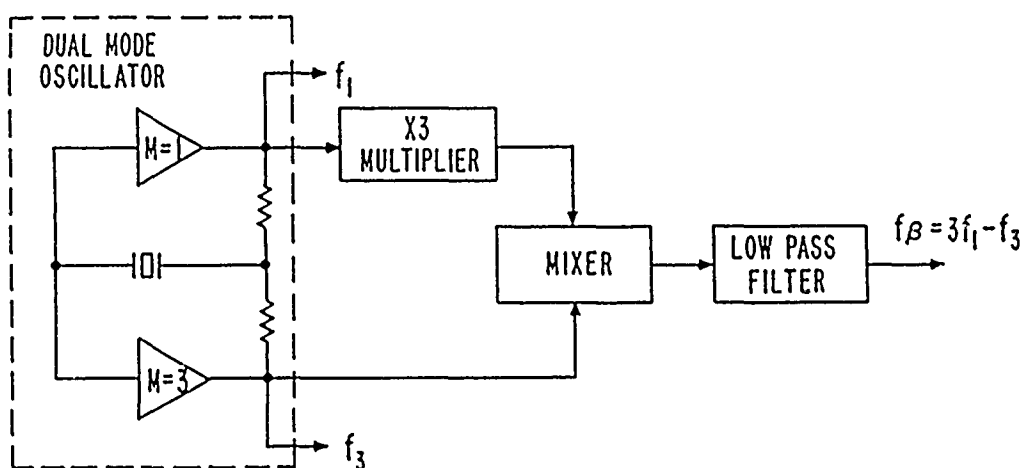


Figure 2. Illustration of the dual c-mode thermometry method.

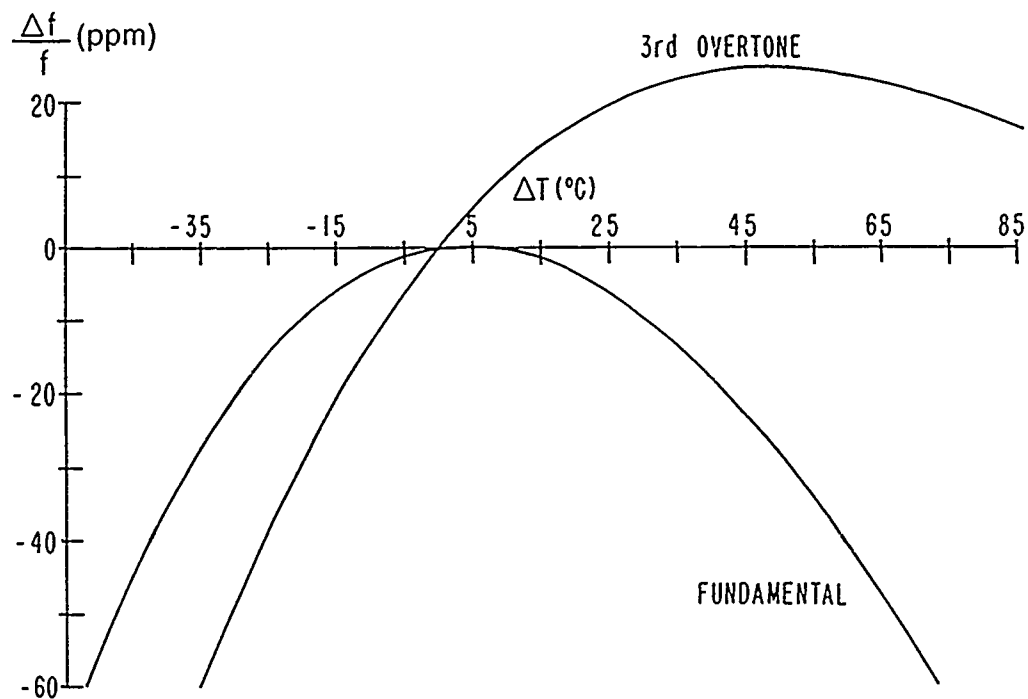


Figure 3. Fundamental and third-overtone characteristics of a typical SC-cut resonator.

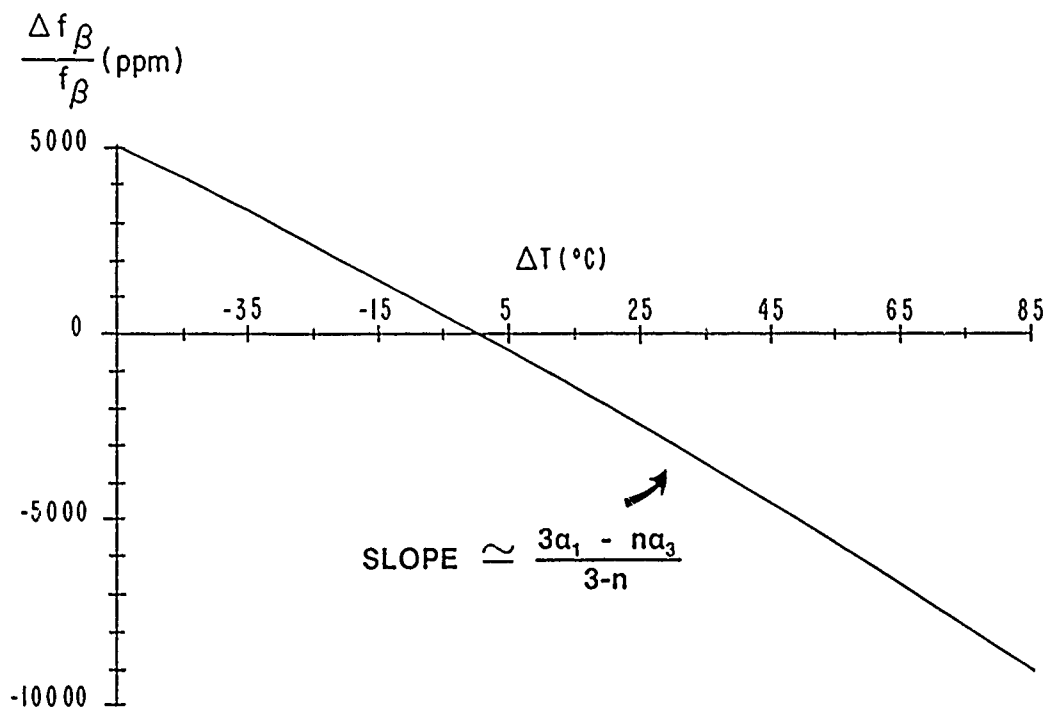


Figure 4. Temperature dependence of the beat frequency.

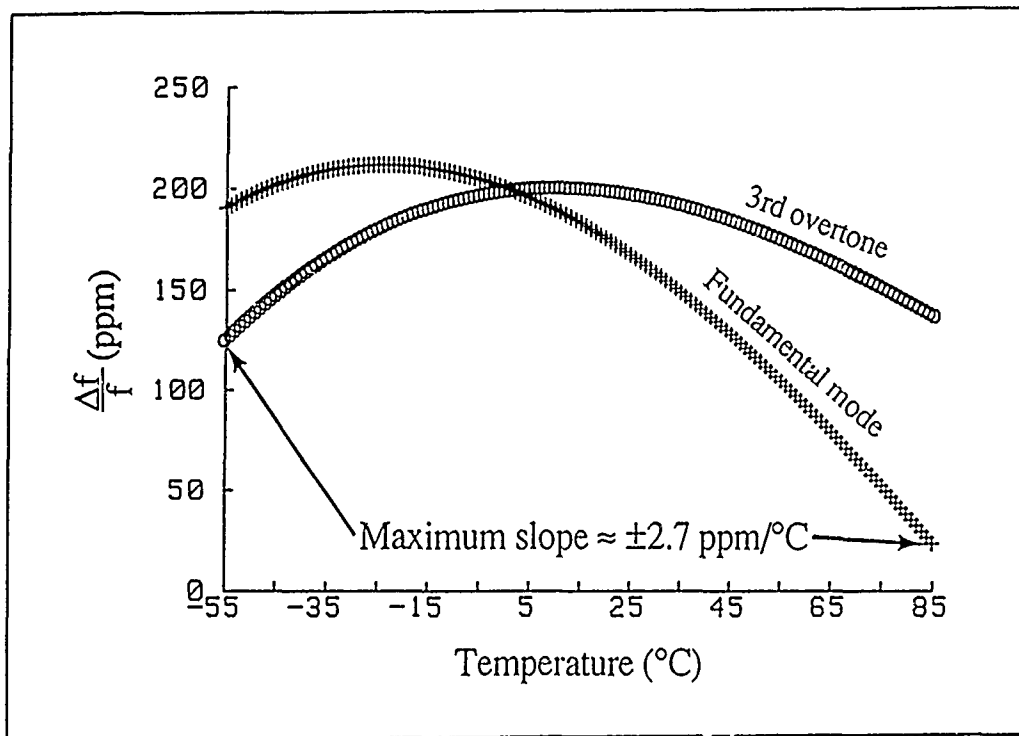


Figure 5. Optimum resonator f vs. T for -55°C to $+85^{\circ}\text{C}$ MCXO.

Table I
MCXO - TCXO Resonator Comparison

Parameter	MCXO	TCXO
Cut, overtone	SC-cut, 3rd	AT-cut, fund.
Angle-of-cut tolerance	Loose	Tight
Blank f and plating tolerance	Loose	Tight
Activity dip incidence	Low	Significant
Hysteresis (-55°C to $+85^{\circ}\text{C}$)	10^{-9} to 10^{-8}	10^{-7} to 10^{-6}
Aging per year	10^{-8} to 10^{-7}	10^{-7} to 10^{-6}

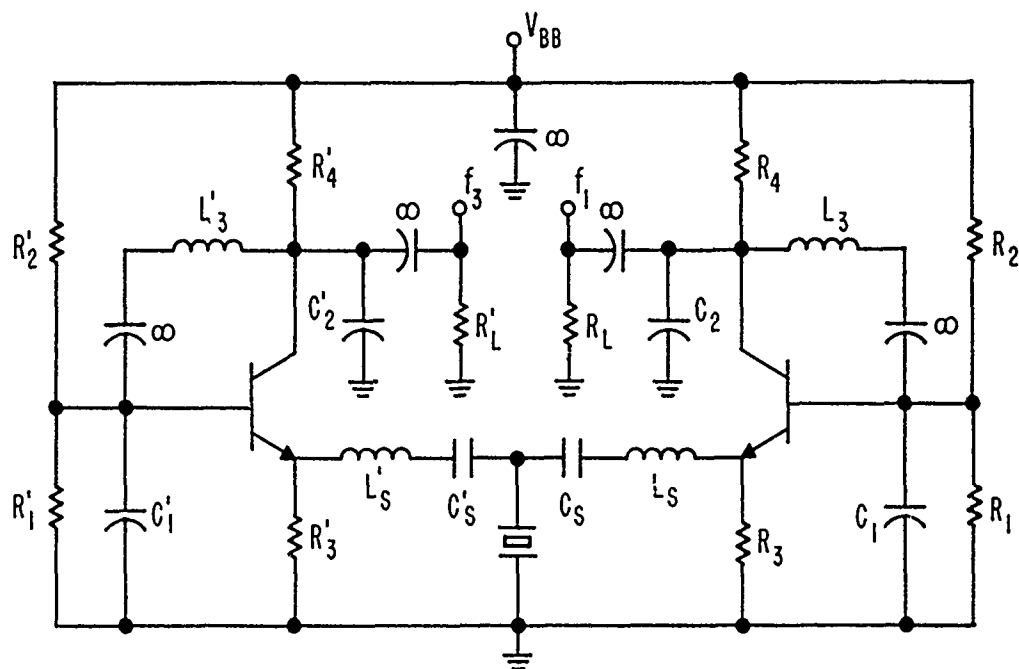


Figure 6. A double-gain-loop DHMXO (emitter degenerative type).

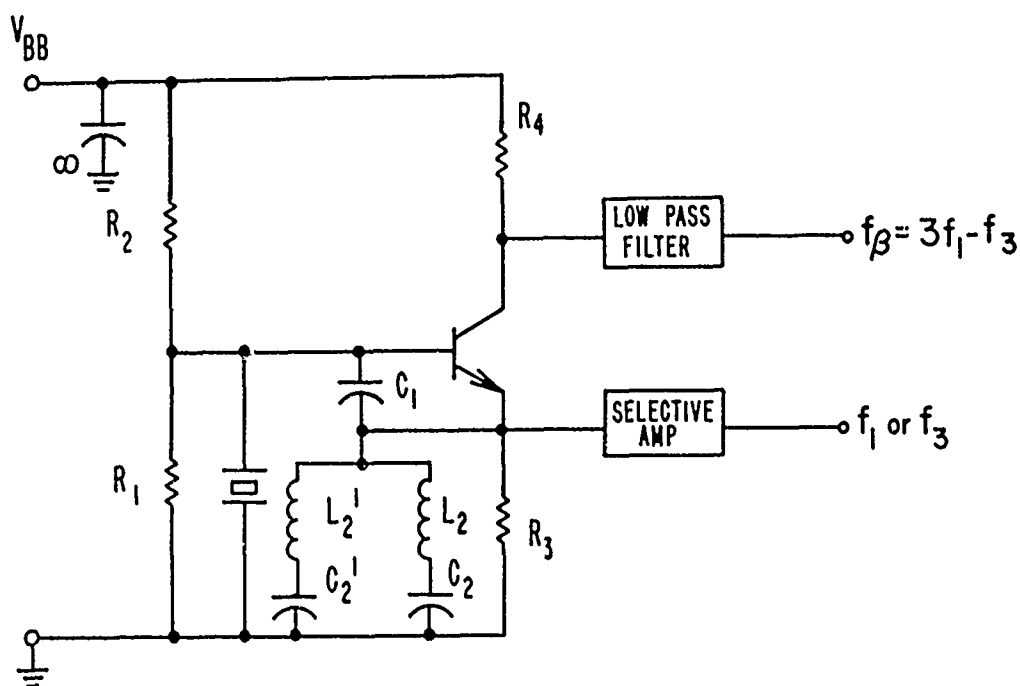


Figure 7. A single-gain-loop DHMXO (colpitts type).

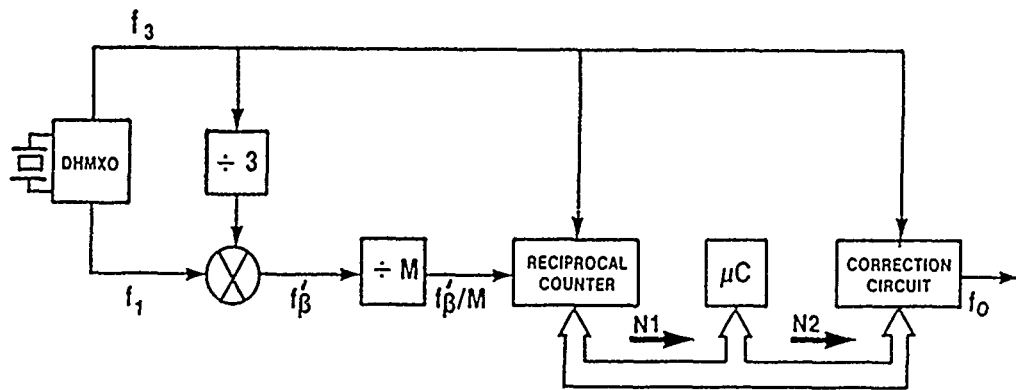


Figure 8. Typical implementation in an MCXO.

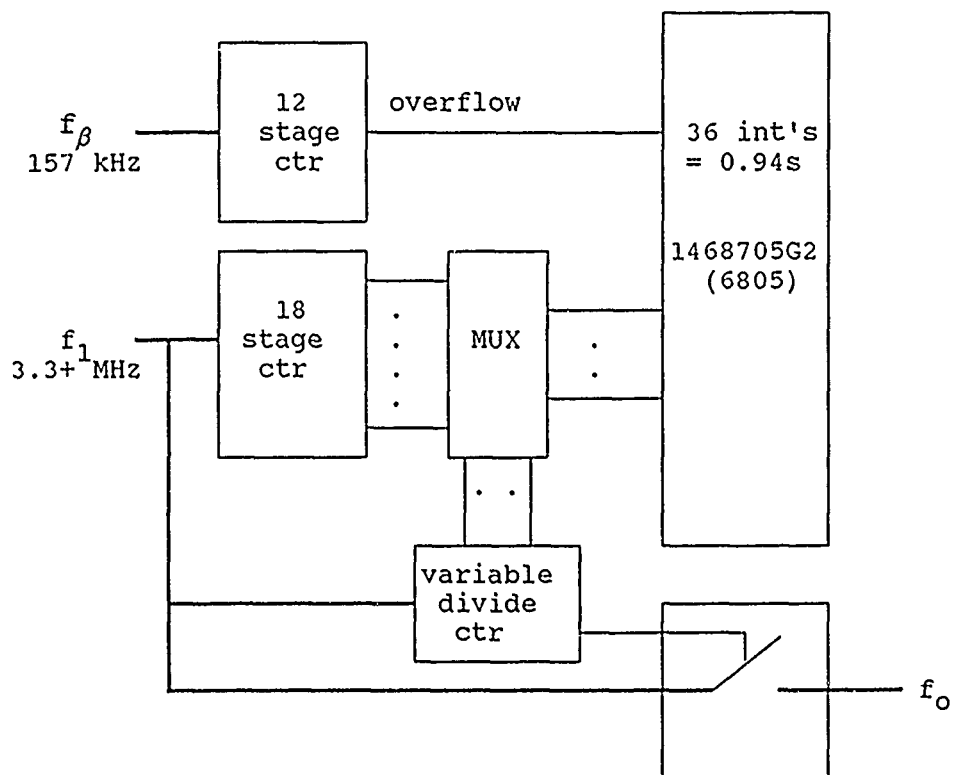


Figure 9. Digital control block diagram (pulse deletion).

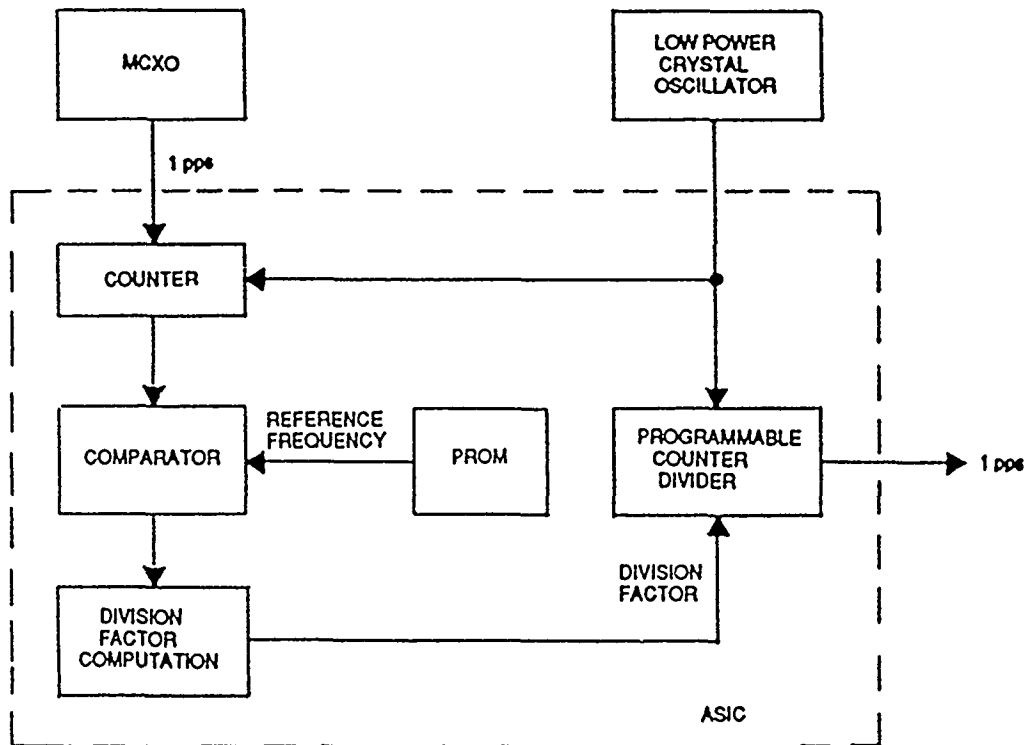


Figure 10. Low-power clock block diagram.

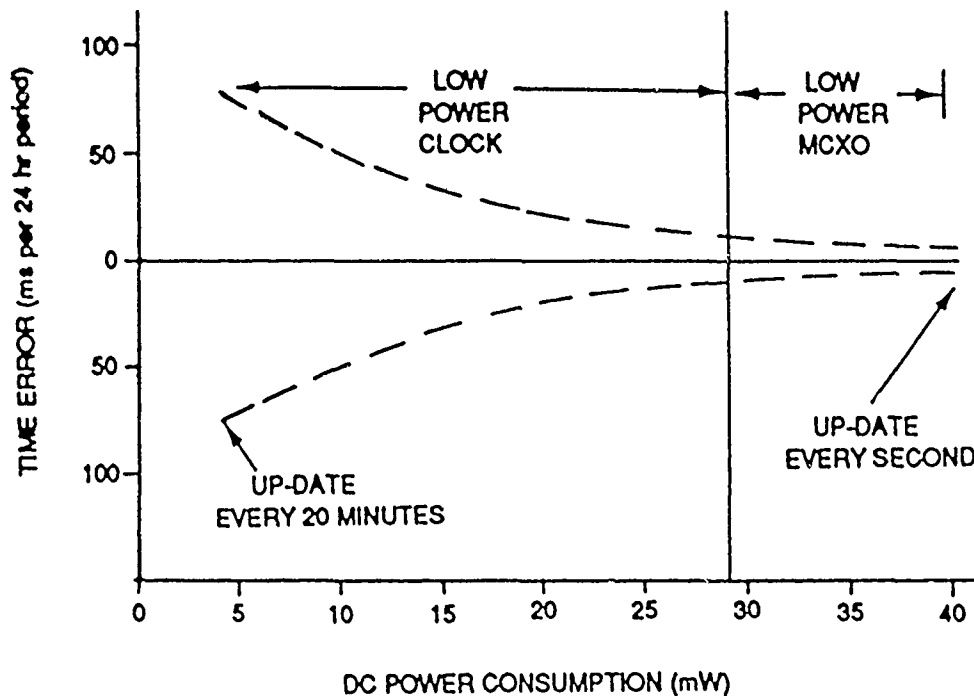


Figure 11. Timing error vs. power consumption.

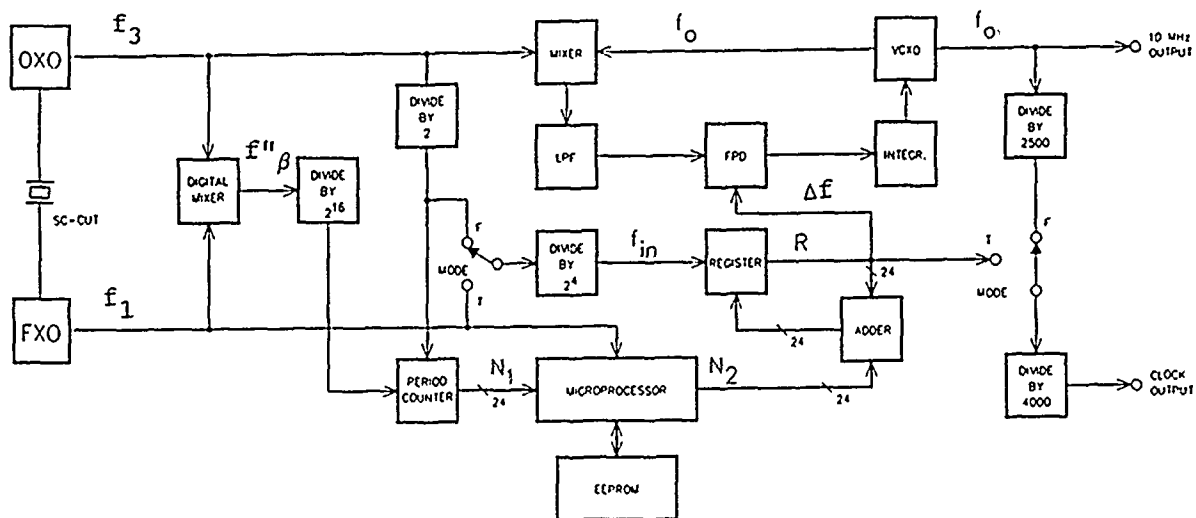


Figure 12. GTS MCXO block diagram.

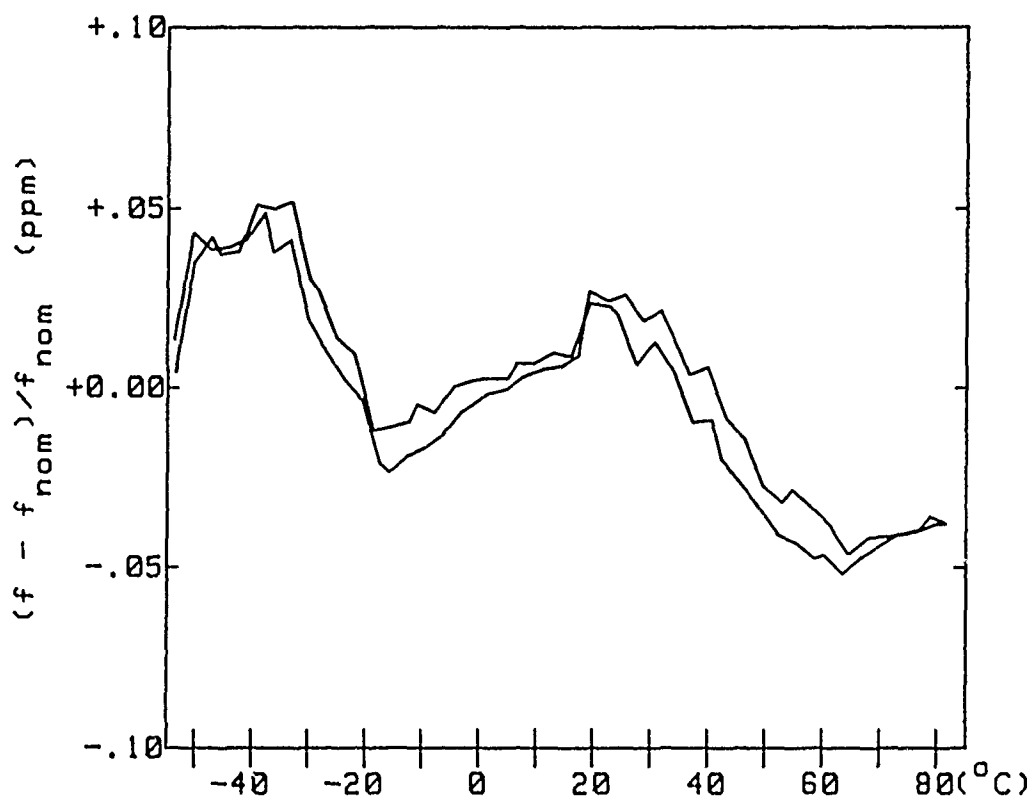


Figure 13. f vs. T characteristic of MCXO 16725.

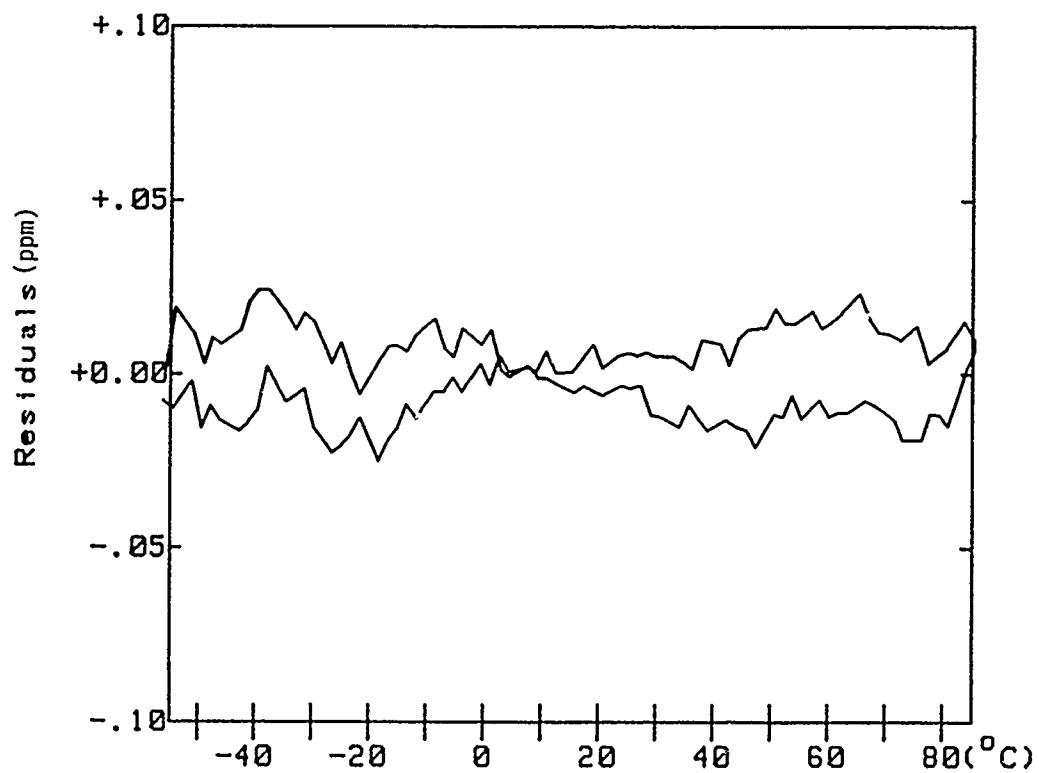


Figure 14. Residuals vs. temperature for the dual-mode oscillator in MCXO 16725.

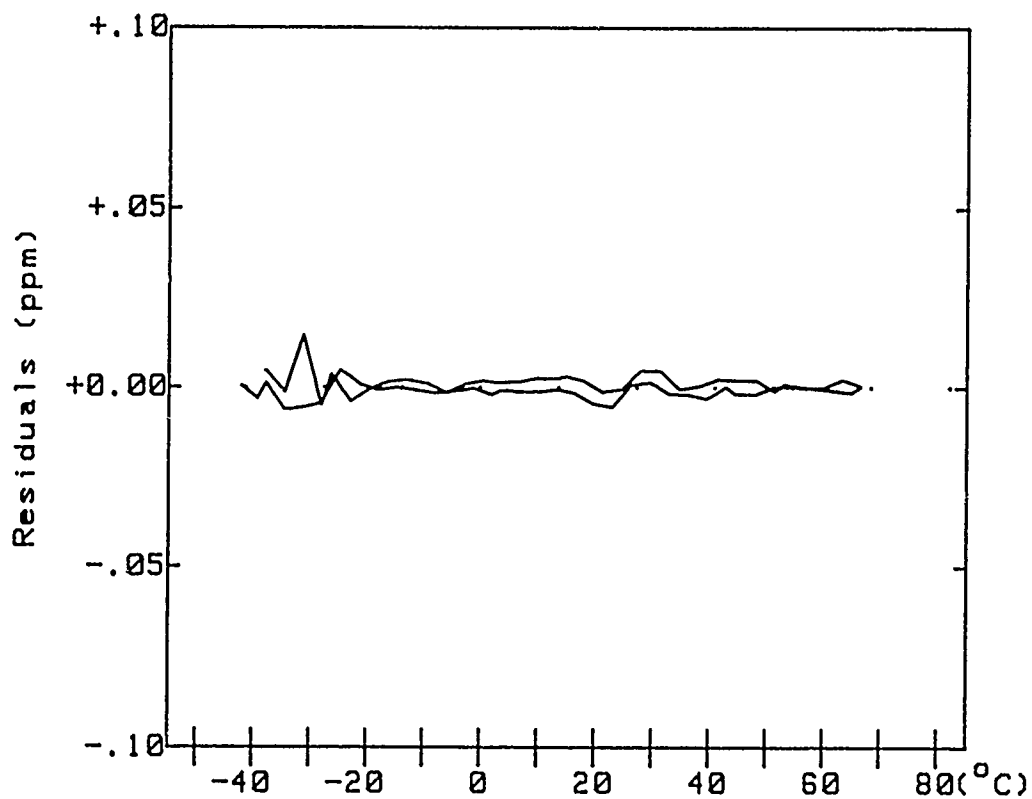


Figure 15. Residuals vs. temperature for the TFR dual-mode oscillator SN AP7.

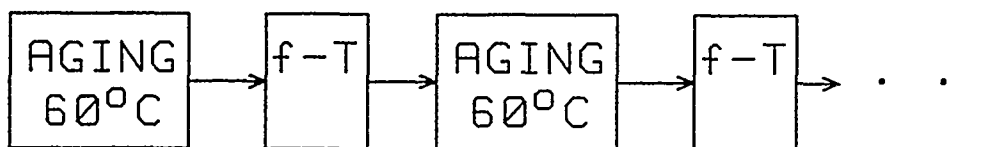


Figure 16. Aging sequence.

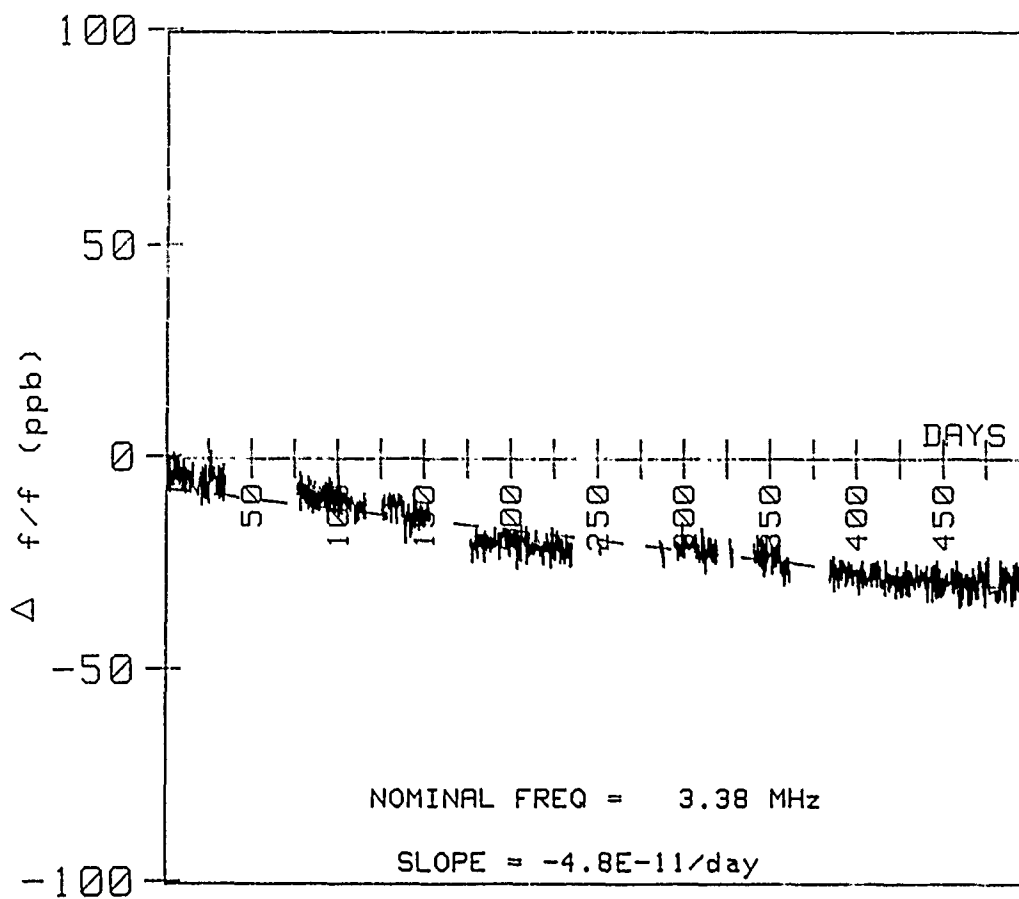


Figure 17. Aging data for MCXO 16725.

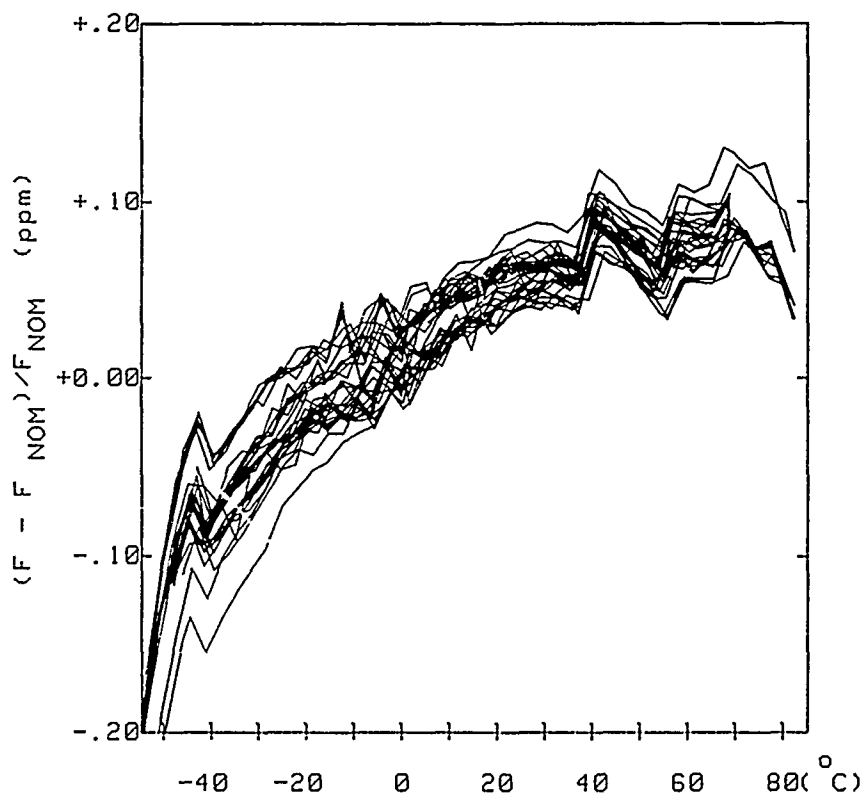


Figure 18. Superposition of 15 f vs. T runs with various parameters for MCXO 16723.

Table II

MCXO PERFORMANCE SUMMARY

Source	Res.	# of f-T	f-T (int) 10^{-8}	f-T (ext) 10^{-8}	Hyst 10^{-8}	Aging $10^{-10}/d$
FEI	LFR	21	12.5	3.2	2	2.0
FEI		19	5.5	-	1	0.6
FEI		17	5.0	2.5	1	1.0
FEI		16	11.0	5.7	4.5	0.3
FEI		15	8.5	3.2	1.5	0.7
GTS	TFR	11	-	1.1	0.5	-
GTS		11	-	3.1	2	-
GTS		1	1.0	-	0.8	-

QUESTIONS AND ANSWERS

MR. REINHARDT: Why can't you just use a varactor and just feed back the information and control the frequency directly?

MR. VIG: In the MCXO a varactor wouldn't work because it would affect the two frequencies differently. The fundamental mode would be pulled much more than the third overtone. It would mess up the compensation. The idea is to avoid having to pull the frequency.

UNIDENTIFIED QUESTIONER: Do you have any data on the phase noise of these oscillators and do you see any increase in phase noise due to amplitude variations in the drive?

MR. VIG: These were initially intended for clocks, so phase noise has not been of concern, although we are finding more and more applications where people want both an accurate clock and a source for carrier frequency control. We are looking at various ways of getting both a good clock output and a good frequency output from the MCXO. The obvious way of doing it is to just phase lock a VCXO to it. That, in fact, is being done in both approaches. When you do that, you will get the phase noise of the VCXO, which will be basically signal-to-noise at the far out frequencies and whatever VCXO's do close to the carrier. Since the temperature is not controlled, the close in phase noise will probably be temperature dependent. There is no unique answer as to what the phase noise will be at one Hertz from the carrier.

MR. REINHARDT: If you let the VCXO run at a different frequency than the MCXO, the offset could be controlled by the information from the MCXO and it could all be done in software.

MR. VIG: Exactly. One application that we have right now will use a 10MHz clock and a 60 Mhz frequency reference, using that kind of approach.

PTTI SYSTEMS ON THE EASTERN TEST RANGE

Christopher S. Duffy
James L. Wright
Computer Sciences Raytheon
P. O. Box 4127, CSR 2230
Patrick Air Force Base, Florida 32925

Abstract

The Eastern Test Range (ETR) is a missile and rocket testing facility available to military and commercial users for the launching and testing of space vehicles. The ETR provides over 4,000 nautical miles of tracking coverage of these vehicles from four major land-based tracking stations and one shipboard tracking station. At each station there are a myriad of Precise Time and Time Interval (PTTI) requirements that must be met. The most demanding requirements are: synchronization accuracy to the United States Naval Observatory (USNO) Master Clock to 100 nanoseconds, frequency accuracy of 1×10^{13} (Tau = 1 day), no single point of failure and continuous (24 hours per day, 365 days per year) PTTI operation. This paper will update a similar paper delivered at the Eighteenth Annual PTTI Applications and Planning Meeting and will describe the techniques employed to meet all of the ETR's PTTI requirements. Philosophical notions such as range PTTI service is much like a highly reliable utility service, synchronization from GPS should not be overemphasized, and gradual corrections are preferred to step corrections will be presented.

BACKGROUND

Figure 1 is a functional ESMC organization chart, showing only that which is germane to this paper. The principal users of PTTI on the ETR are the launch sites at Cape Canaveral Air Force Station (CCAFS) and the downrange tracking stations at Jonathan Dickinson Missile Tracking Annex (JDMTA), Antigua, Ascension, and on the USNS Redstone. There are other ETR sites and instrumentation which require PTTI systems. Refer to Figure 2 for a map of the ETR locations. The ESMC agency responsible for sustaining engineering and modernization of the Eastern Test Range (ETR) is the Deputy Commander for Systems Development (ESMC/DV). ESMC/DV in turn directs the Center Technical Services (CTS) contractor to implement the required engineering services to ETR systems, which include Radar, Telemetry, Command Destruct, Optics, Communications, and Precise Time and Time Interval (PTTI). In most cases the CTS contractor provides systems engineering services to procure and develop systems utilizing equipment available from industry. The CTS contractor engineers are also responsible for the design, development, fabrication, installation, and testing of unique equipment which is not available from the private sector.

In order to satisfactorily accomplish its mission and to support Range customers with their programs, the ETR has numerous PTTI requirements. ETR PTTI systems are often regarded as highly reliable and accurate utility services which are required to operate twenty four hours a day, 365 days a year.

Requirements range from providing a single Time-of- Year display in an aircraft control tower, to a highly reliable system with over 160 output PTTI signals and synchronized within 250 nanoseconds to the DoD Master Clock, to redundant Range Safety systems where no single failure (PTTI systems included) can cause both systems to fail. Each PTTI system is designed to meet both the dependability and accuracy requirements of the using system. To accomplish these objectives in the most cost effective manner, a hierarchy of "Clocks", each closely synchronized to the next higher level, has been established. Thus each user of PTTI on the ETR will benefit from high quality Clocks without incurring the expense of building independent timing systems.

SYNCHRONIZATION HIERARCHY

Each ETR facility, where PTTI services are provided, is traceable to the DoD Master Clock. The Range Clock, collocated with the Station Clock at the Cape, is synchronized and traceable to the DoD Master Clock to within 250 nanoseconds. Each Station Clock is synchronized and traceable to the Range Clock to within 500 nanoseconds. Site requirements determine the synchronization accuracy and traceability of each Site Clock to its local Station Clock. Refer to figure 3 for a composite synchronization diagram.

To achieve and maintain the required synchronization accuracies, time interval and frequency comparisons are made among all local timekeeping equipment (Cesiums, Digital Clocks, Micro Phase Steppers, Time Signal Generators, etc.) and outside reference sources (GPS, LORAN-C, Portable Clock, etc.). These frequent comparisons provide the basis for the thorough understanding of how each equipment behaves relative to all others. Thus when one component fails to compare as expected against all others, whether that component be a Cesium, Micro Phase Stepper, or GPS Receiver, its contribution to the local time scale is discounted and minimized. Consequently no "out of spec performance" from a single equipment or system should cause failure to meet an ETR accuracy specification.

The ETR has resisted adopting GPS as the one and only PTTI system of the future. While GPS is arguably "the best" synchronization source to UTC (DoD MC) and its recent history has demonstrated sub 50 nanosecond (RMS) accuracies to the DoD Master Clock, there have been occasions when UTC (DoD MC) - UTC (GPS) has exceeded 400 nanoseconds. When Selective Availability (SA) is fully implemented, the RMS value of UTC (DoD MC) - UTC (GPS) is expected to be approximately 300 nanoseconds. Thus ETR PTTI systems requiring better than 100 nanosecond accuracies employ Cesium ensembles and synchronization information from Portable Clocks, GPS, LORAN-C, and various other PTTI radio frequency (RF) sources.

RANGE CLOCK

The Range Clock is located in the CCAFS PTTI Center, Range Control Center, Cape Canaveral Air Force Station, Florida. The Range Clock serves as the reference for all time and frequency on the ETR. Its major components are four high performance Cesium Beam Frequency Standards, three Micro Phase Steppers, seven Digital Clocks, two Global Positioning System (GPS) Receivers and two LORAN-C Receivers. The three Micro Phase Steppers are utilized to correct the output frequencies from three of the Cesiums so the resultant frequency is more nearly that of the DoD Master Clock. The Digital Clocks provide time derived from each frequency source (Cesium and Micro Phase Stepper). The GPS and LORAN-C Receivers provide frequent time transfer information from the DoD Master

Clock, used in conjunction with Portable Clock data to derive the long term corrections employed by the Micro Phase Steppers.

PTTI VAULT

Figure 4 is a photograph of the PTTI Vault where much of the Range Clock equipment is installed. This is an environmentally controlled area where the equipment is installed on low frequency shock mounts and the temperature and humidity are closely monitored. Currently temperature is controlled to approximately one degree Celsius. Chart Recorders are used to show the phase relationships of the various frequency sources.

The performance history of a frequency standard can be used to predict its near future time only when it has been continuously operated in a controlled environment and without adjustments. For this reason extensive precautions are taken to insure that the environment is constant and power is always present to all equipment in the PTTI Vault. No adjustments are made to the oscillators, and frequency corrections are made using only the exacting digital features of the Micro Phase Steppers.

The entire PTTI Vault is operated from an Uninterruptable Power Source (UPS). In the event the UPS does fail, all equipment is battery backed-up for approximately 48 hours.

PTTI MONITOR AND CONTROL SYSTEM

Figure 5 is a photograph of the PTTI Monitor and Control System and various PTTI receivers. The computer based monitor system automatically collects time interval measurements made among the various equipments in the PTTI Vault, the PTTI receivers, and the local Station Clock equipment. Measurements are made daily at 1800 UTC, upon restoration of ac power, and upon operator demand. Provisions are also available to set up a "Special Measurement Set" where several measurements can be made more frequently and/or at specified times. The operator may also enter narrative information pertinent to the operating PTTI on the ETR into a "Daily Log" file. Currently, this system is used only to collect and store data, and to assist the operators in determining the Micro Phase Stepper values.

Figure 6 is a diagram of the PTTI Monitor and Control System, as it is now and as it will be when completed. PTTI Monitor and Control Systems will be installed at each Station Clock. They will be networked together in a star configuration with the CCAFS controller at the center of the star. This design will allow the CCAFS controller to retrieve PTTI measurements from all the downrange Station Clocks, schedule GPS and LORAN-C common view measurements between Station Clocks, and effect adjustments to the Micro Phase Steppers. The CCAFS controller software will derive the "Paper Clock" for each Station Clock and output, via the IEEE-488 Bus, Micro Phase Stepper values so the resultant frequency from each Cesium/Micro Phase Stepper pair is corrected to be syntonized to that of the DoD Master Clock. The first "Paper Clock" ensemble algorithm will be similar to the one being used at the USNO Time Service Alternate Station, Richmond Heights, Florida.

Currently PTTI Monitor and Control Systems are installed at the Cape PTTI Center, CCAFS and JDMTA. A partial extension of the CCAFS PTTI Monitor and Control System was implemented at the Antigua PTTI Station Clock several years ago. Until recently the only sub 10 microsecond time transfer system available was LORAN-C. Because Antigua is in a fringe reception area for LORAN-

C the correct cycle tracking is unreliable. The best way to insure proper timing at the unmanned Station Clocks, is to validate its continuous operation by taking frequent time interval measurements between various timing sources after the correct time had been validated by a Portable Clock. At Antigua, automated time interval measurements between the Station Clock Cesium Beam Frequency Standards, Time Signal Generators, LORAN-C Receiver, and GPS Receiver are taken every 6 hours, and transmitted back to the CCAFS PTTI Center. Operators at CCAFS analyze the received data and develop Micro Phase Stepper values used to slowly slew the Antigua Time Signal Generators to be closely synchronized to the Range Clock. One set of measurements is made simultaneously with measurements made at the Range Clock (1800 UTC) so the Antigua Station Clock synchronization is verified using LORAN-C and GPS common view techniques.

Plans will expand the PTTI Monitor and Control System to include automated verification of Site Clock performance. Since unmanned ETR Site Clocks now are driven by Synchronized Time Code Generators, synchronized to the local Station Clock, it has become apparent that Site Clock timing errors (due to loss of input signal, transmission noise, equipment failures, etc.) can go unnoticed indefinitely. Thus it is imperative that a means to monitor the performance of Site Clocks be developed. The Site Clock Monitor System will monitor all the Site Clocks at a given Station (CCAFS, Antigua, Ascension) and provide status information to each PTTI Monitor and Control System. To verify the proper functioning of the Site Synchronized Time Code Generator, an IRIG B120 signal, output from the Generator, will be sent to a digitally controlled switch located at the local Station Clock. A microcomputer will switch select a specific Site Clock IRIG B120 to be decoded for Time-of-Year data and control function data (encoded status bits from the Site Clock). The Site Clock IRIG B120 will also be examined to determine if its phase (time offset) is within predefined values. Any discrepancies will be transmitted to the CCAFS PTTI Monitor and Control System, where operators will be alerted to the potential problems and can initiate responsive action.

CCAFS STATION CLOCK

Since both the Range Clock and the CCAFS Station Clock are collocated in the same facility, the CCAFS Station Clock obtains its sense of time and frequency from the Range Clock. Two Time Signal Generators are synchronized to the Range Clock and are driven from the corrected (Micro Phase Stepped) frequencies of the Range Clock. These Time Signal Generators are capable of producing all IRIG serial time codes and decade pulse repetition rates (1 pulse-per-day through 100 kpps). In addition they generate various non-standard time codes which are required by customers not yet totally in compliance with the IRIG standards identified in Document 200-70, published by the Range Commanders Council. Like outputs from each Time Signal Generator are compared in a Coincidence Monitor Panel, where any synchronization difference greater than 2 microseconds or disagreement in code content activates an audible alarm and illuminates an identifying lamp to indicate which signal pair is in disagreement. Outputs of the manually selected Time Signal Generator are conditioned and then provided to Range Communications for distribution to authorized users within a forty mile radius.

All Station Clocks are scheduled to have these redundant Time Signal Generators and associated Coincidence Monitors replaced with modernized equipment. The new equipment will employ triplicated Time Signal Generators and a Coincidence Monitor which will automatically select the best Time Signal Generator for distribution to PTTI users. Additionally the modernized distribution equipment can sense an output amplifier failure and will select an alternate output amplifier for distribution. The

CCAFS Station Clock is scheduled to receive this new equipment when the Station Clock is relocated to a new facility in the summer of 1991.

Another major PTTI system located at the CCAFS Station Clock is the USNO Monitor system. This system employs the Data Acquisition System (DAS) described by the Automation of Precise Time Reference Stations (PTRS) paper presented by Paul J. Wheeler during the Proceedings of the Fifteenth Annual PTTI Applications and Planning Meeting. With the USNO Monitor System, the Naval Observatory obtains GPS data from a Naval Research Laboratory GPS Receiver and time interval measurements made between the Station Clock, the PTTI Vault Cesiums, and the LORAN-C Receiver 1 pps signals. The Naval Observatory compares readings from this system with those simultaneously made against LORAN-C at their site in Washington D.C. and provides a real-time time transfer measurement utilizing common-view LORAN-C techniques. The results of the USNO data analysis is transmitted to the Range Clock for use in coordinating and steering its local time scale.

CCAFS SITE CLOCKS

Timing signals are distributed to outlying instrumentation sites (Site Clocks) via standard telephone cable plant, video cables, and a local UHF Radio system. Most signals are transmitted over 19 AWG or 22 AWG telephone cables in bipolar pulse form to the Site Clocks where the signals are reconstructed into standard dc level shift or amplitude modulated formats. Newer Site Clocks now employ Synchronized Time Code Generators which input IRIG B120, compensate for transmission delay, and output required IRIG standard codes, decade repetition rates (1 pps through 1 kpps), and decade frequencies (100 Hz through 100 kHz). The Synchronized Time Code Generators also provide "Flywheel" operation through input signal code errors and loss of input signal. Thus site timing signals are uninterrupted and accurate even if there are momentary input faults.

Site Clocks within a forty mile radius of the CCAFS Station Clock can also obtain time via the UHF Radio system. Timing Signals from the Station Clock are Time Division Multiplexed and transmitted 1 millisecond early on a 1750 MHz carrier. Site Clocks with receiver and decoder equipment, demultiplex and output the required signals "on time" (within the 1 microsecond resolution of the delay compensation equipment). This system is now over 20 years old and will be replaced by a new upgraded UHF system. The new system will use the Micro Phase Stepped frequencies from the PTTI Vault to synthesize the 1750 MHz carrier. IRIG B120 and 1Mhz, from the Station Clock, will amplitude modulate the RF carrier. Thus all UHF signals are transmitted coherently and a suitable receiver can output time and frequency closely synchronized and syntonized to the CCAFS Station Clock.

The multiplexed timing signal is also transmitted, via video cable from the Station Clock, to Site Clocks which have requirements for redundant transmission paths from the Station Clock.

Each Site Clock timing signal is provided to the requiring user equipment from a separate buffered amplifier. Thus each user is unperturbed by other users collocated at the instrumentation site. Signal levels are adjustable from 0 to 10 volts (peak-to-peak or base-to-peak depending on signal type).

DOWNRANGE STATION CLOCKS

Station Clocks at each of the downrange Stations employ redundant timing systems similar to those currently employed by the CCAFS Station Clock. However, unlike the CCAFS Station Clock which is driven directly from the Range Clock frequency standards, downrange Station Clock systems are driven from local Cesiums (only Antigua and JDMTA also employ Micro Phase Steppers). Downrange Station Clocks obtain time transfers via semi-annual portable clock calibrations from the Range Clock. Time transfers are also made using GPS, LORAN-C, Transit, GOES, and WWV timing receivers.

Replacement of the redundant downrange Station Clock equipment with the new triplicated systems is currently in progress at JDMTA and will soon be accomplished on the USNS Redstone. Modernization of the Ascension and Antigua Station Clocks is scheduled for completion before the end of 1992.

section*DOWNRANGE SITE CLOCKS Downrange Site Clocks obtain PTTI signals from the local Station Clock and provide signals to users in a manner similar to that of the CCAFS Site Clocks. The only notable difference is the absence of an UHF Radio system, however the Time Division Multiplex system is used via wideband video cables.

SUMMARY

The ETR PTTI systems are continuously being upgraded to meet current and projected requirements. Major considerations for each of the ETR PTTI systems are accuracy, traceability, dependability, remote control automation, and low costs for implementation and operation. Generally, these systems are built using commercially available equipment, perform in various field environments, and are operated and maintained at low costs.

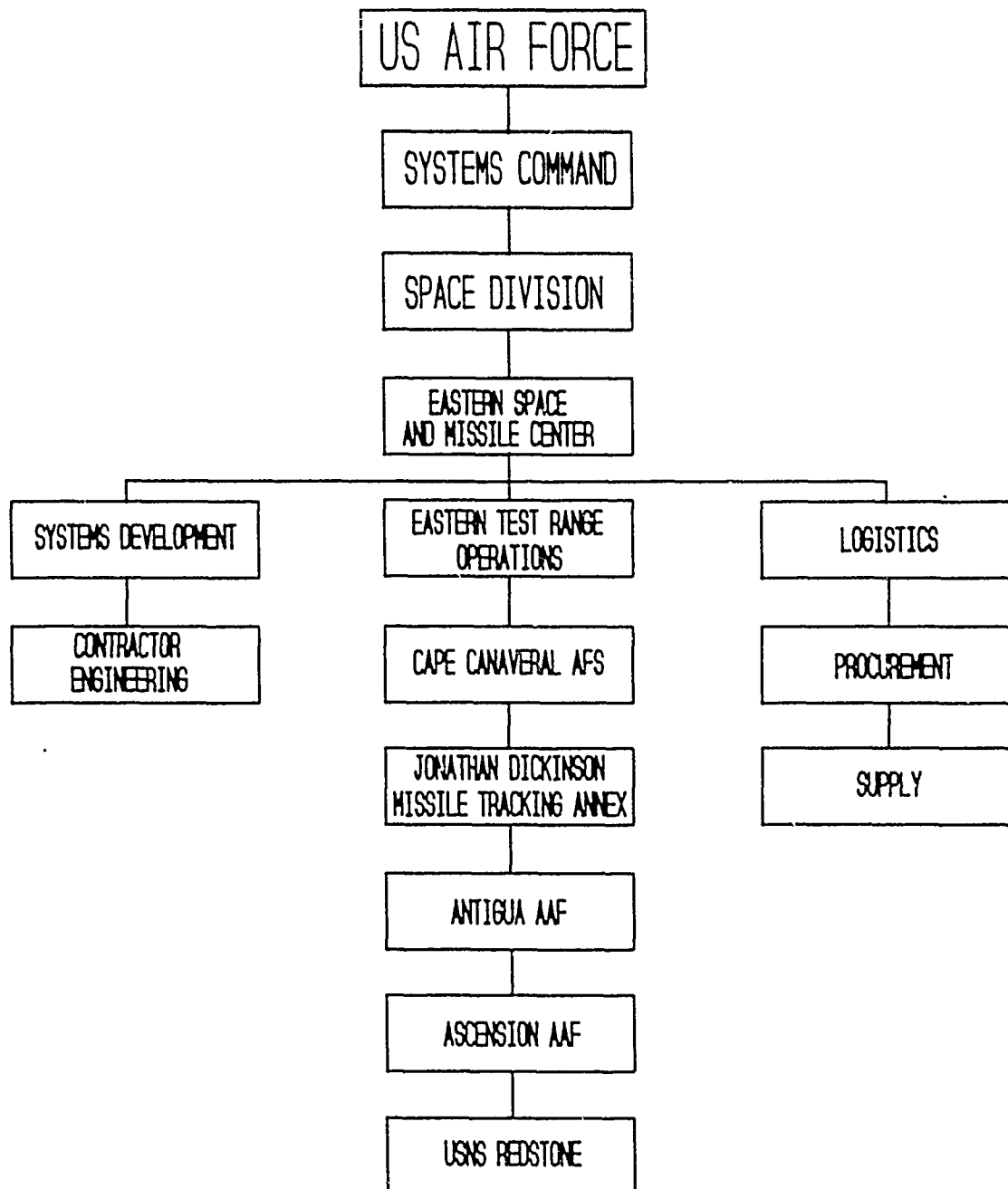


FIGURE 1 FUNCTIONAL ESMC ORGANIZATION CHART

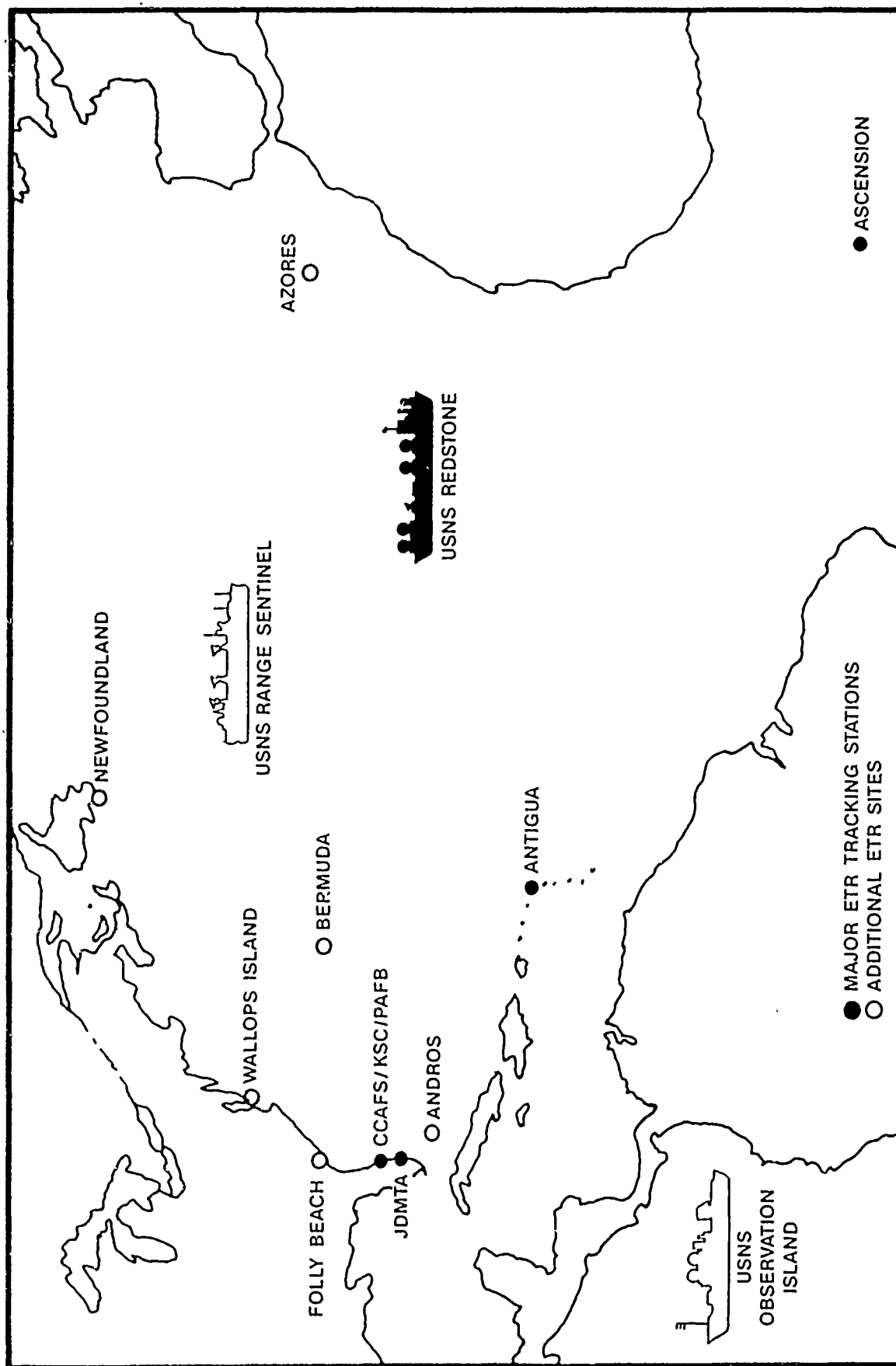
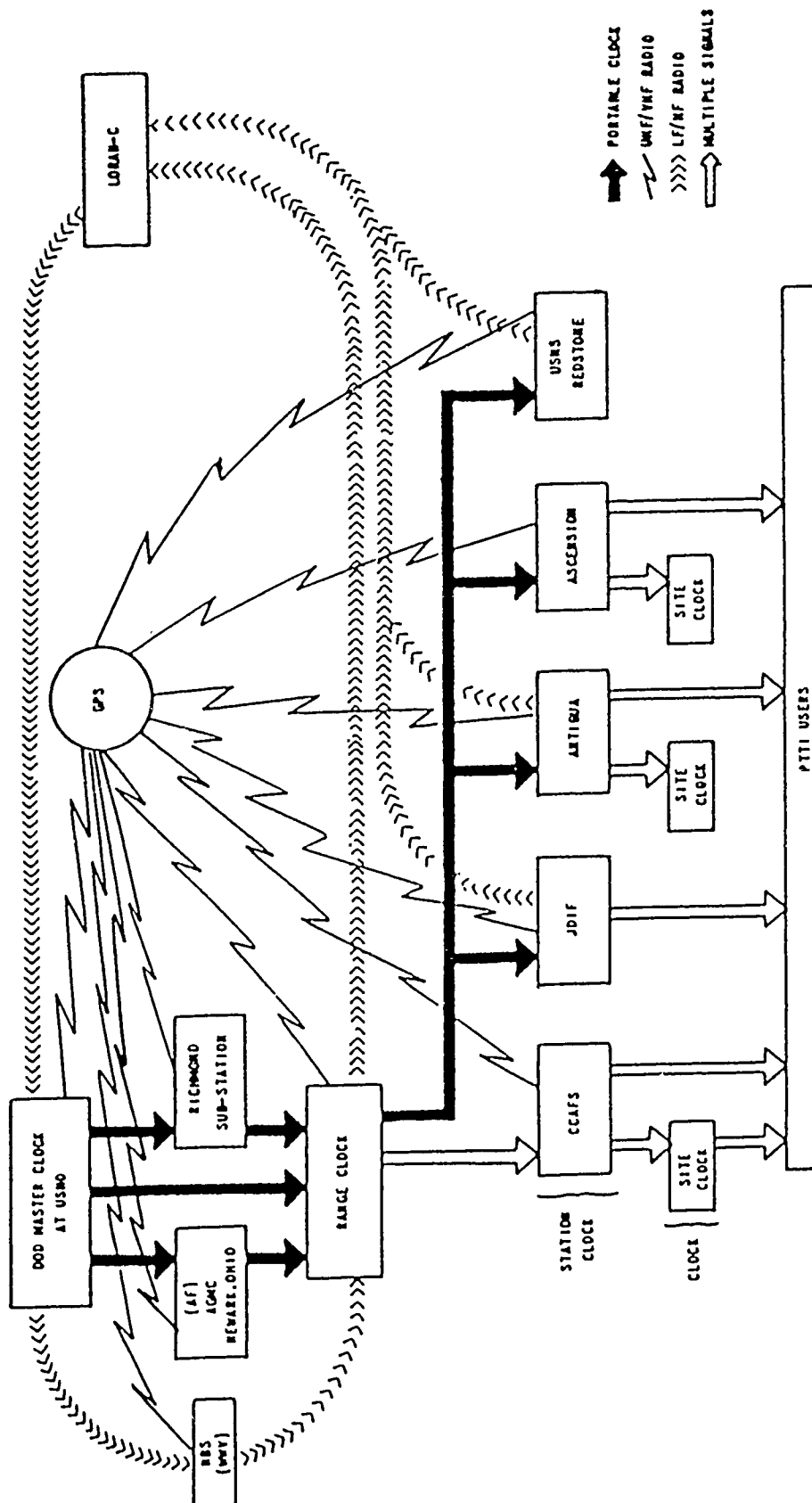


Figure 2. ETR Instrumentation Sites



ETR PTTI SYNCHRONIZATION AND TRACEABILITY

FIGURE 3

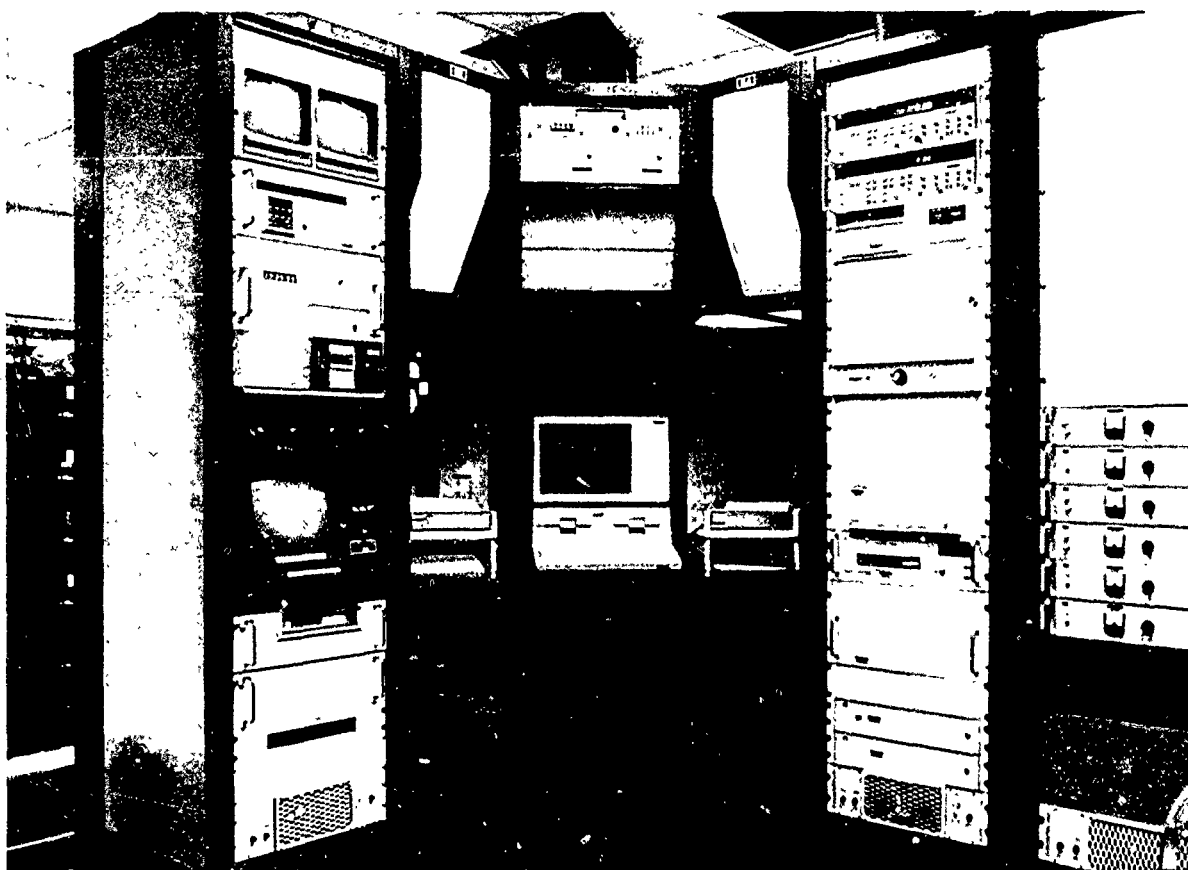
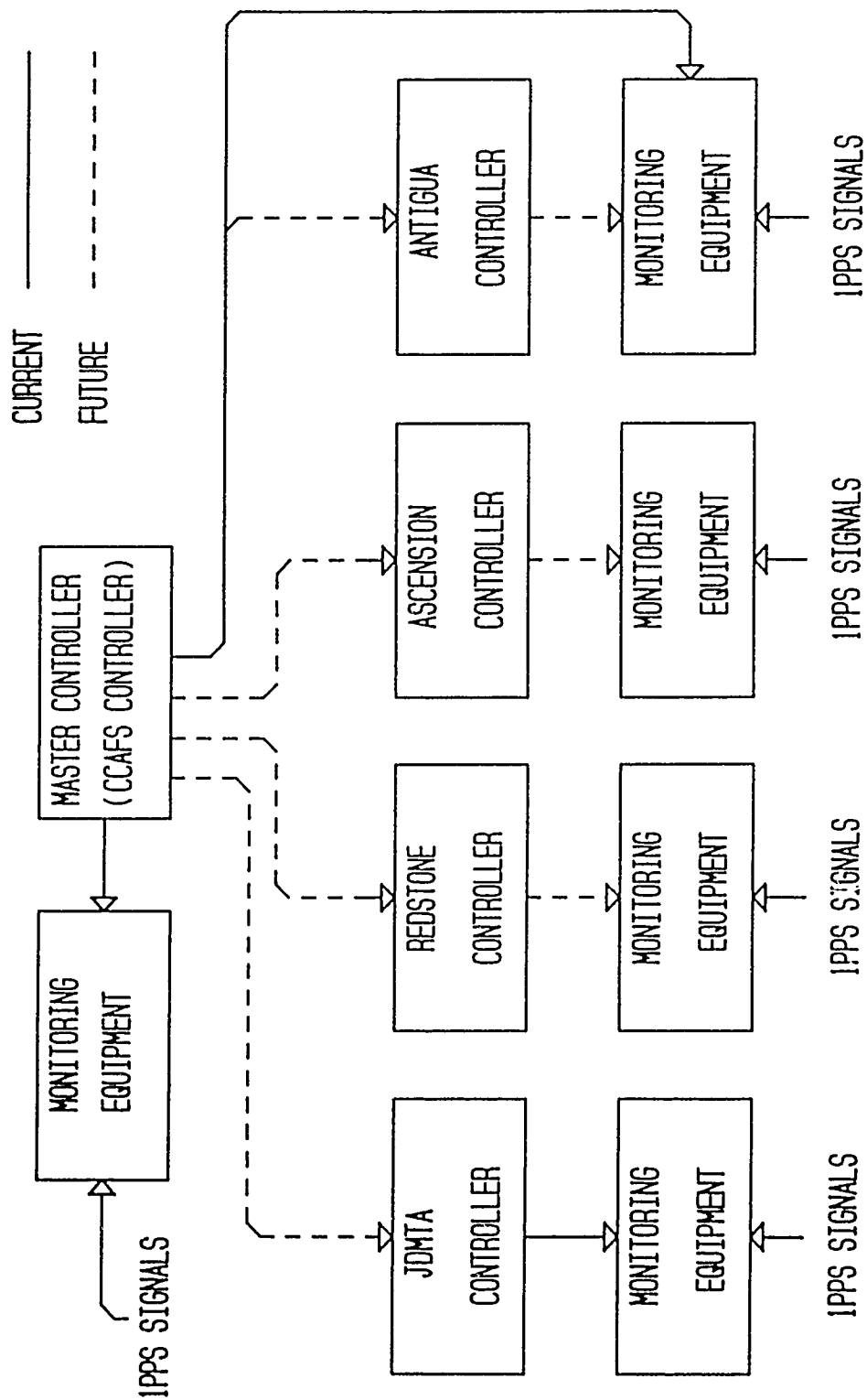


Figure 4. PTTI Monitor and Control System



Figure 5. PTTI Cesium Vault



PTI MONITOR AND CONTROL SYSTEM

FIGURE 8

NASA/JPL DEEP SPACE NETWORK FREQUENCY AND TIMING

Paul F. Kuhnle*
Jet Propulsion Laboratory
California Institute of Technology
4800 Oak Grove Drive
Pasadena, California 91109

Abstract

The Jet Propulsion Laboratory (JPL) supplies, maintains, and operates the NASA Deep Space Network for ground tracking of outer space probes. There are three major complexes which are located near Los Angeles, California; Canberra, Australia; and Madrid, Spain to provide continuous coverage of the desired spacecraft. This paper will describe the Frequency and Timing equipment utilized at the three complexes, and the methods of time synchronization and frequency syntonization between the three complexes and the National Institute of Standards and Technology (NIST).

Diagrams and specifications of today's system and anticipated future requirements will also be presented.

Introduction

NASA/JPL operates the Deep Space Network which consists of three complexes located around the world. These are located at Goldstone, California; near Robledo, Spain; and Tidbinbilla, Australia. From these three sites, continuous coverage of Deep Space probes (e.g., Voyager, Pioneer, Magellan and Galileo) is possible. Each site has multiple antennas for simultaneous coverage of several spacecraft or antenna arraying of a single spacecraft. Each complex has one centralized control room which includes one timing subsystem that is distributed to all users. Time synchronization and frequency syntonization between the three complexes and the National Institute of Standards and Technology (NIST) is accomplished today using the GPS constellation.

Configuration

Each complex (e.g., Goldstone, CA) has a complete Frequency and Timing subsystem. All three complexes have nearly identical equipment and configuration. A typical overall high level block diagram is shown in Figure 1. This is further detailed in several additional block diagrams, each of which is

*This work represents the results of one phase of research carried out at the Jet Propulsion Laboratory, California Institute of Technology, under a contract sponsored by the National Aeronautics and Space Administration

one block from Figure 1. These include the Frequency Standards Group (Figure 2), the Reference Frequency Synthesis and Distribution Group (Figure 3), the Master Clock and Timing Group (Figure 4) and the Monitor and Control Group (Figure 5).

Frequency Standards

The Frequency Standard Group (Figure 2) consists of the atomic frequency standards and accessories. The primary and first backup standards are both active Hydrogen Masers manufactured by the Smithsonian Astrophysical Observatory (SAO). The primary unit is a model VL11B and the backup is a model VLG10. The third and fourth units are Hewlett Packard 5061A Cesium Beam Frequency Standards with the "option 004" High Performance tube. All four are battery backed and are, in addition, connected to the Complex Uninterruptible Power Supply (UPS).

Reference Frequency Synthesis and Distribution

The four frequency standards are connected to the Coherent Reference Generator (CRG). The cabinet provides the switch gear to select one of the four frequency standards, synthesis of several additional frequencies and distribution of these to all users within the complex. The frequencies supplied are 0.1, 1, 5, 10, 10.1, 45, 50, 55 & 100 MHz. The total number of outputs is currently 225. To minimize crosstalk and interference the newer distribution amplifier design has a minimum reverse isolation between outputs of 100 dB. The isolation between the four frequency standards is 140 dB minimum to attenuate crosstalk to below the Hydrogen Maser performance specifications. The CRG is a JPL design that has evolved over the past 17 years and occupies two 7 foot high rack cabinets. It is entirely packaged with plug-in field replaceable modules. The entire assembly is equipped with computer based monitor equipment for hard failure detection (no output) and frequency standard selection.

The Phase Calibration Generator (PCG) transmits a reference frequency from the CRG to the antenna. It uses active (feedback) stabilization of the 20 MHz reference frequency to preserve the Hydrogen Maser stability. The device includes a transmitter, receiver and two comb tone generators. The transmitter-receiver pair provides the frequency stability and the comb tone generators the S & X band comb tone spacing and pulse amplitude that is injected into the antenna feedhorn. This provides the method of measuring the receiver delay stability. The principal uses of the PCG are to deliver a Hydrogen Maser stable reference to the antenna for receiver First Local Oscillator use and comb tones to the receiver for Very Long Baseline Interferometry (VLBI) measurements. The PCG is used in two antennas at each complex: 1) the 70M antenna and 2) the 34M High Efficiency Antenna.

Several users require the 100 MHz reference frequency in the antenna cone areas. To provide stabilized 100 MHz, a frequency multiplier (20 to 100 MHz) is connected to the PCG 20 MHz output. This synthesized 100 MHz is distributed to 4 users, using distribution amplifiers with 100 dB minimum reverse isolation. This equipment is mounted in a temperature controlled container, which is installed in the antenna cone area. This 100 MHz meets the present day required Frequency stability performance requirements. This equipment was designed and developed at JPL.

Master Clock and Timing Group

This group contains the complete set of timing equipment. The major assemblies consist of the Phase Locked Oscillator, Triple Redundant Master Clock (MCA), Time Insertion and Distribution Assembly (TID) and multiple Time Code Translators (TCT).

The Phase Locked Oscillator is a 5 MHz Voltage Controlled Crystal Oscillator that is phase locked to the CRG output (and frequency standard). The purpose of this device is to act as a "flywheel" during reference frequency interruptions. This was implemented to maintain clock service during the 10 to 20 milliseconds reference frequency outage when the CRG switches to another frequency standard.

The master clock contains three independent Time Code Generators which are setup to be in synchronization and driven by the complex atomic frequency standard that is currently in use. All three generators are voted by majority vote logic that selects a minimum of two being within limits as the correct time of day and pulse timing.

The TID is a distribution assembly that formulates a modified IRIG-G code for distribution to all the TCT's in the complex (100 maximum). The requirements are that not only UTC be distributed, but a second time code be available which is titled Simulation (SIM) Time. This code may be offset from UTC to anytime within a year to the nearest second. It is programmable to any or all of TCT's in the complex by the centralized Computer Control console. This SIM time programmability is necessary to meet the requirements of simultaneous multiple antenna users, one of which may be performing a training or software exercise for a future planned event.

The TID generated modified IRIG-G code contains UTC in the same format as specified in the IRIG-G specification. The SIM Time code is inserted in the control functions part of each frame. Flags are inserted in each frame that instruct each TCT on the leap year and leap second function. In addition, an address code is inserted in each frame to instruct a discrete TCT on SIM time and required flags (leap year and leap second). In this manner each TCT may be assigned to UTC or SIM time with the necessary flags. Each address is repeated every 100 frames of TID's code (1 second).

The TCT is really a synchronized Time Code Generator. Each TCT accumulates time from the same 5 MHz reference source as the MCA. The TCT is synchronized and controlled by the modified IRIG-G code. The TCT output contains time code and pulses. The current codes available are NASA PB-1 (millisecond of day and day of year) and BCD (millisecond of day and day of year). Timing pulses available are 1 PPS, 10 PPS, 100 PPS and 1000 PPS.

The Timing Jitter and TCT offset relate to TCT performance. The TCT jitter is inherit within the assembly design and exceeds the requirement by a comfortable margin. Each TCT in the complex may be adjusted to decrease the Master Clock to TCT propagation delay to less than 100 nanoseconds. This offset is adjusted and calibrated when the TCT is installed and subsequently verified at regular intervals.

Time Synchronization

GPS is currently the method for measuring the three DSN complexes timing versus UTC at NIST. The "NBS" (NIST) receiver design is currently in use at the three complexes. Data is acquired daily at each receiver (DSN complexes and NIST) versus selected GPS satellites using a predetermined schedule. This data is accumulated weekly at JPL by the DSN Timing analyst and compared with UTC from

(NIST). The result is the "Common View" measurement technique. Weekly time synchronization and frequency syntonization reports are publicized weekly to the DSN.

Monitor and Control

Figure 5 shows the block diagram configuration of the FTS Monitor and Control. Each major assembly has a dedicated microprocessor computer with keyboard for monitor only or monitor and control purposes. Control is limited to the TID, PCG and CRG. Computer control of the Master Clock and Frequency Standards is intentionally omitted, due to the possibility of erroneous messages causing misadjustment of the equipment. The FTS is normally controlled and monitored from the Centralized Monitor and Control (CMC) console. This console is the central area where the entire complex is controlled and monitored for major functions throughout the complex. Local front panel control at each FTS major assembly has also been provided.

Requirements & Performance

There are many detailed requirements imposed on the DSN Frequency and Timing. These are updated to meet requirements for the future planned Deep Space Missions. Only the most important will be addressed in this paper. These involve stability and offset.

Allan Deviation

Allan Deviation requirements and performance are shown in Figure 6. Various missions overrule the general specifications and have more stringent requirements, some of which are difficult to meet with a Hydrogen Maser, which leaves little margin for the transmission to an antenna that is 300 to 700 meters from the frequency standard. Requirements for the recent Voyager Neptune encounter and the future Galileo and Mars Observer missions are also shown. Note that the Voyager Neptune performance met the mission requirements and this was at the antennas using a non-stabilized coaxial cable that is buried one and one half meters below the ground surface. The section on the antenna structure is exposed and subject to the environment which is the most significant contributor to the stability degradation.

The above described non-stabilized coaxial cable method will not be satisfactory for the Galileo or Mars Observer mission stability requirements. While the PCG is feedback stabilized and will marginally meet the Allan Deviation, other parameters limit the assembly performance. Current work, in process, using fiber optic transmission lines should solve this problem.

Power Spectral Density of Phase

The single sideband phase noise requirements and performance are shown in Figure 7. The requirements for Voyager Neptune and subsequently for Mars Observer were better than Frequency and Timing could support. The recent JPL revisions to the Hydrogen Maser electronics have improved the phase noise performance with a reasonable margin. This was accomplished by replacing the VCO

with a BVA type crystal voltage controlled oscillator (VCO) and frequency multipliers that did not degrade the VCO. The tracking filter was also replaced with the single sided loop bandwidth set to approximately 0.5 HZ. This equipment was installed prior to the Voyager Neptune encounter to support the Radio Science Occultation and Ring Experiment. These revisions are currently being installed in the balance of the DSN.

Offset and Jitter

Table 1 shows the specifications and nominal performance frequency and time offset, timing jitter and TCT offset versus the Master Clock. The frequency and time offset is the maximum permitted between the three complexes and the National Institute of Standards and Technology (NIST). The knowledge of frequency and time offset is specified somewhat tighter; this is not a problem with the present GPS time synchronization and frequency syntonization techniques used in the DSN. These requirements are easily exceeded with a comfortable margin.

Future Requirements and Improvements

Future missions in the planning stage will possibly require tighter specifications than possible with the equipment implemented or in process, at this time. It is estimated these would be required about year 1995 to 2000. Some of these specifications could be:

- Allan Deviation of 1×10^{-16} at sampling times between 1000 and 10,000 seconds. The driver could be Gravitational Wave Experiments.
- Improved Phase Noise of 10 to 20 dB better than the specifications in Figure 7. This will probably be especially true for close to the carrier responses.
- Reduce the knowledge of timing offset to 1 nanosecond between NIST and the three complexes.
- Reduce the maximum permitted time offset between NIST and the three complexes to 1 microsecond.

The near term improvement is to utilize fiberoptic links to distribute the 100 MHz reference to the DSN antennas from the control room. The Allan Deviation and Phase Noise requirements for Galileo and Mars Observer cannot be met with the present configuration using the PCG. A combination of new state of the art fiberoptic transmitters, receivers and near zero temperature coefficient cable appear to meet the requirements from an ongoing test series. It is planned to complete the evaluation, the design in 1991 and to start installation in the antennas during 1992.

Other possible future improvements that are currently being developed or considered by NASA/JPL are:

- Feedback stabilized fiberoptic reference frequency links at 100 MHz to obtain Allan Deviation performance below 1×10^{-15} at 10^4 seconds.
- Fiberoptic reference frequency links at 1GHz to reduce the phase noise contributed by the links.

- Hydrogen Masers with Adiabatic Fast Passage to obtain Allan Deviation performance of 1×10^{-16} at 10^4 seconds.
- Superconducting Cavity Maser Oscillator that is phase locked to a Hydrogen Maser providing a distinct improvement in Phase Noise and short term Allan Deviation performance.
- Mercury Trapped Ion Frequency Standards as a standalone device or as the long term low aging reference to steer a Hydrogen Maser.
- Sapphire Dielectric Resonator Oscillator
- Two-way time transfer to replace or augment GPS, as a method of time synchronization to the one nanosecond level.

These will be considered in the future as project requirements determine the need for DSN implementation.

Summary

Requirements for Frequency and Timing performance have been tightened in the last few years and will undoubtedly continue to in future years. The recent phase noise performance improvements and near future fiberoptic transmission links will meet Galileo and Mars Observer mission Radio Science experiment requirements. Future, yet to be determined, requirements should be met by equipment currently being researched and developed at JPL.

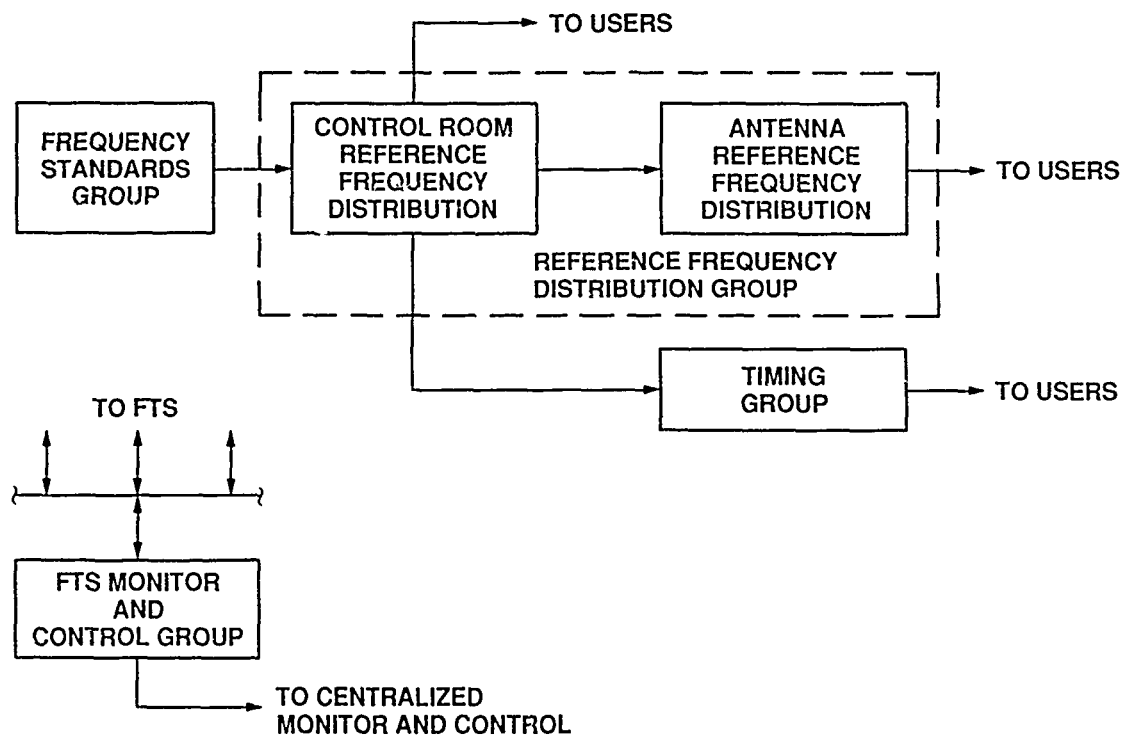


Figure 1. DSN Frequency and Timing Configuration

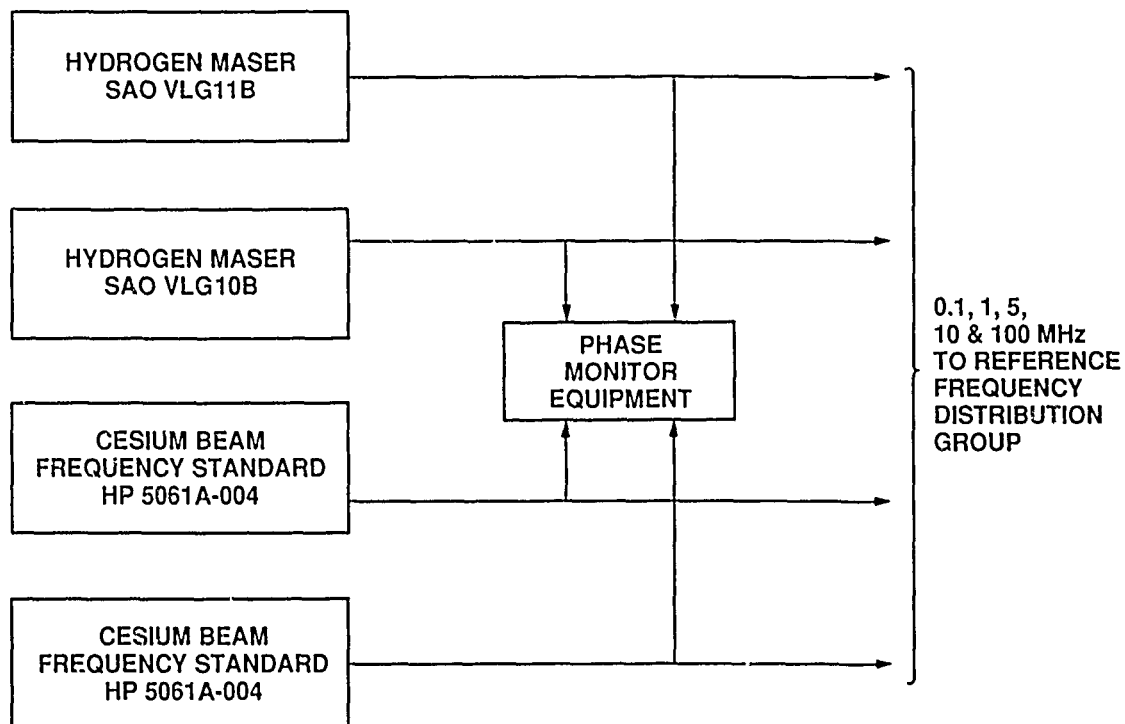


Figure 2. Frequency Standards Group

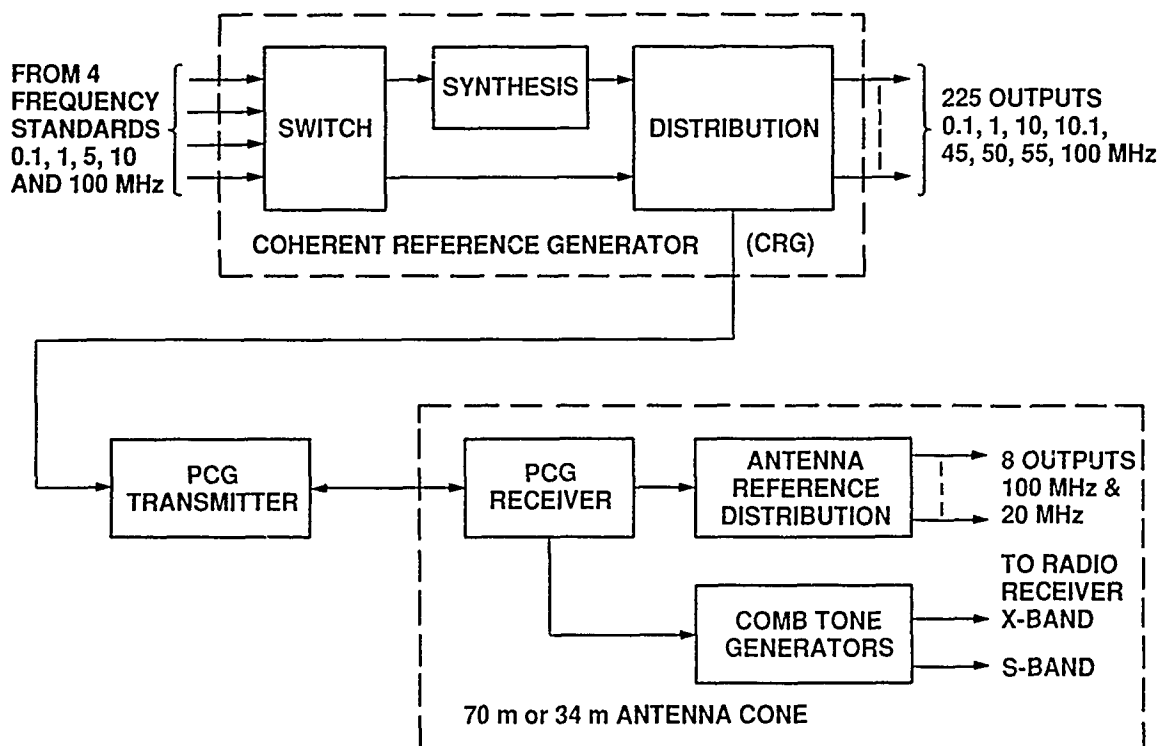


Figure 3. Reference Frequency Synthesis and Distribution Group

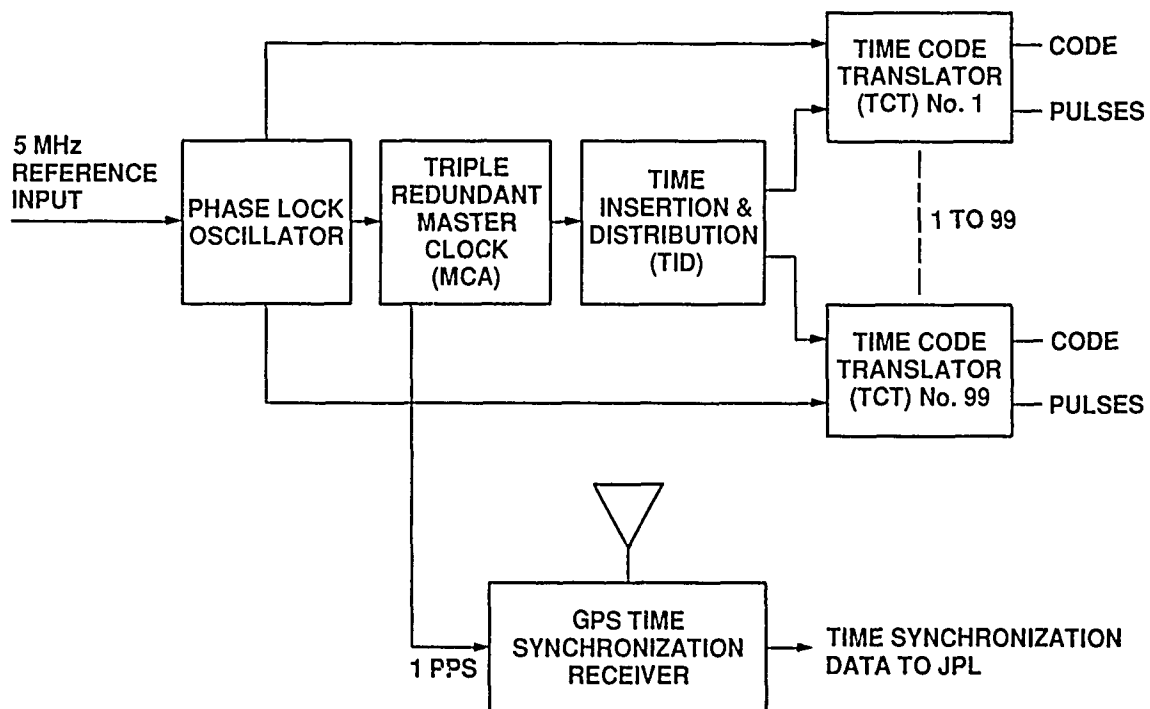


Figure 4. Timing Group

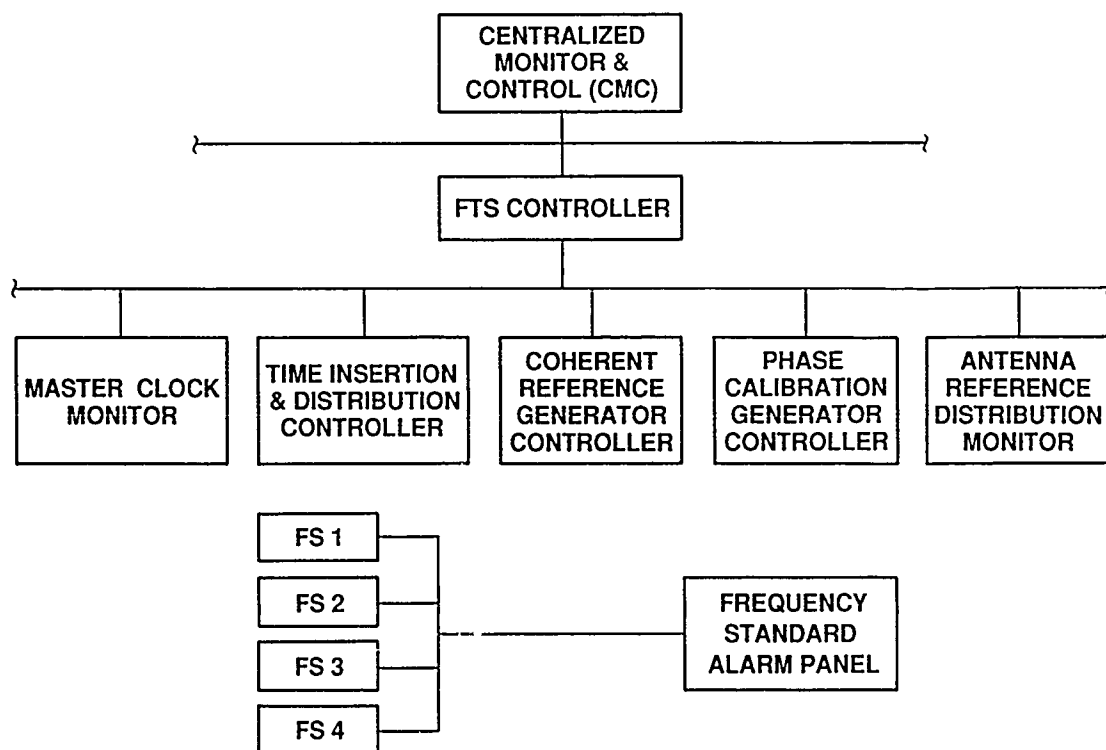


Figure 5. Monitor and Control

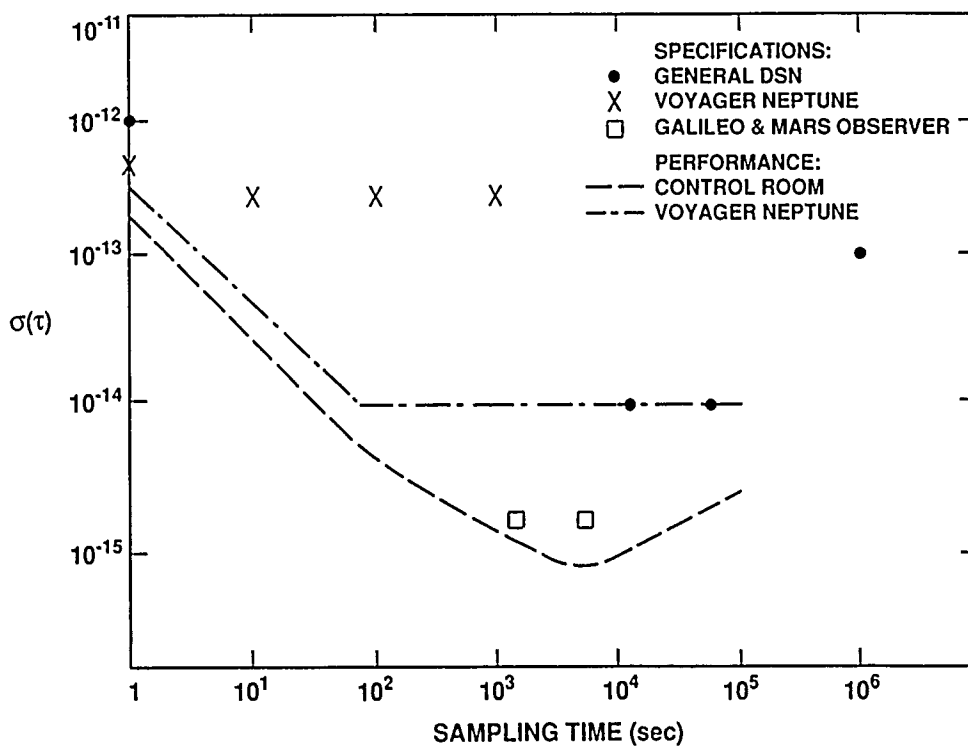


Figure 6. Allan Variance vs Sampling Time

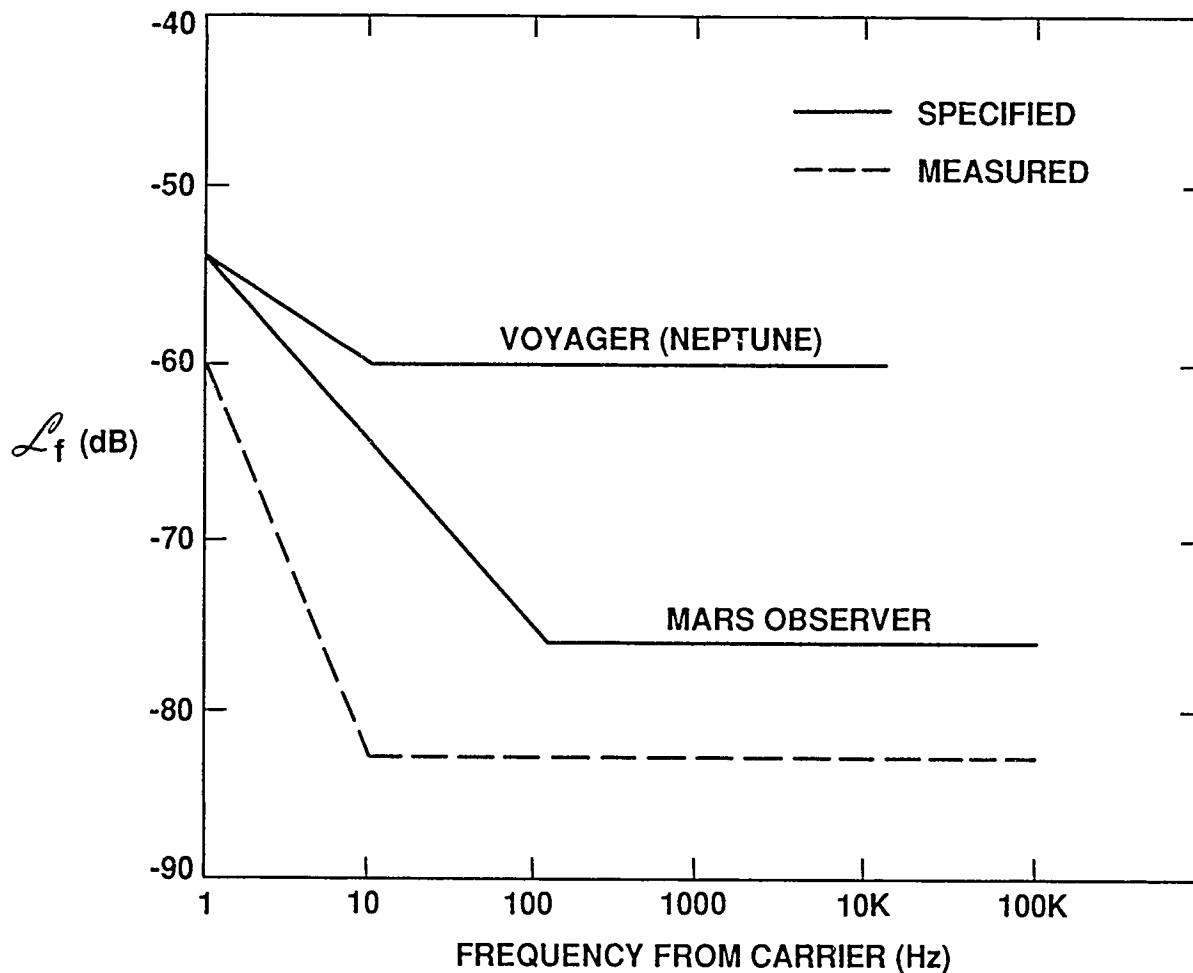


Figure 7. Power Spectral Density of Phase at X-Band

Table 1. Offset and Jitter Requirements and Performance

	<u>SPECIFICATIONS</u>	<u>NOMINAL PERFORMANCE</u>
FREQUENCY OFFSET	9×10^{-13} MAX	$<5 \times 10^{-13}$
FREQUENCY OFFSET KNOWLEDGE	3×10^{-13} MAX	$<1 \times 10^{-13}$
TIME OFFSET	20 μ s MAX	$<5 \mu$ s
TIME OFFSET KNOWLEDGE	10 μ s MAX	<100 ns
TIMING JITTER (1, 10, 100, 1K PPS)	2 ns MAX @ 1σ	<2 ns @ 1σ
TCT OFFSET vs MCA	100 ns MAX	<100 ns

QUESTIONS AND ANSWERS

GERNOT WINKLER, USNO: You mentioned a future requirement for phase or frequency distribution to 1×10^{-15} at the antenna. Over what time interval.

MR. KUHNLE: 1000 to 3600 seconds. It is for some preliminary gravitational wave experiments that they are setting up to do with Galileo.

MR. MCNABB: In one of your early slides, you had cesium standards. I saw no multipliers, but you were coming out with 100 MHz. Where did that 100 MHz come from?

MR. KUHNLE: I left them off the diagram to keep the diagram from becoming too complicated. We do have 5MHz to 100 MHz multipliers and distribution amplifiers in an outboard box with the cesiums.

SYNCHRONIZING LORAN-C MASTER STATIONS TO COORDINATED UNIVERSAL TIME

G.R. Westling, M.D. Sakahara and C.J. Justice

United States Coast Guard
Washington, D.C.

ABSTRACT

In 1987 the Coast Guard, anticipating Public Law 100-223, began improving the synchronization of its Loran-C master stations. Two parallel approaches were begun. One was to develop a hardware addition to the master station's frequency standard rack to provide timing offsets and maintain synchronization with Coordinated Universal Time (UTC) using GPS timing receivers. The other was to examine administrative methods to improve the master station synchronization as reported by the U.S. Naval Observatory (USNO). Three such methods were studied: frequency control, time step control, and modified master station control. These methods were used at three Loran-C master stations: Seneca, NY, Dana, IN, and Malone, FL. All three methods achieved significant synchronization improvement. Key improvement factors were timely and precise time-difference offset reporting by USNO and no-notice timing corrections by the Coast Guard.

INTRODUCTION

The Coast Guard began improvements to the synchronization of its master stations in anticipation of Public Law 100-223, Section 310 (1). This law requires the Coast Guard to synchronize all Loran-C master stations in the United States to within approximately ± 100 nanoseconds (ns) of Coordinated Universal Time (UTC). An accurate and timely method of time transfer from UTC, as maintained by the USNO, to the Loran-C master station's time is one of the keys to successful compliance with the law (2). In March 1987, the Coast Guard began studying two ways to improve the synchronization of its Loran-C master stations:

The first approach was a study conducted by the Coast Guard Electronics Engineering Center, Wildwood, NJ, (EECEN). The EECEN was tasked to develop an addition to the frequency standard rack to provide precise time using the GPS system to transfer time between USNO and the Loran-C station (LORSTA). The EECEN would also study and evaluate methods of coordinating Loran-C time with GPS time to within ± 30 ns. Their equipment would be used to monitor and steer the local cesium oscillators, keeping them synchronized to UTC.

The second approach was a series of experiments using administrative techniques to steer the master station's clocks. The Coast Guard believed that it could approach 200-ns synchronization using the administrative method and, possibly, 100-ns synchronization as the techniques were refined.

Results

The result of these two approaches is that Loran-C offsets have been held within ± 100 nanoseconds of UTC to confidence levels ranging from 61% to 78% for

the four Loran-C chains in the lower 48 states (Northeast U.S. (NEUS), Southeast U.S. (SEUS), Great Lakes (GLAKES), and the U.S. West Coast (USWC)) since 1 May 1989. For the NEUS, SEUS, and GLAKES Chains, these offsets are daily averages of measurements comparing Loran-C signals received at USNO, Washington, D.C. with the USNO master clock. For the USWC chain, the signal is received at a USNO supported Precise Time Reference Station (PTRS) at the Naval Weapons Testing Center, China Lake, CA, and linked to the USNO master clock via GPS time transfer. These chains were chosen for their proximity to USNO monitoring facilities.

The remaining chains required by law to be synchronized to UTC are the Canadian East Coast (CEC) chain, the Gulf of Alaska (GOA) chain, the Central Pacific (CENPAC) chain, the North Pacific (NORPAC) chain, and the two midcontinent expansion project (MEP) chains: the North Central U.S. (NOCUS) and South Central U.S. (SOCUS) chains. Synchronizing the master stations of these chains requires adding to or upgrading USNO PTRS facilities. The Coast Guard intends to include the LABSEA chain, the Canadian West Coast (CWC) chain and the required CENPAC chain, with minimal equipment additions.

This report discusses the administrative efforts from the standpoints of performance, procedures and future recommendations.

IMPROVING THE SYNCHRONIZATION OF LORAN-C MASTER STATIONS ADMINISTRATIVELY

Improving the synchronization of Loran-C master stations using administrative techniques was one of the least expensive alternatives the Coast Guard considered feasible. It could also be implemented quickly at selected chains.

The USNO proposed one method of improving synchronization, and the Atlantic Area Regional Manager (responsible for the NEUS, SEUS, GLAKES, CEC and LABSEA Loran-C chains) proposed two methods.

USNO Proposal

The USNO proposed to develop a steering algorithm to steer the master operate oscillator. This technique uses frequency changes to maintain synchronization. It was tested at LORSTA Seneca, the master station of NEUS.

Atlantic Area Proposals

The first proposal from the Atlantic Area Regional Manager was to retain the current method of controlling master stations and to reduce the offset data averaging period from 30 days to 3. This involves making a combination of time steps and frequency adjustments to the master operate oscillator to maintain synchronization. It was decided to test this technique at LORSTA Malone, the master station of SEUS.

The second proposal from the Atlantic Area Regional Manager was to use daily time steps to "zero" the master station's daily offset. The record of offsets and subsequent corrections would then be used to calculate monthly frequency adjustments to reduce the magnitude and frequency of the time steps needed to maintain synchronization.

To maximize the performance of the new techniques, the Coast Guard suspended the requirement to issue prior user notification of timing corrections being

made to the master stations. The Atlantic Area Regional Manager solicited objections to removing the prior notification requirement and received no response. Therefore, the plan was implemented.

GENERAL ASSESSMENT OF SUCCESS

The Frequency Control Method used at LORSTA Seneca

The USNO is responsible for reporting the timing offset of Loran-C master stations. To do this, USNO compares the arrival time of a Loran-C master signal to the station's time of coincidence (TOC) with the universal second. A modeled propagation time and equipment delay from the station to the monitor point is subtracted from the time difference, or offset, to move the time reference to the master station. The offset data are then averaged over a day. The average offset is published daily in USNO's Series 5 report and biweekly in their Series 4 report. This process is used to monitor all Loran-C master stations under the jurisdiction of the United States. For LORSTA Seneca, USNO uses its PTRS in Washington, DC to directly monitor LORSTA Seneca's signal.

The USNO began by averaging LORSTA Seneca's offset data for 4 days and, based on the averaged data, recommended a frequency correction, if necessary. The correction was entered in a special Electronic Bulletin Board (EBB). At a predetermined time, the watchstander at LORSTA Seneca called the EBB to obtain the day's correction. If a correction was recommended, the watchstander entered the correction and confirmed its entry with the EBB.

The performance of this method is shown in Figure 1. Performance statistics from USNO's steering method are listed in Table 1.

Improved Synchronization at NEUS			
From	To	Mean usec	Sigma usec
Jan. 1, 1988	May 25, 1988	-0.26	0.65
May 25, 1988	Oct. 14, 1988	-0.045	0.139
Oct. 14, 1988	Jan. 17, 1989	-0.109	0.130
Jan. 17, 1989	May 15, 1989	-0.023	0.160
May 15, 1989	Aug. 17, 1989	-0.031	0.061

Table 1. The Synchronization Performance
of Loran-C Station Seneca.

The period from 01 January 1988 through 25 May 1988 shows LORSTA Seneca's performance before 4-day averaging began. The USNO began calculating steering corrections on 03 May 1988. During the start-up period, LORSTA Seneca's offset was reduced approximately 5-fold, as shown in Figure 1. The improvement lessens during the winter of 1988, from 14 October 1988 through 17 January 1989. On 17 January 1989, USNO reduced the minimum time between corrections from four days to three, resulting in another improvement. On 15 May 1989, USNO again decreased the minimum time between corrections from three days to one. The average offset improved somewhat as a result, and the standard deviation of the offset was more than halved.

The goal of this experiment, as with the others, was to attain a zero offset average and to minimize the standard deviation. As Figure 2 shows, about 84%

(79 of the 94 offsets plotted) of the offsets from 15 May through 11 August were within the ± 100 -ns limit of the law.

This experiment was successful. The offset of LORSTA Seneca went from a mean of -0.26 microseconds (usec) and a standard deviation of 0.65 usec before the improvement to a mean of 0.031 usec and a standard deviation of 0.061 usec after the minimum period between corrections was reduced to one day. This is more than a 10-fold improvement.

The Accelerated Coast Guard Master Control Method Used at LORSTA Malone

For the SEUS Loran-C chain (SEUS), the Coast Guard proposed to accelerate the current technique used to maintain master synchronization. Prior to this, daily offset data collected over a 30-day period were analyzed to determine if the station required a time step or frequency adjustment. The proposed technique reduced the 30-day period to about 3 days. The experiment was coordinated by the Coordinator of Chain Operations (COCO) for the SEUS. The synchronization improvement project was started at the same time as that for NEUS.

This method provided a significant improvement in LORSTA Malone's synchronization, as shown in Figure 3. Performance statistics of the technique used at LORSTA Malone are shown in Table 2.

Improved Synchronization at SEUS			
From	To	Mean usec	Sigma usec
Jan. 1, 1988	Oct. 14, 1988	-0.32	0.86
Oct. 24, 1988	Apr. 21, 1989	-0.029	0.188
Apr. 21, 1989	Aug. 17, 1989	-0.006	0.089

Table 2. The Synchronization Performance of Loran-C Station Malone.

The period from 01 January 1988 through 14 October 1988 shows LORSTA Malone's performance before the experiment, including the start-up period beginning on 03 May 1988. LORSTA Malone's synchronization improved significantly using this technique. The average offset was reduced 15-fold, with a 4-fold reduction in the standard deviation. On 21 April 1989 LORSTA Malone's operate oscillator was replaced, and this resulted in an additional 50% reduction in both average offset and standard deviation. The overall performance is shown in Figure 4.

The Time-Step Control Method Used at LORSTA Dana

The technique applied at LORSTA Dana used small time steps to maintain synchronization and occasional frequency adjustments to reduce the number and magnitude of the time steps. The watchstander at LORSTA Dana called the USNO EBB and examined the Series 5 report for the day's offset. If the offset was greater than ± 50 ns, then the offset was "zeroed" using 40-ns time steps. The time steps and offsets were plotted, and frequency adjustments were made, as needed, after 30-days of observation. This technique has the advantage of being able to collect long-term drift data that can be used to steer the cesium frequency standards.

Figure 5 is a plot of offsets for LORSTA Dana, and it shows that synchronization improvement was almost immediate. Performance statistics of the system are shown in Table 3.

Improved Synchronization at GLKS			
From	To	Mean usec	Sigma usec
Jan. 1, 1988	Feb. 24, 1989	-0.08	0.64
Feb. 24, 1989	Aug. 17, 1989	-0.013	0.099

Table 3. The Synchronization Performance of Loran-C Station Dana.

The period from 01 January 1988 through 24 February 1989 shows LORSTA Dana's performance before time-step control was begun. After the start-up period from 12-24 February 1989, this technique produced the largest improvement in the shortest time, nearly an 8-fold decrease in the average offset and a 6-fold decrease in the standard deviation. Figure 6 shows the synchronization performance. There is a gap in the data every weekend, giving a false periodic appearance to the offset plots. The gap occurs because USNO does not issue the Series 5 report on Saturday and Sunday.

Improving Synchronization at Other Loran-C Stations

After the Coast Guard observed the successes in the Atlantic Region, the Pacific Area Regional Manager began using the time-step control technique at LORSTA Fallon, NV, the master station of the USWC chain, on 12 February 1989. This is the same method used at LORSTA Dana. The USNO was unable to furnish daily offset reports with 10-ns resolution (the resolution of the offset reports for NEUS, SEUS and GLAKES) until 17 April 1989.

The offset plot in Figure 7 shows the 100-ns resolution of the offset data used to maintain LORSTA Fallon's synchronization. Note the sinusoidal seasonal drift common to Loran-C in this plot. Once USNO increased the precision of the reported offset data to 10 ns, LORSTA Fallon settled within the ± 100 -ns boundaries. Table 4 lists the progress of improving the synchronization of LORSTA Fallon.

Improved Synchronization at USWC			
From	To	Mean usec	Sigma usec
Jan. 1, 1988	Feb. 24, 1989	-0.151	0.61
Feb. 24, 1989	Apr. 27, 1989	-0.113	0.141
Apr. 17, 1989	Aug. 17, 1989	0.015	0.116

Table 4. Synchronization Performance of Loran-C Station Fallon.

Synchronization improved from a mean offset of -151 ns to one of 15 ns with a 6-fold reduction in standard deviation. The short period between the beginning of the synchronization improvement project (24 February 1989) and when USNO was able to publish daily offset reports with 10-ns resolution (17 April 1989) is not considered significant, but the later synchronization improvements are. Figure 8 shows the performance of LORSTA Fallon from 17 April 1989 through 11 August 1989.

OVERALL PROGRESS AND RESULTS

As shown above, the three techniques (USNO's frequency control (NEUS), modified master control (SEUS) and time-step control (GLAKES, USWC) all provide significant reductions in the synchronization offsets as reported by USNO. Table 5 shows the

Improved Synchronization Performance May 1, 1989 through August 17, 1989				
Station	Mean	Sigma	% of Daily Averages	
			< 100 ns	< 200ns
Seneca	-0.050	0.076	73.5	96.3
Malone	-0.012	0.089	61.8	100.0
Dana	-0.007	0.073	78.4	100.0
Middletown	-0.020	0.116	75.5	89.8

Table 5. Overall Administrative Synchronization Performance.

overall performance of the four master stations involved in the preliminary administrative effort to improve master synchronization with UTC. All four experiments gave synchronization offsets within ± 100 ns at least 60% of the time. The data are from the summer of 1989. The effect of increases in propagation noise during the winter months is to be determined.

CONCLUSIONS

The administrative methods for improving Loran-C master station synchronization evaluated herein have been effective. They have reduced the offsets of the four experimental master stations to within ± 200 ns of UTC 97% of the time. Average offsets were reduced to near zero values and, more significantly, the standard deviations were reduced to near 100-ns.

The Coast Guard will continue testing the three methods of improving the synchronization of Loran-C master stations. The administrative techniques will be refined, and further improvements are expected. This winter season should show the full capability of the methods, including their strengths and weaknesses.

LIMITATIONS OF THE ADMINISTRATIVE CONTROL METHODS

The synchronization improvements shown for the four chains tested are at the limit of feasibility, given the facilities available. Even these significant improvements must be viewed critically, for several reasons.

First, the synchronization experiments run by the four chains were developed to determine the best methods of synchronization and to identify problems. They may have to be further refined to satisfy long-term operational requirements for using synchronized signals.

Second, these results reflect the more quiet spring/summer propagation season and may hide the fact that synchronization accuracy depends strongly on the proximity of the PTRS and the master transmitter. Changes in overland propagation will probably increase the errors in synchronization accuracy. These errors increase with distance from the transmitter. To minimize propagation error for reliable synchronization, a PTRS should be located in the service area of each Loran-C master station and, ideally, it should be relatively close to the master. The receiver site at USNO is just marginally within the service area of the three chains discussed.

SUMMARY

Significant improvements have already been made in Loran-C synchronization to USNO UTC using only administrative techniques. If additional hardware techniques such as two-way satellite time transfer and environmental chambers to increase cesium frequency standard stability are also used, it is highly probable that the requirements of Public Law 100-223 will be satisfied, independent of how that law defines the synchronization confidence limits.

REFERENCES

1. Public Law 100-223, "Airport and Airway Safety and Capacity Expansion Act of 1987."
2. Interim Report #1, "Enhanced Interchain Timing," Coast Guard Electronics Engineering Center, Wildwood, NJ, 01 May, 1989.

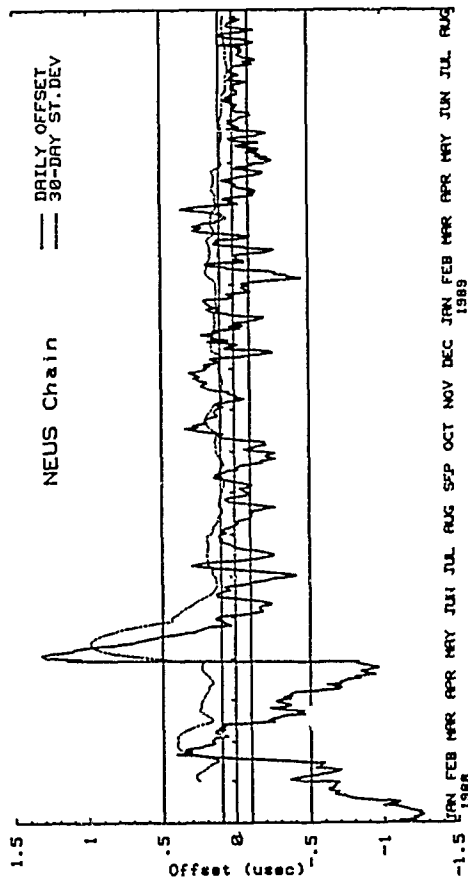


Figure 1. Offset Data for Loran-C Station Seneca, NY.

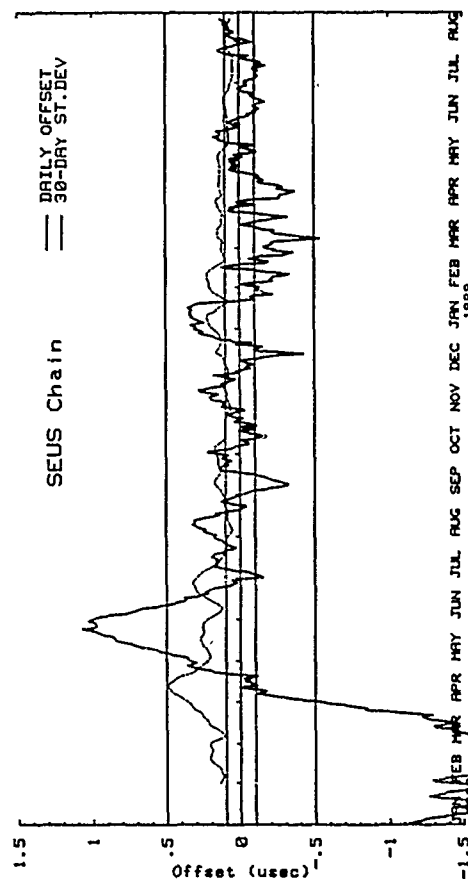


Figure 3. Offset Data for Loran-C Station Malone, FL.

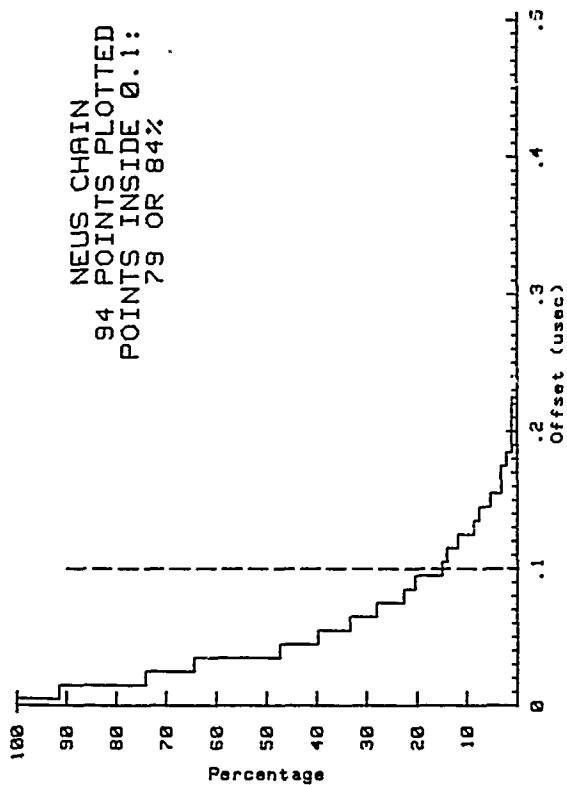


Figure 2. Percentage of Offsets Outside a Given Tolerance for LORSTA Seneca from May 15, 1989 to August 17, 1989.

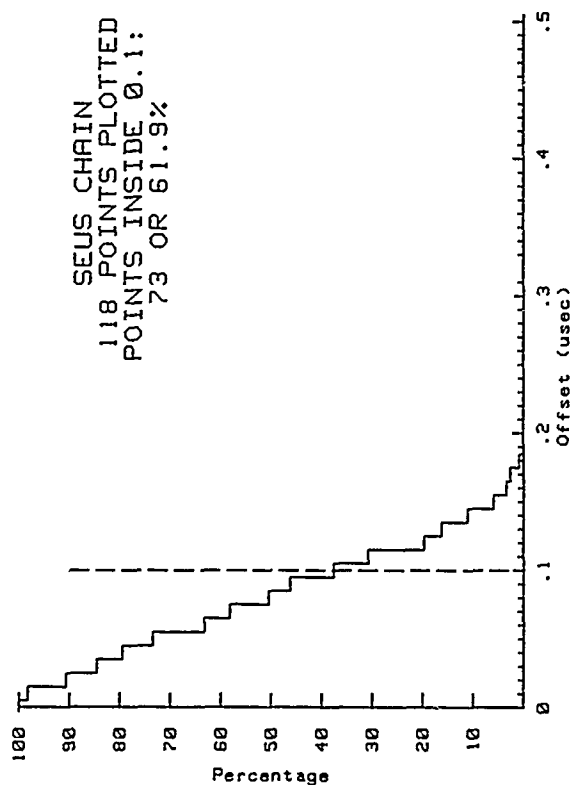


Figure 4. Percentage of Offsets Outside a Given Tolerance for LORSTA Malone from April 21, 1989 to August 17, 1989.

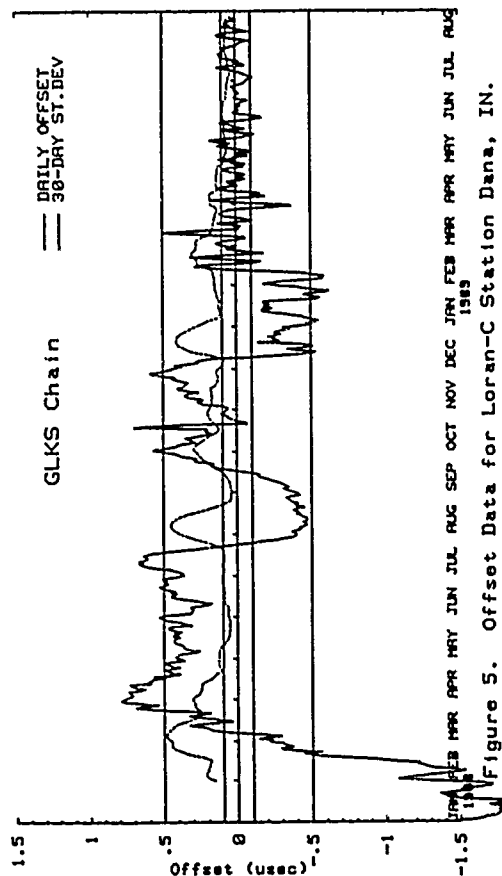


Figure 5. Offset Data for Loran-C Station Dana, IN.

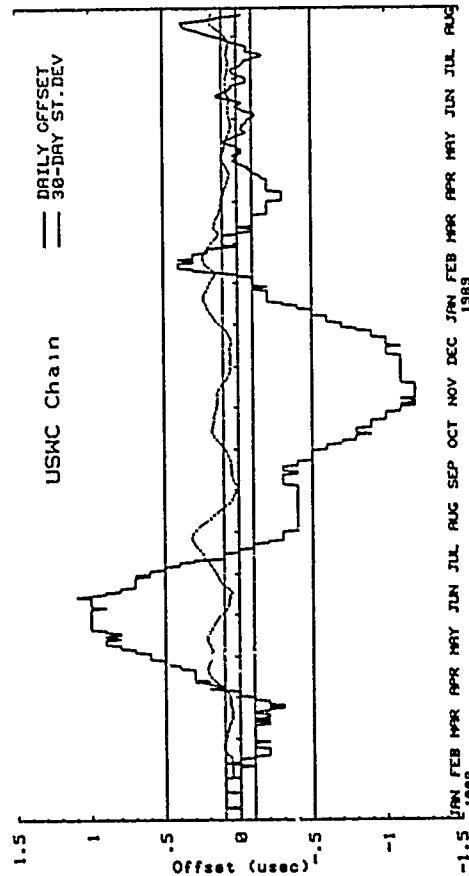


Figure 7. Offset Data for Loran-C Station Fallon, NV.

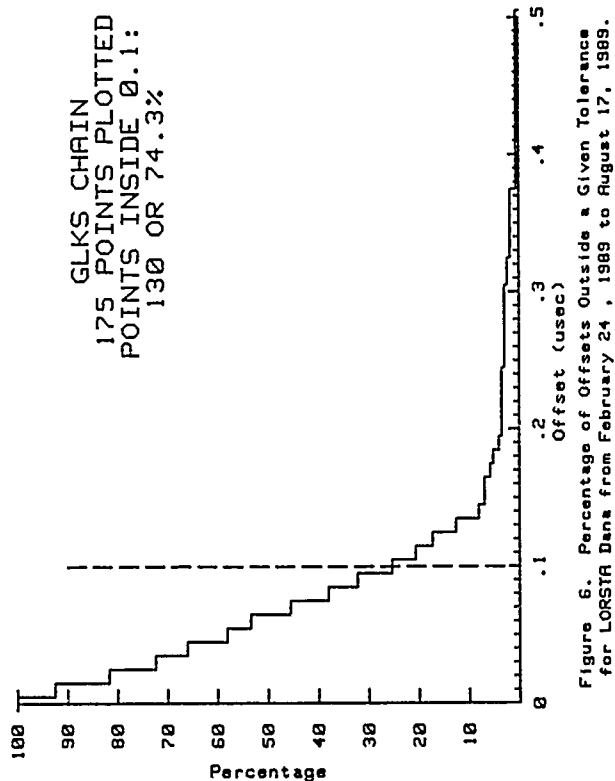


Figure 6. Percentage of Offsets Outside a Given Tolerance for LORSTA Dana from February 24, 1989 to August 17, 1989.

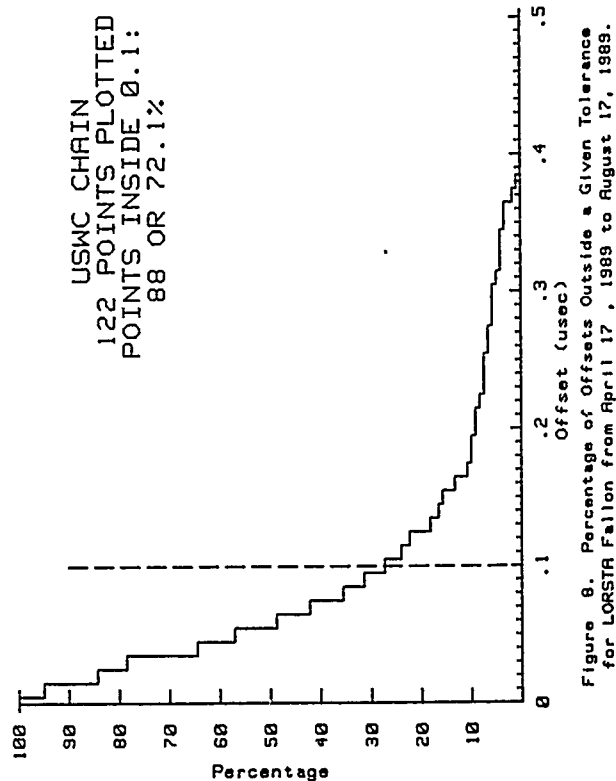


Figure 8. Percentage of Offsets Outside a Given Tolerance for LORSTA Fallon from April 17, 1989 to August 17, 1989.

FREQUENCY AND TIMING SYSTEM
AT THE NATIONAL INSTITUTE FOR STANDARDS (NIS)

Safaa Samuel
National Institute for Standards
Cairo-Egypt

ABSTRACT

The National Institute for Standards (NIS), is charged with the responsibility of establishing and maintaining the national standards of physical measurements and providing means for their effective utilization. Time and frequency division of Egypt makes the international comparison to relate NIS frequency standard to UTC.

Traceable frequency calibrations to NIS of standard clocks kept in other Egyptian scientific organizations, military and industrial laboratories are provided by means of daily television measurements and common-view monitoring of Loran-C signals by the user and by NIS.

This paper describes the Frequency and Timing system used at the NIS and the methods of comparing NIS frequency standard with UTC.

Diagrams and specifications of today's system and plans for future work will be presented.

1. INTRODUCTION:

Time and Frequency Laboratory of Egypt was established in 1967. In that year the National Institute for standards NIS took delivery of its first commercial cesium standard. From then on, it has been developing step by step and its performance level has also progressed gradually. International comparisons are continuously carried out to relate NIS frequency standard to UTC since 1967. Reception of VLF transmissions from GBR (16KHz), Rugby, England was used for phase comparison with good results [1-2].

In March 1982, NIS contracted with AID and National Institute of Standards and Technology NIST, Boulder to improve the time and frequency measurement system. Upon the delivery of receivers, reception of Omega transmissions and LORAN-C navigation signals have been started. The results of continuous phase comparison between Monrovia, Liberia and the NIS frequency standard using the Omega

transmitter (12 KHz) a distance of 5100 km were given in Ref [3] . A study of the receiving conditions using the Loran-C transmissions of the Mediterranean chain was made at NIS to determine the accuracy and reliability of time difference measurements [4] .

2. PRESENT STATUS

2.1. Reference clock system:

The reference clock system currently being used at the NIS consists of the Cesium Beam frequency standard, a secondary Rubidium vapour frequency standard and high quality crystals. The primary frequency standard for the timing system is the HP model 5061A (opt. 004) Cesium beam oscillator. The outputs of the frequency standard are used as reference signals to drive the LORAN-C receivers and other equipment via the distribution amplifier. Battery operated power supply is used to provide uninterrupted power to the standard in the event of a power failure.

2.2. Measurement Facility:

The receiving system comprises two VLF receivers, three automatic Mieco receivers and two 2000 C LORAN-C timing receivers. The data acquisition system is based at present on a personal computer with time-of-day clock, printer and disc store the data system was provided from NIST, Boulder [5] . A functional diagram of the equipment used for the realization of UTC (NIS) is given in Fig.1 and the photo of the timing system is shown in Fig.2. UTC (NIS) is connected permanently to the start terminal of each channel of the 4 channel time interval counter.

Each station is received by means of two types of the Loran-C receivers and the receiver output is connected to the stop terminal. Each measurement is the mean of 400 time difference readings. The computed results, together with a time tag are printed each hour on a floppy disc for permanent storage and subsequent analysis.

3. DATA COLLECTION AND PROCESSING

For many years, Loran-C 7990 Y from Kargaburun, Turkey in the Mediterranean sea chain has been the mainstay of the time link from NIS to the Bureau International de l'Heure (BIH). Regular measurements are made on the automated measurement facility. The time interval counter makes the time interval measurements and transfers them to the computer for storage on disc. When all the necessary data is stored, time position analysis is accomplished by using the

data analysis system.

The data collected at NIS at the last 2 months referencing the NIS to 7990 Y is a good example of problems arising in the received data. The plot shown in Figure 3 shows that around October 23 the data had a sudden jump of about 6 us, then continuing drifting at the same rate. Figure 4 gives the data after removing phase jumps.

In the meantime a continuous check on the accuracy of the 8990 X station clock is carried out [6]. Reception of this signal should be of great value to users in our area and to south Asia because of much shorter distance, 408 km from NIS. Figure 5 gives the relative frequency of the 8990 X station clock.

An example of measurements made over a number of days is shown in Figure 6. The values shown represent the daily accumulated phase shift. The phase shift is measured by comparing the output of a Loran receiver to the cs(NIS) for a period of 24 hours.

4. TIME AND FREQUENCY CALIBRATION AND DISSEMINATION

The dissemination of the time/frequency units within the country is realized by two techniques.

1. Passive TV synchronization technique: Accuracies of 100 us in time and 1×10^{-9} in frequency can be achieved.
2. LORAN-C common view monitoring: Frequency calibration requirements at the level of part in 10^{12} can be achieved using this service.

Calibrations are provided for precision oscillators and reports giving the relative frequency versus cs(NIS) are supplied.

Periodically, the NIS holds workshops intended for engineers and lab technicians involved in the application of time and frequency measurements.

5. FUTURE PLANS

In the near future the developments in the time and Frequency standards field will focus on the development of accurate time comparison techniques via satellites (e.g. GPS, two way communication satellites).

The future goals of the division include also the use of Arabsat as a vehicle for time and Frequency dissemination. This project will help the communications industry to meet some of the timing requirements in digital communication systems.

For all the activities planned and mentioned above, anyone interested in cooperating will be welcomed. The laboratory also welcomes any proposals from other laboratories, for collaboration in this field.

6. CONCLUSION

Current activities in the PTTI area at NIS Egypt has been presented. NIS maintains a cesium beam reference standard, continuously compared with UTC using Loran C signals. NIS clock data is reported. The relative frequency of the clock station 8990 X is given.

ACKNOWLEDGEMENT

Special thanks to Mr George Kamas of the NIST, without whose continued support and encouragement this work should not be possible.

References:

1. A.Loutfy El Sayed, "Frequency Standard work in Egypt," Proc. IEEE (Lett.) 60, No.5 pp. 627-628 (May 1972).
2. S.Samuel, "International Comparison of Atomic Frequency Standards via VLF Radio Signals and Loran-C Navigation Systems," Proc. Second National Radio Science Symposium-Cairo, Egypt, 1984.
3. S.Samuel, "Use of Liberia Omega transmissions for frequency calibration in Egypt," Proc. of the 18th PTTI Meeting, Washington D.C., Dec. 1986.
4. S.Samuel, "Use of the Mediterranean Loran-C transmissions for Frequency Calibration in Egypt," J. Soc. of Eng., Vol.25 No.4, 1986.
5. G.Kamas, M.A.Lombardi, "A new system for Measuring Frequency NCSL 1985 Workshop and Symposium; 1985 July; Boulder, Co.
6. S.Samuel, "Linking Saudi Arabia Loran-C to Mediterranean Chain," Proc. of the 19th PTTI Meeting, Washington D.C., Dec. 1987.
7. D.W.Allan, and M.A.Weiss, "Accurate Time and Frequency Transfer During Common View of a GPS Satellite." Proc. 34th Ann. Symp. on Freq. Control, Philadelphia, PA, p. 334-347, May, 1980

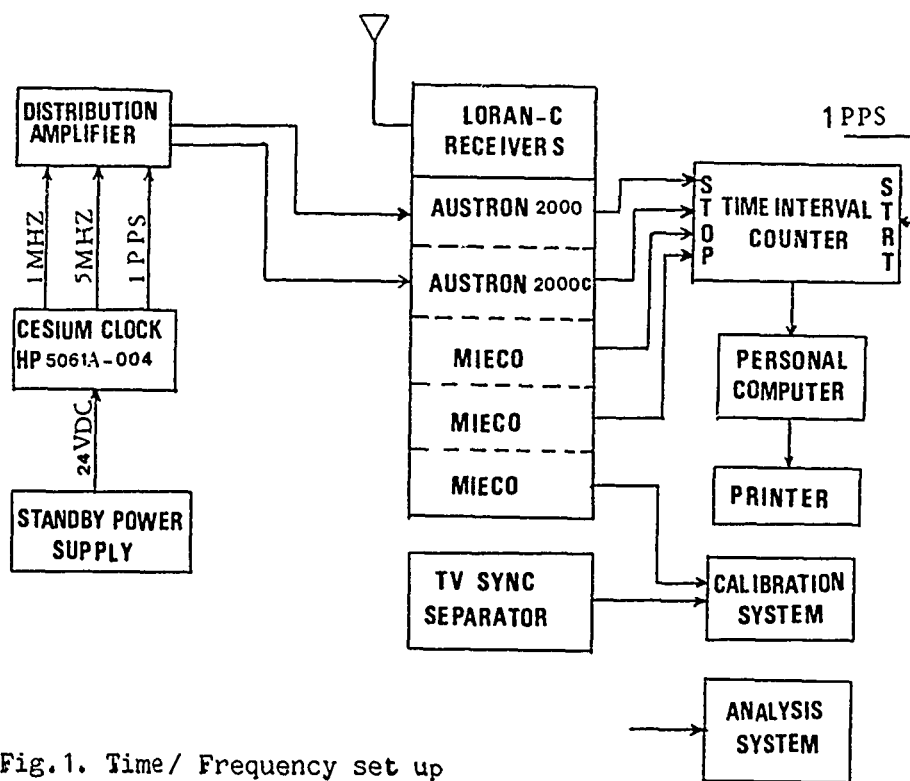


Fig.1. Time/ Frequency set up

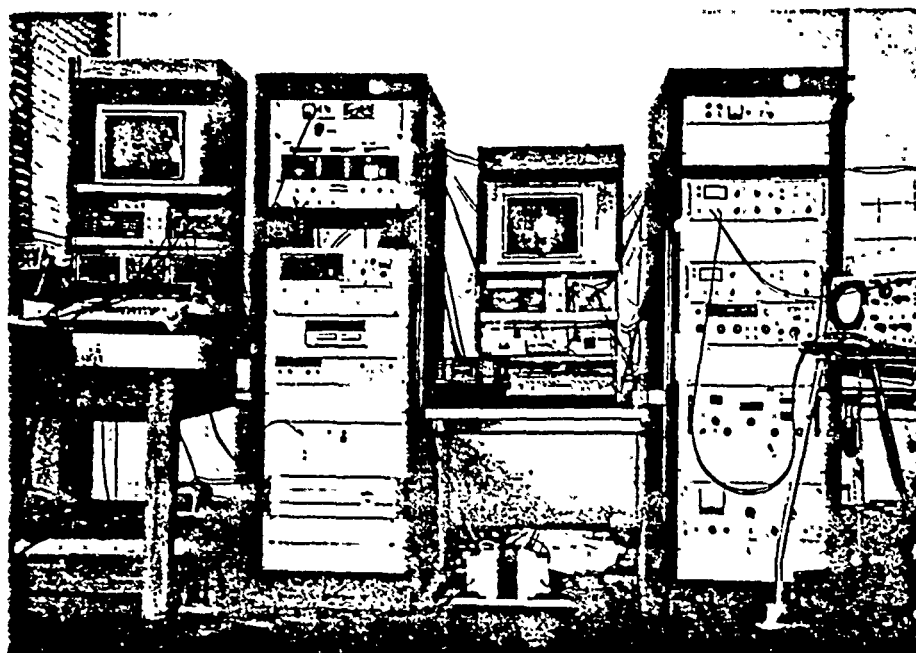


Fig.2. Part of the Time and Frequency Laboratory.

Fig.3. CS VS LORAN 7990Y (M)

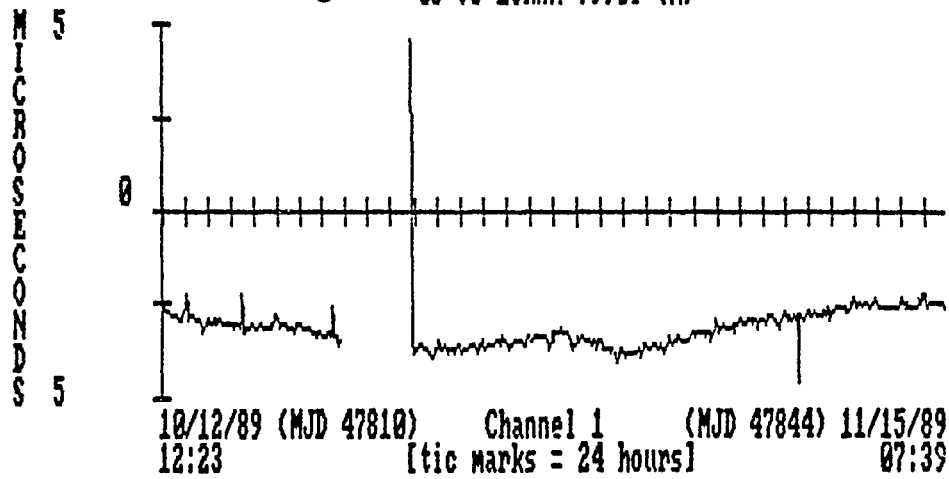
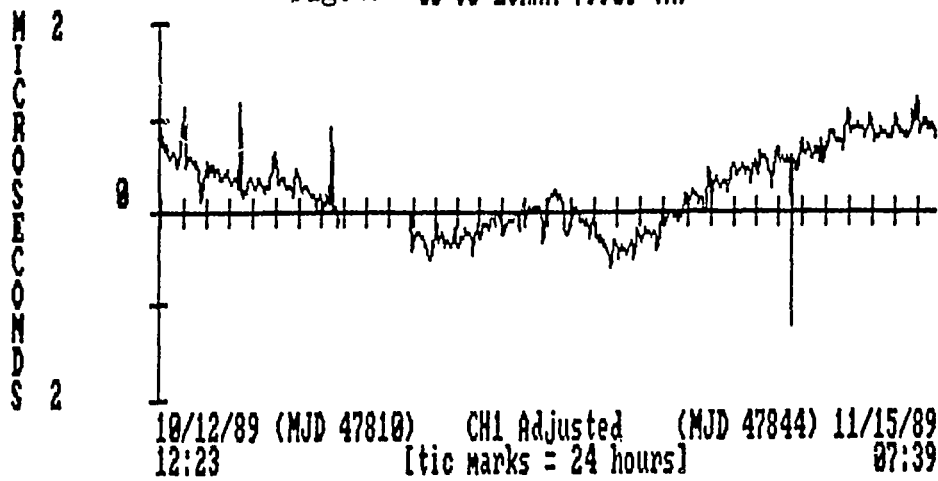


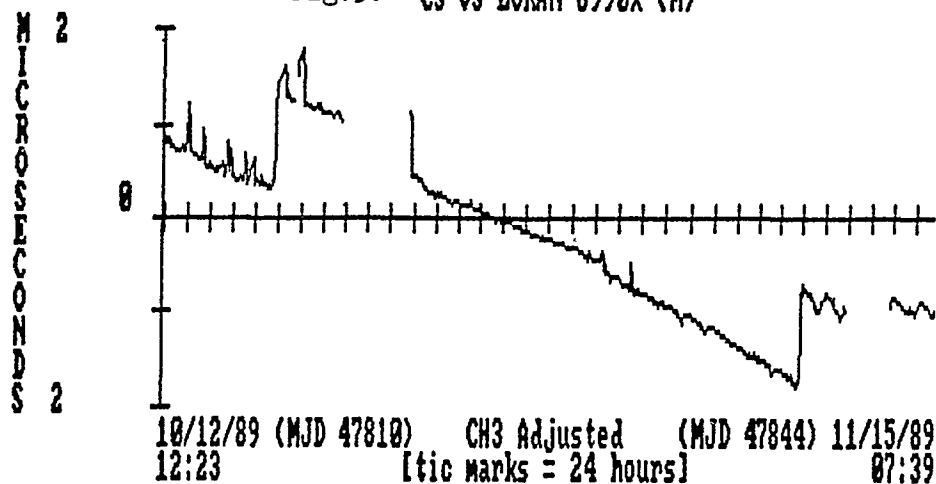
Fig.4. CS VS LORAN 7990Y (M)



The relative frequency is: $+1.52E-13$

Data Points 530

Fig.5. CS VS LORAN 8990X (M)



The relative frequency is: $-9.20E-13$

Data Points 506

Fig.6.

DATE			UTC(NIS)-LORAN PHASE (μ S)	
1989	MJD		LORAN C Turkey (7990-Y)	LORAN C Homyd (8990-X)
Oct	31	47830	+0.23	+0.20
Nov.	1	47831	-0.11	+0.16
	2	47832	-0.23	+0.12
	3	47833	-0.18	+0.12
	4	47834	-0.21	+0.12
	5	47835	-0.05	+0.20
	6	47836	-0.10	+0.16
	7	47837	-0.13	+0.10
	8	47838	-0.10	-0.84
	9	47839	+0.02	-
	10	47840	-0.36	-

QUESTIONS AND ANSWERS

GERNOT WINKLER, USNO: I wonder if there is any possibility of suggesting to the authorities which operate chain 8990 to put it more exactly on frequency, because your numbers indicate a frequency offset of somewhere around 1×10^{-11} . Or am I mistaken?

MS SAMUEL: They don't make an attempt to keep it on frequency.

MR. WINKLER: Then I suggest that they adjust it regularly as is done in the U.S. to keep it very close to the time and frequency of a national reference. In that case, the users could obtain the services directly, for example, frequency calibration.

MS SAMUEL: They don't want to negotiate with Egypt.

ULTRASTABLE QUARTZ OSCILLATOR FOR SPACECRAFT

Jerry R. Norton
The Johns Hopkins University
Applied Physics Laboratory
Johns Hopkins Road
Laurel, Maryland 20707

Abstract

A new series of quartz oscillators that have excellent performance has been developed for use in spacecraft. Some oscillators using this design have demonstrated 24-hour aging rates of less than 1×10^{-11} , 100-s Allan variances of 7×10^{-14} , and a phase-noise floor of -158 dBc.

Variations in resonator performance exceeding factors of 10 have been found during the evaluation of resonators using the same test oscillator; this finding indicates that oscillator performance is still dominated by the quartz resonator. SC cut resonators manufactured by different companies using a variety of mounting techniques and resonator enclosures have been used in this design. Some performance parameters are directly related to resonator type.

The oscillators are designed to survive the rigorous environment of a rocket launch. They are projected to have a minimum useful life of 5 years in a space environment through the use of conservative design margins, high-reliability components, and a rugged mechanical package. A vibration isolation system is incorporated that attenuates the band of frequencies generated by currently available launch vehicles that could potentially damage the oscillator. The oscillators are compact and low weight and have low power consumption.

A dual thermal insulating system using a unique Dewar flask design and a space blanket (alternate layers of a porous spacer and radiation-reflective aluminized Mylar) is used to isolate critical oscillator components from the thermal environment and to reduce power consumption. The design of the Dewar flask, which is made from titanium, requires no pinch-off tubes or other protrusions outside of the basic cylindrical envelope of the Dewar.

A clearly defined frequency versus ambient pressure change was recognized during development of these oscillators. Components used in the oscillator were identified as the main cause of the pressure sensitivity, but after these components were replaced, a pressure sensitivity remained that is related to individual resonators and resonator types.

INTRODUCTION

This paper will present the performance results from a new series of high-performance quartz oscillators developed for use aboard spacecraft. Test results revealed the quartz resonator has a very

heavy impact on oscillator performance. Design features that make this oscillator well suited for use in spacecraft will be discussed. Finally, measurement results and observations of oscillator frequency versus ambient pressure will be presented.

More than 30 oscillators using the same basic design have been fabricated, and 24 of the oscillators have been spaceflight qualified. A 5-MHz third-overtone SC cut resonator controls the output frequency of the oscillator. The resonator and critical oscillator components are housed in a high-stability single proportionally controlled oven that maintains a constant temperature over the ambient operating temperature range to ensure high performance.

ALLAN VARIANCE AND PHASE-NOISE RESULTS

Table 1 contains data selected to illustrate the performance of some of the best and worst oscillators. The mean 100-s Allan variance for the entire oscillator group is very good, and four of the oscillators (S/N4, S/N10, SC5, and SC7-92) achieved an Allan variance in the 10^{-14} range. Data for the series of oscillators designated by SC7 are particularly interesting. Oscillator SC7 is a test oscillator that was used to evaluate resonators, and the dash following SC7 indicates a specific resonator being evaluated. As shown in Figure 1, the 100-s Allan variance for this group of oscillators (SC7, SC7-2, SC7-92, SC7-10, and SC7-38) varies over a wide range (8×10^{-14} to 1.5×10^{-12}). The only difference between these oscillators is the resonator; therefore, performance must be related to the individual resonator. As a further indication that oscillator performance is dominated by the resonator, oscillators SC8-4 and SC7 used the same resonator and performed similarly (see Figure 2), yet they are very different physically and even use different types of electronic components. The mean Allan variance for the group of oscillators and the Allan variance for two of the best performing oscillators SC5 and SN10 are also presented in Figure 2. The Allan variance for τ of 1000 s is heavily influenced by the oscillator aging. For oscillators that have very low aging rates, such as SC5, there is little difference between the 100- and 1000-s Allan variances. Phase-noise data for the oscillators are also presented in Table 1, and a plot of phase noise is depicted in Figure 3. If the Allan variance and phase-noise data for the same oscillator are compared, tracking between the two is not consistent. Actual phase noise is probably 6 to 10 dB better than presented, particularly below 10 Hz, because of two sources of potential error: (1) a low-phase-noise reference oscillator was not always available for phase-noise testing, and (2) the phase-noise test equipment has an error of 10 to 12 dB below 10 Hz. The phase-noise data presented are on the conservative side. Although the data are known to have some error, the oscillator performance is at least as good as shown. All the data presented in this paper do not assume equal noise sources from each oscillator.

Other oscillator performance data are presented in Table 1 without comment except for frequency versus temperature. A design change was implemented, which reduced the temperature coefficient to the mid to low 10^{-13} range per degree Celsius. Resonators from both Bliley Electric and Piezo Crystal have been used in these oscillators; performance from each manufacturer has varied between very good and mediocre.

THERMAL ISOLATION SYSTEM

These oscillators were designed to operate in a space environment where power consumption, size, weight, and the ability to survive the rigors of a rocket launch are always of concern. The method of

providing thermal isolation for the oscillator has a direct influence on these parameters. Glass Dewar flasks have good insulating qualities, but they are bulky, heavy, and fragile. Space blanket or super insulation (alternate layers of a porous spacer and radiation-reflective aluminized Mylar) is extremely efficient but requires a vacuum to be effective. Oscillators at the Applied Physics Laboratory have traditionally used super insulation for thermal isolation; however, requirements for the oscillators to operate at atmospheric pressure have been requested by some of our sponsors. Not being very fond of the penalties imposed by a glass Dewar, we designed the titanium Dewar flask shown in Figure 4, which has very appealing characteristics. The titanium Dewar is light and rugged, has a small cross-sectional area between the walls, and has no pinch-off tubes or other protrusions outside the cylindrical shape of the Dewar. These advantages far outweigh the titanium Dewar's disadvantage of not being as thermally efficient as a glass Dewar. When the titanium Dewar is used in combination with super insulation, a thermal isolation system is realized with a slight increase in size and weight, which permits ground-based operation yet retains the extremely efficient insulation qualities in the vacuum of space.

VIBRATION ISOLATION

A mechanical resonance in the system used to attach the quartz disk to the resonator enclosure will severely damage or destroy the resonator if excited. The frequency of this resonance is in the range of 200 to 1000 Hz. A unique vibration isolation system that is equally effective in all three orthogonal axes is incorporated in the oscillator design to isolate the resonator from the external environment for frequencies above 100 Hz. Figure 5 presents the attenuation characteristics of the isolation system as a function of input excitation frequency. The heart of the system is an elastomeric frustoconical-shaped isolator molded from a low-Q RTV compound. A photograph of the vibration isolation system is shown in Figure 6. By varying the thickness, diameter, and composition of the RTV, the cutoff frequency and attenuation characteristics of the isolator can be tailored to accommodate different weights and vibration profiles. The isolators are carefully processed to eliminate air bubbles during molding and are then baked out in a vacuum to remove volatile components from the molded isolators.

AMBIENT-PRESSURE-INDUCED FREQUENCY CHANGE

During early development of this oscillator, a slow varying frequency change was observed that did not seem related to any known cause. The character of the frequency change suggested it would be related to temperature. Ambient temperature and frequency were monitored, and little correlation was observed between the two. A second oven was added to a test oscillator, but the frequency wander persisted. The frequency wander does not occur during oscillator evaluation in a vacuum that simulates a space environment. After observing the oscillators for several months, the frequency changes in air seemed to be related to weather-front movements. When the atmospheric pressure was recorded and compared with the oscillator frequency changes, correlation between the two was quite good, as shown in Figure 7. Two of the oscillators, SC5 and SC11, have a negative frequency change when the pressure increases, whereas the frequency change of oscillator SC3 is positive with increasing pressure. Figure 8 shows how two oscillators performed during the passage of hurricane Hugo up the East Coast. When pressure increases, frequency changes are larger and the change occurs more rapidly, which may be observed in both Figures 7 and 8. An air dielectric variable piston capacitor used to set the oscillator output frequency was considered to be the most likely component causing

the frequency changes. This capacitor was removed, and indeed the frequency changes were decreased but not eliminated. Tests are continuing to be conducted, but the following observations can be made. The glass-enclosed resonators from Bliley show the largest variation from unit to unit; some have almost no change, whereas others are 10 to 20 times worse. Metal-enclosed resonators from Piezo Crystal have smaller frequency changes than the Bliley units by a factor of 2 to 5; however, only a few samples have been tested. BVA resonators have the best performance, but again the number tested is quite small (< 5).

The size of the oscillator is $5 \times 4 \times 2.2$ in., it weighs 1.7 lb, and it consumes 0.9 W at 27 degrees Celsius.

CONCLUSION

An oscillator has been designed that is well suited to cope with the harsh environment of a rocket launch and the vacuum of space. The oscillator has outstanding performance and perhaps could be even better or at least more consistent if there was a clear understanding of why some quartz resonators perform better than others. This knowledge could then be applied to resonator design and fabrication technology to improve the breed of currently available resonators.

Table 1

SERIAL NO	35 OSC	AVERAGE	S/N4	S/N10	SC4	SC5	SC8-4	SC7	SC7-2	SC7-92	SC7-10	SC7-38
Drift Rate/24 Hr	4 1E-11	6E-12	7 5E-11	2E-10	4E-12	2E-11	3E-11	-4E-11	7E-12	1E-10	2E-10	
ALLAN VARIANCE												
Tau(Sec)												
0 01					6 2E-12	6 9E-12			1 5E-11			
0 1	5 2E-12	4 6E-12	7 7E-12	2 7E-12	2 1E-12	1 4E-12	1 3E-12	2 3E-12	1 1E-12	1 5E-12	4 8E-12	
1	6 5E-13	3 3E-13	6 5E-13	3 1E-13	3 5E-13	4 1E-13	4 9E-13	4 3E-13	1 5E-13	6 1E-13	3 1E-12	
10	1 7E-13	1 6E-13	9 8E-14	2 1E-13	8 9E-14	2 2E-13	2 4E-13	2 5E-13	1 2E-13	9 1E-13	4 8E-12	
100	1 7E-13	8 9E-14	8 4E-14	2 1E-13	6 6E-14	1 8E-13	1 9E-13	3 4E-13	8 1E-14	1 5E-12	7E-12	
1000	9 5E-13	1 4E-13		3 1E-13	7 4E-14	3 1E-13	4 1E-13		3 3E-13			
PHASE NOISE dBc/Hz												
Freq Offset(HZ)												
1	-114 63	-113	-114	-112	-121	-110	-114	-111	-122	-109		
10	-138 75	-141	-141	-142	-139	-135	-141	-135	-136	-134		
100	-148 25	-147	-148	-152	-147	-147	-153	-145	-147	-144		
1000	-151 00	-149	-150	-153	-150	-152	-154	-147	-153	-147		
10000	-152 63	-150	-150	-155	-152	-154	-157	-147	-156	-147		
100000	-153 25	-149	-150	-155	-152	-156	-157	-147	-160	-148		
Freq as Function												
of												
Temperature per °C	1 5E-12	2 1E-12	8 6E-13			6 2E-13						
Load	2 4E-12	2E-12	2 7E-12	5E-12	2E-12		7 0E-10	3 8E-10				
Voltage	2 0E-12	1E-12	3E-12					<1E-12				
Output Characteristics												
Voltage Level	1 55	1 38	1 5	2 1	1 5	1 18	1 9		1 89			
Harmonic (dBc)	-62	-62	<-60	-45	-48				-63			
Spurious (dBc)	-77	-72	<-80									

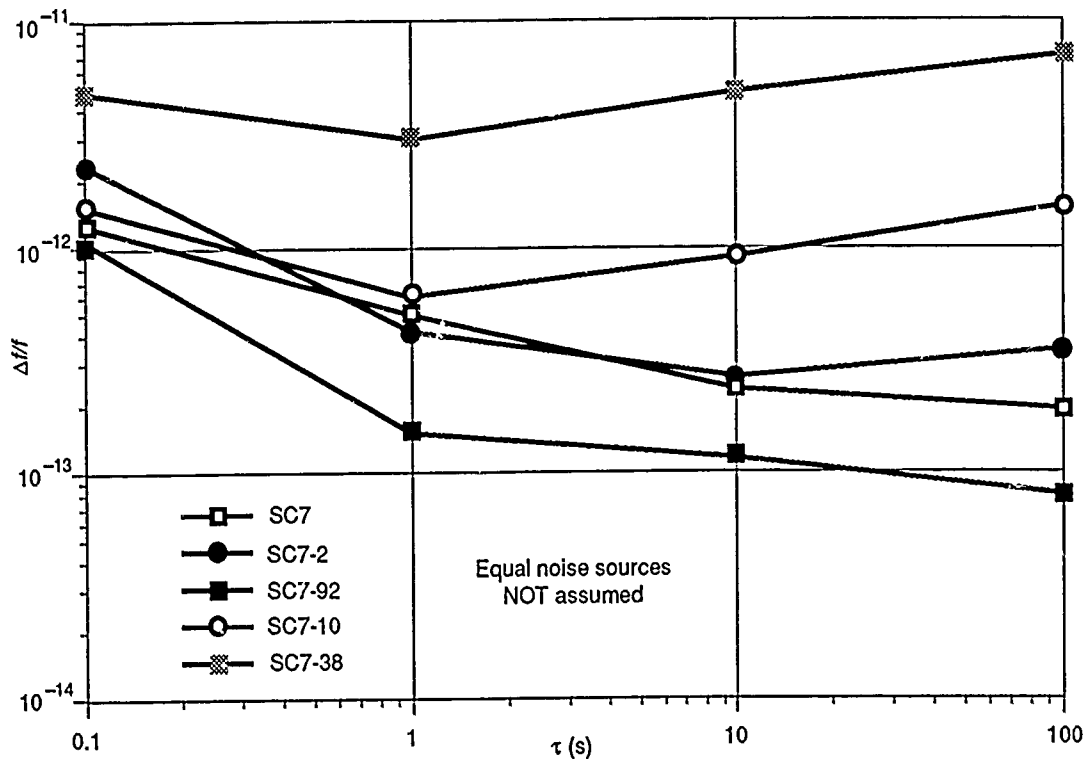


Figure 1. Allan variance of oscillator SC7.

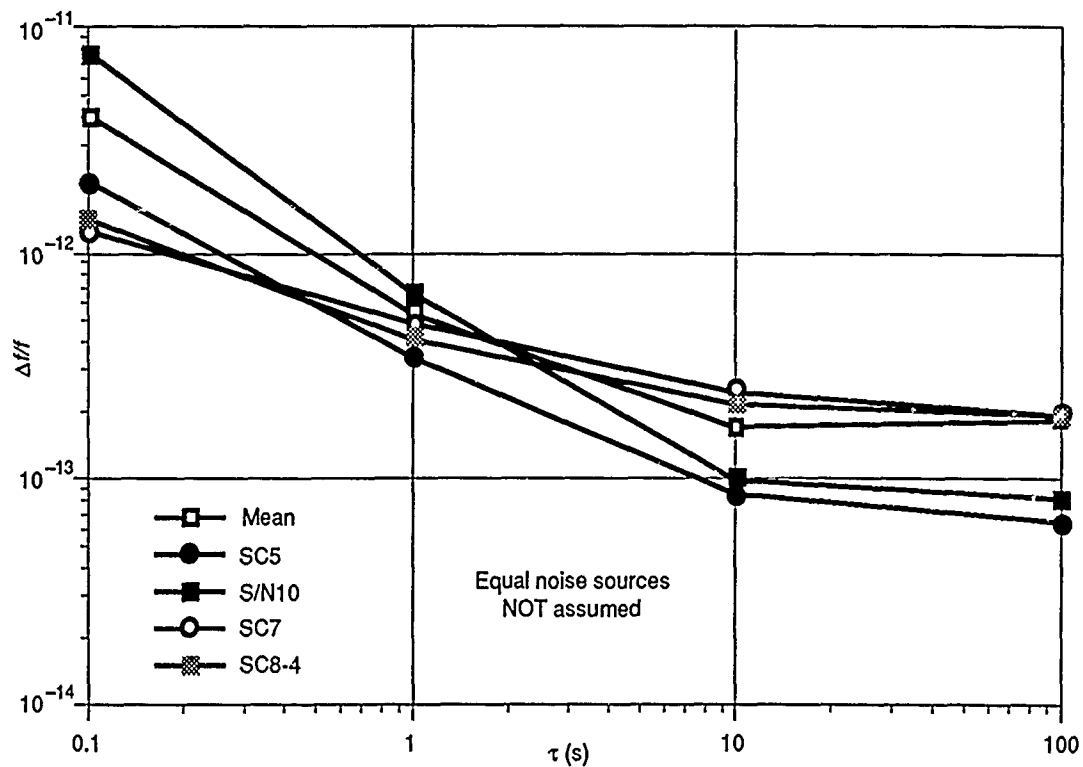


Figure 2. Allan variance of selected oscillators.

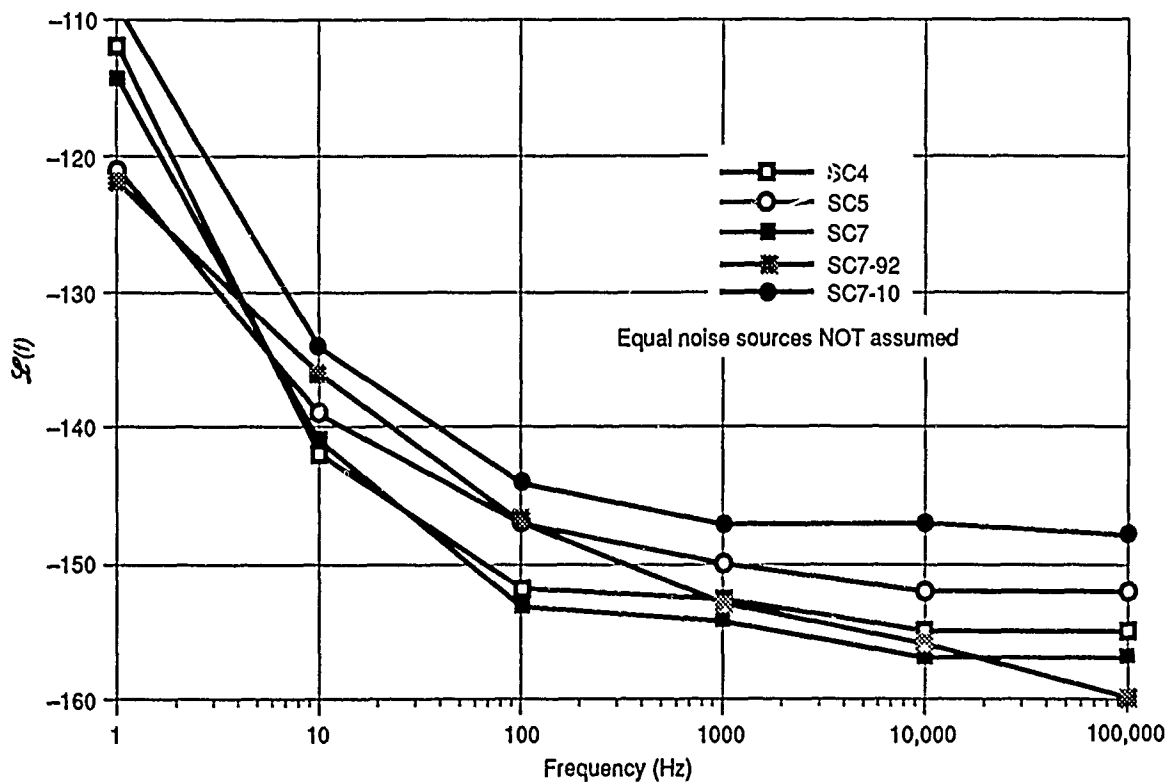


Figure 3. Phase noise of selected oscillators.

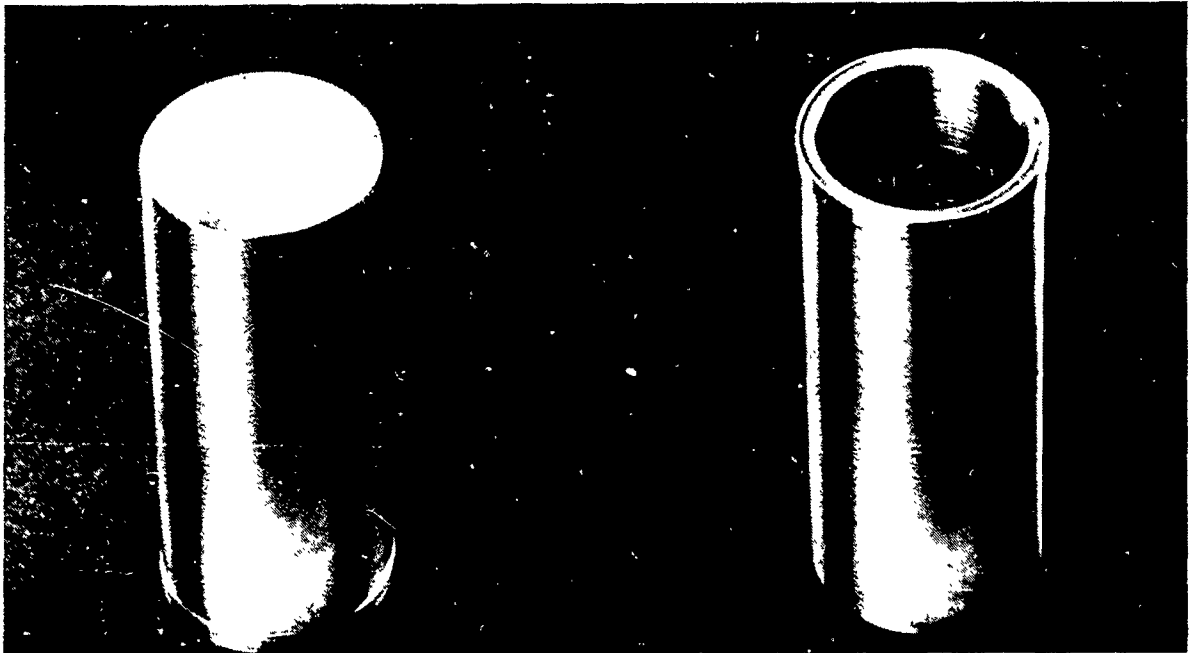


Figure 4. Dewar flask.

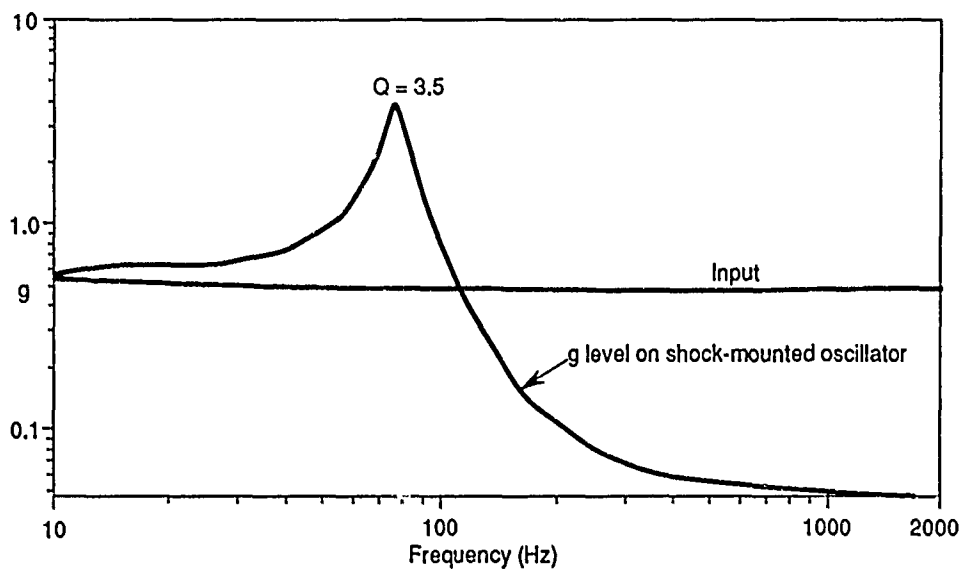


Figure 5. Attenuation characteristics of the isolation system as a function of input excitation frequency.

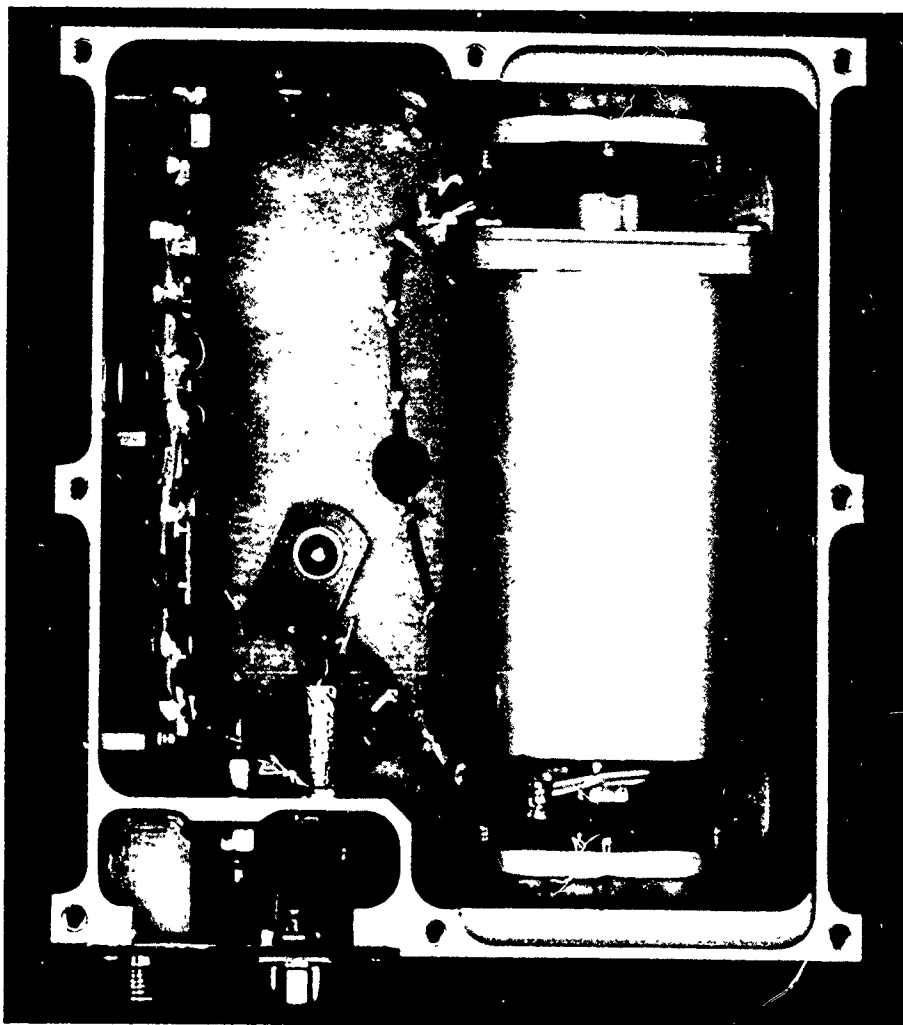


Figure 6. Vibration isolation system.

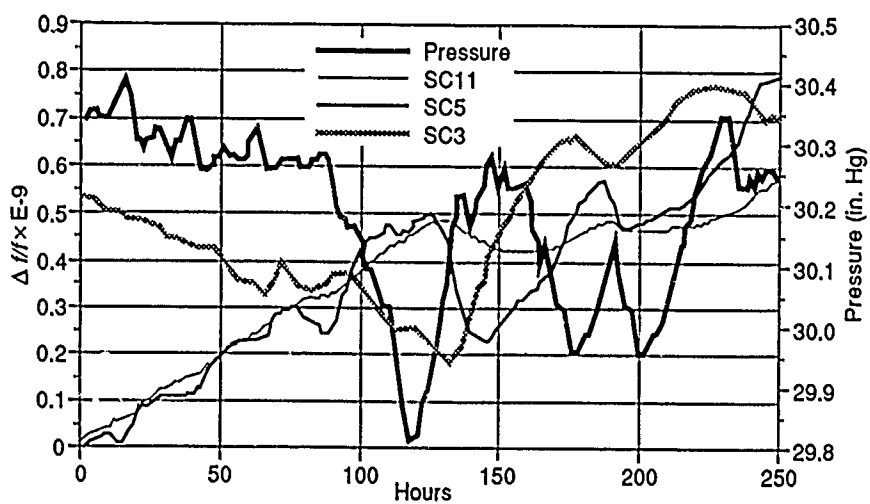


Figure 7. Oscillator SC3, SC5, and SC11 pressure-induced frequency change.

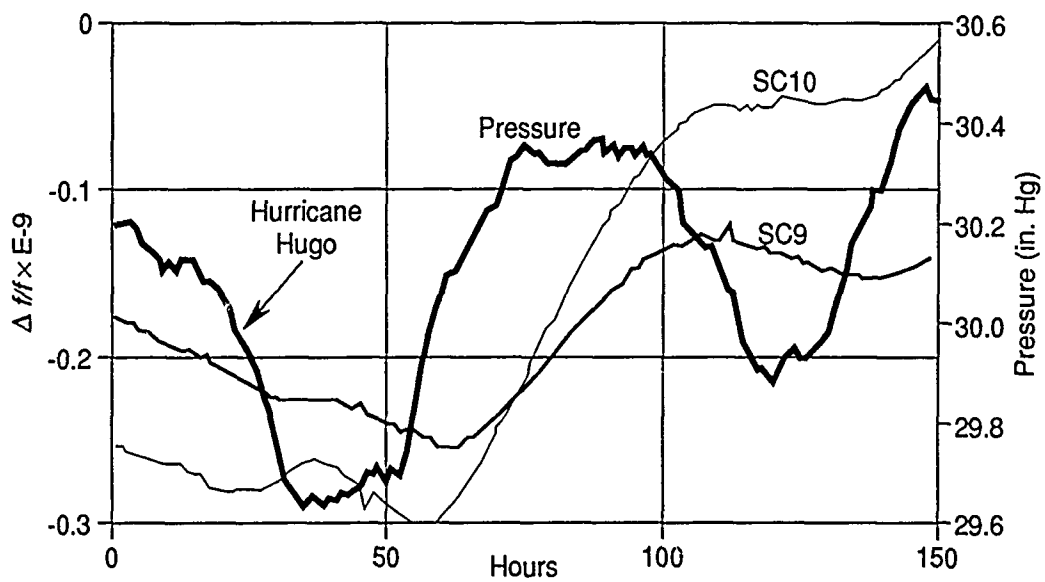


Figure 8. Oscillator SC9 and SC10 pressure-induced frequency change.

QUESTIONS AND ANSWERS

FRED WALLS, NIST: Of the oscillators that reach $\approx 7 \times 10^{-14}$ / , were they just SC cut? Could you comment as to whether they were fifth overtone SC's or what?

MR. NORTON: All the resonators used for this paper were third overtone SC's, 5 MHz. We use resonators from two different manufacturers with at least three different mounting techniques. The oven is a single proportional oven. Is there anything else that you want to know?

MR. WALLS: You are one of the few people that have seen many oscillators drop below 1×10^{-13} and obviously some of your circuit design makes quite a difference. Would you care to comment on what is special about your circuit?

MR. NORTON: To be honest, there is nothing extremely special about it. It is a modified Colpitts oscillator. We have a fairly heavy copper oven which probably helps with the thermal problems. We think that we have a pretty good oven design, which certainly contributes to the overall performance. The measurements in parts in ten to the 14^{14} are not isolated cases. Those are not something that we see once or twice. When the barometric pressure is nice and stable, we see 3 and 5 in ten to the fourteenth for short periods of time. I might mention that the frequency wander that we see—these are spacecraft oscillators and we do qualify them in a thermal vacuum system. Once they get in there, that frequency wander goes away so I think that it would be important to seal oscillators if you were building oscillators for ground based operation.

MR. WALLS: I guess that I would agree with that. It is not just pressure but I believe that humidity plays quite a role. Those that have been hermetically sealed seem to perform substantially better.

MR. NORTON: We haven't run any tests with humidity, but when you get weather front changes you get humidity changes. The environment that these oscillators are tested in is a dual air conditioning system so that, while the humidity is not constant, it doesn't change very rapidly or very far. I would agree that humidity contributes something to it also.

MR. WINKLER: I am going to ask you where the pressure was measured. The reason for the question is that there is a world-wide diurnal cycle which one can see everywhere. I couldn't see that on your data. The suspicion is that it was measured inside some sort of vessel or inside the laboratory.

MR. NORTON: Obviously it is inside a building. The pressure was measured inside the same enclosure with a recording barometer which is capable of measuring to a one/hundredth of an inch of mercury. The barometer and the device under test were separated by 6→8 feet.

MR. WINKLER: It is still strange that one does not see the diurnal effect.

MR. NORTON: Remember that that was for very short intervals, a couple of hundred hours. If you are concerned about the pressure measurements—we are located about 20 miles from BWI, the Baltimore-Washington International airport. We have correlated our data with data from the airport, so I don't think that we have a problem as far as pressure measurements are concerned.

UNIDENTIFIED QUESTIONER: In the oscillator circuit, is the crystal dissipation controlled by self-limiting, or an automatic gain control circuit?

MR. NORTON: It is an automatic gain control circuit.

AN UNBIASED WEIGHTING METHOD FOR DATA IN GPS COMMON VIEW

Zhuang Qixiang, Jian Shuguang, Fan Neng Shanghai Observatory,
Chinese Academy of Sciences

ABSTRACT

The mode parameters for GPS common view time transfer is estimated and an unbiased weighting method (UBWA) for data in GPS common view is discussed in this paper. The one Σ jitter of each time series is determined by the standard deviation of residuals of polynomial regression, which define weights used to compute a weighted average. Averaging the double difference observables during an integral length (30 days), the systematic biases existing between every two time series are corrected in constant monthly relative to a reference time series. The GPS common view data among NRC in Ottawa, NBS in Boulder and USNO in Washington DC, are calculated by using three different methods: UBWA, equal weights average method (EWA), and direct weighting method (DWA). The final weighted averages are compared in terms of Σ (standard deviation of residual), Allan variance (frequency stability) and time discontinuity (caused by increasing or decreasing time series). Results showed that UBWA is superior to the others.

ESTIMATE FOR MODE PARAMETERS

GPS single difference observables between stations reflect receiver clock differences between stations directly and apply to high precision time comparison widely, i.e. the so called common view mode. Its model equation can be expressed as;

$$t_{BAj}(\tau) = t_{Aj}(\tau) - t_{Bj}(\tau) =$$

$$1/c\{R_{Bj}(\tau)\} + ((f_B - f_j)/f_j - 9f_A - f_j)/f_j(\tau - \tau_0) + t_{AB}(ion) + t_{AB}(trop) \quad (1)$$

where A and B refer two stations, i refers the satellite, τ is the epoch for measurement. $t_{Aj}(\tau)$ and $t_{Bj}(\tau)$ are the time readings at stations A and B respectively, and the corrections have been made on these readings for the offset of the receiver system time delay. R_{Aj} and R_{Bj} are the distances from satellite j to stations A and B respectively. f_A and f_B are the receiver clock frequencies at stations A and B respectively. f_j is the satellite clock frequency. $t_{AB}(ion)$ and $t_{AB}(trop)$ are the differenced ionosphere error correction and the differenced troposphere error correction, respectively.

A common view track which repeats every sidereal day defines a time series comparing the clocks at the two stations. Each time series represents the time measurement of signal propagation over a specific path from one station to the satellite to another station. Change in path is caused by different satellite or different measurement time, and forms different time series. Some experiments have reported that the different time series between two stations has not only the different time jitter, but also obvious systematic bias. Through analyses of GPS various difference observables, the reason for existing jitters and biases could be understood. For different measurement geometry and measurement epoch, GPS various error sources which include ephemeris, ionospheric and tropospheric models, receiver coordinates as well as frequency offset between the reference clocks have different effect on GPS single difference observable.

Assuming GPS common view time series is a constant linear discrete time system. For a specific common view time series i , $Z_i(k)$ is defined as the optimal estimate of the i^{th} common view measurement $X_i(k)$ the observation equation is:

$$X_i(k) = \Phi_i Z_i(k) + U_i(k) + E_i(k) \quad (2)$$

Where, for one dimension scalar time comparison, the coefficient matrix $\Phi_i = (1, 0)$: i refers to the i^{th} common view measurement ($i = 1, n$), k refers to the k^{th} day ($k = 1, m$), $U_i(k)$ is the systematic part of the error which includes the frequency offset and drift between the reference clocks, propagation error, ephemeris error as well as receiver coordinates error. $E_i(k)$ is the random perturbation part of error which includes the random perturbation of atomic clocks as well as the measurement noise caused by propagation, ephemeris and receiver.

The systematic bias $U_i(k)$ between the i^{th} time series and the j^{th} time series is determined by the GPS double difference observable $t_{ABij}(\tau_{ij})$ over an integral data length (about 30 days) and the average value is Bias which is used to perform correction in constant relative to reference time series. The simulation of the deterministic properties of a time series is using polynomial,

$$X_i = a + bT_1 + bT_2^2 + \dots + bT_n^n \quad (3)$$

Applying linear regression to measurement data set T_k and $X_i(k)$, the coefficients of the polynomial are determined by least mean-square estimate. Thus Z_i , the optimal estimate of the measurement X_i , is obtained. It is important to examine the confidence in the result by taking the residual $\Delta(k) = X_i(k) - Z_i(k)$ as the estimate of $E_i(k)$.

First, the sampling time, τ , for common view time series is usually one day. Assuming E_i is Gaussian noise process, it includes mainly the white frequency noise and flicker frequency noise. So, E_i is well modeled by equation (4), Allan variance. The mean squared time error is expressed by equation (5).

$$\sigma_y^2(\tau) = (h_0/2)\tau^{-1} + h_{-1}2\ln(2) \quad (4)$$

$$\epsilon^2(\tau) = h_0\tau + 4h_{-1}\ln(2)\tau^2 \quad (5)$$

When the calibration interval $\tau_c = \tau = 1$ day, ϵ^2 is twice as large as σ_y^2 , and it is not divergent.

Secondly, the typical residuals curve for a common view data length of about 135 days is in Figure 1. Let

$$X = [(\Delta(k) - E_m)/\sigma] = 300 \quad (6)$$

$$F(x) = \sqrt{(2\pi)^{-1}} e^{-x^2/2} \quad (7)$$

where, mean value $E_m = 0$ so, the normalized distribution curve $[F(x) - X]$ is in Figure 2. It conforms obviously normal distribution $N(0, \sigma)$.

Hence it is reasonable to have σ , the standard deviation of residuals as the one sigma jitter of time series. RMS, the standard deviation of GPS double difference gives an estimate of measurement noise of double difference observables. The variance of double difference between the i^{th} and the j^{th} common view time series is S_{ij}^2 . Applying the N-corner hat technique, the variance estimate RMS^2 of the i^{th} can be completed:

$$RMS^2 = (n-2)^{-1} \left(\sum_{j=1}^n S^2 - B \right) \quad (8)$$

$$B = (2n-4)^{-1} \left(\sum_{(k=1)}^n \sum_{j=1}^n S_{kj}^2 \right) (S_{ij}^2 = 0) \quad (9)$$

Thus, RMS can be considered as the estimate of measurement noise V_k .

Bias, Σ and RMS are three major parameters of GPS common view time series. The common view data from MJD47011 to MJD47278 among NRC, NBS and USNO are divided and calculated monthly. Table 1 gives the data status. Bias, Σ and RMS are calculated in each data section. Taking an example, Table 2 lists the values of Bias, Σ and RMS for NRC-USNO link and data sections from 1 to 5.

The results in Table 2 are significant.

1. The Biases of time series over five data sections are quite stable the variable value is only several nanoseconds. By using linear regression, the average correlation coefficients are 0.15 and 0.27 for Σ -Bias and RMS-Bias respectively. This indicates a fact that systematic Bias is independent of random perturbation, hence it is acceptable to correct bias in constant.
2. Usually the Σ value is larger than the RMS value. The Σ value seems to be correlative to the data section, e.g. the Σ values for all twelve time series become large in data section 3, but the RMS value is not correlative to the data section. These conform the above analyses: Σ is the sum of system noise and measurement noise, while RMS is mainly the measurement noise.
3. The values of Σ and RMS are correlative to the time series basically, and the Bias for each time series is quite stable. Thus, the time series could be referred to as independent each other and to weight in one over variance is optimum. Because the correlation coefficient of Σ -Bias is small than that of RMS-Bias, to have Σ as one sigma jitter of time series is preferred.
4. The above results are obvious not only for NRC-USNO link but also for NRC-NBS link.

UNBIASED WEIGHTING METHOD

Based on the above analysis, an algorithm for processing data of GPS common view time comparison is recommended to be referred to as Unbiased Weighting Method (UBWA). It has the following features.

1. Averaging the double difference observables during an integral length (~ 30 days), the systematic biases existing between every two time series are corrected in constant monthly relative to a reference time series.
2. The one sigma jitter of each time series is determined by the standard deviation Σ of residuals of polynomial regression, which defines weights in one over Σ square.
3. Using raw measurement data at all, no interpolation or extrapolation for losing data points. For bad points, it can be identified and removed by computer program.

The steps and formulae for UBWA are as follows. The k^{th} day and the i^{th} path common view data between two stations is $X_{ij}(k)$, and the i^{th} path common view data form a time series:

$$X_i(k) \quad (k = 1, m) \quad (10)$$

Where, m is total measurement days, in practice $M=30$ as a data section. $i=1, n$, n is the number of common view paths each day between two stations. So total has n time series. Do least square fit for the i^{th} time series and calculate the standard deviation Σ_i of residuals, then the optimum weight for the i^{th} series is:

$$W_i = 1 / \Sigma_i^2 \quad (11)$$

Choose a reliable and continuous time series as reference one, namely the j^{th} . The double differences for all other series relative to reference one can be calculated,

$$T_{ij}(k) = X_i(k) - X_j(k) \quad (i = 1, n-1; j \neq i; k = 1, m) \quad (12)$$

The average systematic bias S_i between the i^{th} series and j^{th} series is:

$$S_i = \sum_{k=1}^m T_{ij}(k) / m \quad (13)$$

The S_i value is used to correct the daily data of the i^{th} time series,

$$\begin{aligned} X_{ik} &= X_i(k) + S_i & (i \neq j; k = 1, m) \\ & & \} \\ X_{ik} &= X_i(k) & (i = j; k = 1, m) \end{aligned} \quad (14)$$

Considering the losing data points, the daily weight for the i^{th} time series needs to be calculated,

$$\begin{aligned} W_{ik} &= W_i & X_i(k) \neq 0 \\ & & \} \\ W_{ik} &= 0 & X_i(k) = 0 \end{aligned} \quad (15)$$

So,

$$AW_{ik} = W_{ik} / \sum_{i=1}^n W_{ik} \quad (16)$$

Finally, the weighted average of n time series at the measurement epoch of the j^{th} time series can be obtained,

$$X_k = \sum_{i=1}^n AW_{ik} X_{ik} \quad (k = 1, m) \quad (17)$$

RESULTS

The common view data among NRC, NBS and USNO are computed by using three different methods from data files extending for a length of about nine months. The time series of final weighting average are compared in three performance characteristics. The three methods are: Unbiased Weighting method (UBWA), Direct Weighting method (DWA) which does not correct the systematic bias, as well as Equal Weights method (EWA). The three characteristics are: the standard deviation Σ of residuals of polynomial regression, the frequency stability Allan variances at different sampling time and the time discontinuity caused by increasing or decreasing the number of time series. Results showed that UBWA is prior to the others.

1. Data file is divided into ten time sections showed in Table 1 and computed in three methods monthly. The weighted average series UBWA, DWA and EWA are obtained respectively. The standard deviations Σ of residuals of three time series are listed in Table 3. The UBWA results are better than the others, they are about 4.9 ns for NRC-NBS link and about 2.4 ns for NRC-USNO link. The Σ value is the indication of time perturbation of time series.
2. The frequency stability Allan variances at sampling times of 1, 2, 3, 7, 12, 16, and 20 sidereal days are calculated for UBWA, DWA and EWA weighted average time series respectively. Results are plotted in Figure 3 which has coordinates $\log \sigma_y(\tau) - 10 \log \tau$ and τ in seconds. UBWA series has the best frequency

stabilities. The $\sigma_y(\tau)$ is better than 1 part in 10^{13} for sampling times of five days and longer, this meets the requirements of high precision time and frequency comparison between timing laboratories.

3. Because of the existence of systematic bias, the time discontinuity could appear at the conjunction point between two consecutive data section when the weights of time series changed largely or the number of time series increased or decreased especially. Due to correction of Bias, this effect should be not obvious for UBWA method. During data sections 1 to 5 from MJD 47144 to 47278, the number of time series was changed intentionally to exam the possible time discontinuity. The computed results are listed in Table 4 and the time discontinuity is the smallest for UBWA method.

4. In UBWA method, it is required to choose a reference time series and to correct systematic biases for other time series relative to the reference one. For large geographic area or multistation GPS common view data, it is not possible to find a common reference time series. But, this can be solved by using reference time series relay method, and time accuracy could be ensured.

REFERENCES

1. D. W. Allan, J.E.Gray and H.E.Machlan, "The National Bureau of Standards Atomic Time Scale: Generation, Stability, Accuracy and Accessibility,, IEEE Trans. on I&M, IM-21, NO.4, 1972.
2. Probability Research Group, Institute of Mathematics, Academia Sin'ica, "Mathematical Method to Filtering of Discrete Time System", National Defence Industry Press, 1975.
3. M.A.Weiss, Weighting and Smoothing Data in CPS Common-View Time Transfer", Proc. of the 17th PTTI Meeting, 1985.
4. D.W.Allan & L.Ping-Ping, "Estimating Combined Errors Due to Propagation and Ephemeris and their Effect on Time and Frequency Transfer", Proc. of the 41st ASFC, 1987.
5. Zhuang Qixiang & R.J.Douglas, "Analyses of GPS Double Difference Data", Proc. of the ISEM89, Beijing, August, 1989.

Table 1. Data status

section	MJD	Interval (days)	No. of time series
1	47248-47278	31	12
2	47218-47248	31	12
3	47188-47218	31	12
4	47158-47188	31	12
5	47144-47158	15	12
6	47113-47143	31	10
7	47083-47113	31	10
8	47053-47083	31	10
9	47023-47053	31	10
10	47011-47023	13	10

Table 2. Parameter estimate for common view time series (NRC-USNO) (ns)

	Path	031	061	091	092	093	111	112	113	121	122	123	131
Bias	1		-4	23	-13	14	-1	17	23	20	-18	20	16
	2		-5	24	-13	-12	-4	-16	22	18	-16	20	20
	3		-1	28	-7	-13	-4	-15	22	24	-18	25	16
	4		-2	24	-13	-14	-5	-16	23	21	-19	22	17
	5		3	22	-13	-7	0	-14	25	21	-16	21	19
Σ	1	3.6	3.6	3.4	4.1	4.6	3.4	3.8	3.4	4.6	4.5	5.1	3.7
	2	3.8	2.5	3.6	3.1	2.6	4.6	3.3	3.4	4.2	3.3	4.9	3.3
	3	8.6	8.4	12.5	7.4	8.9	8.0	9.9	8.6	9.4	9.2	10.2	6.9
	4	4.8	5.4	5.2	5.2	4.9	4.5	5.3	4.0	4.8	3.4	5.3	5.6
	5	5.2	4.0	4.9	4.2	5.8	4.5	4.7	6.0	6.1	3.3	6.1	4.8
RMS	1	2.8	3.6	3.3	3.2	4.2	4.0	3.0	1.6	4.4	3.5	4.2	3.4
	2	3.1	2.1	5.2	4.5	2.8	4.4	3.0	2.7	3.6	2.7	4.7	3.0
	3	2.7	2.1	5.8	2.3	2.6	2.2	4.8	2.9	2.0	3.3	5.0	3.8
	4	3.2	3.2	4.4	2.8	2.5	1.9	4.6	2.6	5.6	2.4	4.5	3.0
	5	1.6	2.6	5.8	4.9	7.8	1.5	1.7	2.1	4.8	2.2	3.0	3.4

Table 3. Σ values of weighted average time series

section	NRC--NBS (ns)			NRC-USNO (ns)		
	UBWA	DWA	EWA	UBWA	DWA	EWA
1	5.04	4.94	5.08	2.28	2.93	3.02
2	3.79	5.24	5.24	1.73	1.73	1.81
3	10.15	11.86	11.62	8.11	8.16	8.53
4	3.87	4.08	7.02	3.56	3.73	3.78
5	2.93	3.71	3.45	4.02	4.18	4.34
6	5.68	5.91	5.97	4.11	5.32	5.82
7	6.90	7.48	7.75	3.26	3.74	3.67
8	4.38	4.54	4.68	2.76	3.82	5.10
9	4.18	7.82	9.87	4.13	4.26	4.29
10	1.66	2.60	2.71	0.44	4.94	4.10
Σ	4.86	5.82	6.34	3.44	4.28	4.45

Table 4. Time Discontinuity (nanoseconds)

Data section		5 -> 4	4 -> 3	3 -> 2	2 -> 1
Number of time series		12 -> 10	10 -> 12	12 -> 10	10 -> 12
Conjunction Date		47158	47188	47218	47248
NRC	UBWA	+1.7	-2.0	+1.9	-2.0
/	DWA	-1.7	-7.3	+2.3	+3.2
NBS	EWA	+4.2	-4.2	+4.0	-3.7
NRC	UBWA	-2.0	+2.4	-0.4	-1.1
/	DWA	2.2	-1.2	+5.4	-5.2
USNO	EWA	+3.6	-2.3	+3.5	0.7

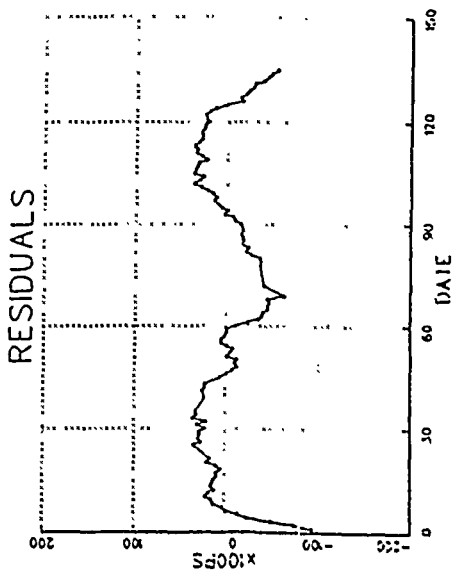


Figure 1. Residuals of time series in dig stream view

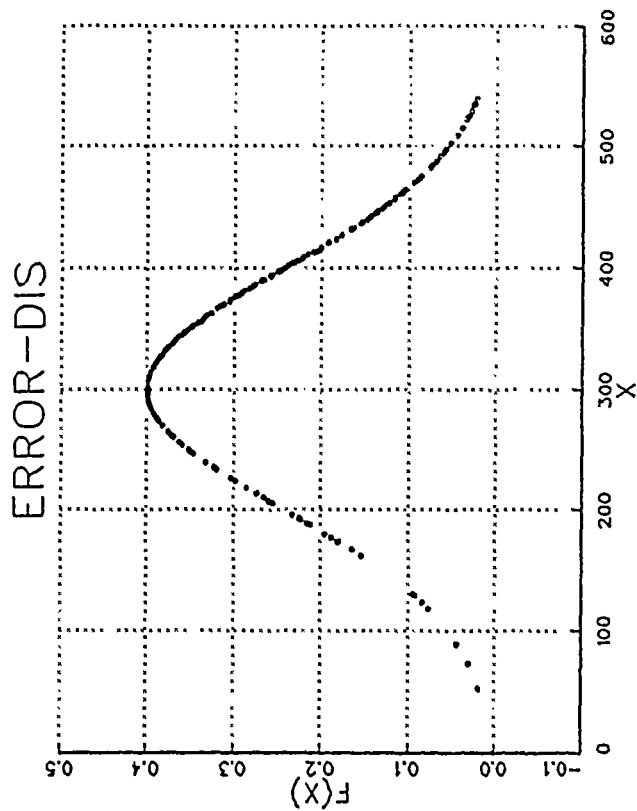


Figure 2. Normal distribution of residuals

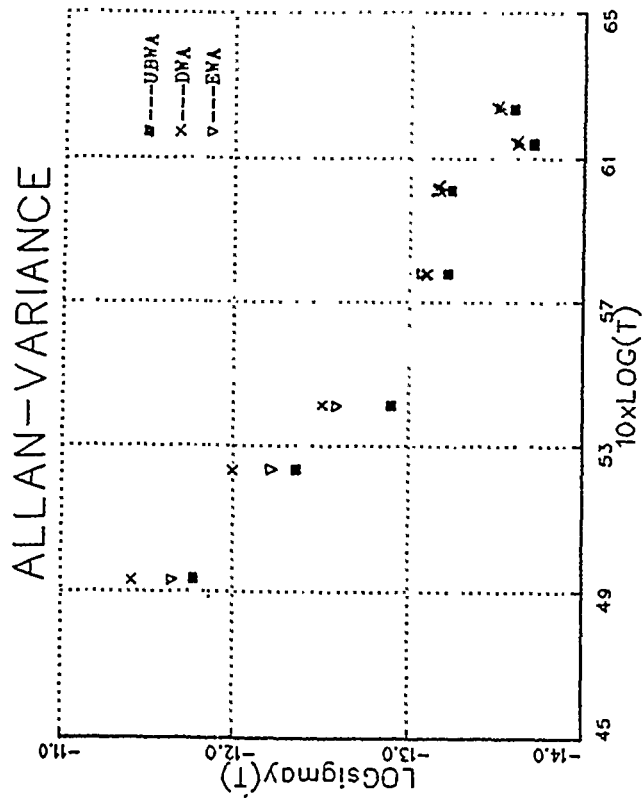


Figure 3. Allan variance results for UBWA, DWA and EWA

Simultaneous Transmission of a Frequency Reference and a Time Code Over a Single Optical Fiber*

G. Lutes and M. Calhoun
Jet Propulsion Laboratory
California Institute of Technology
4800 Oak Grove Drive
Pasadena, CA 91109

Abstract

The Apollo communications station is located at the JPL/NASA Deep Space Communications Complex at Goldstone California. It supports the manned Shuttle flights and Earth-orbiting scientific and communications satellites. This station needs precise frequency and timing references to perform its various tasks. In the past the station used a local Cesium clock to keep track of time which was established with a Loran-C receiver. The station's frequency and timing system has recently been upgraded to improve accuracy and reliability. In the new configuration, a 5 MHz frequency reference and a NASA 36-Bit time code are provided to the station from a central frequency and timing facility located 10 kilometers away. Both signals are transmitted from the frequency and timing facility to the Apollo station over a single optical fiber using a slightly modified commercial fiber optic link. This paper describes this dual channel fiber optic transmission system and gives its performance.

INTRODUCTION

The Apollo Deep Space Station (DSS-16) is located at the JPL/NASA Goldstone Deep Space Communications Complex (DSCC) in the Mojave Desert near Barstow, California. This station supports manned shuttle flights, Earth orbiting scientific satellites, and communications satellites. The Apollo station requires exacting frequency and timing references for precise measurements needed for spacecraft navigation and various science experiments.

Apollo station's frequency and timing system is being upgraded to improve its stability and accuracy and to lower its maintenance and operating costs. The upgrade will also improve the stations synchronization to the central frequency and timing facility and thus to the other stations in the Goldstone complex.

The upgrade consists of a dual channel fiber optic link which provides improved frequency and timing signals to the Apollo station from the complex's central frequency and timing facility. The fiber optic link transmits a 5 MHz reference frequency and a NASA 36 bit time code simultaneously on a single

*This work represents the results of one phase of research carried out at the Jet Propulsion Laboratory, California Institute of Technology, under contract with the National Aeronautics and Space Administration.

fiber over a distance of 10 kilometers from the central frequency and timing facility to the Apollo station. This paper describes the fiber optic link consisting largely of commercial assemblies and compares the quality of the new frequency and timing reference signals to the quality of the previous frequency and timing reference signals.

PREVIOUS FREQUENCY AND TIMING REFERENCE SIGNAL SOURCES

Previous frequency and timing reference signals used at the Apollo station were derived from a WWV receiver, a LORAN-C receiver and a Cesium frequency standard. The WWV receiver was used to determine time within 12 ms eliminating the LORAN-C ambiguity. LORAN-C was then used to refine the time setting to within 1 μ microseconds. The time was checked against a one second tick transmitted over a microwave link from DSS-12. Using this equipment, the time could be set to within about 10 microsecond relative to UTC^[1]. The Cesium frequency standard generated the stations frequency reference and maintained time between updates.

NEW FREQUENCY AND TIMING REFERENCE SIGNAL SOURCES

The frequency and timing signals to be used in the Apollo station's new frequency and timing system are provided by the Goldstone DSCC's central frequency and timing facility. The frequency and timing facility is located in the centralized Signal Processing Center (SPC) located 10 kilometers from the Apollo station.

The 5 MHz frequency reference is provided by one of two H-masers which reside at the centralized frequency and timing facility. The second H-maser is a redundant hot spare. The frequency stability of the H-maser is about 1×10^{-15} for 1000 second averaging times.

The time reference is a GPS receiver which is also located at the central SPC. At the SPC the time can be set to within 100 ns relative to UTC. Time is periodically transferred to a time code generator which generates a NASA 36 bit time code. The time code generator uses the H-maser frequency reference to maintain time between the periodic updates.

The two frequency and timing signals from the SPC are transmitted on a single optical fiber to DSS-16 where they are used as the stations frequency and timing references.

THE FIBER OPTIC DISTRIBUTION SYSTEM

Fig. 1 is a block diagram of the fiber optic frequency and timing distribution system. There is a signal combiner at the input which adds the frequency reference signal and time code signals together into a single signal path. This composite signal is applied to the input of a commercial fiber optic link which transmits the composite signal to the far end of the link. The fiber optic receiver detects the received composite signal and provides the input to a diplexer which separates the frequency reference signal from the time code signal. The signals are then amplified to the desired levels.

The input signal combiner has two inputs, one for the time code, and one for the 5 MHz frequency reference. The time code passes through an active low-pass filter and an amplifier. The low pass filter eliminates high frequency components of the time code above 10 kHz. The signal out of the filter goes to one port of a commercial resistive signal combiner. This signal combiner is of the resistive type to minimize intermodulation distortion which is excessive in transformer type combiners.

The 5 MHz frequency reference signal passes through an isolation amplifier. This amplifier prevents time code signals from feeding back into the frequency reference source which would result in cross modulation between the two signals. After passing through the amplifier the signal goes to the other port of the signal combiner.

The signal out of the signal combiner goes to the fiber optic link which transmits it to the Apollo station. The fiber optic link is a Wavelink model 3290 manufactured by the Grass Valley Group, a subsidiary of Tektronix, Inc. This link utilizes FM pulse modulation. The optical carrier, which is emitted by a laser diode, is AM modulated with a pulse at a subcarrier frequency of 24 MHz. The signal to be transmitted is applied to the FM modulator which frequency modulates the 24 MHz subcarrier. At the receiver end of the link the subcarrier signal is AM detected with a photodiode detector. The transmitted signal is recovered from the detected subcarrier with a frequency discriminator.

When the signal transmitted by the fiber optic link was first tested for frequency stability there was a hump in the Allan deviation which couldn't be accounted for. Further investigation identified the source of the hump. It was frequency modulation generated by the thermal control circuit which stabilized the temperature of the FM modulator in the fiber optic transmitter. This control circuit used pulse width modulation to control the heater. The switching period was around 0.07 Hz.

In an attempt to eliminate the frequency instability resulting from the thermal control circuit it was modified to work as a linear feedback circuit. This was accomplished by replacing a capacitor in the feedback loop filter with a larger value capacitor. This modification successfully eliminated the hump in the frequency stability and resulted in a lower Allan deviation.

Cross modulation products were reduced by adjusting the modulation index and input signal levels in the transmitter. This resulted in the best frequency stability and lowest Allan deviation.

A resistor was changed in the output circuit to modify the output impedance of the receiver from 75 ohms to 50 ohms. Otherwise the receiver was unmodified.

The receiver's output signal goes to a diplexer which separates the 5 MHz frequency reference from the NASA 36 time code. In the diplexer the time code signal passes through an active low-pass filter with gain and then to the output connector. The 5 MHz reference signal is amplified and partially filtered by an amplifier with a low frequency cutoff of 100 kHz.

A quartz frequency standard is used as a filter at the output of the fiber optic link. It is locked, in a 1 Hz bandwidth feedback loop, to the 5 MHz reference frequency from the diplexer. This filter eliminates the time code from the frequency reference signal and reduces its noise bandwidth. The quartz frequency standard is a model 1054A manufactured by FTS, Inc.

PERFORMANCE MEASUREMENTS

Thermal Coefficient of Phase Delay

The change of phase delay through the terminal equipment resulting from a temperature change was measured to determine its Thermal Coefficient of Phase Delay (TCD_ϕ). TCD_ϕ is given in degrees phase change per $^{\circ}\text{C}$ change in temperature.

Knowing the value of TCD_ϕ is important because it can be used to predict Allan deviation if the temperature versus time function is known for the assembly environment.

To measure TCD_ϕ the assembly was placed in an environmental test chamber with a temperature range of 15°C to 35°C . The temperature in the test chamber was then adjusted to an arbitrary reference temperature of 15°C . The phase across the assembly under test was measured at the operating frequency of 5 MHz. The temperature of the test chamber was then changed in 5°C steps. After each temperature change the temperature of the assembly under test was allowed to stabilize then another phase measurement was made. The results were then evaluated.

The measured TCD_ϕ of the transmitter terminal equipment including the fiber optic transmitter, and the signal combiner is 0.12 degrees phase per 1°C change in temperature. For the receiver terminal equipment including the fiber optic receiver, the diplexer, and the clean-up loop the TCD_ϕ is 0.1 degrees phase for a 1°C change in temperature.

Thermal Coefficient of Delay for Fiber Optic Cable

The Thermal Coefficient of Delay (TCD) for cables is usually expressed in change per unit length and given in parts-per-million per $^{\circ}\text{C}$ (ppm/ $^{\circ}\text{C}$). Loose tube single-mode fiber optic cable is used in this installation. Its TCD has previously been measured and found to be 7 ppm/ $^{\circ}\text{C}$.

The delay variations through the buried fiber optic cable at Goldstone have been measured. It was found to be less than 50 picoseconds total variation over 58 kilometers for a period of several days. These measurements were taken when the day to night temperatures in the area varied from about 43°C during the day to about 15°C at night. From this data it is assumed that the delay variations in the fiber optic link are negligible compared to the specified time stability, of 100 ns.

Signal-To-Noise Ratio (SNR)

Because FM modulation is used the SNR of the received signal is virtually constant until the loss in the FO cable and connectors is 28 dB which is equivalent to a transmission distance of 56 km. No signal is received when 28 dB loss is exceeded.

Differential Phase Noise

Differential phase noise is a measure of phase noise added to a signal by the transmission system. It is often defined as double sideband rms phase noise density and is given in dB below the carrier in a one Hz bandwidth (dBc/Hz). The carrier referred to is the transmitted signal.

Differential phase noise is measured across the transmission system. The input signal is used as the reference and the output signal phase noise is measured relative to the input. The phase noise of the signal used as a reference therefore does not contribute to the differential phase noise of the transmission system. The phase noise measured in this manner is only the phase noise contributed by the transmission system.

A block diagram of the measurement system used to measure differential phase noise is shown in Fig. 2. Power splitter splits a 5 MHz input reference signal into two signals. One signal is applied through a phase shifter to a phase detector's LO port. The other signal is applied directly to the phase detector's RF port. The signals applied to the phase detector's LO and RF ports are adjusted to the manufacture's suggested levels, with the use of appropriate amplifiers and attenuators. The phase shifter is adjusted to obtain 90° phase difference between the phase detector's input signals. A phase detector's output voltage is zero for 90° phase difference between its input ports.

To measure the phase noise, the resultant baseband noise out of the phase detector's output port is applied through a low pass filter to the input of a low frequency spectrum analyzer. The phase noise spectrum is read from the spectrum analyzer and recorded.

Table 1 gives the requirements for the new frequency reference signal. Its measured differential phase noise is given in Fig. 3. The time code was transmitted during the phase noise measurement and caused a slight rise in the phase noise between 100 and 1,000 Hz.

Allan Deviation

A block diagram of the system used to measure Allan variance is shown in Fig. 4. An offset generator offsets a 100 MHz frequency reference signal generated by a H-maser frequency standard by 1 Hz. The offset generator used was designed and constructed at JPL. The output of the offset generator drives the LO port of a mixer.

A 5 MHz signal from the same H-maser is transmitted through the fiber optic link along with a NASA 36 time code. At the output of the fiber optic link a tracking filter reduces the noise bandwidth of the transmitted 5 MHz signal to 1 Hz. It also separates the digital time code signal from the 5 MHz frequency reference signal.

The 5 MHz signal out of the tracking filter drives a times 20 frequency multiplier which multiplies the 5 MHz up to 100 MHz. The resulting 100 MHz signal drives the RF port of the mixer. The output of the mixer is the difference frequency between the 100 MHz + 1 Hz from the offset generator and the 100 MHz signal from the times 20 frequency multiplier. This signal which is nominally 1 Hz passes through a low pass filter to an Allan variance test system. This system precisely measures the time interval between zero crossings of the 1 Hz signal from the mixer. The system uses this data to calculate the average frequency between the zero crossing intervals. It then evaluates the equations for Allan^[2] variance and Allan deviation and plots the results.

The Allan deviation for the frequency reference signal provided by the fiber optic distribution system is compared to the Allan deviation of the previously used Cesium^[3] frequency standard in Fig. 5.

CONCLUSION

The stability of the frequency and timing references for the DSS 16 DSCC was improved considerably with the use of a fiber optic link which was assembled primarily from commercial assemblies. This link transmits a 5 MHz reference frequency signal and a NASA 36 time code simultaneously over a 10 km distance on a single optical fiber.

Measurements on the stability of the signals supplied by this fiber optic link verified that the signals are much better than the signals used previously.

The stability of the signals supplied by this fiber optic link is not as good as the stability of signals transmitted by custom fiber optic links used elsewhere in the DSN. However, the system described in this paper is relatively inexpensive and can provide reference signals which are nearly as good as the best reference signals used in the DSN.

REFERENCES

1. Conversation with Paul Kushmeider, Nov. 28, 1989.
2. D. W. Allan, "Statistics of Atomic Frequency Standards," Proc. IEEE, vol. 54, pp. 221-230, February 1966.
3. Manual for the Hewlett Packard 5061B Cesium frequency standard.

TABLE I

SPECIFICATIONS FOR THE NEW FREQUENCY REFERENCE

Amplitude:	1 volt rms,	50 ohms
Harmonics:		-40 dBc
Non Harmonics:		-80 dBc
SSB Phase Noise	(1 Hz Bandwidth):	
	Offset From the Signal	
	1 Hz	-86 dBc
	10 Hz	-124 dBc
	100 Hz	-130 dBc
	1 kHz	-140 dBc
	1 kHz to 100 kHz	-140 dBc

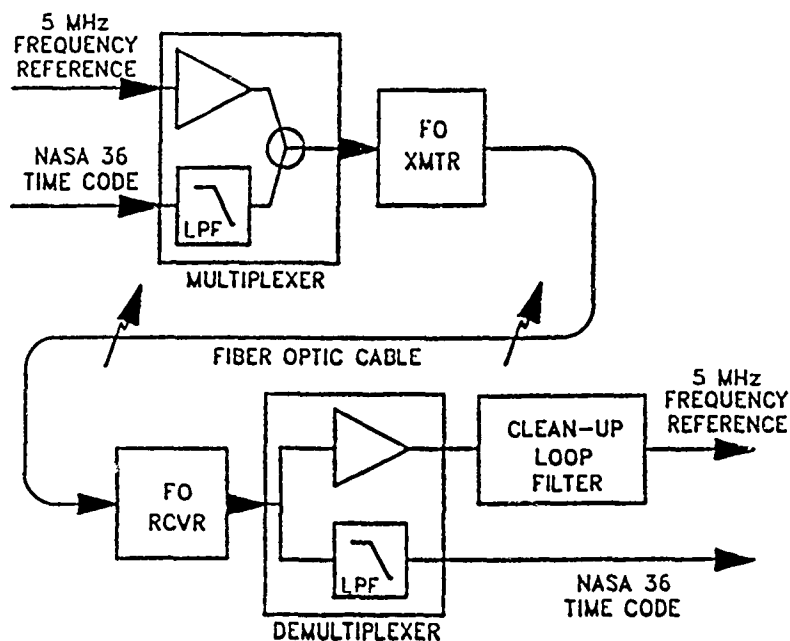


Figure 1. A block diagram of the fiber optic frequency and timing signal distribution system.

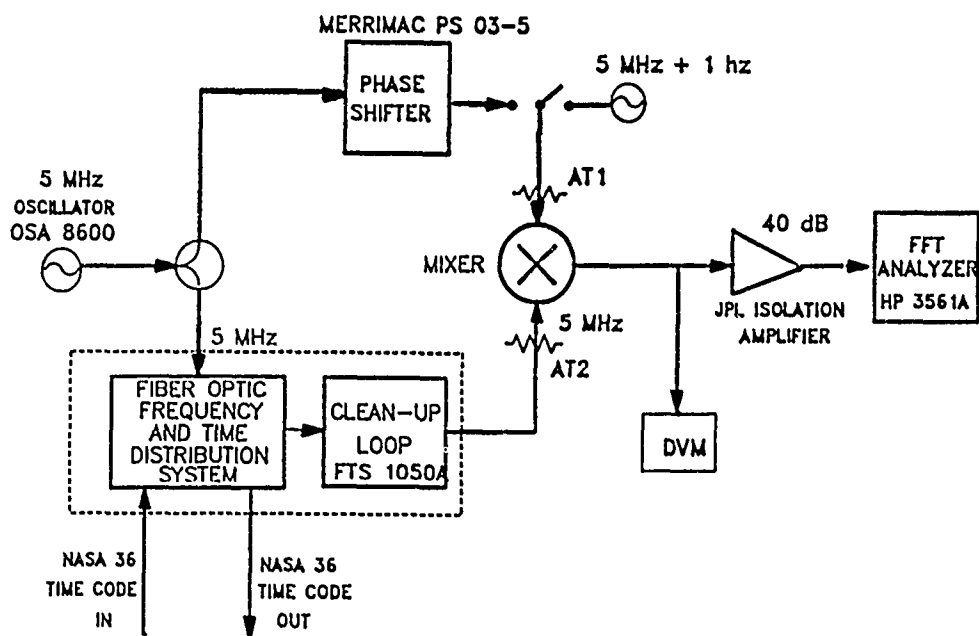


Figure 2. A block diagram of the differential phase noise measurement system.

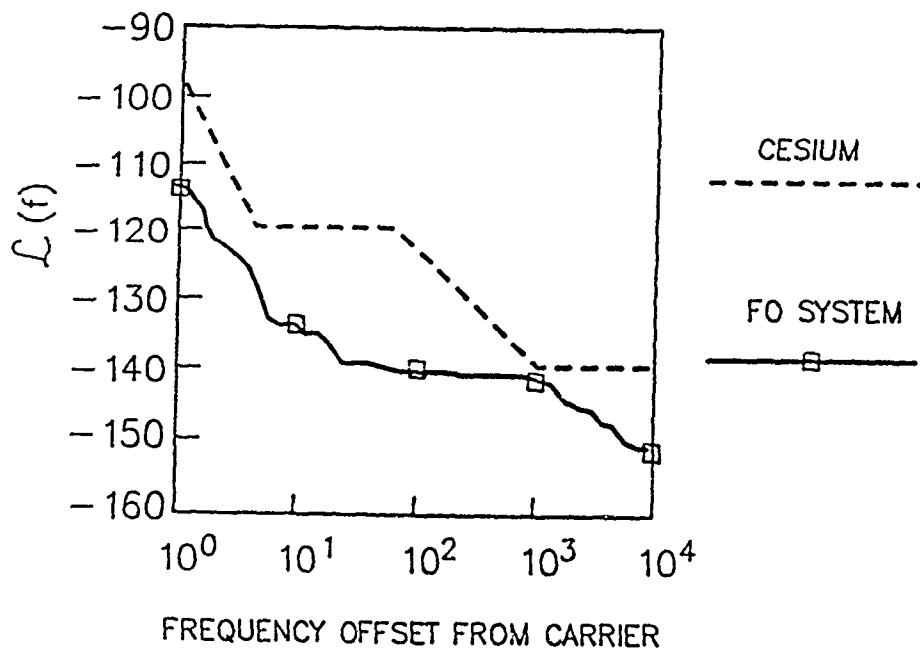


Figure 3. A plot of

- (a) differential phase noise for the fiber optic frequency and timing reference transmission system, and
- (b) the phase noise of the previously used Cesium frequency standard.

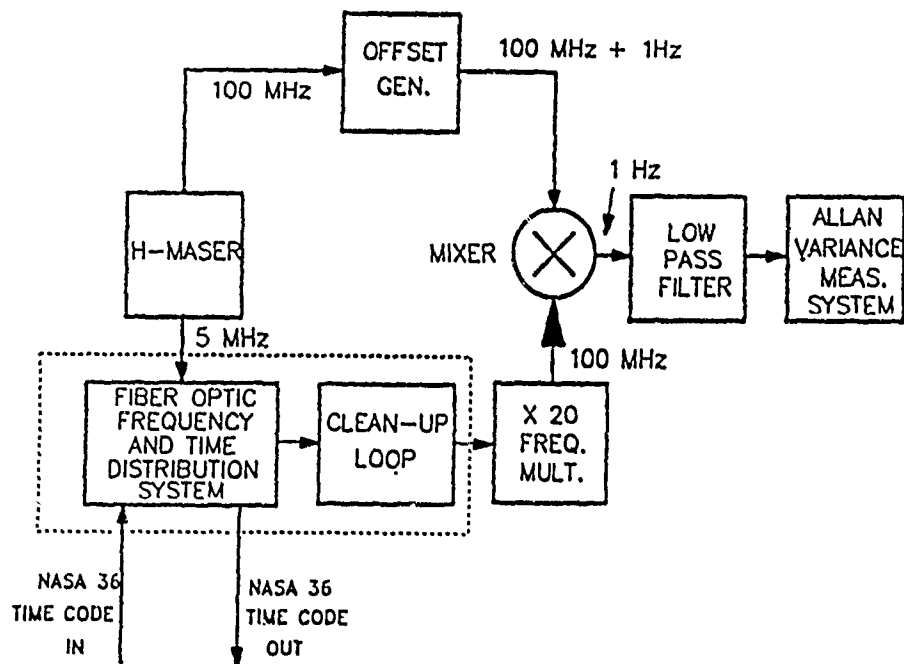


Figure 4. A block diagram of the system used to measure Allan variance.

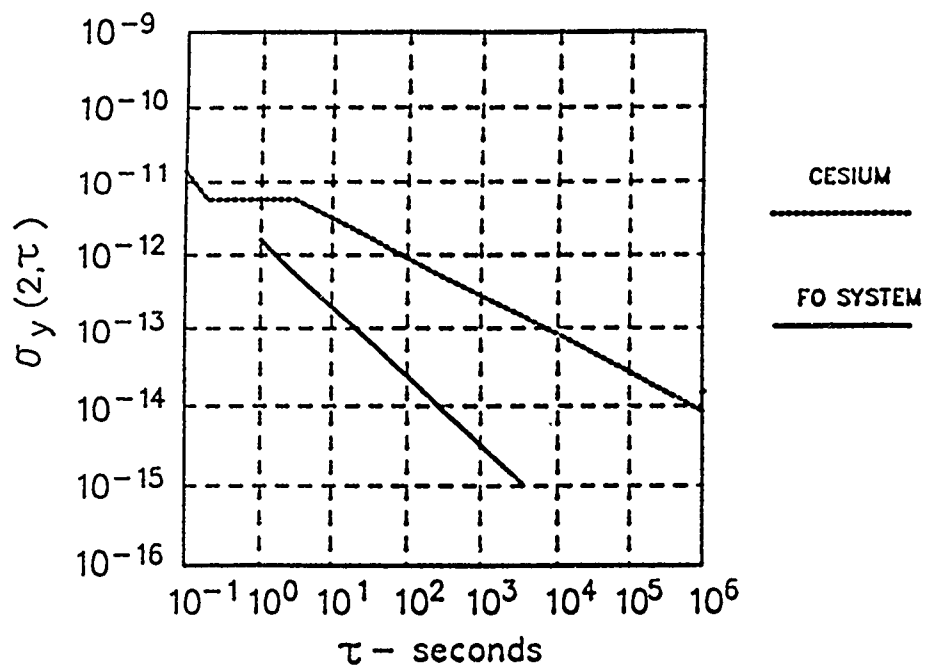


Figure 5. A plot of

- (a) the Allan deviation for the signal transmitted by the fiber optic distribution system,
- (b) the Allan deviation of the previously used Cesium frequency standard,

QUESTIONS AND ANSWERS

PAUL QUINN, ROCKWELL: Did you find it necessary to phase lock the multiplexing frequency with your reference frequency?

MR. CALHOUN: No, there is no multiplexing, just analog addition.

MR. QUINN: There is no degradation due to that?

MR. CALHOUN: There was some cross-talk in the system just due to the non-linearities throughout the system, but I was able to separate the two signals at the analog de-multiplexer with virtually no degradation after I put the disciplined frequency standard in.

MR. QUINN: Does the filter take care of the errors due to multiplexing?

MR. CALHOUN: Yes, it does. The bandwidth on that filter, by the way, is one-half Hertz. It is a very narrow bandwidth tracking filter.

COMMON-VIEW GPS TIME TRANSFER ACCURACY AND STABILITY RESULTS

James R. Semler
Interstate Electronics Corporation
1001 E. Ball Road
Anaheim, California 92803

Abstract

This paper presents the results of time and frequency dissemination research at Interstate Electronics that achieves 10-nanosecond timing accuracy and stability of parts in 10^{14} over continental baselines. Global Positioning System (GPS) receiver data is processed by a differential, common-view technique that cancels most of the cardinal errors. We characterize the noise in the GPS data by using multicorner-hat separation-of-variances techniques. These noise values set Kalman smoother parameters for removal of random noise in the common-view data. The disagreement between various satellite measurements provides a measure of common-view GPS accuracy.

We present a summary of the analytical concepts, followed by the results of real-world data processing in common-view tests between Interstate/Anaheim and the United States Naval Observatory (USNO). The results of side-by-side GPS receiver testing, using the algorithms described here, provide measurements of GPS receiver stability, which can reach levels of 1 nanosecond per sidereal day.

INTRODUCTION — WHAT AND WHY

Although navigation, testing, and sensor data gathering have often required precise, stable time maintenance, currently implemented technology lacks the accuracy required by new military program demands. Correlation of signals recorded by remote sensor data gathering systems needs highly accurate synchronization of several remote sites' frequency standards. Some systems demand synchronization accuracies of 10-nanosecond error or better for meeting their requirements. Testing applications also impose stringent synchronization and time stability requirements, particularly with the Global Positioning System (GPS).

Validation of state-of-the-art time and frequency dissemination accuracy and stability demands "prior-free" analysis techniques that do not depend on a predetermined system model nor the availability of a superior reference clock. The introduction of such a reference merely begs the question, as the reference itself may be invalid. "Who checks the checker?" Other programs demanding high instrumentation accuracy have faced similar problems in validation. The current performance analysis methodology used for GPS, Trident II, and similar navigation/time systems, however, lacks the capability to provide independent estimates of time stability without prior modeling. Kalman filtering and maximum-likelihood estimation require elaborate models for accurate performance estimation. However, they fail to provide parameters needed in the model description, such as GPS clock noise variances. Current accuracy validation techniques implement systems or clocks that must be several times more accurate than the system under test. The technique cannot by itself validate the accuracy of the so-called reference, thus casting doubt on the analysis results.

The long-term stability of GPS-based time and frequency dissemination depends on the long-term repeatability of the GPS ranging signal delays. As such, a GPS receiver designed for precise time transfer has different design priorities from one designed for dynamic navigation. Hence, military users of GPS have not yet reaped all the benefits of the extensive time and frequency dissemination research by the civil and academic communities. Existing military GPS receiver designs emphasize ruggedness, antijam capability, and Kalman-based navigation data processing. These considerations conflict with long-term receiver delay stability needed for precise time maintenance.

To provide cost-effective solutions to these problems, Interstate Electronics Corporation (IEC) has developed the needed time and frequency dissemination technology and performance analysis techniques in support of numerous military applications. In 1989 we completed the program initiated in August 1988 to:

- Demonstrate remote clock synchronization accurate to within 10 nanoseconds or less in real-world testing over baselines ranging from zero to continental distances.
- Develop, implement, and test prior-free algorithms that estimate the stability of each component of a time and frequency dissemination system based on GPS measurements.

To achieve these objectives, we have been:

- Conducting GPS common-view time transfer tests to validate the 10-nanosecond accuracy over a continental baseline.
- Performing GPS common-view time transfer tests over a zero baseline to measure receiver delay stability.
- Implementing the latest multicorner hat separation algorithms to provide quantitative GPS system clock noise variance estimates.
- Teaming with the Time and Frequency Division experts at the National Institute of Standards and Technology (NIST) in developing and implementing these approaches.

COMMON-VIEW GPS — APPROACH AND RESULTS

Our time transfer approach uses a single GPS satellite in common view from two clock locations to provide error cancellations, even over large baselines, which permit us to achieve the accuracy goal. Radio techniques using WWV or WWVH, LORAN, portable clock trips, or single-view GPS do not meet our goals. Timing using the Space Shuttle or laser-based systems is prohibitively expensive^[1]. Thus GPS common view emerged as the most cost-effective solution.

Two stations equipped with GPS receivers can compare their local time standards to nanosecond-level errors by tracking the same satellite simultaneously, and then differencing the measured local time offsets with respect to GPS time. This differential processing cancels most of the major GPS error sources. Variations on this technique allow us to compute the long-term stability of GPS receivers in the Interstate GPS laboratory.

The GPS consists of three segments: space, control, and user. The space segment contains several satellites in semisynchronous orbits that have ground tracks repeating each sidereal day. These satellites emit an RF signal consisting of a carrier wave modulated by a pseudorandom code and a navigation message. The control segment tracks these signals, determines the satellite orbit and clock offset parameters, and uploads these data to each satellite. However, the control segment orbit determination introduces satellite position and time errors into the uploaded data. The user segment

also tracks the satellites, demodulates the orbital data, and computes position and time from the range measurements. These measurements are taken by time-correlation of the pseudorandom code received from the satellite with a copy generated by the user equipment. Because the correlation process introduces the user clock error into the transit time measurement, the user must also solve for time errors. The four variables, three position coordinates and one time correction, require four correlation measurements for a fully determined solution. If the user equipment stores its presurveyed position, then GPS time can be obtained by tracking only one satellite.

Users needing to synchronize their clocks can do so by taking measurements against the GPS time scale and then differencing their local clock offsets from that time scale. If two users agree to track a satellite in common view from both sites simultaneously, the differencing cancels most of the GPS measurement errors, as shown in Figure 1.

The GPS measurements contain several errors from satellite orbit and clock corrections, ionospheric and tropospheric effects, user-surveyed position, and receiver delays. Some errors can, however, be removed. Satellite clock correction error drops out completely because its effect on ranging error is identical in both time offset measurements. The satellite orbital errors project into range measurements as shown in Table 1. When common view satellite measurements are differenced, however, the orbital error cancels to the magnitude of the difference of the projections. The extent of this cancellation depends on the distance between the receivers. The orbital error can dominate the other errors in a common-view GPS measurement if the distance between the receivers is very large, such as intercontinental distances.

Although the common-view technique removes the largest portion of GPS time offset measurement error, some error sources are not reduced by this practice. Ionospheric delays pose particular problems. Unless dual-frequency measurements are available, the user must rely on the broadcast single-frequency model. This model removes only 50 percent of the overall ionospheric error. Common-view measurements over baselines less than 1,000 kilometers, however, tend to remove most of the residual ionospheric errors. Further suppression of the ionospheric error occurs if measurements are taken at night during low ionospheric activity. Tropospheric models provide accuracies less than 1 foot in range, as demonstrated in Reference 2. Errors in receiver coordinate surveys introduce ranging errors similar to ephemeris errors.

The repeatability of the common-view GPS measurement accuracy pivots on the repeatability of receiver delays. Because of the differential comparisons, the magnitude of the delay does not matter so long as the delay is calibrated relative to the other GPS receivers used in common view and that delay remains the same from day to day. Short-term noise introduced by the tracking loops is suppressed by least-squares fitting of raw ranging data. The long-term delay variation depends on RF filter bandwidth, architecture, and environmental sensitivity. Typically the delay variation is a percentage of the absolute delay. For example, a receiver with 100 nanoseconds of delay experiences 1 nanosecond of delay variation from day to day. These stability requirements drive the design of the RF downconverter and tracking loops of the GPS receivers.

To validate the GPS common-view error budget presented in Table 1 in a real-world application on continental baselines, Interstate has collected and analyzed data gathered over such a baseline. We combined data from a NIST GPS receiver situated at the Interstate Anaheim facility and the USNO GPS timing receiver in Washington, D.C. The data analysis took place at IEC, using the separation-of-variances technique and common-view data processing algorithms described in this paper. Fifty days of uninterrupted data concluding on MJD 47636 (20 April 1989) were examined to provide these results. The architecture of the NIST receiver is described in detail by Davis and others in Reference 3.

The GPS tracking schedule for this experiment exploited the repeating ground tracks of the Block I satellites. The new PRN 14 satellite was not used for the experiment due to control segment testing

during the data gathering interval. The schedule is given in Table 2. One notes the extremely low elevation of PRN 12 as seen at Interstate; its track time tends to fall during daytime here. The other tracks tend to occur at nighttime, reducing single-frequency ionosphere error. These times are shifted 4 minutes per solar day to follow the repeating ground track.

The NIST receiver at Interstate measured the phase of an HP 5061 cesium standard relative to GPS. The receiver at USNO provided the phase of UTC (USNO) relative to GPS; these data were downloaded from the USNO dial-up service. We examined the data for missing points. Any gaps were filled with linear interpolation of the local-SV and local-GPS measurements. Then the IEC-GPS and UTC-GPS measurements were differenced to produce six series of common-view GPS measurements of IEC-UTC (USNO) time differences. Each series consists of one time difference measurement per sidereal day from a given GPS satellite.

We analyzed the GPS common-view measurement tracks using the multicorner hat separation-of-variances software (described later in this paper) to produce estimates of the measurement noise found on each repeating measurement track. This makes the implicit assumption that all the variances are constant over the data interval. The noise introduced by each satellite path was estimated via a three-corner hat on the differences between IEC-UTC estimates on separate satellite paths. As the long-term GPS measurement noise has the characteristic of white phase modulation, we scale the Allan deviation by 86,160 seconds to obtain measurement noise filter values. The results are presented in Table 3. One quickly notes that PRN 12 measurements exhibited three times the noise seen on the other paths.

We next estimated the frequency stability of the IEC-UTC difference by applying the separation of variances to the local-GPS tracks. At an averaging time of one sidereal day, we observed stability of 1.03×10^{-13} . This value was used to adjust the common-view time transfer Kalman filter process noise matrix accordingly. We divide the Allan variance at one sidereal day by 86160 to produce the correct process noise matrix frequency noise parameter. Next, a two-state Kalman filter-smoother produced estimates of smoothed IEC-UTC phase and frequency offsets from each common-view track. We apply the smoother to each track individually. The effectiveness of the smoother can be seen by examining the smoothed residual root-mean-square values. The RMS of the difference between the raw common-view data and the smoothed estimates for all tracks is presented in table 4, along with the percentage of measurements accepted by the Kalman filter.

The final step in the time transfer consists of taking a weighted mean of the IEC-UTC phase estimates from the various GPS tracks. The weights are determined from the table 4 values to achieve optimal stability. Another weighted mean omitting PRN 12 was also taken due to the anomalous nature of the PRN 12 path. Figures 2 through 5 show each track's difference from the weighted mean in both cases. We clearly see the biasing of PRN 12 from the rest of the tracks. Its greater noise also compels the weighting algorithm to ignore that track when combining the satellite data. Therefore, comparison of the IEC-UTC (USNO) weighted averages between the two cases revealed differences of 1 nanosecond or less. As a measure of time transfer accuracy and consistency, the RMS of all tracks' differences from the weighted mean is computed by the weighting software. For the all-inclusive weighted mean, the RMS amounted to 13.02 nanoseconds. For the weighted mean omitting PRN 12, the RMS of the differences amounted to 5.6 nanoseconds. It is thus apparent that the results demonstrate the feasibility of 10-nanosecond time transfer using GPS over continental baselines. However, even more room for improvement exists. Improvements in surveying, ionospheric models, and antenna multipath resistance could lead to consistent nanosecond-level performances.

The stability of the IEC-UTC (USNO) difference as estimated by the GPS common-view process is presented in Figure 6. The differences were first fit to a quadratic to remove deterministic frequency bias and drift. The mean clock bias removed was -18069.99 ns. The mean frequency removed was -279.46 ns per sidereal day. The mean frequency drift was 0.0931 ns per sidereal day squared.

ZERO BASELINE TESTS MEASURE RECEIVER STABILITY

We can compute the long-term stability of collocated receivers by driving them off the same local frequency standard, comparing the time offset measurements from the two receivers, and computing the Allan two-sample variance from the data stream. The negligible baseline provides for complete GPS navigation message error cancellation. The errors due to survey and atmospheric modeling cancel if common values are used in both receivers. The remaining difference between the two local-GPS measurements in common view consists of the relative delay between the two receivers plus random error. By applying the smoothing technique described in this paper, we can quantify the long-term receiver delay stability.

Interstate has performed common-view time synchronization tests in the Anaheim laboratory that demonstrate this concept. The test compared the NIST receiver at IEC with a similar time transfer receiver, the Allen Osborne Associates TTR-6 model GPS receiver. We observed a 3.6 nanosecond standard deviation in unsmoothed GPS time differences. We also observed GPS receiver stability to 2 nanoseconds per day. Figure 7 presents the smoothed time differences taken over 40 days. Each point on the plot indicates the difference between the NIST receiver's estimate of local-GPS time bias and that from the Allen Osborne receiver. The mean value of these differences measures the uncompensated cable delays and receiver signal delays. The GPS common-view measurements represented in figures 8 and 9 are a composite of measurements from GPS satellite (PRN) numbers 3, 6, 9, 11, 12, and 13. The smoothed receiver delay comparisons reveal that the NIST and Osborne receivers both have long-term stability of less than one part in 10^{-14} for averaging times of one to eight days. Figure 10 indicates the long-term stability values.

MULTICORNER HAT ALGORITHMS CHARACTERIZE GPS NOISE

The multicorner hat concept overcomes a fundamental limitation of time and frequency measurements by introducing a third oscillator into the measurements to provide observability of each clock's Allan variance. Because oscillator phase measurements can be made only with respect to another clock, either clock could potentially cause the noise quantified by the Allan variances. To resolve which clock is "at fault," we introduce a third clock, then find Allan variances of all three possible differences. If the three clocks are independent, we may assume that the variance of the differences is the sum of the individual clock Allan variances. Three Allan variances of difference data permit us to solve for each clock's Allan variance, removing the effects of the other two clocks. By extending the three-corner hat concept to systems with multiple timing error sources, we can compute the stability of individual clocks within the GPS system. This concept, pioneered by Allan and Weiss in Reference 4, permits us to validate the stability of GPS time synchronization without having to develop and to implement elaborate system error models laden with free parameters. Figure 11 shows the steps performed in the multicorner hat separation of variances. We sort the GPS time difference data into measurements taken each sidereal day. The repeating GPS ground track permits us to eliminate systematic error creeping into the results by enforcing the same geometry on each common-view measurement. We then remove deterministic phase, frequency and frequency drift coefficients through a quadratic fit to the sidereal-day track data. Householder transformations used for the fit ensure numerical accuracy, as described by Bierman in reference 5. The residuals from this quadratic fit contain the random errors, which we can characterize through use of the multicorner hat concept.

We can take three types of time difference measurements with a GPS receiver: local-GPS, local-satellite, and GPS-satellite. Each satellite provides these measurements from each tracking interval.

We can decompose the errors in those measurements into their constituent parts:

- Local frequency standard instability,
- GPS ephemeris and atmospheric errors,
- GPS uploaded satellite clock correction errors,
- GPS master system time instability and
- Satellite oscillator instability.

We difference the local-GPS offset measurements from three satellites to isolate the combined noise due to ephemeris and clock correction error, then apply the three-corner hat to obtain the sum of the Allan variances due to those two error sources for each of the three satellites. The same technique applied to the local-satellite clock offset data produces the sum of the Allan variances of ephemeris and satellite hardware clock noises. We combine these preliminary three-corner hat results from a given satellite with the Allan variances of the original three measurement streams from that satellite to obtain the final separation of variances. We can express the Allan variances of the difference data in terms of their constituent parts, analogous to the three-corner hat. We then invert this expression to solve for the individual error source Allan variances, performing a five-corner hat for each of the three satellites used in the preliminary variance separations. This provides three estimates of local clock stability and GPS time stability that can be averaged to obtain the final stability estimates.

The multicorner hat procedure suffers from the possibility of computing negative variances for some of the stability estimates. Three potential causes of such results are (1) insufficient data to separate all variances; (2) unmodeled correlations between measurements; and (3) one of the clocks in the multicorner hat is much more stable than the others and is thus obscured by noise. We remedy the first problem by gathering more time difference data. The second problem can be solved by modeling correlation terms in the multicorner hat. The occurrence of the third problem indicates that clocks with greater stability are needed. In any case, the nonnegative variances can be accepted as good estimates of stability.

We can see the multicorner hat's applicability to general performance validation problems from the preceding discussions, particularly in navigation applications. Given three independent navigation systems we can compute the accuracy of each system by taking the sample variance of the mutual difference data, then applying the three-corner hat to the resulting values. This provides a prior-free system validation methodology. Extensions of the multicorner hat to include cross-correlation terms between navigation systems can estimate the effects of common system components. For example, if two aided inertial navigators share a common inertial unit but use different range aiding systems, then a correlation term can be added to the multi-corner hat. Extra differences are then required to separate all the variances.

Interstate applied the separation-of-variances technique described above to time difference data gathered in November 1988. Figures 12 to 15 show the excellent time stability of the various clocks in the GPS, as validated by the multicorner hat algorithms. The HP 5061B cesium beam standard exhibited frequency stability 50 times better than specified by the manufacturer, as shown in figure 12. GPS time showed comparable stability to that of the HP cesium in the IEC laboratory, as exhibited in Figure 13. In the short term, however, the HP outperformed the GPS in time stability. From this we can see that GPS time reaches a flicker noise frequency modulation floor of approximately 6×10^{-14} at an averaging time of 3 days.

Our multicorner hat approach allows us to show that in the GPS space segment, proper isolation of rubidium oscillators can provide an environment in which cesium-level performance results. Figure

14 indicates the excellent long-term stability of the cesium beam standard aboard the GPS PRN 3 satellite. A flicker floor of less than 3×10^{-14} occurred between averaging times of 4 and 8 days. In contrast, figure 15 shows that the performance of the GPS PRN 9 rubidium standard actually surpassed that of the spaceborne cesium at averaging times of 1 and 2 days. This short-term superiority is expected in rubidium standards and is further enhanced by the relatively benign environment of the GPS satellite. No apparent force acts on the satellite nor are there extreme temperature fluctuations, thus the usual causes of poor rubidium performance do not pervade the satellite environment. In addition, the PRN 9 rubidium has special heat-dissipation hardware that enhances its performance.

The GPS control segment can benefit from this research by using the multicorner hat approach as an independent performance monitor on the new Block II satellites. In addition, the concepts behind the multicorner hat have application in any performance validation problem where the accuracy of the references is of interest.

ACKNOWLEDGMENTS

The author would like to thank the following persons: Len Jacobson, Dr. Ken Brunn, and Gerry Grayson of Interstate for managerial support of this project; Tony Kurlovich of Interstate for RF receiver stability analysis; Randy Hom, Robert Crane, and Manny Beckers of Interstate for technical support; and David Allan, Marc Weiss, and Dick Davis of NIST for their interest and consulting services throughout the project.

REFERENCES

1. Allan, D. W., "National and International Time and Frequency Comparisons," Time and Frequency Division, National Institute of Standards and Technology, Boulder, CO.
2. Phase 1 Navstar/GPS Major Field Test Objective Report, Tropospheric Correction, Navstar/GPS Joint Program Office, Space and Missile Systems Organization, Los Angeles Air Force Station, Los Angeles, CA., 4 May 1979.
3. Davis, Dick D.; Weiss, Marc A.; Clements, Alvin C.; and Allan, David W., "Remote Synchronization Within a Few Nanoseconds by Simultaneous Viewing of the 1.575 GHz GPS Satellite Signals", Time and Frequency Division, National Institute of Standards and Technology, Boulder, CO.
4. Allan, D. W., and Weiss, M., "Separating the Variances of Noise Components in the Global Positioning System," Proceedings of the Fifteenth Annual Precise Time and Time Interval Applications and Planning Meeting, December 1983.
5. Bierman, G. J., "Factorization Methods for Discrete Sequential Estimation," Academic Press, New York, 1977.

NOTE: References 1, 3, and 4 are also available in documentation supplied as part of the NIST Time Dissemination Service.

Table 1. *The GPS common-view error budget for continental distances shows the domination of satellite ephemeris error. For shorter baselines the orbital error contribution decreases significantly, increasing the potential accuracy.*

Error Source	Contribution (ns)
Ephemeris	8.5
GPS receivers	4.9
Ionosphere	1.4
Troposphere	1.4
Relative Survey	<u>1.4</u>
Root-Sum-Square Total	10.1 ns

Table 2. *GPS tracking schedule 20 April 1989 shows geometry of common-view measurements.*

PRN No.	Time of Track (Zulu)	IEC		USNO	
		Elevation (deg)	Azimuth (deg)	Elevation (deg)	Azimuth (deg)
3	7:18	50	40	61	340
6	2:22	60	124	62	242
9	3:12	88	273	47	288
11	3:56	38	31	58	351
12	13:18	21	61	60	90
13	5:28	44	30	56	342

Table 3. *Common-view measurement noise estimates from multicorner hat show poor PRN 12 performance.*

PRN No.	One-Day Allan Variance	Equivalent Measurement Variance (ns ²)	Noise Sigma (ns)
3	1.14×10^{-26}	84.63	9.20
6	6.33×10^{-27}	46.99	6.85
9	8.40×10^{-27}	62.36	7.90
11	8.17×10^{-27}	60.65	7.78
12	8.16×10^{-26}	605.76	24.61
13	8.70×10^{-27}	64.58	8.04

Table 4. *Common-view smoothed residual RMS values indicate higher noise on PRN 12 path.*

PRN No.	Smoothed RMS Variance	Percentage Accepted
3	5.31	100
6	4.73	100
9	5.43	100
11	5.37	100
12	11.30	100
13	4.45	100

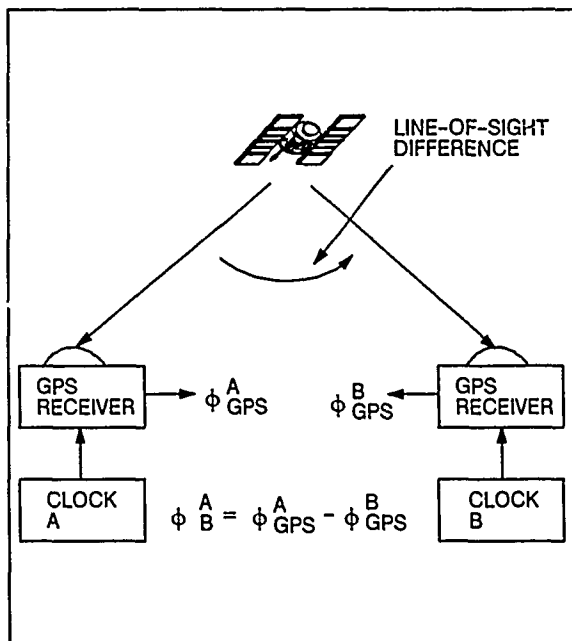


Figure 1. Common-view GPS provides high ephemeris error cancellation, permitting time transfer to nanoseconds of error.

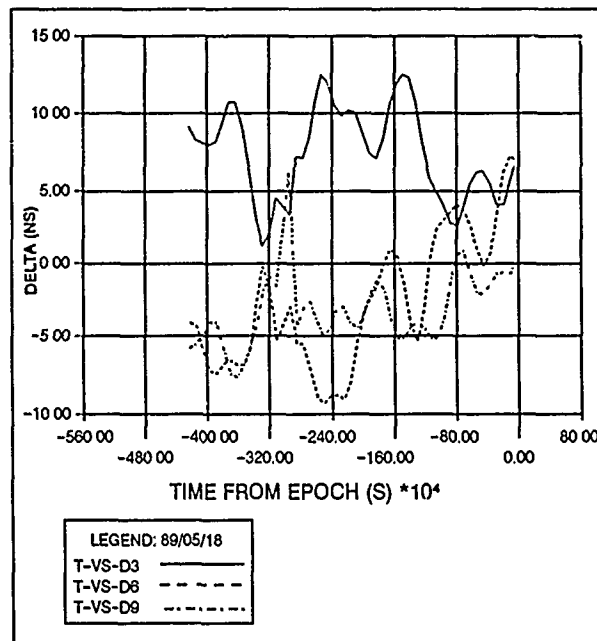


Figure 2. Differences from weighted mean for PRNs 3, 6, and 9 show agreement to 5 nanoseconds RMS.

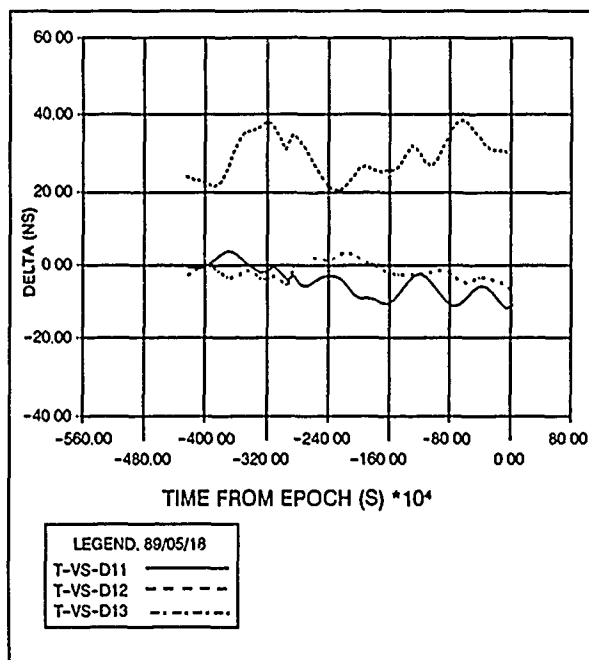


Figure 3. Weighted mean differences clearly indicate biaslike error in PRN 12 track. Extra noise is also evident.

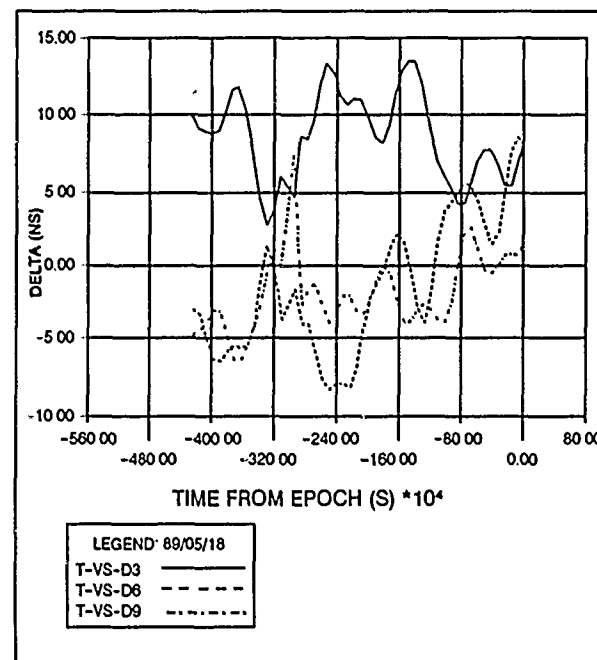


Figure 4. Excluding PRN 12 produced only 1-nanosecond change in weighted mean differences.

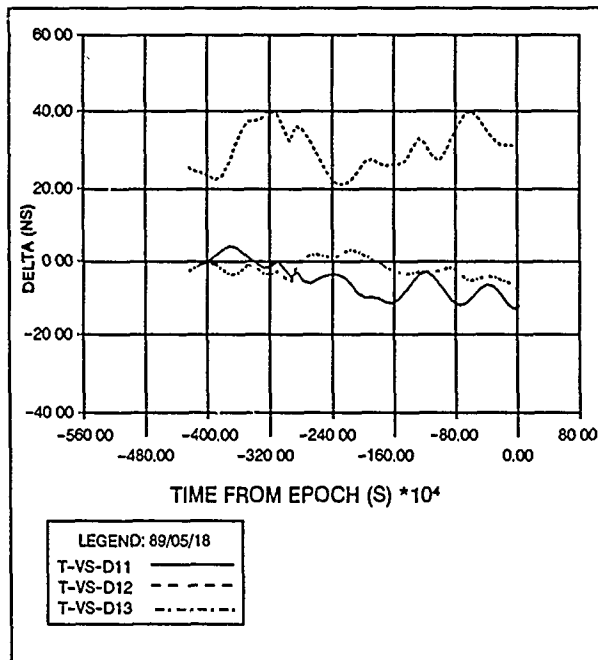


Figure 5. All-inclusive weighted mean ignores PRN 12, as shown by little change in differences when PRN 12 is excluded.

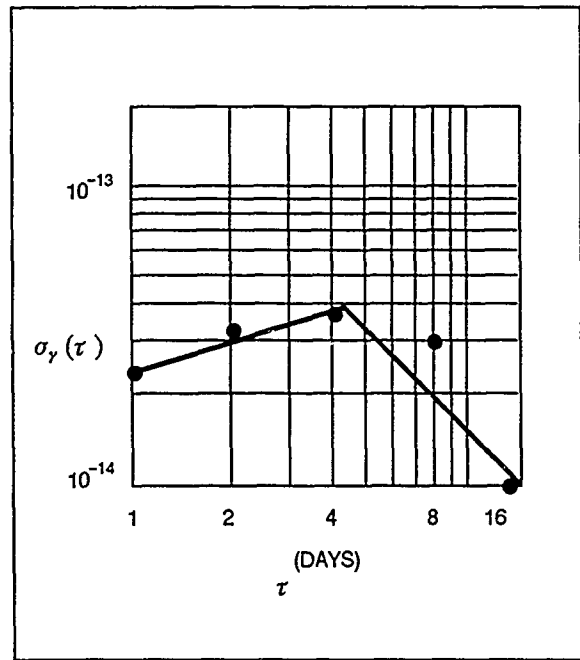


Figure 6. An HP 5061B cesium at Interstate exhibits excellent smoothed frequency stability versus UTC (USNO).

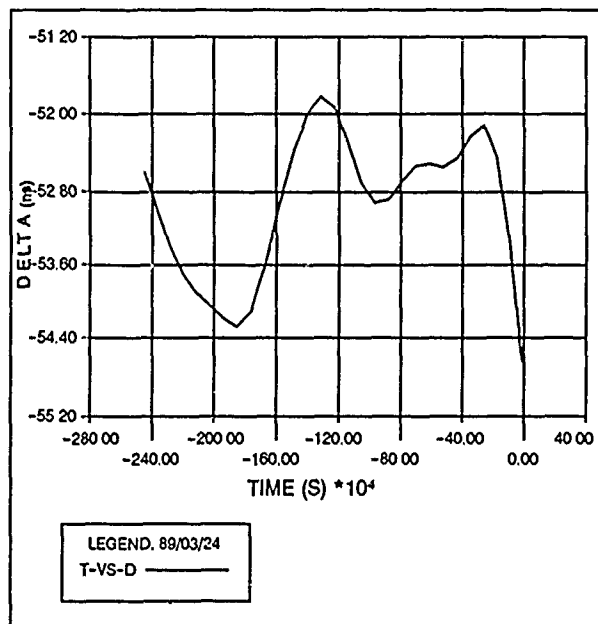


Figure 7. Common-view weighted mean error shows 0.7-nsec deviation.

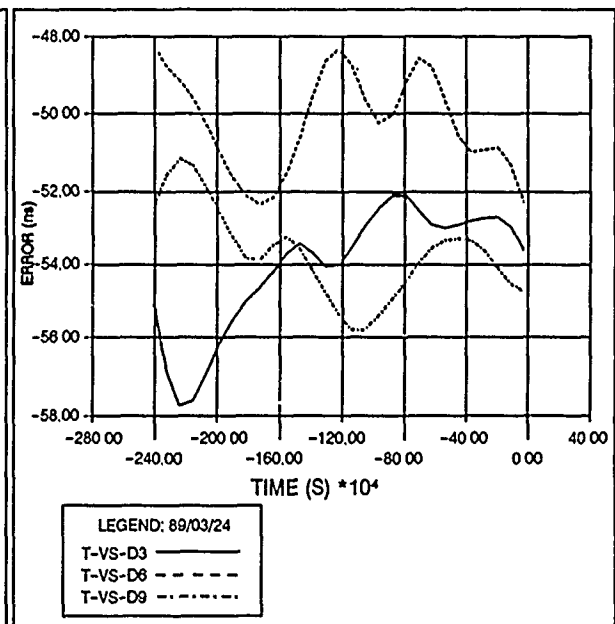


Figure 8. Common-view smoothed tracks show satellite-by-satellite deviations for PRNs 3, 6 and 9.

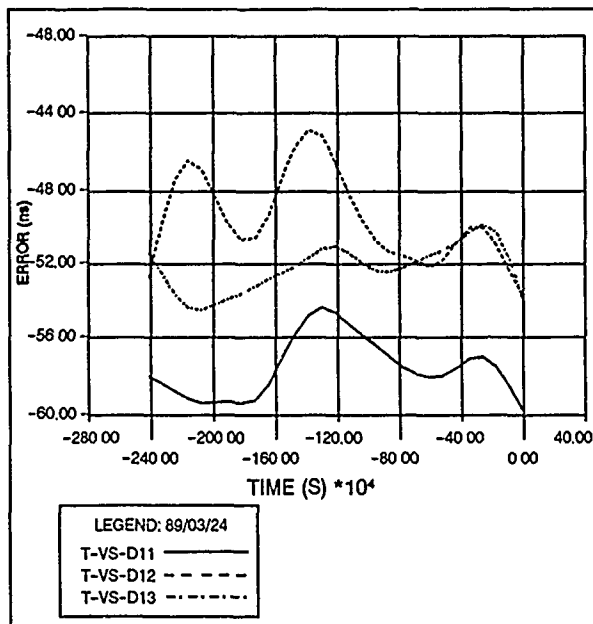


Figure 9. Common-view smoothed tracks show satellite-by-satellite deviations for PRNs 11, 12, and 13.

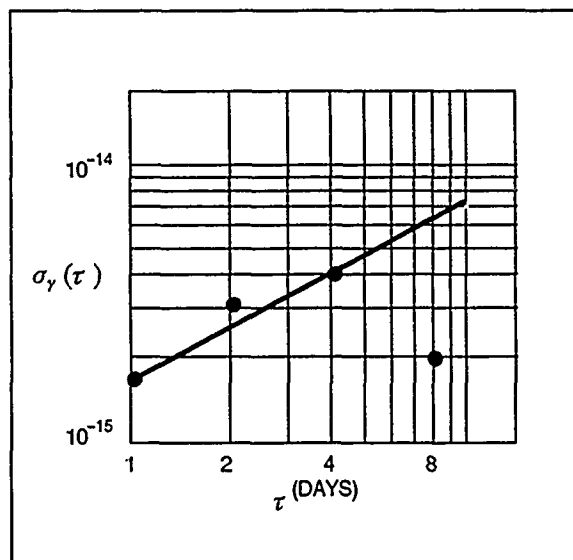


Figure 10. Smoothed receiver time stability is less than one part in 10^{14} .

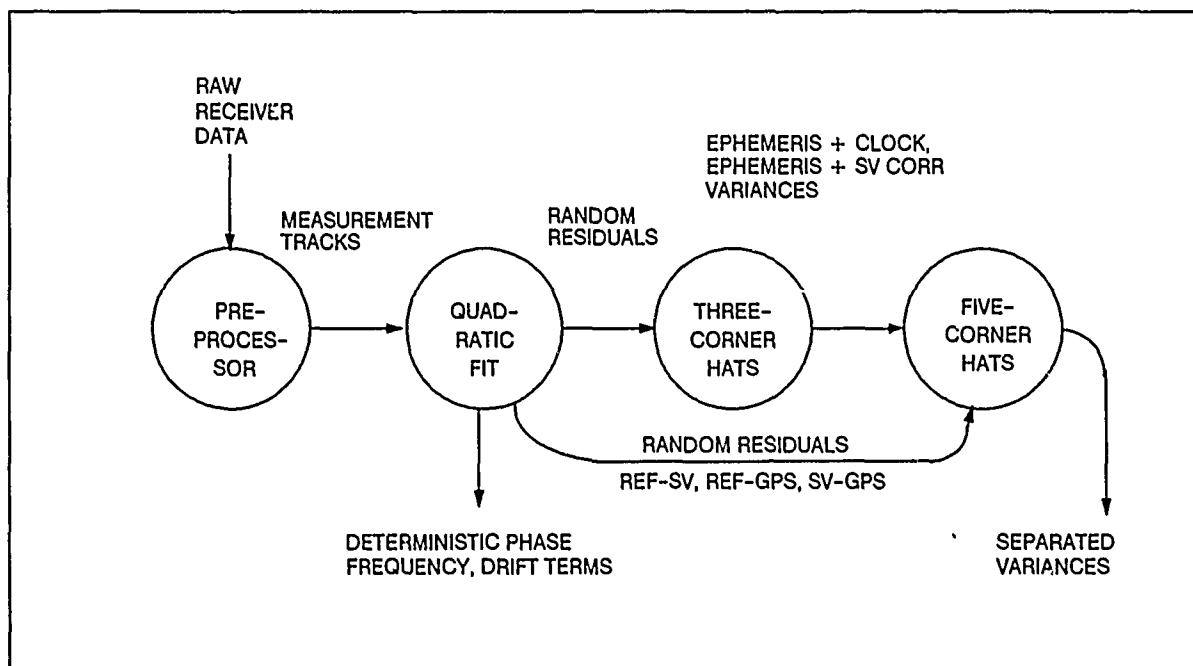


Figure 11. Data flow shows procedure for multicorner hat.

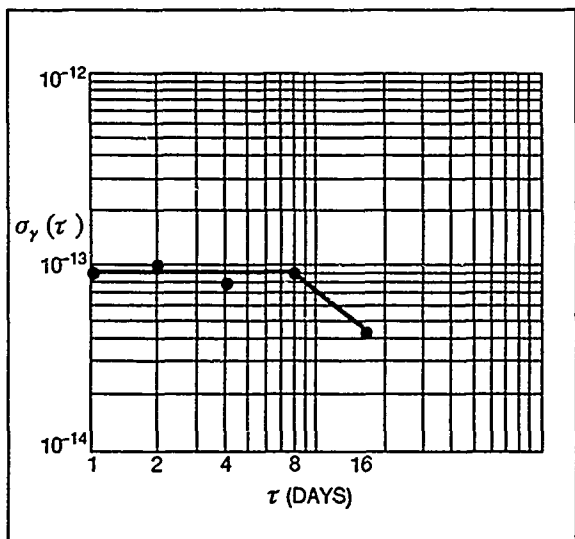


Figure 12. Standard HP 5061B cesium shows performance fifty times better than specification.

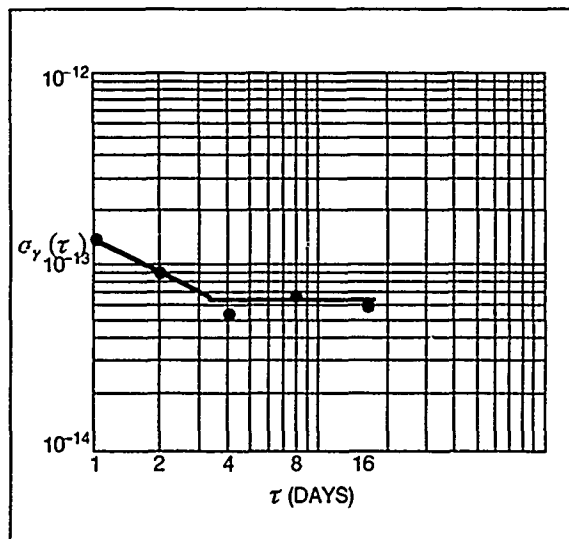


Figure 13. GPS master control segment clock reaches flicker floor at 4 days.

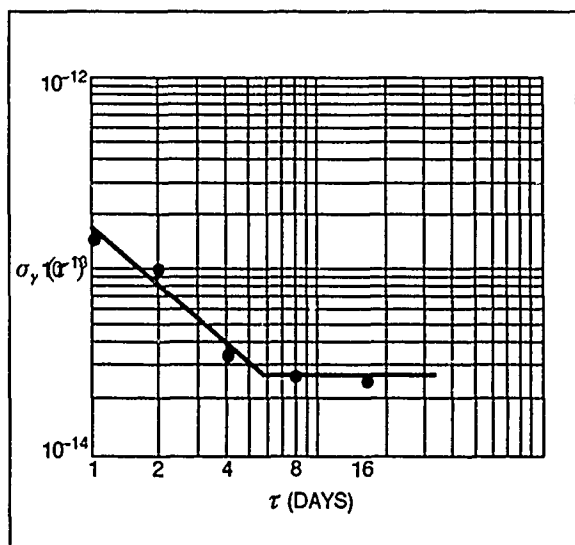


Figure 14. SV 3 cesium shows excellent long-term stability.

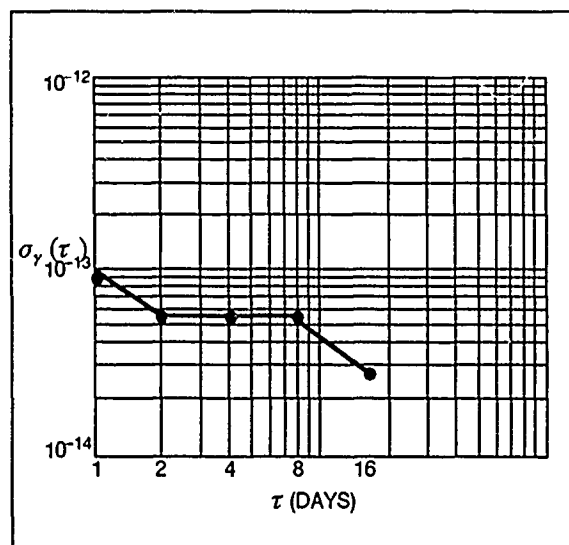


Figure 15. SV 9 rubidium performs better than cesium in short term.

1989 PTTI CONFERENCE ATTENDEES LIST

Charles A. Adams
Hewlett-Packard
5301 Stevens Creek Boulevard (MS 51U/23)
Santa Clara, CA 95052
408-553-2440

David W. Allan
National Institute of Standards and Technology
Time and Frequency Division
325 Broadway
Boulder, CO 80303
303-497-5637

Carroll O. Alley
University of Maryland
Department of Physics and Astronomy
College Park, MD 20742
301-454-3405

Alfred Anderman MTS/FB96
Space Transportation and Systems Group
Rockwell International Corporation
12214 Lakewood Boulevard
Downey, CA 90241
213-922-2522

John D. Anderson
Jet Propulsion Laboratory 301-230
4800 Oak Grove Drive
Pasadena, CA 91109
818-354-3956

Duane A. Andre
United States Navy
OFF ASS'T SECNAV (RE&S)
Pentagon, 4D145
Washington, D.C. 20350-1000
202-695-2395

Ronald J. Andrukitis
U.S. Naval Observatory
Time Service Alternate Station
11820 Southwest 166th Street
Miami, FL 33177
305-235-0515 A 791-6213

Bob M. Austin
Telecom Solutions
85 West Tasman Drive
San Jose, CA 95134
408-433-0910

Joshua P. Auzenne
USAF Space Systems Division
SSD/M2UF
Los Angeles AFB, CA 90009
213-643-0590

Rob Avery
Telecom Solutions
85 West Tasman Drive
San Jose, CA 95134
408-433-0910

Alice K. Babcock
U.S. Naval Observatory
11820 Southwest 166 Street
Miami, FL 33177
305-235-0515

James F. Barnaba
Newark Air Force Base
Newark, OH 43057-5475
614-522-7792

James A. Barnes
Austron, Inc.
P.O. Box 14766
Austin, TX 78761-4766
512-251-2313

Thomas R. Bartholomew
TASC
1190 Winterson Road
Linthicum, MD 21044
301-850-0070

Kimber Barton
Science Applications International Corp.
1980 North Atlantic Avenue
Suite 330
Cocoa Beach, FL 32931

Francoise S. Baumont
Observatoire de la Cote D'azur
(OCA/CERGA)
Avenue Nicolas Copernic
Grasse, France 06130
33/93 3658 49

Ronald L. Beard
Naval Research Laboratory
Code 8320
4555 Overlook Avenue, Southwest
Washington, D.C. 20375-5000
202-767-2295

Roger E. Beehler
National Institute of Standards and Technology
325 Broadway
Boulder, CO 80303
303-497-3281

Jeffrey S. Bergdahl
Space and Naval Warfare Systems Command
9533 Poplar Leaf Court
Fairfax, VA 22031
703-352-3515

Laurent-Guy Bernier
Observatoire Cantonal de Neuchatel
Rue de l'Observatoire 58
CH-2000 Neuchatel, Switzerland
(41) 38 31 88 31 FAX (41) 38 24 59 41

Professeur Raymond J. Besson
Ecoll Nationale Superieure
de Mecanique et des Microtechniques
La Bouloie - Route de Gray
35030 Besancon Cedex, France
Besancon, France 25030
81500569

Nat D. Bhaskar
The Aerospace Corporation
P.O. Box 92957 MS N2/25J
Los Angeles, CA 90009
213-336-8091

Stephen M. Bloor
Department of Defense
7929 Barnhill Circle
Severn, MD 21144-1805
301-859-4625

Lt. Sheldon B. Blue
U.S. Coast Guard EECEN
Engineering Center
P.O. Box 60
Wildwood, NJ 08260-0060
609-727-8955

Stephen G. Boemler
Naval Air Type II Standards Laboratory
NADEP, Code 46200, Building 3220
NAS Pensacola, FL 32508
904-452-3277

Jean-Simon Boulanger
National Research Council of Canada
Montreal Road
Ottawa, Ontario, Canada KIA ORG
613-993-5698

William H. Bourke
Electronic Research Company
7618 Wedd
Overland Park, KA 66204
913-631-6700

Dan E. Brannen
HRB Systems
Science Park Road, P.O. Box 60
State College, PA 16804-0060
814-238-4311

Lee A. Breakiron
U.S. Naval Observatory
Time Service Department
34th and Massachusetts Avenue, N.W.
Washington, D.C. 20392
202-653-1888

Edward T. Bryan
Rockwell International
P.O. Box 4509
Irvine, CA 92216
213-797-3783

James A. Buisson
Naval Research Laboratory
Code 8320
4555 Overlook Avenue, Southwest
Washington, D.C. 20375-5000

Dr. Giovanni Busca
Observatoire Cantonal de Neuchatel
Rue de l'Observatoire 58
CH-2000 Neuchatel, Switzerland
(41) 38 24 18 61 FAX (41) 38 24 59 41

Edgar W. Butterline
AT&T, Room 3C130E
Routes 202 and 206 North
Bedminster, NJ 07921
201-234-4545

Malcolm D. Calhoun
Jet Propulsion Laboratory
4800 Oak Grove Drive MS 298/100
Pasadena, CA 91109
818-354-9763

James C. Camparo M2/253
The Aerospace Corporation
P.O. Box 92957
Los Angeles, CA 90009
213-336-6944

Carol J. Cardoza
SIMCO Electronics (WSMC/PMEL)
Building 1737 Airfield Road
P.O. Box 6318
Vandenberg AFB, CA 93437
805-866-6595/7369

Bill Cashin
Ball Corporation, Efratom Division
3 Parker
Irvine, CA 92718-1605
714-770-5000

Miguel Cerezo
Jet Propulsion Laboratory/CALTECH
4800 Oak Grove Drive MS/125-B18
Pasadena, CA 91109
818-354-0193

James W. Chaffee
ARINC Research Incorporated
4055 Hancock Street
San Diego, CA 92110
619-222-7447

Laura G. Charron
U.S. Naval Observatory
Time Service Department
34th and Massachusetts Avenue, N.W.
Washington, D.C. 20392-5100
202-653-

Mary C. Chiu
The Johns Hopkins University
Applied Physics Laboratory
Johns Hopkins Road
Laurel, MD 20707
301-953-5818

Philip A. Clements
Jet Propulsion Laboratory
4800 Oak Grove Drive
Pasadena, CA 91109
818-354-2933

James M. Cloeren
The Johns Hopkins University
Applied Physics Laboratory
Johns Hopkins Road
Laurel, MD 20707
301-953-5000

Debra A. Coleman
Bonneville Power Administration - EEDC
P.O. Box 3621
Portland, OR 97208-3621
503-230-3769/4341

Jimmie B. Collie
Space and Naval Warfare System Command
National Center One
Crystal City
Arlington, VA 20360

Franco Cordara
Istituto Elettrotecnico Nazionale
91 Strada Delle Cacce
Turin, Italy 10135
011/3488933

Jeff Crockett
Ball Corporation, Efratom Division
3 Parker
Irvine, CA 92718-1605
714-770-5000

Leonard S. Cutler
Hewlett-Packard
P.O. Box 10350
Palo Alto, CA 94303-0867
415-857-5259

Peter R. Dachel
Bendix Field Engineering Corporation
10210 Greenbelt Road, Suite 700
Seabrook, MD 20706
301-794-3500

Peter Daly
University of Leeds
Department of EE
Leeds, UK LS2 9JT
0532 332073

Sam Dang
Naval Weapon Station
Seal Beach, CA 90740-5000
213-594-7224

Mitchell H. Dazey
Retiree, The Aerospace Corporation
1120 Via Nogales
Palos Verdes Est., CA 90274
213-375-5298

Gerrit DeJong
Van Swinden Laboratory b.v.
P.O. Box 654
Delft, Netherlands 2600 AR
15 691 623

Patricia A. De Laere
Jet Propulsion Laboratory
4800 Oak Grove Drive MS 298/100
Pasadena, CA 91109
818-354-7055

Andrea DeMarchi
Universita' Di Ancona
Via Brece Bianche
Ancona, Italy 60131
011/39/71/5893-463 (FAX 835)

Edoardo Detoma
SEPA SpA (FIAT)
Corso Giulio Cesare, 294
Torino, Italy 10154
0039(11)205-3371

Wayne P. Dewey
Kinematics/Truetime
3243 Santa Rosa Avenue
Santa Rosa, CA 95407
707-528-1230

John Dick
Jet Propulsion Laboratory
4800 Oak Grove Drive MS 298/100
Pasadena, CA 91109
818-354-6393

William A. Diener
Jet Propulsion Laboratory
4800 Oak Grove Drive MS 298/100
Pasadena, CA 91109
818-354-9762

Thomas P. Donaher
Spectracom Corporation
101 Despatch Drive
East Rochester, NY 14445
716-381-4827

Robert C. Dreyer
B and J Marketing
17074 Dearborn Street
Northridge, CA 91325
818-993-0048

Raymond Eastwood
Magnavox Advanced Products and Systems
2829 Maricopa Street
Torrance, CA 90503
213-618-1200

Chris Eckoff
Austron, Incorporated
P.O. Box 14766
Austin, TX 78761-4766
512-251-2313

Robert F. Ellis
Austron, Incorporated
P.O. Box 14766
Austin, TX 78761-4766
512-251-2313

Edward Eng
Lockheed Missiles and Space Company
P.O. Box 3504 B195A/04872
Sunnyvale, CA 94088
408-756-3989

Tom English
Ball Corporation, Efratom Division
3 Parker
Irvine, CA 92718-1605
714-770-5000

John W. Evans
Defense Communications Agency (DCA)
1860 Wiehle Avenue
Reston, VA 22090
703-437-2598

Bennie W. Falin
Jet Propulsion Laboratory
4800 Oak Grove Drive
Pasadena, CA 91109
818-354-5549

Sheila C. Faulkner
U.S. Naval Observatory
Time Service Department
34th and Massachusetts Avenue, N.W.
Washington, D.C. 20392-5100
202-653-1460

William A. Feess
The Aerospace Corporation
2350 East El Segundo Boulevard
El Segundo, CA 90245
213-336-4397

Dr. Stephen J. Feltham
European Space Agency
Keplerlaani
2200 AG Noordwijk, Holland
INT-31-1719-83948/84649

Michael M. Fisher
Trimble Navigation
645 North Mary Avenue
Sunnyvale, CA 94088-3642
408-730-2900

Henry F. Fliegel
The Aerospace Corporation
2350 El Segundo Boulevard
El Segundo, CA 90235
213-336-1710

Donald L. Foiani
Retiree U.S. Army Atmospheric Sciences Lab
5035 Las Alturas Drive
Las Cruces, NM 88001
505-522-7603

D. Louis Foiani II
Department of Defense
9800 Savage Road
Fort Meade, MD 20755-6000
301-859-4721

D. Earl Fossler
Trak Systems
4726 Eisenhower
Tampa, FL 33634
813-884-1411

Cordell J. Fox
United States Air Force 2SCS-6P5
Falcon Air Force Base, Colorado
719-550-2525

Christopher J. Franks
Hewlett-Packard
5301 Stevens Creek Boulevard
Santa Clara, CA 95052-8059
408-553-2243

Robert P. Frueholz
The Aerospace Corporation
P.O. Box 92957
Los Angeles, CA 90009
213-336-6975

Jean C. Gaignebet
Observatoire De La Cote D'Azur
OCA/CERGA
Avenue Nicolas Copernic
Grasse, France 06130
33/93365849

R. Michael Garvey
Frequency and Time Systems, Inc.
34 Tozer Road
Beverly, MA 01915
508-927-8220

Mike Gawarecki
Austron, Incorporated
P.O. Box 14766
Austin, TX 78761-4766
512-251-2313

Gary L. Geil
Datum, Inc.
1363 South State College Boulevard
Anaheim, CA 92806-5790
714-533-6333

Guy A. Gifford
Naval Research Laboratory
Code 8320
4555 Overlook Avenue Southwest
Washington, D.C. 20375-5000
202-767-2595

Asbjorn M. Gjelsvik
The Mitre Corporation
Burlington Road
Bedford, MA 01730
617-271-3903

Michel Granveaud
LPTF/Observatoire Paris
61, AV. Observatoire
7501L Paris, France
L0512223

Charles A. Greenhall
Jet Propulsion Laboratory
4800 Oak Grove Drive 298-100
Pasadena, CA 91109
818-354-5434

Lloyd F. Griffith
Federal Electric Corporation/ITT
P.O. Box 5728 SD 210
Vandenberg Air Force Base 93437
805-866-3108

Albert E. Guevara
United States Air Force 25CS
2745 Frazier Lane
Colorado Springs, CO 80922
719-574-2950/550-6377

Captain James B. Hagen
U.S. Naval Observatory
34th and Massachusetts Avenue, N.W.
Washington, D.C. 20392-5100
202-653-1538

Shinichi Hama
CRL, Japan
893 Hirai, Kashima, Ibaraki, 314

Robert L. Hamell
Jet Propulsion Laboratory
4800 Oak Grove Drive MS 298/100
Pasadena, CA 91109
818-354-4944

Tadayoshi Hara
Division of Earth Rotation
National Astronomical Observatory
2-12 Hoshigaoka-Machi
Mizusawa, Japan 023
197-24-7111

Robert Hardin
Ball Corporation, Efratom Division
3 Parker
Irvine, CA 92718-1605
714-770-5000

Walter R. Harding
Navel Electronic Systems Engineering Center
P.O. Box 55, Code 336WH
Portsmouth, VA 23705-0055
804-396-7992

Robert W. Harris
Telecom Australia Research Laboratories
770 Blackburn Road
Clayton UC Australia 3168
6135416124 FAX No. 6135436001

Ilan Havered
Datum, Inc.
1363 South State College Boulevard
Anaheim, CA 92806-5790
714-533-6333

Helmut W. Hellwig
National Institute of Standards and Technology
A526 Administration Building
Gaithersburg, MD 20899
301-975-3690

Robert J. Hesselberth
Spectracom Corporation
101 Despatch Drive
East Rochester, NY 14445
716-381-4827

David Hessick
Magnavox
2829 Maricopa Street
Torrance, CA 90503
213-618-1200

Ken Ho
Hewlett-Packard
5301 Stevens Creek Boulevard
Santa Clara, CA 95052-8059
408-553-3205

Jerome B. Hodge
United States Navy
1501 Crystal Drive #1125
Arlington, VA 22202
703-418-3816

Dave A. Howe
National Institute of Standards and Technology
325 Broadway
Boulder, CO 80303
303-497-3277

Quyen D. Hua
Stanford Telecom
2421 Mission College Boulevard
Santa Clara, CA 95054
408-987-5520

John P. Hurrell
The Aerospace Corporation
P.O. Box 92957
Los Angeles, CA 90009
213-336-6508

John F. Hynes
United States Air Force
1842 EEG (AFCC)
Scott Air Force Base, IL 62225-6348
618-256-4182

Bernardo Jaduszliwer
The Aerospace Corporation
P.O. Box 92957 M2/253
Los Angeles, CA 90009
213-336-9217

Nicolette M. Jardine
U.S. Naval Observatory
Time Service Department
34th and Massachusetts Avenue, N.W.
Washington, D.C. 20392-5100
202-653-1662

James L. Jespersen
National Institute of Standards and Technology
325 Broadway
Boulder, CO 80302
303-497-3849

Walter A. Johnson
The Aerospace Corporation
2350 East El Segundo Boulevard
El Segundo, CA 90245
213-336-7174

Edward C. Jones
Naval Research Laboratory
Code 8320, 4555 Overlook Avenue
Washington, D.C. 20375-5000
213-643-0608

Sandra L. Joy
Lockheed Missiles and Space Company
POB 3504 0/62-35 B/150
Sunnyvale, CA 94089
408-742-2275

Rick Karlquist
Hewlett-Packard
5301 Stevens Creek Boulevard
Santa Clara, CA 95052-8059
408-553-2194

Peter Kartaschoff
Swiss PTT RES & DEV
Swiss PTT R&D
CH 3000 Bern 29 Switzerland
41 31 624380 FAX 41 31 62 5747

Sarunas K. Karuza
The Aerospace Corporation
2350 East El Segundo Boulevard
El Segundo, CA 90245-4691
213-336-7174

Richard E. Keating
U.S. Naval Observatory
Time Service Department
34th and Massachusetts Avenue, N.W.
Washington, D.C. 20392-5100
202-653-1022

Douglas E. Keefer
Navy Astronautics Group
Building 389, PMTC
Point Mugu, CA 93042
805-989-4344

Nancy E. Key
Jet Propulsion Laboratory
4800 Oak Grove Drive
Pasadena, CA 91109
818-354-5434

Amarpal Khanna
Avantek
3175 Bowers Avenue
Santa Clara, CA 95054
408-970-2889

Albert Kirk
Jet Propulsion Laboratory
4800 Oak Grove Drive MS 298/100
Pasadena, CA 91109
818-354-7854

Charles W. Kissire
Allen Osborne Associates
756 Lakefield Road, Building J
West Lake Village, CA
805-495-8420

William J. Klepczynski
U.S. Naval Observatory
Time Service Department
34th and Massachusetts Avenue, N.W.
Washington, D.C. 20392-5100
202-653-1521

Charles M. Klimcak
The Aerospace Corporation
2350 El Segundo Boulevard
El Segundo, CA 90250
213-336-6069

David J. E. Knight
National Physical Laboratory
Department Trade and Industry
Queens Road
Teddington, MIDDX UK TW11 OLW
01-943-6796

Paul A. Koppang
Sigma Tau Standards Corporation
P.O. Box 1877
Tuscaloosa, AL 35403
205-553-0038

Timothy P. Krisher
Jet Propulsion Laboratory
4800 Oak Grove Drive
Pasadena, CA 91109
818-354-7577

Paul F. Kuhnle
Jet Propulsion Laboratory
4800 Oak Grove Drive MS 298-100
Pasadena, CA 91109
818-354-2715

Robert E. Kursinski
Jet Propulsion Laboratory
4800 Oak Grove Drive
Pasadena, CA 91109
818-354-7533

Paul J. Kushmeider
Bendix Field Engineering Corporation
MS/VLBI
One Bendix Road
Columbia, MD 21045
301-964-7672

Jack Kusters
Hewlett-Packard
5301 Stevens Creek Boulevard
Santa Clara, CA 95052-8059
408-553-2041

Graybill Paul Landis
Naval Research Laboratory, Code 8320
4555 Overlook Avenue, Southwest
Washington, D.C. 20375-5000
202-404-7067

Jim Lanphear
N-5 Westronics
4062 Oak Pt. Ct.
Hayward, CA 94542
415-537-9462

Julius C. Law
Jet Propulsion Laboratory
4800 Oak Grove Drive MS 298/100
Pasadena, CA 91109
818-354-2988

Felix Lazarus
Hewlett-Packard AG
150 Route Du Nant D'Avril
CH 1217 Meyrin 2, Switzerland
41 22/780 8140

Christoph Lehrer
DFVLR/GSOC-ZDRS
Postfach 156
8120 Weilheim, West-Germany
08809/140

Albert A. Leong
The Aerospace Corporation
2350 Ease El Segundo Boulevard
El Segundo, CA 90245
213-336-7174

Judah Levine
National Institute of Standards and Technology
Time and Frequency Division, 576
325 Broadway
Boulder, CO 80303
303-497-3903

Liong Lew
Rockwell International
2600 Westminster Boulevard
P.O. Box 3644
Seal Beach, CA 90740-7644
213-797-3036

Weodzimierz Lewandowski
BIPM
Pavillon de Breteuil
92312 Sevres Cedex, France
(33) (1) 45 07 70 63

Funming Li
Ball Corporation, Efratom Division
3 Parker
Irvine, CA 92718-1605
714-770-5000

Gil Lieberman
Israel Military Industries (IMI)
P.O.B. 1044/77
Ramat Hasharon Israel 47100
U.S.-to-Israel 011-972-3-5426167

Bruce M. Lohrey
Physics and Engineering Lab
Department of Scientific and Industrial
Research (DSIR)
P.O. Box 31313 Lower Hutt, New Zealand
64-4-666919 FAX 64-4-690117

Roger D. Loiler
Allen Osborne Association
757 Lakefield
Westlake, CA 91361
805-495-8420

James G. Lopez
Jet Propulsion Laboratory
4800 Oak Grove Drive MS 298/100
Pasadena, CA 91109
818-354-6800

George F. Lutes
Jet Propulsion Laboratory
4800 Oak Grove Drive MS 298/100
Pasadena, CA 91109
818-354-6210

Lute Maleki
Jet Propulsion Laboratory
4800 Oak Grove Drive MS 298/100
Pasadena, CA 91109
818-354-3688

Rudolf Manetsberger
DLR
Postfach 156
8120 Weilheim, West Germany
08809/140

Charles S. Mangleburg
Naval Surface Warfare Center
Dahlgren, VA 22443
703-663-1586

Kenneth E. Martin
Bonneville Power Administration - ELIP
5411 Northeast Highway 99
P.O. Box 491
Vancouver, WA 98666
206-690-2694

Edward M. Mattison
Smithsonian Astrophysical Observatory
60 Garden Street, MS-59
Cambridge, MA 02138
617-495-7265

Thomas B. McCaskill
Naval Research Laboratory
Code 8320
4555 Overlook Avenue, Southwest
Washington, D.C. 20375-5000

Thomas A. McClelland
Frequency Electronics, Inc.
55 Charles Lindbergh Boulevard
Mitchel Field, NY 11553
516-794-4500

Hunter McConnell, Jr.
Jet Propulsion Laboratory, Caltech
4800 Oak Grove Drive MS 125-B18
Pasadena, CA 91109
818-354-3033

David A. McGillivray
EG&G/EM, Inc.
680 Sunset Road
Las Vegas, NE 89109
702-295-3094

Colleen H. McKenzie
The Aerospace Corporation
2350 East El Segundo Boulevard
El Segundo, CA 90245-4691
211-336-4386

Patricia A. McMaster
Naval Research Laboratory
4555 Overlook Avenue, Southwest
Washington, D.C. 20375-5000
202-767-2655

Jack S. McNabb
Trak Systems
4726 Eisenhower Boulevard
Tampa, FL 33634
813-884-1411

Arlene F. Meadows
Racal-Dana Instruments, Incorporated
4 Goodyear Street
Irvine, CA 92718
714-859-8999

Marvin P. Meirs
Frequency Electronics, Incorporated
55 Charles Lindbergh Boulevard
Mitchel Field, NY 11553
516-794-4500, Ext. 5019

William G. Melbourne
Jet Propulsion Laboratory
4800 Oak Grove Drive
Pasadena, CA 91109
818-354-5071

Gary R. Miller
Computer Science Corporation
P.O. Box 446
Edward Air Force Base, CA 93523
805-277-2004

Gills Missout
Hydro Quebec
1800 Montee Street Julie
Varenes Quebec, Canada JOL2PO
516-652-8086

Don Mitchell
Austron, Incorporated
P.O. Box 14766
Austin, Texas 78761-4766
512-251-2313

Shawn P. Monaghan
CSE
P.O. Box 9703, Terminal
Ottawa, Ontario, Canada K1G 3Z4
613-998-6850

Robert D. Montesi
Hewlett-Packard
5301 Stevens Creek Boulevard, MS 23
Santa Clara, CA 95052
408-553-3088

Craig R. Moore
The Johns Hopkins University
Applied Physics Laboratory
Johns Hopkins Road, Building 4-342
Laurel, MD 20707
301-953-5920

David D. Morabito
Jet Propulsion Laboratory
4800 Oak Grove Drive
Pasadena, CA 91109
818-393-0665

Derek Morris
National Research Council
Montreal Road
Ottawa, Canada K1A 0R6
613-993-9340

Paul Naepflin
Ball Corporation, Efratom Division
3 Parker
Irvine, CA 92718-1605
714-770-5000

Robert A. Nelson
Department of Physics and Astronomy
University of Maryland
College Park, MD 20742
301-454-3405

Clyde C. Norris
Computer Sciences Corporation
P.O. Box 217
Clearfield, UT 84015
801-777-4845

Jerry R. Norton
The Johns Hopkins University
Applied Physics Laboratory
Johns Hopkins Road
Laurel, MD 20707
301-792-5000

Philip J. Norton
NAVASTROGRU
Building 389
Point Mugu, CA 93042
805-989-4338

Allen W. Osborne
Allen Osborne Associates
756 Lakefield Road, Building J
Westlake Village, CA 91361
805-495-8420

Allan Oster
Air Force Space Systems Division
Code CWNUI
WPC P.O. Box 92960
Los Angeles, CA 90009
213-643-1202

Terry N. Osterdock
Stellar Navigation, Inc.
19075 Skyline Boulevard
Los Gatos, CA 95030
408-354-0733

Ralph E. Partridge
Los Alamos National Laboratory
P.O. Box 1663, MS P947
Los Alamos, NM 87545
505-665-1617

Benjamin Parzen
Consulting Engineer
3634 7th Avenue
San Diego, CA 92103
619-291-0567

I. Pascaru
Frequency Electronics, Inc.
55 Lindburgh Boulevard
Uniondale, NY
516-794-4500

Peter Z. Paulovich
Navelex Systems Engineering Center
P.O. Box 55
Portsmouth, VA 23701
804-396-0287

Bruce Penrod
Austron, Incorporated
P.O. Box 14766
Austin, TX 78761-4766
512-251-2313

Donald B. Percival
University of Washington
7541 20th Avenue Northeast
Seattle, WA 98115
206-523-8147

James C. Perry
National Aeronautics and Space
Administration/Code 531.3
Greenbelt Road
Greenbelt, MD 20770
301-286-3471

Harry E. Peters
Sigma Tau Standards Corporation
P.O. Box 1877
Tuscaloosa, AL 35403
205-553-0038

Wolfgang Pflaum
Ball Corporation, Efratom Division
3 Parker
Irvine, CA 92718-1605
714-770-5000

Bundesanstalt Physikalisch-Technische
Library
Bundesallee 100, P.O. Box 3345
D-3300 Braunschweig
Federal Republic of Germany

William G. Pixton
Ford Aerospace
3825 Fabian Way
Palo Alto, CA 94303
415-852-7209

H. Richard Potts
Bendix Field Engineering Corporation
One Bendix Road
Columbia, MD 21045
301-964-7075

Edward D. Powers
Naval Research Laboratory, Code 8320
4555 Overlook Avenue, Southwest
Washington, D.C. 20375-5000
202-404-7066

John D. Prestage
Jet Propulsion Laboratory
4800 Oak Grove Drive
Pasadena, CA 91109
818-354-3515

Robert E. Price
Bendix Field Engineering Corporation
One Bendix Road
Columbia, MD 21045
301-964-7437

Arthur M. Quaas
Rockwell International Corporation
3370 Miraloma Avenue
Anaheim, CA 92803
714-762-7847

Paul M. Quinn
Rockwell International Corporation
3370 Miraloma Avenue
Anaheim, CA 92803
714-762-7847

George L. Ramsey
E-Systems, Incorporated
P.O. Box 1056
Greenville, TX 75401
214-457-4663

Jerry Rayne
Ball Corporation, Efratom Division
3 Parker
Irvine, CA 92718-1605
714-770-5000

Victor S. Reinhardt
Hughes Aircraft Company
SC S12 V322, P.O. Box 92919
Los Angeles, CA 90009
213-416-0160

Eugene A. Rheingans
Rockwell International Corporation
2606 Pampas Street
Orange, CA 92665
714-637-1959

William J. Riley
EG&G Frequency Products Division, Inc.
35 Congress Street
Salem, MA 01970
508-745-3200

Paul N. Risinger
Telecom Solutions
85 West Tasman Drive
San Jose, CA 95134
408-943-9403

Ron Roloff
Austron, Incorporated
P.O. Box 14766
Austin, TX 78761-4766
512-251-2313

Joseph R. Romanosky
Department of Defense
R632
Fort George G. Meade, MD 20755
301-859-4722

Safaa Samuel
National Institute for Standards
92A Ahmed Orabi Street
Apartment #1005 El Mohandseen
Cairo, Egypt
13460713

Harrison A. Sarrafian
The Aerospace Corporation
Systems Evaluation Department
P.O. Box 92957
Los Angeles, CA 90009
213-336-4376

Gary Sasaki
Hewlett-Packard
5301 Steven Creek Boulevard
Santa Clara, CA 95052-8059
408-553-2243

Arthur L. Satin
The Aerospace Corporation
2350 East El Segundo Boulevard
El Segundo, CA 90245-4691
213-336-4499

Todd J. Schlosser
Computer Sciences Corporation
P.O. Box 446
Edwards Air Force Base, CA 93523
805-277-0312

John M. Schmitt
1842EEG (AFCC)
1842EEG/EETSA
Scott Air Force Base, IL 62225-6348
618-256-2679

Wallace A. Schnitger
Science Systems
P.O. Box 880
Midway City, CA 92655
714-744-1909

Malvin C. Schwalje
EG&G Frequency Products Division, Inc.
35 Congress Street
Salem, MA 01970
508-745-3200

James R. Semler
Interstate Electronics Corporation
1001 East Ball Road
Anaheim, CA 92803
714-758-2754

Richard T. Sharpe
Magnavox Advanced Products and Systems
Company
2829 Maricopa Street
Torrance, CA 90503
213-618-1200

Soon Shin
Ball Corporation, Efratom Division
3 Parker
Irvine, CA 92718-1605
714-770-5000

Julian R. Skorupski
McDonnell Douglas
3855 Lakewood Boulevard
Mail Code 28-10
Long Beach, CA 90846
213-593-2000

Samuel R. Stein
Ball Aerospace
P.O. Box 1235
Broomfield, CO 80020
303-460-2017

Charles S. Stone
Brightline Corporation/FEI
P.O. Box 1299
Cedar Park, TX 78613
512-258-3701

David A. Stowers
Jet Propulsion Laboratory MS 298/100
4800 Oak Grove Drive
Pasadena, CA 91109
818-354-7055

Emil R. Straka
Hewlett-Packard
5301 Stevens Creek Boulevard
Santa Clara, CA 95051
408/553-2887

Seiji Sugihara
The Aerospace Corporation
Systems Evaluation Department
P.O. Box 92957
Los Angeles, CA 90009
213-336-4387

Richard L. Sydnor
Jet Propulsion Laboratory
4800 Oak Grove Drive MS 298/100
Pasadena, CA 91109
818-354-2763

Roland E. Taylor
Jet Propulsion Laboratory
4800 Oak Grove Drive MS 298/100
Pasadena, CA 91109
818-354-6670

Dorsey L. Thacker
Interferometrics, Incorporated
8150 Leesburg Pike
Vienna, VA 22151
703-321-7167

Pierre Thomann
Oscilloquartz
Brevards 16
Neuchatel, Switzerland CH-2002
41-38-258501 or 41-38-318831

Dr. Claudine Thomas
Bureau International des Poids et Mesures
Pavillon de Breteuil
92372 Sevres Cedex, France
(1) 45-07-70-73

Robert N. Treuhaft
Jet Propulsion Laboratory
4800 Oak Grove Drive MS 238-700
Pasadena, CA 91109
818-354-6216

Thomas K. Tucker
Jet Propulsion Laboratory MS 298/100
4800 Oak Grove Drive
Pasadena, CA 91109
818-354-2164

Kenneth M. Uglow
P.O. Box 2260
Sarasota, FL 34230
813-955-5856

Pierre Uhrich
LPTF/Observatoire de Paris
61 Avenue de l'Observatoire
75014 Paris, France
011.33.1.40.51.22.16

Jacques Vanier
National Research Council
Montreal Road
Ottawa, Canada KIA OR6
613-993-9326

Christian Veillet
Observatoire De La Cote D'Azur
(OCA/CERGA)
Avenue Nicolas Copernic
Grasse, France 06130
33/93 3658 49

Robert F. C. Vessot
Smithsonian Astrophysical Observatory
60 Garden Street
Cambridge, MA 02138
617-495-7276

John R. Vig
United States Army LABCOM
Attention: SLCET-EQ
Fort Monmouth, NJ 07703
201-544-4275

Frank J. Voit
The Aerospace Corporation
2350 East El Segundo Boulevard
El Segundo, CA 90245
213-336-7174

Hank Vorwerk
Ball Corporation, Efratom Division
3 Parker
Irvine, CA 92718-1605
714-770-5000

Fred L. Walls
National Institute of Standards and Technology
Time and Frequency Division, 576
325 Broadway
Boulder, CO 80303
303/497-3207

Ronald L. Walsworth
Harvard University
Department of Physics
Lyman Laboratory of Physics
Cambridge, MA 02138
617-495-9077 or 495-7272

Harry T. M. Wang
Hughes Research Labs
3011 Malibu Canyon Road
Malibu, CA 90265
213-317-5431

S. Clark Wardrip
Bendix Field Engineering Corporation
726 Foxenwood Drive
Santa Maria, CA 93455
805-865-3214

Toney Warren
Telecom Solutions
85 West Tasman Drive
San Jose, CA 95134
408-943-9403

Werner Weidemann
Ball Corporation, Efratom Division
3 Parker
Irvine, CA 92718-1605
714-770-5000

Marc A. Weiss
National Institute of Standards and Technology
325 Broadway, 576
Boulder, CO 80303
303-497-3261

Paul J. Wheeler
U.S. Naval Observatory
Time Service Department
34th and Massachusetts Avenue, N.W.
Washington, D.C. 20392-5100
202-653-0516

Joe D. White
U.S. Naval Research Laboratory
Code 8321
4555 Overlook Avenue
Washington, D.C. 20375
202-404-7060

Robert E. Wilson
Western Area Power Administration
1250A South Plaza Way
Flagstaff, AZ 86001
602-527-7501

Warren L. Wilson
Lockheed Missiles and Space Company
707 Spindrift Drive
San Jose, CA 95134-1346
408-743-1213

Dr. Gernot M. R. Winkler
U.S. Naval Observatory
34th and Massachusetts Avenue, N.W.
Washington, D.C. 20392-5100
202-653-1520

Bosco Wong
Hewlett-Packard
5301 Stevens Creek Boulevard
Santa Clara, CA 95052-8059
408-553-2418

Valerie A. Wooden
(Pan Am) World Services, Incorporated
2003 Byrd Spring Road
Huntsville, AL 35802
205-883-9690

Woody Wordsworth
Austron, Inc.
P.O. Box 14766
Austin, TX 78761-4766
512-251-2313

Nicholas F. Yannoni
Rome Air Development Center
RADC/ESE, Hanscom Air Force Base
Bedford, MA 01731
617-377-2206

Eric C. Youngberg
Hewlett-Packard
5301 Stevens Creek Boulevard MS 55/16
Santa Clara, CA 95052
408-553-2308

Edward Yrisarri
Ball Corporation, Efratom Division
3 Parker
Irvine, CA 92718
714-770-5000

Patrick T. Yun
Pacific Bell
2600 Camino Ramon, Room 3S400N
San Ramon, CA 94583
415-823-

Walter A. Zarris
Frequency and Time Systems
34 Tozer Road
Beverly, MA 01915
508-927-8220

Stephen A. Zielinski
Naval Avionics Center
6000 East 21st Street
Indianapolis, IN 46219
317-351-4664